

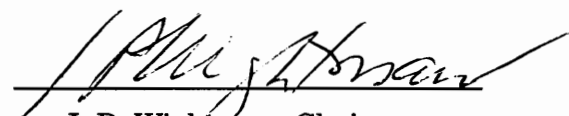
**Characterization of the Molecular Structure at Modified
Polymer Surfaces and Polyphenylene Sulfide / Copper
Interphases**

By

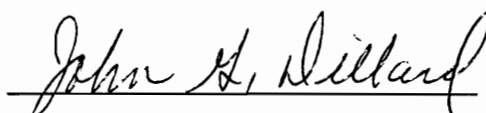
H. Francis Webster II

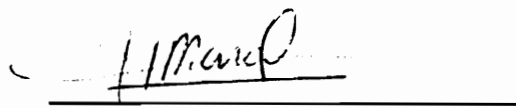
Dissertation submitted to the faculty of the
Virginia Polytechnic Institute and State University
In partial fulfillment of the requirements for the degree of
Doctor of Philosophy
in
Chemistry

APPROVED:


J. P. Wightman, Chairman


T. C. Ward


J. G. Dillard


H. Marand


M. R. Anderson

August, 1992
Blacksburg, Virginia

Characterization of the Molecular Structure at Modified Polymer Surfaces and Polyphenylene Sulfide / Copper Interphases

By

H. Francis Webster II

Committee Chairman: James P. Wightman

Chemistry

(Abstract)

The interphase region at modified polymer surfaces or at polymer \ metal interfaces may be critical in determining the strength and durability in adhesive applications. Methods to investigate these regions are limited however and this research has focused on the use of infrared reflection absorption spectroscopy (IRRAS) and x-ray photoelectron spectroscopy (XPS) to investigate the molecular structure of both modified and unmodified thin films. The optical constants of polyphenylene sulfide (PPS) were determined and exact optical theory was utilized to simulate spectra for a variety of reflectance techniques. This method was also utilized to confirm the ordered state of thin spin coated PPS films.

The surface modification of polystyrene, polyphenylene sulfide, and poly(arylene ether) phosphine oxides was also examined by these techniques and optical theory used to optimize experimental conditions. Results after plasma treatment indicated a very thin modified surface layer (< 10 nm) where the thickness and specific surface chemistry depended on the polymer and plasma gas used. The interaction of an epoxy resin with a surface modified PPS film showed that while most of the modified surface layer is removed after this treatment, a remaining amount can serve to cross-link a thin adsorbed epoxy film. Results for the oxygen plasma treatment of poly(arylene ether) phosphine oxides showed the formation of a surface phosphate layer that inhibited further plasma etching. The kinetics of formation and the particular

chemistry involved were examined in detail.

A new technique, variable temperature reflection absorption spectroscopy (VTRAS) was developed as a method to investigate the reorganization of thin PPS films on a variety of substrates. Both the crystallization and melting temperatures could be determined for quenched coatings on a variety of substrates. While degradation under vacuum was not observed on chromium and aluminum surfaces, PPS films on copper surfaces showed a loss in crystallizability, and did not return to the original ordered state after exposure to temperatures near 300°C. Loss of cuprous oxide was also observed, and chain scission mechanisms were postulated. Additional measurements on thin sputtered cuprous oxide films showed less degradation for the same temperature treatments, emphasizing the role of the underlying metal in the degradation process. Spin coated films of polyetherimide were shown to be oriented after spin coating, and the relaxation to a more random state could also be observed by the VTRAS technique.

Degradation of PPS films in air was examined and the diffusion of copper species into the bulk of the film with the formation of copper carboxylates was observed. The use of the VTRAS technique in air also was useful in determining the temperature needed for the onset of degradation. Bonded PPS/ copper laminates were investigated and results showed that the particular surface chemistry was crucial in determining the peel strength observed. After a simple thermal oxidation pretreatment for copper foil, an increase in the peel strength of almost one order of magnitude was observed over non-oxidized foils. Chemical oxidation with alkaline persulfate solutions resulted in a needle-like surface oxide morphology, and bond strengths were also increased by this pretreatment method. Failure surface analysis and model interaction studies with PPS tetramer showed that the formation of excess cuprous sulfide at the interface was the most probable cause of poor adhesion in these systems. Foil pretreatment by thermal oxidation gave the highest peel strength, and also exhibited the lowest amount of interfacial cuprous sulfide.

*Hold on to the rope
for the eagle leads the way
and my canoe goes faster
I weep with joy over the sea.*

Julie Watson
Kiriwina, Papua New Guinea

ACKNOWLEDGEMENTS

The author would like to acknowledge the following people who helped in various ways to make this dissertation possible:

Dr. J.P. Wightman, for his guidance and friendship now dating back almost ten years. Certainly, without his influence, I would not have pursued either graduate degree at Virginia Tech. The freedom given to pursue many projects while here certainly resulted in many of the more interesting results found in this work.

The members of my committee, Dr. T.C. Ward, Dr. J.G. Dillard, Dr. H. Marand, and Dr. M. R. Anderson. A particular thanks must go to Dr. Dillard for the use of his lab for the infrared work and for putting up with all the mess. Dr. Marand must be acknowledged for his help in the interpretation of data, especially concerning aspects of polymer crystallization. Dr. Anderson is acknowledged for all his help with various aspects of infrared spectroscopy and it is hoped that further collaboration will continue in the future.

Phillips Petroleum, for the funding of this project and particularly, Dr. Tim Johnson, for his help in almost all aspects of this work. Not only did he help provide all materials needed for this project, but the constant correspondence by phone or mail will be remembered as one of the best aspects of the work. The trip to Bartlesville will also be remembered as a highlight of my stay, and the helpful discussions of every person I met at Phillips is certainly recognized.

Bob Ross and Melvin Shaver for their help both in the design and construction of the variable temperature vacuum cell used in this work. Without their input, this part of the project would not have been possible, and thanks must also go to Fred John, and Dave for the many helpful discussions concerning many aspects of this work. The time spent with all the people in the Physics shop will be remembered as one of the best times in graduate school.

Larry Jackson, for the many discussions on just about every subject, and all his help with the electronic and computer problems associated with this work. Thanks must also go to Jim Hall and Jim Coulter for their patience in answering the untold

number of questions during the past three years.

Andy Mollick for building the vacuum system for the VTRAS cell and for all the helpful discussions on how to make it work properly.

Frank Cromer, whose advise and technical expertise has influenced almost every aspect of this work. It is still hard to believe that a person can be asked so many questions and still keep a smile. A special thanks is also a must for the use of his tools and other equipment during my time here.

Renaldo Gonzalez, for being a good friend and for all of the helpful discussions concerning optical theory and computer programming. The use of his program to calculate electric field intensities is particularly acknowledged.

Charlie Potter, for the nifty algorithm to evaluate the Kramers-Kronig integral. This saved a tremendous amount of time in the calculation of optical constants and made life a lot easier.

Peng, in Materials Engineering, for his original ellipsometry software. Part of this served as the core of the optical simulation programs.

Carrington Smith, for all the collaborative work on the plasma treatment of poly(arylene ether) phosphine oxides and for the useful discussions about chemistry and many other subjects. This is truly a case where a single discussion between two students can blossom into an interesting and significant collaborative effort between research groups.

Cheryl Heisey, for running the DSC analysis of PPS. This saved me a alot of time near the end of my stay here.

My wife, Janet, for her patience and understanding during the last several years, and for not holding me to statements written in New Guinea concerning my attitude towards further education. Not many women would have done all that she has had to do with work, school, and a baby, while putting up with a husband in a Ph.D. program, so my thanks and love go to her. A special acknowledgement goes to my daughter, Rebekah, for giving her dad the proper perspective on life while writing this dissertation.

Table of Contents

CHAPTER 1.	1
1.0 INTRODUCTION.	1
 CHAPTER 2	
THIN FILM CHARACTERIZATION.	3
2.1 LITERATURE REVIEW.	3
2.1.1 Introduction.	3
2.1.2 Fundamentals of Optical Theory.	7
2.1.2.1 Optical Constants of Polymers.	11
2.1.2.2 Refractive Index Effects.	13
2.1.3 Applications of Reflection Absorption Spectroscopy.	15
2.1.3.1 Characterization of Polymer Surface Modification.	15
2.1.3.1.1 Atomic Oxygen Degradation.	17
2.1.3.2 Interphase Characterization.	18
2.1.3.3 Molecular Orientation.	19
2.1.4 Materials / Polyphenylene Sulfide.	22
2.1.4.1 Chemistry.	22
2.1.4.2 Properties.	23
2.1.4.3 Thermal Cure.	25
2.1.4.4 Crystallinity and Crystallization.	28
2.1.4.5 Infrared Analysis.	32
2.1.4.6 Applications.	32
2.2 EXPERIMENTAL.	35
2.2.1 Analysis of Polyphenylene Sulfide Films.	35
2.2.1.1 High Temperature Spin Coating.	35
2.2.1.2 Thin Film Preparation.	38
2.2.1.3 Extruded Films.	41
2.2.1.4 Molded PPS.	41
2.2.2 Analysis of Plasma Modified Polymer Surfaces.	41

2.2.3	Experimental Methods.	42
2.2.3.1	Infrared Analysis.	42
2.2.3.1.1	Determination of Optical Constants.	42
2.2.3.1.2	Simulation of Optical Spectra.	45
2.2.3.1.3	Transmission.	45
2.2.3.1.4	Reflection Methods.	46
2.2.3.2	Ellipsometry.	49
2.2.3.3	X-ray Photoelectron Spectroscopy.	49
2.3	RESULTS AND DISCUSSION.	50
2.3.1	Infrared Analysis of Polyphenylene Sulfide (PPS).	50
2.3.1.1	Optical Constants.	50
2.3.1.2	Transmission Spectroscopy.	50
2.3.1.3	Attenuated Total Reflectance.	53
2.3.1.4	Reflection Absorption Spectroscopy.	57
2.3.1.4.1	Reflection at the Brewster Angle	57
2.3.1.4.2	Thin Films / Reflecting Substrates.	60
2.3.1.4.3	Thin Films / Infrared Transparent Substrates.	75
2.3.2	Analysis of Plasma Modified Polymer Surfaces.	83
2.3.2.1	Theoretical Considerations.	83
2.3.2.2	Surface Analysis of Plasma Modified Polystyrene.	92
2.3.2.2.1	Ellipsometry.	92
2.3.2.2.2	X-ray Photoelectron Spectroscopy (XPS).	92
2.3.2.2.3	Infrared Reflection Absorption Spectroscopy.	95
2.3.2.3	Surface Analysis Plasma Modified PPS.	101
2.3.2.3.1	Ellipsometry.	101
2.3.2.3.2	X-ray Photoelectron Spectroscopy.	101
2.3.2.3.3	Infrared Reflection Absorption Spectroscopy.	108
2.3.2.3.4	XPS Analysis of Epoxy Interactions.	113
2.3.2.3.5	IRRAS Analysis of Epoxy Interactions.	116
2.3.2.4	Surface Analysis of Plasma Modified PEPO's.	118
2.3.2.4.1	Ellipsometry and Surface Acoustic Wave Analysis.	118
2.3.2.4.2	X-ray Photoelectron Spectroscopy.	124
2.3.2.4.3	Infrared Reflection Absorption Spectroscopy.	138
2.4	SUMMARY AND CONCLUSIONS.	144
2.5	REFERENCES.	147

CHAPTER 3.	154
ANALYSIS OF THE REORGANIZATION IN THIN PPS FILMS BY VARIABLE TEMPERATURE REFLECTION ABSORPTION SPECTROSCOPY (VTRAS).	154
3.0 INTRODUCTION.	154
3.1 LITERATURE REVIEW.	155
3.1.1 Interphase Studies.	155
3.1.2 Variable Temperature Infrared Spectroscopy.	156
3.1.2.1 Frequency Shifts.	157
3.1.2.2 Intensity Changes.	158
3.1.3 Variable Temperature Infrared Spectroscopy.	163
3.2 EXPERIMENTAL.	163
3.2.1 Sample Preparation.	163
3.2.2 Variable Temperature Infrared Analysis.	165
3.2.3 Variable Temperature Reflection Absorption Spectroscopy.	165
3.2.4 Data Manipulation.	171
3.3 RESULTS AND DISCUSSION.	172
3.3.1 Theoretical Considerations.	172
3.3.2 Differential Scanning Calorimetry.	177
3.3.3 Variable Temperature Infrared Analysis of PPS Films.	180
3.3.4 Variable Temperature Reflection Spectroscopy.	183
3.3.4.1 Polyphenylene Sulfide Coatings.	183
3.3.4.1.1 Chromium.	183
3.3.4.1.2 Aluminum.	198
3.3.4.1.3 Copper.	198
3.3.4.1.4 Copper Oxide (Cu ₂ O).	210
3.3.4.2 Polyetherimide.	217
3.4 SUMMARY AND CONCLUSIONS.	224
2.5 LITERATURE REVIEW.	226

CHAPTER 4.	229
ANALYSIS OF THE MOLECULAR STRUCTURE AT PPS / COPPER INTERPHASES AND ITS ROLE IN ADHESION.	229
4.0 INTRODUCTION.	229
4.1 LITERATURE REVIEW.	230
4.1.1 Surface Analysis of Copper.	230
4.1.1.1 X-ray Photoelectron Spectroscopy.	230
4.1.1.2 Infrared Reflection Absorption Spectroscopy.	235
4.1.1.3 Ellipsometry.	237
4.1.2 Copper Catalyzed Thermoxidative Degradation of Polymers.	237
4.1.3. Analysis of Polymer/Copper Adhesion.	242
4.1.3.1 Copper Surface Pretreatment.	242
4.1.3.2 Analysis of the Interphase.	243
4.1.3.3 Test Methods.	244
4.2 EXPERIMENTAL.	245
4.2.1 Analysis of the Thermoxidative Degradation of PPS Coatings.	245
4.2.1.1 Sample Preparation.	245
4.2.1.2 X-ray Photoelectron Spectroscopy.	246
4.2.1.3 Infrared Reflection Absorption Spectroscopy.	246
4.2.2 Analysis of Copper / PPS Adhesion.	247
4.2.2.1 Sample Preparation.	247
4.2.2.2 Scanning Electron Microscopy (SEM).	248
4.2.2.3 Bonding.	250
4.2.2.4 Peel Test Analysis.	250
4.2.2.5 Interphase Characterization: Failure Surface Analysis.	250
4.3 RESULTS AND DISCUSSION.	252
4.3.1 Analysis of the Copper Catalyzed Oxidative Degradation of PPS.	252
4.3.1.1 XPS Analysis.	252
4.3.1.2 IRRAS Analysis.	257

4.3.2 Bonding Studies.	265
4.3.2.1 Analysis of Surface Pretreatment.	265
4.3.2.2 Peel Test Analysis.	270
4.3.2.3 Failure Surface Analysis.	275
4.3.3 Interphase Characterization: Model Studies with PPS Tetramer.	287
4.4 SUMMARY AND CONCLUSIONS.	294
4.4.1 Thermoxidative Degradation of PPS.	294
4.4.2 Analysis of PPS / Copper Adhesion.	294
4.7 REFERENCES.	296
CHAPTER 5.	302
5.0 OVERALL CONCLUSIONS.	302
APPENDIX 2.1.	305
APPENDIX 2.2.	313
APPENDIX 3.1.	334
VITA.	355

List of Figures and Tables

CHAPTER 2

Figure 2.1 Two methods for obtaining ir spectra of thin films: arrows indicate direction of the E field component. Both *p* polarization (lower figure), and *s* polarization (upper figure) are shown for reflection. (9)

Figure 2.2 Formulation of the problem of the interaction of light with a series of stratified isotropic layers. (11)

Figure 2.3 Optical constants for Cu_2O . Both *n* and *k* spectra were calculated using Eqns. [21]-[27] and values of ρ_j , γ_j , and ν_j from Ref. 68. Experimental data points were taken from Ref. 42.

Figure 2.4 Infrared spectra of cadmium arachidate for (a) six monolayers on silver with **E** normal to the substrate, and (b) eighteen monolayers on silver bromide with **E** parallel to substrate. (Text and figure taken from Ref. (23).

Figure 2.5 Plots shown for (a) thermal gravimetric analysis of polymers under nitrogen for (1) polyvinylchloride; (2) polymethylmethacrylate; (3) polystyrene; (4) polyethylene; (5) PTFE; (6) PPS and (b) thermal gravimetric analysis for (1) PTFE under nitrogen; (2) PPS under nitrogen; and (3) PPS in air. (79)

Figure 2.6 A typical differential scanning calorimeter trace for polyphenylene sulfide showing heating traces for (—), quenched amorphous and (---), annealed crystalline; samples; and (···), the cooling curve from the melt. (81)

Figure 2.7 General reaction scheme of polyphenylene sulfide cure. (95)

Figure 2.8 Postulated reaction schemes for the thermal cure of polyphenylene sulfide under vacuum conditions. (106)

Figure 2.9 (a) Crystal structure of polyphenylene sulfide, projected on the *ab* plane. (b) polymer chain conformation, projection in the *bc* plane. (119)

Figure 2.10 Infrared spectrum of PPS powder in KBr. (117)

Figure 2.11 Schematic diagram of the high temperature spin coating unit.

Figure 2.12 Typical heating rates for both "cold" and "hot" starts using the high temperature spin coater.

Figure 2.13 Chemical structures for Bis-A-PEPO, polysulfone; and BP-PEPO.

Figure 2.14 Schematic diagram of (a) the retro mirror reflection attachment, and (b) schematic of modifications to the holder design for high temperature operation.

Figure 2.15 Illustration of the Seagull™ multipurpose reflection attachment. (114)

Figure 2.16 Optical constants for PPS in the 400-2000 cm^{-1} spectral region. Shown are plots for both (a) k and (b) n values.

Figure 2.17 Comparison of the infrared spectrum of a 1.55 μ free standing crystalline PPS film for (a) an experimentally measured spectrum and (b) a simulated spectrum using exact optical theory.

Figure 2.18 Comparison of the infrared spectrum for a (a) quenched and (b) annealed 1.55 μ free standing spin coated PPS film.

Figure 2.19 Comparison of the infrared spectra of amorphous and crystalline 2.5 μ spin coated PPS films. Shown are the spectra for (a) quenched, and (b) melted at 320°C and show cooled. The difference spectrum (c) is also shown.

Figure 2.20 Comparison of infrared ATR spectrum for an extruded PPS films at (a) 50° and (b) 42° incidence angles. The 50° spectrum was multiplied by a factor of 0.75 and the 42° spectrum by a factor of 0.375 for scaling purposes.

Figure 2.21 Comparison of the simulated infrared ATR spectrum for PPS using optical theory for incidence angles of (a) 50° and (b) 42°.

Figure 2.22 Comparison of the infrared RAS spectrum for 0.16 mm molded PPS panel at (a) 50° (b) 60° and (c) 70° angles of incidence.

Figure 2.23 Comparison of the simulated infrared RAS spectra for surface reflection from a bulk PPS sample at (a) 50°, (b) 59°, and (c) 70° incidence angles.

Figure 2.24 Thickness versus concentration for PPS coated ferrotype plates. All thicknesses were determined by ellipsometry based on a refractive index of 1.65 for PPS.

Figure 2.25 IRRAS spectra of an (a) amorphous and a (b) crystalline 30 nm PPS film on a chromium substrate. Fig. (c) shows the difference spectrum.

Figure 2.26 Plot of absorbance versus thickness in angstroms for absorbance bands located at (a) 1474 (b) 1075 and (c) 814-820 cm^{-1} for both amorphous and crystalline films. Absorbance was calculated as $-\log(R/R_0)$ where R_0 represents a film with a k value of 0.

Figure 2.27 Infrared RAS band intensity ratio dependence on annealing time for a 60 nm amorphous PPS film on chromium for the (a) 1075 / 1094 cm^{-1} and (b) 820 / 1474 cm^{-1} ratios.

Figure 2.28 *In-situ* IRRAS analysis of the crystallization of a 70 nm PPS film on a ferrotype plate (see Fig 2.13b)

Figure 2.29 Infrared RAS spectrum of a 60-70 nm PPS film on a chromium (ferrotype) substrate after (a) drying at 110-120°C and (b) further annealing at 150-160°C under vacuum.

Figure 2.30 Infrared RAS spectrum of a 60-70 nm PPS film on an oxidized vapor deposited aluminum substrate after (a) drying at 110-120°C and (b) further annealing at 150-160°C under vacuum.

Figure 2.31 Infrared RAS spectrum of a 60-70 nm PPS film on 20 nm oxidized sputter coated copper film on a chromium substrate after (a) drying at 110-120°C and (b) further annealing at 150-160°C under vacuum.

Figure 2.32 Plot of the electric field intensities (x,y,z) for light reflection from a 100 nm film of PPS on copper. Values of 1.65 and 0.3 were taken as n and k values of the 1474 cm^{-1} ring stretch vibration. Values of n_s and k_s for copper were interpolated as 4 and 42.7 respectively from published values. (111)

Figure 2.33 Schematic diagram of the PPS/ Cu_2O /Cr system for optical simulation.

Figure 2.34 Infrared RAS spectrum for the PPS/ Cu_2O /Cr system, described in Fig. 2.33 showing the (a) simulated spectrum using exact optical theory, and (b) the experimental spectrum for the same system. Optical constant values for copper oxide were calculated from Ref. 34 while values for chromium were interpolated from literature values (111,122).

Figure 2.35 Infrared RAS spectrum of a 1% (wt/wt) PPS solution spin coated from benzophenone onto methanol degreased ETP 110 copper foil for (a) quenched and (b) annealed at 150°C under nitrogen.

Figure 2.36 Plot of the electric field intensities (x,y,z) for light reflection from a 100 nm film of PPS on germanium. Values of 1.65 and 0.3 were taken as n and k values for the 1474 cm^{-1} ring stretching vibration. Values of n_s and k_s for germanium were taken as 4 and 0 respectively (117).

Figure 2.37 Infrared transmission spectrum of a 200 nm PPS film on germanium for both (a) quenched and (b) annealed samples. Annealing was done at 150°C in air.

Figure 2.38 Comparison of the infrared spectra for (a) a 200 nm crystalline PPS film on a germanium substrate using transmission and (b) for the same film using p-polarized light and reflection at 60°.

Figure 2.39 Proposed orientations of lamellae in films of different thicknesses: (A) thickness on the order of nanometers; (B) thickness on the order of hundreds of nanometers; (C) thickness on the order of tens of hundreds of nanometers (transcrystalline regions). (119)

Figure 2.40 Schematic diagram of the problem of the IRRAS analysis of a surface modified polymer film.

Figure 2.41 Simulated spectrum of a 2 nm surface layer of polymethylmethacrylate on a polystyrene film of varying thicknesses: (a) 0.5 μ , (b) 0.1 μ , and (c) 0.05 μ on gold. The optical constants of gold were calculated from Ref (111).

Figure 2.42 Simulated difference spectra for a 2 nm polymethylmethacrylate surface layer on a polystyrene film of varying thicknesses: (a) 1 μ (b) 0.5 μ (c) 0.25 μ (d) 0.1 μ and (e) 0.05 μ on gold.

Figure 2.43 The angular dependence of the z component of the electric field intensity for the infrared analysis of a modified surface layer of a film on chromium. Optical constants of the surface layer were taken as 1.5 and 0.35 for n and k respectively for a typical carbonyl absorbance. The film was taken to be nonabsorbing with a refractive index of 1.59 and the n and k values of chromium were estimated to be 5 and 25 (112,122) respectively. Plots are shown for varying film thicknesses, and calculations were done for a z position in the center of the surface modified layer.

Figure 2.44 Calculated absorbance for a typical carbonyl absorbance in the surface modified layer as a function of both underlayer film thickness and angle of incidence. The optical constants used are the same as given in Fig. 2.43.

Figure 2.45 Calculated absorbance for a typical carbonyl absorbance in a surface layer as a function of both underlayer thickness and polarization state of the incident light. The optical constants used are the same as given in Fig. 2.43.

Figure 2.46 Thickness removed for polystyrene thin films as a function of oxygen plasma etch time.

Figure 2.47 C1s line shape for untreated, oxygen plasma, and ammonia plasma treated polystyrene films at (a) 90°, (b) 30°, and (c) 10° exit angles.

Figure 2.48 IRRAS difference spectra of a (a) one minute oxygen plasma treated polystyrene film and a (b) two minute ammonia plasma treated film. The reference was multiplied by a factor to account for the amount of polymer removed.

Figure 2.49 IRRAS difference spectra for a one minute plasma treated polystyrene film taken (a) immediately after treatment and (b) after 72 hours under nitrogen.

Figure 2.50 Thickness removed for PPS thin films as a function of oxygen and ammonia plasma etch time.

Figure 2.51 XPS analysis of atomic concentration changes for PPS thin films versus oxygen plasma treatment time.

Figure 2.52 C1s line shape for untreated and oxygen plasma treated PPS films at both 90° and 10° exit angles.

Figure 2.53 S2p line shape for untreated and oxygen plasma treated PPS films at both 90° and 10° exit angles.

Figure 2.54 XPS analysis of atomic concentration changes for PPS thin films versus ammonia plasma exposure time.

Figure 2.55 C1s line shape for untreated and ammonia plasma treated PPS films at both 90° and 10° exit angles.

Figure 2.56 IRRAS spectra of a 30 nm PPS film before (A) and after (B) a one minute oxygen plasma exposure.

Figure 2.57 IRRAS difference spectrum of a one minute oxygen plasma treated PPS film. The reference was multiplied by a factor to account for the amount of polymer removed.

Figure 2.58 IRRAS difference spectrum of a two minute ammonia plasma treated PPS film. The reference was multiplied by a factor to account for the amount of polymer removed.

Figure 2.59 C1s line shape for a one minute oxygen and ammonia plasma treated PPS films before (---) and after (—) exposure to epoxy followed by 3 CCl₄ rinses.

Figure 2.60 IRRAS difference spectra of a one minute oxygen plasma treated PPS film exposed to epoxy at 100°C after: (a) one CCl₄ rinse (b) two CCl₄ rinses (c) three CCl₄ rinses. Spectrum (a) was multiplied by a factor of 0.16 for scaling purposes.

Figure 2.61 IRRAS difference spectrum of a one minute ammonia plasma treated PPS film exposed to epoxy at 100°C followed by three CCl₄ rinses.

Figure 2.62 IRRAS difference spectrum of untreated PPS films exposed to epoxy at 100°C followed by three CCl_4 rinses.

Figure 2.63 Relative thickness decrease for polysulfone and BP-PEPO films as a function of oxygen plasma exposure time.

Figure 2.64 Surface acoustic wave analysis of the relative etch rates of polysulfone and BP-PEPO after oxygen plasma exposure.

Figure 2.65 XPS analysis of atomic concentration changes for polysulfone thin films versus oxygen plasma treatment time.

Figure 2.66 XPS analysis of atomic concentration changes for BP-PEPO thin films versus oxygen plasma treatment time.

Figure 2.67 XPS analysis of the O1s / P2p ratio for BP-PEPO as a function of oxygen plasma exposure time. Also shown is a similar analysis for the O1s / S2p ratio of Udel polysulfone.

Figure 2.68 XPS analysis of the P2p photopeak for BP-PEPO as a function of oxygen plasma treatment time shown for (a) 0 (b) 0.08 (c) 0.17 (d) 0.33, (e) 1 (f) 5 and (g) 10 minutes. All spectra have been normalized to the C1s line intensity.

Figure 2.69 XPS analysis of the O1s line shape for BP-PEPO as a function of oxygen plasma exposure time shown for (a) 0, (b) 10 minutes and (c) a polyphosphoric standard. All spectra have been normalized to identical intensities for comparison.

Figure 2.70 XPS analysis of the relative changes in peak area for the curve fit spectra in the P2p photopeak for BP-PEPO as a function of oxygen plasma exposure time.

Figure 2.71 XPS analysis of the C1s lineshape for both polysulfone and BP-PEPO as a function of oxygen plasma exposure time. For BP-PEPO (upper figure), times of (a) 0.08 (b) 0.17 (c) 0.33 (d) 1 (e) 5 and (f) 10 minutes are shown, while for polysulfone (lower figure) times are shown for (a) 0.17 (b) 1 (c) 5 and (d) 7.5 minutes.

Figure 2.72 XPS analysis of (■), the C-O / C-H ratio from the curve fit C1s photopeak of BP-PEPO as a function of oxygen plasma exposure time and (Δ), the C_{ox} / C-H ratio for the same analysis. C_{ox} represents the remainder of oxidized carbon species that could not be accounted for by C-O functionality in the curve fit C1s spectra.

Figure 2.73 Theoretically expected elemental ratios for a polyphosphate structure as a function of i , the degree of polymerization, and X , the average number of carbon atoms per pendant group.

Figure 2.74 IRRAS analysis of 70-90 nm spin coated films of polysulfone and Bis-A-PEPO on ferrotype substrates.

Figure 2.75 IRRAS difference spectrum of a five second and five minute oxygen plasma treated polysulfone film. The reference was multiplied by a factor to account for the amount of polymer removed.

Figure 2.76 IRRAS difference spectrum of a 15 second and five minute oxygen plasma treated BP-PEPO film. The reference was multiplied by a factor to account for the amount of polymer removed.

Table 2.1 Infrared Absorbance Band Assignments for Polyphenylene Sulfide. (117)

Table 2.2 Typical Parameters for Spin Coating Thin Polyphenylene Sulfide Films (see Fig. 11).

Table 2.3 XPS Analysis of the Major Elements Present for Oxygen and Ammonia Plasma Treatment of Polystyrene.

Table 2.4 XPS Analysis of the Atomic Concentrations Found for Plasma Treated PPS Before and After Exposure to Epoxy Followed by Several CCl₄ Washes.

Table 2.5a Atomic Concentrations (Measure/Calculated) for the XPS Analysis of Polysulfone and PEPO polymers.

Table 2.5b Atomic Concentrations (Before/After) for the XPS Analysis of a five Minute Oxygen Plasma Treatment of PEPO and Polysulfone.

Table 2.6 IR Band Assignments for Polysulfone and Bis-A-PEPO. (130)

CHAPTER 3

Figure 3.1 Plot of peak intensity versus temperature for the 782 cm⁻¹ C-H rocking absorbance band of n-C₁₉H₄₀ (32).

Figure 3.2 Plot of absorbance versus temperature for the polyimide 1780 cm⁻¹ band. The plot shows both experimental points and theoretical results based on equation [2] (33).

Figure 3.3 Typical heating and cooling temperature profile for variable temperature transmission experiments.

Figure 3.4 Schematic diagram of the experimental design used in all variable temperature reflection absorption measurements.

Figure 3.5 Schematic diagram of the sample holder for variable temperature RAS measurements.

Figure 3.6 Typical heating temperature profile for variable temperature RAS measurements.

Figure 3.7 Plot of the dependence of the peak intensity ($-\log(R/R_0)$) on (a) the substrate k value (k_s), and (b) the substrate n value (n_s). The hypothetical absorbance band used were given values of 1.5 and 0.4 for n_f and k_f respectively, and a substrate n value of 3.0 was used for plot (a) and a k value of 40 for plot (b). The frequency was taken as 1740 cm^{-1} .

Figure 3.8 Plot of the dependence of the peak intensity ($-\log(R/R_0)$) on the film refractive index. Substrate n and k values were taken as 3.0 and 40 and the other parameters are given in Fig. 2.7.

Figure 3.9 Plot of the RAS absorbance band peak frequency as a function of (a) the percent decrease in the initial k value for two peak widths, and (b) the percent increase in peak width for two initial k values.

Figure 3.10 Differential scanning calorimetry trace for Ryton™ polyphenylene sulfide taken at a ramp rate of $2.5^\circ\text{C} / \text{minute}$. Plots are shown for both (a) the first run of a quenched sample, and (b) the second run for fully crystalline PPS.

Figure 3.11 Relative peak intensity changes for the variable temperature transmission analysis of an approximately 2.5 micron quenched PPS film on a salt plate substrate. All bands have been normalized to the initial peak intensity at room temperature.

Figure 3.12 Relative peak position changes for the variable temperature transmission analysis of an approximately 2.5 micron PPS film on a salt plate substrate. All bands frequencies have been referenced to the room temperature peak frequency.

Figure 3.13 Relative peak intensity changes for the transmission analysis of an approximately 2.5 micron spin coated PPS film on a salt plate substrate. The film had been crystallized from the melt and all bands frequencies have normalized to the peak intensity at room temperature.

Figure 3.14 Relative peak area changes for the transmission analysis of an approximately 2.5 micron spin coated PPS film on a salt plate substrate. The film had been crystallized from the melt and all bands areas have normalized to the peak area at room temperature.

Figure 3.15 Absolute peak intensity changes for the variable temperature RAS analysis of a 60-70 nm PPS film on a chromium substrate showing plots for bands at (a) $814 - 820\text{ cm}^{-1}$, (b) 1474 cm^{-1} , (c) 1011 cm^{-1} , and (d) 1390 and 1574 cm^{-1} .

Figure 3.16 Absolute peak frequency shifts for the variable temperature RAS analysis of a 60-70 nm PPS film on a chromium substrate showing plots for bands at (a) 814 - 820 cm^{-1} , (b) 1474 cm^{-1} , (c) 1011 cm^{-1} , and (d) 1574 cm^{-1} .

Figure 3.17 Plot of the absolute peak frequency shifts for both variable temperature transmission and RAS analysis of bands at (a) 814 - 820 cm^{-1} , and (b) 1474 cm^{-1} .

Figure 3.18 Plot of the absolute peak frequency shifts for both variable temperature transmission and RAS analysis showing plots of bands at (a) 1011 cm^{-1} , and (b) 1390 cm^{-1} .

Figure 3.19 Relative peak intensity changes for both variable temperature transmission and RAS analysis. All band intensities have normalized to the peak intensity at room temperature, and plots are shown for peaks at (a) 814 - 820 cm^{-1} , (b) 1474 cm^{-1} , (c) 1011 cm^{-1} , and (d) 1574 cm^{-1} .

Figure 3.20 VTRAS analysis of the absolute peak intensity and position for the 814 - 820 cm^{-1} C-H out-of-plane band for both first and second scans for a 60-70 nm PPS film on a chromium substrate.

Figure 3.21 VTRAS analysis of peak area versus temperature for the 814 - 820 cm^{-1} absorbance band of a 60 - 70 nm PPS film on a chromium substrate.

Figure 3.22 VTRAS analysis of the absolute (a) peak intensity and (b) peak position changes for the the 1011 cm^{-1} C-H in-plane band for both first and second scans.

Figure 3.23 Analysis of the derivative plots for the (a) first and (b) second scans using variable temperature RAS analysis of the peak intensity versus temperature data for the 814 - 820 cm^{-1} absorbance band of PPS on a chromium substrate.

Figure 3.24 VTRAS analysis of the absolute peak intensity changes for a 60-70 nm PPS film on an oxidized aluminum substrate showing plots for bands at (a) 814 - 820 cm^{-1} , (b) 1474 cm^{-1} , (c) 1011 cm^{-1} , and (d) 1390 and 1574 cm^{-1} .

Figure 3.25 VTRAS analysis of the absolute peak frequency shifts for a 60-70 nm PPS film on an oxidized aluminum substrate showing plots for bands at (a) 814 - 820 cm^{-1} , (b) 1474 cm^{-1} , (c) 1011 cm^{-1} , and (d) 1574 cm^{-1} .

Figure 3.26 VTRAS analysis of the absolute peak intensity and position for the 814 - 820 cm^{-1} C-H out-of-plane band for both the first and second scans of a 60-70 nm PPS film on oxidized aluminum.

Figure 3.27 RAS spectrum of a 60-70 nm PPS film on a pre-oxidized vapor deposited copper substrate.

Figure 3.28 XPS analysis of a preoxidized vapor deposited copper substrate.

Figure 3.29 VTRAS analysis of the absolute (a) peak intensity and (b) peak position of the $814 - 820 \text{ cm}^{-1}$ absorbance band for both first and second scans in the analysis of a 60-70 nm PPS film on copper.

Figure 3.30 VTRAS analysis of the absolute peak area of the 650 cm^{-1} absorbance band for both the first and second scans in the analysis of a 60 - 70 nm film on copper.

Figure 3.31 VTRAS analysis of the relative peak area changes for the $814 - 820 \text{ cm}^{-1}$ absorbance band of a 60-70 nm PPS film on a copper substrate showing plots of both the first and second runs for films quenched from $320 - 340^\circ\text{C}$, and for a sample quenched after heating to $350 - 370^\circ\text{C}$.

Figure 3.32 RAS difference spectrum for the analysis of 60 - 70 nm PPS films on copper. Shown are spectra for (a) the difference between the spectrum after the first scan and the initial spectrum, and (b) the difference between the spectrum after the second scan and the spectrum after the first scan.

Figure 3.33 VTRAS analysis of the absolute (a) peak intensity and (b) peak position of the $814 - 820 \text{ cm}^{-1}$ absorbance band for both first and second scans in the analysis of 60 - 70 nm PPS films on copper oxide.

Figure 3.34 RAS spectrum for the analysis of 60 - 70 nm PPS films on copper oxide shown for (a) the original spectrum, (b) the spectrum taken after the first scan, and (c) the spectrum taken after the second scan.

Figure 3.35 RAS difference spectrum for the analysis of 60 - 70 nm PPS films on copper oxide. Shown is the difference spectrum between the spectrum after the first run and the initial spectrum.

Figure 3.36 VTRAS analysis of the absolute peak area for the 650 cm^{-1} absorbance band for both the first and second scans in the analysis of a 60 - 70 nm film on copper oxide.

Figure 3.37 XPS analysis of the (a) $\text{Cu}2p_{3/2}$ photopeak and the (b) Cu (LVV) photopeak for the analysis of methanol cleaned copper foil as a function of temperature under argon. Shown are 30 minute heat treatments at (A) room temperature, (B) 120°C , (C) 220°C , and (D) 320°C .

Figure 3.38 RAS spectrum of a thin spin coated film of polyetherimide on a 'brite dip' (See chapter 2, section 2.2.1.2) acid cleaned copper foil substrate.

Figure 3.39 RAS difference spectrum comparing a polyetherimide thin film taken after the first temperature scan and the original spectrum after drying.

Figure 3.40 VTRAS analysis of the absolute peak intensity of the 1738 cm^{-1} carbonyl absorbance band for both the first and second scans in the analysis of a thin polyetherimide film on copper foil.

Figure 3.41 VTRAS analysis of the absolute peak intensity for the 1363 cm^{-1} C-N absorbance band for both the first and second scans in the analysis of a thin polyetherimide film on copper foil.

Table 3.1 Infrared absorbance band assignments for Ultem™ polyetherimide.

CHAPTER 4

Figure 4.1 XPS analysis of the Cu 2p photopeak for copper metal and cupric and cuprous copper oxides (13). Figure 3.8 Plot of the dependence of the peak intensity ($-\log(R/R_0)$) on the film refractive index.

Figure 4.2 Illustration of the copper metal, oxide, and hydroxide layered structure typically found for the ambient oxidation of copper surfaces (15).

Figure 4.3 Typical Wagner plot for various copper compounds (11)

Figure 4.4 Proposed mechanism for the copper catalyzed degradation of polyethylene (36).

Figure 4.5 Illustration of the method of thermal oxidation of copper foil prior to bonding.

Figure 4.6 Schematic of the laminate structure used in the bonding of PPS to copper foil.

Figure 4.7 XPS analysis of the (a) C 1s and O 1s photopeak, and (b) Cu 2p and S 2p photopeak intensities at different aging times on copper foil at 210°C in air.

Figure 4.8 XPS analysis of the Cu 2p and O1s photopeaks at aging times of (a) 1 hour (b) 10 hours (c) 22 hours and (d) 85 hours for PPS films on copper foil at 210°C in air.

Figure 4.9 XPS analysis of the S 2p photopeak at aging times of (a) 1 hour (b) 10 hours (c) 22 hours and (d) 85 hours for PPS films on copper foil at 210° in air.

Figure 4.10 XPS analysis of the (a) C 1s and O 1s photopeak, and (b) Zn 2p and S 2p photopeak intensities at different aging times on zinc foil at 210°C in air.

Figure 4.11 *Ex-situ* IRRAS analysis of PPS aging (1% spin coated) on a copper foil substrate after 15 minutes at 210°C.

Figure 4.12 *In-situ* VTRAS analysis of a 2% (wt/wt) spin coated PPS film on copper foil in air. Spectra are shown at (a) room temperature, (b) 204°C, and (c) 221°C for a 5°C / min temperature ramp rate.

Figure 4.13 *In-situ* VTRAS analysis of a 2% (wt/wt) spin coated PPS film on copper foil in air in the 1300 - 1700 cm^{-1} spectral region. Spectra are shown at (a) room temperature, (b) 204°C, and (c) 221°C for a 5°C / min temperature ramp rate.

Figure 4.14 VTRAS analysis of the integrated peak areas versus temperature for the (a) 620 - 650 cm^{-1} , and (b) 1012 cm^{-1} absorbance bands. Plot (b) was multiplied by a factor of 17.0 for scaling purposes.

Figure 4.15 VTRAS analysis of a 1% (wt/wt) spin coated PPS film on a ferrottype substrate with spectra shown for (a) room temperature, (b) 194°C, and (c) 218°C. Also shown is the analysis for a 2% (wt/wt) spin coated PPS film on a sputtered cuprous oxide film for (a) room temperature, (b) 201°C, and (c) 223°C. A ramp rate of 5°C / min was used in all analyses.

Figure 4.16 VTRAS analysis of a 2% (wt/wt) spin coated PPS film on an aluminum foil substrate. Shown are spectra for (a) room temperature, (b) 216°C, (c) 250°C, and (d) 282°C.

Figure 4.17 XPS analysis of the Cu 2p and Cu(LVV) spectral lines for (a) methanol washed, (b) nitric acid treated, and (c) 'brite dip' treated copper foil.

Figure 4.18 XPS analysis of the Cu 2p and Cu(LVV) spectral lines for (a) 'brite dip' treated, and (b) thermally oxidized copper foil.

Figure 4.19 XPS analysis of the Cu 2p and Cu(LVV) spectral lines for (a) 'brite dip' treated and (b) chemically oxidized copper foil.

Figure 4.20 SEM analysis of copper foil surfaces for (a) 'brite dip'treated, and (b) thermally oxidized samples.

Figure 4.21 SEM analysis of a chemically oxidized copper foil sample.

Figure 4.22 XPS analysis of the Cu 2p and Cu(LVV) lines for failure surfaces of PPS bonded to methanol degreased copper foil showing (a) the foil surface before bonding, (b) the foil failure surface, and (c) the adhesive failure surface.

Figure 4.23 XPS analysis of the S 2p photopeak of failure surfaces for PPS bonded to methanol degreased copper foil for (a) the adhesive failure surface, and (b) the foil failure surface.

Figure 4.24 XPS analysis of the S 2p and Cu(LVV) peaks for failure surfaces of PPS bonded to 'brite dip' etched copper foil showing (a) the foil surface before bonding, (b) the foil failure surface, and (c) the adhesive failure surface.

Figure 4.25 XPS analysis of the S 2p and Cu(LVV) peaks for failure surfaces of PPS bonded to nitric acid etched copper foil showing (a) the foil surface before bonding, (b) the foil failure surface, and (c) the adhesive failure surface.

Figure 4.26 XPS analysis of the S 2p and Cu(LVV) peaks for failure surfaces of PPS bonded to thermally oxidized copper foil showing (a) the foil surface before bonding, (b) the foil failure surface, and (c) the adhesive failure surface.

Figure 4.27 XPS analysis of the S 2p and Cu(LVV) peaks for failure surfaces of PPS bonded to chemically oxidized copper foil showing (a) the foil surface before bonding, (b) the foil failure surface, and (c) the adhesive failure surface.

Figure 4.28 XPS analysis of the S 2p photopeaks for copper and aluminum foil samples after exposure to PPS oligomer for five minutes at 320 - 340°. Shown are spectra for (a) heat treatment without oligomer, (b) heat treatment with oligomer and no solvent wash, and (c) treatment with oligomer followed by several solvent washes.

Figure 4.29 XPS analysis of the S 2p photopeaks for (a) 'brite dip' etched foil, (b) thermally oxidized, and (c) chemically oxidized copper foil after exposure to PPS oligomer for five minutes at 320 - 340° followed by several solvent washes.

Figure 4.30 XPS analysis of the Cu 2p and Cu (LVV) peaks (a) before, and (b) after exposure to PPS oligomer for five minutes at 320 - 340° followed by several solvent washes for 'brite dip' etched, thermally oxidized, and chemically oxidized copper foil.

Table 4.1 XPS Analysis of Photopeak Positions for Several Copper Compounds.

Table 4.2 Maximum Rate of Oxidation (R_o) as Functions of Catalyst Surface Area.

Table 4.3 XPS Atomic Concentrations for Pretreated Copper Foil Surfaces.

Table 4.4 Peel Test Analysis of Copper/PPS Adhesion.

Table 4.5 XPS Atomic Concentrations for Copper Foil/PPS Failure Surfaces.

Table 4.6 XPS Atomic Concentrations for Copper Foil/PPS Failure Surfaces.

Table 4.7 XPS Analysis of Relative Concentrations of Inorganic and Organic Sulfur For Foil Failure Surfaces.

Table 4.8 XPS Analysis of Relative Concentrations of Inorganic and Organic Sulfur for PPS Oligomer Treated Copper Foil.

Table 4.9 XPS Atomic Concentrations for Oligomer Treated Copper Foil Surfaces.

Chapter 1: Introduction

Due in part to the explosive growth in the electronics industry in the last two decades, there has followed an increase in research efforts focusing on the analysis of thin polymeric films. These have been shown to offer a number of advantages over inorganic coatings when incorporated into electronic devices. Further interest in thin films also comes from applications in the coatings industry, new applications for non-linear optics systems, and thin films can also serve as model systems to evaluate interactions across interfaces in adhesion applications.

While films and coatings play a major role in many industries, literature data on the characterization of extremely thin polymer films is lacking. The unique nature of polymers having both temperature and time dependent properties is well known for bulk polymer materials, and many characterization techniques are available including differential scanning calorimetry, and measurements that involve the external application of mechanical or electrical oscillations. Few techniques are available, however, to characterize the dynamic nature of thin films on surfaces. Polymer orientation and relaxation phenomena for thin films might be expected to be quite different than the bulk due to surface effects, and thus play a critical role in determining the overall film properties. These considerations, then, lead to a number of questions that must be addressed both theoretically and experimentally in the characterization of thin films: (1) What are the factors important in polymer organization of solid surfaces and can orientation be induced by the method of preparation? (2) What role does the surface play in altering polymer molecular motions at the surface as a function of temperature for both crystalline and amorphous polymers? (3) What are the degradation processes that occur in various environments and how does this affect the overall film properties?

In another application, polymer films are often modified by chemical or physical means to alter only the surface region, leaving the bulk of the polymer unaltered. This type of treatment has been shown to improve the adhesion to other materials in many cases. The chemistry of this layer may be quite different than the bulk, but

while such a treatment can dramatically alter surface properties such as wettability, characterization of the surface layer has been limited. Several important questions can again be asked: (1) What are the functional groups present in the surface modified layer, and what is the molecular mechanism behind the increased adhesive performance often seen? (2) What is the depth of the modified layer, and can the depth be changed by altering the experimental conditions? (3) How does the modified layer change with time and environment?

Unfortunately, many of these fundamental questions have not been answered due to the problem that both thin polymer films or modified surface layers represent only a fraction of the material needed for analysis by conventional techniques.

This dissertation focuses on the use of relatively new methods to analyze both the orientation in thin films and their dynamic behavior as a function of temperature on solid surfaces. The use of optical theory has only recently been applied to polymer thin film systems and Chapter 2 extensively uses these methods to characterize orientation in thin polyphenylene sulfide films. Surface modification by plasma treatment is also analyzed in Chapter 2 from both a theoretical and experimental perspective and the infrared analysis reflection absorption spectroscopy represents some of the first data available for plasma modification of thin films. In addition, the mechanism of the interaction of a model adhesive with a plasma modified layer can also be determined by this technique. Chapter 3 introduces a new technique, variable temperature reflection absorption spectroscopy (VTRAS), in the analysis of thin film re-organization on surfaces. This technique allows characterization of thermal transitions by analyzing small frequency and intensity changes for various absorption bands. Also, distinctions can be made in the specific interactions for a variety of substrates. Chapter 4 includes a study of the degradation processes occurring in polyphenylene sulfide / copper interphases to deduce the mechanisms involved. *In-situ* variable temperature infrared reflection absorption spectroscopy was utilized in this analysis. Bonding studies of PPS and copper were also performed to determine the mechanisms responsible for the poor adhesion usually seen for this system. Recommendations for methods to improve adhesion are also put forth.

Chapter 2: Thin Film Characterization

2.1 LITERATURE REVIEW

2.1.1 Introduction

Infrared spectroscopy has been utilized for many decades to help understand the bonding structure of molecules. In the analysis of polymers alone, IR spectroscopy has been used to investigate polymer properties including conformation, crystallinity, and crosslinking among others (1). The infrared absorption process is quantized with light absorption giving rise to excitation of molecules to higher energy states. Absorption at only certain frequencies can occur and the change in energy is related to frequency of light by the well known equation: $E=h\nu$. Light absorption in the infrared spectral region (2.5 - 15 micrometers) is associated with molecular vibrations, and for absorption to occur, there must be an electrical dipole oscillating at the same frequency as the incoming radiation. The alignment of the dipole derivative, or transition moment will determine the degree of energy transfer between the oscillating dipole and the standing electric field from the incident infrared light.

The most widely used infrared method is transmission spectroscopy where the intensity of the transmitted light (I) is related to the incident light by the equation:

$$I = I_0 e^{-4\pi\nu kd} \quad [1]$$

where ν is the frequency in wavenumbers (cm^{-1}), d is the thickness in centimeters and k is an extinction coefficient which measures the extent of absorption. To better understand this term, the attenuation of the wave amplitude for one vacuum wavelength is defined as $e^{-2i\pi k}$ (2). Often, the terms $4\pi\nu k$ are combined to give an absorption coefficient β with units of reciprocal centimeters (cm^{-1}). This equation can also be rearranged to yield the more commonly found form of the Beer-Lambert equation as:

$$A = \rho cd = -\log\left[\frac{I}{I_0}\right] = \frac{4\pi\nu kd}{2.303} \quad [2]$$

where ρ represents another version of the extinction coefficient, c is the concentration, and l the cell path length.

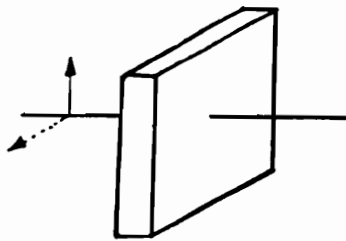
For absorption to occur, there must be coupling between a particular absorbing group and the standing electric field. Having an absorbing group first implies that there is a non-zero transition dipole moment. Parallel alignment of this transition moment with the infrared electric field vector results in maximum coupling, and therefore maximum absorbance, while perpendicular alignment of the two gives no energy absorption. The absorbance seen experimentally then depends, for a given mass, on the alignment of the transition moment and the direction of the electric field vector. For transmission through a film, the electric field vector is parallel to the surface of the film, and can only interact with absorbing groups having a component of the dipole transition moment parallel to the surface. Experimentally, when coupled with polarized infrared light, this means that one examines transition moments in the x and y directions (in the plane of the substrate), and this forms the basis for measurements of dichroic ratios, used for many years to analyze orientation in polymer films (1). In order to obtain information in the z direction (perpendicular to the substrate plane), the sample must be tilted. Fina and Koenig have discussed both the practical and theoretical aspects of such an analysis to fully characterize three dimensional orientation in polymer films (3).

The interpretation of transmission spectra is relatively straightforward, correlating experimentally determined band frequencies to the molecular "groups" they represent (4). Quantification is also simple, following the Beer-Lambert law in the linear range of the detector used. In addition to standard transmission measurements, there are a number of commonly used 'surface' infrared techniques including reflection absorption spectroscopy (RAS), attenuated total reflectance spectroscopy (ATR), diffuse reflectance spectroscopy (DRIFT), as well as the more recent developments of surface electromagnetic wave spectroscopy (SEWS), and metal overlayer ATR (5). For these reflectance techniques, the interpretation of band shapes and intensities can be more difficult and require an understanding of reflection optics.

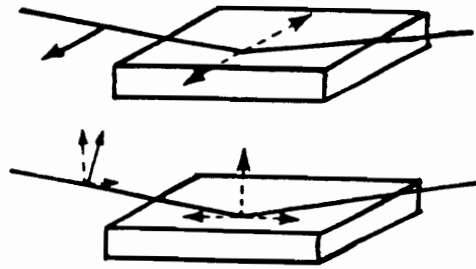
Focusing on external reflection, the early work of Francis and Ellison (6) and Greenler (7) provided the first quantitative analysis of external reflectance for the infrared analysis of thin films on metals and Greenler coined the phrase "reflection absorption spectroscopy" to describe this technique. While several authors have discussed both the theory and application of this technique (5,8-10), the fundamental principles will be reviewed here.

For the reflection of light from a surface, the incident beam can be resolved into its two components, one parallel to the plane of incidence (*p* polarization) and one perpendicular to the plane of incidence (*s* polarization). For the reflection from a metal, *s* polarization undergoes almost a 180° phase shift at all angles of incidence, and this results in a standing electromagnetic field with a node at the surface. With negligible electric field intensity at the surface, absorption will be extremely small using this state of polarization. For *p*-polarization, however, the reflected beam undergoes a shift of 0° to 180° depending on the angle of incidence. At grazing angles, the incident and reflected light can combine constructively (~ 90° phase shift) to give a standing elliptical electric field with a non-zero field intensity at the surface of the metal. Figure 2.1 shows a schematic representation of this process for transmission, and for both states of polarization in reflection. Increased sensitivity over an equivalent transmission experiment is therefore possible, and a second feature is that the field is anisotropic, with the major component of the electric field vector normal to the surface.

Greenler also showed that an absorbance band intensity for a particular polarization of the incident light can have a complicated dependence on the optical properties of the film and substrate under study (7). While general predictions from theory can aid in the experimental design for simple polymer/metal systems, the use of exact optical theory is necessary to help predict the nature of experimental reflection spectra, which often can appear quite different than those obtained in transmission spectroscopy. Also, theory can aid in the comparison of spectra obtained utilizing different reflection techniques (5).



Transmission



Grazing Incidence Reflection

Figure 2.1 Two methods for obtaining ir spectra of thin films: arrows indicate direction of the E field component. Both *p* polarization (lower figure), and *s* polarization (upper figure) are shown for reflection. (9)

2.1.2 Fundamentals of Optical Theory

Figure 2.2 shows a schematic representation of the interaction of an infinite propagating electromagnetic wave with a series of stratified isotropic layers. The diagram represents a typical problem often found in adhesive applications for a polymer coating on an oxide covered metal. In the simplest case, each layer is assumed to be isotropic and described by a complex refractive index:

$$\hat{n} = n_1 - ik_1 \quad [3]$$

where n_1 is the refractive index, and k_1 is the attenuation coefficient. The refractive index, \hat{n} , can be cast in terms of the complex dielectric constant, $\hat{\epsilon}$, as

$$\hat{\epsilon} = (\hat{n})^2 = \epsilon' - i\epsilon'' \quad [4]$$

where

$$\epsilon' = n^2 - k^2 \quad [5]$$

and

$$\epsilon'' = 2nk \quad [6]$$

Using equations [5] and [6] and rearranging yields the following equations for n and k in terms of ϵ' and ϵ'' :

$$n = \sqrt{\frac{1}{2}(\sqrt{\epsilon'^2 + \epsilon''^2} + \epsilon')} \quad [7]$$

$$k = \sqrt{\frac{1}{2}(\sqrt{\epsilon'^2 + \epsilon''^2} - \epsilon')} \quad [8]$$

In Fig. 2, E_j^+ / E_1^+ represents the electric vector sum of all multi-reflected waves traveling in the direction shown. The quantity E_1^- / E_1^+ represents the amplitude ratio of the reflected vector to the incident vector, and is termed the reflectivity (r), while

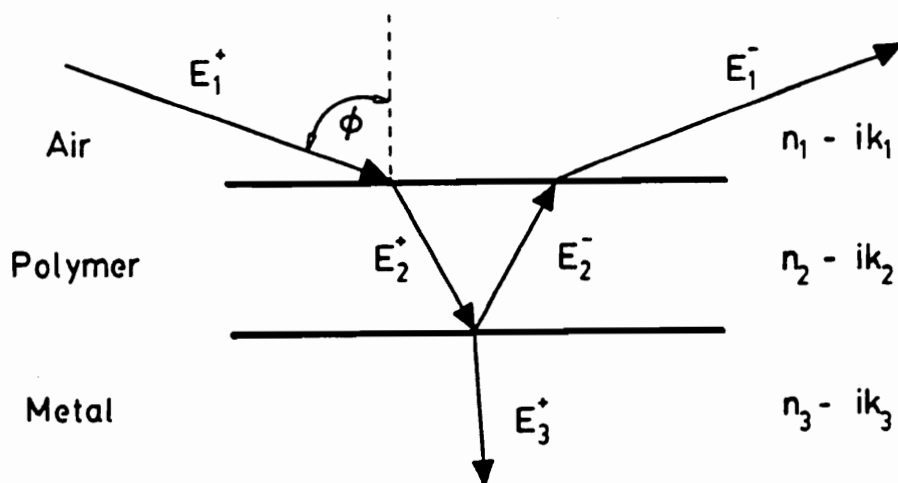


Figure 2.2 Formulation of the problem of the interaction of light with a series of stratified isotropic layers (11).

E_3^+/E_1^+ represents the same ratio for the transmitted vector and is termed the transmissivity (\mathfrak{t}). Both \mathfrak{r} and \mathfrak{t} are complex quantities that can be defined for either state of incident light polarization and contain both amplitude and phase information. Since experimental infrared measurements are concerned with the measurement of absolute power loss, the terms \mathfrak{r} and \mathfrak{t} must be multiplied by the corresponding complex conjugate terms \mathfrak{r}^* and \mathfrak{t}^* to yield either reflectance (\mathbf{R}) or transmittance (\mathbf{T}).

The method for evaluation of the reflectance and transmittance for the system described in Fig. 1. involves solving Maxwell's equations for the electric and magnetic vectors in each layer and applying the appropriate boundary conditions across each interface (2,12). A more thorough summary of Heaven's treatment is given in Appendix 2.1 (2). The outcome of these treatments leads to the well known Fresnel relationships describing the reflectivity and transmissivity at a given interface for p and s polarization:

$$\hat{r}_p = \frac{n_0 \cos \phi_1 - n_1 \cos \phi_0}{n_0 \cos \phi_1 + n_1 \cos \phi_0} \quad [9]$$

$$\hat{r}_s = \frac{n_0 \cos \phi_0 - n_1 \cos \phi_1}{n_0 \cos \phi_0 + n_1 \cos \phi_1} \quad [10]$$

$$\hat{t}_p = \frac{2n_0 \cos \phi_0}{n_0 \cos \phi_1 + n_1 \cos \phi_0} \quad [11]$$

$$\hat{t}_s = \frac{2n_0 \cos \phi_0}{n_0 \cos \phi_0 + n_1 \cos \phi_1} \quad [12]$$

The reflectance and transmittance are therefore defined as:

$$\mathbf{R} = \hat{p} \times \hat{p}^* \quad [13]$$

and

$$\mathbf{T} = \frac{n_1}{n_0} [\hat{e} \times \hat{e}^*] \quad [14]$$

In general, for Eqns. [9]-[12] n_i will be replaced by \hat{n}_i , and ϕ_i can be found by Snells law:

$$\cos\phi_i = \sqrt{1 - \left(\frac{\hat{n}_0}{\hat{n}_i} \sin\phi_0\right)^2} \quad [15]$$

where ϕ is a complex quantity and no longer represents the simple angle of refraction.

The above treatment gives the reflectance and transmittance across a single interface. For the case of a film covered substrate, one must account for reflectance and transmittance at each interface, multiple reflections through the film, and phase shift corrections due to the film thickness. Accounting for these factors yields the following equations for the single film model (2):

$$r = \frac{r_1 e^{i\delta_1} + r_2 e^{-i\delta_1}}{e^{i\delta_1} + r_1 r_2 e^{-i\delta_1}} \quad [16]$$

$$t = \frac{t_1 t_2}{e^{i\delta_1} + r_1 r_2 e^{-i\delta_1}} \quad [17]$$

where r and t are the appropriate reflectivity and transmissivity coefficients. The term δ_1 represents the phase change upon traversing the film thickness once and is given by $(2\pi d/\lambda)\hat{n}_1 \cos\phi$ where d is the film thickness and λ is the wavelength. For the two film system shown in Fig. 2, the following more complex equations result:

$$R = \frac{r_1 + r_2 e^{-2i\delta_1} + r_3 e^{-2i(\delta_1 + \delta_2)} + r_1 r_2 e^{-2i\delta_2}}{1 + r_1 r_2 e^{-2i\delta_1} + r_1 r_3 e^{-2i(\delta_1 + \delta_2)} + r_2 r_3 e^{-2i\delta_2}} \quad [18]$$

$$t e^{-i\delta_2} = \frac{t_1 t_2 t_3 e^{-i(\delta_1 + \delta_2)}}{1 + r_1 r_2 e^{-2i\delta_1} + r_1 r_3 e^{-2i(\delta_1 + \delta_2)} + r_2 r_3 e^{-2i\delta_2}} \quad [19]$$

Analysis of the reflectance and transmittance in this form is cumbersome, and Heavens (2) and Born and Wolf (12) have shown convenient matrix formulations to calculate reflectance and transmittance for any number of layers. A description of Heavens's approach is given in Appendix 2.1.

2.1.2.1 Optical Constants of Polymers

To fully utilize exact optical theory to analyze the infrared spectra of polymers, the complex refractive index, \hat{n} , must be known in the spectral region of interest. The optical constants of many inorganic materials including metals and semiconductors have been compiled (13), and methods of optical constant determination evaluated (14). Little data is available however for the optical properties of organic solids in the infrared. Methods have been developed, however, to determine \hat{n} in the infrared region for organic liquids using transmission techniques (15-18), and techniques based on attenuated total reflectance (19-22).

Only recently has data been compiled for the optical constants of polymers in the infrared. Ribbegaard and Jones extended a method previously proposed for the analysis of liquid films to examine the optical properties of thin free-standing commercial polymer films (23). The technique involved calculation of n and k by analyzing transmission measurements using an iterative process. The method involved estimation of k from the transmission spectrum, determination of n through a Kramers-Kronig transformation, calculation of a theoretical transmission spectrum using exact optical theory, and refinement of k values until convergence occurred with the original transmission spectrum. A detailed analysis of this procedure has been

given (15-18,23). A similar iterative process has been used by Allara et al. to determine optical parameters for polymethylmethacrylate (PMMA) in the carbonyl region (24). Ishida also used this process to determine the optical constants of PMMA, polyvinylchloride (PVC) and polystyrene (PS) (25). Graf et al. also have recently developed the technique of infrared ellipsometry to measure directly the optical constants of polymer films on substrates (26) and have extended its use to the analysis of bulk samples by analyzing reflection near the Brewster angle (27). In a different approach, Pacansky et al., used classical dispersion analysis to analyze the absorption bands in polymer infrared spectra as a collection of damped oscillations with specified peak positions, widths, and strengths (28,29). Knowing these specific parameters for all absorbances, the complex dielectric constant could be calculated from the following equations:

$$\epsilon_r = \epsilon_o + \sum_{j=1}^W 4\pi\rho_j v_j^2 \frac{v_j^2 - v^2}{(v_j^2 - v^2)^2 + \gamma_j^2 v^2} \quad [20]$$

$$\epsilon_i = \sum_{j=1}^W 4\pi\rho_j v_j^2 \frac{\gamma_j v}{(v_j^2 - v^2)^2 + \gamma_j^2 v^2} \quad [21]$$

where ϵ_r and ϵ_i are the real and imaginary parts of ϵ , v_j is the oscillator position, ρ_j is a measure of the oscillator strength, and γ_j is the full width at half height. The term ρ_j can be related to peak absorbance by:

$$\rho_j = \frac{\frac{\bar{n}}{h} \int_{v_a}^{v_b} \ln\left(\frac{T_o}{T}\right) dv}{4\pi^3 v_j^2} \quad [22]$$

where (T_o/T) represents the reciprocal of the transmittance spectrum over the peak from v_a to v_b , \bar{n} is the mean refractive index, and h is the film thickness.

In yet another approach, Mielczarski et al. used a classical oscillator fitting routine combined with analysis at different angles of incidence and states of polarization to obtain n and k (30). This method, also an iterative process, required initial trial values of the polarizability parameters.

2.1.2.2 Refractive Index Effects

While infrared transmission spectroscopy is affected to only a small extent by the refractive index of the material under study, absorbance bands in reflection spectroscopy can be distorted by refractive index effects. With normal dispersion, the refractive index will decrease with decreasing frequency (31). In the vicinity of an absorption band, however, the refractive index goes through an anomalous dispersion and an example of this is shown in Figure 2.3 for the n and k values of cuprous oxide (Cu_2O) for the absorption band at approximately 610 cm^{-1} . Greenler et al. showed in an early theoretical treatment, that while refractive index effects only slightly distort the transmission spectrum for the copper oxide absorbance band, the grazing angle (87°) external reflection spectrum showed that the peak maximum was blue shifted 32 cm^{-1} (32). Calculations also predicted peak splitting for thicker films with one peak maximum due to the maximum in the k spectrum and the other due to the minimum found in the n spectrum. Experimental efforts to verify this band splitting, however, were not successful. Boerio and Armogan did later experimentally verify band splitting for thermally grown copper oxide layers (33). More recent work by Machefert et al. has theoretically investigated the reflectance spectra of Cu_2O on copper and Cr_2O_3 on chromium as a function of thickness (34). Simulating reflectance spectra for Cu_2O as a function of thickness, multiple peak splitting was observed due to optical effects for thicknesses ranging from $1\text{-}3\mu$. Experimental verification of the predicted effects was performed for copper oxide films formed at 300°C .

While Greenler et al. predicted that shifts and spectral distortions for absorbance bands with small k values (<0.1) would be minimal (32), Allara et al. showed that the carbonyl peak maximum for a reflection spectrum of polymethylmethacrylate exhibited a 10 cm^{-1} blue shift when compared to transmission

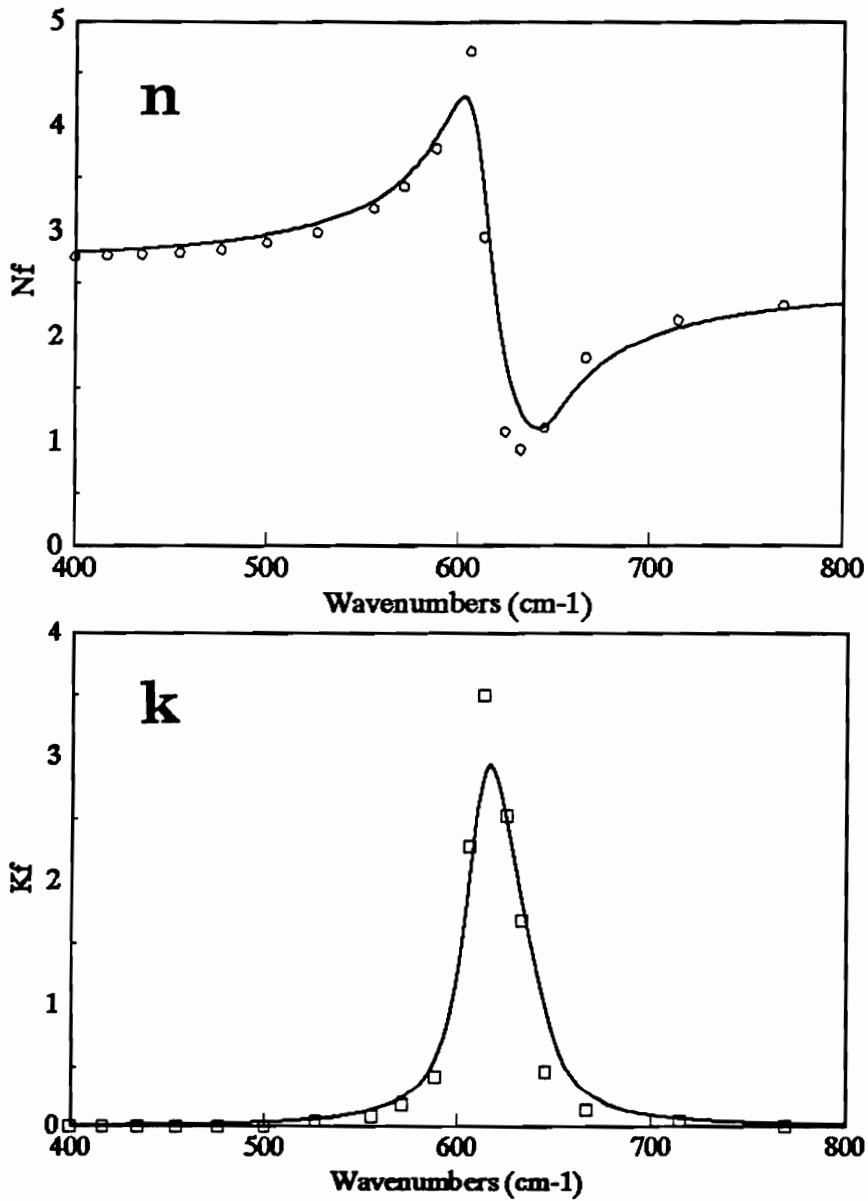


Figure 2.3 Optical constants for Cu₂O. Both n and k spectra were calculated using Eqns. [21]-[27] and values of ρ_j , γ_j , and ν_j from Ref. 34. Experimental data points were taken from Ref. (42).

(24). Nguyen et al. also investigated spectral distortions for reflectance spectra of epoxy coatings on steel and found that distortions were larger at grazing angles and increased thickness (35). While these studies have involved the analysis of absorbing films on metal substrates, relatively little work has been performed to characterize more infrared transparent materials where both states of incident light polarization can be analyzed.

Wong and Yen, in the analysis of the reflectance spectra of SiO_2 films on silicon, showed that while measurements taken with perpendicular polarized light generally reflected the profile of k values for SiO_2 , the use of parallel polarized light yielded severe peak shifts and distortions that were strongly dependent on the angle of incidence (36). Calculations showed that these effects were associated with the dispersion in refractive index values. Another interesting point was that unlike spectra for films on metal substrates, spectra taken for films on silicon showed band inversion, or increased reflectance through an absorbance band when compared to a substrate without a film. This is a result of the low k value of the substrate, and band inversion has also been shown by other authors (24,37).

2.1.3 Applications of Reflection Absorption Spectroscopy

With the advent of inexpensive FT-IR infrared spectrophotometers and inexpensive attachments, a tremendous amount of research has been done in the past decade to analyze thin coatings on metals. More recently, the interest has expanded to include substrates that are relatively infrared transparent. A number of workers have recently reviewed both the theoretical and experimental aspects of reflection absorption spectroscopy (5,9,10). The technique has been applied to a variety of experimental problems including thin film characterization, polymer/metal interfacial characterization, orientation of molecules at surfaces, and adsorption of small molecules.

2.1.3.1 Characterization of Polymer Surface Modification

Often in adhesion applications it is desirable to modify the surface of a polymer

or other material to induce specific chemical or physical changes which enhance the bond strength or durability. In the case of polymers, it is often necessary to modify the surface without altering the bulk properties of the polymer. One method commonly used to modify polymer surfaces is by using wet chemical techniques. Here, modification is controlled by the specific chemistry involved, and depth of modification can be controlled by a variety of experimental factors including time and temperature. Whitesides et al. have analyzed the oxidation of polyethylene by chromic acid using the techniques of contact angle titration and attenuated total reflectance (38). McCarthy has used both contact angles, XPS, and ATR to analyze the surface functionalization of fluorinated polymers prepared by a variety of synthetic routes (39,40). The use of reflection absorption spectroscopy has been limited, but in a recent work, Lee et al. used reflection absorption spectroscopy to study the modification of polyimide surfaces by potassium and sodium hydroxide. Treatment resulted in a polyamate surface layer that could be treated with acid to yield polyamic acid. By using a calibration curve for peak absorbance versus thickness for the 1740 cm^{-1} band, the thickness of the modified layer could be estimated (41).

A second commonly used method to increase adhesive strength is the surface modification by low pressure gas plasma treatment. The advantage of such a treatment is that the modification is usually restricted to the uppermost layers of the substrate, thus not affecting the overall desirable bulk properties of the substrate adherend. The energetic environment of the plasma creates surface free radicals that can lead to the possible cleaning, ablation, cross-linking or chemical modification of the substrate surface (43).

To analyze the chemical modification of polymer substrates, many studies have used x-ray photoelectron spectroscopy (XPS), while comparatively few other spectroscopic techniques have been utilized. These have included the use of secondary ion mass spectrometry (SIMS) and neutron activation analysis (NAA) to study nitrogen and ammonia plasma treatment of polystyrene and polycarbonate (44). The use of infrared techniques has also proven useful in a limited number of studies. Attenuated total reflectance has been used to study the ammonia plasma treatment

of polytetrafluoroethylene (45) while reflection absorption spectroscopy has been used to investigate the surface modification by various plasma gases on thin polymer films (46,47).

2.1.3.1.1 Atomic Oxygen Degradation

It is well known that exposure of polymeric materials to the atomospheric conditions found in low earth orbit (LEO) often results in unacceptable surface erosion due to interaction with atomic oxygen. Due to the importance of polymer coatings on the exterior of space structures (e.g. thermal blankets), there has been extensive research to find polymeric materials that are resistant to atomic oxygen and remain intact over the lifetime of the particular application. Studies have been performed where the erosion rates have been measured for polymers exposed to LEO environment (48). Often, however, exposure to a microwave or radio frequency generated plasmas is used to monitor ablation rates of polymers (49,50). While plasmas have a wide range of excited oxygen species and the flux and energy are much different than that encountered in LEO, the method provides a good qualitative evaluation of polymer stability in an aggressive oxygen environment.

Many studies have focused on the use of inorganic coatings that provide protection to the underlying polymer (49,51). Concern exists, however, that pinholes or cracks in such coatings would lead to localized erosion in the substrate polymer. Clearly, one component polymer films which show atomic oxygen resistance as well as superior mechanical properties would be desirable. To date, only silicone based polymers seem to offer significant improvements in the resistance to atomic oxygen degradation. This has been attributed to the formation of a non-volatile surface silicate layer which protects the underlying polymer from further erosion (52). It has been shown for polyimide-polydimethylsiloxane copolymer systems that the siloxane segments segregate to the surface and are then transformed to a silicate like structure upon exposure to atomic oxygen (53,54).

Little work has been performed to investigate the oxygen plasma treatment of phosphorus containing polymers. A recent investigation of polyphosphazenes by x-ray

photoelectron spectroscopy (XPS), however, did show a reduced etch rate when exposed to atomic oxygen and oxygen plasmas (55). Results showed an enrichment of both oxidized nitrogen and phosphorus surface species.

While several studies have deduced the mechanism of atomic oxygen resistance for siloxane containing materials by XPS (53,54,56), little complementary infrared data can be found due primarily to the limited amount of material in the thin surface layer (52). Clearly, new infrared techniques are needed analyze the chemical changes associated with exposure to LEO.

2.1.3.2 Interphase Characterization

Reflection absorption spectroscopy has been used extensively to help understand the interaction of polymers with metal substrates. This is of great importance in adhesively bonded systems where interfacial characteristics may be critical in determining bond performance or bond durability.

Carter et al. investigated the interaction of a dicyandiamide cured epoxy with zinc oxide and zinc metal (57). On curing, the reduction of the dicyandiamide by metallic zinc was implicated with no reaction occurring when the polymer was coated with zinc oxide. Ishida analyzed the interaction of epoxy resin on acid cleaned copper surfaces at a temperature of 150°C and found that a cured epoxy film of approximately 20 nm remained on the surface after treatment (58). It was postulated that such surface film formation could explain the increased shear strength of epoxy/steel plate bonds where the steel had previously been heat treated in uncatalyzed epoxy resin (59). In an analysis of modified polyethylenes, Ishida et al. showed that for poly(ethylene- co-butylacrylate) films, a shifting of the carbonyl absorbance maximum from 1735 cm⁻¹ to 1727 cm⁻¹ was interpreted as an indication of hydrogen bonding between the modifier and the aluminum surface (60). Boerio and Ondrus, in analyzing the interphase of cured epoxy films on copper and aluminum, determined that the anhydride curing agent reacted with copper substrates to etch the surface oxide and form a carboxylate salt (61). Carboxylates were also detected on aluminum surfaces, but no oxide etching occurred.

While infrared reflection absorption has been used primarily to study systems involving films or absorbed species on flat reflective substrates, recent efforts have extended the analysis to samples of different geometries. Xue et al. obtained the external reflectance spectra of iron and copper wires using diffuse reflectance optics (62). They showed that the failure surface of steel cord in reinforced rubber could be analyzed by this technique. Claybourn et al. using spectra reflectance with an infrared microscope, analyzed several opaque polymer pellets using a near normal incidence angle (63). Approximations of the n and k spectra were obtained from the reflectance spectrum using a commercially available Kramers-Kroenig transform based on an algorithm described by Harbecke (64). Analysis of hard opaque samples can also be analyzed by reflection at the Brewsters's angle to yield a spectrum more indicative of the true k spectrum and free from refractive index effects (37,27).

2.1.3.3 Molecular Orientation

Due to the technological importance of thin films in the design of optical and electronic devices, there is a tremendous interest in understanding the chemical and physical aspects of thin ordered films (4). Due to the anisotropic nature of the electric field vector upon reflection from a surface, RAS as well as other reflection techniques (ATR, IR ellipsometry) have become important complementary techniques to more classical techniques of x-ray or electron diffraction in the determination of molecular order in thin films.

Given the highly ordered nature of Langmuir-Blodgett (LB) films and spontaneously ordered monolayers, a number of studies have investigated the orientation of such films against a variety of solid surfaces. Allara and Swalen used RAS to help analyze LB films of cadmium arachidate on silver (65). By using reflection spectroscopy, which is sensitive to dipole transition moments perpendicular to the surface, and comparing these spectra with simulated spectra based on bulk data using optical theory, it was concluded that the cadmium arachidate layers were adsorbed at the surface via the carboxylate group, with aliphatic tails extending almost perpendicular to the surface. This type of analysis was extended to deduce the

orientation of spontaneously formed n-alkanoic acid monolayers on aluminum (66). Rabolt et al. also studied cadmium arachidate LB films and determined the orientation present by a combination of reflection absorption spectroscopy on silver and transmission measurements of films deposited on silver bromide (67). In transmission, the resulting electric field vector is parallel to the surface while RAS at grazing angles generates an electric field vector perpendicular to the surface. By combining these two techniques, both absorbances with dipole transitions moments parallel and perpendicular to the surface can be sampled. Figure 2.4 shows the results of this analysis and clearly demonstrates the anisotropic nature of the film. The symmetric -CO_2 stretching vibration is enhanced in reflection while the asymmetric -CO_2 mode is enhanced in transmission. Analysis of all absorbance modes showed that aliphatic chains must pack in an orthorhombic crystalline structure with aliphatic chains perpendicular to the surface (67). Chollet et al. also used a combination of reflection and transmission spectroscopy to determine orientation in stearamide monolayers on fluorite (68). The analysis indicated a greater degree of tilt ($\sim 25^\circ$) of monolayer tails for this system compared to the aliphatic tails above. Debe and Field have used reflection absorption spectroscopy to study orientation of phthalocyanine films on copper substrates (69). The films were ordered with the main b axis perpendicular to the surface when deposited at 8°C but ordered parallel to the surface when deposition was carried out at 70°C .

While studies have used optical modeling to show orientation by deviation of experimental spectra from simulated spectra based on bulk optical properties (65,66), recent studies have attempted to simulate anisotropic spectra for uniaxially anisotropic monolayers. Ishino and Ishida, using a combination of infrared ellipsometry to determine the extraordinary optical constants (n_e, k_e) and transmission measurements to determine the ordinary optical constants (n_o, k_o), used exact optical theory to simulate anisotropic spectra (70). The procedure follows Drude's original approach (64) and involved using n_e, k_e, n_o and k_o in modified Fresnel equations to calculate reflectivity at each interface. The results showed that experimental spectra could be closely simulated using this approach. Fina and Tung theoretically

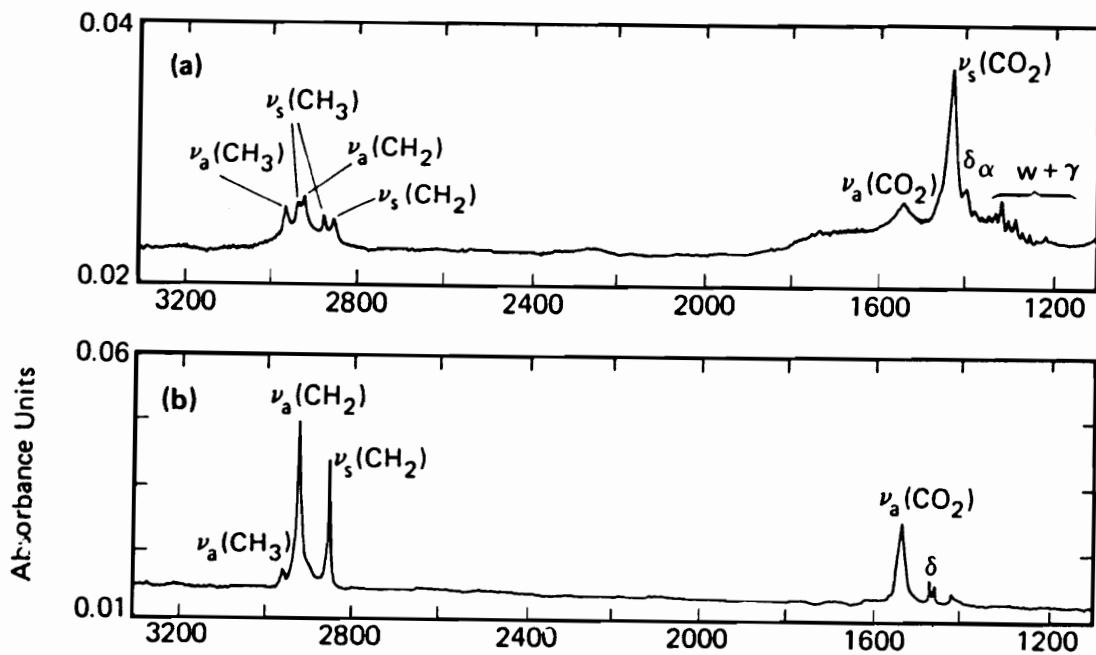


Figure 2.4 Infrared spectra of cadmium arachidate for (a) six monolayers on silver with **E** normal to the substrate, and (b) eighteen monolayers on silver bromide with **E** parallel to substrate. (Text and figure taken from Ref. (9)).

investigated the problems associated with analyzing uniaxially anisotropic monolayers on water surfaces (71). The approach here was to model the optical constants in the x and z direction, and incorporate these into Fresnel formulae as outlined by Schopper (72). Effects of the angle of incidence and polarization were explored to optimize conditions necessary for the detection of orientation in thin films.

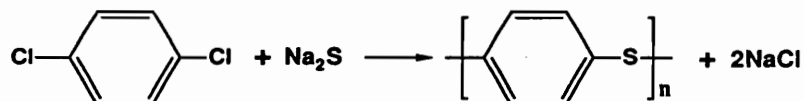
Unlike the well ordered nature of Langmuir-Blodgett (LB) films or spontaneously ordered monolayers, the orientation of polymer films in contact with solid surfaces has received little attention both theoretically or experimentally. A number of studies have alluded to, however, the unique ordering of polymers against surfaces. Ishida, using reflection absorption spectroscopy, demonstrated the unique orientation of PEEK against graphite single crystals (73). Comparing spectra obtained from both quenched and annealed thin films as well as by analyzing model compounds, perpendicular orientation was indicated between the surface normal and the main polymer chain direction. Application of optical theory also helped to eliminate optical effects. Boerio and Chen analyzed adsorbed epoxy films on both copper and iron, and showed that very thin films (~ 1.5 nm) were adsorbed on both surfaces (74). Analysis of infrared peak intensities by IRRAS also indicated that the films were adsorbed in a vertical conformation. More recent efforts to understand orientation of polymers at surfaces were made by Novotny et al. in the investigation of polyperfluoropropylene oxide (PPFPO) thin films against silver surfaces (75). They demonstrated by monitoring peak intensity ratios, that the polymer conformation in films less than 10 nm is much different than that found for the bulk, and suggested that polymer chains were oriented in the plane of the substrate.

2.1.4 Materials/Polyphenylene Sulfide (PPS)

2.1.4.1 Chemistry

Although thought of as a relatively new engineering thermoplastic, the first reports of the synthesis of PPS type resins date back almost 100 years (76). Although many synthesis routes have been proposed in early studies, Phillips Petroleum developed an improved method process based on the polycondensation of

p-dichlorobenzene with sodium sulfide in N-methyl-2-pyrrolidone at high temperatures and pressures:



This synthesis route forms the basis of the commercial production that started almost two decades ago. Modifications to this process were reported later to include alkaline metal carboxylate compounds which result in PPS of much higher molecular weight (77). A thorough review of the mechanisms involved has been recently presented (78).

2.1.4.2 Properties

Since polyphenylene sulfide contains only carbon-sulfur, carbon-carbon and carbon-hydrogen bonds that are relatively thermodynamically stable, this polymer exhibits superior stability at elevated temperatures. To demonstrate this, Figure 2.5 shows the thermogravimetric analysis of PPS compared to several other polymers. The high temperature resistance of PPS is clearly demonstrated here and the oxidative resistance is also demonstrated by the fact that PPS degradation in air is less than of polytetrafluorethylene which was run under a nitrogen environment. Thermal stability and the tendency to char upon burning also translates into superior flame resistance for PPS (79,80). The stability of the PPS backbone not only aids in resistance to thermal or oxidative degradation, but also imparts a high resistance to chemical solvent attack. In fact, there are no known solvents for this polymer below 200°C (79,80).

PPS is a semi crystalline polymer possessing a high crystalline melting point (T_m) of approximately 285°C, as determined by differential scanning calorimeter (DSC) (10°/min) (80). In amorphous samples, a relatively low glass transition temperature (T_g) of 85°C was indicated by DSC, followed by an exothermic

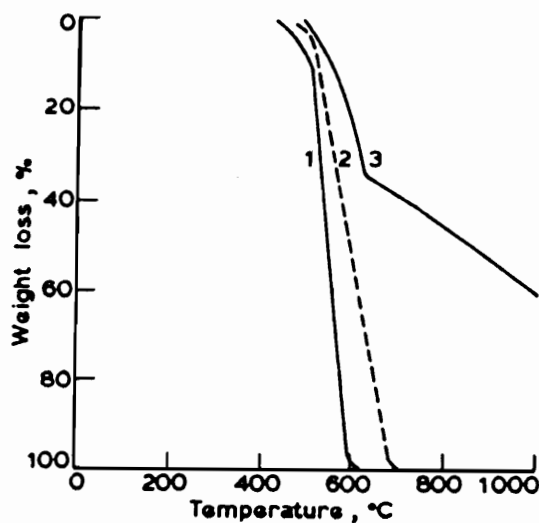
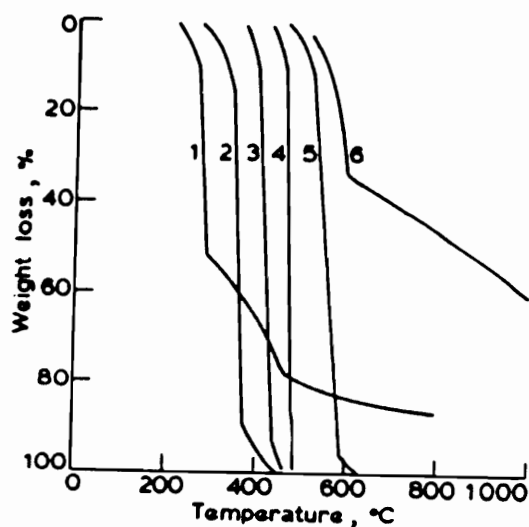


Figure 2.5 Plots shown for (a) thermal gravimetric analysis of polymers under nitrogen for (1) polyvinylchloride; (2) polymethylmethacrylate; (3) polystyrene; (4) polyethylene; (5) PTFE; (6) PPS and (b) thermal gravimetric analysis for (1) PTFE under nitrogen; (2) PPS under nitrogen; and (3) PPS in air. (79)

crystallization (T_{cc}) peak at 120-130°C. For samples cooled from the melt (10°/min), a crystallization exotherm (T_{mc}) was indicated at 220°C. A typical DSC trace is shown in Figure 2.6.

2.1.4.3 Thermal Cure

Under appropriate conditions, polyphenylene sulfide has the unique property of possessing both characteristics of a thermoset as well as a thermoplastic polymer. Upon heating in air at elevated temperatures, PPS will undergo a series of chemical changes that result in properties that are associated with an increase in molecular weight, (e.g. increase in melt viscosity) (79,80). Curing at moderate temperatures (175°-280°) results in a tougher material that can then be later processed, and this method provides a convenient method of tailoring melt viscosity for a particular application. Curing at temperatures exceeding the crystalline melting point results in an intractable material, and this method is useful for the formation of tough, flexible coatings (82).

The chemistry of PPS cure is not completely understood but seems to involve a variety of reactions, and several studies have been performed to help elucidate the mechanism of PPS cure (83-85). Although the results depended somewhat on the exact experimental conditions, evidence seems to indicate C-S bond homolysis with subsequent crosslinking of the polymer. Oxidation reactions and evolution of small chain fragments were also observed. In a detailed study of both PPS polymer and oligomers, Hawkins showed that cure involved chain extension involving disproportionation reactions, oxidative cross linking, thermal cross linking, and oxygen uptake followed by SO₂ loss (86). Figure 2.7 shows a schematic representation of those processes thought to be involved in the cure. Infrared analysis was consistent with this scheme and showed the presence of aryl ether functionality, tri-substituted ring structures and decreased C-S moieties.

While curing below the crystalline melting point had little effect on crystallinity, crystallization was significantly reduced upon remelting and annealing the polymer (87). This is consistent with the formation of crosslinks upon

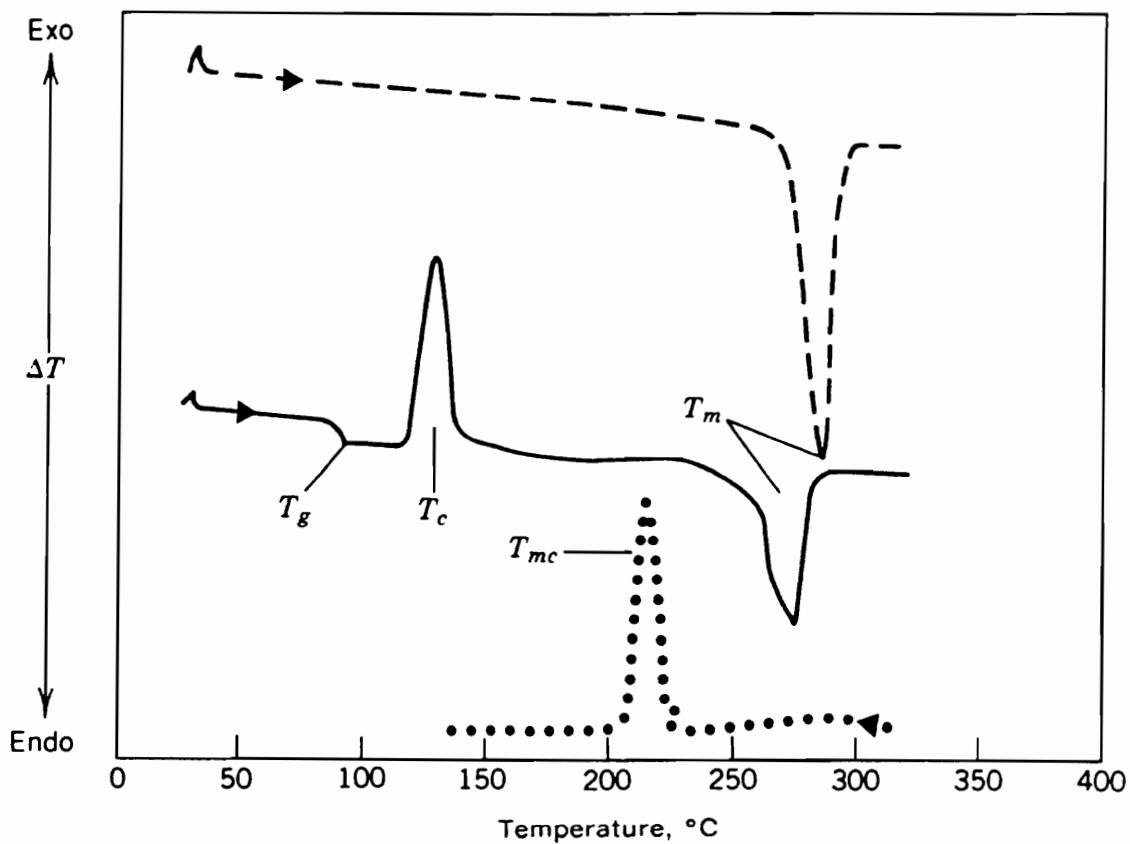


Figure 2.6 A typical differential scanning calorimeter trace for polyphenylene sulfide showing heating traces for (—), quenched amorphous; (---), annealed crystalline; and (···), the cooling curve from the melt. (81)

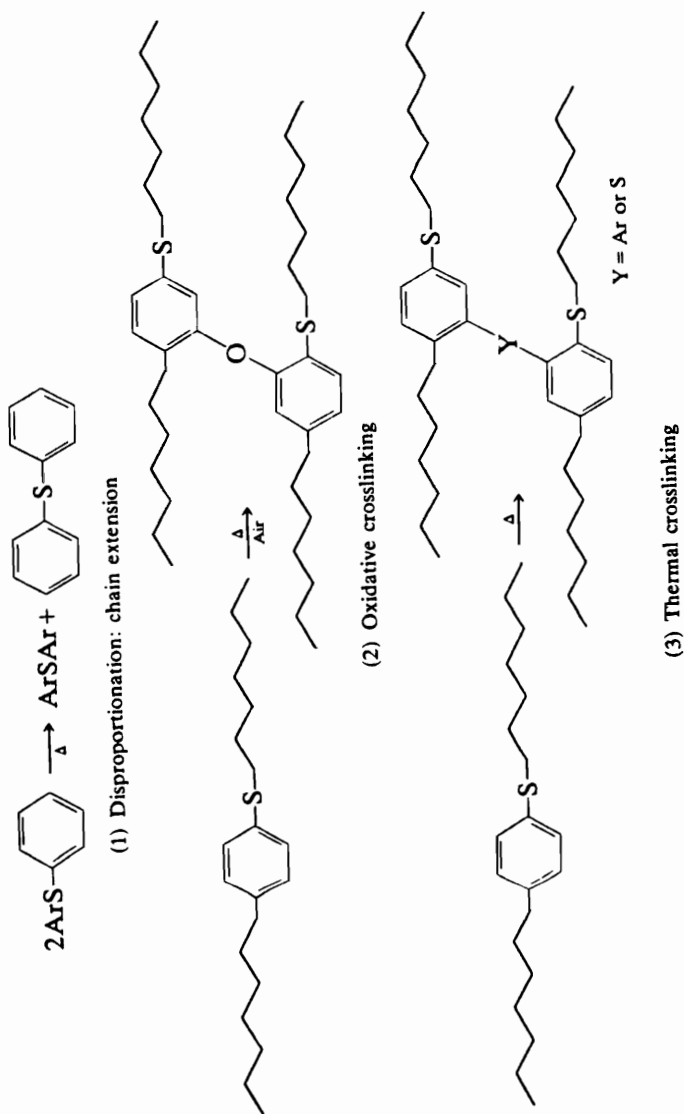


Figure 2.7 General reaction scheme of polyphenylene sulfide cure. (79)

cure. PPS coatings have also been analyzed, and Joshi and Radhakrishnan have examined the effect of cure for PPS coatings on aluminum substrates by SEM, x-ray diffraction, and attenuated total reflectance (88). Results showed only small amounts of crystallinity on annealing films cured at lower temperatures (350-370°C), and no crystallization for films cured at higher temperatures. Infrared results suggested tri- and tetra- substitution suggesting crosslinking as well as the possible presence of five member ring structures indicating possible dibenzothiophene structures. While curing is typically performed in air, degradation studies have also been performed under vacuum conditions (83). Thermogravimetric analysis of PPS degradation under these conditions showed negligible weight loss up to approximately 350°C (heating rate of 2.5°/min) and heating at higher temperatures resulted in a variety of volatile compounds where hydrogen sulfide was the major component. Other chain fragments were detected including diphenyl sulfide, dibenzothiophene, and thianthrene among others (83). Figure 2.8 shows postulated reaction schemes. Curing reactions have also been carried out under nitrogen and have been shown to be much slower than in an air atmosphere (89). Curing of oligomers under nitrogen showed that while disproportionation reactions continue, virtually no cross linking occurs (86).

2.1.4.4 Crystallinity and Crystallization

PPS is a highly crystalline material possessing a crystallinity index of 65% as determined by x-ray diffraction measurements (87). The crystal structure of PPS has been determined by x-ray diffraction to be very similar to that of poly-p-phenylene oxide (90) and an orthorhombic unit cell is indicated with lattice parameters $a = 0.867$ nm, $b = 0.561$ nm and c (chain axis) = 1.026 nm. The structure of the unit cell is shown in Figure 2.9 and shows two molecular chains passing through the unit cell, one in the center and one at the corners. A bond angle of 110° is indicated with alternating phenylene groups $\pm 45^\circ$ to the (100) plane. Amorphous samples of PPS (< 5% crystallinity by x-ray diffraction) can be easily prepared by heating samples slightly above the crystalline melting point and quenching. Crystallization has been shown to occur rapidly upon heating above 120°C (87). In depth analysis of the

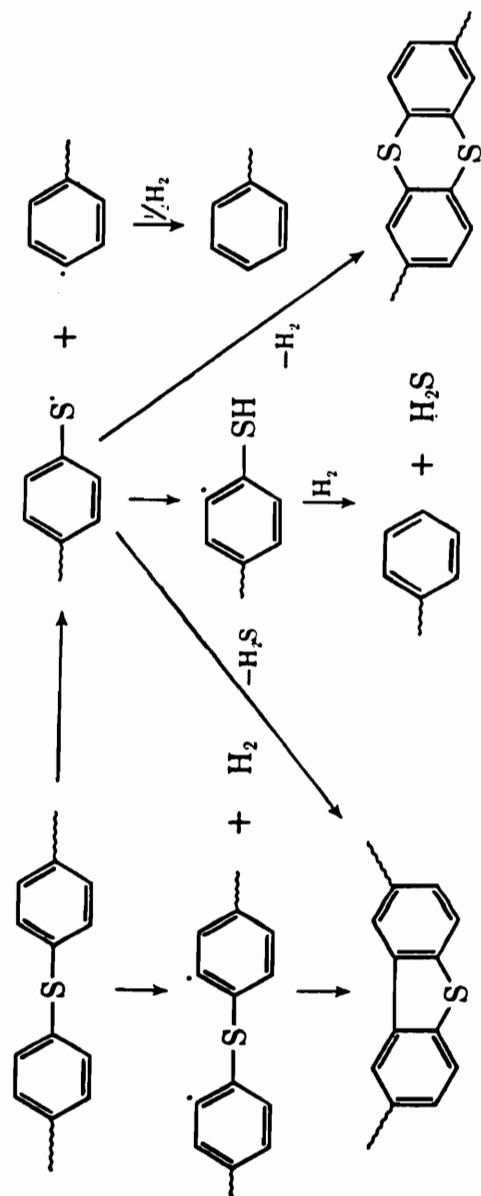


Figure 2.8 Postulated reaction schemes for the thermal cure of polyphenylene sulfide under vacuum conditions. (83)

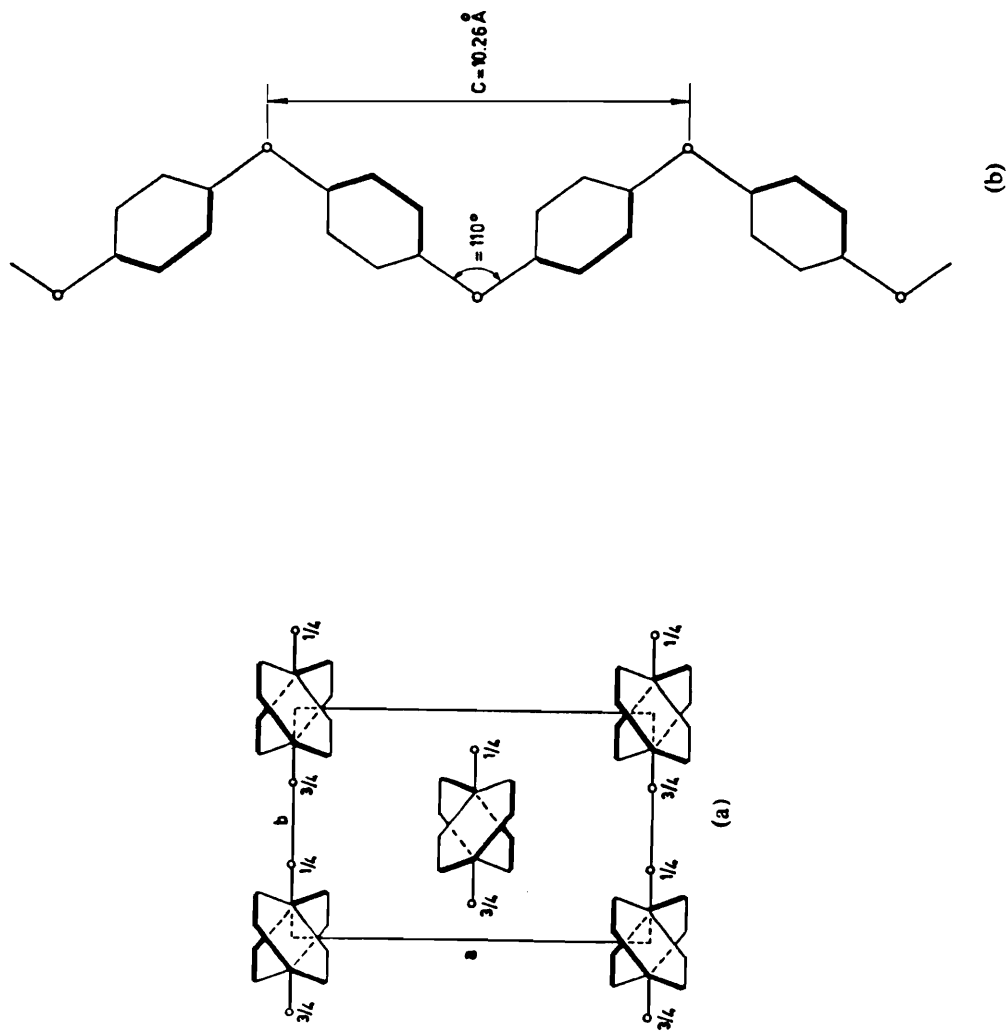


Figure 2.9 Illustrations for (a) the crystal structure of polyphenylene sulfide, projected on the *ab* plane, and (b) the polymer chain conformation, projection in the *bc* plane. (90)

isothermal crystallization kinetics of bulk PPS has been performed as a function of molecular weight (91), and branching agent content (92). Non-isothermal crystallization studies have also been reported (93).

Due to the increasing importance of semicrystalline polymer resins (PPS, PEEK) in composite systems, there is a tremendous interest in studying the effects of reinforcing unidirectional fibers on the morphology of the matrix phase. In particular, many studies have examined the role of the reinforcing fiber on the initiation of heterogeneous nucleation at the surface. Such nucleation can lead to transcrystalline growth, where the lamellae will grow in one direction only, perpendicular to the fiber surface.

A number of studies have been reported to detail the conditions under which transcrystalline growth can be initiated. The results are often contradictory, indicating that particular processing conditions involved may have a large effect on the development of transcrystalline growth. Many factors have been studied including substrate chemistry (94), substrate crystalline morphology (95), and surface energy (96).

While many studies have focused on carbon, glass, or polymer fibers, transcrystallinity has also been observed in a copper/polypropylene systems where it was found to alter the pullout characteristics of embedded copper wires (97). Schonhorn and Ryan found that the adhesive joint strengths for polyethylene/epoxy bonds could be enhanced by first molding a polyethylene film against high energy aluminum under conditions producing a transcrystalline surface layer (96). Foenkes et al. suggested that polymer orientation at surfaces due to flow induced stresses could produce sheets of chain extended crystalline morphology (98). For polyphenylene sulfide, Johnson and Ryan have shown that transcrystallinity can develop in carbon fiber/PPS systems (99). López and Wilkes also examined the crystallization morphology in carbon fiber/PPS systems and demonstrated that many factors are involved in the development of transcrystalline surface morphology including the cooling rate from the melt and polarity of the fiber surface (100). Inducing an interfacial shear stress also resulted in an increase in transcrystalline growth, and

this result is in agreement with results from other studies (98,101).

2.1.4.5 Infrared Analysis

While infrared analysis of polyphenylene sulfide has been published in a number of studies (83,102-106), the spectra are of various quality, due to the difficulty in preparing thin uniform infrared transparent films of PPS. Although tentative absorbance band identification has been attempted, unambiguous assignment has come only recently with an in depth analysis of PPS oligomers and polymer by infrared and raman spectroscopy (107). Figure 2.10 shows the IR spectrum obtained for a sample of PPS powder in KBr and Table 2.1 gives the assignments made for all bands seen. As can be seen all peaks present are due either to local ring motions or sulfur-phenyl groups. Infrared analysis of both amorphous and crystalline PPS indicate that there are several spectral features associated with the amorphous content of the sample. Brady found an increase in absorbances at 7.2μ (1389 cm^{-1}) and 10.35μ (966 cm^{-1}), and a change in shape for the absorption at 12.2μ (820 cm^{-1}) after crystallizing amorphous PPS samples (87). Clarke et al. found that absorptions at 482 , 560 , 1097 , and 1900 cm^{-1} increased with increasing crystallinity while bands at 1080 and 1575 cm^{-1} decreased (103). A shifting of the out of plane C-H bending absorption from 810 to 822 cm^{-1} was also observed. Piaggio et al. suggested that the band intensity at 1571 , 1181 , 1075 , 741 , 706 and 630 cm^{-1} could be related to the amorphous content of the material (107). Cole et al., using diffuse reflectance infrared spectroscopy, monitored the ratio of peak intensities for the 1075 and 1093 cm^{-1} absorbance bands as a measure of crystallinity for composite prepreg surfaces (108). A linear relationship was found between this ratio and the enthalpy of crystallization as determined by differential scanning calorimetry.

2.1.4.6 Applications

Due to its characteristics of chemical resistance, ease of processing molded parts, as well as low dielectric constant and dissipation factor over a wide temperature range, PPS has found wide application in the electrical / electronics industry (109).

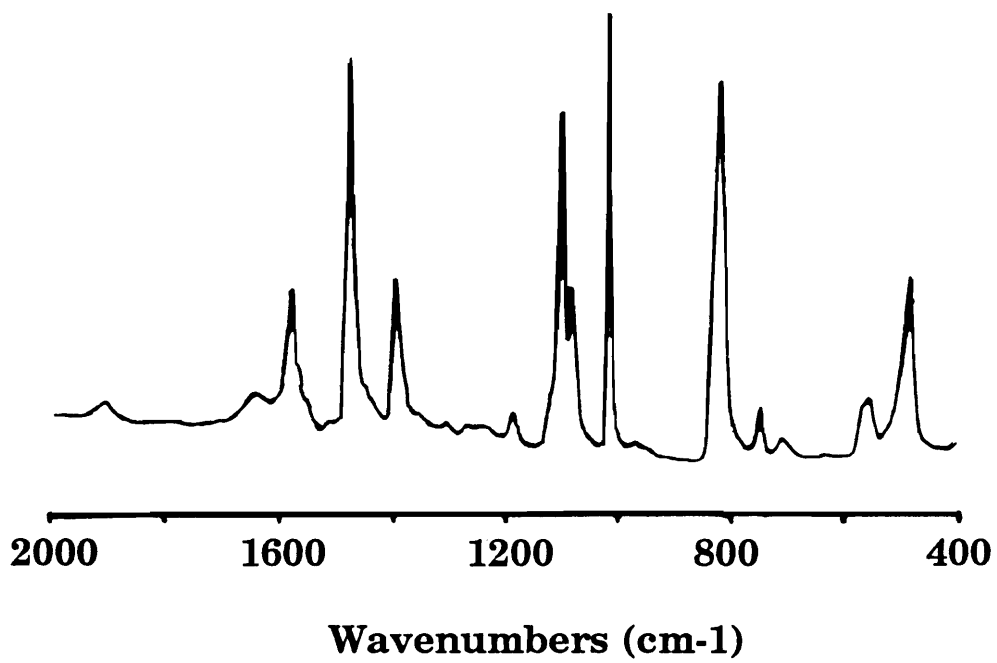


Figure 2.10 Infrared spectrum of PPS powder in KBr. (107)

Table 2.1 Infrared Absorbance Band Assignments for Polyphenylene Sulfide. (117)

<u>Peak Position</u>	<u>Assignment</u>
1572*	ring stretch
1471	(s) ring stretch
1390	(ms) ring stretch
1181*	C-H in-plane bend
1109	(w) ring-S stretch
1096	(s) ring-S stretch
1075	(s) ring-S stretch
1010	(s) C-H in-plane bend
818	(vs) C-H out-of-plane bend
812*	
743*	C-H out-of-plane bend
630*	ring in-plane bend
566*	ring-S deformation
556	(mw) ring-S deformation
483	(ms) ring-S deformation

* - depends of the amorphous content

vs - very strong; s - strong; m - medium; mw - medium weak; w - weak; vw - very weak

Molded parts include electrical connectors, feed throughs, switch components, housings, and attempts have been made to encapsulate wire-bonded integrated circuits. Due to excellent mechanical properties and chemical resistance, pump components can be molded from PPS for use with solvents or corrosive materials (79). The automotive industry also has found use for PPS molded parts when heat and chemical resistance as well as dimensionally precise and stable parts are needed (79). Another use for PPS has been in the area of specialty coatings (82). Applications that can utilize the chemical resistance properties of PPS to form protective coatings have been used to coat pipes. When Teflon™ is incorporated with PPS, coatings can be made combining the thermal and chemical properties of PPS with the release properties of Teflon™. These coatings have been used to coat metal substances by electrostatic powder coating, fluidized bed coating, or powder spraying, and can be used as "non-stick" coatings in cookware (79,82). Curing in air is done after deposition of the coating to ensure a non-crystalline moderately crosslinked film (82).

2.2 EXPERIMENTAL

2.2.1 Analysis of Polyphenylene Sulfide Films

2.2.1.1 High Temperature Spin Coating

Since there is no known solvent for polyphenylene sulfide below approximately 200°C, new methods were developed to coat uniform films of this polymer. A high temperature spin coating unit was designed and a schematic is shown in Figure 2.11. Operation consisted of either a "cold" start where a sample was placed in the chamber at room temperature, purged with nitrogen for a given length of time, and then rapidly heated to the set temperature, or a "hot" start where the heating chamber was removed at temperature, a sample placed in the chamber, and the purged oven immediately replaced. The first technique had the advantage of limiting substrate oxidation, while the second minimized the time required between coatings. Typical heating rates are given in Figure 2.12 for both "hot" and "cold" heating procedures, and temperatures reported are for a ferrotype plate measured with a surface temperature probe (OMEGA, Inc., Model 88012K)). Other critical operation

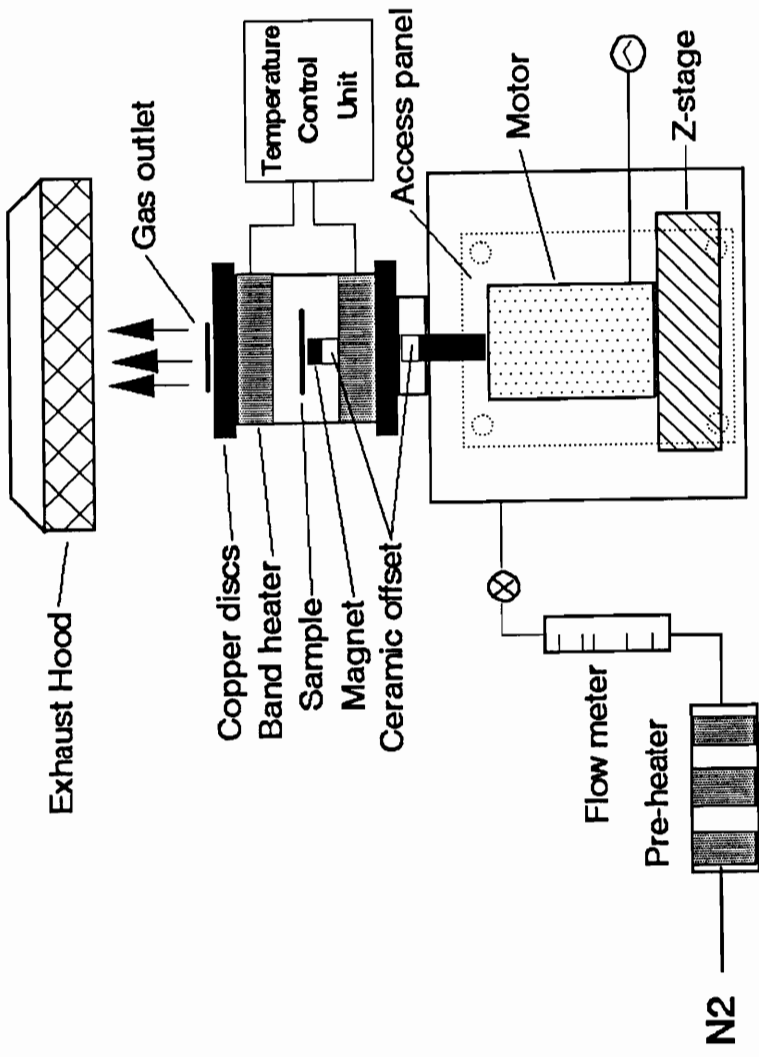


Figure 2.11 Schematic diagram of the high temperature spin coating unit.

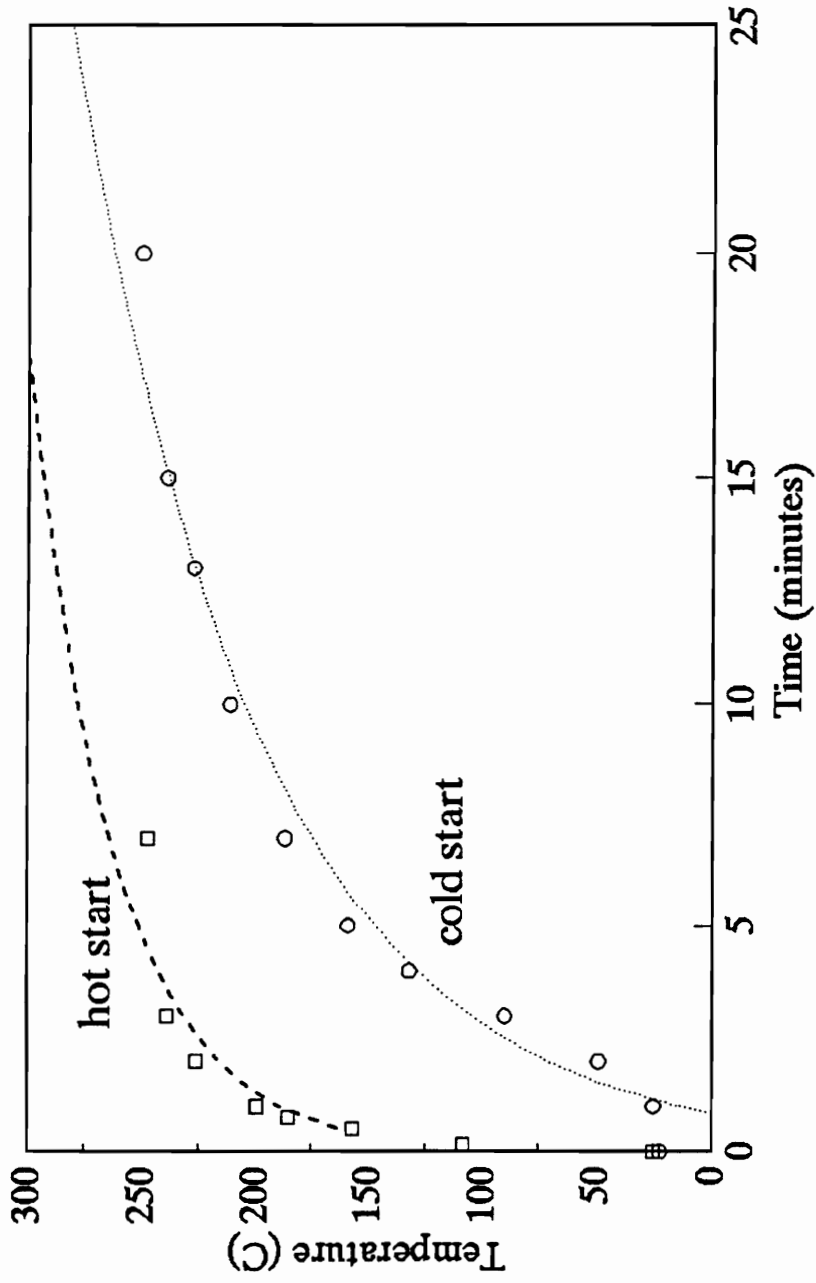


Figure 2.12 Typical heating rates for both "cold" and "hot" starts using the high temperature spin coater.

parameters are given in Table 2.2. After coating, the coating oven was typically purged with nitrogen or air at temperature until residual vapor had evaporated. Several suitable solvents for PPS were found including benzophenone, diphenyl ether, benzyl benzoate, diphenyl sulfone, and α -chloronaphthalene. All dissolved PPS under slightly different temperature ranges and concentrations, but benzophenone (Fisher, reagent grade) was selected as the solvent of choice due to the limited degradation at elevated temperatures and low toxicity. This solvent was also found to be extremely suitable for preparation of poly(ether-ether-ketone) (PEEK) films. To minimize oxidation, solvent samples were degassed with nitrogen at 70°C for 1 hour prior to use.

The metal substrate used was ferrotype plate obtained from Thompson Photo Products (Bedford Park, IL) consisting of a 0.51 mm steel base plate with an approximately 80 nm surface layer of chromium. Typically, plates (3.81 cm \times 3.81 cm maximum) were secured to the shaft via the attached magnet, but to coat other types of materials, one of several methods was needed: (1) metals, including aluminum, copper, and silver were vapor deposited on acid cleaned ferrotype plates; (2) foil samples were attached to the underlying ferrotype substrate and secured by crimping the foil at the plate edges; (3) other rigid nonmagnetic samples were secured to ferrotype plates using ceramic cement (Omega, Inc.) and later detached after coating.

2.2.1.2 Thin Film Preparation

Chromium

Chrome plated steel substrates (ferrotype) were first cleaned using a radio frequency (13.56 MHz) plasma generator (Tegal Plasmod™). Samples were treated by two 15 minute oxygen plasma etches followed by rinses with water and acetone, and the substrate optical constants determined at 632.5 nm by ellipsometry. Solutions of PPS in benzophenone were then spin coated using the high temperature spin coating technique previously described.

Solution concentrations ranged from approximately 0.5 to 1.5 % (wt/wt), and after coating, plates were immediately brought to room temperature. The coated

Table 2.2 Typical Parameters for Spin Coating Thin Polyphenylene Sulfide Films (see Fig. 2.11).

Oven wall temperature	375°C
Oven volume	292 ml
Preheater temperature	120 - 140°C
Purge gas flowrate	2 - 3 LPM
Solvent	benzophenone
Solvent melting point	50°C
Solvent boiling point	306°C
Solution temperature	280°C
Transfer pipet temperature	280°C
Plate temperature (at coating)	240 - 250°C
Rotation speed	1550 rpm
Typical spin time	1 minute
Time to coat: cold start	20 minutes
Time to coat: hot start	7 minutes

plates were then used as prepared, or reheated to 340°C for 2 minutes under a stream of nitrogen and quenched in liquid nitrogen. For annealing studies, samples were held at 150°C for 5-60 minutes in air to crystallize the thin PPS film. Ellipsometric analysis of both amorphous and crystalline thin films was then performed.

Copper

Two types of copper samples were prepared. Copper foil (Olin, Inc. ETP 110 grade) was either used after a methanol wipe, or cleaned by an acid polish. Chemical polishing was done using a "brite dip" solution consisting of a 70:26:4 ratio of acetic acid (Fisher, glacial, 99.7%), phosphoric acid (Fisher, 85%), and nitric acid (Fisher, 70%) by volume. An etch time of 15 seconds was used followed by two distilled water washes, and the sample dried under a stream of nitrogen.

Copper films were prepared by vapor deposition on ferrotype (3.81 cm x 3.81 cm) chrome plates that had been previously etched in a 20% solution of hydrogen peroxide in concentrated sulfuric acid at approximately 60°C. Vapor deposition was carried out using pure copper wire (99.9985%, Johnson Matthey, Inc.) in a vacuum evaporator (Ladd Research Industries) operated at a pressure of approximately 1×10^{-6} torr. Copper oxide films were prepared by a sputter process using an Edwards (Model S1503) sputter coater utilizing an ETP grade copper foil covered copper cathode. The substrates were plasma cleaned ferrotype plates and after coating, films were fully oxidized by heating in air at 150°C for 15 - 30 minutes. Solutions of PPS in benzophenone (~ 1%, (wt/wt)) were then prepared using high temperature techniques previously described, and brought to room temperature immediately after coating. Samples were then dried at 110°C - 130°C for approximately 12 hours under vacuum. For quenched films, samples were heated rapidly to approximately 320°C under nitrogen and quenched in liquid nitrogen. Total time at this elevated temperature did not exceed two minutes.

Aluminum/Silver

Aluminum and silver vapor deposited samples were prepared in a manner as

described for copper, using aluminum (99.999%) or silver (99.9985%) wire (Johnson Matthey, Inc.). After vapor deposition, aluminum samples were oxidized in air at 150°C for 30 minutes. Solutions were spin coated and dried as described for copper.

Germanium

Germanium disks (0.2mm, Wilmad, Inc.) were cleaned prior to use by a two minute argon plasma etch using a Tegal Plasmod™ rf plasma generator operated at 13.56 MHz and 50 watts. A treatment time of two minutes was used and samples were then rinsed with distilled water and dried under a stream of nitrogen. Substrate optical constants were then determined by ellipsometry, and the substrates coated with PPS films from solution. Film thickness was then be determined by ellipsometry.

2.2.1.3 Extruded Films

For analysis of PPS films by attenuated total reflectance, slot extruded PPS films were obtained from Phillips Petroleum. The amorphous films were clear, and amber in color. Crystalline films were prepared by heating amorphous films above the glass transition temperature at approximately 200°C for 30 minutes in air.

2.2.1.4 Molded PPS

Molded resin was prepared by compression molding PPS powder (Ryton, Phillips Petroleum) between copper sheets using a 10.2 cm × 10.2 cm × 0.16 cm mold at 320°C and approximately 625 psi. Samples were first quenched in a cold press and then annealed in air at 150°C. The foil could then be easily peeled away to yield an approximately 16 mm thick molded specimen.

2.2.2 Analysis of Plasma Modified Polymer Surfaces

To investigate the surface modification of polyphenylene sulfide, films were prepared on ferrotype plates using high temperature spin coating methods (see section 2.2.1.1). For polystyrene, a well characterized standard was used with a molecular

weight of 104,000 and a polydispersity of 1.05 (Polysciences, Inc.). Samples were dissolved in chloroform in the concentration range of 0.5 - 1.0% (wt / vol). Solutions were then spin coated on plasma cleaned ferrotype plates previously analyzed by ellipsometry (see section 2.2.1.2). Film thicknesses were then analyzed by multiple angle ellipsometry. The poly(arylene ether) phosphine oxides used are shown in Figure 2.13 along with polysulfone. The synthesis and characterization of these polymers have been described elsewhere (130). and polysulfone was obtained commercially (Udel, Union Carbide). All samples were dissolved in either chloroform or chlorobenzene and spin coated from solution onto ferrotype substrates.

For the plasma treatment of thin films, a Tegal Plasmod™ was used to produce a radio frequency (13.56 MHz) generated 50W plasma of oxygen or ammonia. The pressure inside the treatment chamber was typically 1.2 torr.

2.2.3 Experimental Methods

2.2.3.1 Infrared Analysis

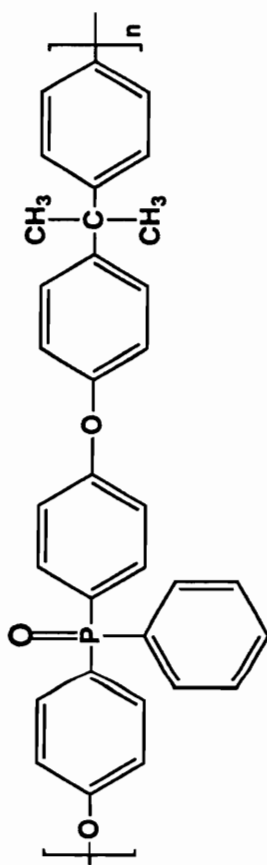
2.2.3.1.1 Determination of Optical Constants

Estimation of the PPS optical constants was done by experimentally measuring the transmission spectrum of thin free standing PPS film and applying the iterative method outlined by Ribbegård and Jones [14]. First, an infrared transmission spectrum was taken at 2 cm⁻¹ resolution and digitally stored as frequency vs transmittance. Initial k values were then estimated by Eqn. [2] and initial n values through the use of the Kramers-Kronig transform given as:

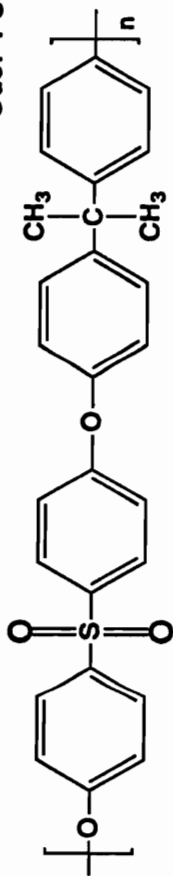
$$n_1 = n_\infty + \frac{2}{\pi} P \int_{\tilde{\nu}_a}^{\tilde{\nu}_b} \frac{\tilde{\nu} k(\tilde{\nu})}{\tilde{\nu}^2 - \tilde{\nu}_1^2} d\tilde{\nu} \quad [23]$$

The initial n and k values were then used in the calculations outlined by Eqns. [9] through [19], using exact theory, to simulate the transmittance spectrum. Differences between the experimental spectrum and calculated spectrum were then used to

Bis A PEPO



Udel PSF



BP PEPO

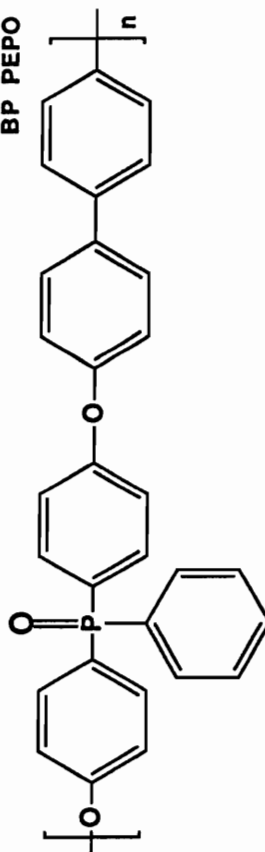


Figure 2.13 Chemical structures for Bis-A-PEPO, polysulfone, and BP-PEPO.

generate correction factors for k . New n values could then be calculated and the process repeated and the program for this calculation is given in Appendix 2.2 (Program NK10). Typically ten iterations gave satisfactory convergence.

To accurately determine the optical constants of spin coated PPS, both the refractive index at high frequency (n_{∞}) and the thickness of the film are needed. Unfortunately, due to the insolubility of PPS, preparation of samples amenable to optical measurements is difficult, and little data is available giving refractive index values. Also, due to the crystalline nature of PPS, optical properties may depend on the method of preparation and light scattering in crystalline samples may cause errors. To provide an estimate of the refractive index for spin coated samples, films ranging in thickness from 30 - 150 nm were spin coated on chromium substrates, heated to 320°C under a nitrogen stream, and quenched in liquid nitrogen. The refractive index was then determined by ellipsometry at a wavelength of 623.8 nm. The value obtained was 1.65 ± 0.02 . While the value for isotropic crystalline samples would be expected to be slightly higher than this, the orientation induced by spin coating could lead to an anisotropic refractive index, and ellipsometry would be sensitive only to the extraordinary component, perpendicular to the surface. Such anisotropy has been reported for polyimide films where the n_{\parallel} value was quite different than the n_{\perp} value (110). Due to this uncertainty, the n_{∞} values for amorphous samples were used as an approximation. Thickness values were then estimated using the Harrick method:

$$d = \frac{m}{2 ((n_f^2 - \sin^2\phi)^{\frac{1}{2}} \Delta)} \quad [24]$$

where n_f is the refractive index, ϕ is the incidence angle, and Δ is the interference fringe spacing for fringe interval m . An incidence angle of 5° was used in all measurements and fringes measured in the range of 500 - 7000 cm^{-1} .

2.2.3.1.2 Simulation of Optical Spectra

Using the determined values of n and k for PPS, optical spectra can be simulated for a variety of techniques including transmission, reflection absorption, and attenuated total reflectance using Eqns. [9] - [19]. A program (Program RAS14, Appendix 2.2) was written in Microsoft™ fortran for personal computer use. Optical constants for metals (Al, Cu, Au, Ag) were estimated using the Drude approximation:

$$\epsilon_1 = \epsilon_\infty - \frac{\omega_p^2}{\omega^2 + \omega_\tau^2} \quad [25]$$

$$\epsilon_2 = \epsilon_\infty - \frac{\omega_p^2 \omega_\tau}{\omega^3 + \omega \omega_\tau^2} \quad [26]$$

and n and k could be determined using Eqns. [7] - [8]. The values of the plasma frequency, ω_p , and the damping frequency, ω_τ , for these metals have been compiled by Ordall et al. (111). The optical constants for chromium were obtained from previously tabulated results (112,122).

2.2.3.1.3 Transmission Spectroscopy

All infrared measurements were made using a nitrogen purged Nicolet 510 spectrophotometer employing a triglycine sulfate (TGS) detector. A typical resolution of 4 cm^{-1} was used and 100 - 1000 scans were taken to achieve the desired signal-to-noise levels.

Samples for transmission measurements were prepared in one of two ways. In the first, solutions of PPS in benzophenone were spin coated onto unpolished 2.54 cm KBr windows. Samples were then dried at 110 - 130°C under vacuum (10^{-1} - 10^{-2} torr) for

approximately 12 hours to remove residual solvent present. Quenched samples were prepared by heating the sample on a hot plate oven to 320 - 340°C under nitrogen and quenching in liquid nitrogen. Residence times at these temperatures were less than five minutes. Annealing was done at 150°C in air to fully crystallize the amorphous film. The second method was identical to the first except that PPS solutions (1-10% wt/wt) were coated on polished KBr windows. After drying and quenching, an aluminum holder (1.52 cm x 3.56 cm) with a 0.635 mm center circular opening was attached to the film via double stick tape. The salt was then dissolved to yield a uniform free standing film. Films ranging in thickness from approximately 1 - 5 μ could be prepared in this manner

2.2.3.2.4 Reflection Methods

Retro-Mirror Design

Figure 2.14a shows a schematic diagram of the retro mirror reflection accessory. Typically, the incident light was polarized before reflecting from the sample, and careful laser alignment of the sample allowed angles up to 85° (from the surface normal) to be utilized.

In-situ thermal analysis

To analyze the IRRAS spectrum of thin PPS coatings at elevated temperatures, a modification to the retro-mirror design was necessary and a diagram of the design is shown in Fig. 2.14b. The modification consisted of an aluminum heater with a front surface retaining bracket for mounting film samples. The base was machined from high temperature ceramic (Macor) to insulate the lower metal holder. This design typically allowed operation temperatures up to 350°. The heater also allowed rapid heating, and a temperature of 320°C could be achieved in several minutes from room temperature.

Harrick Seagull™ Design

Figure 2.15 shows an illustration for the Harrick Seagull™ reflection attachment.

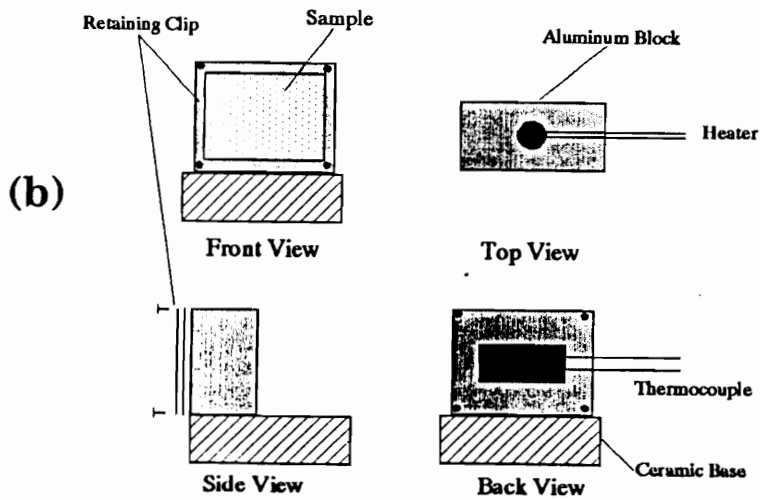
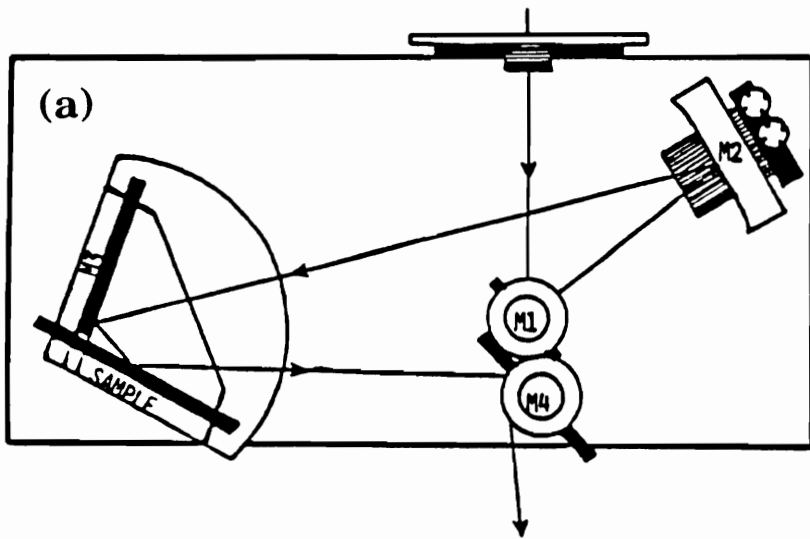


Figure 2.14 Schematic diagram of (a) the retro mirror reflection attachment, and (b) schematic of modifications to the holder design for high temperature operation.

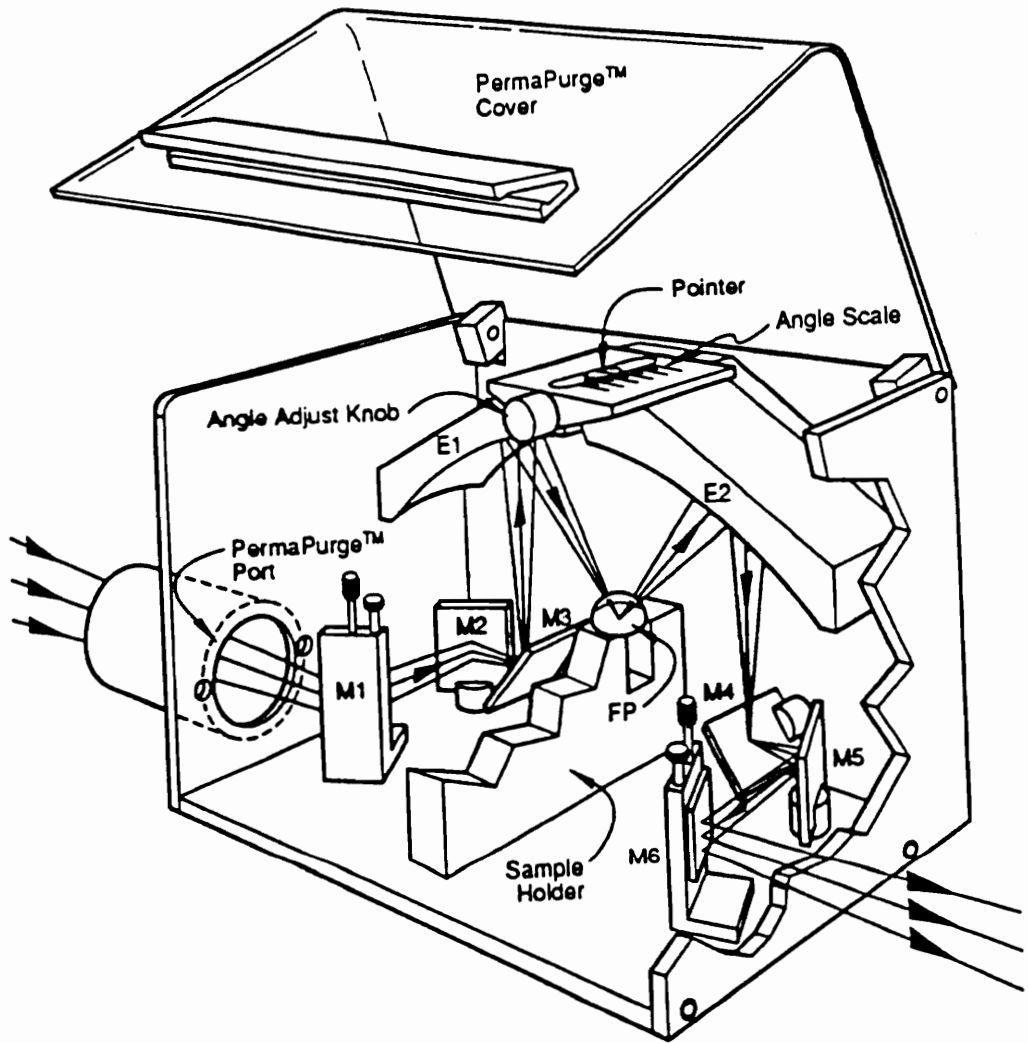


Figure 2.15 Illustration of the Seagull™ multipurpose reflection attachment. (114)

This attachment is a multipurpose unit, allowing measurements to be made in the external reflectance, internal reflectance, and diffuse reflectance modes. The use of a polarizer (Spectra Tech, Inc.) allowed both *p* and *s* states of polarization to be examined. The angle of incidence could be easily varied from 5 - 85° with a resolution of 0.5°. Variable angle attenuated total reflectance measurements were made using a zinc selenide hemispherical crystal. Details of the design and use of this attachment have been recently published (114).

2.2.3.2 Ellipsometry

Ellipsometry was used to determine the film thicknesses of the spin coated samples. The instrument used was a Gaertner L116A dual mode automatic ellipsometer. Both linear and circular polarizations were used and a continuous rotating analyzer was employed with automatic data sampling at 72 points for each state of polarization. A 1 mW helium-neon laser (632.8 nm) was used as the incident light source and the spot size analyzed was 1 mm.

All films were assumed to be transparent at this wavelength, i.e. $k_r = 0$. The optical constants of the substrate were always determined after cleaning and prior to polymer deposition. The refractive index of polystyrene was taken to be 1.58 (11) and that of the poly(arylene ether) phosphine oxides and polysulfone were determined by measurement at a 70° angle incidence for solution concentrations ranging from 0.5-1% in chloroform. For polyphenylene sulfide, only amorphous films were measured (after quenching), as the state of crystallinity in extremely thin PPS films and its variation with thickness are not known.

All thickness were confirmed by measurement at 30, 50, and 70° incidence angles to determine the correct period, since the measured parameters in ellipsometry (ψ, Δ) are periodic functions for transparent films.

2.2.3.3 X-ray Photoelectron Spectroscopy

XPS analysis was performed using a Perkin-Elmer PHI 5400 spectrometer employing a Mg K_α (1253.6 eV) achromatic X-ray source operated at 15 keV with a

total power of 400 W. Typical operating pressures were $< 1 \times 10^{-7}$ Torr and the surface area analyzed was either a 1 mm circular spot or a 1×3 mm rectangle. The spectrometer was calibrated to the $4f_{7/2}$ photopeak of gold at 83.8 eV and the $2p_{3/2}$ photopeak of copper at 932.4 eV, and all binding energies were referenced to the main C-H photopeak at 285 eV.

Angular resolved XPS analysis was done by varying the "takeoff angle" between the surface normal and direction of electron detection. Values between 10° and 90° were typically used in this analysis.

2.3 RESULTS AND DISCUSSION

2.3.1 Infrared Analysis of Polyphenylene Sulfide

2.3.1.1 Optical Constants

Determination of the optical constants by any method using the form of the Kramers-Kronig analysis in a limited frequency range requires the knowledge of n_∞ , the high frequency refractive index. This value has been taken to be that just outside the chosen integral region (24), while others have used the refractive index in the visible region (28,29). Errors in the estimation of n_∞ (or thickness) in this type of analysis will have the effect of altering the fringe pattern in the simulated spectrum. Convergence to the experimental spectrum will still occur but residual fringes will occur in the n and k spectra.

Figure 2.16 shows the average n and k spectrum for crystalline PPS in the range of $400\text{-}2000\text{ cm}^{-1}$ for films ranging from one to five microns. Little evidence for residual fringes is seen in the k spectrum even though it represents an average over a wide thickness range.

2.3.1.2 Transmission Spectroscopy

Figure 2.17a shows the transmission spectrum for a $1.55\ \mu$ freestanding film of crystalline PPS. Figure 2.17b shows the simulated spectrum calculated using exact optical theory. As can be seen, almost exact agreement between the two is obtained,

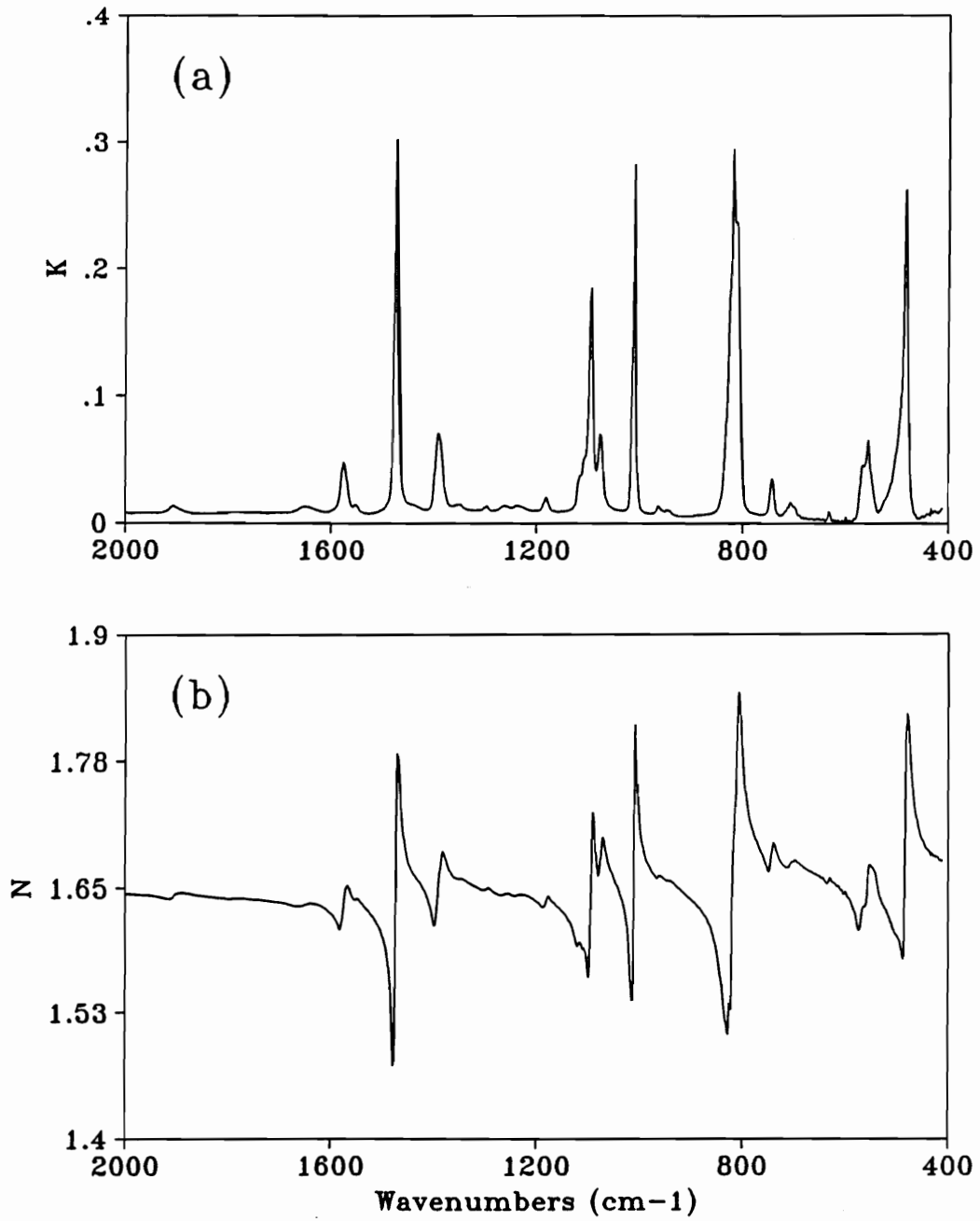


Figure 2.16 Optical constants for PPS in the 400-2000 cm^{-1} spectral region. Shown are plots for both (a) k and (b) n values.

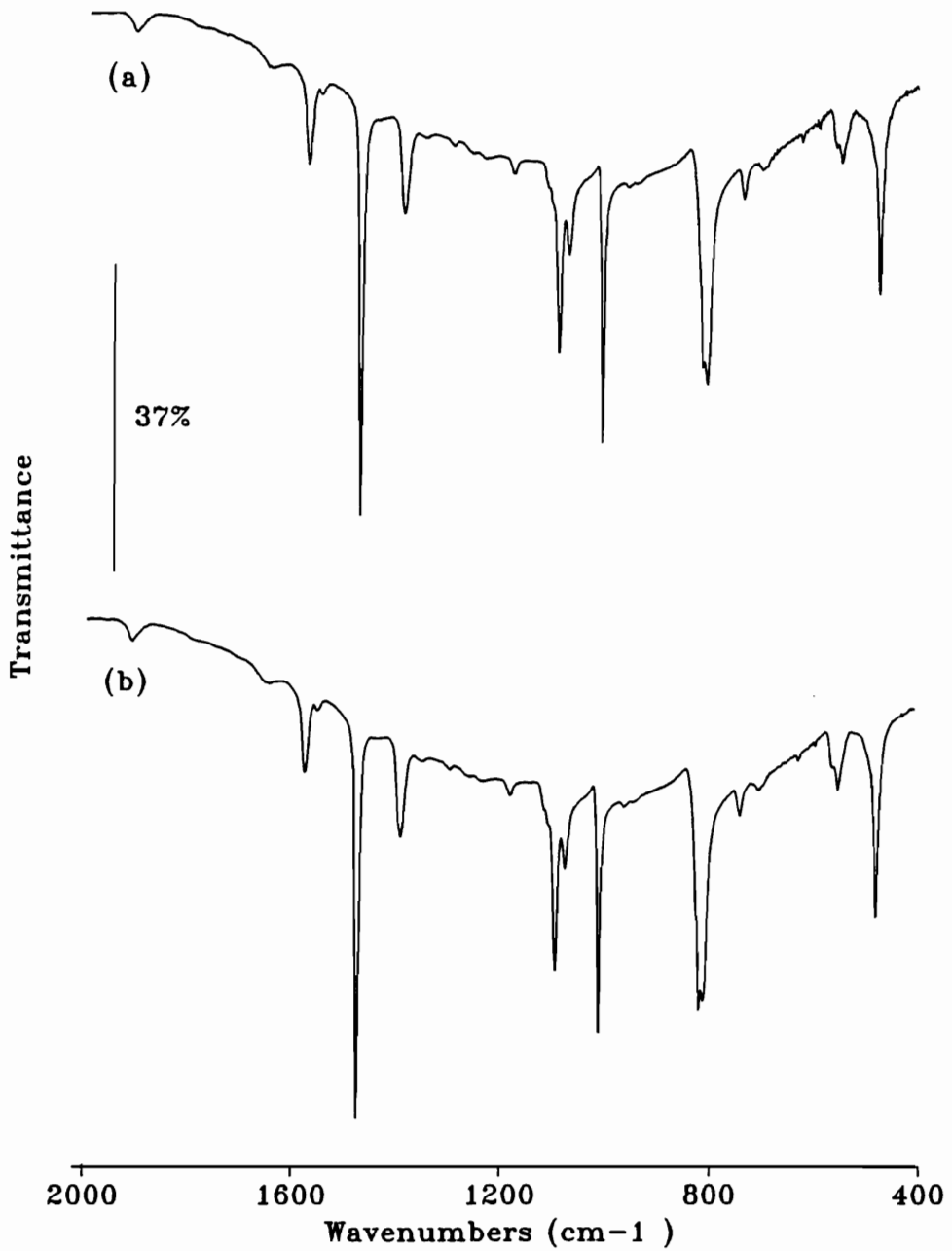


Figure 2.17 Comparison of the infrared spectrum of a 1.55μ free standing crystalline PPS film for (a) an experimentally measured spectrum and (b) a simulated spectrum using exact optical theory.

and the curvilinear baseline representing a broad interference fringe shows the usefulness of spectral simulations in predicting optical effects. Figure 2.18 shows the comparison between amorphous (quenched) and crystalline annealed films for free standing PPS films. Crystalline films were coated and dried under vacuum at 150°C for 12 hours. Little change was detected in most peak frequencies, although the out-of-plane bending vibration developed a shoulder at 819 cm⁻¹. Increases in intensity were noted for bands at 1473, 1389, 1093, and 1010 cm⁻¹ while decreases were noted for bands at 1574 and 1074 cm⁻¹.

Figure 2.19 shows the transmission spectra for an approximately 2.5μ spin coated PPS film supported on a salt disc. These samples had been heated to 320°C at a rate of 2.5°C / minute and slowly cooled to crystallize the film. Very similar changes are seen when compared to Fig. 2.17 although slight differences can be attributed to whether the film was crystallized from the amorphous state or from the melt. In the difference spectrum shown, the shoulder near 820 cm⁻¹ is more prominent and the peak absorbances at 1473 cm⁻¹ and 1010 cm⁻¹ only undergo slight shifts in the frequency with little change in intensity.

2.3.1.3 Attenuated Total Reflectance (ATR)

Figure 2.20 shows the experimentally determined ATR spectra of a 0.178 mm crystalline extruded PPS film at both 42° and 50° incidence angles. Although the difference in the incidence angle used was only 8 degrees, the effect on the resultant spectrum is considerable. This effect is due to optical effects above and below the critical angle, ϕ_c , the angle at which total internal reflectance occurs. This angle can be calculated from the equation:

$$\sin\phi = \frac{n_f}{n_s} \quad [27]$$

where n_f is the refractive index of the polymer, and n_s represents the refractive index of the ATR crystal. Using a refractive index value of 1.65 for PPS, and a refractive

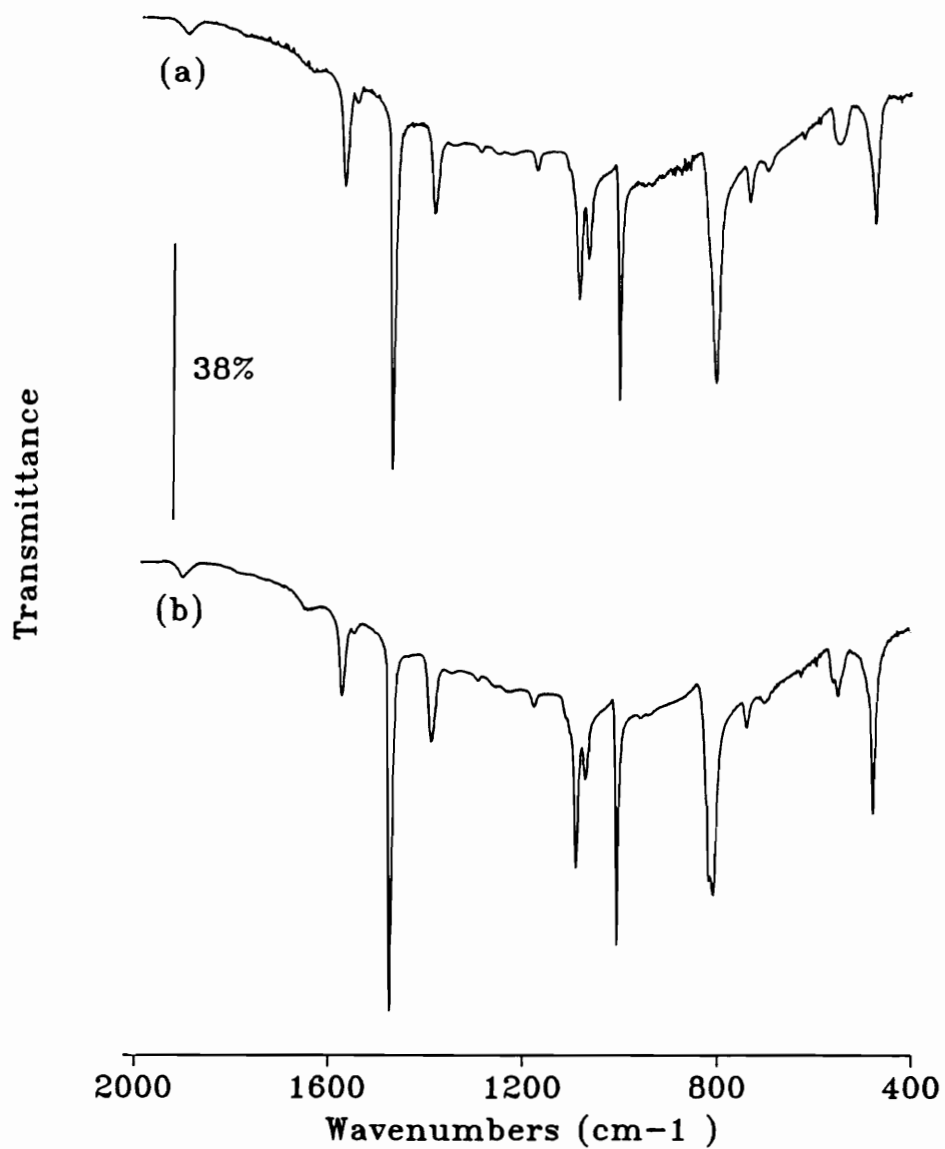


Figure 2.18 Comparison of the infrared spectrum for a (a) quenched and (b) annealed 1.55 μ free standing spin coated PPS film.

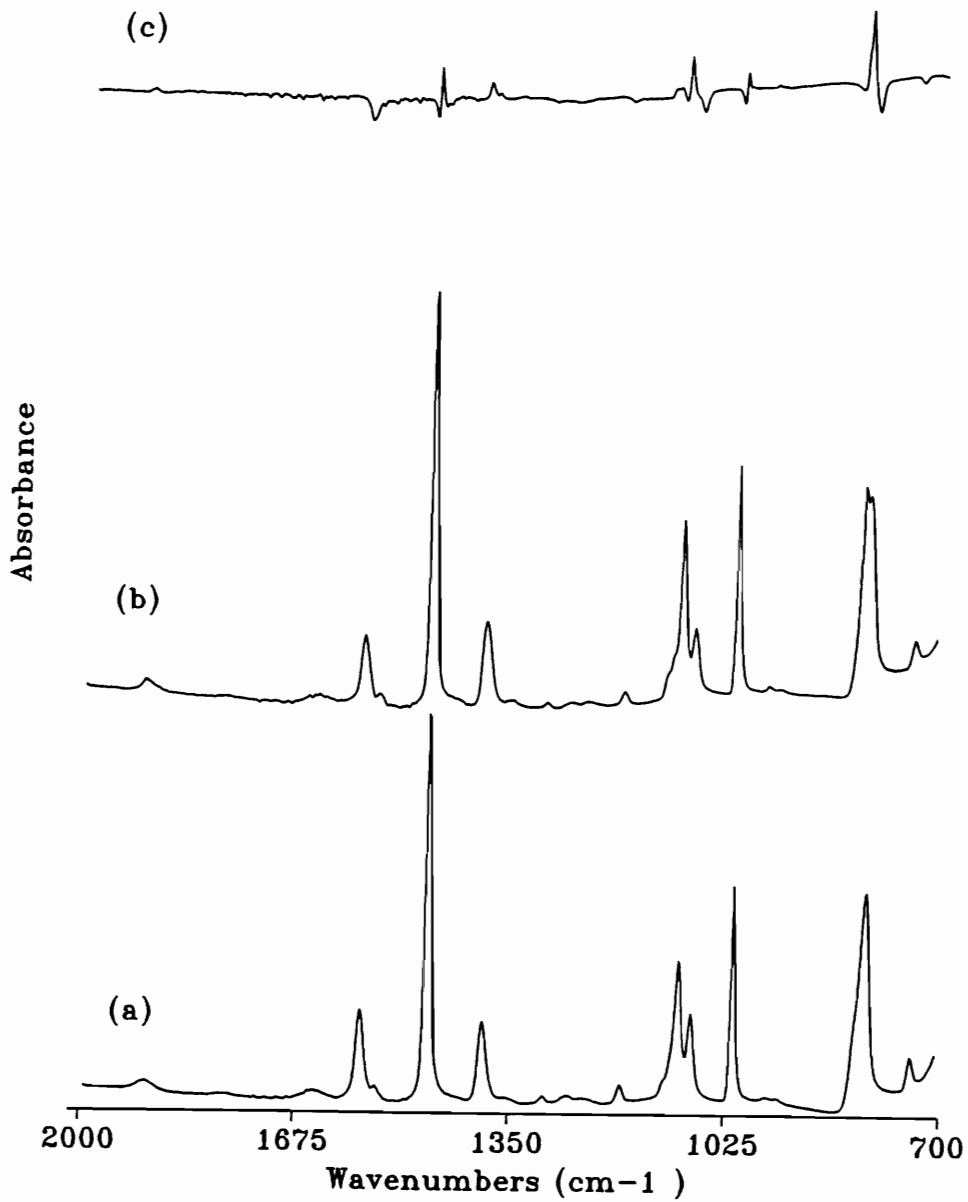


Figure 2.19 Comparison of the infrared spectra of amorphous and crystalline 2.5 μ spin coated PPS films. Shown are the spectra for (a) quenched, and (b) melted at 320°C and show cooled. The difference spectrum (c) is also shown.

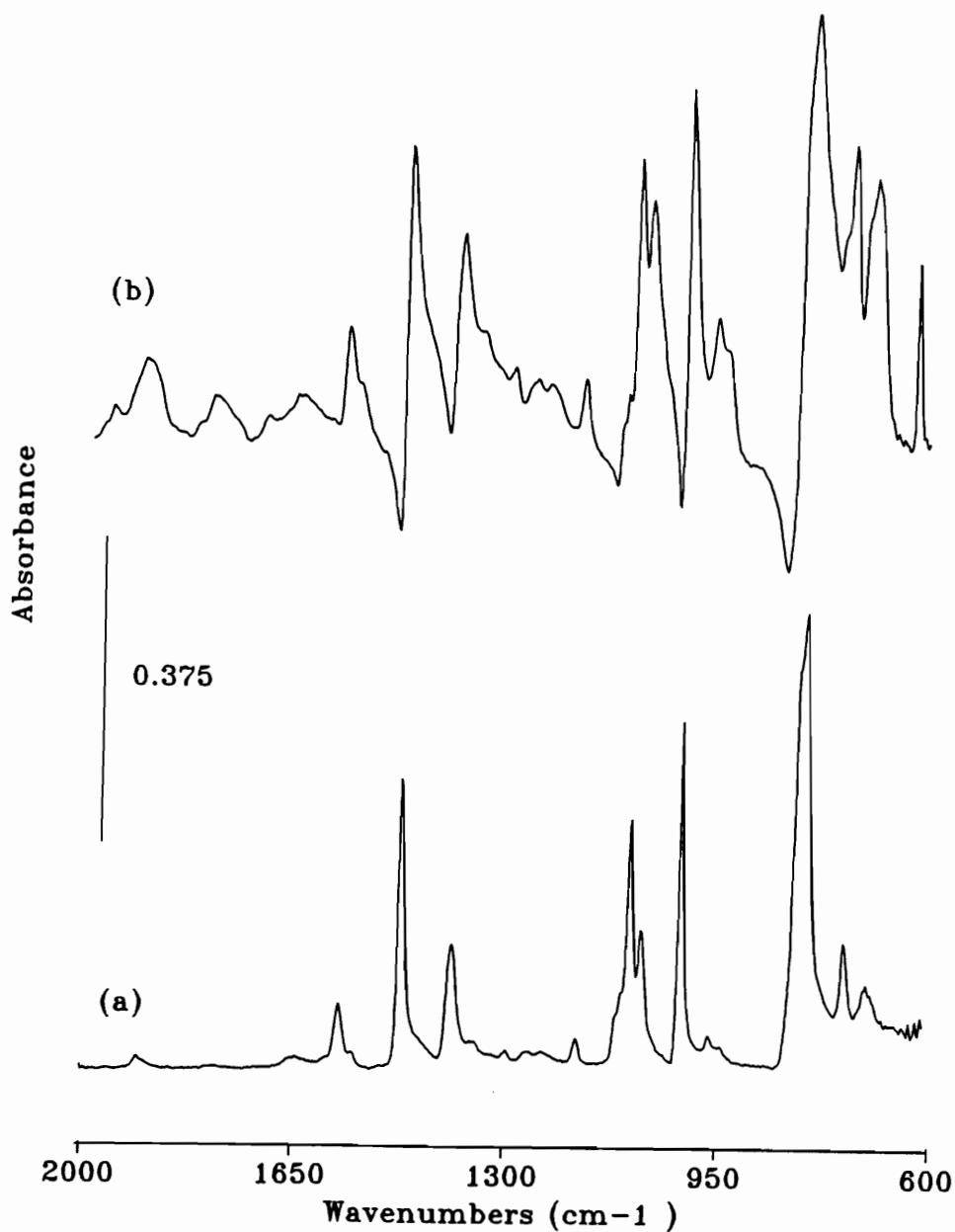


Figure 2.20 Comparison of infrared ATR spectrum for an extruded PPS films at (a) 50° and (b) 42° incidence angles. The 50° spectrum was multiplied by a factor of 0.75 and the 42° spectrum by a factor of 0.375 for scaling purposes.

index value of 2.429 at 2000 cm^{-1} for the ZnSe hemispherical crystal used (115) gives a ϕ_c value of 43° . Figure 2.21 shows the simulated spectra, and indicates that even though the angle used is only slightly below the critical angle, distortions in the spectrum are evident, showing the great advantage of applying exact optical theory to predict reflectance spectra. Below the critical angle, the spectrum generally reflects the dispersion in the refractive index, while above ϕ_c , the spectrum more closely resembles the k spectrum. Also, since the simulated spectra were calculated using experimentally determined n and k values, errors in these values must not be excessive. The simulated spectrum at 50° shows the enhanced intensity of the 810 cm^{-1} absorbance band relative to the other bands present and most of the relative intensities are in general agreement. The overall intensities of the spectra, however, were much greater than experimentally determined and probably reflect imperfect contact of the polymer film and crystal. Calculations, of course, assume perfect contact.

2.3.1.4 Reflection Absorption Spectroscopy

2.3.1.4.1 Reflection at the Brewster Angle

Often, it is of interest to analyze rigid opaque materials that are too stiff for analysis by attenuated total reflectance. This is typically the case for many composite laminates where a resin rich surface region has an opaque but somewhat reflective surface. Molded PPS samples also have similar characteristics and are difficult to analyze by conventional infrared techniques. Figure 2.22 shows reflectance spectra for a molded PPS sample at 50° , 60° and 70° incidence angles. Clearly, the spectra at 50° and 70° reflect the dispersion in the refractive index values, the former resembling the refractive index dispersion curve while the latter resembles its mirror image. The spectrum at 60° , however, is quite free from refractive index effects and seems very similar to the true absorbance (k) spectrum although band intensities are somewhat different.

Given the approximate refractive index of 1.65 for PPS, the Brewster angle can

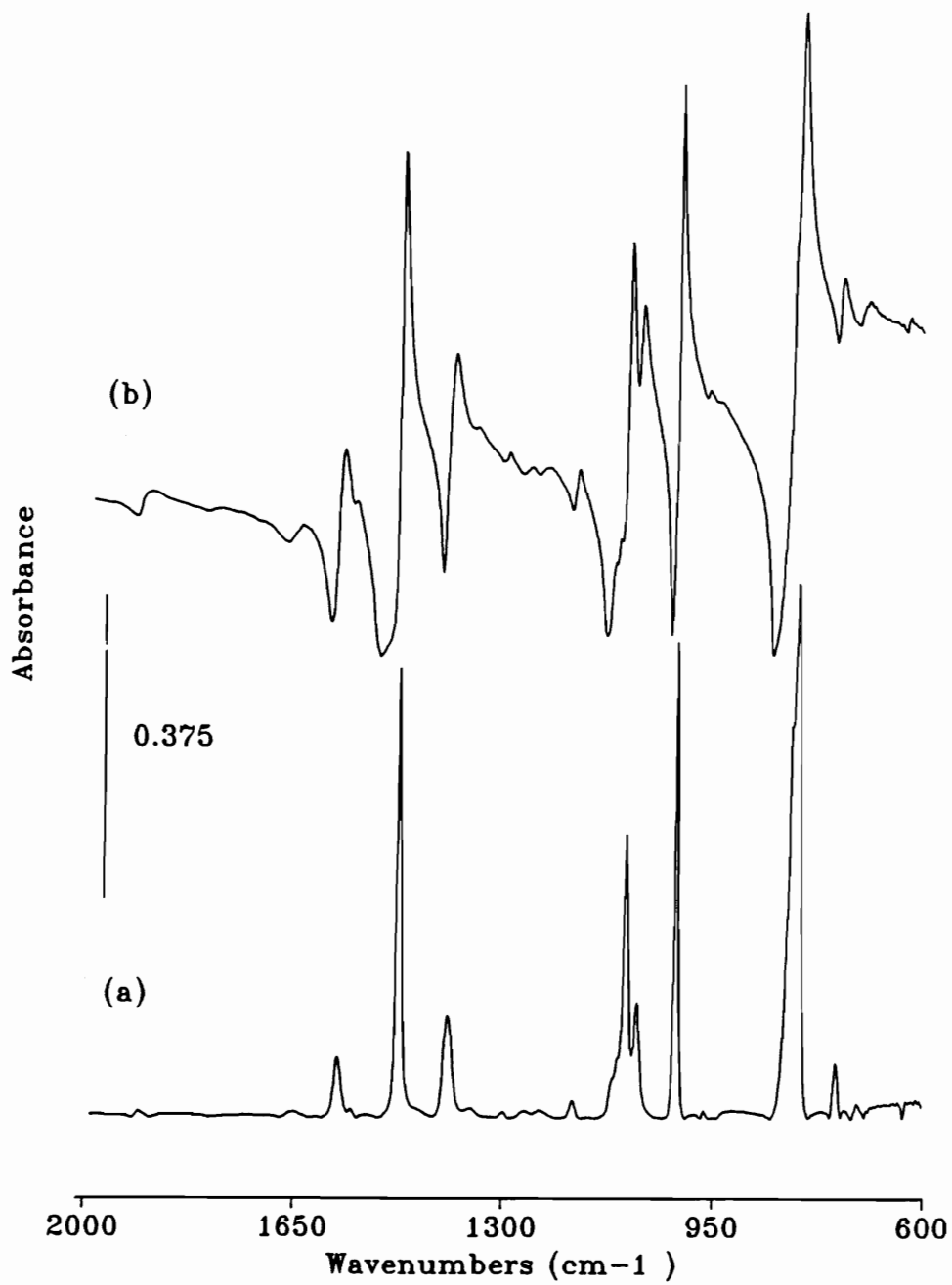


Figure 2.21 Comparison of the simulated infrared ATR spectrum for PPS using optical theory for incidence angles of (a) 50° and (b) 42° .

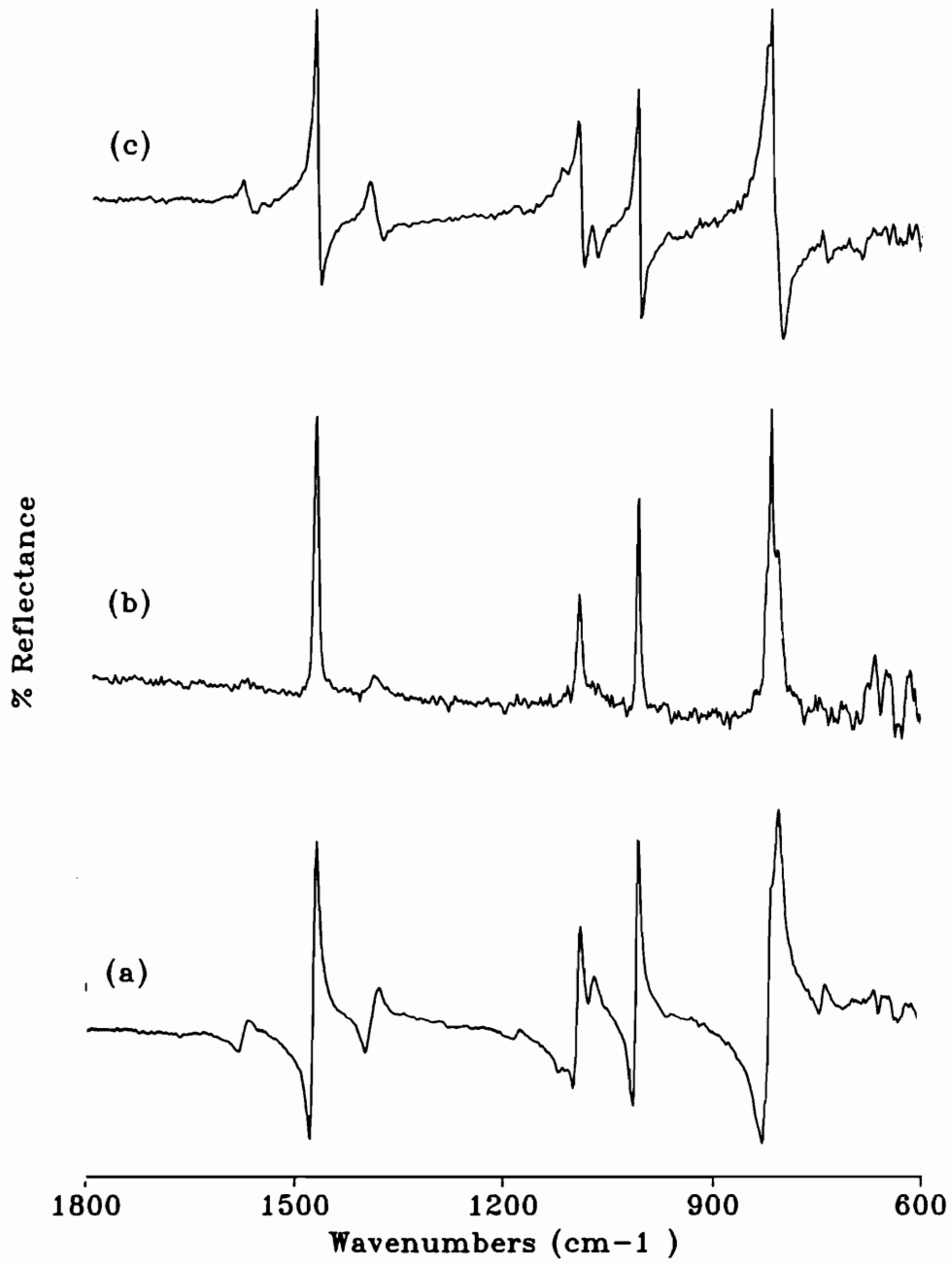


Figure 2.22 Comparison of the infrared RAS spectrum for 0.16 mm molded PPS panel at (a) 50° (b) 60° and (c) 70° angles of incidence.

be calculated using the eqn:

$$\tan\phi_b = \frac{n_f}{n_o}$$

where ϕ_b is the Brewster angle, n_f is the refractive index of PPS and n_o is the refractive index of air. This equation yields a Brewster angle of approximately 59° , slightly lower than the 60° incidence angle used experimentally. Figure 2.23 shows the simulated spectra using exact optical theory. Comparing Figs. 2.22 and 2.23 clearly shows the agreement between optical theory and experiment, and theory predicts the enhanced absorption of the 1474 cm^{-1} band over the neighboring absorbances at 1574 and 1389 cm^{-1} at the Brewster angle, and the shift of 810 cm^{-1} band, found in transmission, to approximately 820 cm^{-1} . The 810 cm^{-1} remains as a second peak of lower intensity and the increased intensity of this band is also accurately simulated.

2.3.1.4.2 Thin Film Analysis/Metal Substrates

Figure 2.24 shows the thickness versus solution concentration for thin PPS films coated on chromium substrates using high temperature spin coating. The curvilinear form of the plot is in agreement with the analysis by Weill and Dechenaux (131). Refractive index values (n_s , k_s) experimentally determined for ferrotype substrates of 3.8 ± 0.1 and 4.2 ± 0.1 are in good agreement with published values of 3.63 and 4.57 at a frequency of 600 nm (111). The findings suggest that the chromium substrate must only be covered with a thin oxide layer which would otherwise significantly increase the error in the optical values experimentally determined.

Figure 2.25 shows the spectrum of a spin coated 30 nm PPS film on a chromium substrate. This figure includes both amorphous (quenched) and crystalline (annealed in air for 30 min at 150°C) spectra and the difference spectrum is also included for emphasis. On crystallization, a number of spectral changes can be observed including slight decreases in the ring in-plane stretch and C-H bend at 1473

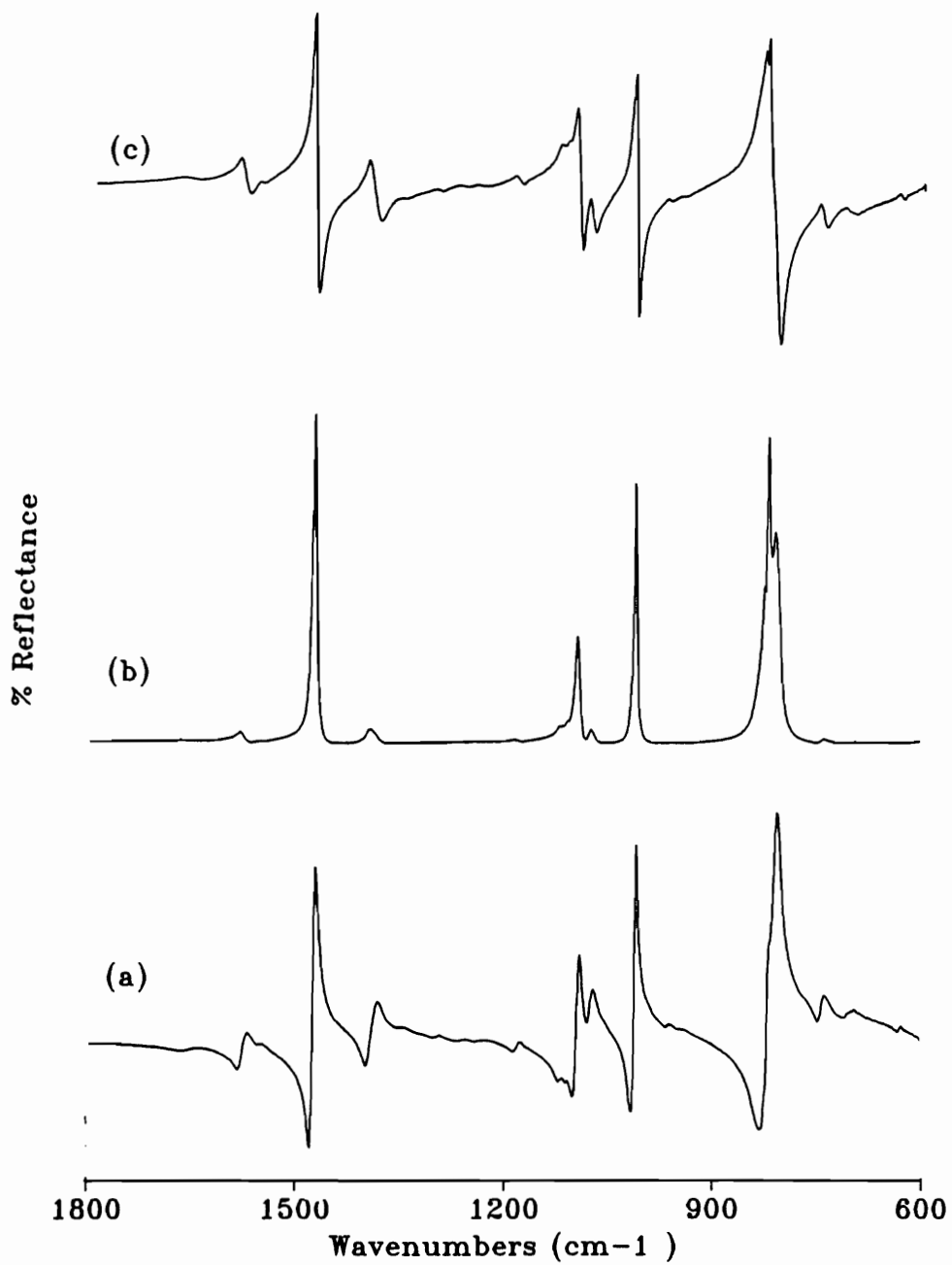


Figure 2.23 Comparison of the simulated infrared RAS spectra for surface reflection from a bulk PPS sample at (a) 50°, (b) 59°, and (c) 70° incidence angles.

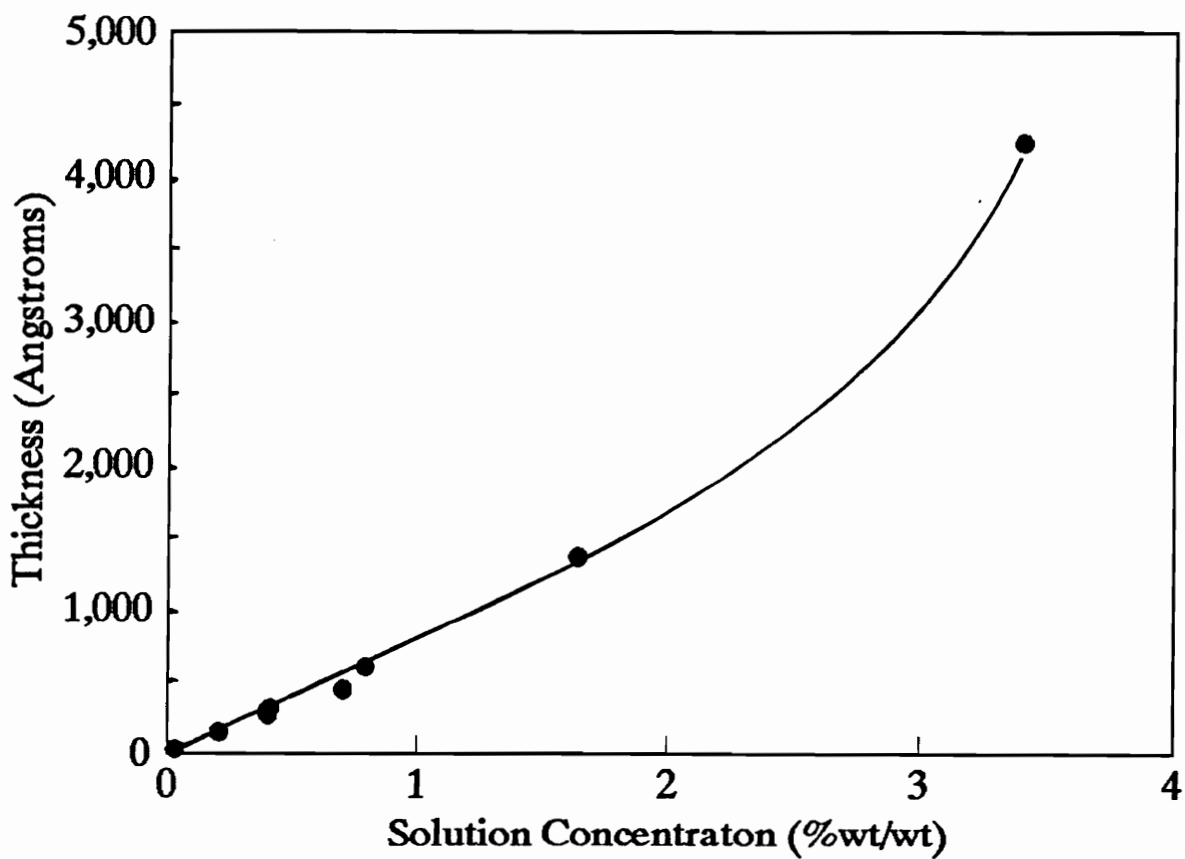


Figure 2.24 Thickness versus concentration for PPS coated ferrotype plates. All thicknesses were determined by ellipsometry based on a refractive index of 1.65 for

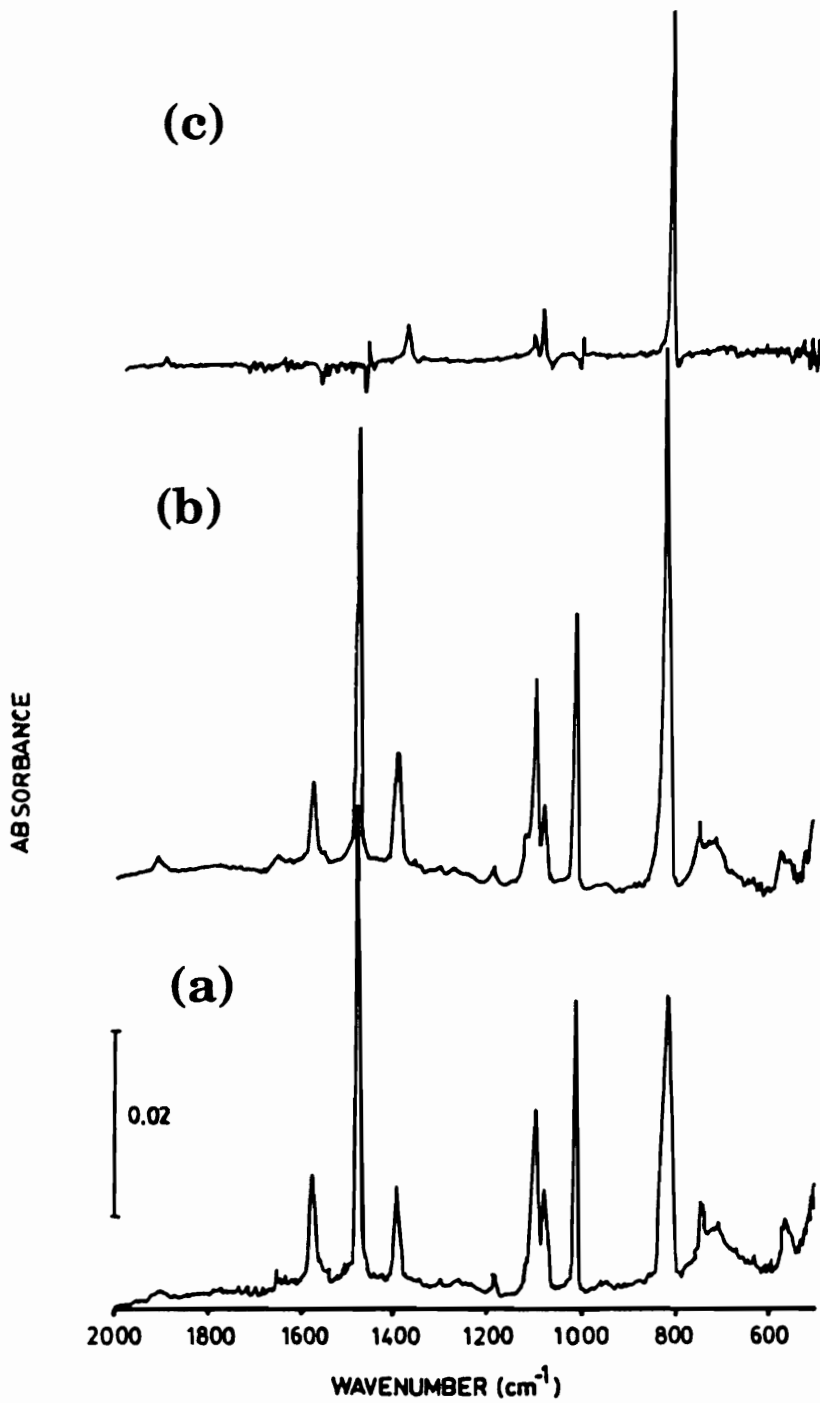


Figure 2.25 IRRAS spectra of an (a) amorphous and a (b) crystalline 30 nm PPS film on a chromium substrate. Fig. (c) shows the difference spectrum.

and 1011 cm^{-1} , respectively. The absorbance at 1574 cm^{-1} decreases in intensity while that at 1387 cm^{-1} increases. The intensity of the peak at 1094 cm^{-1} , recently assigned to the phenyl-sulfur asymmetric stretch, increases in intensity while the intensity for the neighboring band at 1075 cm^{-1} decreases substantially on crystallization. Figure 2.26 shows the plot of the absorbance of several bands measured as a function of film thickness. Curvilinear plots are found and the intensity changes associated with crystallization are also shown for three absorbance bands. The out-of-plane absorbance band at 811 cm^{-1} undergoes a dramatic increase over the entire thickness range shown, while the 1075 cm^{-1} peak decreases in intensity. The ring stretch at 1474 cm^{-1} remains relatively unchanged, but does seem to undergo a slight decrease in intensity at lower thicknesses. Clearly, by examination of the transmission spectra of both amorphous and crystalline free standing films and coatings, the large increase in the 811 cm^{-1} peak cannot be explained in terms of bulk crystallization effects. To increase in intensity, the transition moment for this group must align with the electric field vector, perpendicular to the surface, and this indicates preferential chain alignment with respect to the surface. The large increase in the 820 cm^{-1} band, which also increases somewhat in the transmission spectra of crystalline samples, may also reflect a deviation from the normal crystalline packing structures of PPS due to surface effects, the thickness of the film used, or spin coating induced orientations.

To qualitatively examine the kinetic aspects of PPS crystallization on chromium, Figure 2.27 shows the results of annealing a quenched 60 nm film of PPS for varying lengths of time at 150°C in air. As can be seen, crystallization at this temperature is very rapid and no further absorbance changes in the $820\text{ cm}^{-1}/1474\text{ cm}^{-1}$ or $1075\text{ cm}^{-1}/1094\text{ cm}^{-1}$ peak ratios are detected after the first five minutes. In another qualitative attempt to measure crystallization, an *in situ* RAS analysis was performed by rapidly heating quenched samples to approximately 130°C and monitoring the changes in intensity and peak position of the 811 cm^{-1} absorbance band found in amorphous samples. Figure 2.28 shows the results of this analysis and the difference spectrum shown clearly demonstrates that rapid crystallization occurs, and shows the promise of this technique as an analytical tool to monitor reorganization of thin

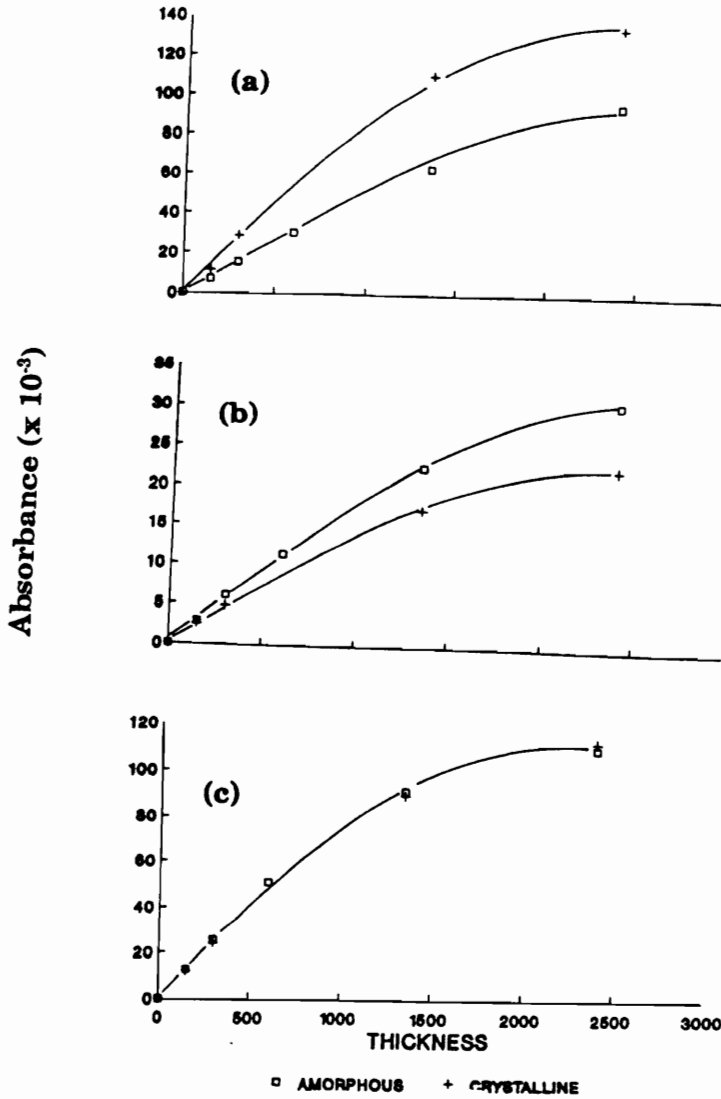


Figure 2.26 Plot of absorbance versus thickness in angstroms for absorbance bands located at (a) 1474 (b) 1075 and (c) 814-820 cm^{-1} for both amorphous and crystalline films. Absorbance was calculated as $-\log(R/R_0)$ where R_0 represents a film with a k value of 0.

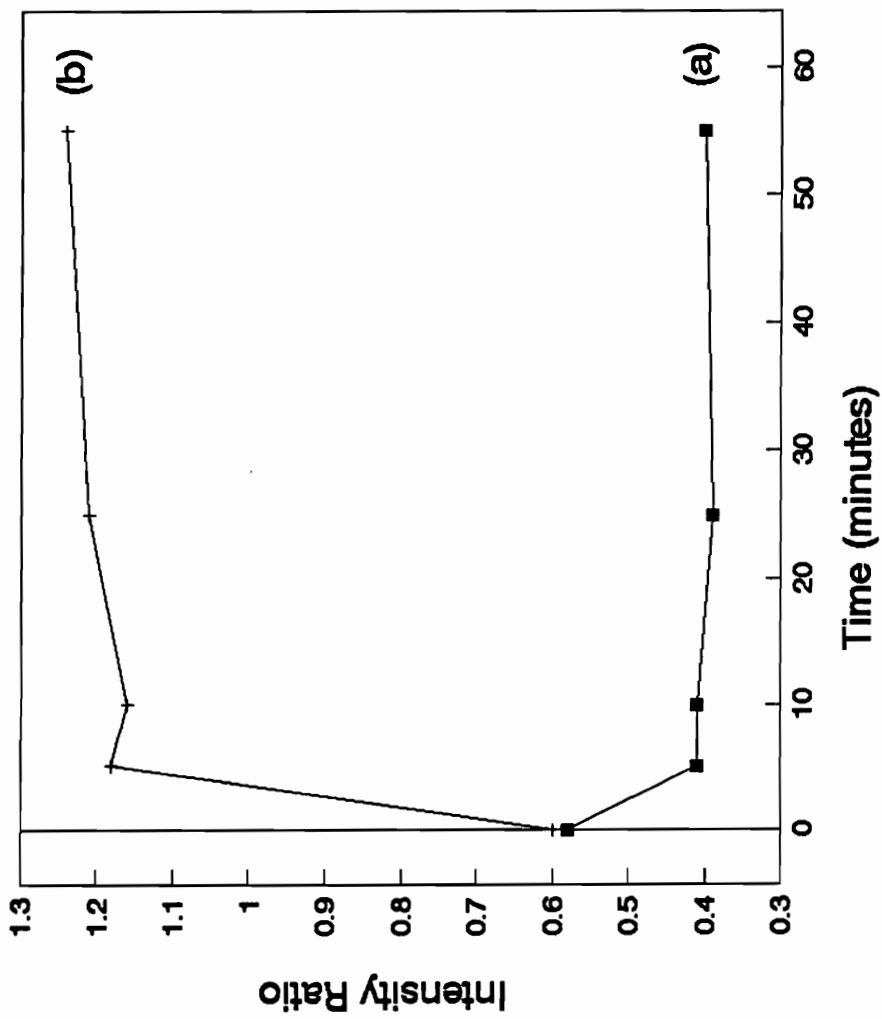


Figure 2.27 Infrared RAS band intensity ratio dependence on annealing time for a 60 nm amorphous PPS film on chromium for the (a) 1075 / 1094 cm^{-1} and (b) 820 / 1474 cm^{-1} ratios.

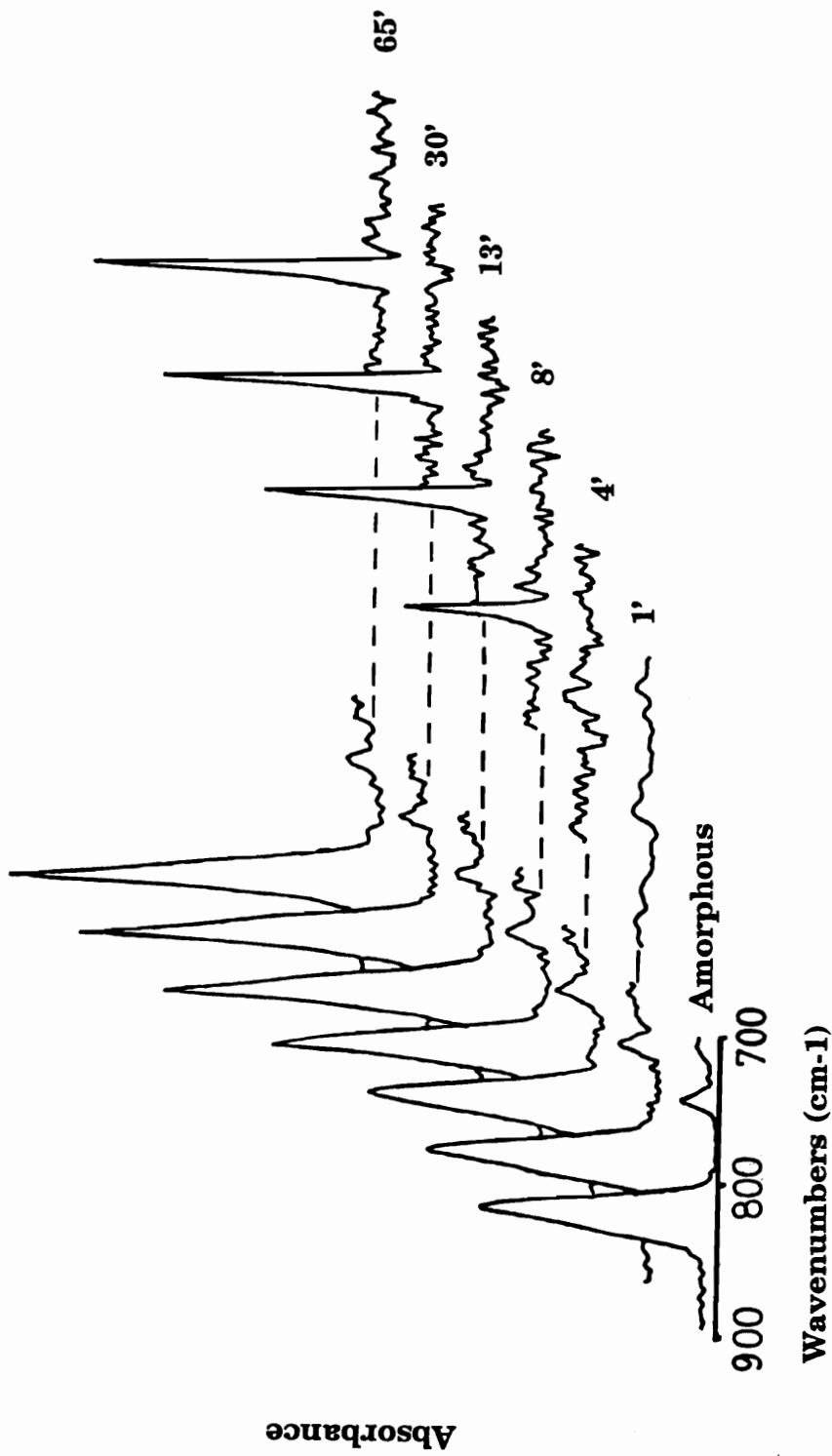


Figure 2.28 *In-situ* IRRAS analysis of the crystallization of a 70 nm PPS film on a ferrotype plate (see Fig 2.13b)

crystalline films on surfaces.

While quenching molten films in liquid nitrogen provides a convenient method to produce thin amorphous films, such a step may in fact promote unique ordering of crystalline polymers at surfaces. In studies of the development of heterogeneous nucleation of crystalline polymers against surfaces, transcrystallinity could be produced in some cases by inducing a shear stress at the interface (98,101). While spin coating certainly would provide a shearing stress for the flow direction in the plane of the substrate, quenching would provide a substantial thermal stress due to the mismatch in thermal expansion coefficient between polymer and metal substrate. Another point is that although heating above the melt in bulk samples usually erases memory of prior processing steps, thin films against surfaces may be restricted due to adsorbed polymer segments, and may be unable to assume bulk configurations.

To examine samples that had not been quenched, Figure 2.29a shows the infrared spectrum for 60-70 nm PPS film after coating and drying at approximately 110-120°C under vacuum. As can be seen by monitoring the 1094/1075 cm^{-1} absorbance band ratio or the out-of-plane C-H bending peak intensity at 811 cm^{-1} , the film appears amorphous in character. It has been shown that heating above 120°C is required to initiate crystallization (87) in bulk PPS samples. Figure 2.29b, however, shows that after annealing at 150-160°C under vacuum for one hour, crystallization of the surface film is apparent. Therefore, the ordered nature of the surface film is formed during the deposition process, and quenching of the film is not prerequisite.

In order to understand if the film structure formed is unique to chromium, several other substrates were also investigated. Figure 2.30 shows the infrared spectra of a 60-70 nm film of PPS on a pre-oxidized vapor deposited aluminum surface. Since the spectra were taken relative to a gold background, the appearance of the absorbance band at 960 cm^{-1} clearly shows the presence of aluminum oxide (Al_2O_3). As can be seen, after drying under vacuum, the film remains essentially amorphous. After annealing the sample, a similar spectrum is seen to that shown before for a crystallized film on chromium, with a large increase in the out-of-plane bending vibration and decreases in the in-plane ring stretch and C-H bending mode

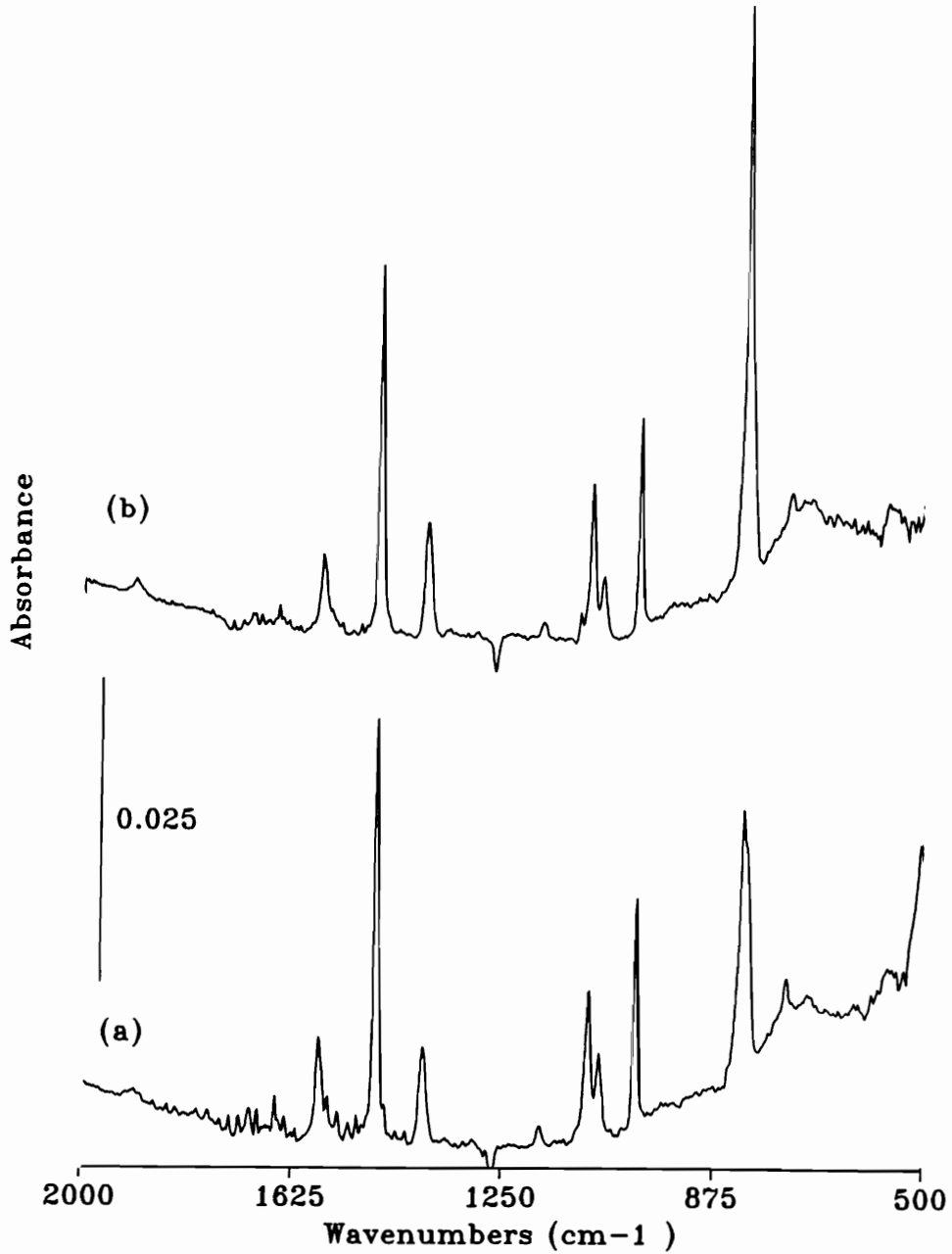


Figure 2.29 Infrared RAS spectrum of a 60-70 nm PPS film on a chromium (ferrottype) substrate after (a) drying at 110-120°C and (b) further annealing at 150-160°C under vacuum.

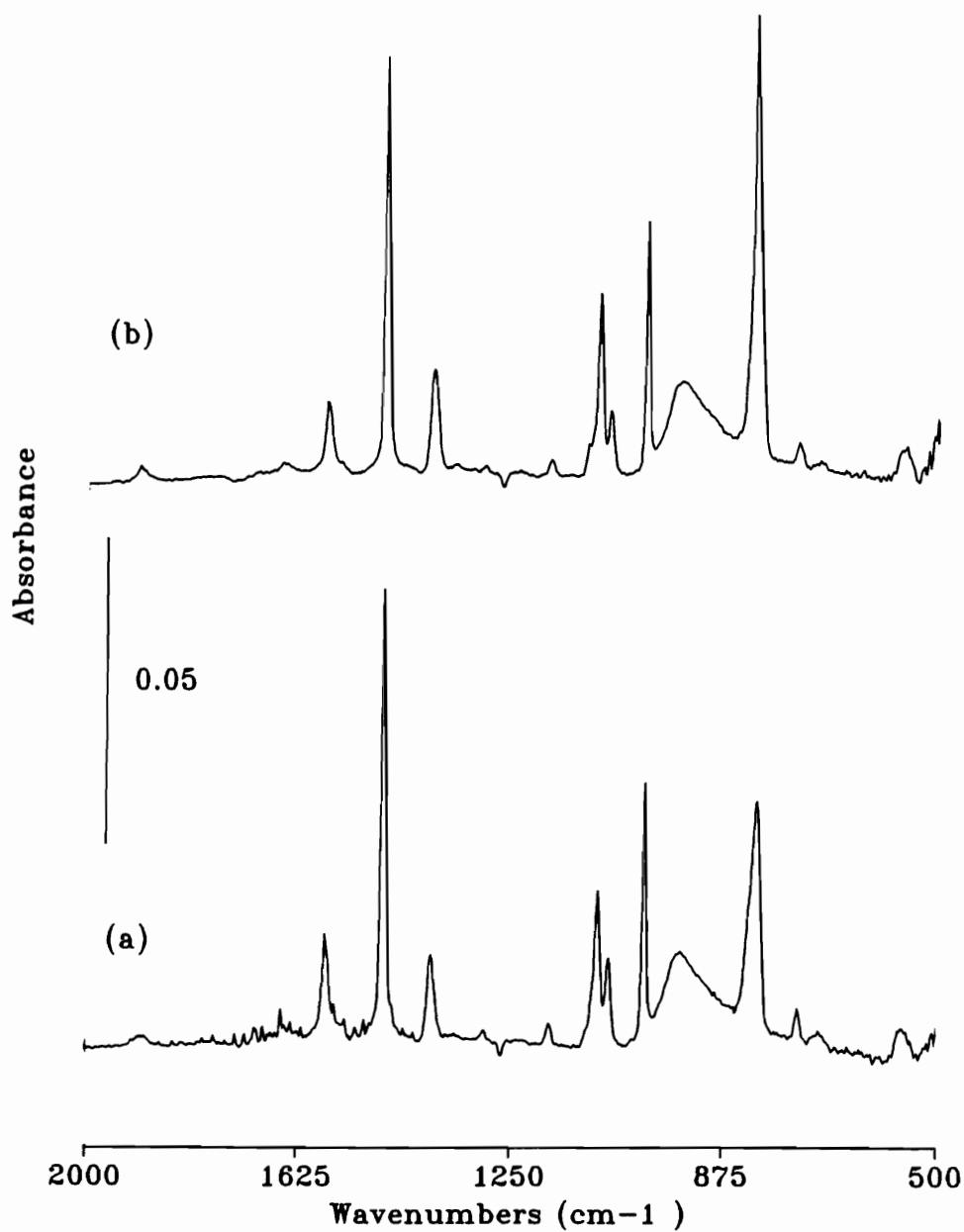


Figure 2.30 Infrared RAS spectrum of a 60-70 nm PPS film on an oxidized vapor deposited aluminum substrate after (a) drying at 110-120°C and (b) further annealing at 150-160°C under vacuum.

absorbance, showing that the structure formed is not unique to chromium. Figure 2.31 shows the spectra of a 60-70 nm film of PPS coated on a 20 nm layer of Cu_2O on a chromium substrate. The same spectral changes on crystallization are observed for this substrate as well after annealing under vacuum.

When comparing spectra taken in the reflection mode to those measured by transmission, optical effects must be taken into account to fully understand the spectral changes associated with the reflectance technique. To better judge the magnitude of optical effects and show the true anisotropic nature of the film, the RAS spectrum can be simulated based on the optical properties determined for thick spin coated samples. These optical constants, due to the fact that they were determined in transmission measurements, represent optical properties in the plane of the substrate, or n_o and k_o , the ordinary refractive index and extinction coefficient, respectively. Any deviation from the calculated reflectance spectrum and the experimental reflectance spectrum, represents anisotropy in the surface film, since for the IRRAS at grazing angles, essentially only the z component of the surface electromagnetic field vector is present.

This is demonstrated in Figure 2.32 which depicts the electric field intensity as a function of the angle of incidence for the IRRAS technique simulated for a 100 nm film of PPS on a copper substrate. The x, y, and z components are shown, and calculations were performed using a procedure for multiple layers similar to that outlined by Hansen (116), and the z position was taken as the midpoint in film thickness. The fortran program found in Appendix 2.2 was used to generate all data for the plot seen. While p polarization contains both x (in the direction of light propagation) and z (vertical to the surface) components, the x component is negligible at grazing incidence angles. Therefore, if an anisotropic film were present, this technique at grazing angles would be sensitive only to the component normal to the surface, or the extraordinary optical constant values (n_e and k_e).

Figure 2.33 shows a schematic diagram of the system modeled for the two layer system experimentally prepared. Copper oxide thickness was determined by ellipsometry and polymer thickness was estimated by coating the same polymer

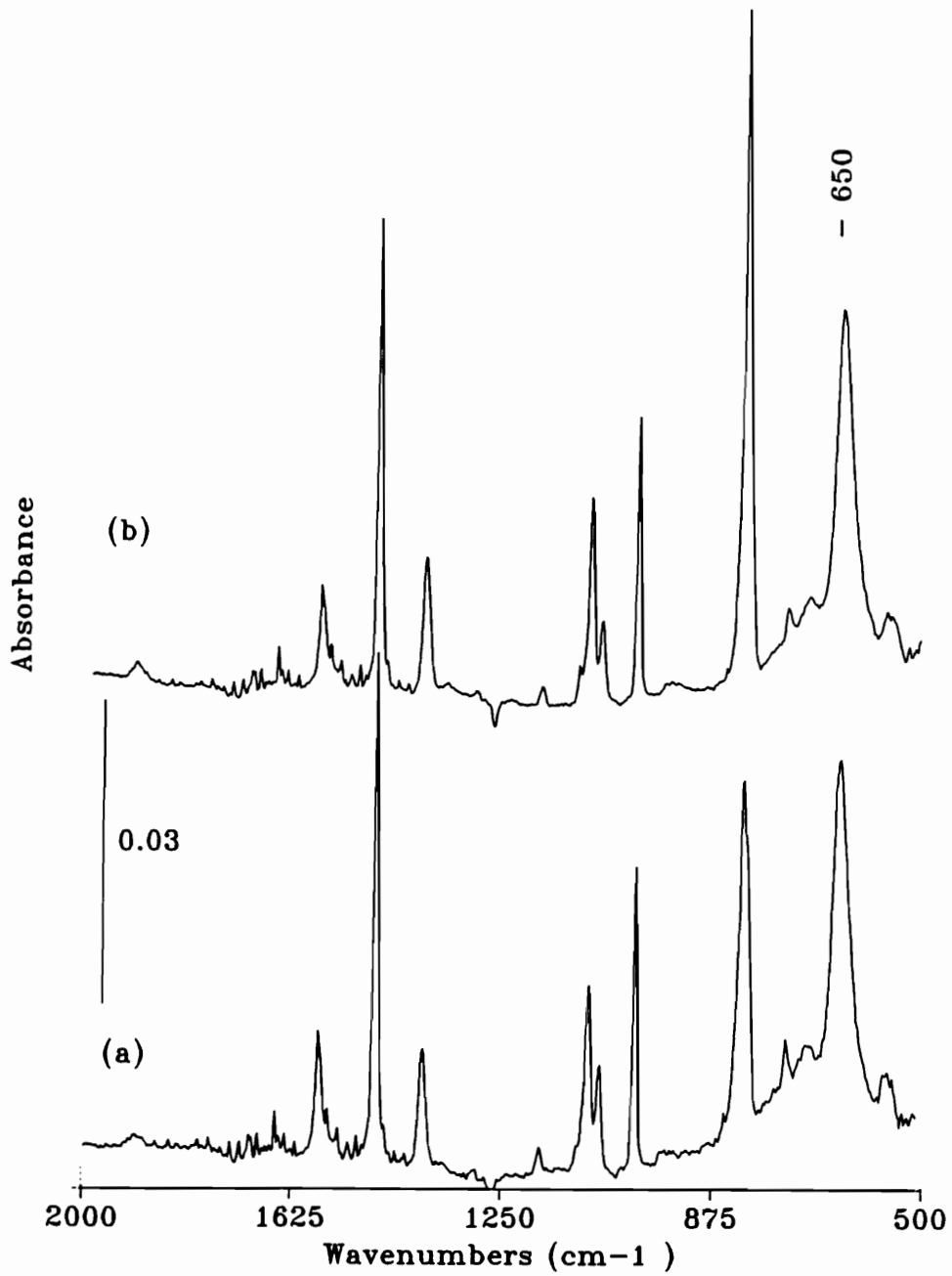


Figure 2.31 Infrared RAS spectrum of a 60-70 nm PPS film on 20 nm oxidized sputter coated copper film on a chromium substrate after (a) drying at 110-120°C and (b) further annealing at 150-160°C under vacuum.

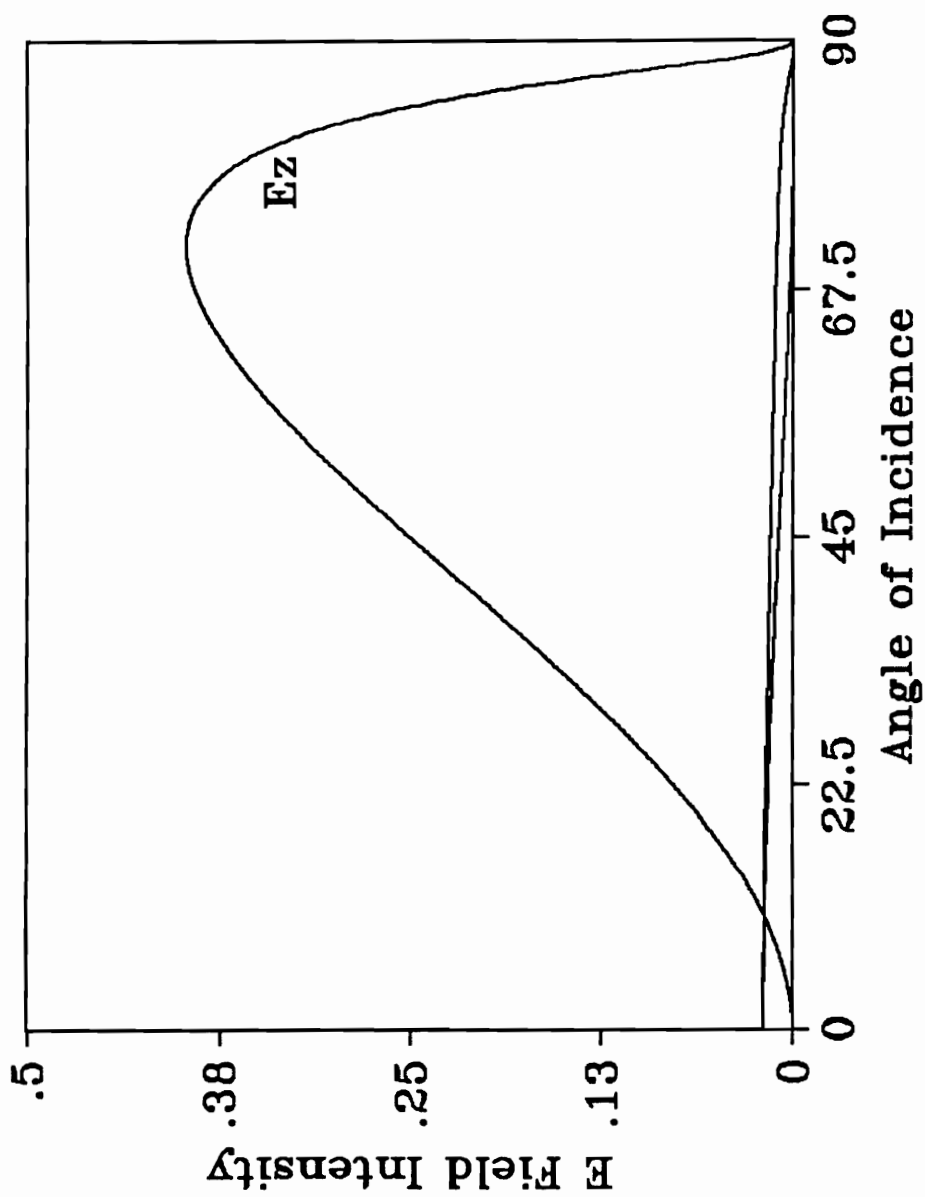


Figure 2.32 Plot of the electric field intensities (x,y,z) for light reflection from a 100 nm film of PPS on copper. Values of 1.65 and 0.3 were taken as n and k values of the 1474 cm^{-1} ring stretch vibration. Values of n_s and k_s for copper were interpolated as 4 and 42.7 respectively from published values. (111)

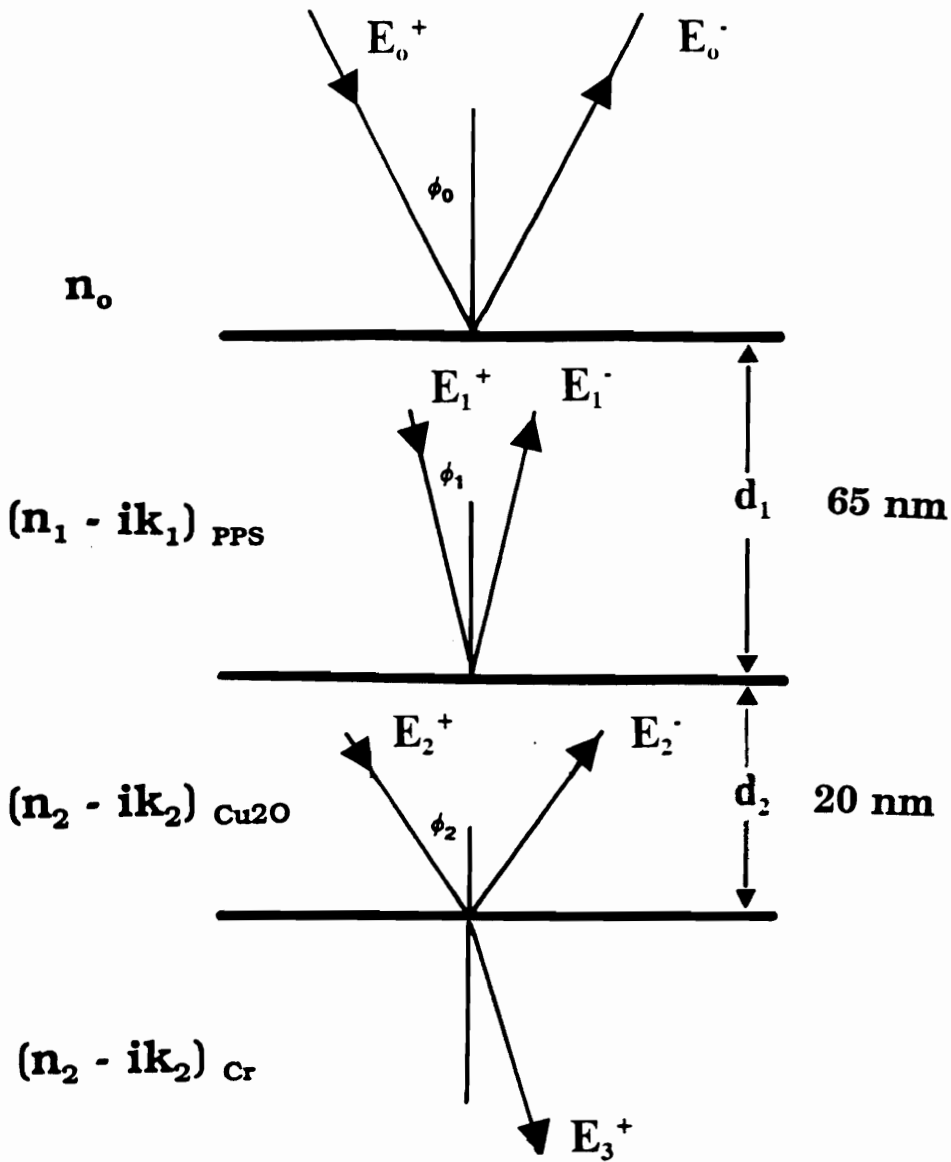


Figure 2.33 Schematic diagram of the PPS/Cu₂O/Cr system for optical simulation.

concentration on chromium substrates and determining thickness by ellipsometry. Figure 2.34b shows the experimental spectrum for this system, while Fig. 2.34a gives the simulated spectrum, calculated from exact optical theory. The simulated spectrum shown clearly indicates the utility of simulation as the calculated spectrum reasonably predicts both the intensity and position of the Cu_2O absorbance band at 650 cm^{-1} . In transmission measurements, the peak position has been reported near 610 cm^{-1} , showing the large shift due to optical effects, and all calculated peak positions for PPS bands are shifted to slightly higher frequencies due to anomalous dispersion in the refractive index. Although the peak intensities may vary somewhat due to error in the polymer thickness used in the calculations, the agreement is reasonable. The clear difference between experimental and calculated spectra can be seen by monitoring the out-of-plane to in-plane peak intensities. For the simulation shown, the ratio of the 820 cm^{-1} band to the 1474 cm^{-1} and 1011 cm^{-1} bands yield values of 0.60 and 0.95 respectively. For the experimental spectrum shown in Fig. 2.34b, however, the dramatic reversal in these peak ratios can be seen with a $820 / 1474\text{ cm}^{-1}$ ratio of 1.43 and the $820 / 1012\text{ cm}^{-1}$ ratio of 2.36. These ratios, when compared to the simulated spectrum, represent an approximately 2.5 fold increase in out-of-plane to in-plane absorbance intensities, clearly indicating the anisotropic nature of the thin surface film. Simulations for all other substrates show the same trend, indicating that the structure formed is fairly independent of the nature of the substrate.

While this analysis has utilized relatively smooth rigid metal surfaces, copper foil samples also show similar spectral changes on crystallization as this is seen in Figure 2.35, indicating the usefulness of the technique in analyzing many substrate types.

2.3.1.4.3 Thin Films / Infrared Transparent Substrates

While simulation of optical spectra has been found to be useful in the determination of the ordering of PPS films at surfaces, if infrared transparent substrates are used, a direct measure of film anisotropy can be made by one of two comparison methods. These involve either: (1) the comparison of transmission and

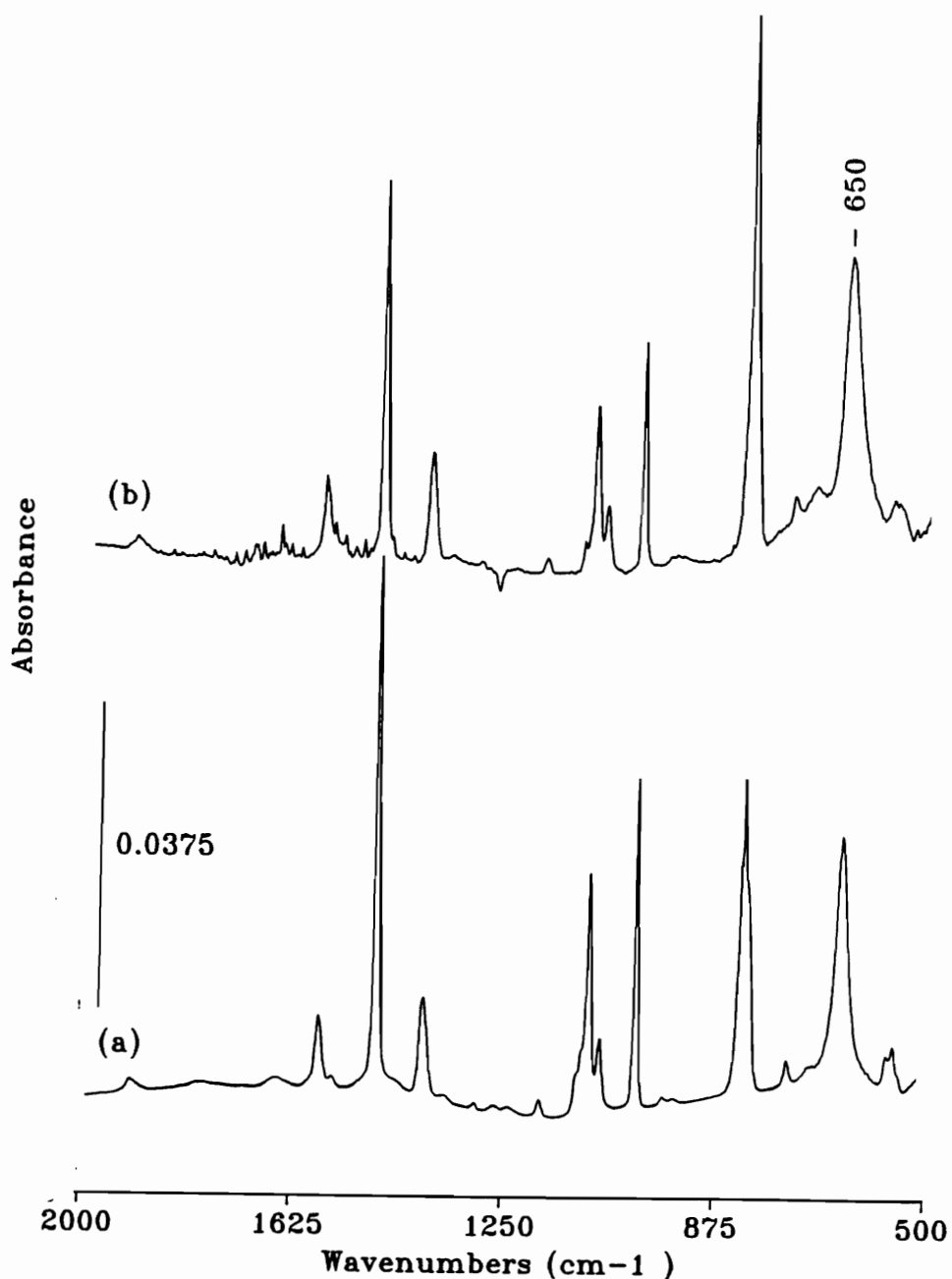


Figure 2.34 Infrared RAS spectrum for the PPS/Cu₂O/Cr system, described in Fig. 2.33 showing the (a) simulated spectrum using exact optical theory, and (b) the experimental spectrum for the same system. Optical constant values for copper oxide were calculated from Ref. 34 while values for chromium were interpolated from literature values (111,122).

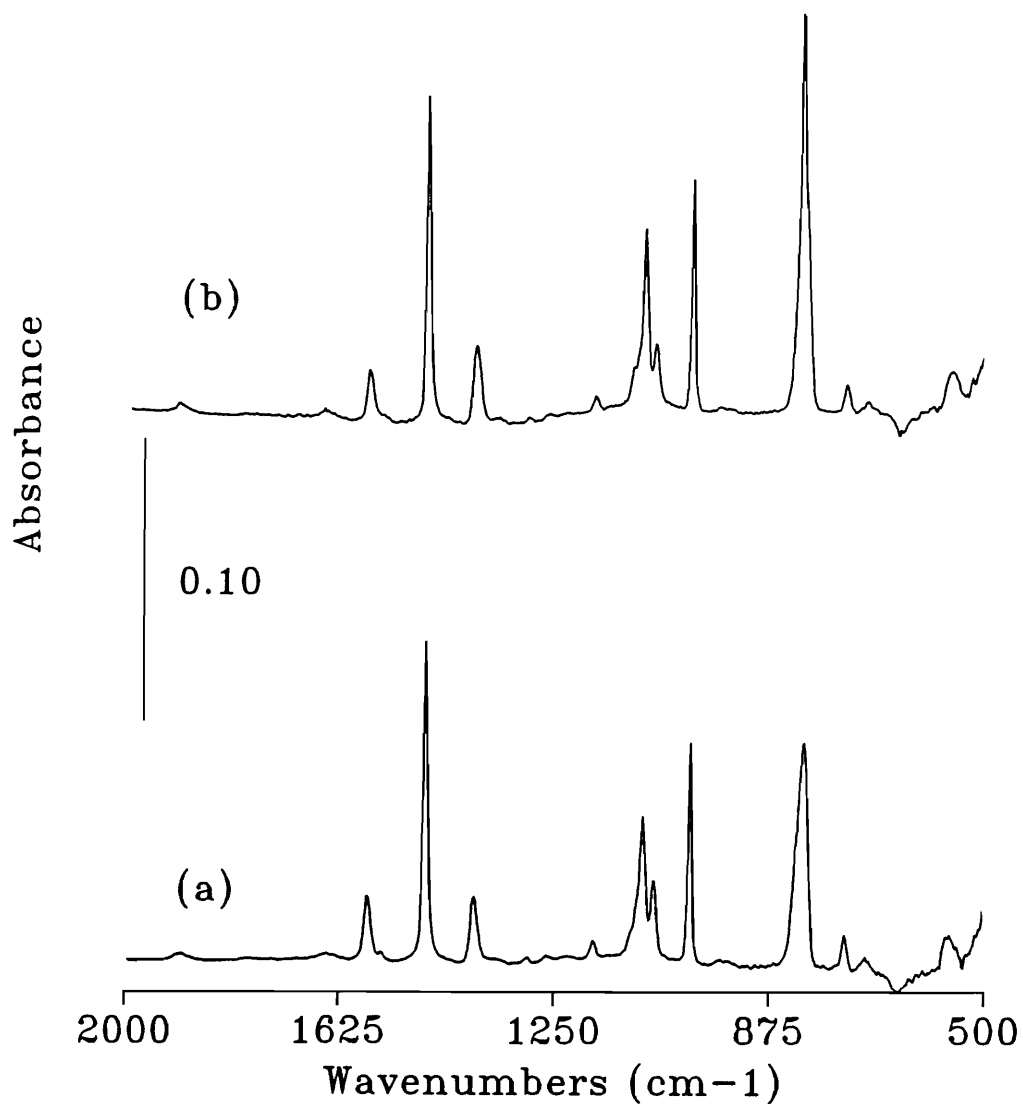


Figure 2.35 Infrared RAS spectrum of a 2.2% (wt/wt) PPS solution spin coated from benzophenone onto methanol degreased ETP 110 copper foil for (a) quenched and (b) annealed at 150°C under nitrogen.)

reflection spectra (using p-polarized light) or (2) comparison of reflection measurements for both p and s states of polarization. Unlike the results shown for Fig. 2.32, reflection of light from a relatively transparent substrate (low k_x values) results in a standing electric field at the surface that has a sizable contribution for the x, y, and z components. Figure 2.36 shows the results obtained for the electric field intensities for x, y and z components for reflection from a germanium substrate with a 100 nm surface PPS film. At normal incidence, only absorbances having a component of the dipole transition moment parallel to the plane of the substrate can give rise to absorption, while near a 45° incidence angle, electric field intensities of all components are of almost equal in intensity. This allows interaction with groups aligned both parallel and perpendicular to the plane of the sample to be analyzed. At higher incidence angles, the z component becomes dominant but is never completely independent of the x component. This means that at grazing angles, a mixture of absorbances for both parallel and perpendicular orientation will result for p polarized light. Also, while reflection from metals using s polarized light results in negligible absorbances at any angle of incidence, for germanium substrates, the y component can be substantial. To analyze orientation, transmission spectra (E_t) can be compared to p-polarized light reflection ($E_{\parallel} + E_{\perp}$) and the differences noted. Although in the reflection mode, the anisotropy of the electric field is not purely in the z direction and the average resultant absorbance should reflect the perpendicular component, as averaged with the parallel. Also reflection using s-polarized light will give information concerning absorbances in the substrate plane, and this can be compared with results using p-polarized light.

To investigate the changes associated with crystallization of thin films on germanium, transmission measurements were made, and Figure 2.37 shows the spectral changes associated with crystallization of a thin film on this substrate. While crystallization on the metal substrates using the IRRAS technique resulted in slight decreases in the 1474 and 1011 cm^{-1} bands and a large increase in the 820 cm^{-1} peak, analysis shows that these absorbance bands in transmission show the exact opposite behavior. In this case, there are increases in the in-plane ring modes for the

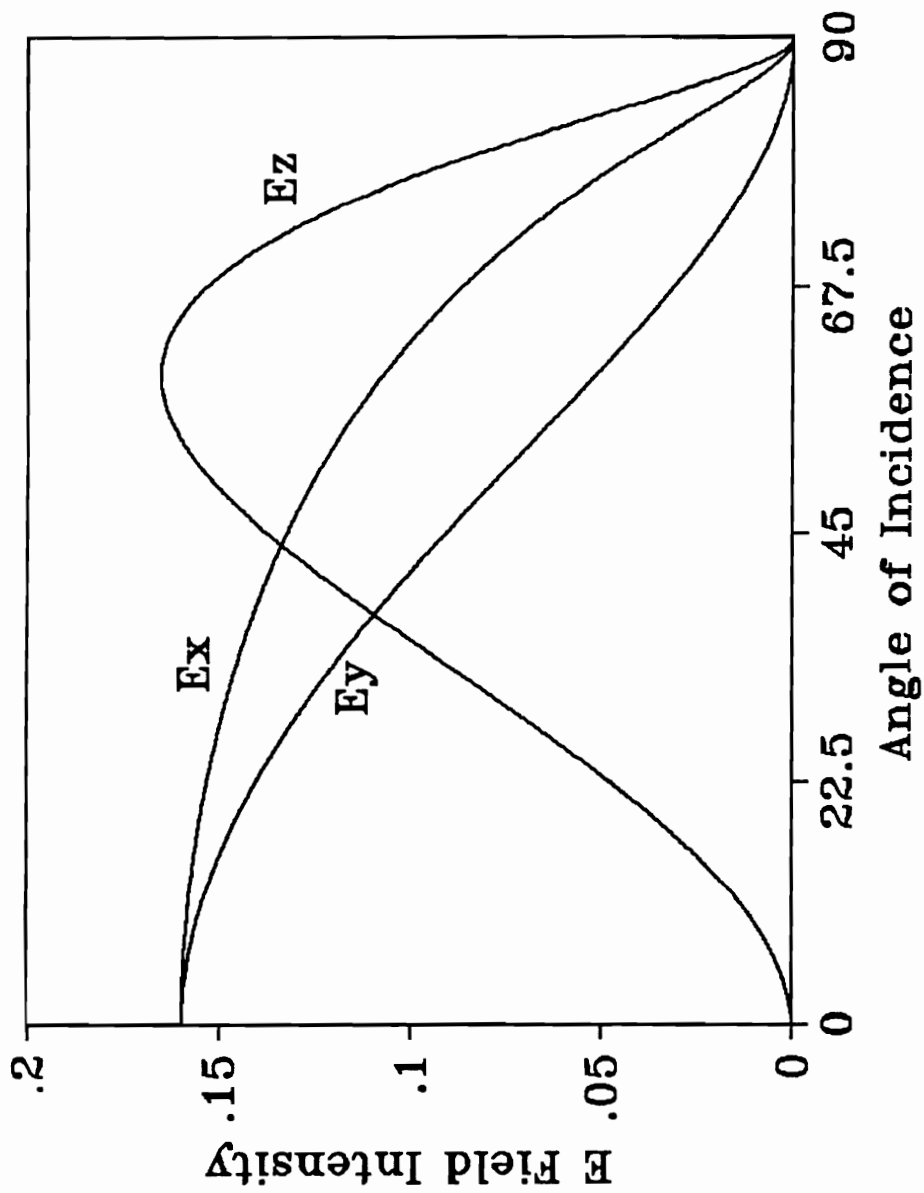


Figure 2.36 Plot of the electric field intensities (x, y, z) for light reflection from a 100 nm film of PPS on germanium. Values of 1.65 and 0.3 were taken as n and k values for the 1474 cm^{-1} ring stretching vibration. Values of n_s and k_s for germanium were taken as 4 and 0 respectively. (117)

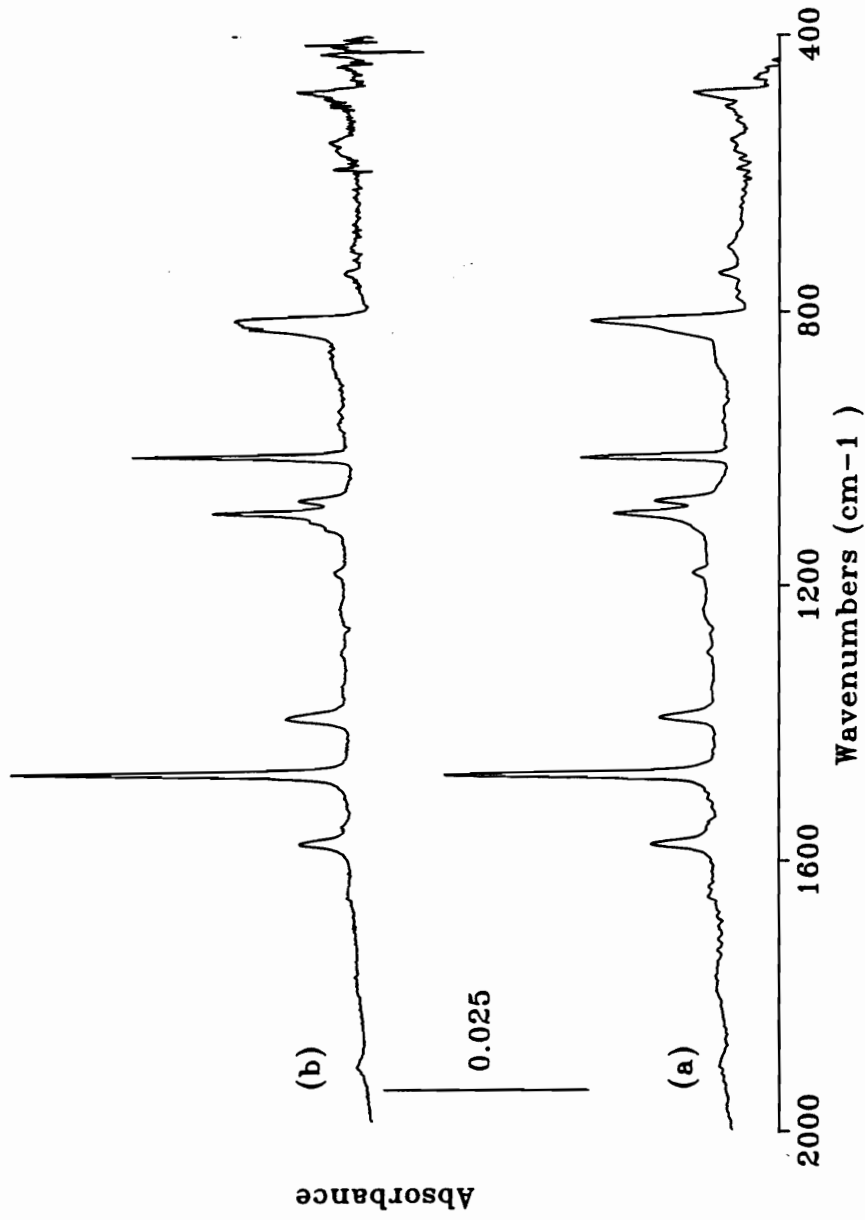


Figure 2.37 Infrared transmission spectrum of a 200 nm PPS film on germanium for both (a) quenched and (b) annealed samples. Annealing was done at 150°C in air.

ring-stretching vibration (1474 cm^{-1}) and the CH-bending vibration (1011 cm^{-1}) and decreases in the out of plane C-H bending mode at 820 cm^{-1} . To examine the dipole transition moments perpendicular to the surface, Figure 2.38 shows the comparison between the transmission spectrum of a crystalline PPS film and a reflectance spectrum using 60° reflection and p-polarized light. Although the reflection spectrum will reflect both x and z components of the electric field, the large increase in the absorbance at 820 cm^{-1} is clearly evident relative to the in-plane modes. This clearly shows the anisotropic nature of the surface film and confirms the previous conclusions based on the simulation of optical spectra.

The results for both metals and non-metals are consistent with the orientation of the aromatic rings in the backbone structure of crystallized polymer primarily in the plane of the substrate. This would enhance in-plane modes in transmission and out-of-plane absorbances in reflection. For PPS, qualitative dichroic measurements have shown that the C-H out-of-plane mode giving rise to the 820 cm^{-1} band is oriented primarily perpendicular to the polymer chain direction (107). The large increase in this functionality when sampling modes perpendicular to the surface in reflection implies that the direction of the backbone chain extension is parallel to the plane of the substrate. This is also in the same direction as flow during the spin coating procedure, and this method may play a critical role in the anisotropy seen. Sampling modes with dipole transition moments parallel to the substrate in transmission show a decrease in this absorbance, with an increase in in-plane modes consistent with this model. The extreme sensitivity of the 820 cm^{-1} band relative to the in-plane modes is most likely due to the fact that this absorbance is sensitive primarily to the crystalline regions while the 1474 , and 1012 cm^{-1} absorbances have not been shown to be particularly sensitive to crystallinity. Therefore the changes due to orientation may in fact be "diluted" by the amorphous regions present.

Previous studies of the orientation of thin ($<100\text{ nm}$) crystalline films on solid substrates has been limited, but Nguyen and Ishida have shown, using the IRRAS technique that poly(ether-ether ketone) ketone polymer chains were oriented perpendicular to the surface for coatings on graphite single crystals. Studies of thicker

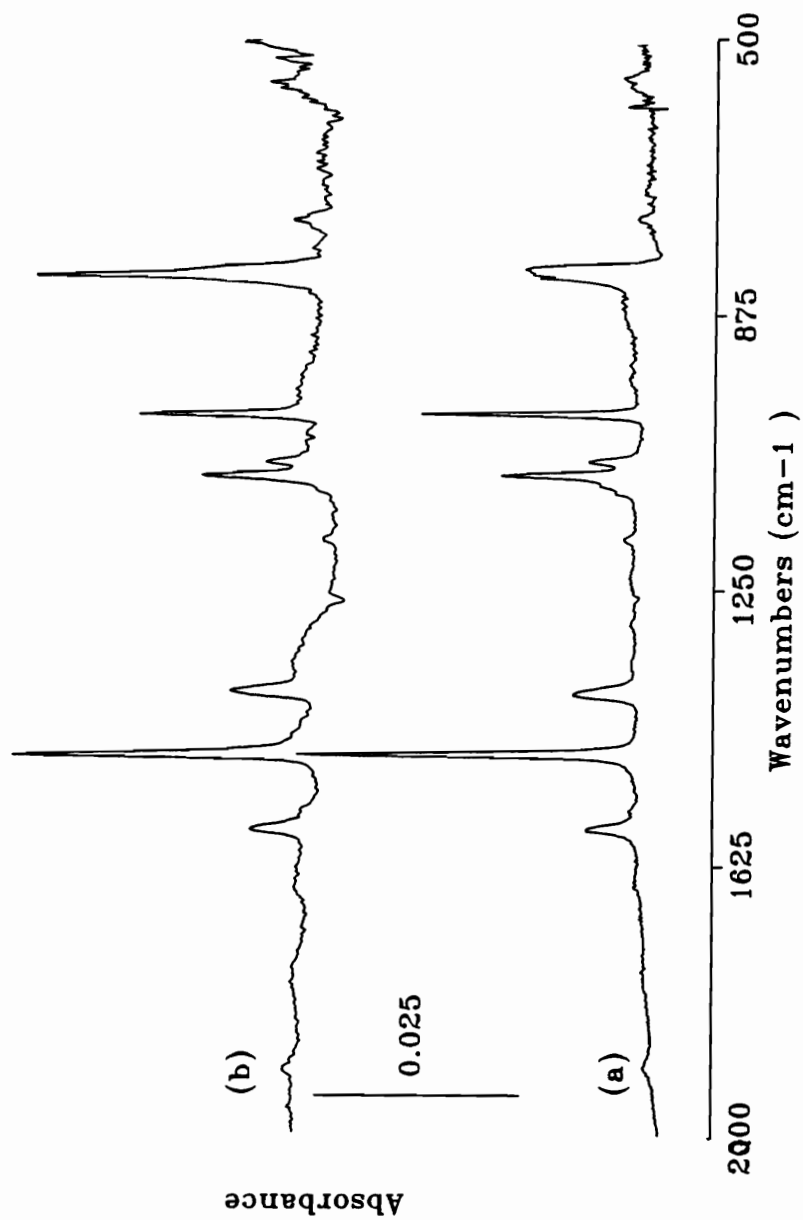


Figure 2.38 Comparison of the infrared spectra for (a) a 200 nm crystalline PPS film on a germanium substrate using transmission and (b) for the same film using p-polarized light and reflection at 60°.

PEEK films on cleaved mica by electron diffraction showed a parallel alignment of the polymer chains with the surface and a parallel growth direction (118). Studies of much thicker transcrystalline regions show parallel alignment against the surface and a growth direction perpendicular to the substrate (119). Figure 2.39 shows an illustration of the orientation postulated for these studies (119), and shows that orientation depends on film thickness, and also probably on particular sample preparation. While in this analysis, films of PPS appear to orient with the main chain direction parallel to the surface, clearly, the technique cannot distinguish between orientation given by Fig. 2.39 b and Fig. 2.39 c.

2.3.2 Analysis of Plasma Modified Polymer Surfaces

2.3.2.1 Theoretical Considerations

Figure 2.40 shows a schematic diagram of the problem of analyzing a thin modified surface region on a thicker underlayer of unmodified polymer. The diagram indicates that the polymer exists as a thin film on a metal substrate, a situation that can be readily examined experimentally by infrared reflection absorption spectroscopy. While this technique has been used in a limited number of studies to investigate modified surfaces (46,47), no studies have considered the theoretical aspects of the situation where a two layer system is involved. Such an analysis could give insight into methods to optimize experimental conditions for such a system.

To simulate the spectrum of a plasma modified polymer film, exact optical theory was used as outlined in Eqns. [9] through [19] using the fortran program RAS14 in Appendix 2.2. For the substrate polymer, optical constants for polystyrene were determined from the analysis of Pacansky et. al (29). The chemical composition, and therefore the optical constants, for an oxygen plasma treated polystyrene surface layer are not known, but investigations have suggested a number of oxidized carbon species including ether, carbonyl, carboxylate, and carbonate functionalities (120,121). Therefore, to simulate the surface layer, the optical constants of polymethylmethacrylate were used and calculated using the same method as for polystyrene (29). While this can serve as only an approximation of the chemistry found in the oxygen

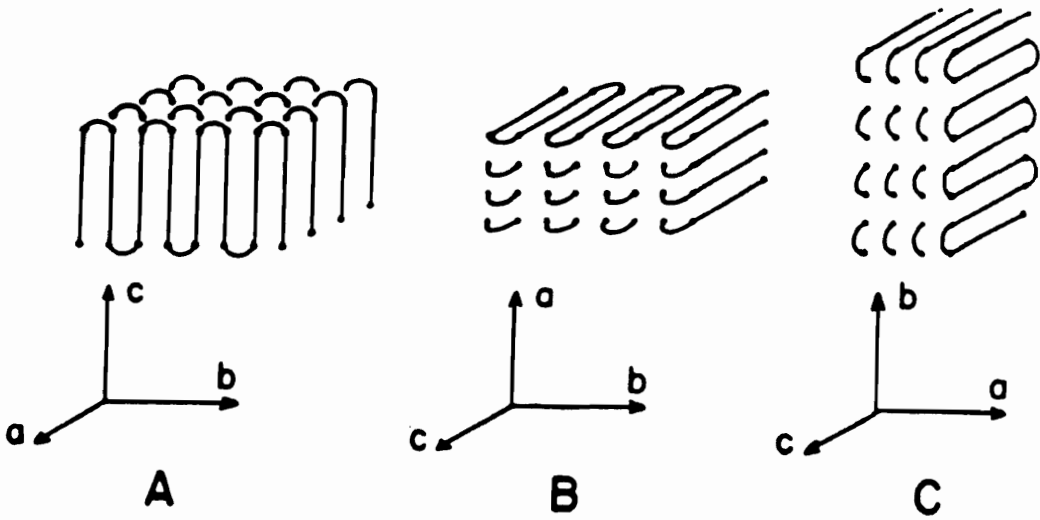


Figure 2.39 Proposed orientations of lamellae in films of different thicknesses: (A) thickness on the order of nanometers; (B) thickness on the order of hundreds of nanometers; (C) thickness on the order of tens of hundreds of nanometers (transcrystalline regions). (119)

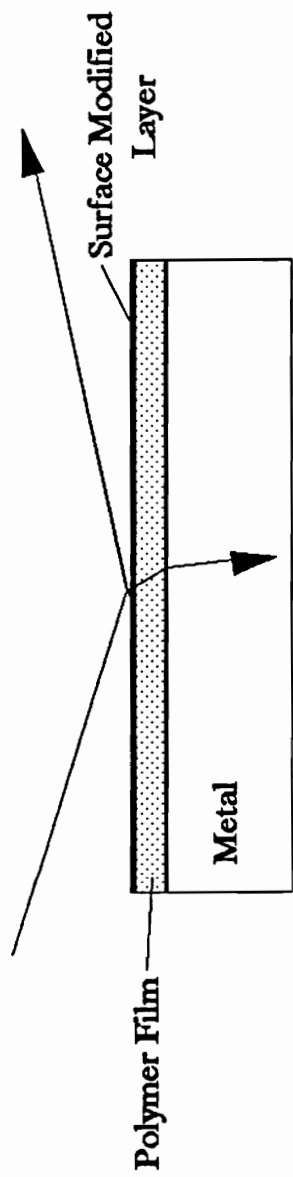


Figure 2.40 Schematic diagram of the problem of the IRRAS analysis of a surface modified polymer film.

plasma treated layer, the optical properties of carbonyl and C-O functionalities would not be expected to differ dramatically.

Figure 2.41 shows the simulated spectra of a 2 nm thick surface layer of PMMA on varying thicknesses of polystyrene substrates. As can be seen, only at the lowest polystyrene thicknesses, can any indication of the surface layer be observed in the raw spectra. The peak near 1600 cm^{-1} is assigned to the ring stretching mode for polystyrene. Often, subtraction techniques are used to analyze small chemical changes in infrared analysis, and Figure 2.42 shows the difference spectra in the carbonyl region for the plots spectra in Fig. 2.41. In this case, a simulated reference spectrum for unmodified polystyrene was used for subtraction. The intensity of the absorbance band for the carbonyl absorbance is weak ($4\text{-}5 \times 10^{-4}$) and strongly dependent on the thickness of the underlying polymer. In fact, given typical baseline instrumental signal to noise levels, carbonyl absorbance bands for polystyrene thicknesses in excess of 500 nm would be difficult to observe. To better understand this effect, Figure 2.43 shows the angular dependence for the z component of the electric field vector at the surface. The falling absorbance (see Fig. 2.42) is due to a diminishing electric field intensity as the modified layer is moved farther from the surface by the underlying polystyrene film. This, of course, depends of the angle of incidence, and Figure 2.44 shows the absorbance $(R - R_0) / R_0$ of the carbonyl peak intensity of a 2 nm PMMA film on an underlying polystyrene film of varying thickness. As shown, at 85° , the highest sensitivity for the detection of the surface layer is calculated for the case where the underlying film is relatively thin. However, a rapid decay in the peak intensity is observed with increase in polystyrene film thickness, and at higher thicknesses the higher angle of incidence offers no advantage in sensitivity.

While it can be shown from theory that both the x and z components of the electric field intensity diminish with increasing underlayer thickness, the y component, however, increases with distance from the surface. To investigate this effect, Figure 2.45 shows the predicted absorbance for a 2 nm film of PMMA on a substrate of polystyrene of varying thickness. An interesting result is obtained and shows that if the polystyrene underlayer thickness is chosen correctly ($1.1\text{-}1.2\mu$), an almost 5 fold

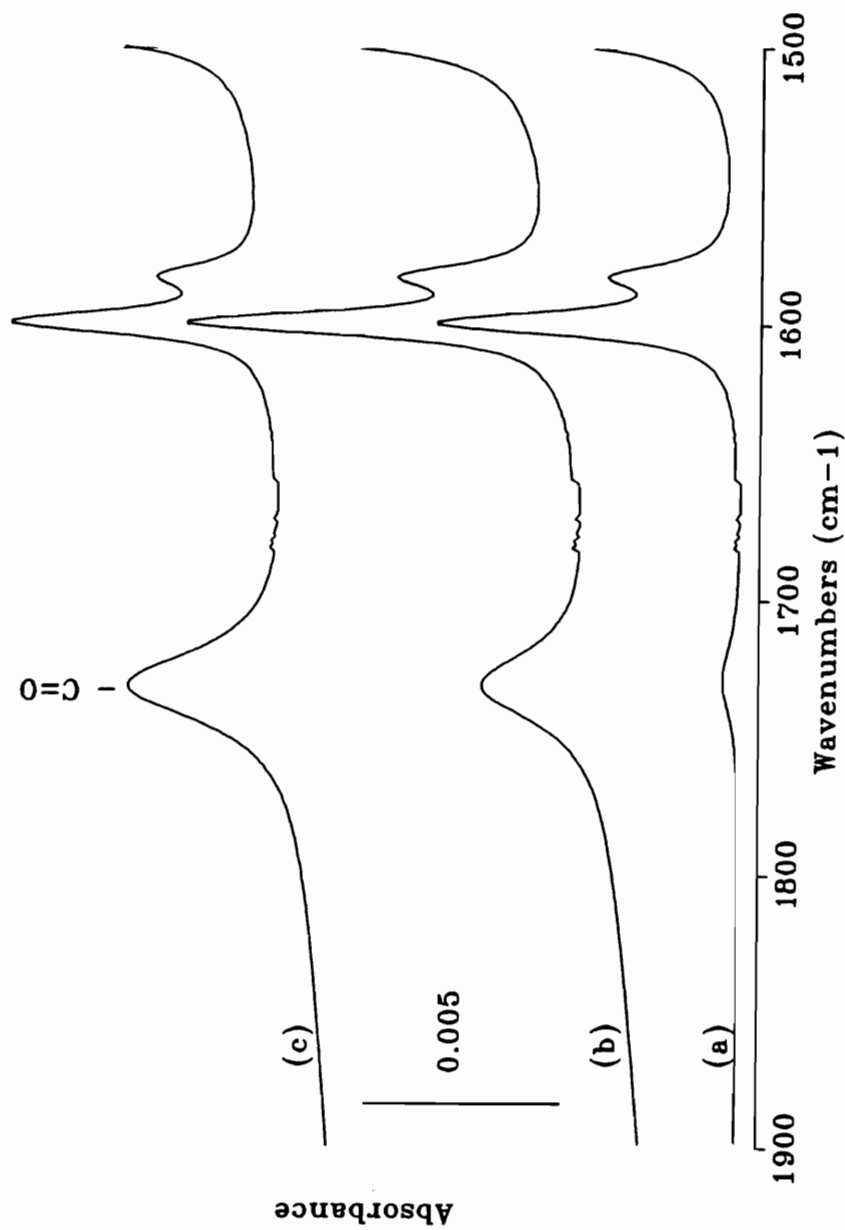


Figure 2.41 Simulated spectrum of a 2 nm surface layer of polymethylmethacrylate on a polystyrene film of varying thicknesses: (a) 0.5μ , (b) 0.1μ , and (c) 0.05μ on gold. The optical properties of gold were calculated from Ref (111).

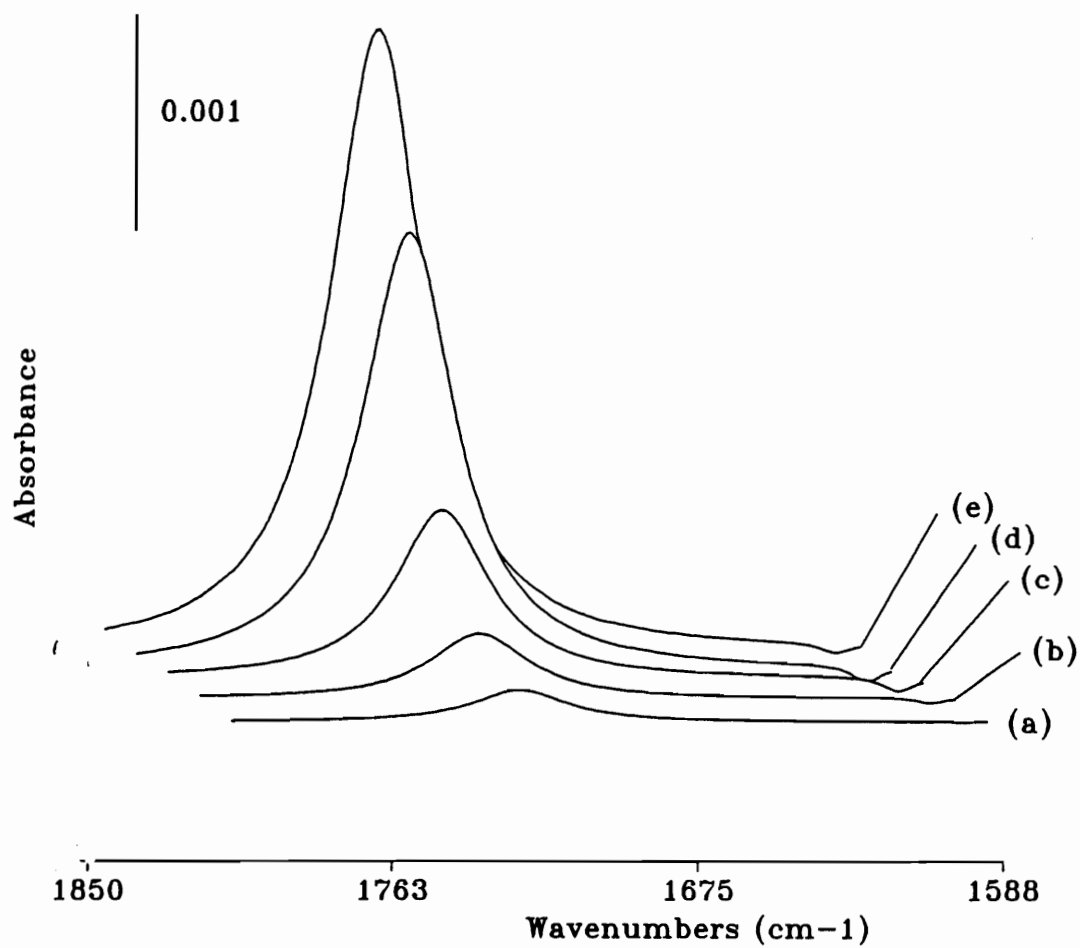


Figure 2.42 Simulated difference spectra for a 2 nm polymethylmethacrylate surface layer on a polystyrene film of varying thicknesses: (a) 1μ (b) 0.5μ (c) 0.25μ (d) 0.1μ and (e) 0.05μ on gold.

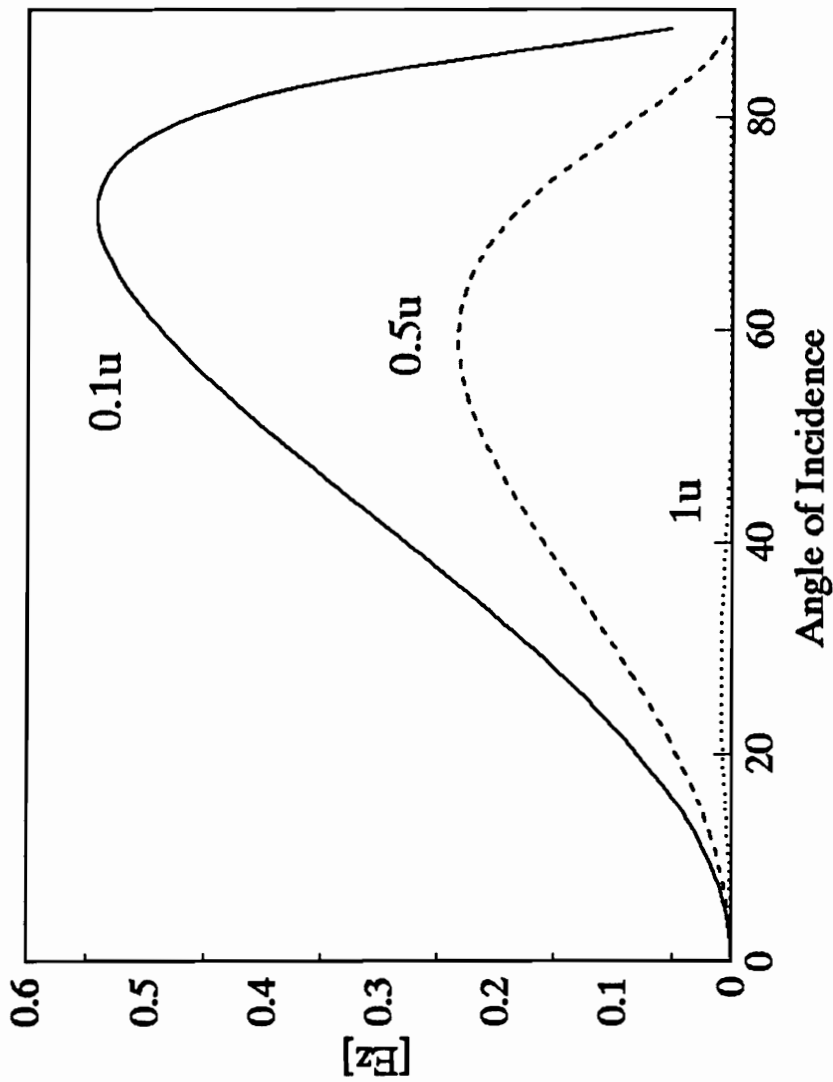


Figure 2.43 The angular dependence of the z component of the electric field intensity for the infrared analysis of a modified surface layer of a film on chromium. Optical constants of the surface layer were taken as 1.5 and 0.35 for n and k respectively for a typical carbonyl absorbance. The film was taken to be nonabsorbing with a refractive index of 1.59 and the n and k values of chromium were estimated to be 5 and 25 (112,122) respectively. Plots are shown for varying film thicknesses, and calculations were done for a z position in the center of the surface modified layer.

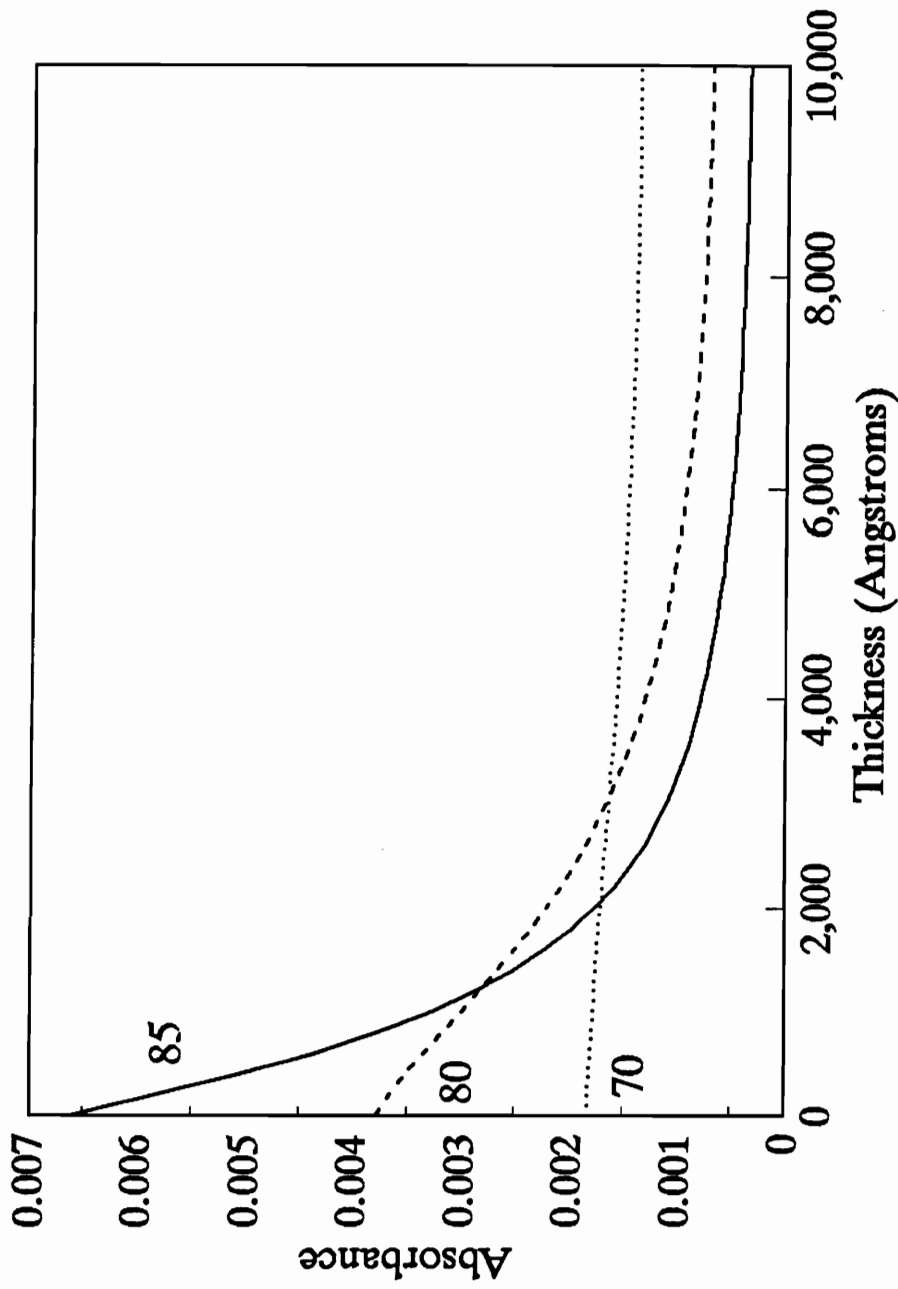


Figure 2.44 Calculated absorbance for a typical carbonyl absorbance in the surface modified layer as a function of both underlayer film thickness and angle of incidence. The optical constants used are the same as given in Fig. 2.43.

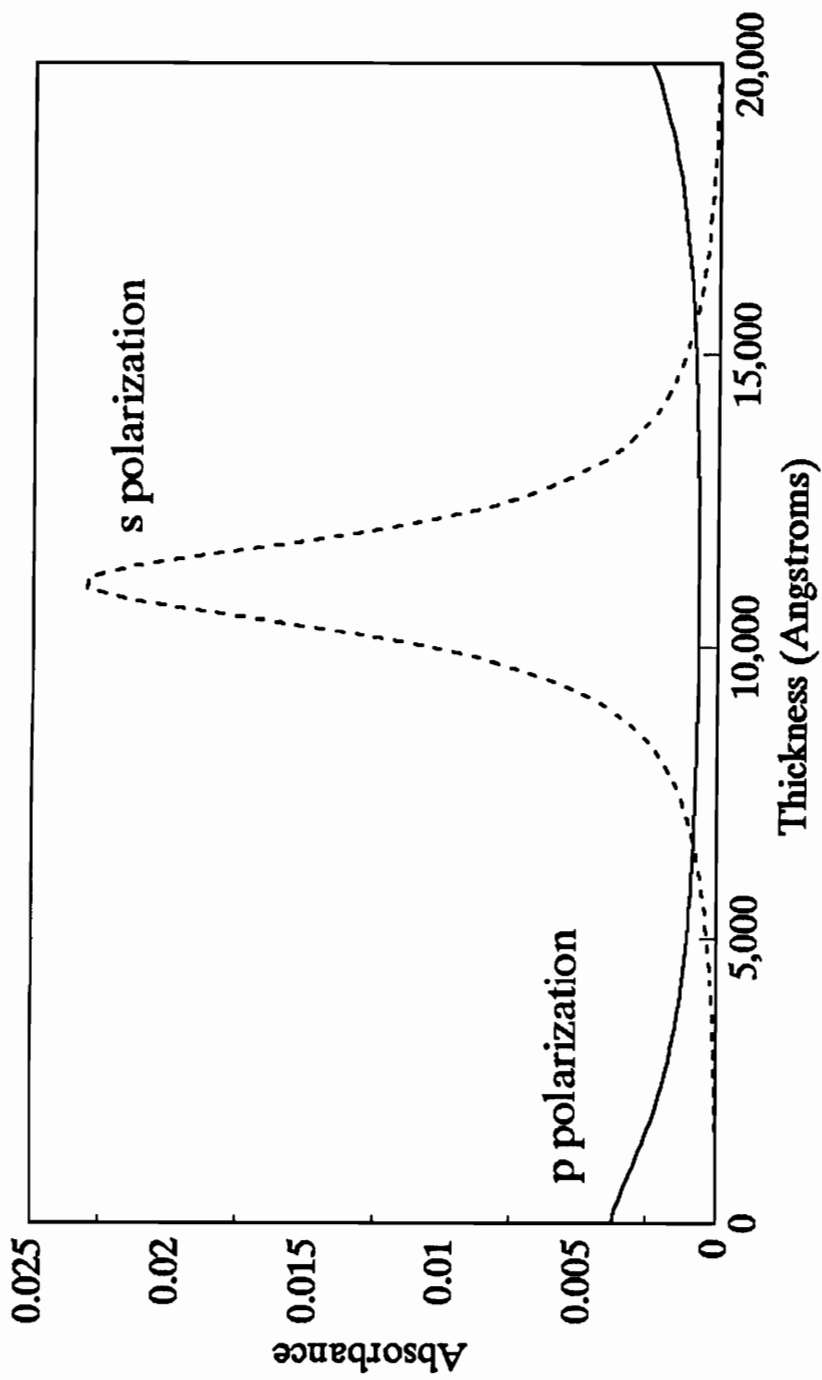


Figure 2.45 Calculated absorbance for a typical carbonyl absorbance in a surface layer as a function of both underlayer thickness and polarization state of the incident light. The optical constants used are the same as given in Fig. 2.43.

enhancement in the signal for the carbonyl absorbance is observed for s-polarization over even the most sensitive measurement that can be made with p-polarization. For p-polarization, however, the choice of a thin (< 10nm) underlayer is desirable to achieve maximum sensitivity (see Fig. 2.44).

2.3.2.2 Surface Analysis of Plasma Modified Polystyrene

2.3.2.2.1 Ellipsometry

Figure 2.46 shows the ellipsometric analysis of polystyrene etching by an Rf generated oxygen plasma. A near linear plot is indicated, and regression analysis shows an etch rate of approximately 5 nm/minute. Although other methods including gravimetric analysis or laser interferometry can be used to monitor material loss during plasma exposure, ellipsometry has the advantage of detecting extremely small changes in thickness (<1 nm resolution), therefore allowing the initial stages of etching to be examined. The technique should also lend itself to *in-situ* analysis. The disadvantage of ellipsometry is that due to the isotropic single layer model used, use of this technique is only valid when the surface modification layer is thin and similar in optical properties to the underlying substrate. Two layer models can be used, but the analysis becomes complicated as the optical constants and thickness of the surface layer are not known a priori. Another requirement is that the polymer must be cast in a thin film form on a reflective substrate. These criteria are probably met for many polymeric systems where the surface modification is estimated to be thin, but errors will arise when analyzing siloxane containing materials, where it has been shown that a SiO₂ layer forms at the surface during plasma treatment (91,92).

2.3.2.2.2 X-ray photoelectron Spectroscopy

Table 2.3 gives the results for XPS analysis of the atomic concentrations of elements present after oxygen and ammonia plasma treatment for varying lengths of time. For untreated films, no oxygen was detected, while after oxygen plasma treatment, the oxygen content increases dramatically to approximately 25%, and does

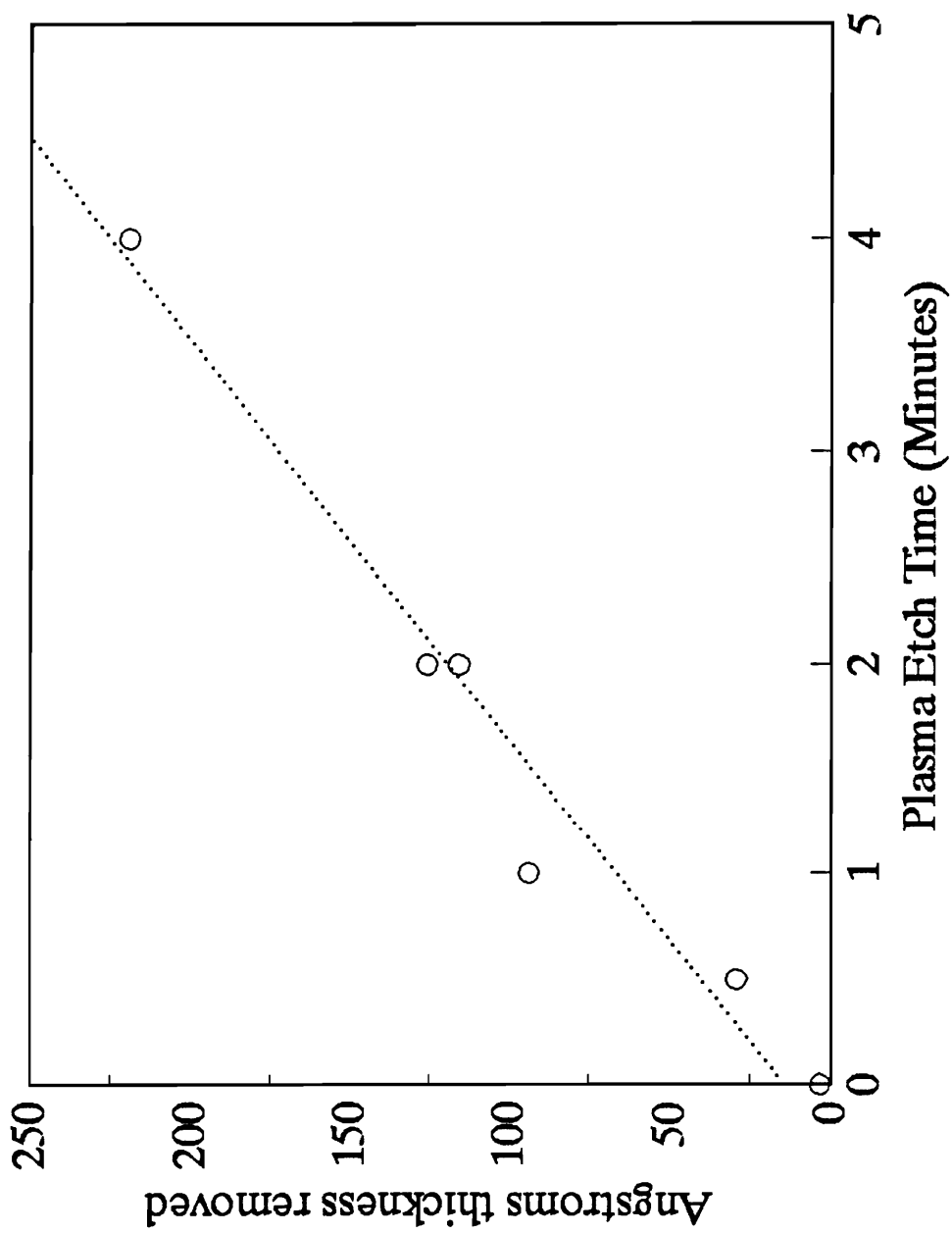


Figure 2.46 Thickness removed for polystyrene thin films as a function of oxygen plasma etch time.

Table 2.3 XPS Analysis of the Major Elements Present for Oxygen and Ammonia Plasma Treatment of Polystyrene.

<u>Time</u>	<u>Oxygen Plasma</u> ¹			<u>Ammonia Plasma</u> ²		
	<u>C1s</u>	<u>O1s</u>	<u>N1s</u>	<u>C1s</u>	<u>O1s</u>	<u>N1s</u>
0	100%	0	0	100%	0	0
0.5	75%	25%	---	---	---	---
1	75.1%	24.9%	---	---	---	---
2	74.3%	25.7%	---	90.6%	2.2%	5.9%
3	---	---	---	89.8	2.9	5.9
4	---	---	---	88.5	3.3	6.7

¹ All samples showed a small nitrogen signal in the wide scan, and this was not included in the atomic concentrations shown.

² Air dried samples showed a small chlorine signal due to residual solvent after etching and accounts for approximately 1% for these samples.

not vary in the limited time range analyzed. For ammonia plasma treatment at somewhat longer exposure times, there is incorporation of 6 - 7% nitrogen and 2 - 3% oxygen. The incorporation of oxygen is probably due to the reaction of chemically active surface species with air during transfer to the spectrometer. The high percentage of carbon relative to nitrogen after ammonia plasma treatment shows that direct functionalization by this gas is much less than when compared to that for oxygen plasma treatment.

To further examine the nature of the surface modified layer, Figure 2.47 shows the C1s narrow scan spectra for a control and a one minute oxygen plasma treated samples at 90°, 30°, 10° exit angles. For the control sample, a single symmetrical peak could be fit to the data using a 75% gaussian / 25% lorentzian envelope with a full width at half maximum intensity of 1.25 eV. The absence of any oxygen bound carbon species correlates with the atomic concentration of 100% carbon. Upon plasma treatment, however, a large number of functionalized carbon species are detected at higher binding energies. Although curve fitted peaks are not shown, a number of oxidized species have been postulated including ether, carbonyl, carboxylate, and carbonate species (107). The spectra for a 10° takeoff angle shows the large increase in the oxidized carbon species relative to the main hydrocarbon peak intensity, indicating an increased concentration of oxidized species in the near surface region. The C1s spectrum of a two minute ammonia plasma treated polystyrene film is also shown in Fig. 2.47 and curve fitting at 90° shows only two new carbon groups at approximately 286 and 287 eV which combined probably represent new C-N or C-O species. At 10°, however, a small peak corresponding to C=O species can be seen.

2.3.2.2.3 Infrared Reflection Absorption Spectroscopy (IRRAS)

Figure 2.48a shows the results of the IRRAS analysis of an oxygen plasma treated 30 - 40 nm polystyrene film on a ferrotype substrate. The spectrum actually represents the difference spectrum between treated and untreated films, and takes into account the thickness of polymer removed. The largest peak in the spectrum is

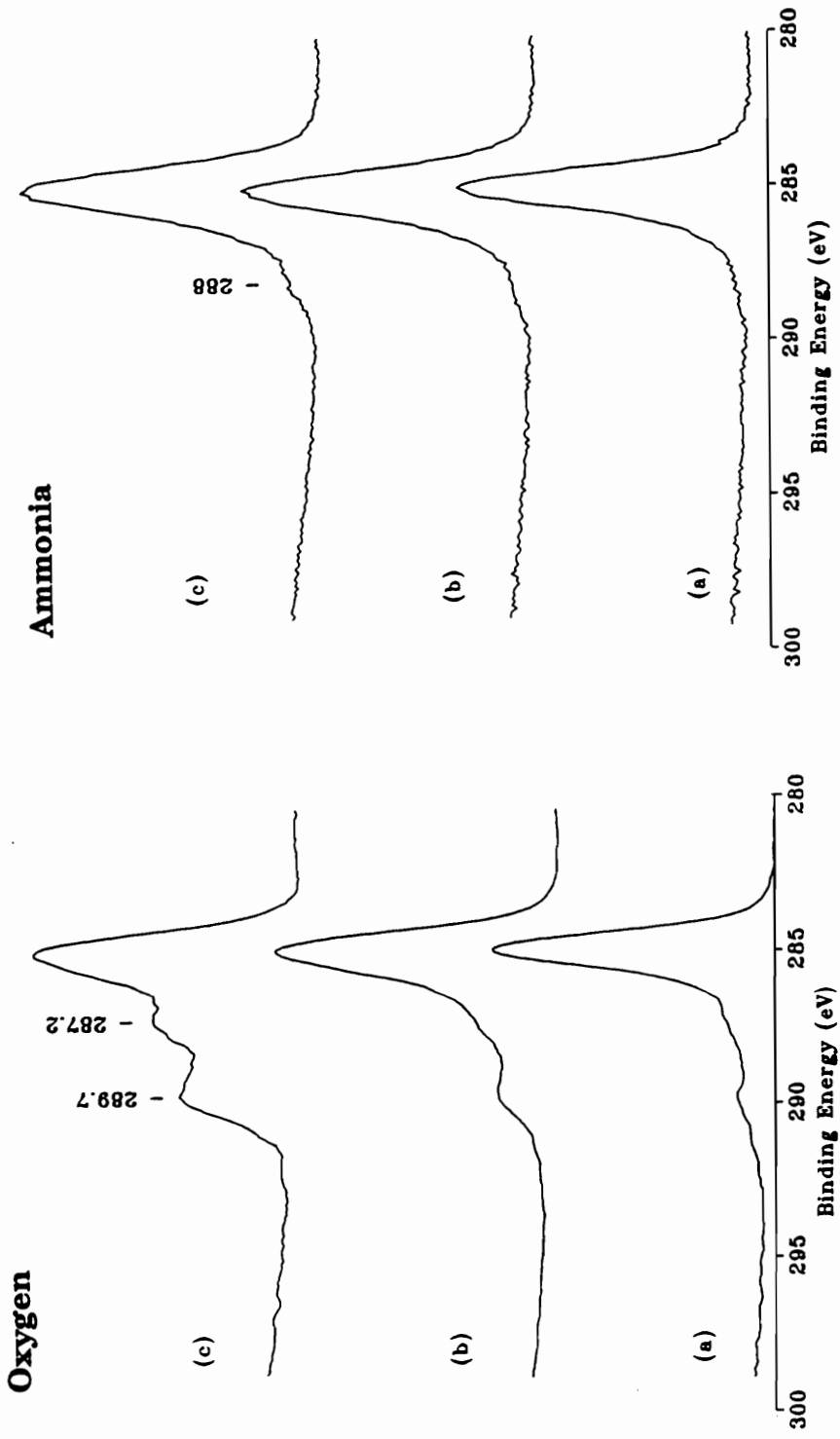


Figure 2.47 C1s line shape for untreated, oxygen plasma, and ammonia plasma treated polystyrene films at (a) 90°, (b) 30°, and (c) 10° exit angles.

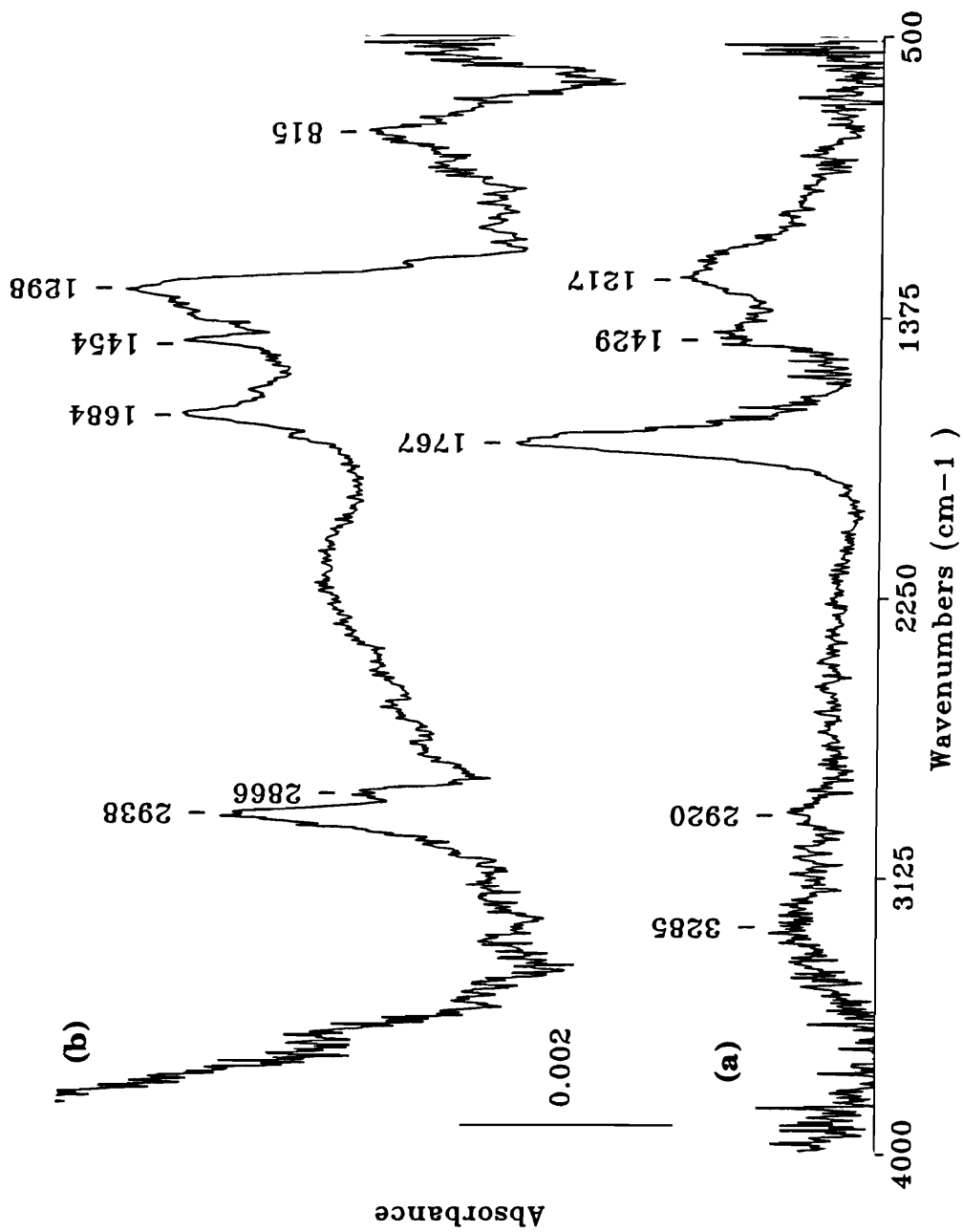


Figure 2.48 IRRAS difference spectra of a (a) one minute oxygen plasma treated polystyrene film and a (b) two minute ammonia plasma treated film. The reference was multiplied by a factor to account for the amount of polymer removed.

located at 1767 cm^{-1} and the peak width of more than 100 cm^{-1} clearly indicates a wide range of carbonyl species present. A typical carbonyl absorbance in a polymer backbone structure would be approximately an order of magnitude narrower. The peak maximum, however, may indicate ester functionality, and the high frequency suggests possible conjugation with the ester single-bonded oxygen as would be found in phenyl or vinyl acetates (1770 cm^{-1}) (4). The second most intense peak at 1217 cm^{-1} may suggest C-O or more probably aryl-O groups that would be present in ether or ester groups. The 1435 cm^{-1} absorbance band can be attributed to a C-H bending mode and there is also a small absorbance due to C-H stretching in aliphatic hydrocarbon species. A rather broad absorption band is present in the $2400 - 3500\text{ cm}^{-1}$ region which may indicate some carboxylic acid species (4). The observed carbonyl band has an intensity of approximately 3.5×10^{-3} absorbance units, and using optical theory, the thickness of the modified layer can be estimated. With typical optical constants of 1.5 and 0.3 - 0.4 for n and k values, respectively, of a typical polymer containing a carbonyl functionality (24,28), and optical constants of polystyrene taken as 1.59 and 0 in the carbonyl region (28), the thickness of the modified layer can be estimated to be in the range of 1.0 to 1.5 nm. For comparison, the thickness of modified surface layers for plasma treated polymers have been generally estimated in the range of 2 to 20 nm for a number of plasma treated polymers (43).

Figure 2.48b shows the IRRAS spectrum for a two minute ammonia plasma treated polystyrene film, and shows the dramatically different functionalization of the polystyrene surface produced by this gas. The most noticeable features are the strong bands at 2938 and 2866 cm^{-1} indicative of a C-H stretch and shows the increase in the aliphatic hydrocarbon nature of the surface layer. This result shows the great promise of using a surface sensitive vibrational method to complement XPS analysis, which cannot distinguish between aliphatic and aromatic carbon moieties. The absorbance band at 1454 cm^{-1} can be assigned to a C-H bending vibration, and the broad medium intensity band at 1684 cm^{-1} may be assigned to several possible groups. The shoulder near 1600 cm^{-1} may be attributed to a N-H scissoring mode, and therefore the band at 815 cm^{-1} would represent the out-of-plane absorbance for this group. Identification

of primary or secondary amines requires a N-H stretch, but this absorbance is difficult to assign due to the poor signal to noise in the 3000 - 4000 cm^{-1} region. The 1684 cm^{-1} could be assigned to an amide functionality, however, XPS indicated that only a small percentage of C=O groups were present in the surface layer. Another possibility is that the peak represents imine groups (-N=N-) on the surface which would have absorbances in this spectral region (4). Estimation of the thickness of the surface modified layer is more difficult due to the wide range of k values for typical hydrocarbon C-H stretching absorbances. If a range of k values from 0.02 - 0.08 is taken as for typical polymers (28), the thickness can be estimated to fall in the range of 3 - 10 nm, and shows a thicker modified layer than was found for oxygen plasma treatment.

To explore the stability of the surface layer with time, IRRAS spectra were taken immediately after treatment, and after 72 hours in a nitrogen environment. The results are shown in Figure 2.49 and dramatic spectral changes after aging are evident. The spectrum shows a large increase in the C-O functionality at approximately 1213 cm^{-1} and a shifting and broadening of the carbonyl band to lower frequencies ($\sim 1750 \text{ cm}^{-1}$). The broad absorption from approximately 2800 - 3500 cm^{-1} may indicate increased hydroxyl concentration and an increase in the peak intensity at 2935 cm^{-1} is indicative of higher concentrations of hydrocarbon. Although the results do not represent a thorough study, the IRRAS technique is clearly sensitive to a large scale restructuring of the plasma modified region. A broad hydroxyl absorbance, coupled with a shifting of the carbonyl to lower frequencies and an increase in C-O functionalities are consistent with an increase of carboxylic acid species. This may indicate possible hydrolysis reactions with residual amounts of water present. The increased hydrocarbon and C-O functionalities may also indicate contamination of the newly formed hydrophilic surface after treatment. Although analysis by XPS did indicate increased C-O functionality after storage, dramatic changes were not seen, and analysis required extensive curve fitting. This, again shows the usefulness of IRRAS as a complementary technique to XPS.

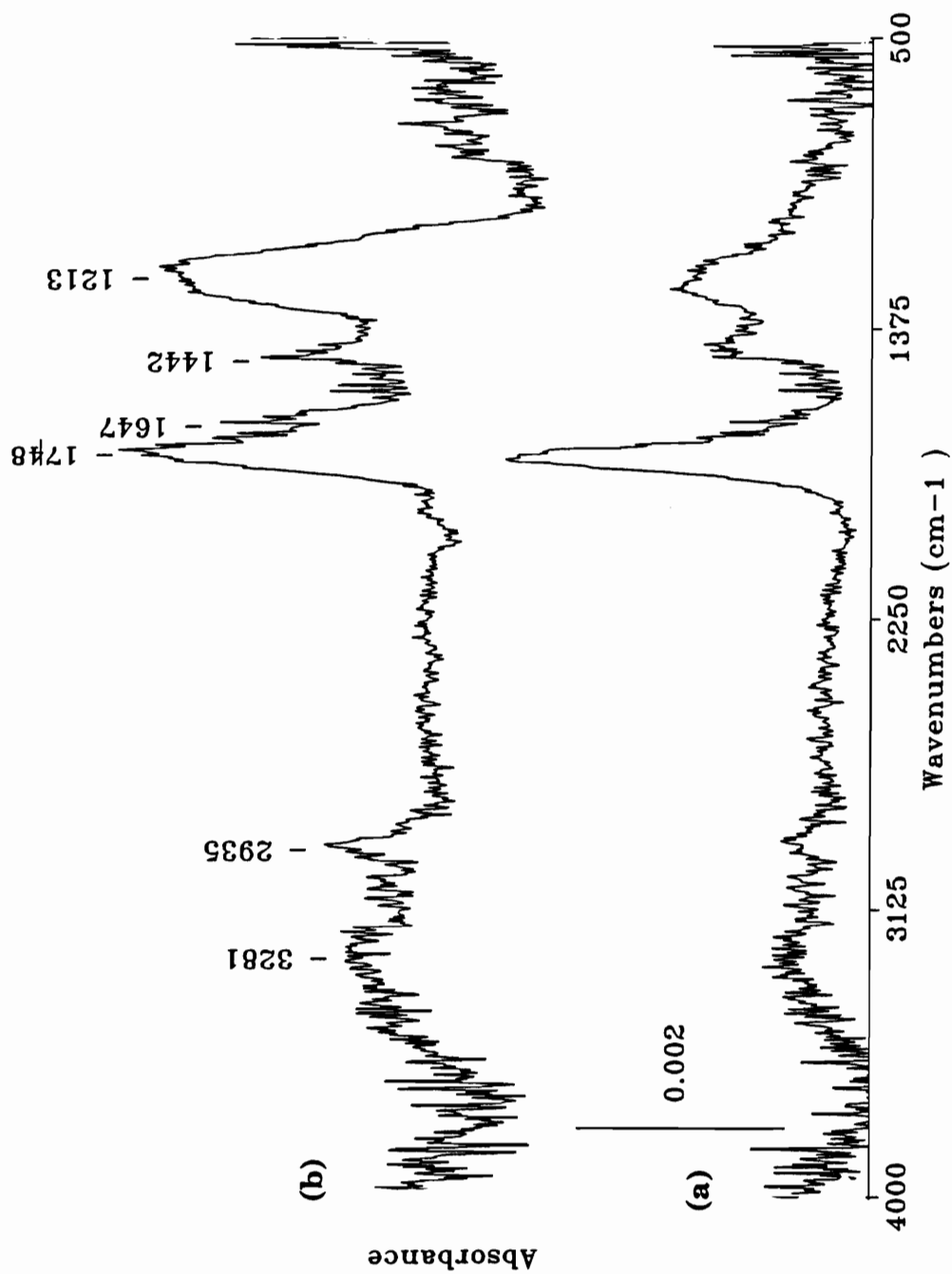


Figure 2.49 IRRAS difference spectra for a one minute plasma treated polystyrene film taken (a) immediately after treatment and (b) after 72 hours under nitrogen.

2.3.2.3 Analysis of Plasma Modified PPS

2.3.2.3.1 Ellipsometry

Figure 2.50 shows the results of the thickness removed by etching versus time of exposure for both oxygen and ammonia treated PPS. The original thickness values for these films ranged from 30 - 50 nm. The results for oxygen plasma treatment show a limited and almost linear ablation rate. By contrast, the ammonia plasma treatment shows a relatively rapid etch rate but then the plot seems to plateau after 2 - 3 minutes. Due to the thermal treatment of the film following plasma treatment and prior to the thickness determination (re-melt and quench), the results can only be viewed as approximate, although the relative rates of etching for ammonia and oxygen plasma are certainly valid.

2.3.2.3.2 X-ray Photoelectron Spectroscopy

Figure 2.51 shows the atomic concentrations of major elements found after various oxygen plasma treatment times of PPS. The plot shows a rapid incorporation of oxygen reaching almost 30% after only one minute exposure time. In comparison with the ellipsometry results, the relatively unchanging atomic concentration levels with time after the first measurement (30 seconds) indicate that steady state conditions must exist for the plasma conditions used. Figure 2.52 shows the C1s narrow scan spectrum of PPS after one minute oxygen plasma treatment. The C1s spectrum for the control sample with no treatment is also given and shows no oxidized carbon species, indicating that little oxidation occurred during the elevated temperature coating procedure. The shake-up satellite at about 291.5 eV, due to the aromatic nature of the polymer, is also evident. The spectrum for the plasma modified PPS shows the presence a number of oxidized carbon species ranging from 0.8 to almost 5 eV higher than the main C-H photopeak position at 285 eV. Curve resolution of the carbon spectrum indicates four peaks at 285.8, 287.5, 288.5, 289.6 eV. Although all individual binding energies are somewhat lower than that reported for oxygen plasma treatment of polystyrene (120), the photopeaks may be tentatively assigned to C-O, C=O, O-C=O, and carbonate species. By lowering the exit angle from 90° to 10°, the

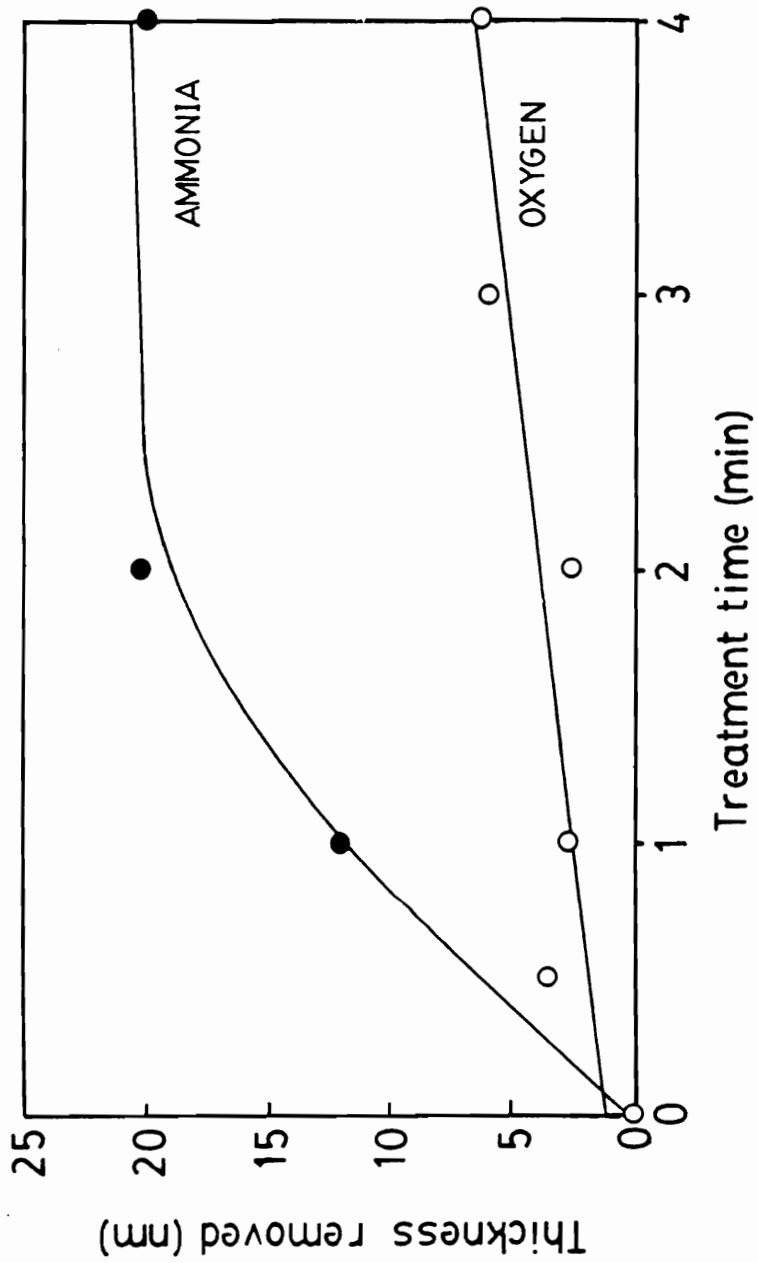


Figure 2.50 Thickness removed for PPS thin films as a function of oxygen and ammonia plasma etch time.

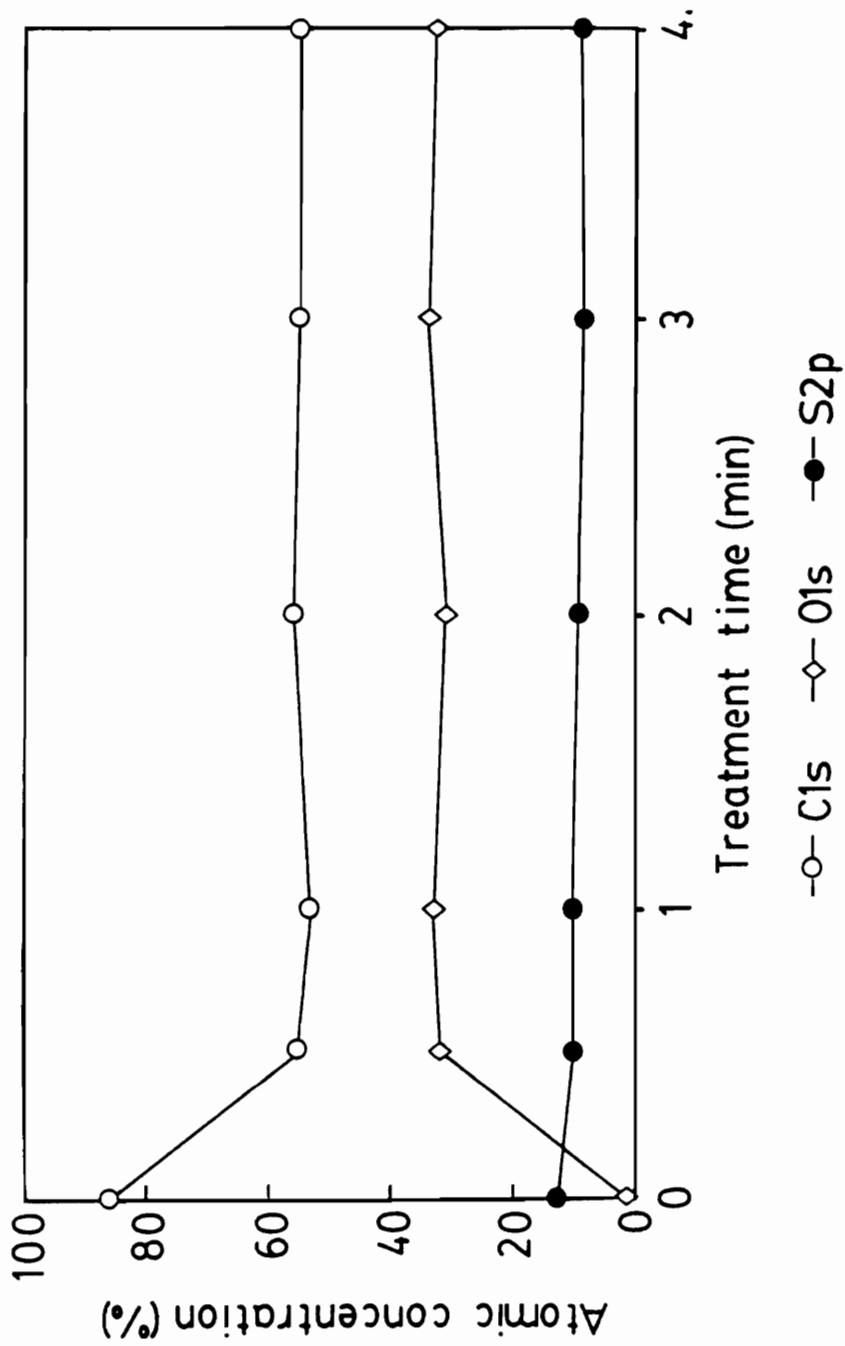


Figure 2.51 XPS analysis of atomic concentration changes for PPS thin films versus oxygen plasma treatment time.

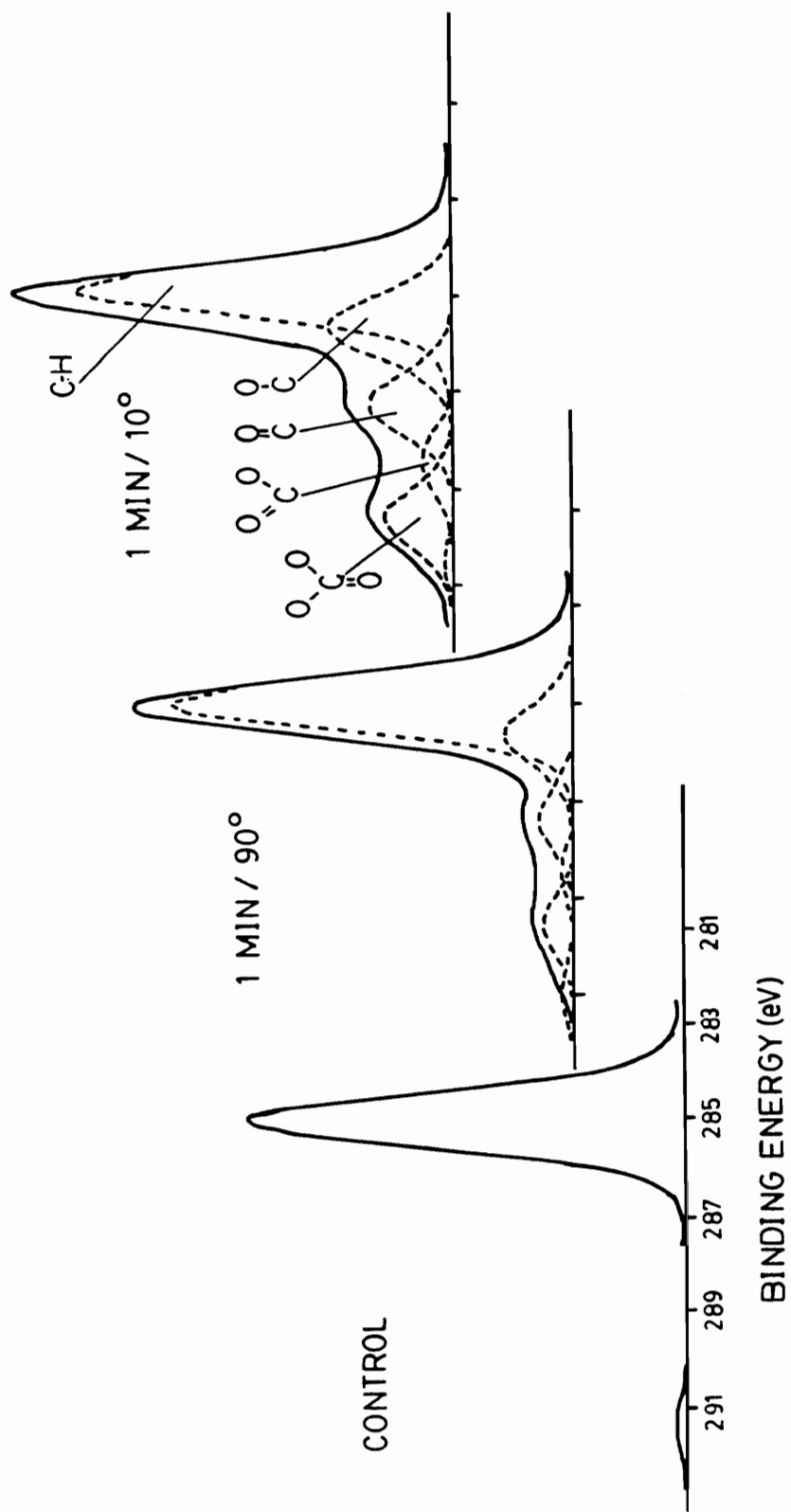


Figure 2.52 C1s line shape for untreated and oxygen plasma treated PPS films at both 90° and 10° exit angles.

mean sampling depth can be decreased and the technique made more surface sensitive. If the mean free path (λ) for the C1s electron is taken as approximately 1.4 nm (123), the sampling depth can be calculated as approximately $3\lambda \sin \phi$ where ϕ is the takeoff angle. Therefore, the sampling depths for 90° and 10° are found to be 4.2 and 0.7 nm respectively. Fig. 52 also shows the narrow scan spectrum for a 10° "take off" angle. Here, the relative intensity of the oxidized carbon species to the main C-H photopeak has increased, indicating that the modifications due to plasma treatment are restricted to the topmost layers of the PPS substrate.

Analysis of the S2p photopeak in Figure 2.53 shows that oxygen plasma treatment results in a broad higher binding energy photopeak at 169.4 eV, clearly separated from the sulfide doublet at 163.8 and 164.8 eV. This high binding energy can be attributed to highly oxidized forms of sulfur, and the wide peak indicates more than one oxidized form. Similar results were obtained for PPS composites exposed to atomic oxygen in low earth orbit (124). This may show the usefulness of plasma treatment in simulating at least some of the effects expected for candidate materials for space applications. The dramatic increase in the oxidized sulfur species compared to non-oxidized substrate sulfur when a 10° exit angle is used shows again that the plasma modification is restricted to the top surface layers of PPS.

Analysis of the atomic concentration found by XPS for various exposure times of PPS to ammonia plasma discharge is shown in Figure 2.54. Increase in nitrogen content from zero to 6-7% is observed, and the N1s binding energy was approximately 400 eV indicating an amine type functionality. There was also a similar smaller increase in oxygen content. The increase in oxygen content with non-oxygen containing plasmas is a common phenomenon found in many studies (45,120), and can possibly be due to oxidation of residual free-radicals when the sample is exposed to air. The increase in nitrogen and oxygen content was accompanied with a 50% reduction in sulfur content and little change in carbon. The sulfur narrow scan showed little difference when compared to control samples indicating that the reduction in sulfur concentration most probably is attributed to an overlayer of modified material containing little sulfur. As with oxygen plasma treatment, steady

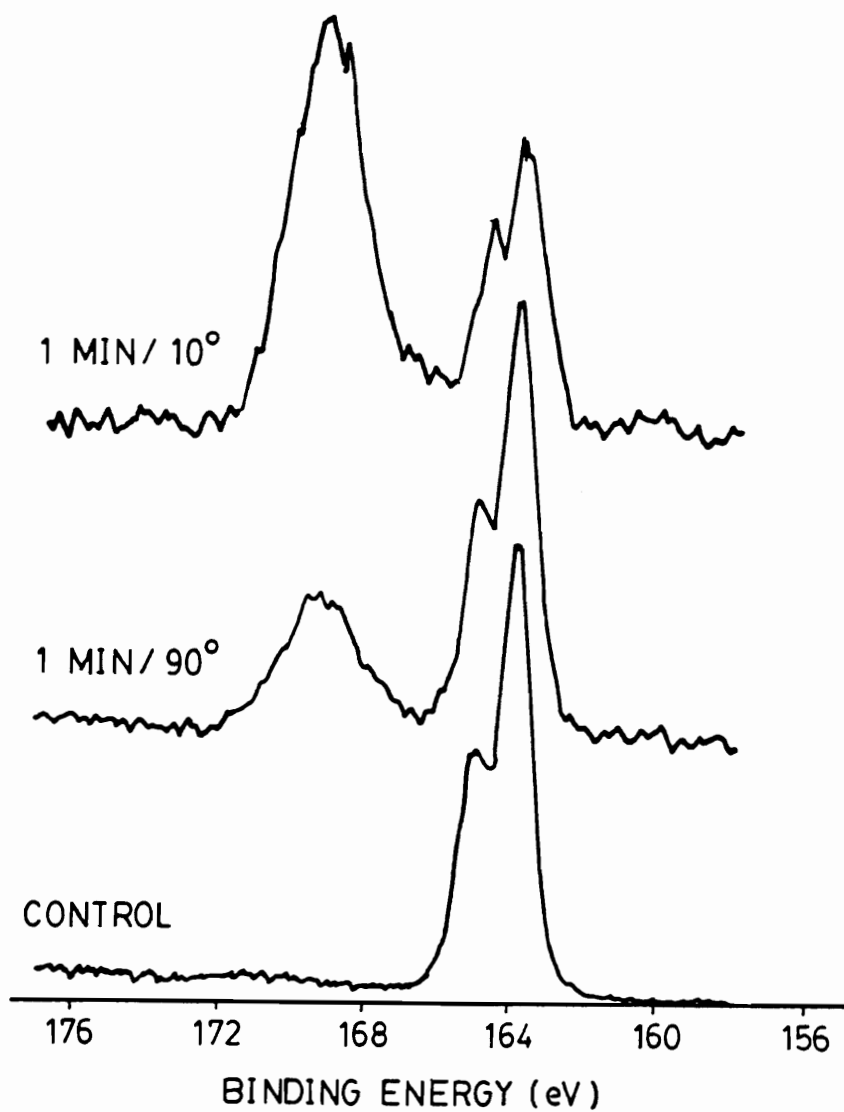


Figure 2.53 S_{2p} line shape for untreated and oxygen plasma treated PPS films at both 90° and 10° exit angles.

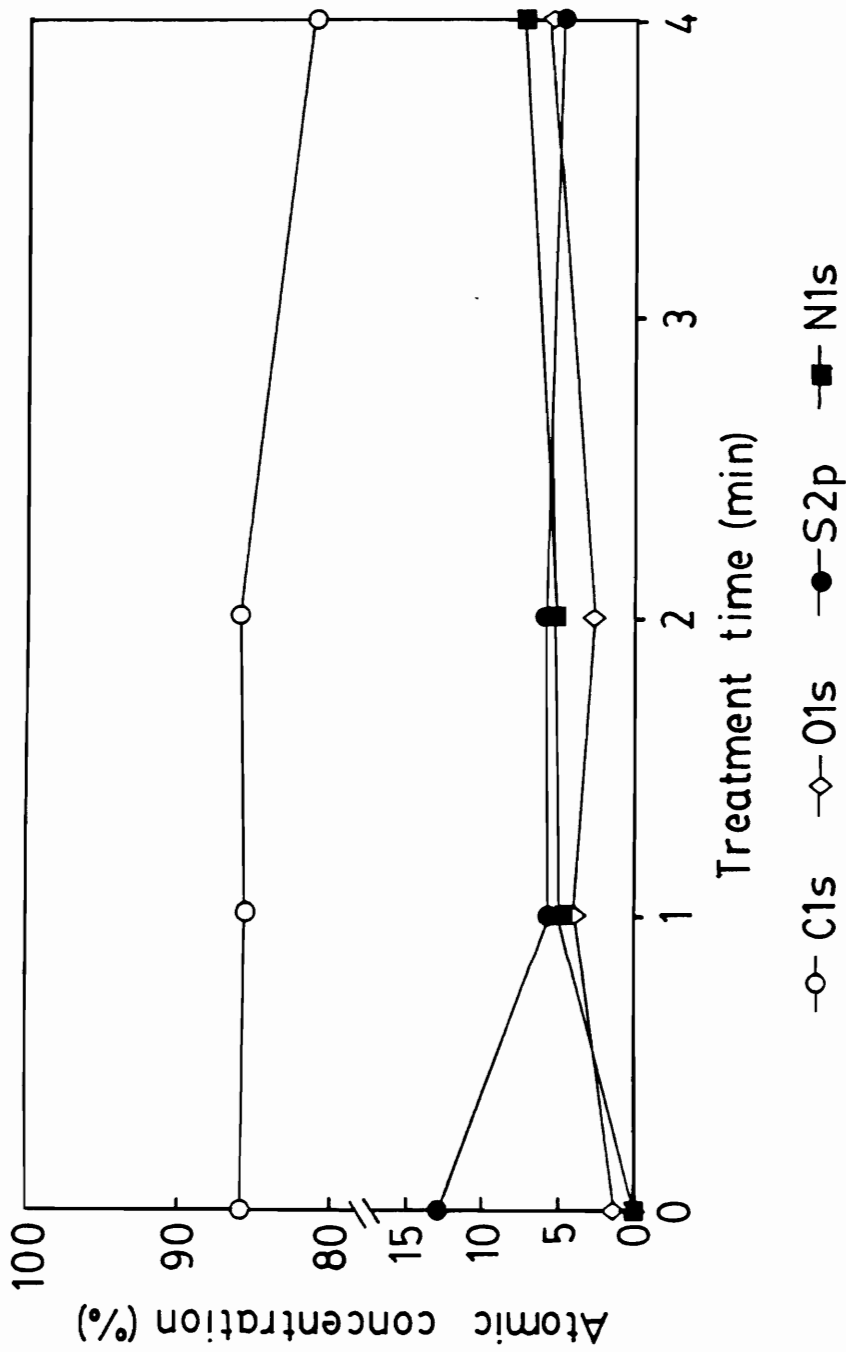


Figure 2.54 XPS analysis of atomic concentration changes for PPS thin films versus ammonia plasma exposure time.

state was achieved within one minute even though ellipsometry indicated significant ablation of the surface film by the ammonia plasma. The C1s narrow scan spectrum in Figure 2.55 shows a new photopeak curve fitted at approximately 0.8 - 1 eV higher than that of the main C-H peak and this peak can be assigned to C-N or C-O functionality. However, even with incorporation of oxygen, no evidence for higher oxidation states of carbon is seen.

2.3.2.3.3 Infrared Reflection Absorption Spectroscopy (IRRAS)

The IRRAS spectrum of a 30 nm thick polyphenylene sulfide film before and after oxygen plasma treatment is shown in Figure 2.56. The plasma induced changes are evident in the C-O (1250 cm^{-1}) and C=O (1750 cm^{-1}) absorbance regions. Figure 2.57 shows the difference spectrum where the untreated PPS film is used as a reference and its intensity reduced by a factor to account for the amount of material removed during plasma treatment. Two relatively intense and broad absorption bands are located at 1760 and 1230 cm^{-1} again indicating mainly C=O and C-O functionalities. The breadth of the carbonyl peak indicates a wide range of functional groups created during treatment including possibly ketone, aldehyde, ester, and carboxylic acid moieties. Relatively little absorbance is seen, however, in the OH stretch region indicating little hydroxyl or carboxylic acid formation. The large absorption band due to primarily C-O functional groups is also in agreement with XPS data that show these to be in the largest relative concentration compared to other forms of oxidized carbon. The C-O absorbances may be associated with various ether groups as well as with ester or carboxylate groups. Oxidized forms of sulfur should also be detected in this region and the absorbance bands associated with these groups probably overlap with various C-O absorbances. For example, absorbance bands for the asymmetric and symmetric stretches of sulfonic acids fall in the range $1340 - 1350\text{ cm}^{-1}$ and $1150 - 1165\text{ cm}^{-1}$ respectively (4), which are well within the envelope observed.

The difference spectrum of ammonia plasma treated PPS is shown in Figure 2.58. All bands are relatively weak although the absorbance band at 2940 cm^{-1} can be assigned to a C-H stretch associated with increased hydrocarbon functionality after

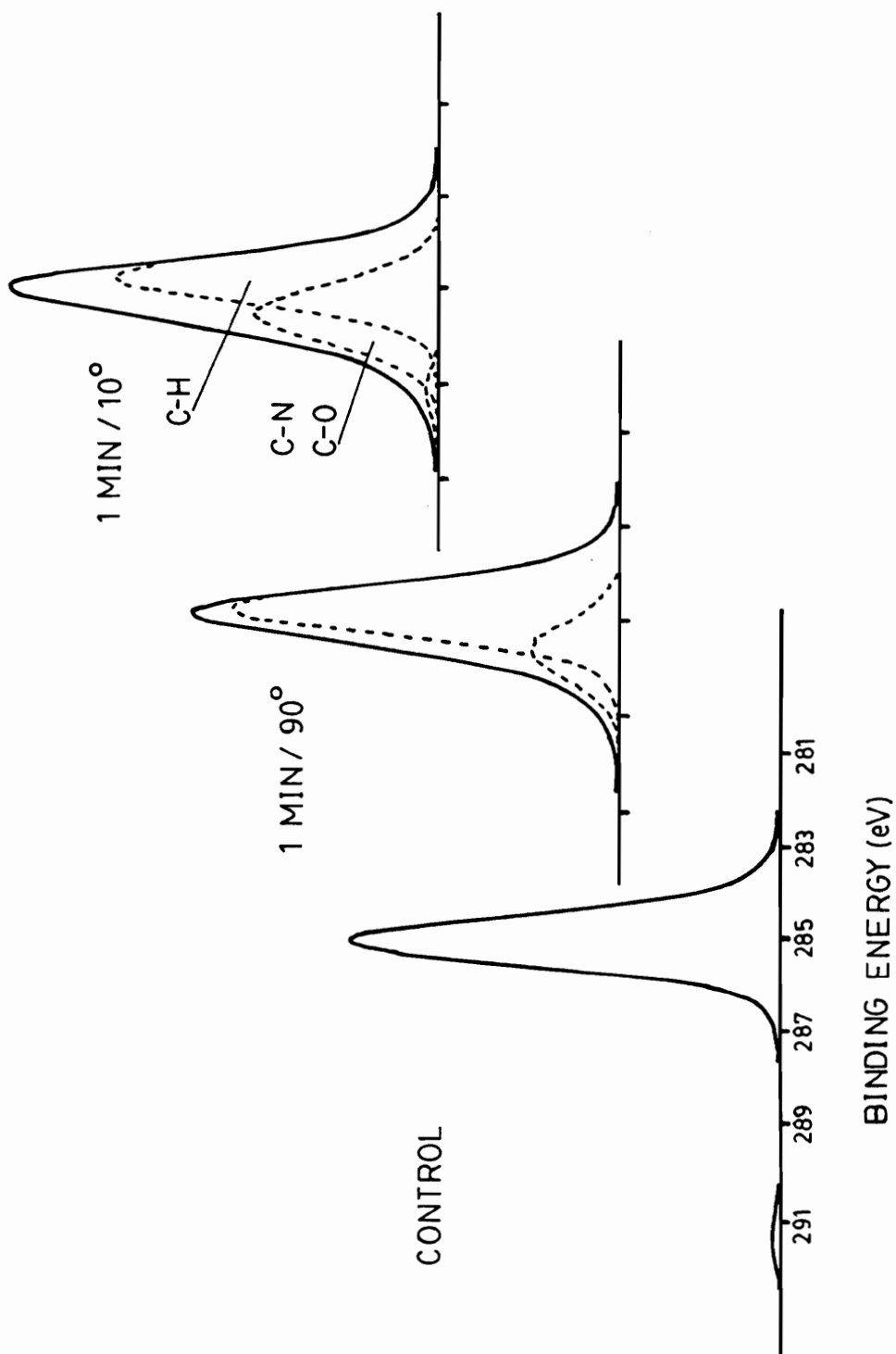


Figure 2.55 C1s line shape for untreated and ammonia plasma treated PPS films at both 90° and 10° exit angles.

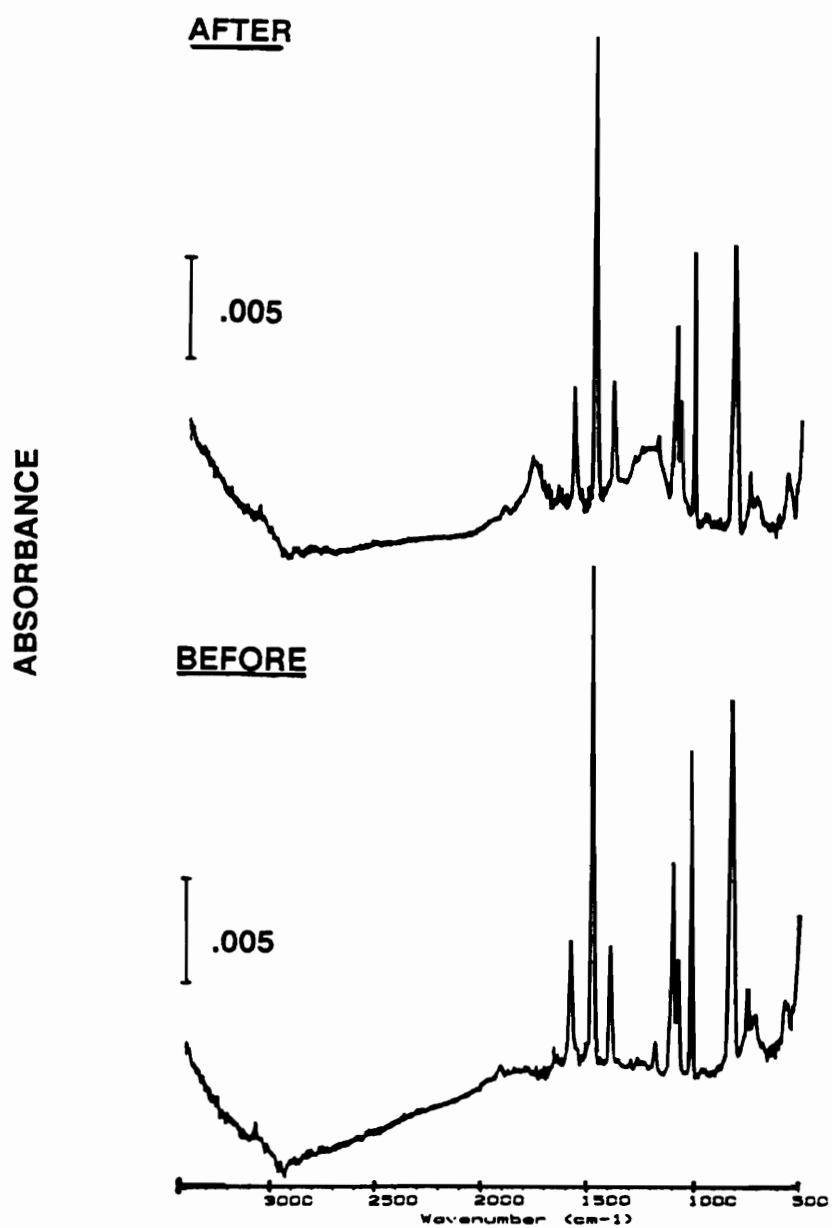


Figure 2.56 IRRAS spectra of a 30 nm PPS film before (A) and after (B) a one minute oxygen plasma exposure.

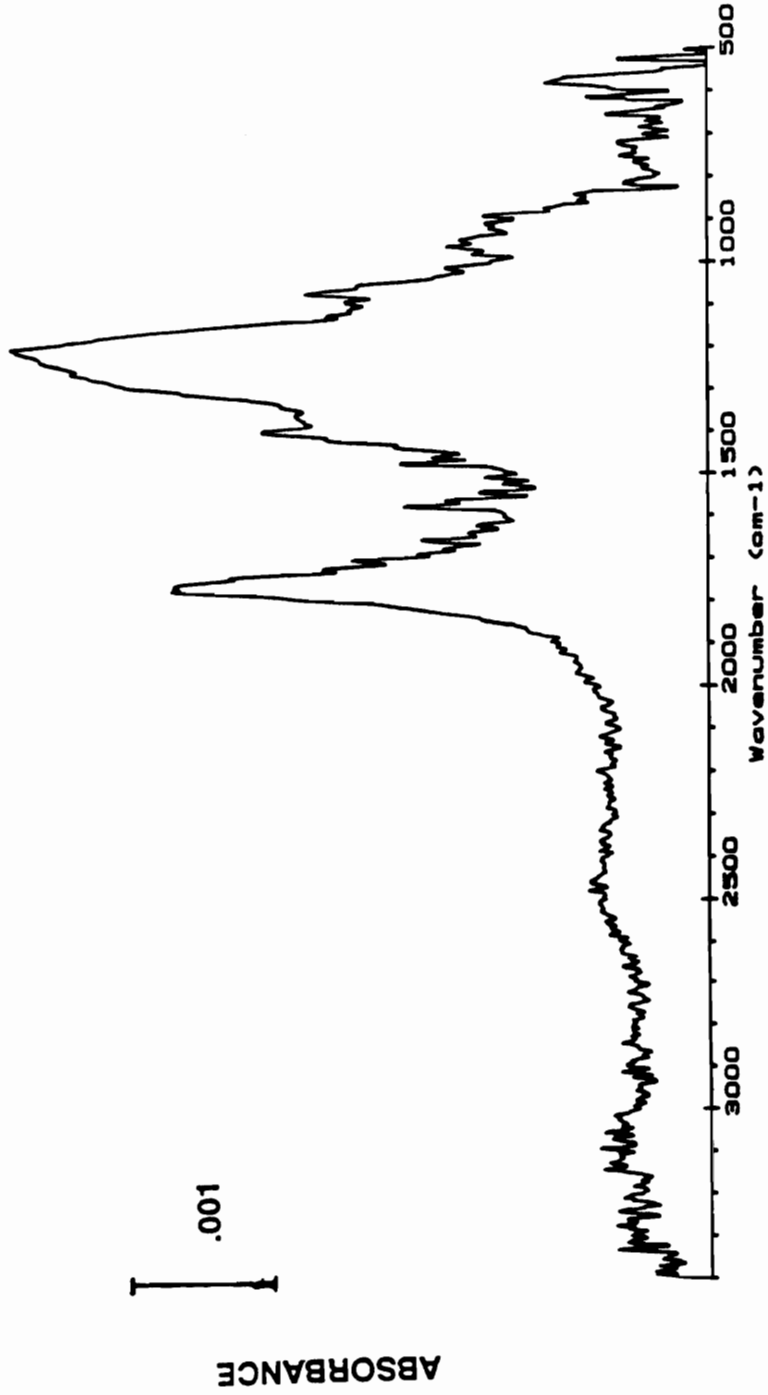


Figure 2.57 IRRAS difference spectrum of a one minute oxygen plasma treated PPS film. The reference was multiplied by a factor to account for the amount of polymer removed.

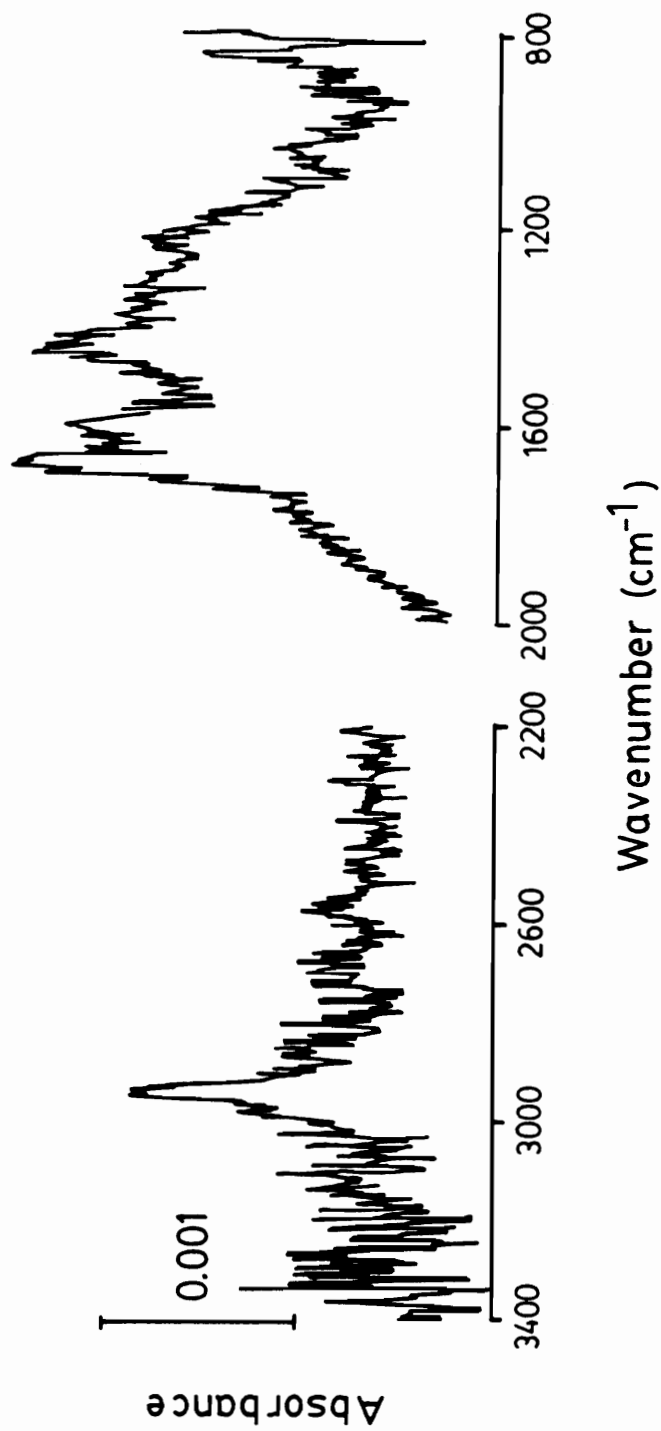


Figure 2.58 IRRAS difference spectrum of a two minute ammonia plasma treated PPS film. The reference was multiplied by a factor to account for the amount of polymer removed.

ammonia plasma treatment. Absorbance bands at 1690 and 1450 cm^{-1} are most probably due to the C=C stretch and C-H deformation bend in CH_2 groups respectively. Similar spectra have been shown for the ammonia treatment of polytetrafluoroethylene (45). The shoulder at 1600 - 1650 cm^{-1} may also indicate a N-H deformation absorbance band although poor signal-to-noise does not allow assignment of a N-H stretch absorbance in the region above 3000 cm^{-1} . The apparent absence of C-O absorbances indicates that the XPS curve fit C1s peak at 285.8 - 286 eV can most probably be assigned to C - N functionality. The absence of carbonyl absorbance bands is in agreement with the XPS curve fitted results.

2.3.2.3.4 XPS Analysis of Epoxy Interactions

Table 2.4 shows the atomic concentrations obtained for one minute oxygen and ammonia plasma treated surfaces before and after exposure to epoxy with subsequent CCl_4 washes. For the oxygen plasma treated PPS surfaces, the oxygen content is dramatically reduced after epoxy treatment while the carbon and sulfur content increased. The sulfur fraction has been divided into both oxidized (ox) and non-oxidized species, and the epoxy treatment resulted in complete removal of all surface oxidized sulfur species. For ammonia plasma treatment, the most noticeable change is the almost complete loss of nitrogen functionality with a doubling of the sulfur content.

For both cases, the results seem consistent with the loss of much of the surface functionality induced by plasma treatment. To further support this assumption, the XPS C1s narrow scan spectrum is shown in Figure 2.59. For the oxygen treatment, only C-O functionality remains with no higher oxidation states of carbon present. For ammonia plasma treatment, the curve fitted peak previously assigned to either C-N or C-O functionality is greatly reduced. Also, for both cases, the shakeup satellite is significantly increased, probably indicating the exposure of an unmodified PPS surface. These results are consistent with the loss of oxygen and nitrogen functionalities seen for oxygen and ammonia plasma treatment, respectively. XPS results, therefore, indicate that only C-O functionality for oxygen plasma and C-O or

Table 2.4 XPS Analysis of the Atomic Concentrations Found for Plasma Treated PPS Before and After Exposure to Epoxy Followed by Several CCl₄ Washes.

	Oxygen			Ammonia	
	<u>Control</u>	<u>Initial</u>	<u>w/Epoxy</u> ¹	<u>Initial</u>	<u>w/Epoxy</u> ¹
C1s	86.5	61.8	82.2	85.0	85.1
O1s	0-1	28.4	10.0	2.4	3.3
N1s	0	0	--	6.8	0.8
S2p	12.5	6.7	7.8	5.9	10.8
S2p(ox) ²	0	3.1	0	0	0

¹ After exposure to epoxy and washed with carbon tetrachloride.

² Denotes high binding energy sulfur component at 169.4 eV.

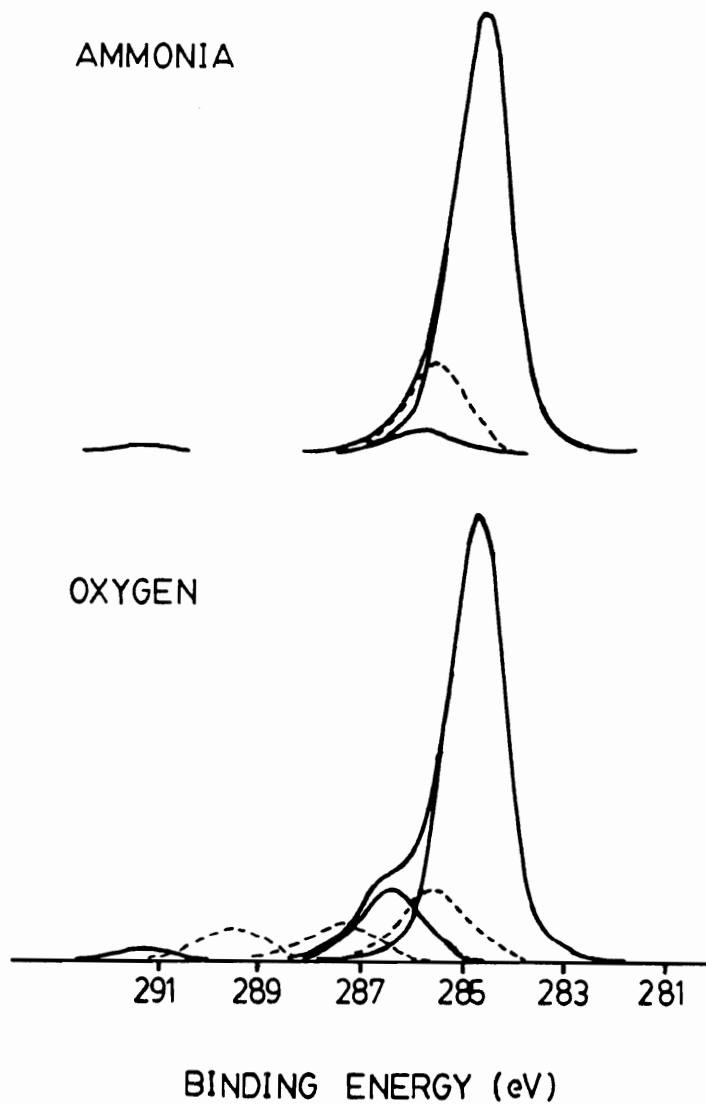


Figure 2.59 C1s line shape for a one minute oxygen and ammonia plasma treated PPS films before (---) and after (—) exposure to epoxy followed by 3 CCl₄ rinses.

C-N for ammonia plasma are present after exposure to epoxy followed by CCl_4 rinses.

3.3.2.3.5 IRRAS Analysis of Epoxy Interactions

Infrared analysis can be used to identify the chemical nature of the residual functionality seen above in the XPS analysis after epoxy treatment of plasma modified PPS. IRRAS analysis of plasma treated PPS exposed to epoxy is shown in Figure 2.60. The spectra represent the difference spectra between plasma modified PPS after exposure to epoxy with a varying number of CCl_4 washes, and control samples receiving no treatment. Therefore, the spectra represent both modification due to the plasma treatment as well as any spectral changes due to the epoxy / CCl_4 treatment. The first solvent wash after removal from the epoxy bath shows a relatively thick layer of residual epoxy remaining on the surface. The thickness of this film, as measured by ellipsometry, was in the range of 50 - 70 nm. All bands can be assigned to the epoxy structure and assignments can be found elsewhere (125). Clearly, however, the epoxy ring vibration is present at 916 cm^{-1} indicating no crosslinking in this film. After the second wash, however, several interesting spectral features can be noted. The most evident is the complete lack of carbonyl functionality previously seen in Fig. 2.57 for oxygen plasma treatment of PPS. This is consistent with the XPS results and must again indicate that much of the surface modification can be removed after epoxy treatment, therefore possibly contributing little to bonding. A second feature is the absence of the epoxy ring vibration compared to other absorbance bands present. Also, an absorbance band at approximately 1120 cm^{-1} can be detected that may be assigned to C-O stretching vibration of either an alcohol or alkyl ether structure. This absorbance is much weaker in intensity than that seen for the plasma modified surface before epoxy treatment and has shifted from the peak maximum at 1230 cm^{-1} seen previously (see Fig. 2.57). The loss of the epoxy vibration with a relatively intense C-O absorbance band is consistent with the spectrum of a cured epoxy film, indicating that crosslinking has occurred in the surface film. Similar spectral features have been seen for the transmission spectra of epoxy films crosslinked with a variety of curing agents (126). The particular curing agent involved

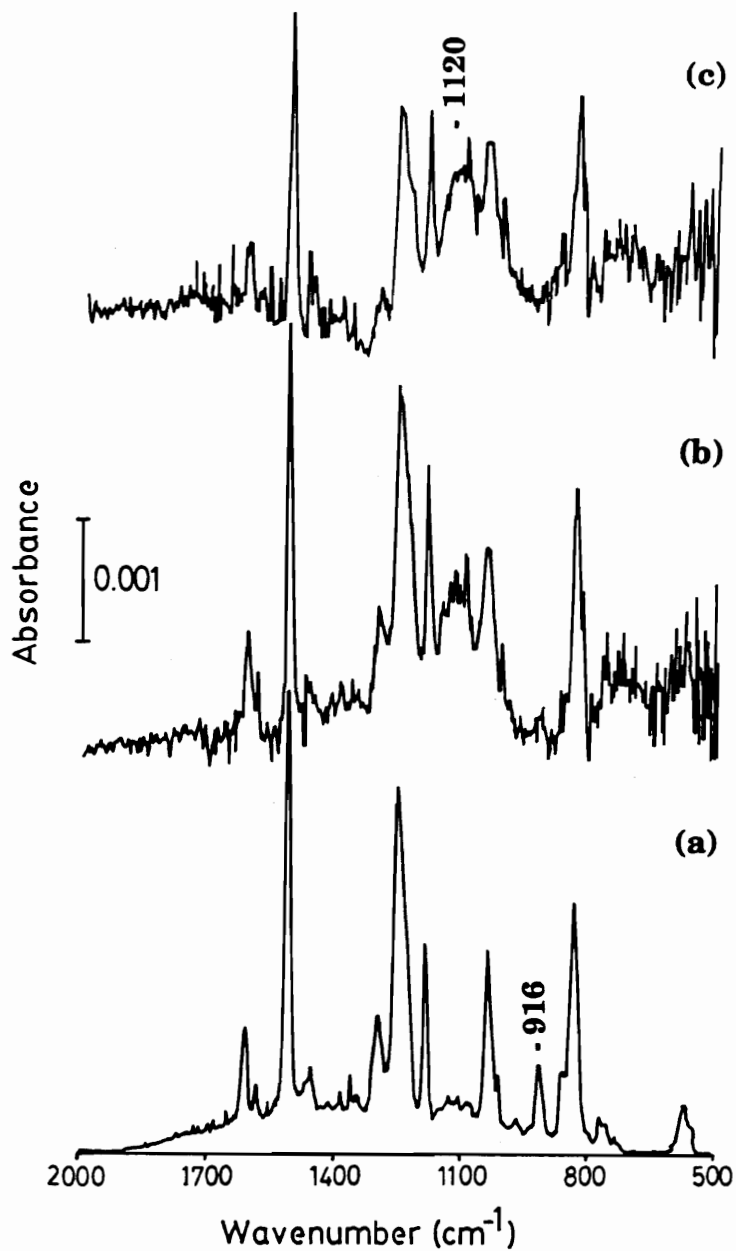


Figure 2.60 IRRAS difference spectra of a one minute oxygen plasma treated PPS film exposed to epoxy at 100°C after: (a) one CCl_4 rinse (b) two CCl_4 rinses (c) three CCl_4 rinses. Spectrum (a) was multiplied by a factor of 0.16 for scaling purposes.

here is not known although the lack of carbonyl absorbance bands indicates that it does not contain this moiety. Reaction with a number of functional groups including ketones, alcohols, or acetals could possibly lead to C-O absorbance bands, although the conditions required for reaction can be varied (126). The overall low concentration of reactive groups at the surface may be below the detection limits of the IRRAS technique, and the poor signal to noise levels in the hydroxyl region unfortunately does not allow detailed analysis in this region of the spectrum.

The IRRAS difference spectrum for an ammonia plasma treated PPS surface after treatment with epoxy and three CCl_4 washes is shown in Figure 2.61. A similar spectrum is obtained to that found with oxygen plasma treatment although the amount present seems to be much less. The absence of the epoxy ring vibration again indicates crosslinking, and the C-O absorbance is also evident at 1150 cm^{-1} although the band is not as intense.

To test for epoxy interaction with PPS samples without plasma treatment, control samples were heat treated with epoxy under the same conditions and the difference spectrum is shown in Figure 2.62. The spectrum clearly shows that epoxy will adsorb to untreated PPS surfaces, although the presence of the epoxy ring vibration at 915 cm^{-1} shows that the polymer is adsorbed in a non cross-linked form. Also, no C-O absorption bands are detected in the region of $1100\text{-}1200\text{ cm}^{-1}$. The mechanism of adsorption is not known, although it most probably consists of a combination of dispersion forces, and more importantly, acid-base contributions. Since carbon tetrachloride is a neutral solvent, even weak acid-base interactions would not be disrupted by this solvent, and maximum adsorption would occur. In work reported earlier by Fowkes (127), the use of this solvent was shown to give the maximum adsorption of basic PMMA on acidic silica.

2.3.2.4 Surface Analysis of Plasma Modified PEPO's

2.3.2.4.1 Ellipsometry and Surface Acoustic Wave Analysis

Figure 2.63 shows the relative etch rates for oxygen plasma exposure of Bis-A-PEPO and the polysulfone analog. The much slower etching of the phosphorus

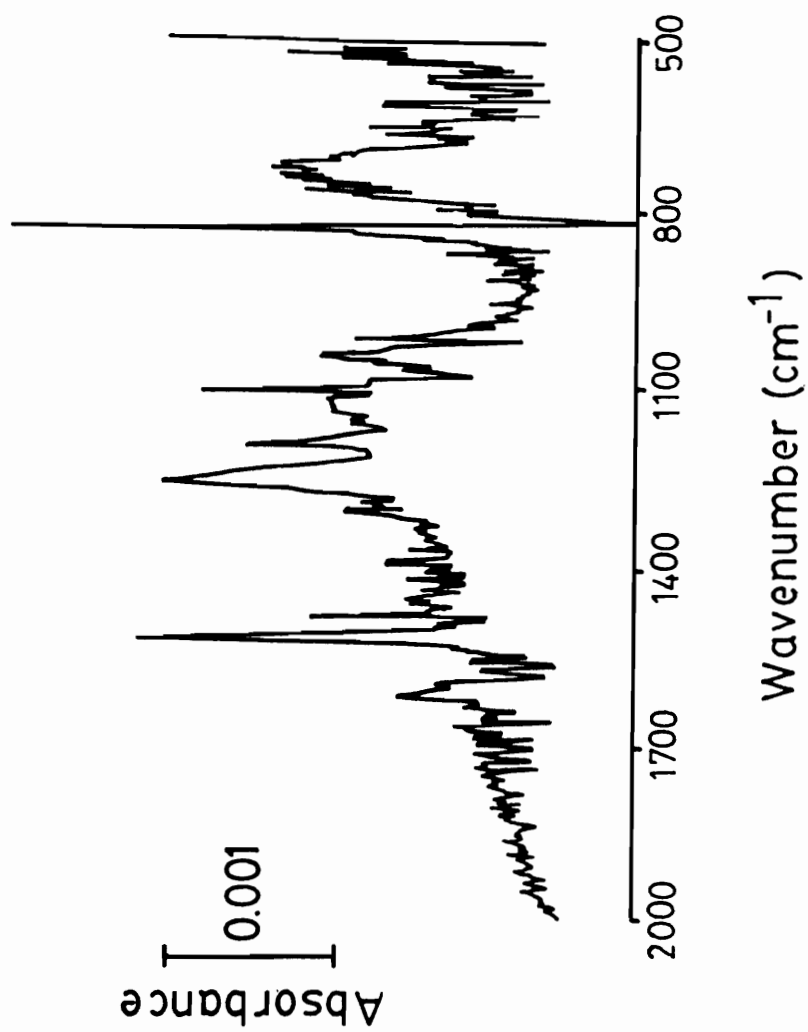


Figure 2.61 IRRAS difference spectrum of a one minute ammonia plasma treated PPS film exposed to epoxy at 100°C followed by three CCl₄ rinses.

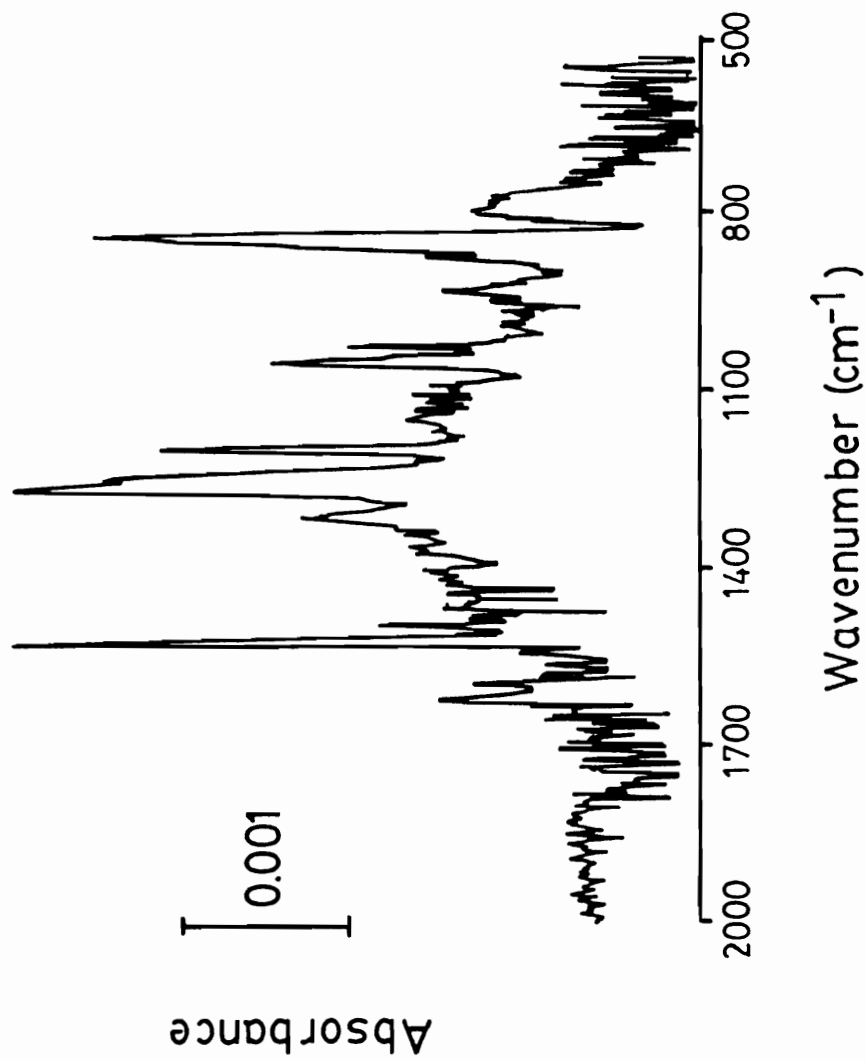


Figure 2.62 IRRAS difference spectrum of untreated PPS films exposed to epoxy at 100°C followed by three CCl₄ rinses.

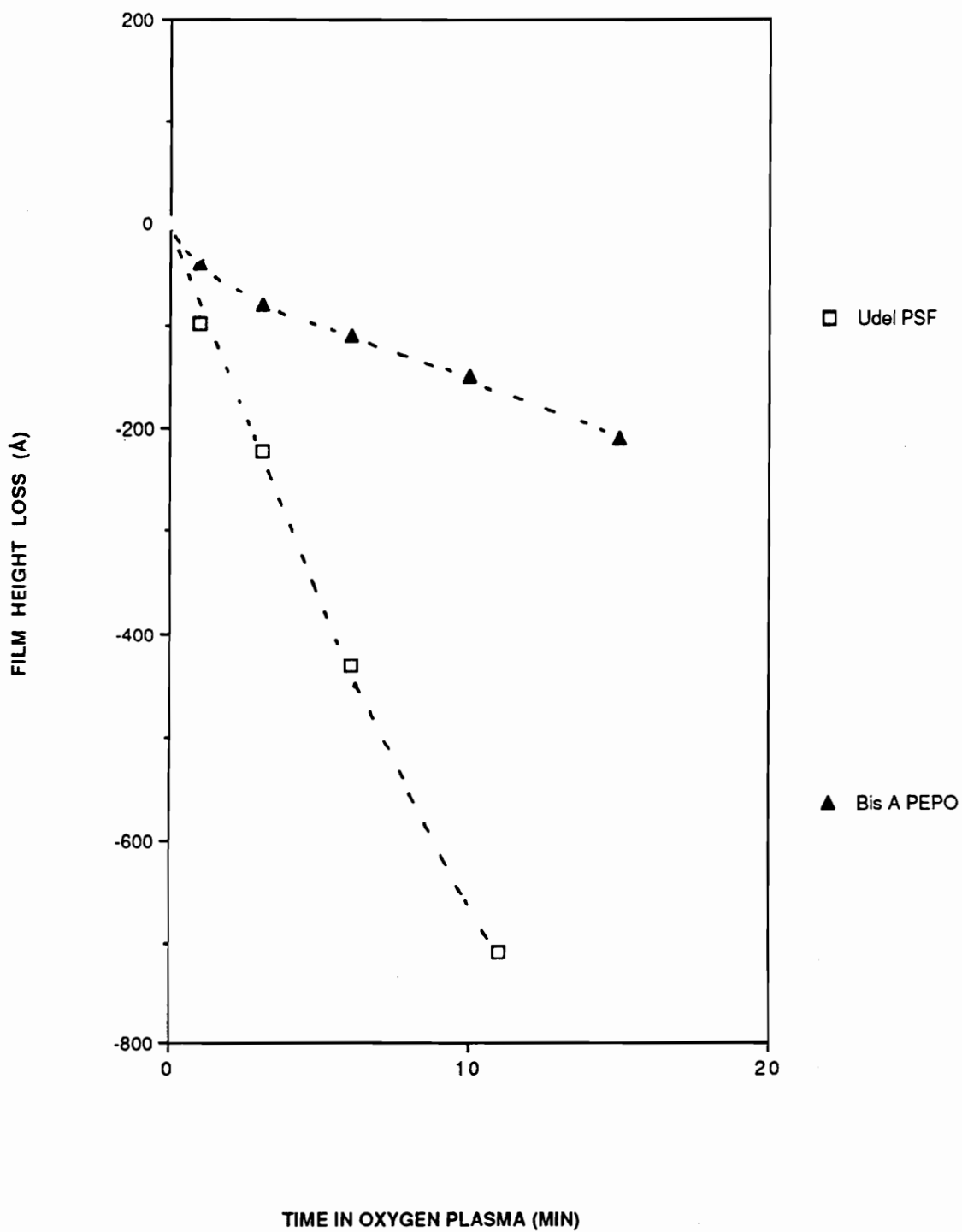


Figure 2.63 Relative thickness decrease for polysulfone and BP-PEPO films as a function of oxygen plasma exposure time.

containing polymer is evident, with an etch rate of approximately 1.5 nm / minute compared with 7 nm / minute for polysulfone. While ellipsometry is useful in analyzing initial etch rates, long term durability under plasma exposure is not easily studied due to the thin polymer films required. To study thicker films exposed to the oxygen plasma for longer periods of time, surface acoustic wave analysis (SAW) was used. This technique is similar in principle to a quartz crystal microbalance which has been shown to be useful for analysis of the plasma etching of polymers (151). Upon loading of the device with the polymer film, the frequency of the crystal (33 MHz) is depressed by an amount depending on the mass loading used. The relationship governing the change in frequency (Δf) with film thickness can be given by a well known Sauerbrey equation (129):

$$\Delta f = 2.3 \times 10^6 F^2 \frac{M_s}{A} \quad [29]$$

where F is the frequency of the crystal, M is the film mass, and A is the film area. Given the surface selectivity of plasma treatment, and that the polymers used were well below the glass transition temperature, the frequency shift should only reflect changes in h, the polymer thickness.

As the polymer is etched away, the frequency will increase proportionally with the decrease in thickness. Figure 2.64 shows the results of this analysis and indicates the dramatic difference between polysulfone and BP-PEPO. While a linear increase in frequency with etch time is seen for polysulfone, the BP-PEPO sample undergoes an initial 3 KHz increase with a subsequent very slow change in frequency, indicating that mass loss is minimal. Combining these results with ellipsometry indicates that for BP-PEPO, after an initial decrease in thickness (determined by ellipsometry and a small increase in frequency for the SAW device), polymer etching has essentially stopped. This is an interesting result as few organic polymers show this level of resistance to oxygen plasma treatment.

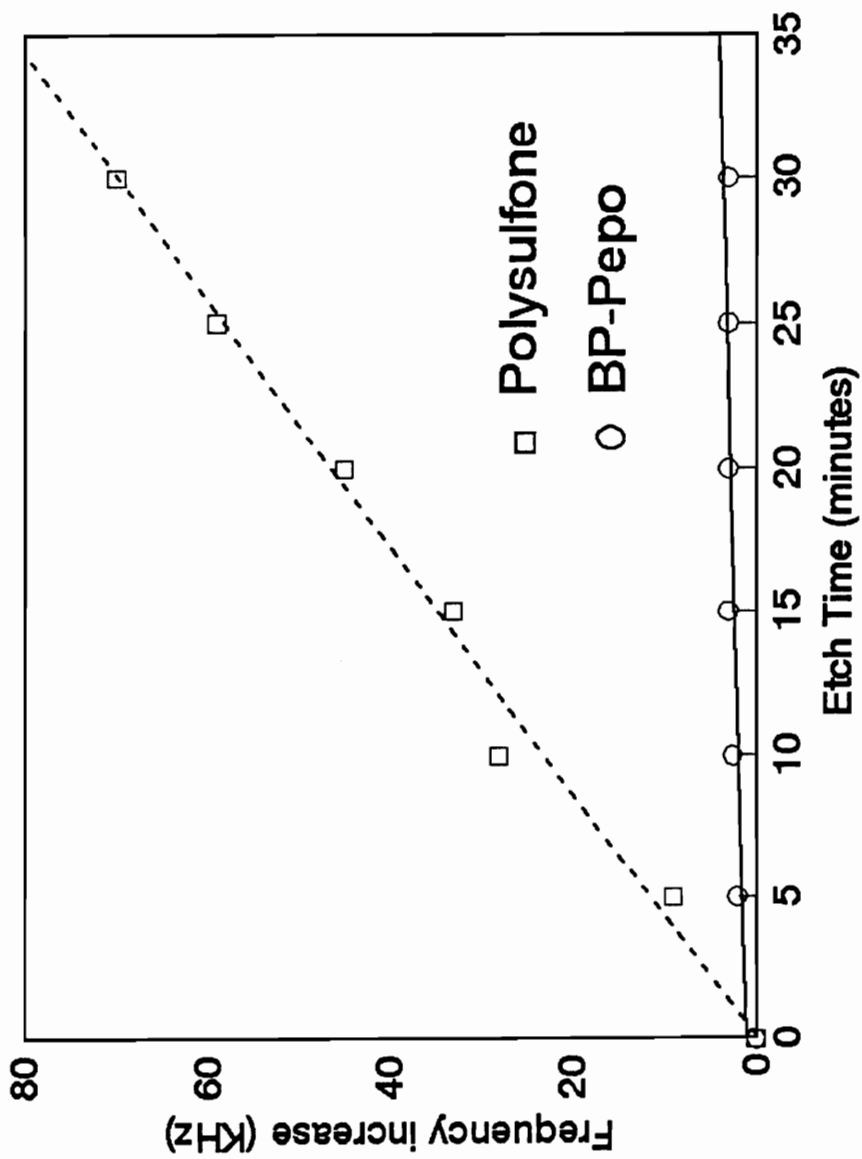


Figure 2.64 Surface acoustic wave analysis of the relative etch rates of polysulfone and BP-PEPO after oxygen plasma exposure.

2.3.2.4.2 X-ray Photoelectron Spectroscopy (XPS)

Table 2.5a shows the atomic concentrations found for polysulfone, Bis-A-PEPO, and BP-PEPO control samples. Also given in Table 2.5a are the expected atomic concentrations expected given the backbone structure. For comparison, the atomic concentrations for both control samples and polymers after a five minute oxygen plasma exposure are shown in Table 2.5b. For polysulfone, a 25% decrease in the carbon content and a 2.5 fold increase in oxygen is found, while the sulfur content remains essentially unchanged. By comparison, for the PEPO containing polymers, a dramatic decrease of approximately 50% for carbon is seen, with a 5-6 fold increase in oxygen content. Also, the phosphorus content increases by 3-4 times for both polymers. To analyze the atomic concentration changes in more detail, Figure 2.65 shows the results of XPS analysis of the atomic concentration changes on plasma exposure for polysulfone and shows that after an initial exposure of 10 seconds, the atomic concentrations remain relatively constant for all treatment times. This is in agreement with the results previously seen for polystyrene and polyphenylene sulfide. Figure 2.66 shows the results for BP-PEPO, and the difference with this polymer is evident. Instead of reaching a plateau in atomic concentrations, the values given for carbon, oxygen, and phosphorus concentrations show significant change over the exposure time. It is interesting to note also that the rate of change for oxygen and phosphorus are similar, while a much faster decrease in carbon content is indicated. After a dramatic increase in phosphorus and oxygen concentrations, and a decrease in carbon concentrations during the initial treatment time of five seconds, the values continue to change showing the continual 'evolution' of new chemistry at the surface. Figure 2.67 shows the change in the O1s / P2p and O1s / S2p ratio for BP-PEPO and polysulfone, respectively. This figure again shows the relatively unchanging ratio for polysulfone with treatment time, while the BP-PEPO sample undergoes a rapid decrease in the O1s / P2p ratio to a leveled value of approximately 3.4. The scatter in the ratio for polysulfone is due primarily to the error seen in the low value for the sulfur content. Due to excessive etching of polysulfone, thicker samples (2% spin coated solutions) were used at times greater than five minutes, and even with this,

Table 2.5a Atomic Concentrations (Measure/Calculated) for the XPS Analysis of Polysulfone and PEPO polymers.

<u>Element</u>	<u>BP-PEPO</u>	<u>Bis-A-PEPO</u>	<u>Polysulfone</u>
Carbon	88.3 / 88.2	89.2 / 89.2	84.0/84.4
Oxygen	8.5 / 8.8	7.6 / 8.1	13.0 / 12.5
Sulfur	-----	-----	3.0 / 3.1
Phosphorus	3.2 / 2.9	3.1 / 2.7	-----

Table 2.5b Atomic Concentrations (Before/After) for the XPS Analysis of a five Minute Oxygen Plasma Treatment of PEPO and Polysulfone.

<u>Element</u>	<u>BP-PEPO</u>	<u>Bis-A-PEPO</u>	<u>Polysulfone</u>
Carbon	88.3 / 46.0	89.2 / 42.0	84.0 / 63.0
Oxygen	8.5 / 40.6	7.6 / 43.0	13.0 / 32.3
Sulfur	-----	-----	3.0 / 3.2
Phosphorus	3.2 / 11.3	3.1 / 11.3	-----

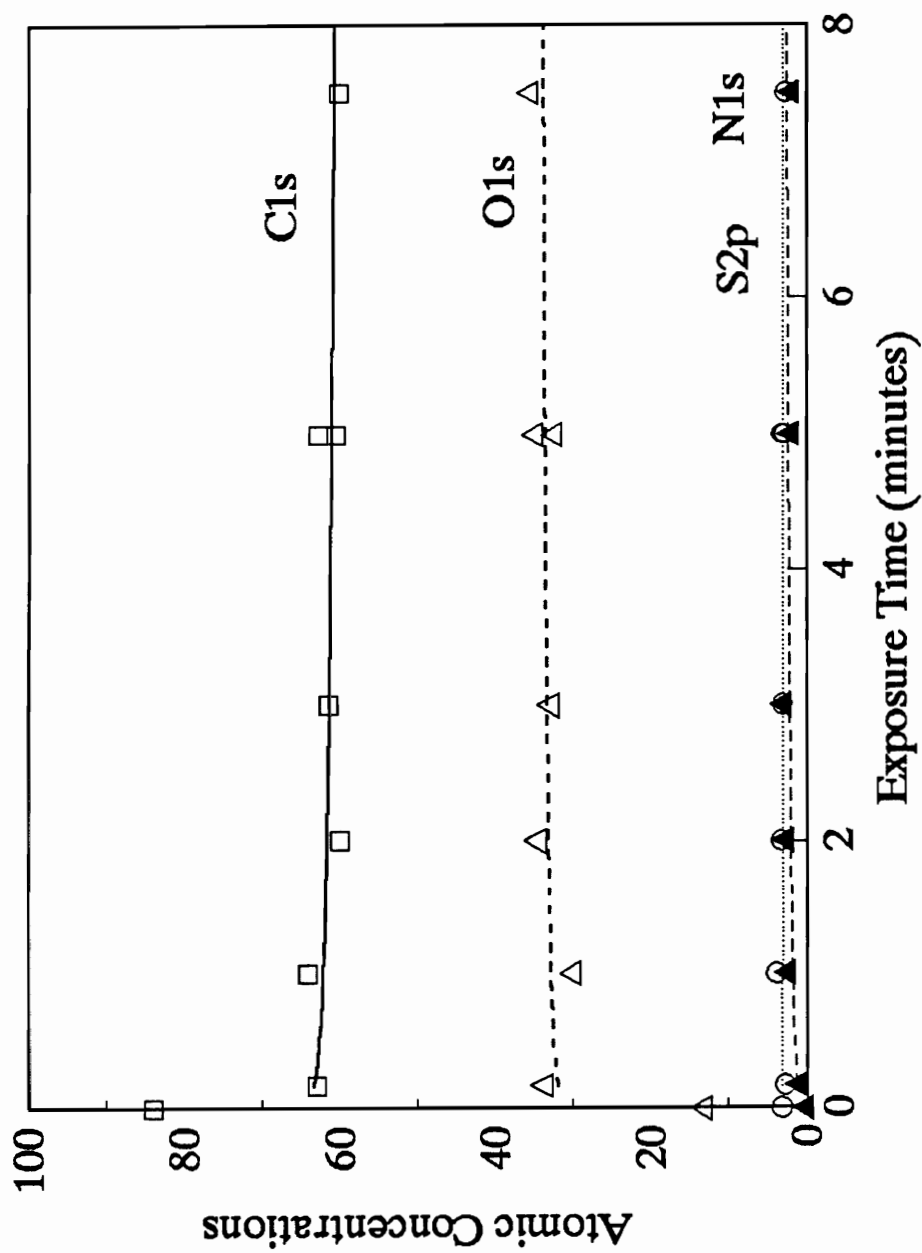


Figure 2.65 XPS analysis of atomic concentration changes for polysulfone thin films versus oxygen plasma treatment time.

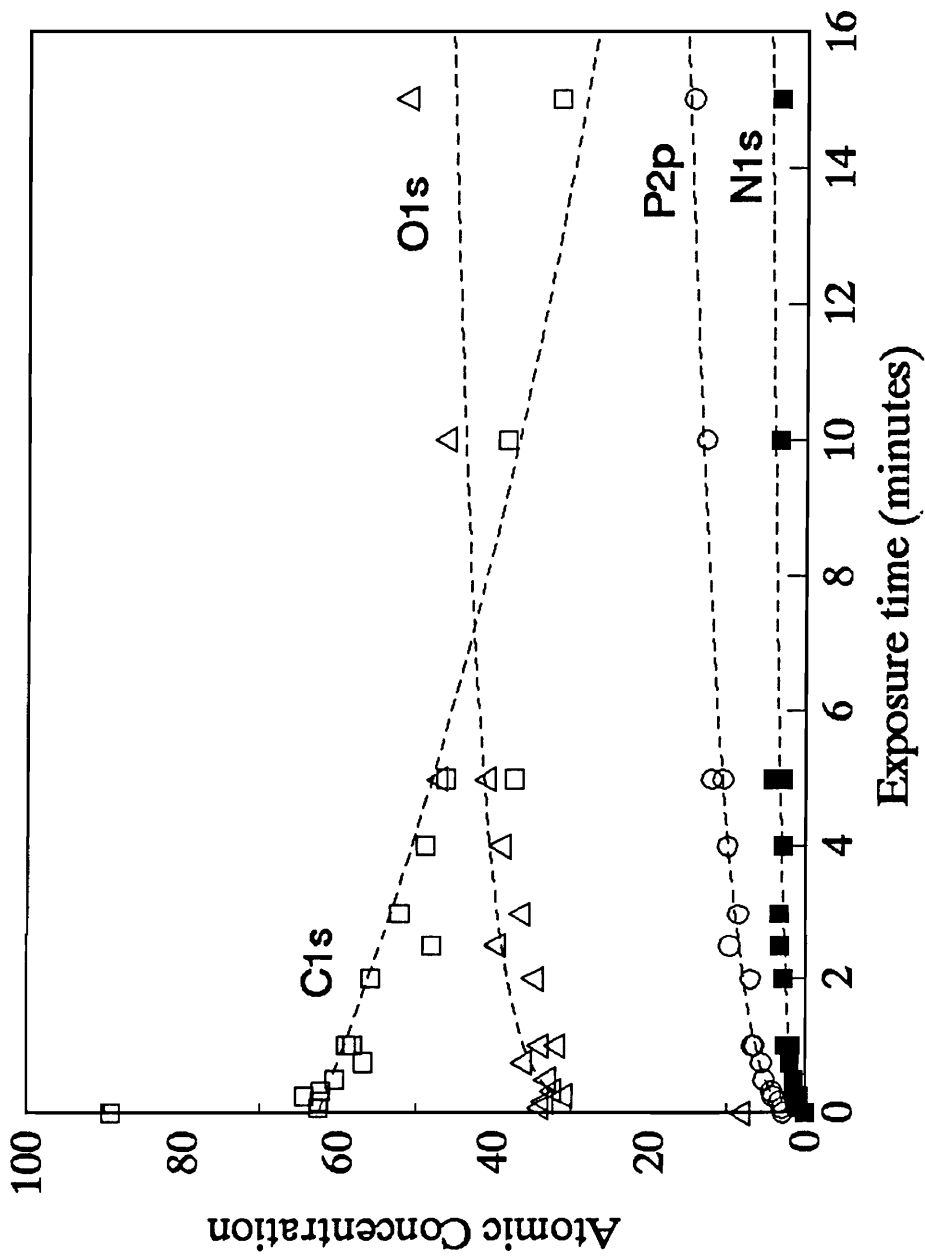


Figure 2.66 XPS analysis of atomic concentration changes for BP-PEPO thin films versus oxygen plasma treatment time.

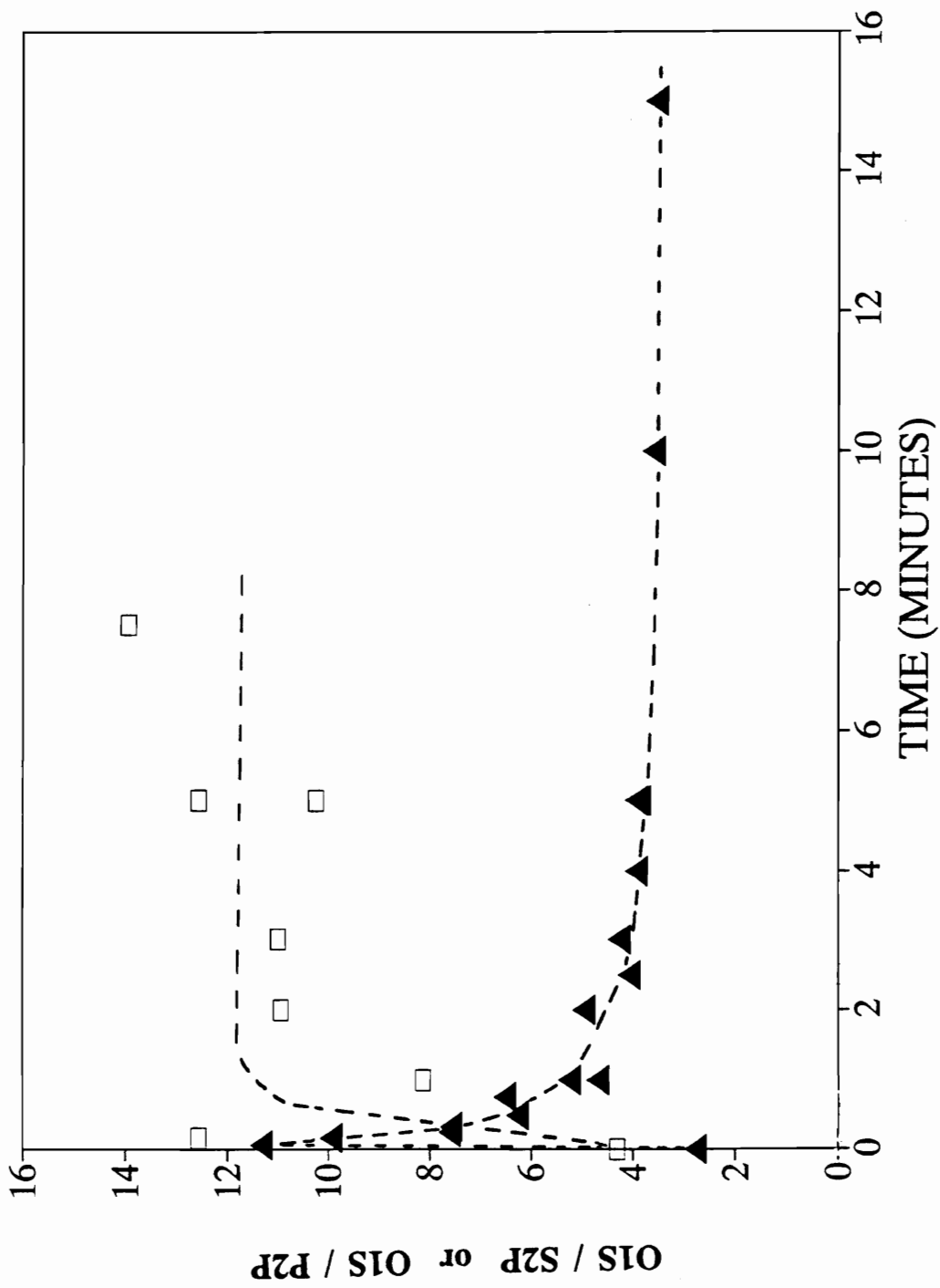


Figure 2.67 XPS analysis of the O1s / P2p ratio for BP-PEPO as a function of oxygen plasma exposure time. Also shown is a similar analysis for the O1s / S2p ratio of Udel polysulfone.

times greater than 7.5 minutes exposure time showed a chromium signal due to the substrate.

To better characterize the surface chemical changes and understand the mechanisms behind increased oxygen plasma resistance, analysis of the narrow scan spectra was also performed. Figure 2.68 shows narrow scan spectra for the P 2p photopeak as a function of oxygen plasma exposure time. In this figure, the peak intensities have been normalized to the C1s peak intensity. The control spectrum shows an unresolved doublet for the P=O functionality with a peak maximum at 132.5 eV with a separation of approximately 0.9 - 1.0 eV between the 2p 3/2 and 2p 1/2 photopeaks. Upon oxygen plasma exposure, however, there is a large broadening of the peak with a shift to higher binding energies. At longer exposure times, an intense peak develops at 135 eV. Figure 2.69 shows a more simple analysis for the O1s photopeak and clearly shows the transition from a doublet corresponding to P=O and C-O functionality at 530.7 eV and 533.7 eV respectively to a much broader photopeak with a maximum at 533.7 eV. No evidence of the O=P photopeak is seen at longer exposure times.

To quantify this transition for the phosphorus photopeak, the control photopeak and the photopeak after long exposure times (15 min) were curve fit assuming a ratio of the 2p 3/2 to 2p 1/2 photopeaks of 2:1 and an approximate separation of 0.9 - 1 eV. By applying these criteria to spectra at all exposure times, any area not included in the two known peaks could be attributed to intermediate oxidation states. Monitoring the loss of the P=O absorbance near 132.5 eV, the growth of the new 135 eV photopeak, and the change in intermediate oxidation states can give an indication of the relative rate of change of these species. Figure 2.70 shows the results of this analysis and shows the dramatic loss of P=O functionality and growth of a highly oxidized phosphorus species. The intermediate oxidation species undergo an immediate increase after initial plasma treatment, and then slowly decrease in concentration. The results are consistent with the oxidation of phosphorus through a series of mixed intermediates to reach a highly oxidized final state. The high binding energy of this phosphorus species is probably indicative of a phosphate species, and

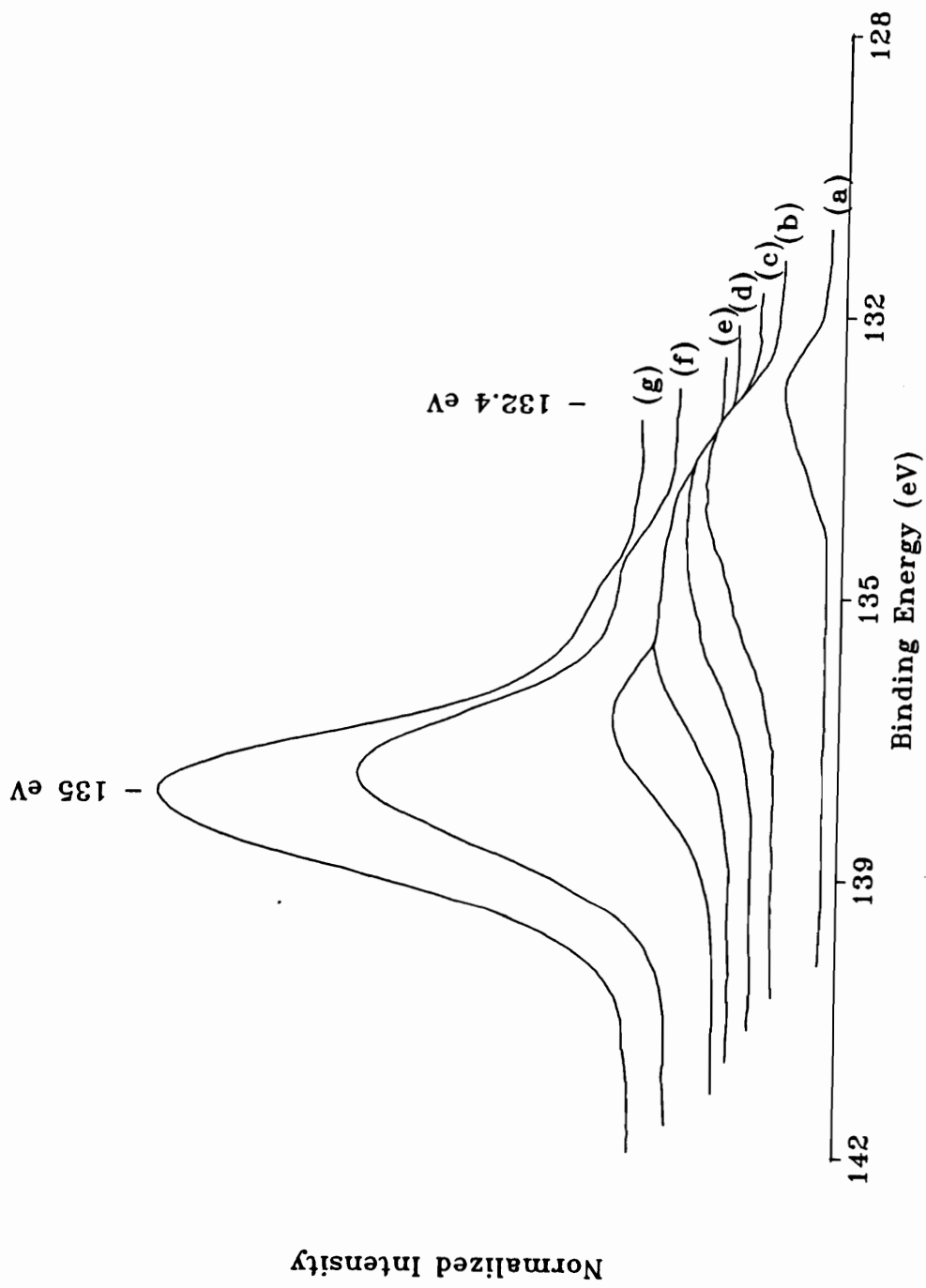


Figure 2.68 XPS analysis of the P2p photopeak for BP-PEPO as a function of oxygen plasma treatment time shown for (a) 0 (b) 0.08 (c) 0.17 (d) 0.33, (e) 1 (f) 5 and (g) 10 minutes. All spectra have been normalized to the C1s line intensity.

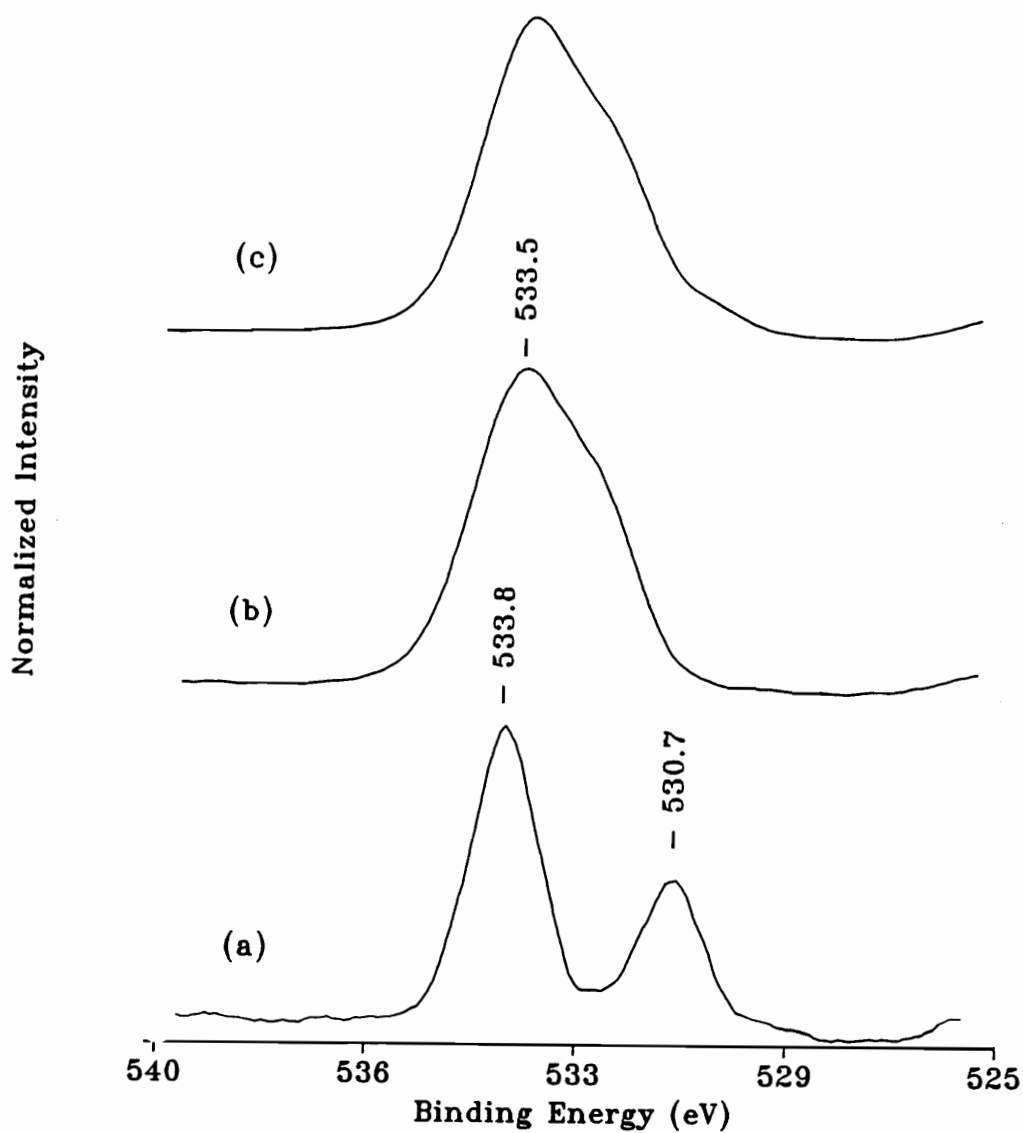


Figure 2.69 XPS analysis of the O1s line shape for BP-PEPO as a function of oxygen plasma exposure time shown for (a) 0, (b) 10 minutes and (c) a polyphosphoric standard. All spectra have been normalized to identical intensities for comparison.

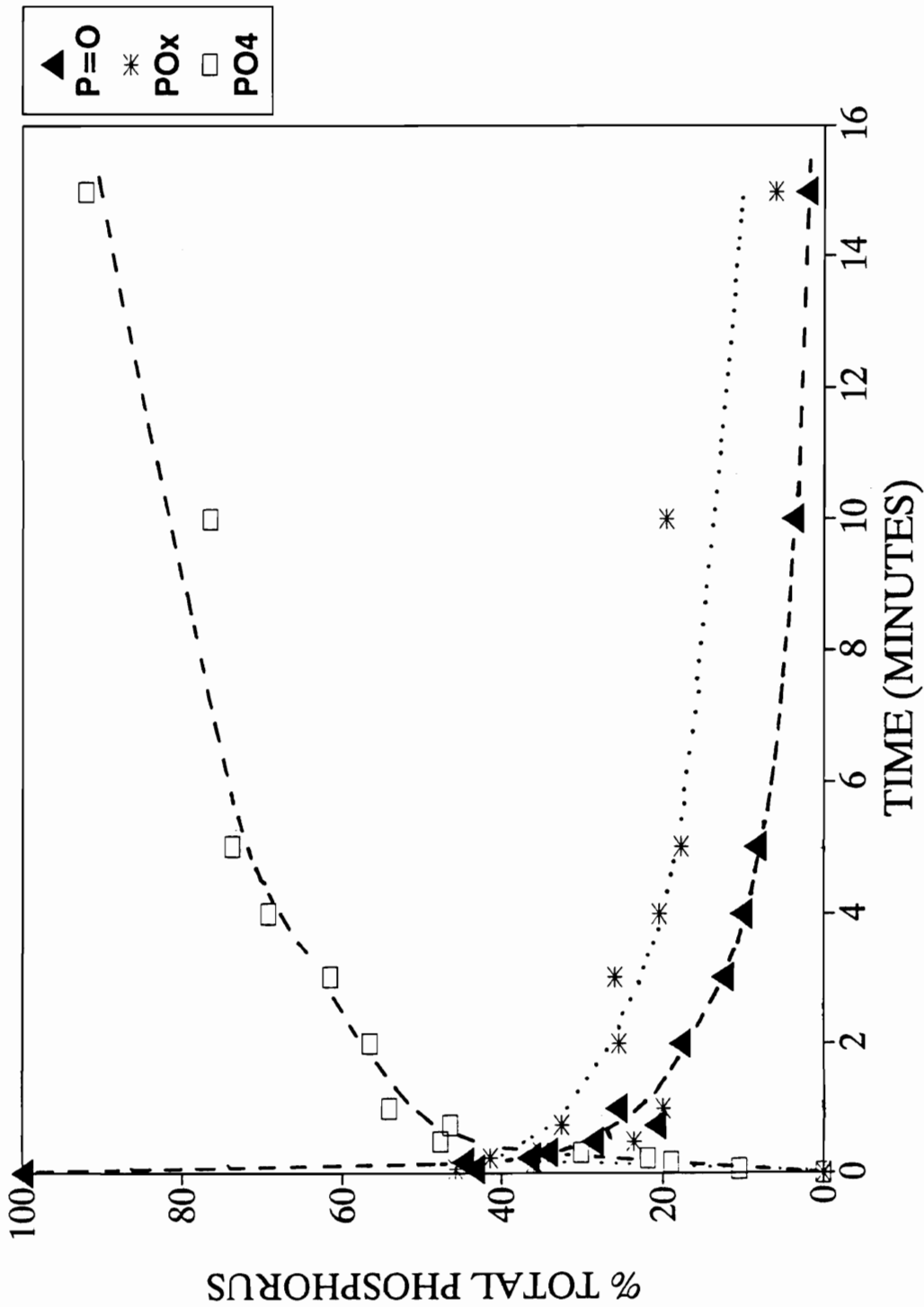


Figure 2.70 XPS analysis of the relative changes in peak area for the curve fit spectra in the P2p photopeak for BP-PEPO as a function of oxygen plasma exposure time.

XPS analysis of the P2p photopeak for triphenyl phosphate gave a peak position of 134.8 eV, similar in position to that seen experimentally found for plasma treated samples. The O1s / P2p ratio of 3.4 - 3.5 (see Fig. 2.67) is lower than the value of near 4:1 found experimentally for the triphenylphosphate standard. This probably indicates that the surface phosphate is polymeric in nature. A di-phosphate would yield a value of 3.5, close to that seen experimentally, while a true polyphosphate would yield a value of 3:1 for the O1s / P2p ratio. XPS analysis of polyphosphoric acid yielded a value for this ratio of 3.9 closer to the theoretically expected value. Also, the P2p photopeak position of 135eV and the O1s position of 533.5 eV agree with the experimentally observed positions for the plasma modified films.

To better understand the surface chemical changes, the C1s photopeak was analyzed, and the results are shown in Figure 2.71 for both polysulfone and BP-PEPO. For polysulfone, the large number of oxidized carbon species are evident by the presence of several higher binding energy components after a 10 second oxygen plasma treatment. At longer exposure times, there is some decrease in the amount of oxidized species initially, but a constant residual amount of highly oxidized carbon species is evident in all spectra. This indicates that although ellipsometry has indicated polymer etching, the surface composition of oxidized carbon is unchanged, suggesting a 'steady state' process. The C1s profile for BP-PEPO at short times resembles that for polysulfone, indicating that the early oxidation processes may be similar. At longer times, however, the amount of higher oxidation states for carbon is significantly reduced, showing that while these chemical processes are important in the initial stages of treatment, the surface chemistry at later times is altered to significantly reduce further oxidation of carbon in the surface region. To quantify the changes in the concentrations of oxidized surface carbon, Figure 72 shows the plots of the change in oxidized species as a function of treatment time. The plot shows the changes in the peak area relative to the main hydrocarbon peak at 285 eV for the curve fit C-O species at approximately 286.4 eV. Also shown is the change in relative peak area for the remaining peak area associated with more highly oxidized carbon species. As can be seen, there is relatively little change in the C-O concentration,

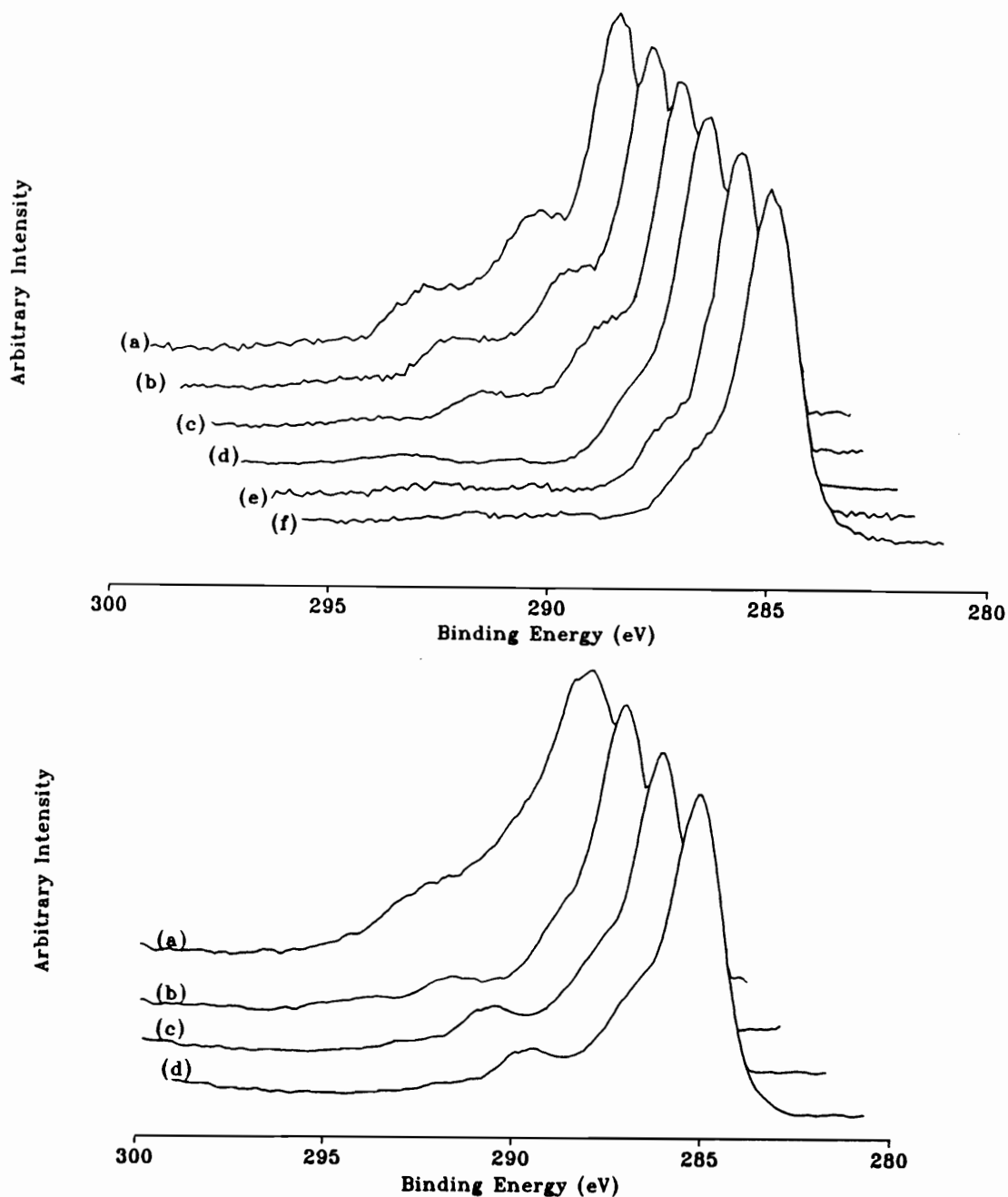


Figure 2.71 XPS analysis of the C1s lineshape for both polysulfone and BP-PEPO as a function of oxygen plasma exposure time. For BP-PEPO (upper figure), times of (a) 0.08 (b) 0.17 (c) 0.33 (d) 1 (e) 5 and (f) 10 minutes are shown, while for polysulfone (lower figure) times are shown for (a) 0.17 (b) 1 (c) 5 and (d) 7.5 minutes.

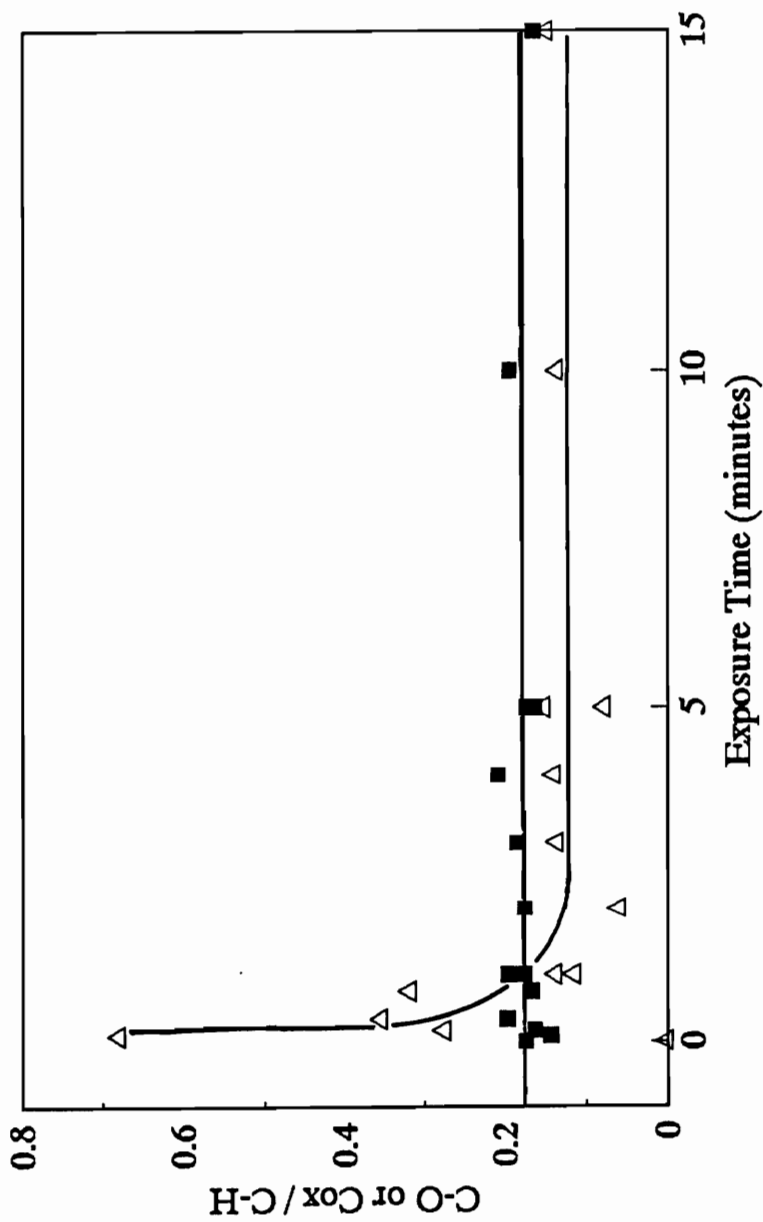
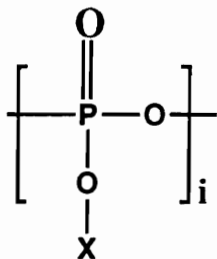


Figure 2.72 XPS analysis of (■), the C-O / C-H ratio from the curve fit C1s photopeak of BP-PEPO as a function of oxygen plasma exposure time and (Δ), the C_{ox} / C-H ratio for the same analysis. C_{ox} represents the remainder of oxidized carbon species that could not be accounted for by C-O functionality in the curve fit C1s spectra.

while the remaining oxidized species undergo a large increase after initial treatment to a value of 0.7, and then rapidly decays to a $C_{ox} / C-H$ ratio of approximately 0.17, indicating a small amount of residual oxidized carbon in the surface region.

The combined results suggest the formation of a surface phosphate of the possible structure:



where i shows that the phosphate may be polymeric in nature and X represents the number of carbon atoms in various carbon functionalities. The presence of a nitrogen photopeak at 402.4 eV indicates that a smaller amount of -N-O- functionality is present, and this type of functional group has been suggested for the oxygen plasma treatment of polyphosphazenes (55). From the curve fit analysis, a photopeak at 291.5 eV due to the π to π^* shakeup transition is always present indicating that at least some aromatic functionality remains.

To fully interpret the results, Figure 2.73 shows the changes theoretically expected in the O1s / C1s, O1s / P2p, C1s / P2p and C-O / C-H ratios for the chemical phosphate structure proposed as a function of both i and X . The C-O / C-H ratio is independent of i , and the average experimental value of 0.17 for all exposure times compares with a value of 0.2 expected if X represented phenyl moieties ($X = 6$). The O1s / P2p ratio is independent of the X functionality but is dependent of the value of i . An experimental O1s / P2p ratio of 3.5 (see Fig. 66) at a 15 minute plasma exposure shows that a di-phosphate may be indicated. Even though this analysis would be somewhat in error by any P-N-X functional groups, this functional group would be expected to have a binding energy near 400 eV (93), much lower than that observed in this case. The C1s / P2p ratio also gives some indication of the X functionality, and the experimental value of 2-3 (see Fig. 2.66) at 15 minutes compares with an X

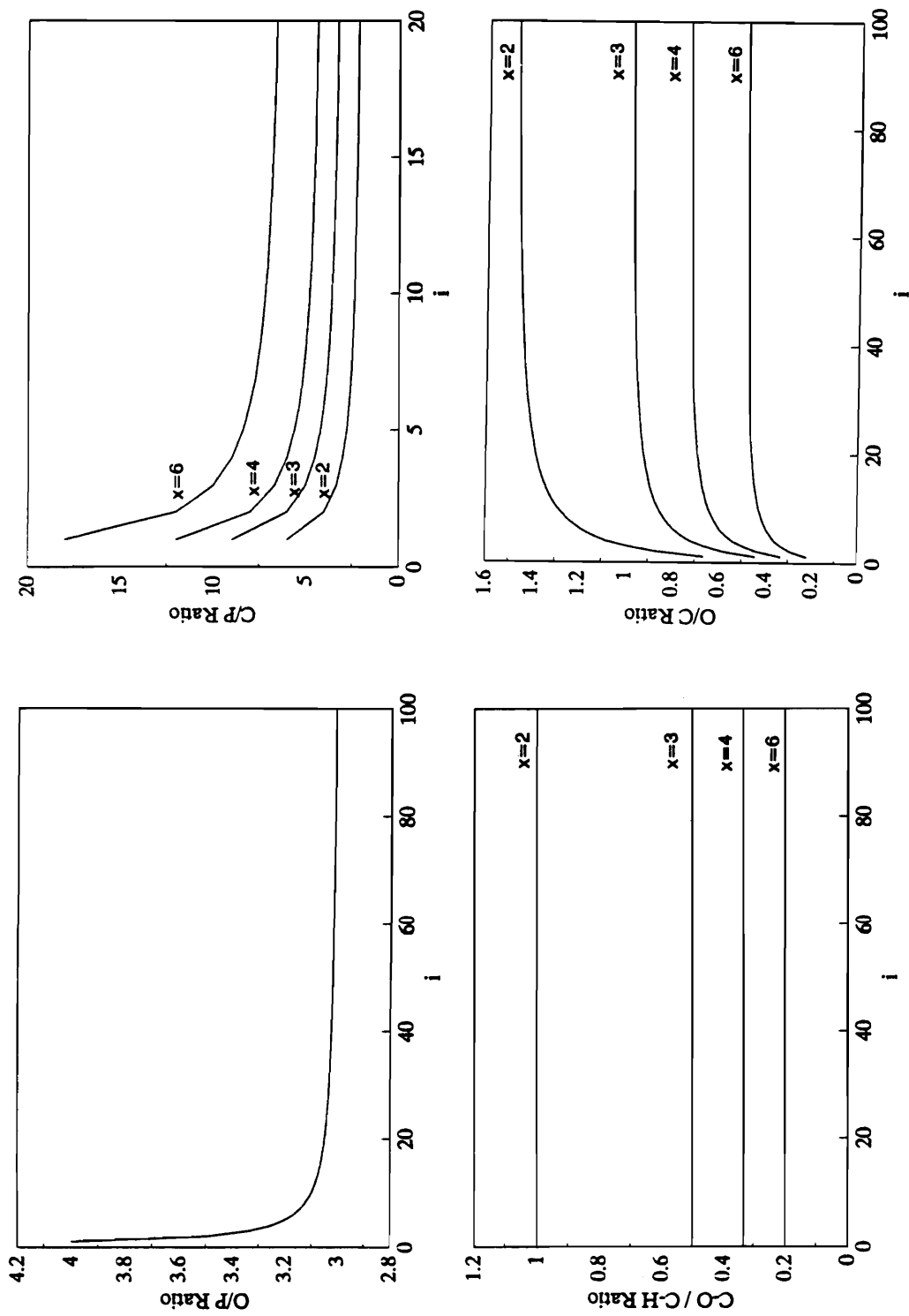


Figure 2.73 Theoretically expected elemental ratios for a polyphosphate structure as a function of i , the degree of polymerization, and X , the average number of carbon atoms per pendant group.

composed of between 1 and 3 carbon atoms for a polyphosphate. A O1s / C1s ratio of 3 - 0.75 would be expected for a polyphosphate with an X group containing 1 - 3 carbon atoms, and this compares with an experimentally determined value of 1.66 (see Fig 2.66).

The results for the analysis of O1s / C1s, O1s / P2p, and C1s / P2p seem to indicate that a polymeric surface phosphate species exists with an $n \geq 2$. Analysis of these element ratios indicates that the X species contains 2 - 3 carbon atoms and this seems to contradict the C-O / C-H results which indicated approximately 6 carbon atoms. The discrepancy can arise from several factors. The first is that some residual more highly oxidized carbon is seen in the curve fitted carbon spectra and this would introduce error in the analysis. Also, and more importantly, the presence of P-OH groups would drastically lower the C1s / P2p ratio and increase the O1s / C1s ratio, while the C-O / C-H ratio would be independent of the amount of hydroxyl species present. This explanation seems more likely, indicating that while phenyl groups are present, a significant amount of hydroxyl functionality is also present. The presence of phenyl groups is supported by the π to π^* shakeup feature seen.

2.3.2.4.3 Infrared Reflection Absorption Spectroscopy

A complementary technique to XPS analysis, infrared RAS analysis was used to examine thin spin coated films of polysulfone and Bis-A-PEPO.

Figure 2.74 shows the infrared spectrum of the untreated polymer films, and the similarity in structure is indicated by the closely matching spectra. Table 2.6 gives the major peaks found, and the assignments for each absorbance band. The only major difference in the spectra are associated with the sulfone (1150 and 1324 cm^{-1}) and phosphine oxide (1193 cm^{-1}) moieties in polysulfone and Bis-A-PEPO, respectively.

Figure 2.75 shows the difference spectra for oxygen plasma treated polysulfone films for both 5 second and 5 minute treatment times. At 5 seconds, the presence of broad absorbances at 1770 cm^{-1} and 1250 cm^{-1} indicate a wide range of C=O and C-O functionalities. At a longer time of five minutes, although there are subtraction problems due to excessive polymer etching, there is still the clear indication of similar

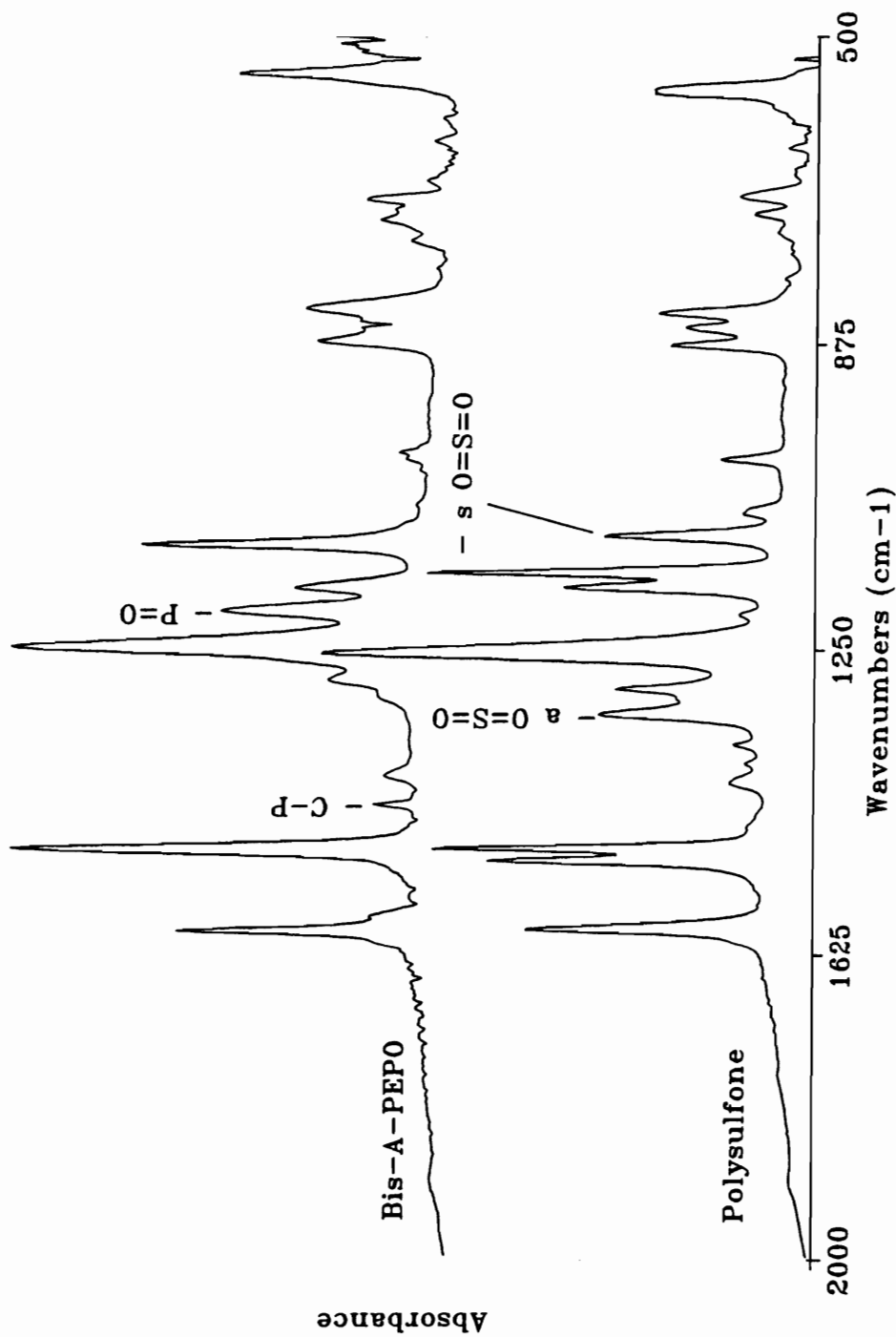


Figure 2.74 IRRAS analysis of 70-90 nm spin coated films of polysulfone and Bis-A-PEPO on ferrotype substrates.

Table 2.6 IR Band Assignments for Polysulfone and Bis-A-PEPO. (130)

Polymer (cm⁻¹)		Assignments	
<u>Bis-A-PEPO</u>	<u>Udel</u>	<u>Bis-A-PEPO</u>	<u>Udel</u>
3063	3061	Aromatic C-H	Aromatic C-H
1590,1494	1586,1505	Aromatic C=C	Aromatic C=C
1436	----	Aromatic C-P	-----
-----	1324	-----	Asymm. O=S=O
1245	1242	Aromatic C-O-C	Aromatic C-O-C
1193	----	P=O stretch	-----
----	1150	-----	Symm. O=S=O
750	----	C-P stretch	-----

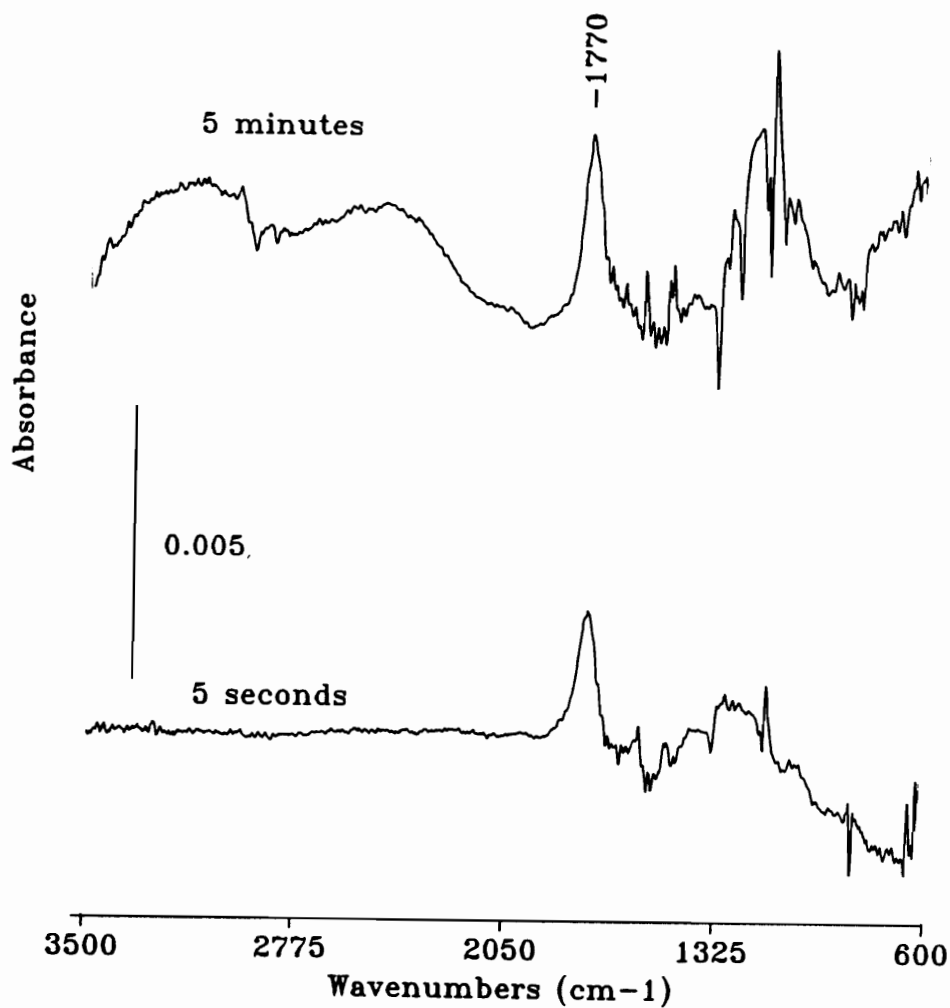


Figure 2.75 IRRAS difference spectrum of a five second and five minute oxygen plasma treated polysulfone film. The reference was multiplied by a factor to account for the amount of polymer removed.

concentrations of highly oxidized carbon functionalities, and this is agreement with results from XPS analysis. Figure 2.76 shows a similar analysis for the oxygen plasma treatment of Bis-A-PEPO. At a treatment time of 15 seconds, the spectrum is very similar to that found for polysulfone at early treatment times, with the appearance of a broad carbonyl absorbance at approximately 1760 cm^{-1} and a C-O absorbance at 1240 cm^{-1} . At longer times, however, there is a dramatic difference in spectral features when compared to polysulfone. First, although a residual amount remains, there is a marked decrease in carbonyl functionality, and this is also in agreement with XPS results for the C1s photopeak. Since this technique samples the entire film thickness, the reduction in oxidized carbon species seen in XPS is not due to the limited sampling depth of the technique (5-10 nm). Also, there is a strong broad absorbance with a peak maximum of 1275 cm^{-1} which is consistent in position with that seen for many phosphate species (155). IRRAS analysis of a tri-butyl phosphate standard showed a P-O stretching absorbance at 1284 cm^{-1} although the peak was narrow and not the most intense in the spectrum. The difficulty in obtaining a subtraction spectrum without spectral distortions is no doubt related to the build up of a surface layer. The best results for this analysis are probably obtained where the surface modified layer is completely different than the underlying substrate. In this case, residual material increases at the surface with treatment time, and finding a suitable reference peak for subtraction is difficult. Even with these difficulties, the advantages of the analysis of the thin plasma modified layer using a vibrational technique are clear.

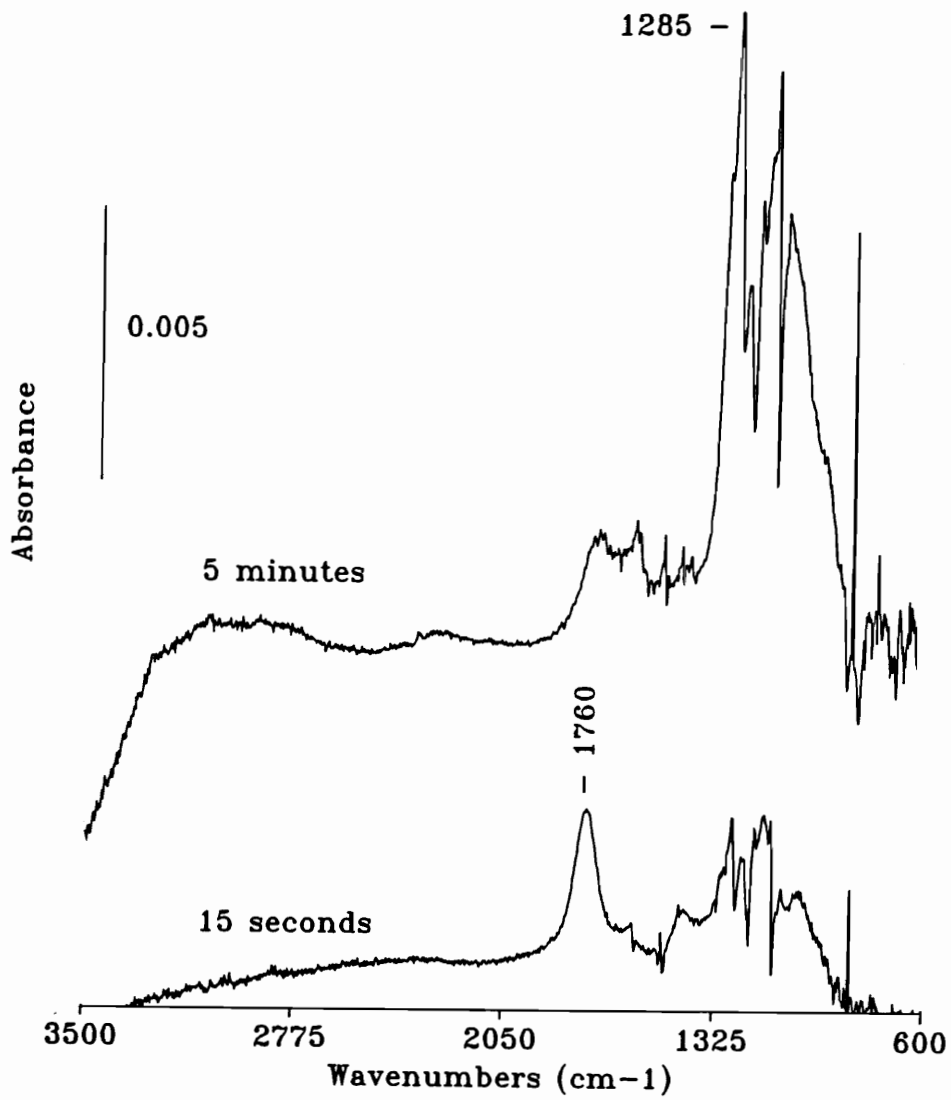


Figure 2.76 IRRAS difference spectrum of a 15 second and five minute oxygen plasma treated BP-PEPO film. The reference was multiplied by a factor to account for the amount of polymer removed.

2.4 SUMMARY AND CONCLUSIONS

The use of exact optical theory has been shown to be a great aid in the prediction of reflectance spectra for PPS films, coatings, and molded samples using a variety of experimental techniques including transmission spectroscopy, reflection absorption spectroscopy, attenuated total reflectance spectroscopy, and reflectance spectroscopy at the Brewster angle. The theoretical predictions for these cases were confirmed almost exactly by experiment. The use of optical theory in the analysis of polymers has been limited to efforts by only a few investigators in the past decade (5,24,28,29,75). The clear advantage of predicting spectra under any experimental conditions can aid in the interpretation of optical distortions that are usually present, evaluation of orientation, and help in the development of new reflectance techniques. Spectral simulations, however, must have well known optical parameters and unfortunately, the analysis for polymers has been limited to only a few simple polymers (24-26,28,29). Almost no data exists for more recently developed high performance polymers, and the spectral analysis in this work provides the first data for PPS.

By comparing simulated spectra from exact optical theory to experimental results, thin spin coated PPS films on a variety of metal and metal oxide substrates were shown to be anisotropic in nature, with the major polymer chain direction parallel to the surface. This alignment may be induced by the spin coating procedure used which has been shown to produce orientation in polyimide films (110). Although the use of optical theory is of great utility in deducing orientation, the analysis of coatings on infrared transparent substrates can show orientation directly if spectra are taken in both the transmission and reflection techniques modes. For spin coated PPS film on germanium, the results again indicate an anisotropic film, in agreement with the conclusions using optical theory. While IRRAS has been used in many studies to analyze orientation in Langmuir Blodgett films and spontaneously ordered monolayers (65-68), few studies exist to show orientation in thin polymer coatings (73,75).

XPS has shown that the oxygen plasma treatment of PPS results in an overall increase in the oxygen content of the surface region. This oxygen was associated with both oxidized forms of carbon and sulfur. Ammonia plasma treatment resulted in the incorporation of nitrogen and oxygen as either a C-N or a C-O functionality. Treatment with epoxy followed by CCl_4 rinses, however, seemed to remove most surface functionalities, leaving only C-O or C-N moieties, as determined by the C 1s narrow scan XPS spectra. IRRAS showed that this was, in part, due to C-O functional groups from a thin epoxy layer at the surface. The absence of the epoxy ring vibration indicated a crosslinked surface film for both oxygen and ammonia plasma treated PPS surfaces although the surface density or thickness was much less for the ammonia treatment. Although the specific curing site could not be identified, it certainly resulted from the plasma surface treatment. Epoxy treatment of non-plasma treated PPS films showed that an uncured film could also adsorb to the PPS surface. The use of IRRAS as a complementary tool to XPS has shown great promise in the determination of the mechanisms involved between plasma modified surfaces and a model adhesive. The indication of a direct bond between a plasma induced surface species and epoxy shows some of the first evidence for the formation of covalent bonds in the interphase for such a system.

Surface analysis of the plasma treatment of poly(arylene ether phosphine oxide) by XPS yielded results consistent with the loss of oxidized carbon species and the formation of a phosphate surface layer. The development of such a surface structure may be responsible for its resistance to degradation in an oxygen plasma determined by both ellipsometry and surface acoustic wave analysis. The evolution of the surface structure with time could be easily monitored using XPS and this technique showed that most of the surface conversion occurred within several minutes of oxygen plasma exposure. The use of IRRAS in the analysis of the surface modified region showed that carbon oxidation was reduced after a five minute plasma exposure time with the build up of the surface phosphate species. This response to oxygen plasma is quite different to that seen for a polysulfone analog and other engineering thermoplastics where the surface concentrations remain constant with various exposure times. The

excellent resistance to polymer degradation by oxygen plasma may make poly(arylene ether) phosphine oxides ideal candidate materials for space applications.

2.4 REFERENCES

1. Zbinden, R. In *Infrared Spectroscopy of High Polymers*; Academic: New York, 1964.
2. Heavens, O. S. *Optical Properties of Thin Solid Films*; Dover: New York, 1965; Chapter 4.
3. Fina, L. J.; Koenig, J. L. *J. Polym. Sci.: Part B: Polym. Phys.* **1986**, *24*, 2508.
4. Bellamy, L. J. *The Infrared Spectra of Complex Molecules*; John Wiley: New York, 1964.
5. Ishida, H. *Rubber Chem. Tech.* **1987**, *60*, 497.
6. Francis, S. A.; Ellison, A. H. *J. Opt. Soc. Amer.* **1959**, *49*, 131.
7. Greenler, R. G. *J. Chem. Phys.* **1966**, *44*, 310.
8. Boerio, F. J.; Boerio, J. P.; Bozian, R. C. *Appl. Surf. Sci.* **1988**, *31*, 42.
9. Swalen, J. D.; Rabolt, J. F. In *Fourier Transform Infrared Spectroscopy, Applications to Chemical Systems*; Ferraro, J. R., Basile, L. J., Eds.; Academic: New York, 1985, p. 283.
10. Golden, W. G. In *Fourier Transform Infrared Spectroscopy, Applications to Chemical Systems*; Ferraro, J. R., Basile, L. J., Eds.; Academic: New York, 1985, p. 315.
11. Webster, H. F. *M.S. Thesis 1985* Virginia Polytechnic Institute and State University, Blacksburg, VA.
12. Born, M.; Wolf, E. *Principles of Optics*; Pergamon: Oxford, 1975.
13. *Handbook of Optical Constants of Solids II*; Palik, E. D., Ed.; Academic: New York, 1991.
14. Pelletier, E. In *Optical Constants of Solids II*; Palik, E. D., Ed.; Academic: New York, 1991; p. 57.
15. Hawranek, J. P.; Neelakantan, P.; Young, R. P.; Jones, R. N. *Spectrochim. Acta* **1976**, *32A*, 75.

16. Hawranek, J. P.; Neelakantan, P.; Young, R. P.; Jones, R. N. *Spectrochim. Acta* **1976**, 32A, 85.
17. Hawranek, J. P.; Jones, R. N. *Spectrochim. Acta* **1976**, 32A, 99.
18. Hawranek, J. P.; Jones, R. N. *Spectrochim. Acta* **1976**, 32A, 111.
19. Cameron, D. G.; Escolar, D.; Goplen, T. G.; Nadeau, A.; Young, R. P. *Appl. Spectrosc.* **1980**, 34, 646.
20. Goplen, T. G.; Cameron, D. G.; Jones, R. N. *Appl. Spectrosc.*, **1980**, 34, 652.
21. Crawford, Jr., B.; Goplen, T. G.; Swanson, D. In *Advances in Infrared and Raman Spectroscopy*; Clark, R. J. H., Hester, R. E., Eds.; Heyden: London, 1978; Vol. IV, Chap. 2.
22. Harrick, N. J. In *Internal Reflection Spectroscopy*; John Wiley: New York, 1967.
23. Ribbegård, G. K.; Jones, R. N. *Appl. Spectrosc.* **1980**, 34, 638.
24. Allara, D. L.; Baca, A.; Pryde, C. A. *Macromolecules* **1978**, 11, 1215.
25. Graf, R. T.; Koenig, J. L.; Ishida, H. *Appl. Spectrosc.* **1985**, 39, 405.
26. Graf, R. T.; Koenig, J. L.; Ishida, H. *Anal. Chem.* **1986**, 58, 64.
27. Ishino, Y; Ishida, H. *Appl. Spectrosc.* **1992**, 46, 504.
28. Pacansky, J.; England, C. D.; Waltman, R. J. *Appl. Spectrosc.* **1986**, 40, 8.
29. Pacansky, J.; England, C. D.; Waltman, R. J. *J. Polym. Sci.: Part B: Polym. Phys.* **1987**, 25, 901.
30. Mielczarski, J. A., Milosevic, M., Berets, S. L., *Appl. Spectrosc.* **1992**, 46, 1040.
31. Hecht, E.; Zakac, A. In *Optics*; Addison-Wesley: Reading, 1944; Chap. 3.
32. Greenler, R. G.; Rahn, R. R.; Schwartz, J. P. *J. Catal.* **1971**, 23, 42.
33. Boerio, F. J.; Armogan, L. *Appl. Spectrosc.* **1978**, 32, 509.
34. Machefert, J. M.; Le Calvar, M.; Lenglet, M. *Surf. Interf. Anal.* **1992**, 18, 39.
35. Nguyen, T.; Byrd, E.; Tsao, A. *J. Appl. Polym. Sci.* **1986**, 32, 6339.

36. Wong, J. S.; Yen, Y. *Appl. Spectrosc.* **1988**, *42*, 598.
37. Hanake, M.; Milosevic, M.; Harrick, N. J. *Vib. Spect.* **1991**, *1*, 251.
38. Holmes-Farley, S. R.; Reamey, R. H.; McCarthy, T. J.; Deutch, J.; Whitesides, G. M. *Langmuir* **1985**, *1*, 725.
39. Lee, K. W.; McCarthy, T. J. *Macromolecules*, **1988**, *21*, 3353.
40. Lee, K. W.; McCarthy, T. J. *Macromolecules*, **1988**, *21*, 309.
41. Lee, K. W.; Kowalczyk, S. P.; Shaw, J. M. *Macromolecules* **1990**, *23*, 2097.
42. Ribbing, C. G.; Roos, A. In *Handbook of Optical Constants of Solids II*; Palik, E. D., Ed.; Academic: New York, 1991; p.875.
43. Liston, E. M. *J. Adhesion* **1989**, *30*, 199.
44. Lub, J.; van Vroonhoven, F. C. B. M.; Brunix, E.; Benninghoven, A. *Polymer* **1989**, *30*, 40.
45. Inagaki, N.; Tasaka, S.; Kawai, H. *J. Adh. Sci. Technol.* **1989**, *3*, 637.
46. Dunn, D. S.; McClure, D. J. *J. Vac. Sci. Technol.* **1987**, *A5*, 1327.
47. Grant, J. L.; Dunn, D. S.; McClure, D. J. *J. Vac. Sci. Technol.* **1988**, *A6*, 2213.
48. Leger, L.; Visentine, J.; Santos-Mason, B. *Sampe Q.* **1987**, *18*, 48.
49. Rutledge, S. K.; Mihelcic, J. A. *Surf. Coat. Technol.* **1989**, *39/40*, 607.
50. Rutledge, S. K.; Banks, B. A.; DiFlippo, F.; Brady, J.; Dever, T.; Hotes, D. *NASA Tech. Memo.* **1986**, No. 100122.
51. Ritahie, I.; Gjerde, H. D. *Surf. Coat. Technol.* **1989**, *39/40*, 599.
52. Chou, N. J.; Tang, C. H.; Paraszczak, J.; Babich, E. *Appl. Phys. Lett.* **1985**, *46(1)*, 31.
53. Arnold, C. A.; Chen, D.; Chen, Y. P.; Graybeal, J. D.; Bott, R. H.; Yoon, T.; McGrath, B. E.; McGrath, J. E. *High Perform Polym.* **1990**, *2*, 83.
54. Webster, F.; Wightman, J. P. Final Report to NASA, Langley Research Center, Grant NAG-1-521, **1989**.

55. Fewell, L. L. *J. Appl. Polym. Sci.* **1990**, 41, 391.
56. Brandt-Andolino, P. J. *Ph.D. Dissertation*, Virginia Polytechnic Institute and State University, 1985.
57. Carter III, R. O.; Dickie, R. A.; Holubka, J. W.; Lindsay, N. E. *I & EC Research* **1989**, 28, 48.
58. Yoshida, S.; Ishida, H. *J. Adhesion* **1984**, 16, 217.
59. Tanaka, I.; Yanagihara, E.; Watanbe, Y. 16th Meeting Adhesion Soc. of Japan **1978**, 69.
60. Ulrén, L; Hjertberg, T.; Ishida, H. *J. Adhesion* **1990**, 31, 117.
61. Boerio, F. J.; Ondrus, D. J. *J. Colloid Surf. Sci.* **1990**, 139, 446.
62. Xue, G.; Liu, S.; Jin, Y.; Jiang, S. *Appl. Spectrosc.* **1987**, 41, 1172.
63. Claybourn, M.; Colombel, P.; Chalmers, J. *Appl. Spectrosc.* **1991**, 45, 279.
64. Harbecke, B. *Appl. Phys. A* **1986**, 40, 151.
65. Allara, D. L.; Swalen, J. D. *J. Phys. Chem.* **1982**, 86, 2700.
66. Allara, D. L.; Nuzzo, R. G. *Langmuir* **1985**, 1, 52.
67. Rabolt, J. F.; Burns, F. C.; Schlotter, N. E.; Swalen, J. D. *J. Chem. Phys.* **1983**, 78, 946.
68. Chollet, P. A. *Thin Solid Films* **1978**, 52, 343.
69. Debe, M. K.; Field, D. R. *J. Vac. Sci. Technol. A* **1991**, 9, 1265.
70. Ishino, Y.; Ishida, H. *Langmuir* **1988**, 4, 1341.
71. Fina, L. J.; Tung, Y. *Appl. Spectrosc.* **1991**, 45, 986.
72. Schopper, H. Z. *Phys.* **1952**, 132, 146.
73. Nguyen, H. X.; Ishida, H. *Makromol. Chem., Macromol. Symp.* **1986**, 5, 135.
74. Boerio, F. J.; Chen, S. L. *Appl. Spectrosc.* **1979**, 33, 121.

75. Novotny, V. J.; Hussla, I.; Turlet, J. M.; Philpott, M. R. *J. Chem. Phys.* **1989**, 90, 5861.
76. Genresse, P. *Bull. Soc. Chim. Fr.* **1897**, 17, 599.
77. Hill, H. W. *Ind. Eng. Chem. Prod. Res. Develop.* **1979**, 18, 252.
78. Fahey, D. R.; Ash, C. E. *Macromolecules* **1991**, 24, 4242.
79. Shue, R. S. *Dev. Plast. Technol.* **1985**, 2, 259.
80. Geibel, J. F.; Campbell, R. W. In *Comprehensive Polymer Science*; Eastmond, G. C., Ledwith, A., Russo, S., Sigwalt, P., Eds.; Pergamon: Oxford, 1989; Chapter 32.
81. Hill Jr., H. W.; Brady, D. G. In *Encyclopedia of Polymer Science and Engineering*; Kroschwitz, J. I., Ed.; John Wiley: New York, 1988; p.531
82. Hill, H. W.; Brady, D. G. *J. Coatings Technol.* **1977**, 49, 33.
83. Ehlers, G. F. L.; Fisch, K. R.; Powell, W. R. *J. Polym. Sci.* **1969**, 7, 2955.
84. Black, R. M.; List, C. F.; Wells, R. J. *J. Appl. Chem.* **1967**, 17, 269.
85. Smith, H. A.; Hadlovits, C. E. ASD-TDR-62-322. *Phenylene Sulfide Polymers* **1962**, , 18.
86. Hawkins, R. T. *Macromolecules* **1976**, 9, 189.
87. Brady, D. G. *J. Appl. Polym. Sci.* **1976**, 20, 2541.
88. Joshi, S. G.; Radhakrishnan, S. *Thin Solid Films*, **1986**, 142, 213
89. Port, A. B.; Still, R. H. *Polym. Degradation Stab*, **1980**, 2, 1.
90. Tabor, B. J.; Magré, E. P.; Boon, J. *Eur. Polym. J.* **1971**, 7, 1127.
91. López, L. C.; Wilkes, G. L. *Polymer*, **1988**, 29, 106.
92. López, L. C.; Wilkes, G. L.; Geibel, J. F. *Polymer*, **1989**, 30, 147.
93. López, L. C.; Wilkes, G. L. *Polymer* **1989**, 30, 882.
94. Fitchmun, D. R.; Newman, S. *J. Polym. Sci. A2*, **1970**, 8, 1545.

95. Chatlerjee, A. M.; Price, F. P.; Newman, S. J. *Polym. Sci.: Polym. Phys. Ed.* **1975**, 13, 2369.
96. Schonhorn, H.; Ryan, F. W. *J. Polym. Sci. A2* **1968**, 6, 231.
97. Huso, M. G.; McGill, W. J. *J. Polym. Sci.: Polym. Phys. Ed.* **1985**, 23, 21.
98. Folkes, M. J.; Harwick, S. T.; Wong, W. K. *In Polym. Composites*; Sedlacek, B., Ed; W. de Gruyter: Berlin, 1986; p. 33.
99. Johnson, T. W.; Ryan, C. L. *Int. SAMPE Symp. Exhib.* **1986**, 32, 1537.
100. López, L. C.; Wilkes, G. L. *Polym. Prep.* **1989**, 30, 207.
101. Gray, D. G. *J. Polym. Sci. Polym. Letters Ed.* **1974**, 12, 645.
102. Radhakrishnan, S.; Nadkarni, V. M. *Polym. Eng. Sci.* **1984**, 24, 1383.
103. Clarke, T. C.; Kanazawa, K. K.; Lee, V. Y.; Rabolt, J. F.; Reynolds, J. R.; Street, G. B. *J. Polym. Sci. Polym. Phys. Ed.* **1981**, 75, 1919.
104. Schacklette, L. W.; Elsenbaumer, R. L.; Chance, R. R.; Echhardt, H.; Frommer, J. E.; Baughman, R. H. *J. Chem. Phys.* **1981**, 75, 1919.
105. Zuk, A.; Juedk, M. W.; Rogal, E. *Polymer*, **1978**, 19, 438.
106. Schock, Jr., K. F.; Bartko, J. *Polymer* **1987**, 28, 556.
107. Piaggio, P.; Cuniberti, C.; Dellepiane, G.; Campani, E.; Gorini, G.; Masetti, G.; Novi, M.; Petrillo, G. *Spectrochim. Acta.* **1989**, 3, 347.
108. Cole, K. C.; Noël, D.; Hechler, J.; Wilson, D. *Mikrochim. Acta.* **1988**, I, 291.
109. Goosey, M. T. *In Plastics for Electronics*; Goosey, M. T., Ed.; *Elsevier Applied Science*: London, 1985; Chapter 10.
110. Russell, T. P.; Gugger, H.; Swalen, J. D. *J. Polym. Sci.: Poly. Phys. Ed.* **1983**, 21, 1745.
111. Ordal, M. A.; Long, L. L.; Bell, R. J.; Bell, S. E.; Bell, R. R.; Alexander Jr., R. W.; Ward, C. A. *Appl. Optics* **1983**, 22, 1099.
112. Ganin, G. V.; Kirillova, M. M.; Nomerovannaya, L. V. *Shirokovskiy Fiz. metal. metalloved.* **1977**, 43, 907.

114. Milosevic, M.; Harrick, N. J.; Berets, S. L. *Appl. Spectrosc.* **1991**, *45*, 126.
115. Ward, L. In *Handbook of Optical Constants of Solids II*; Palik, E. D., Ed.; Academic: New York, 1991: p. 737.
116. Hansen, W. N. *J. Opt. Soc. Am.* **1968**, *58*, 380.
117. Potter, R. F. In *Handbook of Optical Constants of Solids*; Palik, E. D., Ed.; Academic: New York, 1985; p. 465.
118. Lovinger, A. J.; Davis, D. D. *J. Appl. Phys.* **1985**, *58*, 2843.
119. Nguyen, H. X.; Ishida, H. *Polym. Comp.* **1987**, *8*, 57.
120. Clark, D. T.; Wilson, R. J. *J. Polym. Sci.: Polym. Chem. Ed.* **1983**, *21*, 837.
121. Anonymous *Application Note No. 8401*, Perkin-Elmer Corp., Physical Electronics Division, Eden Prairie, MN.
122. Lynch, D. W.; Hunter, W. R. In *Handbook of Optical Constants of Solids II*; Palik, E. D., Ed.; Academic: New York, 1991; p. 376.
123. Clark, D.T.; Thomas, H. R. *J. Polym. Sci., Polm. Chem. Ed.* **1977**, *15*, 2843.
124. C. Evans & Associates, *Application Note* **1990**, 5(2).
125. Filbey, J. *Ph.D. Dissertation*, Virginia Polytechnic Institute and State University, Blacksburg, VA 1988.
126. Lee, H.; Neville, K. In *Handbook of Epoxy Resins*; McGraw-Hill: New York, 1964.
127. Fowkes, F. M.; Mostafa, M. A. *Ind. Eng. Chem. Prod. Res. Dev.* **1978**, *17*, 3.
128. Fracassi, F.; Coburn, J. W. In *Plasma Processing*; Coburn, J. W., Gottscho, R. A., Hess, D. W., Eds.; Pittsburgh: Mat. Res. Soc. Symp. Proc., 1986; Vol. 68, p.407.
129. Sauerbrey, G. *Z. Phys.* **1959**, *155*, 206.
130. Smith, C. D. *Ph.D. Dissertation*, Virginia Polytechnic Institute and State University, Blacksburg, VA 1991.
131. Weill, A.; Dechenaux, E. *Polym. Eng. Sci.* **1988**, *28*, .

Chapter 3: Analysis of the Reorganization in Thin PPS Films by Variable Temperature Reflection Absorption Spectroscopy (VTRAS)

3.0 INTRODUCTION

The physical and chemical nature of the interphase or transition region between a polymer in contact with a rigid inorganic substrate can be of critical importance in many areas of interest including adhesion, flocculation, polymer adsorption, and filled polymer systems. Polymer structure and properties in this region may be reasoned to be different than that found for the bulk polymer, with the difference decreasing as further distances from the surface are sampled. One factor involved is the loss in the number of polymer conformations possible as the polymer chains are adsorbed to the surface, thus representing a decrease in entropy. This must be balanced by favorable segmental interaction with the surface to give an exothermic enthalpy contribution, and a combination of the two factors drives the system to minimum free energy at the interface. For crystalline polymers, the surface sites can also serve as nucleation centers from which unique transcrystalline regions can grow. Surface characteristics including surface energy (1,2), and surface chemistry (3) have been postulated to play roles in heterogeneous nucleation on surfaces. For a particular polymer/substrate combination, interaction terms may involve London dispersion forces as well as acid-base contributions, and Fowkes has shown the importance of interfacial acid-base chemistry in determining the adsorption properties of polymethylmethacrylate on acidic and basic substrates (4). Specific polymer properties will also be important, including chain flexibility, number of entanglements, crystallinity and polymer intermolecular forces which will combine with interfacial interactions to determine the structure of the interphase.

In addition to the "static view" of the interphase, dynamic considerations involving time and temperature must be introduced. Polymer property variations with time and temperature are generally well known in the bulk, but often neglected with regard to interphase or surface phenomena. In this region, the environment must also be included with time and temperature as a critical variable. Polymer dynamics

including thermal expansion and thermal transitions may be profoundly influenced by the local environment or chemical reactions in the interfacial region. The method of preparation may also profoundly affect the dynamics involved if non-equilibrium states are formed. In general, polymer molecules in the vicinity of a solid surface may be expected to exhibit motions and relaxations different than those in bulk samples. Experimentally, however, techniques to probe this difference are restricted to high surface area substrates, while studies involving relatively flat substrates are rare.

3.1 LITERATURE REVIEW

3.1.1 Interphase Studies

Several analytical techniques have been used to probe the structure and dynamics of the interphase region. Inverse gas chromatography can be used to investigate the interaction of probe molecules with both inorganic and polymer matrices. Braun and Guillet have used this technique to determine the glass transition temperature for polyvinylchloride (5) and have also found that the T_g of polystyrene increased as the thickness of the support media film coating decreased (6).

XPS is another useful tool, particularly for surface structure, and Ratner and coworkers have used this technique to study the surface rearrangement of polar polymers grafted onto nonpolar polymer substrates when changing from an aqueous to ambient air environment (7,8). Studies of surface segregation of siloxane containing copolymers are common and analysis of the extent of interphase segregation has been shown to depend on the acid/base character of the substrate (9). Interfacial studies of single component polymer systems are difficult to interpret due to the usually small changes that are observed. Sample damage with exposure of the interface and contamination are also problems.

Nuclear magnetic resonance provides the most direct means of studying interfacial dynamics, although due to the lack of sensitivity, the analysis is restricted to high surface area substrates. This technique has been extremely useful in studying the

dynamics of alkyl chains for alkyl-modified chromatographic supports (12,13). It has also been used to investigate the chain mobility of polyethylene oxide adsorbed on silica (9,10).

The study of interfacial phenomena in filled polymer systems has received much attention in recent years due to its importance in the area of composite systems and because the systems are amenable to more classical methods of analysis including dynamic mechanical thermal analysis (DMTA). Although the results are not in complete agreement, many studies have shown that polymer/filler interactions can lead to decreased polymer mobility in the interphase region and affect the mechanical properties of the composite system. Studies have shown an increase in the polymer glass transition temperature due to polymer/filler interactions (14,15). Richard, et al. showed that the improvement of mechanical properties and filler dispersion properties for a CaCO_3 filled polyvinyl chloride system correlated with the degree of acid/base interfacial interaction (16). Stupp and Weldert also showed that when a glass filler was electrostatically charged, polymer wettability increased while polymer mobility, as measured by thermally stimulated discharge (TSD), decreased (17). Using dielectric thermal analysis (DETA), Ko, et al. showed that the glass transition temperature increased and the loss peak broadened for polysulfone coatings coated on both acid cleaned and anodized aluminum surfaces for thicknesses even in the micron range (18). This, again, indicates how specific surface/polymer interactions can dramatically affect polymer dynamics in the interphase region.

3.1.2 Variable Temperature Infrared Spectroscopy

While infrared spectroscopy of polymers is a common tool in polymer characterization, studies of thermal effects on the infrared spectra of polymers are relatively few. Many studies have dealt with the irreversible spectral changes associated when certain polymers crystallize (19,20). While investigations concerning the temperature dependence of the width of absorbance bands on temperature have

been investigated (21), variable temperature studies have usually involved the measurement of either peak frequency or peak intensity as a function of temperature. While the exact theoretical explanations behind these changes are not completely understood at present, a number of explanations have been given for the changes observed.

3.1.2.1 Frequency Shifts

The frequency of an absorbance band for a simple diatomic molecule can be given by the simple relationship:

$$\nu = \frac{1}{2} \pi \left(\frac{K}{\mu} \right) \quad [1]$$

where K , the force constant, is related to the potential energy surface for the vibrational excitation of interest and μ is the reduced mass. Changes in the potential energy surface, then, would lead to shifts in frequency for the absorbance peak. It has been postulated that the intermolecular force field around a particular group would contribute to the potential energy for a vibration, and therefore a decrease in intermolecular forces with thermal expansion would lead to a decrease in frequency (22, 23). This would be particularly important in polymeric systems where intermolecular forces are known to play an important role in polymer physical properties. The decrease in frequency with increasing temperature has been observed in a number of studies (22,23,24) and the often linear rate seen has been attributed to the linear temperature dependence for the thermal expansion in polymers (22). Herber, in studying organotin compounds, found that for covalent solids where intermolecular forces were small, the frequency of absorbance bands was insensitive to changes in temperature (23). For the compounds studied that formed polymeric networks, strong dependencies of peak frequency on temperature were seen, and were attributed to intermolecular interactions.

While many of the early studies showed the qualitative usefulness of variable temperature infrared analysis, more recent analyses have attempted to identify and quantify the infrared spectral changes. In a comprehensive analysis, Joss, et. al studied the non-equilibrium state of polyvinylchloride and polystyrene, and developed expressions to explain the peak frequency shifts in terms of both intermolecular and intramolecular contributions (24). The intramolecular contribution could be monitored by following skeletal vibrations, and was attributed to chain strain effects. This term disappeared in properly annealed samples, leaving the intermolecular contribution to frequency shifting due only to changes in temperature and volume. This contribution could be expressed by the following equation (24):

$$\frac{d\nu}{dT} = \frac{-\gamma_i \nu_i \alpha_{g,i}}{1 + \alpha_{g,i} (T - T_g) - \beta_o} \quad [1]$$

where γ_i is the three dimensional Grueneisen coefficient, α_g and α_i are the thermal coefficients of expansion below or above the T_g respectively, ν_i is the frequency of interest, and β_o is a constant. This expression shows the interchain contribution to frequency shifting. Both the T_g and the Grueneisen coefficient γ_i (at T_g) were determined for PVC and polystyrene (24). From this work and that with PMMA (25), it was speculated that by monitoring main chain skeletal absorbance bands, intramolecular contributions to frequency shifting with temperature could be monitored, while pendant group absorbance frequencies may monitor the intermolecular environment.

3.1.2.2 Intensity Changes

The second and perhaps more common variable temperature infrared method is

to examine changes in peak intensity or integrated absorbance with temperature. As with frequency shifts, a number of explanations for polymeric systems have centered around the fact that the cubic expansion of the polymer with temperature would alter intermolecular forces for a particular chemical group in the polymer backbone, thus changing the observed absorbance or peak intensity. In early studies, Anton showed that by monitoring integrated peak absorbance versus temperature for certain absorbance bands, the glass transition temperature of polystyrene and polyvinylacetate could be determined (26). Ogura also monitored the temperature dependence of the CH and CH₂ bending absorbances at 1333 cm⁻¹ and 1427 cm⁻¹ respectively, for PVC to detect the T_g of this polymer (27). Fukawa rationalized that the observed peak absorbance changes could be correlated with refractive index changes in the polymer (28), although given the wide sensitivity for various absorbance bands, this explanation has been disputed (32). Huang and Koenig found that by monitoring the out-of-plane bending mode absorbance at 841 cm⁻¹ for polystyrene, the δ transition at 50 K and the β transition at 240 K could be detected, showing the usefulness of this technique in detecting polymer transitions other than the T_g (29). The thermal changes were attributed to variations in intermolecular forces as the polymer expanded, and a linear decrease in peak absorbance with increasing temperature was observed. Reversible thermal changes in polyethylene terephthalate were also monitored by Lin and Koenig, and both peak absorbance and frequency shifts were monitored to yield linearly decreasing plots with increasing temperature (30). The sensitivity of individual vibrating modes was explained as a reflection of the changes in the specific environment of the group monitored as both intramolecular and intermolecular forces were altered with thermal expansion. Magonov, et al. studied changes in absorbance and frequency of both quenched and annealed polystyrene, and reasoned that changes in intermolecular forces were responsible for the observed decreases in frequency and absorbance for the bands monitored (31). In this work, the T_g was also determined, and the slope of the

frequency and absorbance plots with temperature was dependent on the thermal history of the samples. Snyder, et al. studied the change in the intensities for particular infrared bands for crystalline n-alkanes and polyethylene and an example of the temperature dependence of the 782 cm⁻¹ rocking band of n-C₁₉H₄₀ is shown in Figure 3.1. The 30% decrease in intensity for the phase I to phase II solid-solid transition is clearly seen in the plot. In this analysis, it was determined that changes in density, refractive index or Boltzmann factors could not account for the large reversible changes in the intensity for the bands monitored (32). However, the decrease in band intensities was correlated with the polymer thermal expansion. In another recent work, Snyder, et al. showed that Boltzmann effects could not explain the large decrease in intensity for the carbonyl absorbance for a PMDA/ODA polyimide (33). The expression developed to predict the absorbance decrease due to the reduction in ground state species was given as:

$$\frac{A_{T_2}}{A_{T_1}} = \frac{e^{\left(\frac{-hc\nu}{kT_1}\right)} + 1}{e^{\left(\frac{-hc\nu}{kT_2}\right)} + 1} \quad [2]$$

The comparison of experimental and theoretical results based on Eqn.[2] for the 1780 cm⁻¹ carbonyl band is shown in Figure 3.2, and the deviation between calculated and measured absorbances is shown. It was reasoned that conformational changes involving the imide ring altered the magnitude of the dipole moment, thus directly affecting the strength of absorption.

When compiling the available literature for variable temperature infrared studies, unambiguous mechanisms to explain the frequency and absorbance changes for all absorbance bands in every polymer system studied do not exist. Clearly, however,

the changes in intermolecular environment with temperature due to thermal

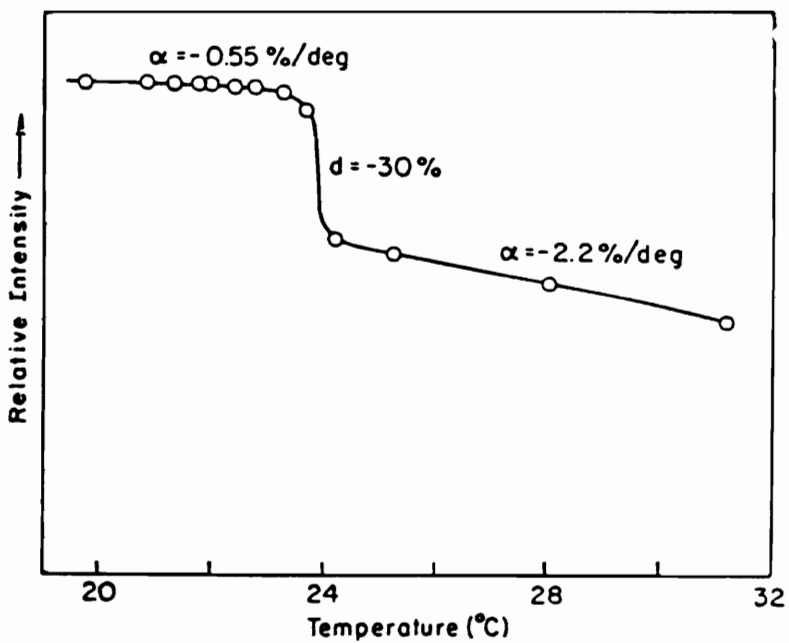


Figure 3.1 Plot of peak intensity versus temperature for the 782 cm⁻¹ C-H rocking absorbance band of n-C₁₉H₄₀ (32).

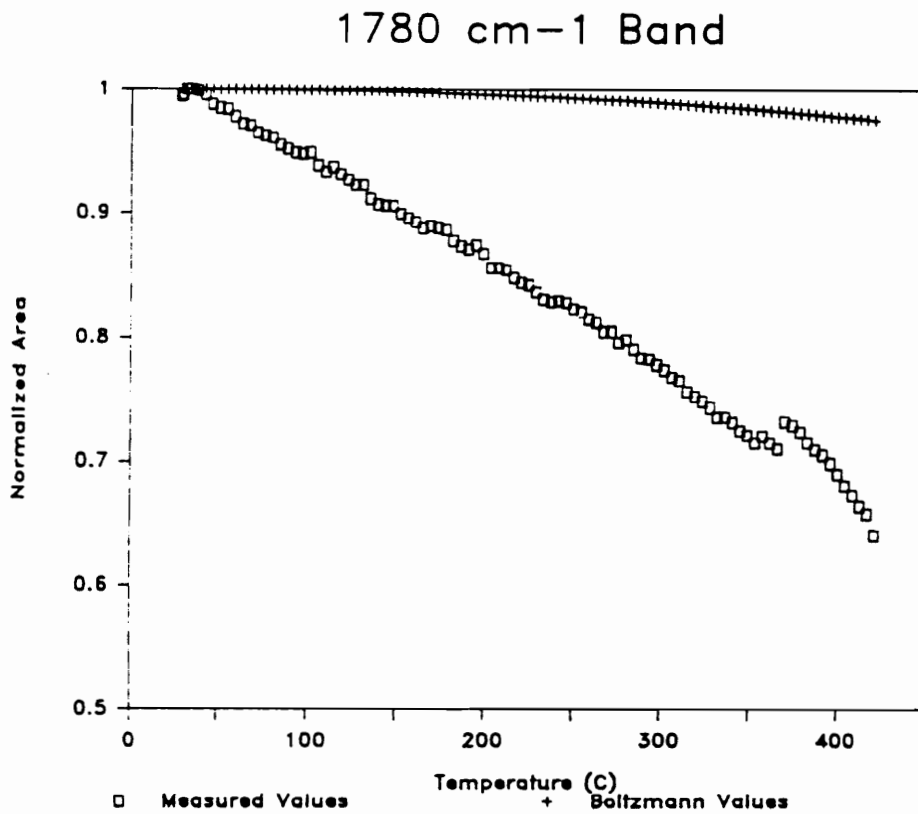


Figure 3.2 Plot of absorbance versus temperature for the polyimide 1780 cm⁻¹ band. The plot shows both experimental points and theoretical results based on equation [2] (33).

expansion plays a central role in the spectral changes. If this is the case, processes altering polymer mobility including interfacial chemical reactions, cross linking, or surface adsorption of polymer segments should be detected by this technique.

3.1.3 Variable Temperature Infrared Spectroscopy

The combination of thermal analysis with reflection infrared techniques is almost nonexistent. Studies by Schlotter and Rabolt (34) and Swalen, et al. (35) have investigated spectral features at various temperatures for ordered monolayers, but no quantitative measurements of peak absorbance or frequency were presented. Spectral changes with temperature did show conformational disorder with increasing temperature due to gauche defects. The use of this technique to investigate increasing disorder with elevated temperatures for thin films of poly(di-n-alkylsilanes) was reported by Rabolt, et al. (36) and qualitative spectral changes for a polymethylmethacrylate film on silver have been shown by Schlotter and Rabolt (34). However, no quantitative study was attempted. The use of this technique has most probably been limited by the small database of information for variable temperature infrared measurements, and the difficulty in predicting the effects of temperature of the optical properties of both the polymer film and the substrate. This technique, however, does offer advantages due to the ability to monitor orientational changes in surface films.

3.2 EXPERIMENTAL

3.2.1 Sample Preparation

Copper, chromium, and aluminum substrates were prepared by vapor deposition of the metal of interest on acid cleaned ferrotype plates (see section 2.2.1.2). For vapor deposited copper samples, substrates were oxidized at 140-150°C for two minutes and aluminum samples were pre-oxidized at approximately 150°C for 30 minutes before coating. Thin PPS coatings were prepared by high temperature spin

coating procedures previously outlined (see section 2.2.1.1). After coating, samples were dried under vacuum (10^{-1} - 10^{-2} torr) for 12 hours at approximately 140 - 150°C. Samples were then quenched in liquid nitrogen after a rapid heating in a nitrogen atmosphere to 320 - 340°C on a hot plate oven. Heating times at this temperature did not exceed two minutes. Some PPS coated copper samples were held at higher temperatures (350 - 370°C) for two minutes and quenched in liquid nitrogen. Samples for transmission measurements were prepared by spin coating more concentrated PPS solutions in benzophenone (10% wt/wt) on unpolished salt plates to yield films of approximately 2.5 microns thickness. Samples were then dried under vacuum and heated to 320 - 340°C under nitrogen for 10 minutes followed by quenching in liquid nitrogen.

Differential scanning calorimetry (DSC) was used to analyze the major thermal transitions for Ryton™ PPS using a ramp rate of 2.5°C / minute. To prepare samples with a similar thermal history to those prepared by spin coating, samples were dissolved in degassed benzophenone at 280°C and held at this temperature for approximately 15 minutes. The solution was then poured into a 25:75 water / methanol solution and the PPS precipitate filtered and washed with pure methanol several times. The sample was then dried overnight at 120°C under vacuum. Samples were then melted at approximately 320°C under nitrogen in a DSC sample pan and quenched in liquid nitrogen prior to analysis.

Films of polyetherimide were prepared by spin coating solutions ranging from 0.1 to 10% (wt/vol) in chloroform onto chemically polished copper foil (see section 2.2.1.2). Samples were then dried under vacuum at 140 - 150°C for six hours to remove all solvent.

3.2.2 Variable Temperature Infrared Analysis

Variable temperature infrared transmission measurements were made on spin coated PPS films using a heated transmission cell (Spectra Tech, Inc.). The temperature was monitored with a type K thermocouple mounted in the center between the coated salt plate, and a second uncoated salt plate. The two were then positioned in the center of the heating unit and the temperature monitored with a digital thermometer (Omega, Inc., model 660). The analog output signal (10 mV / °C) was sent to a personal computer via an 8 channel high speed data acquisition and control interface (Model DAS-8, MetraByte, Inc.), and a program was written in QuickBasic™ (Microsoft, Inc.) for personal computer use to monitor and control the temperature. The program incorporated proportional, integral, and derivative control features and allowed multiple set points and ramp rates. Typically for these studies, a ramp rate of 2-3°C per minute was employed, and a plot of the temperature versus time for a 2.3°C / minute ramp rate is shown in Figure 3.3. Data was collected using a nitrogen purged Nicolet 510 infrared spectrophotometer employing a triglycine sulfate (TGS) detector. Approximately 120 scans were recorded per spectrum at a resolution of 4 cm⁻¹, resulting in one spectrum taken every 1 - 2 minutes for typical instrument mirror velocities. This resulted in temperature resolution of 2.5 - 5°C.

3.2.3 Variable Temperature Reflection Absorption Spectroscopy

Figure 3.4 shows a schematic diagram of the variable temperature design used for all variable temperature reflection measurements. Essentially, the system consists of a U-shaped holder with an attached sample heater, centered in a cylindrical vacuum chamber. Figure 3.5 shows a more detailed diagram of the sample holder configuration. The holder was mounted on a ceramic shaft to insulate the external components from excessive heating. The entire assembly was fastened to a four inch stainless steel high vacuum flange mounted on a 360° precision turntable (Edmund Scientific). A liquid nitrogen trapped oil diffusion pump was used to achieve operating

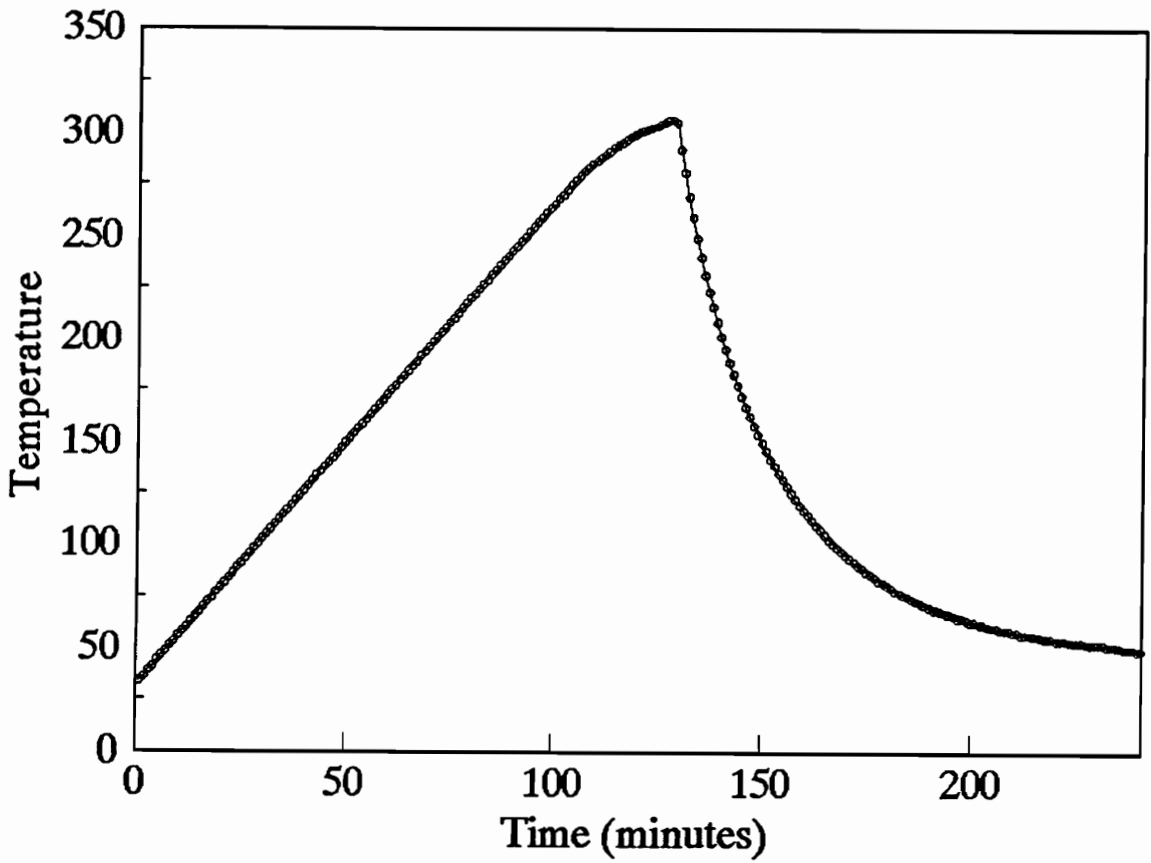


Figure 3.3 Typical heating and cooling temperature profile for variable temperature transmission experiments.

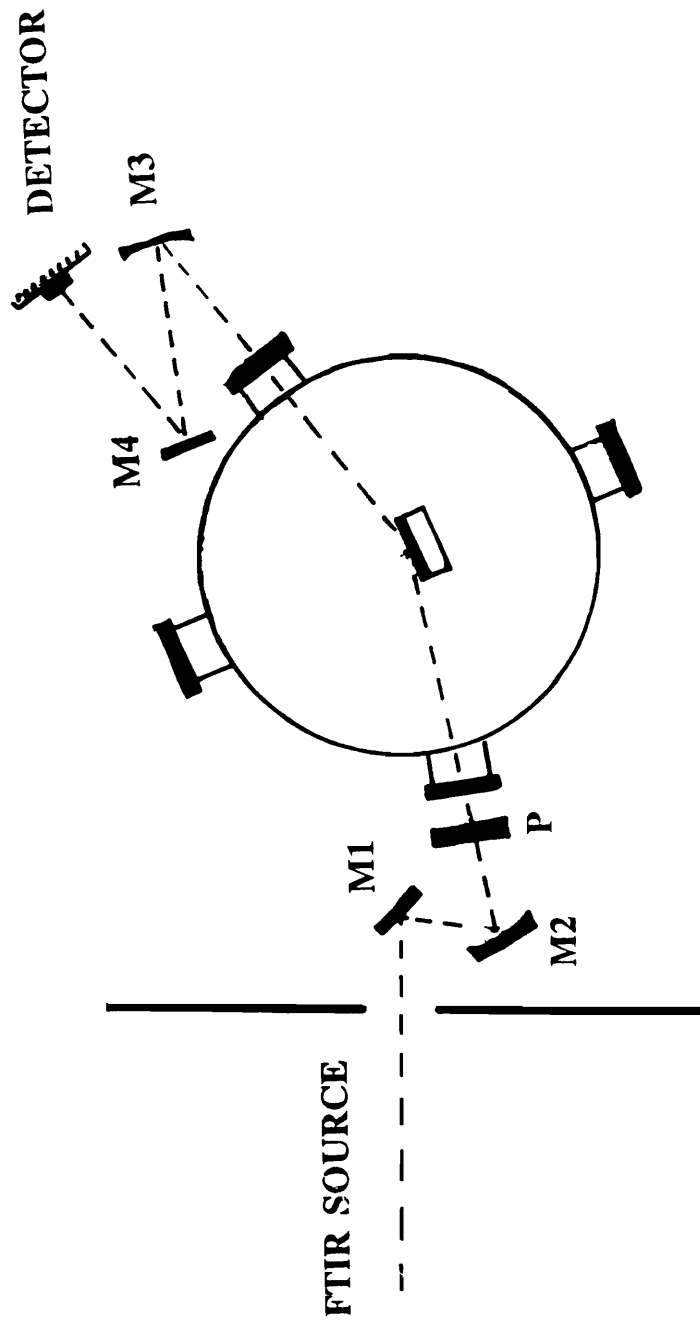


Figure 3.4 Schematic diagram of the experimental design used in all variable temperature reflection absorption measurements.

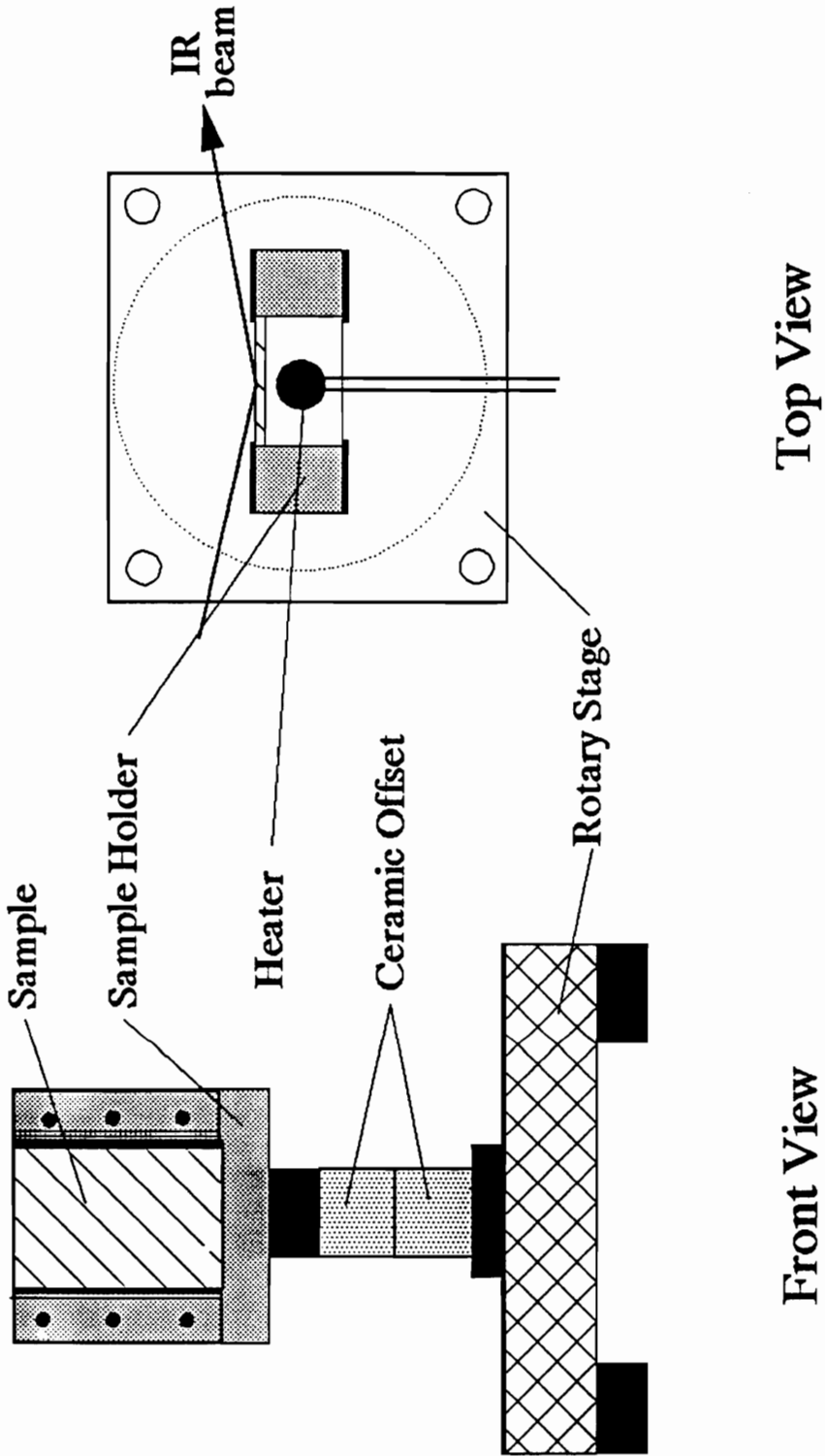


Figure 3.5 Schematic diagram of the sample holder for variable temperature RAS measurements.

pressures of 5×10^{-4} - 5×10^{-5} torr and the pressure was continually monitored using a nitrogen gas calibrated ion gauge. The infrared beam was directed outside the FTIR optical bench, and into the chamber via a series of transfer optics designed to match those of the internal bench chamber. The vacuum chamber was isolated from the external environment by o-ring sealed KBr windows, and the entire optics assembly was maintained under a nitrogen purged environment to minimize water and carbon dioxide absorption. The unit had machined optical ports designed to allow measurements in both the reflection (80°) or transmission mode (0°). The incidence angle was calibrated by laser alignment of the substrate after removal of the external chamber and rotating the sample until the 0° point was established by turning the beam back onto itself. The sample could be then rotated to 80° and the external chamber replaced and rotated until normal alignment of the windows with the incident laser. A polarizer was placed in the infrared beam path before entering the sample chamber and typically p-polarization was used. After exiting the vacuum chamber, the light was focused onto a liquid nitrogen cooled mercury cadmium telluride (MCT) detector.

The surface temperature was measured using a 1.59 mm diameter stainless steel K type thermocouple (Omega, Inc.) mounted through a high vacuum Swagelok™ fitting into the vacuum chamber. The tip of the thermocouple was pressed directly against the front surface of the film covered substrate. Contact was ensured by sealing any air gaps between the thermocouple end and sample plate with silver paint (E. F. Fullam, Inc.), and cementing the thermocouple to the substrate using high temperature ceramic cement (Omega, Inc.). The temperature was monitored and controlled using electronic components and computer software previously described for transmission measurements. For the studies here, a ramp rate of $2\text{-}3^\circ\text{C} / \text{minute}$ was employed, and a plot of time versus temperature for a $2.4^\circ\text{C} / \text{minute}$ ramp rate is shown in Figure 3.6. To obtain a linear ramp rate under vacuum, the software

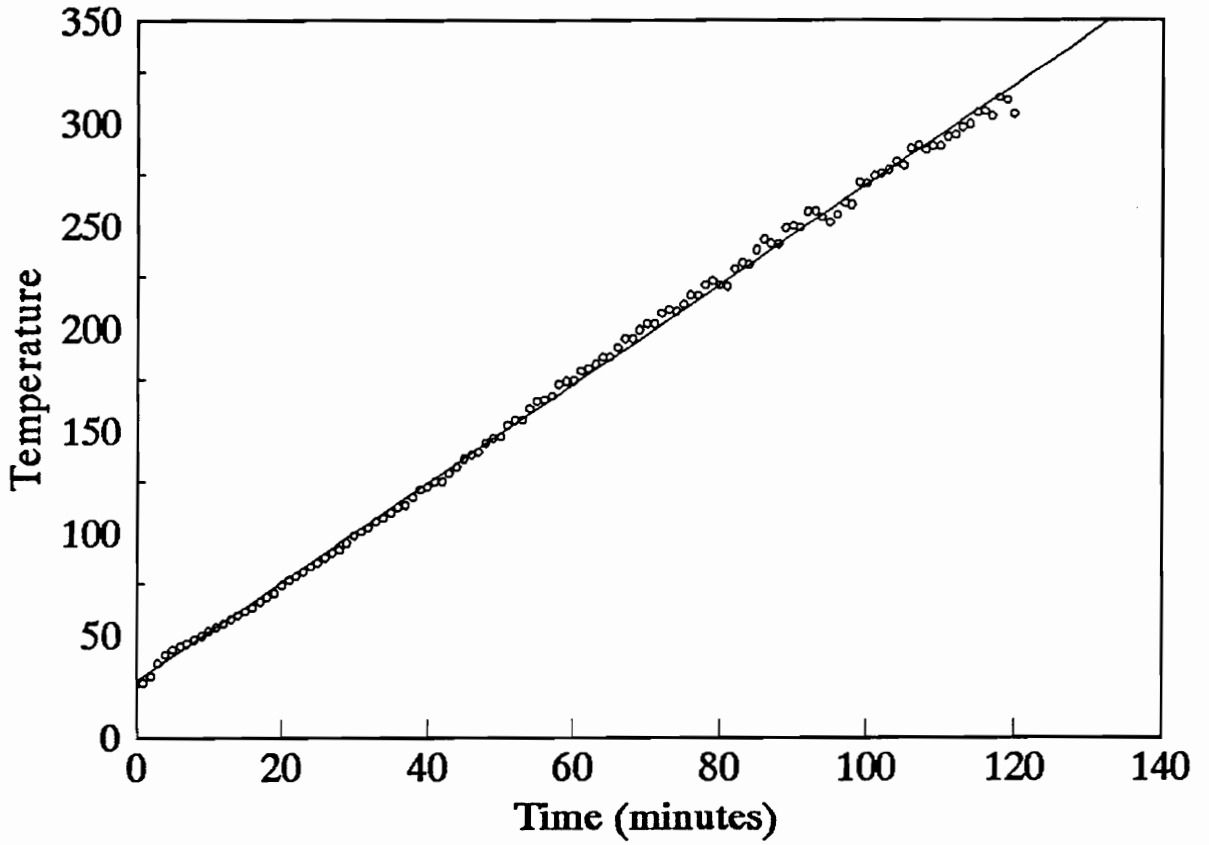


Figure 3.6 Typical heating temperature profile for variable temperature RAS measurements.

parameters for proportional and derivative control had to be carefully selected. The values used under vacuum and ambient nitrogen conditions are given in Appendix 3.1.

3.2.4 Data Manipulation

The experiments for this work involved data collection using two instruments. The infrared spectrophotometer collected spectral information, and stored data as the infrared spectrum taken versus time. Temperature information was collected using an IBM™ personal computer and stored as temperature versus time. To ensure equivalent times for both instruments, the personal computer internal clock was synchronized with the clock from the infrared spectrophotometer before each run. A computer program was written in QuickBasic™ (Microsoft, Inc.) to allow accurate determination of the time taken for each spectral scan, and can be found in Appendix 3.1. The calculated time was for the mid-point of each temperature scan, and once known, the temperature for each spectrum was found by interpolation from stored temperature versus time data.

Since the information of interest was spectral changes for peak position, intensity, and area with temperature, methods were developed to determine these parameters for large numbers of data files. To do this, a custom program was written in ArrayBasic™ (Galactic, Inc.) and was designed to be used within the LabCalc™ (Galactic, Inc.) working environment. The specifics of the program and operation are given in Appendix 3.1. In general, the program incorporates LabCalc™ peak picking and quantification software to generate the quantity of interest, i.e., peak position, peak intensity, or peak area versus spectrum number for any number of multiple data files. Once this file is stored, it is merged with spectrum number versus temperature data previously determined. All software is given in Appendix 3.1.

3.3 RESULTS AND DISCUSSION

3.3.1 Theoretical Considerations

While changes in refractive index have sometimes been used to explain the changes in peak intensity with temperature for absorbance bands, the sensitivity of infrared spectra to refractive index is small in transmission and such arguments have been disputed (36). Therefore, the changes in band intensities with temperature primarily reflect changes in k , the extinction coefficient. In reflection, however, a more complicated dependence of the resultant spectral features such as band position, intensity, and shape on the optical parameters of the system exists. These can be expressed by the following relation where the state of polarization, frequency, and angle of incidence are fixed:

$$A(T) = -\log\left(\frac{R(T)}{R_o(T)}\right) = f(n_f(T), k_f(T), n_s(T), k_s(T), d(T)) \quad [3]$$

where n_f and k_f denote the optical constants of the polymer film, n_s and k_s represent the optical constants of the substrate and d is the thickness of the layer. All variables will be sensitive to changes in temperature and this effect must be quantified to understand the resultant spectra. The ideal experiment would be one where a direct comparison of changes in bulk k values with temperature measured in transmission could be compared with changes in k values in the reflection mode to investigate the potential role of surface interactions. Due to optical effects, including the anomalous dispersion in the refractive index, it is often difficult to compare directly transmission and reflection changes (see section 2.1.2). To quantify the potential changes due to these factors, and therefore possibly optimize experimental conditions, exact optical theory was employed to determine the significance of each variable.

The increase in thickness due to thermal expansion would be offset by a decreasing density given that the number of molecules in the beam path remains

relatively constant. This would probably be expected for thin surface films where lateral flow would be negligible, and therefore the effect on absorbance due to thickness changes would be minimal.

To investigate the spectral changes with changes in substrate optical parameters, Figure 3.7a shows the dependence of the intensity of a hypothetical absorbance peak as a function of the k value of the substrate for several incidence angles. The refractive index of the substrate was taken as 3.0 for a typical metal, and values for n_r and k_r were taken as 1.5 and 0.4 respectively, which are typical for a polymer carbonyl band. The frequency was taken as 1740 cm^{-1} , also indicative of a carbonyl functionality. These results are similar to those reported by Greenler (37) and show that only at the highest angles of incidence and lowest k values is there a significant dependence. This means that the contribution to peak intensity or area due to changes in substrate k values for metals would be minimal except at extremely grazing angles. The effect for of substrate refractive index, n_s , is shown in Figure 3.7b and little change in the absorbance peak intensity will arise due to changes in this variable. The fact that the absorbances can be made insensitive to the substrate is fortunate since although data is available for the temperature dependence of some metals in limited frequency ranges, an extensive list of n_s and k_s values versus temperature over a wide spectral range does not exist for many substrate materials.

While the anomalous dispersion in the refractive index causes distortions in the reflectance spectra (see section 2.1.2.2), the magnitude of this effect for a single peak band shape, given a known angle of incidence, state of polarization, and frequency, will depend on the magnitude of the k value and its full width at half maximum. These two variables are not independent and can be connected through the Kramers-Kronig relation. The intensity of the resulting absorbance band can depend, however, on the 'anchor point' for the dispersion through the absorbance band, which can be taken as the high frequency refractive index (n_∞) for a single isolated band (38,39). Figure 3.8 shows the change in intensity for the simulated carbonyl stretching

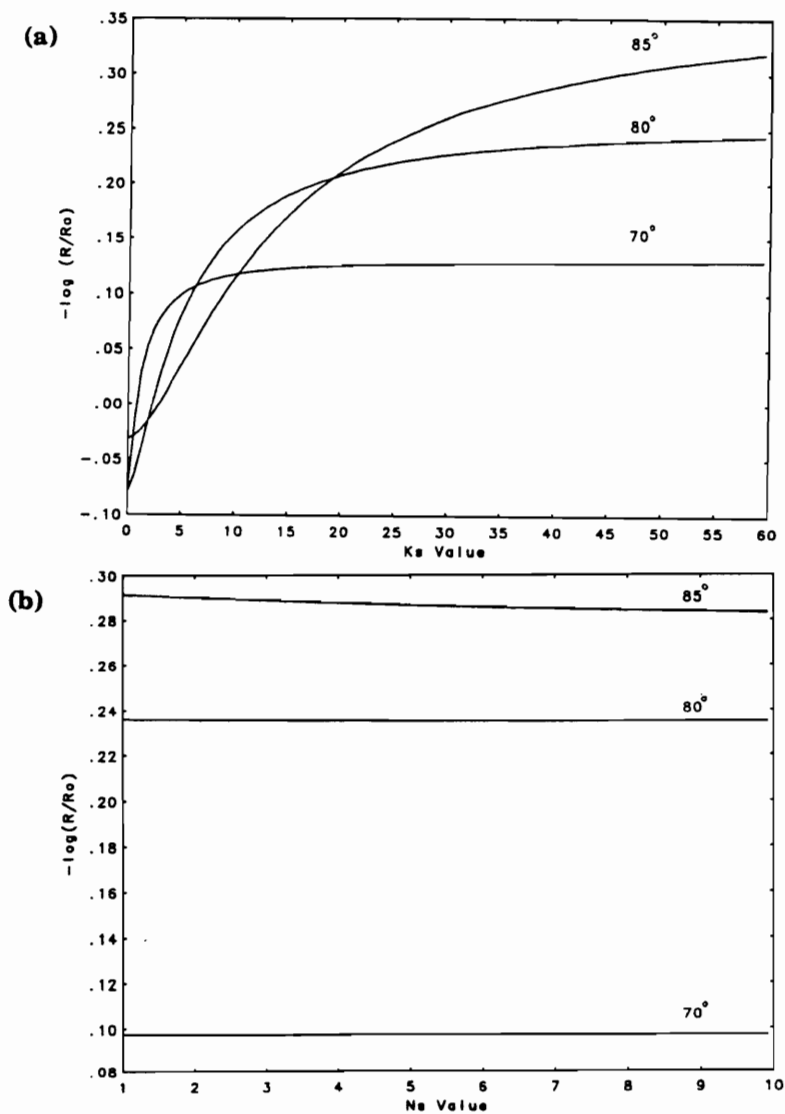


Figure 3.7 Plot of the dependence of the peak intensity ($-\log(R/R_0)$) on (a) the substrate k value (k_s), and (b) the substrate n value (n_s). The hypothetical absorbance band used was given values of 1.5 and 0.4 for n_r and k_r respectively, and a substrate n value of 3.0 was used for plot (a) and a k value of 40 for plot (b). The frequency was taken as 1740 cm^{-1} .

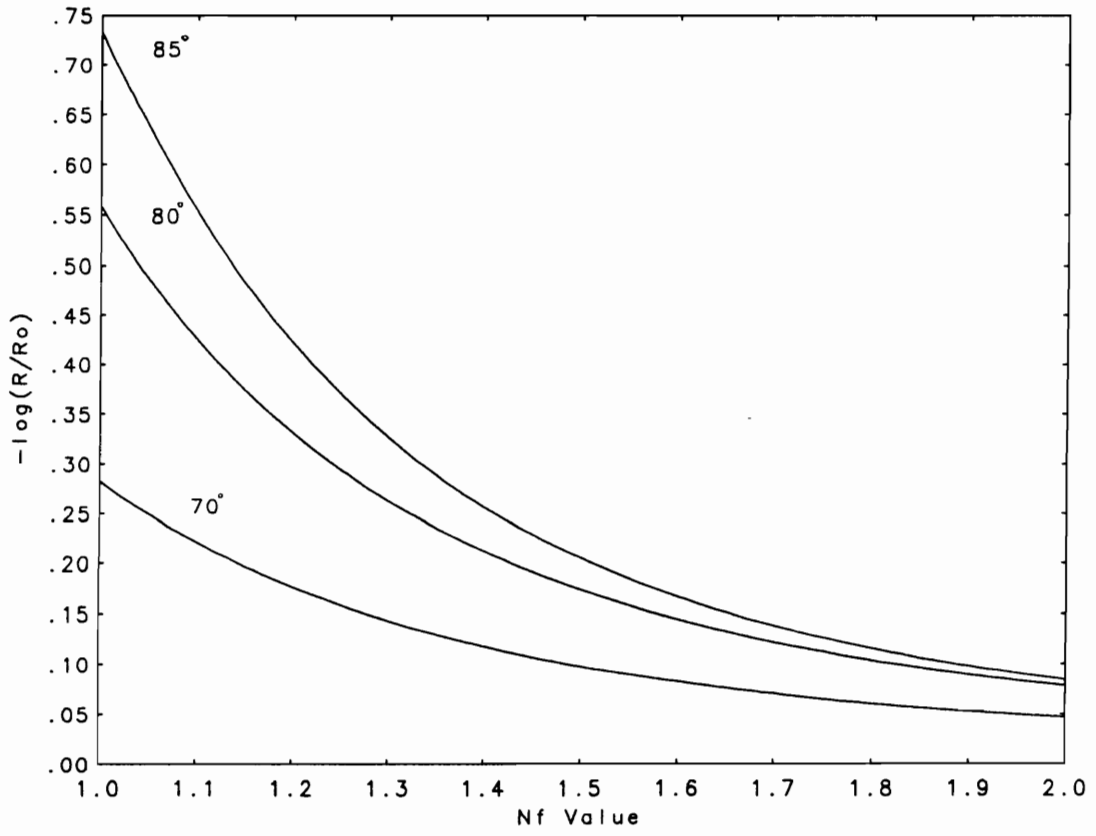


Figure 3.8 Plot of the dependence of the peak intensity ($-\log (R/R_0)$) on the film refractive index. Substrate n and k values were taken as 3.0 and 40 and the other parameters are given in Fig. 3.7.

absorbance used previously as a function of n_{∞} , for several angles of incidence. In this case, the n_s and k_s values were fixed at 3 and 40, respectively, to correspond to values for copper at 1740 cm^{-1} (47). The strong dependence at high angles decreases with decreasing

incidence angle and becomes less sensitive to this parameter in the refractive index range of 1.4 to 1.7. Since this range of values is typical for many polymers, the result indicates that while the peak position and intensity will be dependent on changes in k_r , the intensity due to changes in refractive index with temperature will be less important for polymers if the experimental conditions are chosen carefully.

The last variable to investigate is k_r which can be described in terms of $\nu(\text{max})$, $k(\text{max})$, $\Delta_{1/2}$ for a given isolated band, where $\nu(\text{max})$ is the frequency of maximum intensity in the k spectrum, $k(\text{max})$ is the maximum k value, and $\Delta_{1/2}$ represents the full width at half height for the peak. For a given frequency, $\nu(\text{max})$ in the k spectrum, there will be a corresponding $\nu(\text{max})_R$ in the reflectance spectrum that will generally be somewhat blue shifted for external reflectance and depend on the film thickness and other set experimental parameters. It is of interest to examine the effect of changes in the peak position, intensity, and width of the k profile on the peak position in the reflectance spectrum. Since transmission measurements approximate the k spectrum, this would allow a direct comparison of transmission and reflection spectra.

Holding $k(\text{max})$ and $\Delta_{1/2}$ constant, changes in peak position $\nu(\text{max})$ should show a corresponding change in $\nu(\text{max})_R$ for a given film thickness. This means that while absolute comparisons of reflectance and transmittance spectra are difficult to make, relative changes in the k spectrum maximum, holding $k(\text{max})$ and $\Delta_{1/2}$ constant should correspond to relative frequency changes in the reflectance spectrum. Of course with increasing temperature, the peak intensity generally decreases in transmission (22,30,32) and the peak width broadens (21). To examine the effects of these parameters, optical modeling can be used to predict changes in the reflectance

spectrum with changes in the k spectrum. To do this a Lorentzian band shape was assumed with given $\nu(\text{max})$, $k(\text{max})$, and $\Delta_{1/2}$ values. Holding $\nu(\text{max})$ and $\Delta_{1/2}$ constant, Figure 3.9a shows the change in absorbance peak position for the reflectance spectrum versus the percent decrease in $k(\text{max})$ for several initial $k(\text{max})$ values. The plot assumes an 80° incidence angle and a film thickness of 100 nm and shows a slight dependence with a maximum shift of -1.5 cm^{-1} for a width of 20 cm^{-1} and a 50% reduction from the initial k value. Clearly, the wider the original peak, the greater is the effect. On the other hand, if $\nu(\text{max})$ and $k(\text{max})$ are held constant, and the percent increase in $\Delta_{1/2}$ monitored, it can be seen in Figure 3.9b that the maximum effect for an original k value of 0.4 and a 50% increase in peak width would result in a positive frequency shift of 1.5 cm^{-1} . Given the typical range of k values (<0.4) and peak widths ($<40 \text{ cm}^{-1}$) for many absorbance peaks in polymers (41), the shifts due to decreases in k and peak broadening would be expected to somewhat cancel each other resulting in a minimal effect of the resulting reflectance spectrum. The results, however, only apply for a polymer thickness of less than 100 nm for reflectance from metals. Thicker films or films on infrared transparent substrates can display more severe distortions in the observed absorbance bands and the dependence on changes in optical parameters may be more severe.

2.3.2 Differential Scanning Calorimetry

Figure 3.10 shows a DSC trace for the Phillips Ryton™ polyphenylene sulfide used in this study. As can be seen, the first trace exhibits an exothermic crystallization peak (T_∞) at 117°C and a melting endotherm (T_m) at 284°C . Evidence for the glass transition temperature is seen during the first scan as a slope change near $85 - 90^\circ\text{C}$. On the second scan, one melting peak is seen at 284°C and these results are in general agreement with previous results shown for Ryton™ PPS (See Chapter 2, Fig. 2.6)

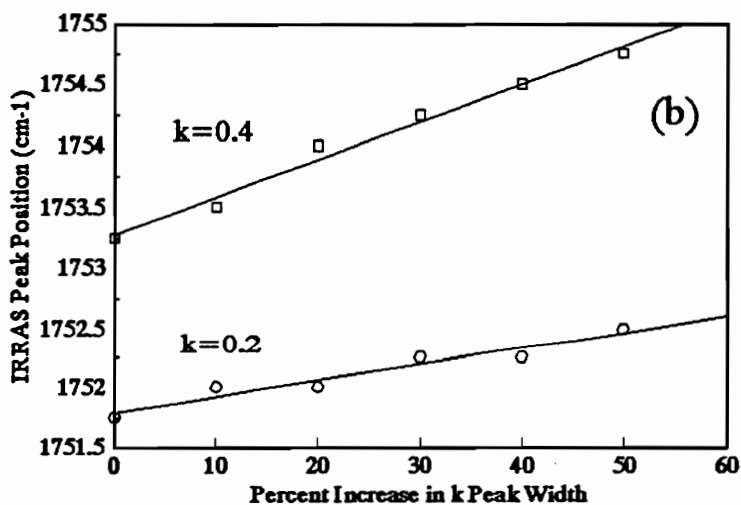
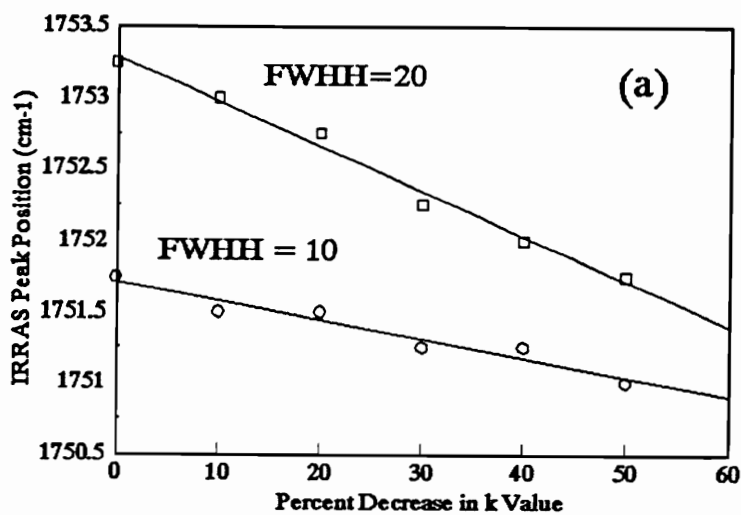


Figure 3.9 Plot of the RAS absorbance band peak frequency as a function of (a) the percent decrease in the initial k value for two peak widths, and (b) the percent increase in peak width for two initial k values.

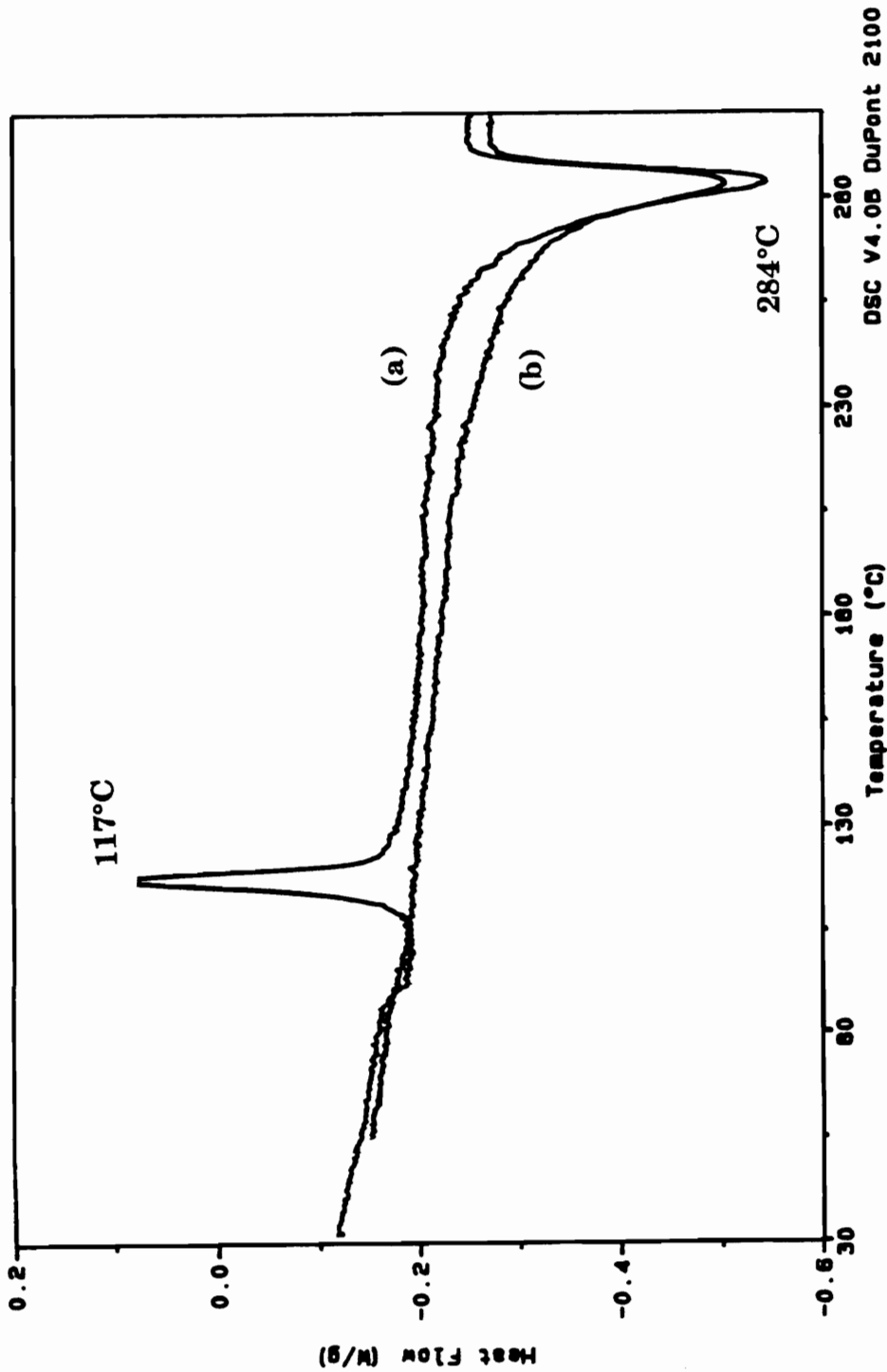


Figure 3.10 Differential scanning calorimetry trace for Ryton™ polyphenylene sulfide taken at a ramp rate of 2.5°C / minute. Plots are shown for both (a) the first run of a quenched sample, and (b) the second run for fully crystalline PPS.

3.3.3 Variable Temperature Infrared Analysis of PPS Films

Figure 3.11 shows the relative peak intensity changes for the 814-820, 1474, 1011, 1387, and 1574 cm^{-1} absorbance bands for an approximately 2.5 micron thick spin coated PPS film. The range of 814 to 820 cm^{-1} for the C-H out-of-plane bending mode indicates that this peak is composed of two components, the higher frequency band being dependent on the crystallinity of the polymer. While peak areas are sometimes used as a better measure of absorbance changes with temperature (32), the scatter in the data for quenched samples was too severe. The absorbance doublet at 1093 and 1074 cm^{-1} was not analyzed due to excessive band broadening of these closely spaced bands at elevated temperatures. Clearly, a non-linear response of peak intensity with temperature is seen, probably indicating a complex crystallization behavior from the quenched state. The process may involve crystallization to form various sized spherulites which may melt again at a higher temperatures and reform larger spherulites, giving a complicated dependence of peak intensity with temperature. However, all bands except the 1387 cm^{-1} peak show a break in slope near 145°C indicative of the onset of crystallization. Smoothing and calculation of the first derivative yields a T_{∞} value of 144°C ($\pm 5^{\circ}\text{C}$) for this sample. The temperature is higher than the value of 117°C obtained by differential scanning calorimetry, and may reflect the smaller number of nucleation sites for the thin film used. Both the 1011 cm^{-1} in plane C-H bending mode and the 1474 cm^{-1} in plane ring stretching mode show increases in intensity upon crystallization with little change in the C-H out-of-plane bending mode at 814 cm^{-1} . All peaks show a second break in the slopes in the temperature range of 270 to 280°C which represents the melting temperature (T_m). While sensitivities to the T_{∞} and T_m depend on the particular absorbance band, the clearest indication of both transitions is given by the 1574 cm^{-1} absorbance band. Figure 2.12 shows a similar analysis for the shift in peak position as a function of temperature. Again, a break in slope at 144°C indicates the onset of crystallization while the T_m is indicated at 277°C. An interesting point is that although the T_{∞} and

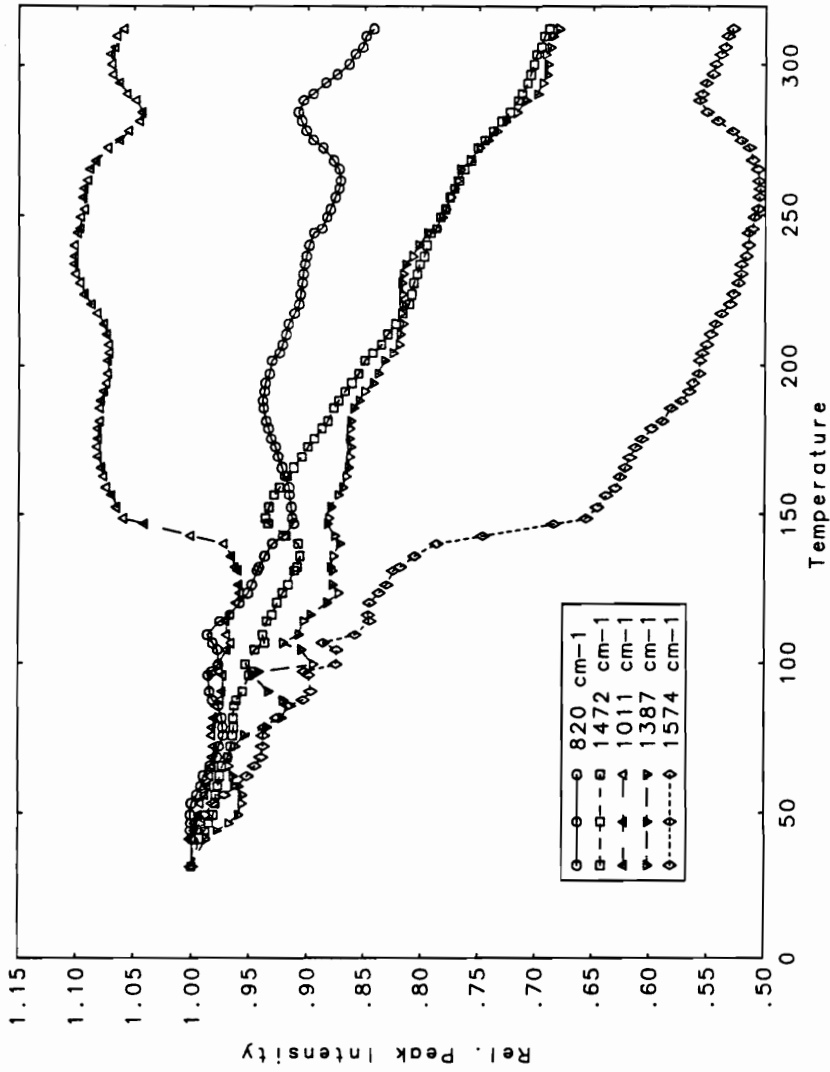


Figure 3.11 Relative peak intensity changes for the variable temperature transmission analysis of an approximately 2.5 micron quenched PPS film on a salt plate substrate. All bands have been normalized to the initial peak intensity at room temperature.

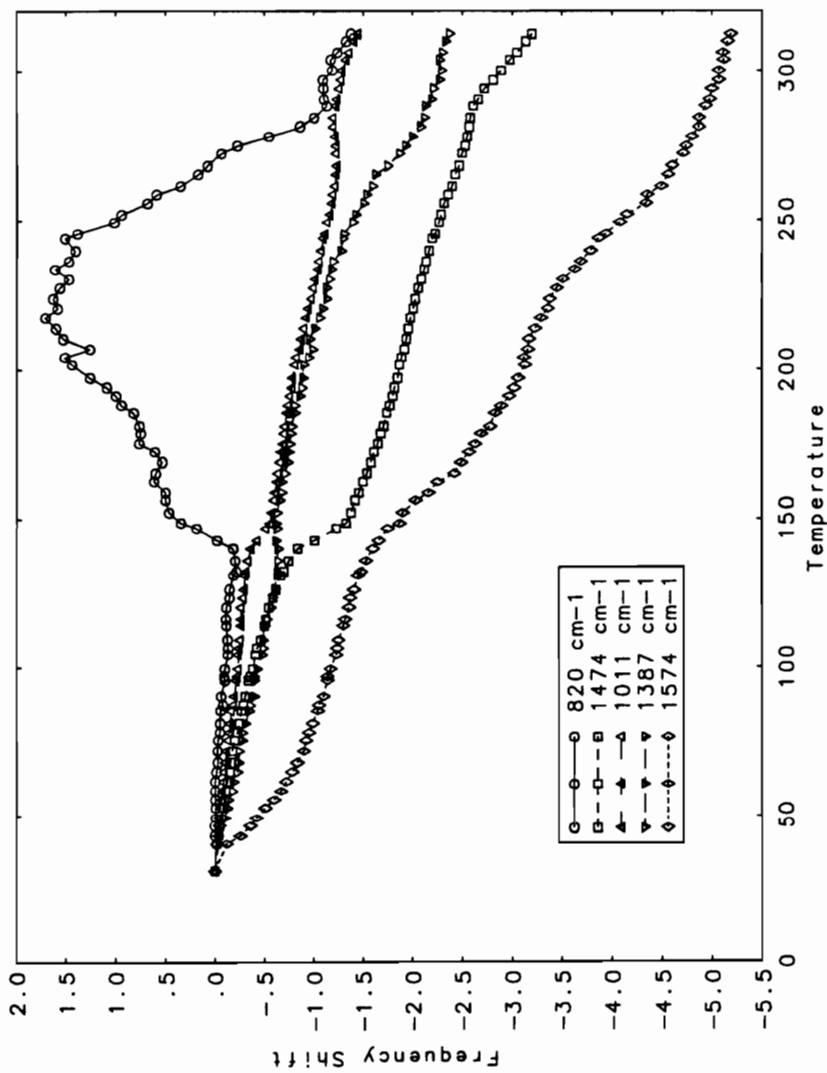


Figure 3.12 Relative peak position changes for the variable temperature transmission analysis of an approximately 2.5 micron PPS film on a salt plate substrate. All bands frequencies have been referenced to the room temperature peak frequency.

T_m are clearly visible in such plots, the frequency shifts range from only -5 to $+2$ cm^{-1} . Combined with the results from monitoring peak intensities, the T_m value of $278 \pm 5^\circ\text{C}$ agrees well with results from DSC. Again, the increase in the T_∞ peak probably reflects the thin nature of the PPS film used.

To analyze films crystallized from the melt, Figure 3.13 shows a plot of relative peak intensity versus temperature for a quenched PPS film heated at $2.5^\circ\text{C} / \text{minute}$ to 320°C and allowed to cool from the melt. A typical temperature cooling profile was shown in Fig. 3.3. As is indicated in the plot, much of the irregular shaped plot for quenched samples has been replaced with smoothly changing curvilinear plots. Again, a large change in slope at $280 \pm 5^\circ\text{C}$ indicates the T_m under the conditions used. A similar analysis for peak intensity is shown in Figure 2.14 and indicates that peak intensities do not always follow the identical trends as are found with peak areas. Again, the T_m is clearly indicated as sharp changes in slope for all peaks shown. For both the peak intensities and areas, the plot slopes are generally negative as has been observed for a number of polymer systems (22,32). One exception is the band at 1011 cm^{-1} which increases both in intensity and peak area. This is extremely unusual, and rarely seen for this type of analysis.

3.3.4 Variable Temperature Reflection Spectroscopy

3.3.4.1 Polyphenylene Sulfide Coatings

3.3.4.1.1 Chromium

Figure 3.15 shows the analysis of the peak intensity changes for a $60 - 70$ nm quenched film of PPS on chromium for the $814 - 820$, 1474 , 1011 , 1390 and 1574 cm^{-1} absorbance bands of PPS. For all peaks shown, two transitions are indicated, the lower one representing the onset of crystallization, and the higher one, the onset of the crystalline melting point. The $814 - 820$ cm^{-1} band for the C-H out-of-plane bending mode undergoes a 1.7 fold increase in intensity and this is primarily associated with the sharp 820 cm^{-1} band indicative of crystalline PPS. The 1474 and

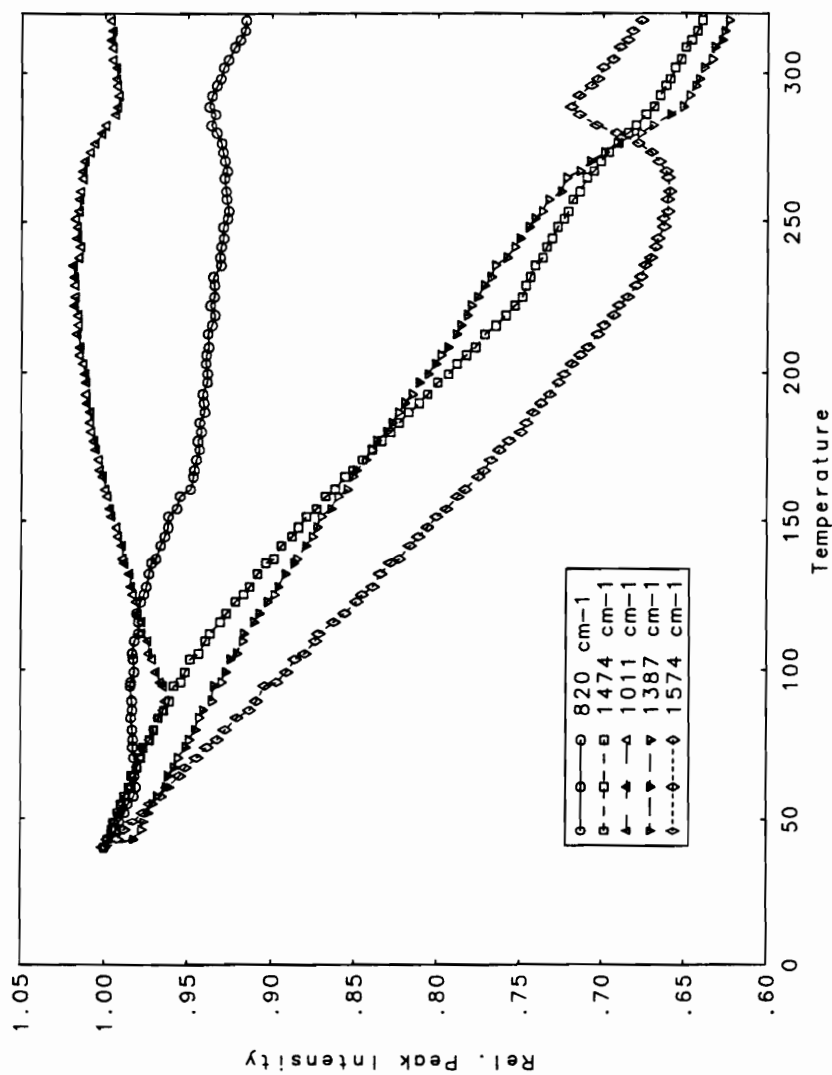


Figure 3.13 Relative peak intensity changes for the transmission analysis of an approximately 2.5 micron spin coated PPS film on a salt plate substrate. The film had been crystallized from the melt and all bands frequencies have normalized to the peak intensity at room temperature.

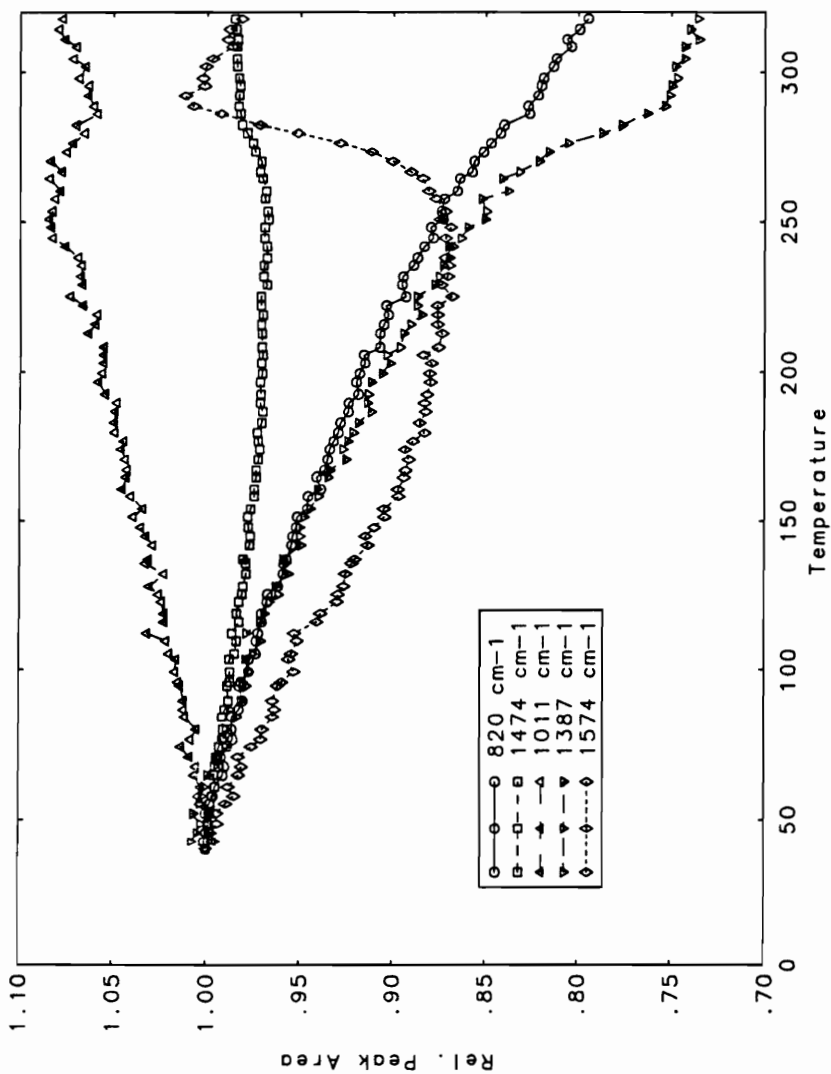


Figure 3.14 Relative peak area changes for the transmission analysis of an approximately 2.5 micron spin coated PPS film on a salt plate substrate. The film had been crystallized from the melt and all bands areas have normalized to the peak area at room temperature.

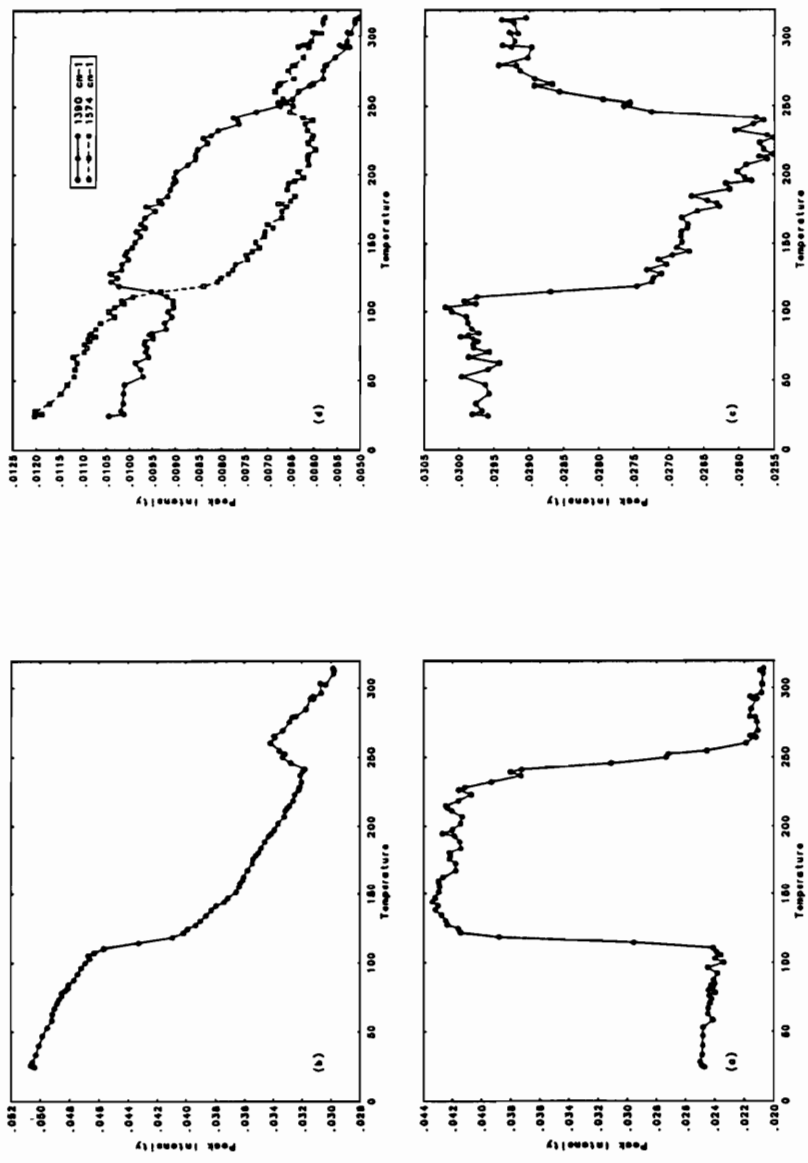


Figure 3.15 Absolute peak intensity changes for the variable temperature RAS analysis of a 60-70 nm PPS film on a chromium substrate showing plots for bands at (a) 814 - 820 cm^{-1} , (b) 1474 cm^{-1} , (c) 1011 cm^{-1} , and (d) 1390 and 1374 cm^{-1} .

1011 cm^{-1} bands undergo a 10 - 15% decrease in intensity upon crystallization in agreement with the formation of an oriented surface film as observed in previous *ex-situ* measurements (See chapter 2). The bands for the 1390 and 1574 cm^{-1} ring modes act inversely with respect to each other, the former increasing in intensity and the latter decreasing in intensity on crystallization. The cross over point of the two plots provides a convenient index to measure T_{∞} and T_m . If the plots are smoothed using a seven point Savitsky-Golay smoothing routine, and the first derivative taken, the temperature at the inflection points on crystallization or melting can be averaged to yield a T_{∞} value of 112°C and a T_m value 245°C. For a given plot, the error associated with these values is approximately $\pm 5^\circ\text{C}$ and primarily reflects the resolution in the temperature profile. By comparison, the cross over point for the 1390 and 1574 cm^{-1} peaks yields similar values of 112°C and 253°C for the T_{∞} and T_m temperatures, respectively. For comparison, Figure 3.16 shows the relative changes in peak position with temperature for the bands shown in Fig. 3.15. All bands indicate the T_{∞} temperature and to a lesser extent, the T_m temperature. The large shift in the position of the 814 cm^{-1} to 820 cm^{-1} is due to the growth and decay of the 820 cm^{-1} band arising from crystalline PPS. For comparison to transmission results, Figures 3.17 and 3.18 show the comparison of peak position with temperature for both reflection and transmission experiments. All bands show an increase in frequency in the reflection mode due to the effect of the anomalous dispersion in the refractive index as would be expected (30,39). The large changes in the reflection mode show the dramatic difference in the results depending on the mode of analysis.

Figure 3.19 shows a comparison of the relative peak intensity changes with temperature for the reflection and transmission analysis. For the 814 - 820 cm^{-1} absorbance band, the dramatic difference between the two techniques is easily seen with the band increasing very little in transmission. Other peaks are also compared and the 1474 cm^{-1} undergoes an increase in transmission, and a decrease in reflection on crystallization. A similar result is seen for the 1011 cm^{-1} absorbance band and

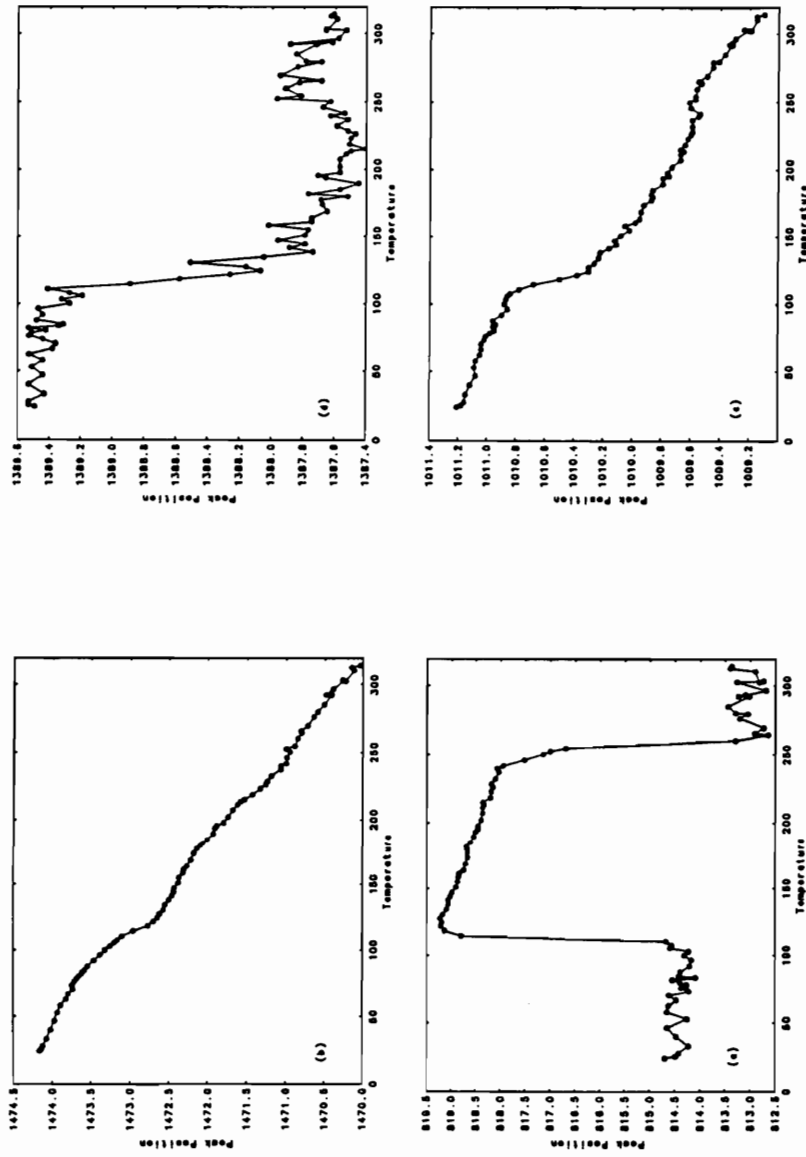


Figure 3.16 Absolute peak frequency shifts for the variable temperature RAS analysis of a 60-70 nm PPS film on a chromium substrate showing plots for bands at (a) 814 - 820 cm^{-1} , (b) 1474 cm^{-1} , (c) 1011 cm^{-1} , and (d) 1574 cm^{-1} .

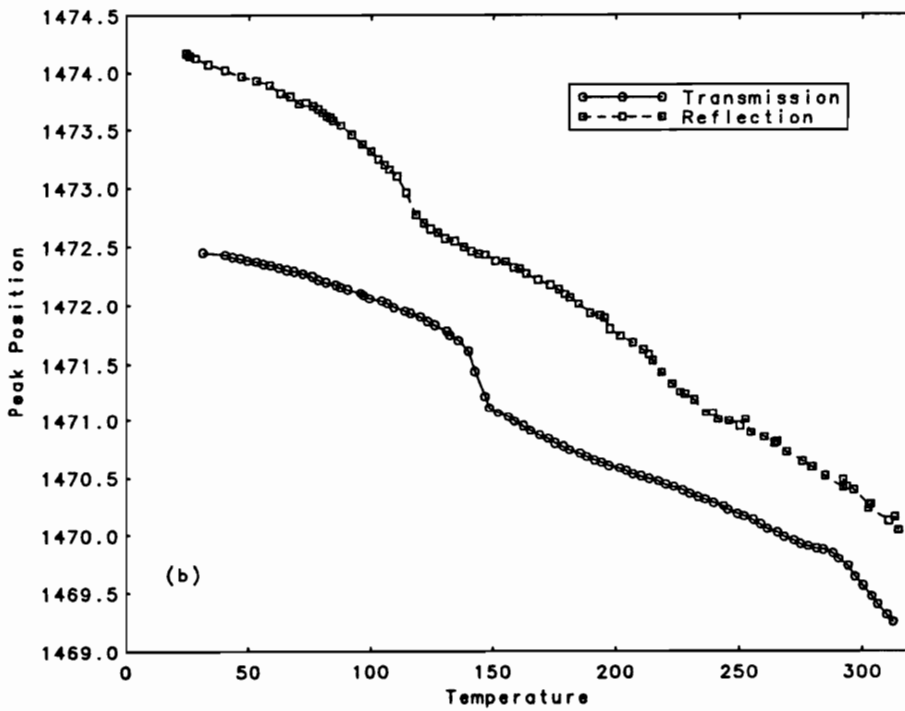
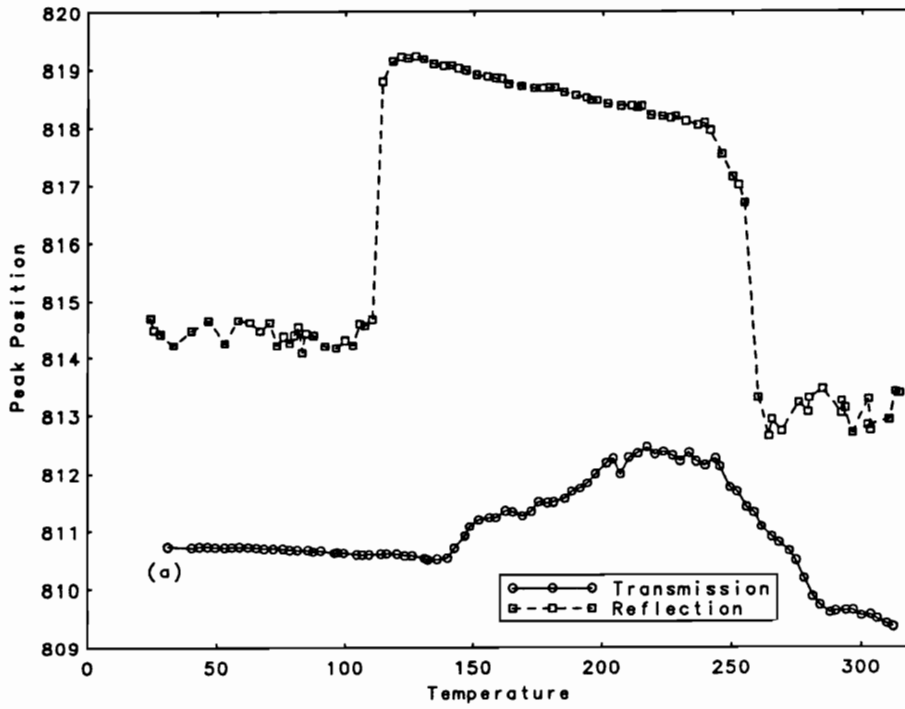


Figure 3.17 Plot of the absolute peak frequency shifts for both variable temperature transmission and RAS analysis of bands at (a) 814 - 820 cm^{-1} , and (b) 1474 cm^{-1} .

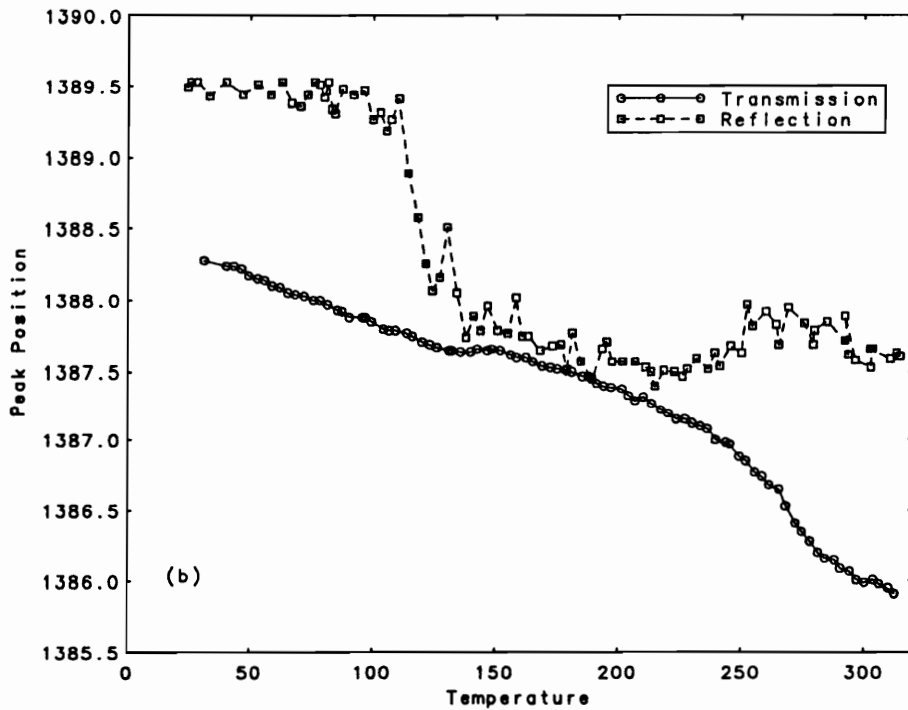
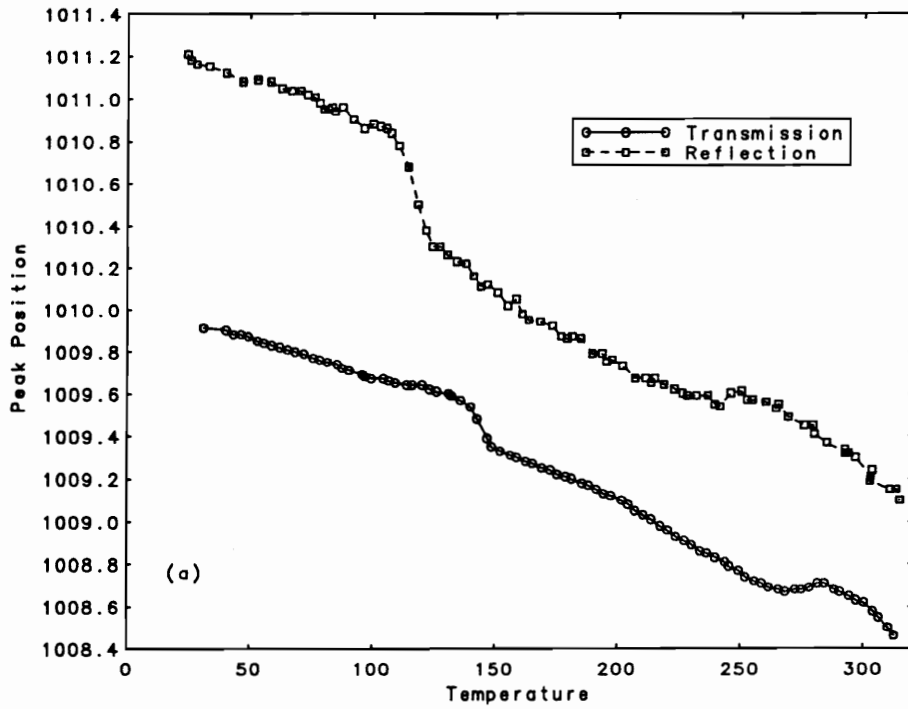


Figure 3.18 Plot of the absolute peak frequency shifts for both variable temperature transmission and RAS analysis showing plots of bands at (a) 1011 cm^{-1} , and (b) 1390 cm^{-1} .

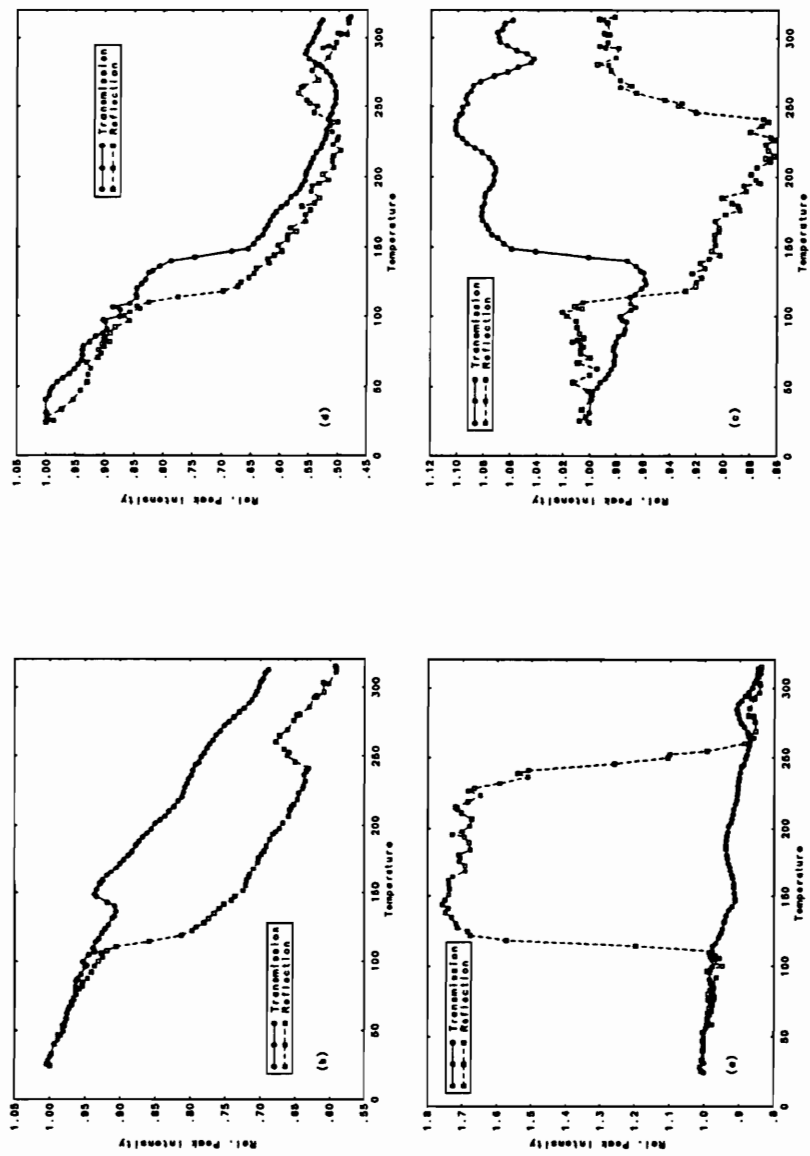


Figure 3.19 Relative peak intensity changes for both variable temperature transmission and RAS analysis. All band intensities have normalized to the peak intensity at room temperature, and plots are shown for peaks at (a) 814 - 820 cm^{-1} , (b) 1011 cm^{-1} , (c) 1474 cm^{-1} , and (d) 1574 cm^{-1} .

which again reflects orientation effects in the thin PPS coatings. The 1574 cm^{-1} bands show almost identical trends in peak intensity except that both the T_{∞} and T_m transitions are shifted to lower temperatures in reflection. An interesting point in many plots is that the relative peak intensity changes with temperature for both the reflection and transmission analysis are almost the same in the amorphous ($<T_{\infty}$) and in the melt ($>T_m$) for the 1474 , 1574 , and 814 cm^{-1} bands. This seems to indicate that the material response (i.e. thermal expansion around a given group) in these temperature regions is very similar between bulk surface films. The large difference in the crystalline regions can be attributed to specific orientation effects for thin spin coated PPS films against surfaces.

To analyze the effect of prolonged exposure of PPS coatings to elevated temperatures, Figure 3.20 shows the comparison of the first and second scans where the second represents the analysis of a fully crystalline film slowly cooled from the melt on a chromium substrate under vacuum. While there are some clear breaks in the intensity versus temperature plot for the 820 cm^{-1} band, monitoring peak intensity could lead to irregularities in the peak position or intensity due to small changes in the peak shape. Peak area is often a better measure, and Figure 3.21 shows a plot of the peak area for the $814 - 820\text{ cm}^{-1}$ band versus temperature. The data points were smoothed with a cubic spline smoothing function. Clearly, the plot shows only one transition corresponding to the melting of the crystalline PPS film. Figure 3.22 shows the same analysis for the intensity changes for the 1011 cm^{-1} band and shows a similar pattern of one transition corresponding to the melting temperature. The T_m temperature on the first run, taken as an average of all frequency, intensity, and area data yielded a value of 247°C representing an average of twelve values. The temperature for T_m found for the second run was determined to be 245°C , the same as the first scan within the error of the measurement. This shows that little polymer degradation of PPS has occurred against the chromium surface. The crystallization and melting points were obtained by smoothing the plots and determination of the

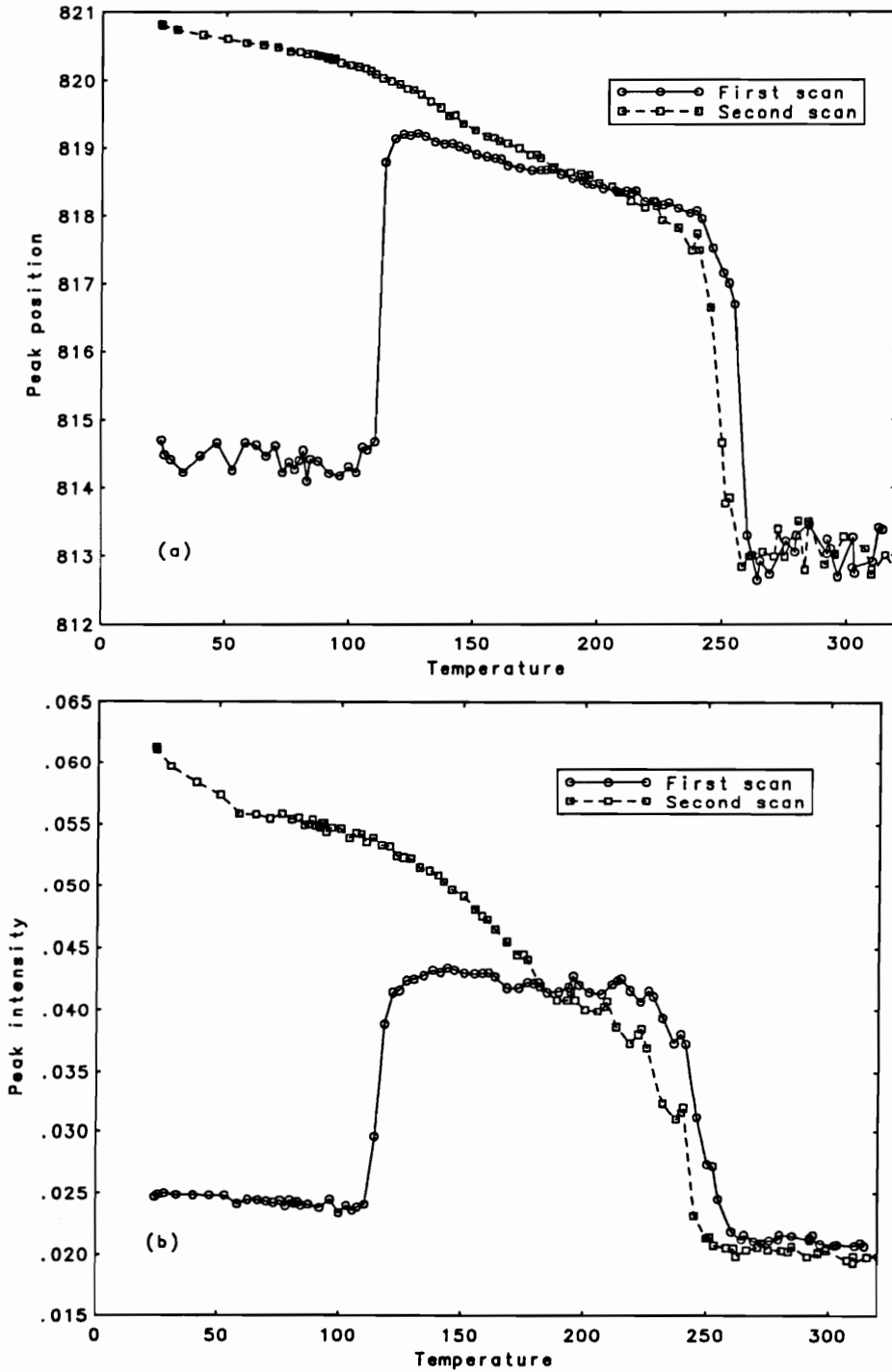


Figure 3.20 VTRAS analysis of the absolute peak intensity and position for the the 814 - 820 cm^{-1} C-H out-of-plane band for both first and second scans for a 60-70 nm PPS film on a chromium substrate.

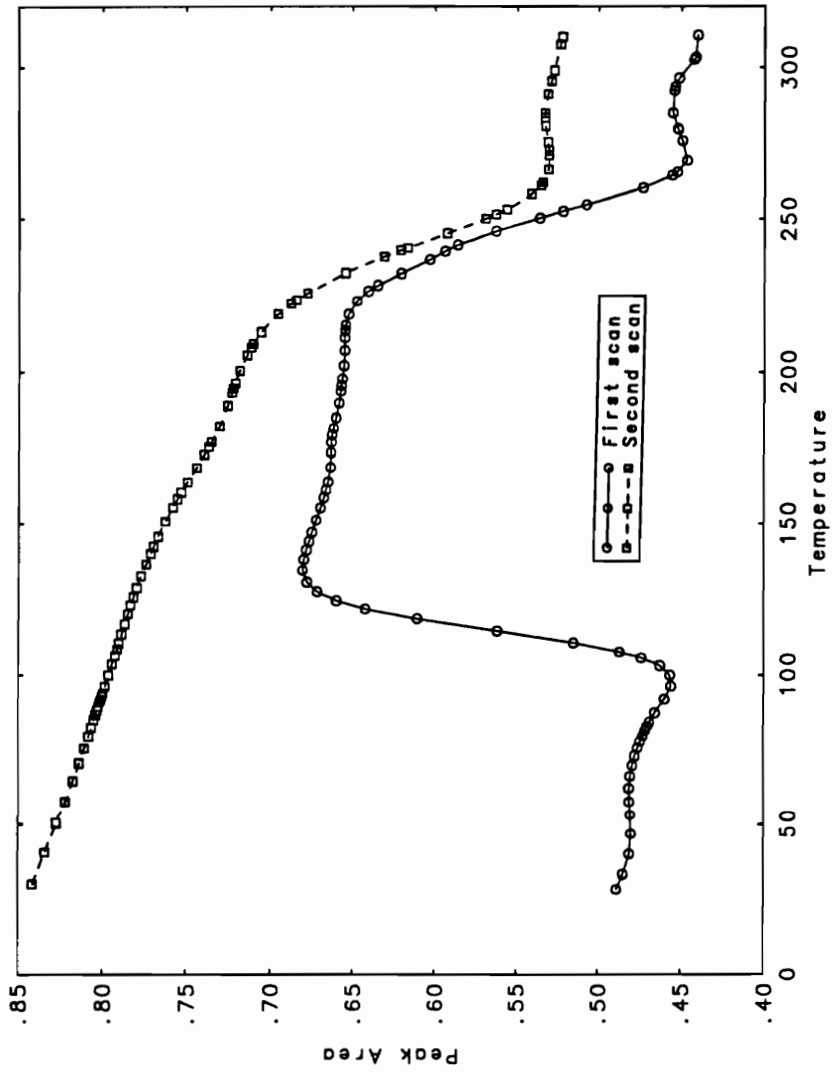


Figure 3.21 VTRAS analysis of peak area versus temperature of the 814 - 820 cm^{-1} absorbance band for a 60 - 70 nm PPS film on a chromium substrate.

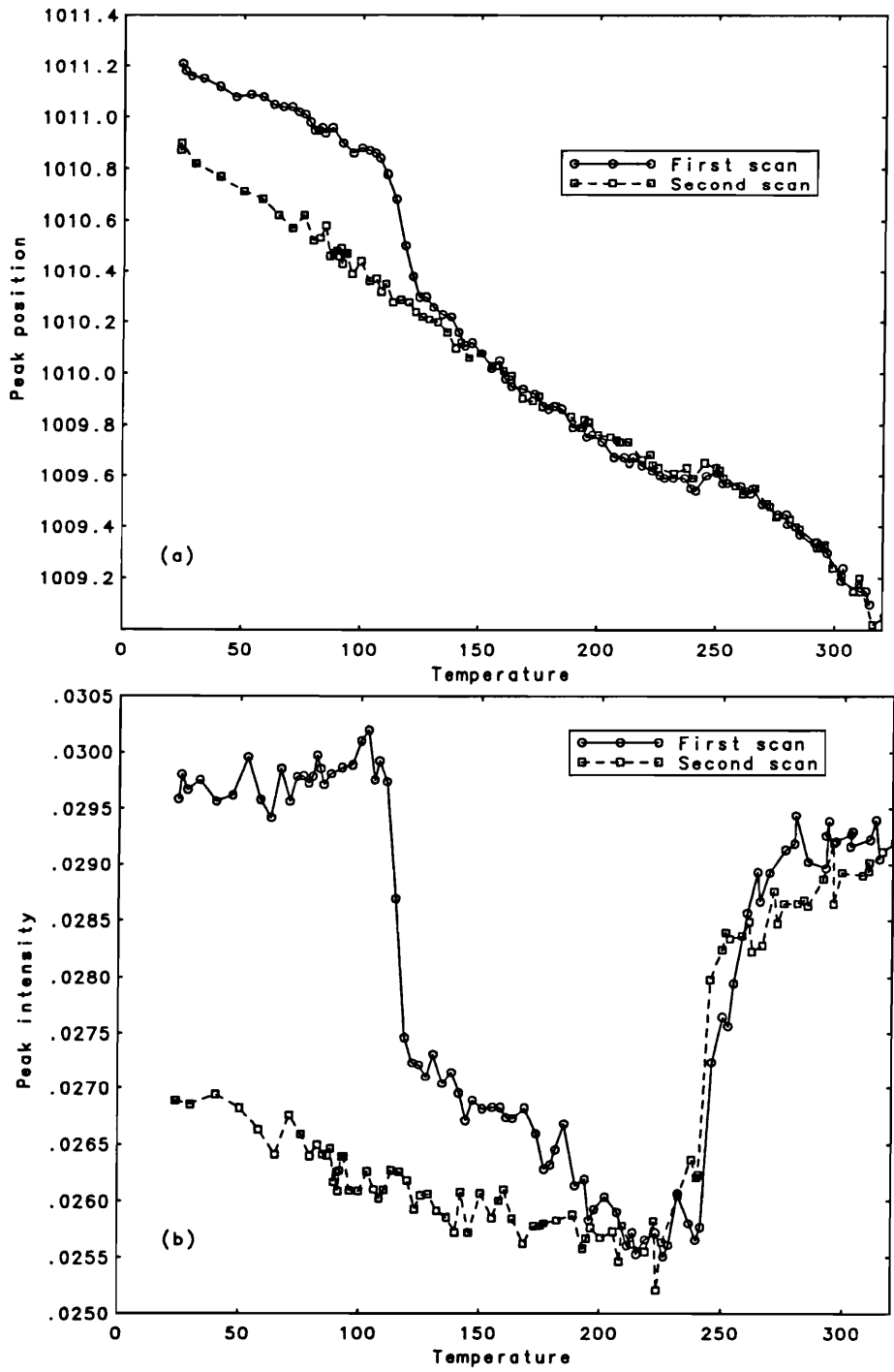


Figure 3.22 VTRAS analysis of the absolute (a) peak intensity and (b) peak position changes for the the 1011 cm^{-1} C-H in-plane band for both first and second scans.

first derivative. Figure 3.23 shows a typical derivative trace for both the first and second scans.

Another interesting observation is that the plot of peak intensity versus temperature for the 814 - 820 cm^{-1} band remains relatively flat upon crystallization from the quenched state during the first scan. This shows that volume increases for the crystalline regions due to thermal expansion are much less than were noted previously for thicker films in transmission. Hannon and Koenig showed in early work on thermal analysis of polyethylene terephthalate by infrared spectroscopy, that certain band absorbances for quenched samples showed a much smaller temperature dependence than those of annealed samples. They reasoned that if the peak changes with temperature reflected the thermal expansion of the polymer, quenching created severe molecular strains that caused a decrease in the thermal expansion coefficient. Motion would be locked in until a sufficient temperature was reached to allow large scale segmental motion. Quenching of the thin PPS films against the surface would create a strain due to the large mismatch in thermal expansion coefficients of polymer and metal. This would lock the polymer into a limited number of configurations upon crystallization. The large strain produced would therefore cause reduced thermal expansion in the crystalline regions until the T_m was reached, and would lead to a reduced change in peak intensity with temperature. After reaching the melt, however, the polymer can relax and slow cooling would allow the polymer time to adopt more favorable configurations. The almost 40 percent increase in the band intensity for the 820 cm^{-1} peak after cooling from the melt during the first run also suggests a more ordered film at the start of the second scan. These effects would be more dramatic for absorbance bands for crystalline regions, and therefore the 820 cm^{-1} band would be particularly sensitive. A plot of peak position or peak intensity versus temperature for the 820 cm^{-1} band also shows an increased slope for the second scan. Given eqn. [1], this increase, holding other factors constant could be due to a change in the thermal expansion coefficient for the polymer. However, quenched-in strain effects have also

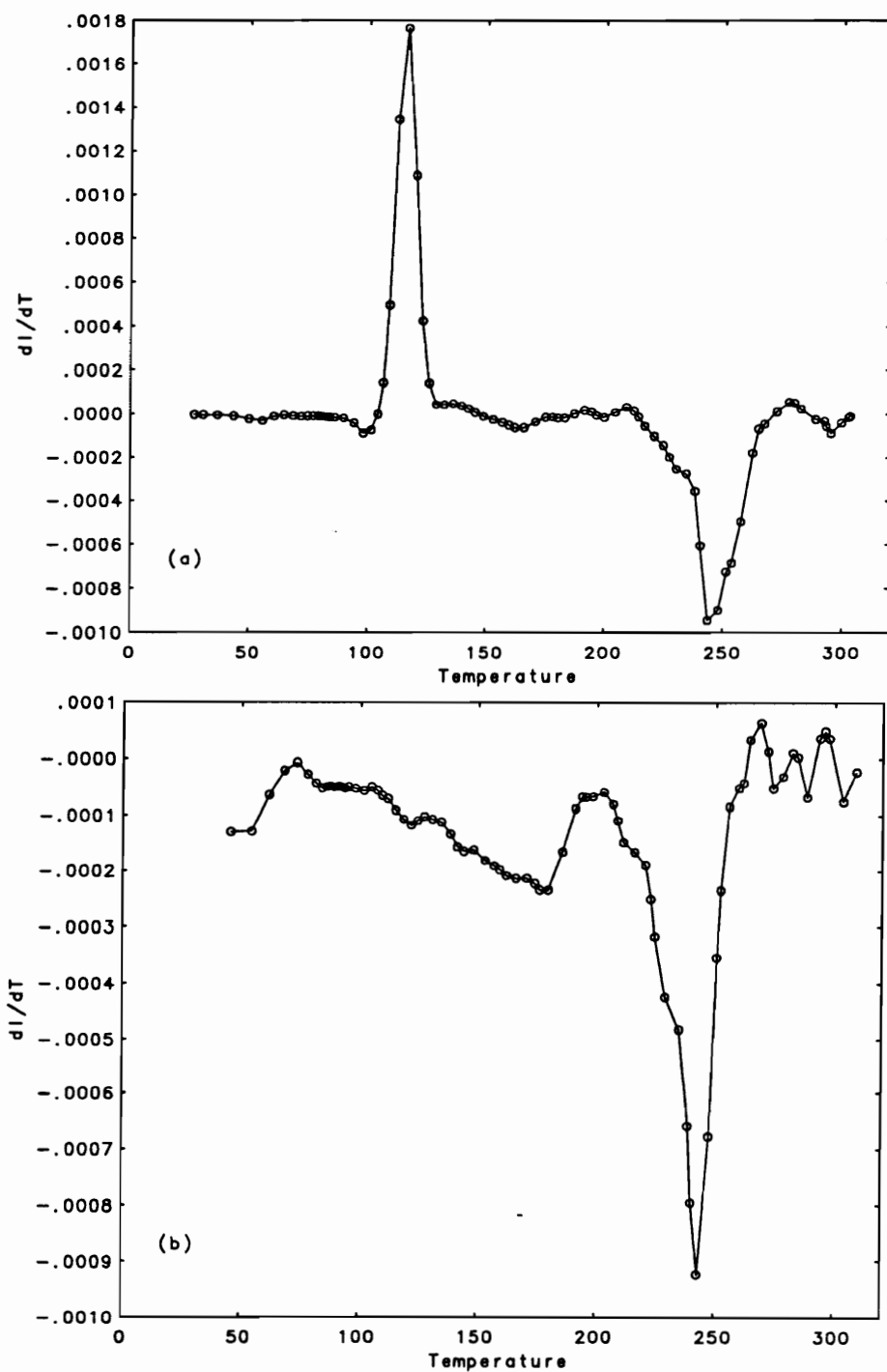


Figure 3.23 Analysis of the derivative plots for the (a) first and (b) second scans using variable temperature RAS analysis of the peak intensity versus temperature data for the 814 - 820 cm^{-1} absorbance band of PPS on a chromium substrate.

been shown to alter the change in peak frequency versus temperature for polymers (24,25).

3.3.4.1.2 Aluminum

To understand whether the reorganization of PPS thin films on surfaces is general in nature, VTRAS analysis was used to investigate thin films of PPS on aluminum/aluminum oxide surfaces. Figures 3.24 and 3.25 show the results of this analysis for both the peak intensities and peak frequencies for the same bands previously shown for chromium. Similar results are seen for an aluminum substrate, and an average T_{cc} value of 118°C and a T_m value of 254°C agree well with the values obtained for a chromium substrate. These values were calculated as an average of all intensity and peak position data. Figure 3.26 shows the results for the first and second scan for the change of peak intensity and peak position of the 814 - 820 cm^{-1} absorbance band versus temperature. Similar results to those previously observed for chromium are found, and little change in T_m is observed indicating little damage to the polymer after exposure to temperatures above the crystalline melting point under vacuum.

3.3.4.1.3 Copper

Figure 3.27 shows the infrared spectrum for a thin PPS film (60-70nm) on a vapor deposited copper substrate that had been previously oxidized at 150°C for two minutes to produce a thin oxide layer. The appearance of the absorbance band near 655 cm^{-1} clearly indicates the presence of the oxide as cuprous oxide (Cu_2O) and not cupric oxide (CuO) which would show an absorbance band near 570 cm^{-1} (40,41). Results from XPS analysis of a similarly prepared surface before coating are shown in Figure 3.28 and show a prominent oxygen 1s photopeak at 530.5 eV due to the presence of cuprous oxide. The Cu 2p_{3/2} photopeak is located at 932.7 eV and the x-ray induced Auger photopeak (LVV) at 337.2 eV together indicate a Cu^+ oxidation state. Analysis

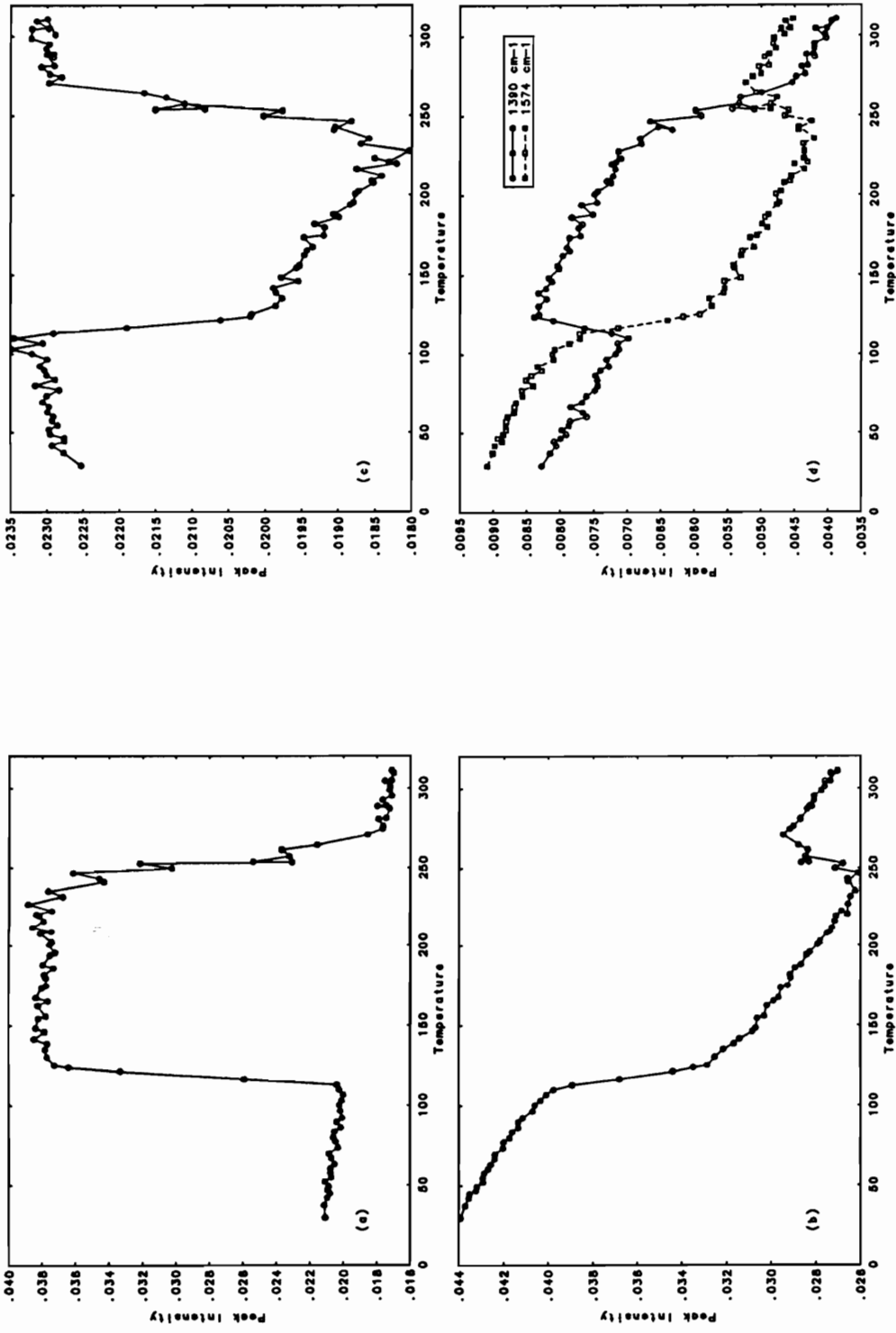


Figure 3.24 VTRAS analysis of the absolute peak intensity changes for a 60-70 nm PPS film on an oxidized aluminum substrate showing plots for bands at (a) 814 - 820 cm^{-1} , (b) 1474 cm^{-1} , (c) 1011 cm^{-1} , and (d) 1390 and 1574 cm^{-1} .

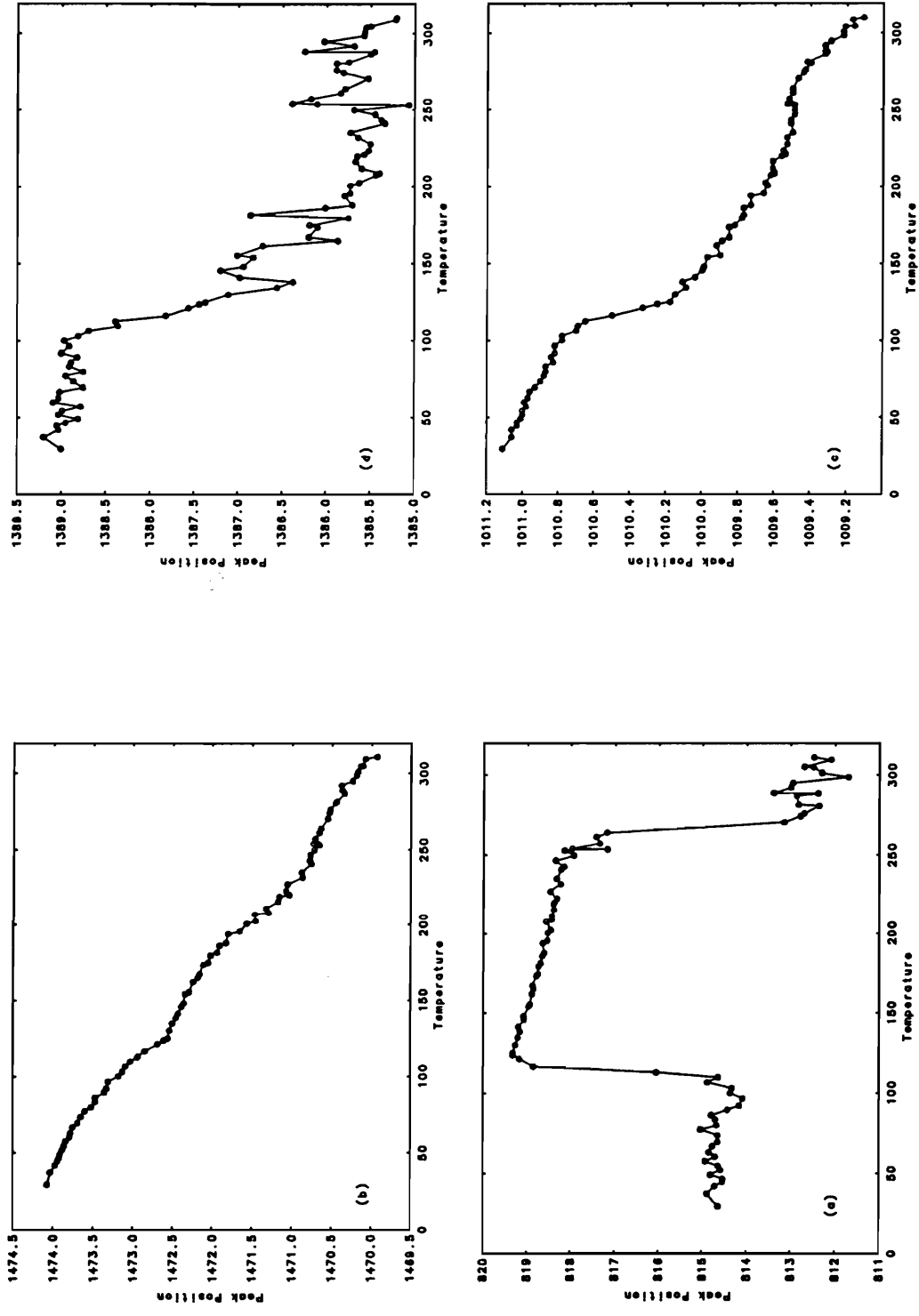


Figure 3.25 VTRAS analysis of the absolute peak frequency shifts for a 60-70 nm PPS film on an oxidized aluminum substrate showing plots for bands at (a) 814 - 820 cm^{-1} , (b) 1474 cm^{-1} , (c) 1011 cm^{-1} , and (d) 1574 cm^{-1} .

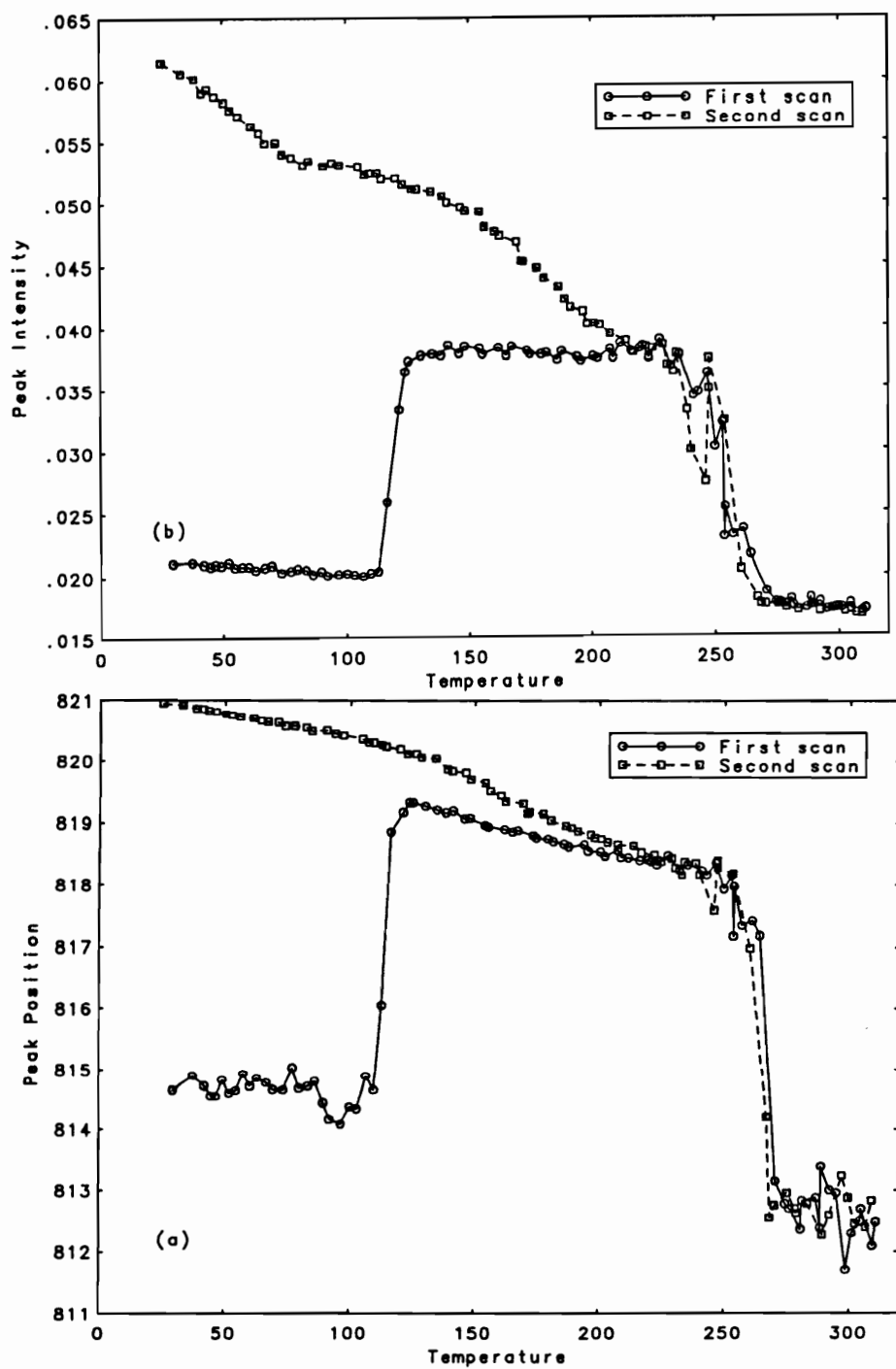


Figure 3.26 VTRAS analysis of the absolute peak intensity and position for the 814 - 820 cm^{-1} C-H out-of-plane band for both the first and second scans of a 60-70 nm PPS film on oxidized aluminum.

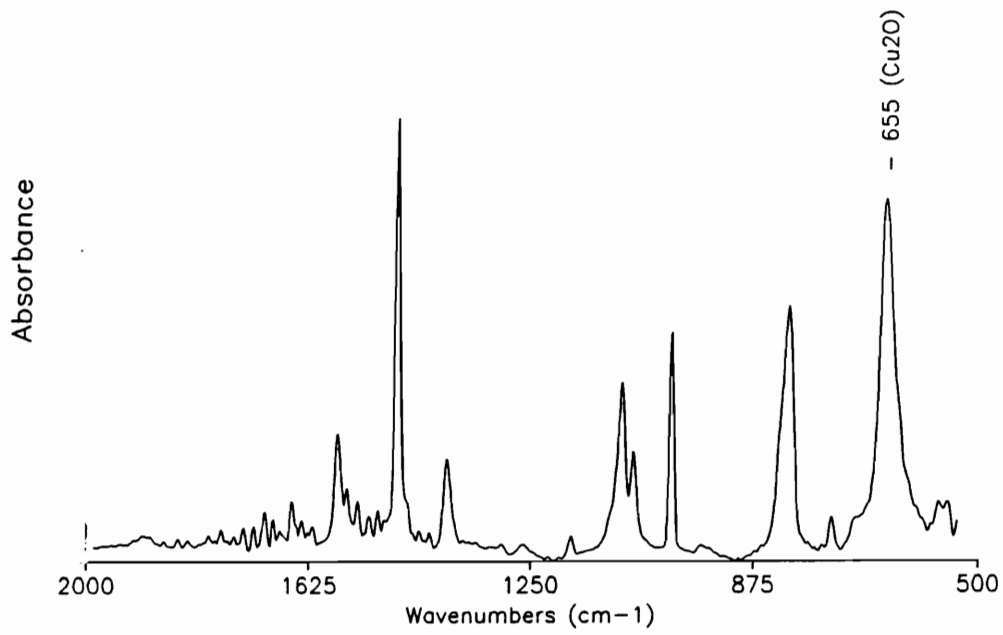


Figure 3.27 RAS spectrum of a 60-70 nm PPS film on a pre-oxidized vapor deposited copper substrate.

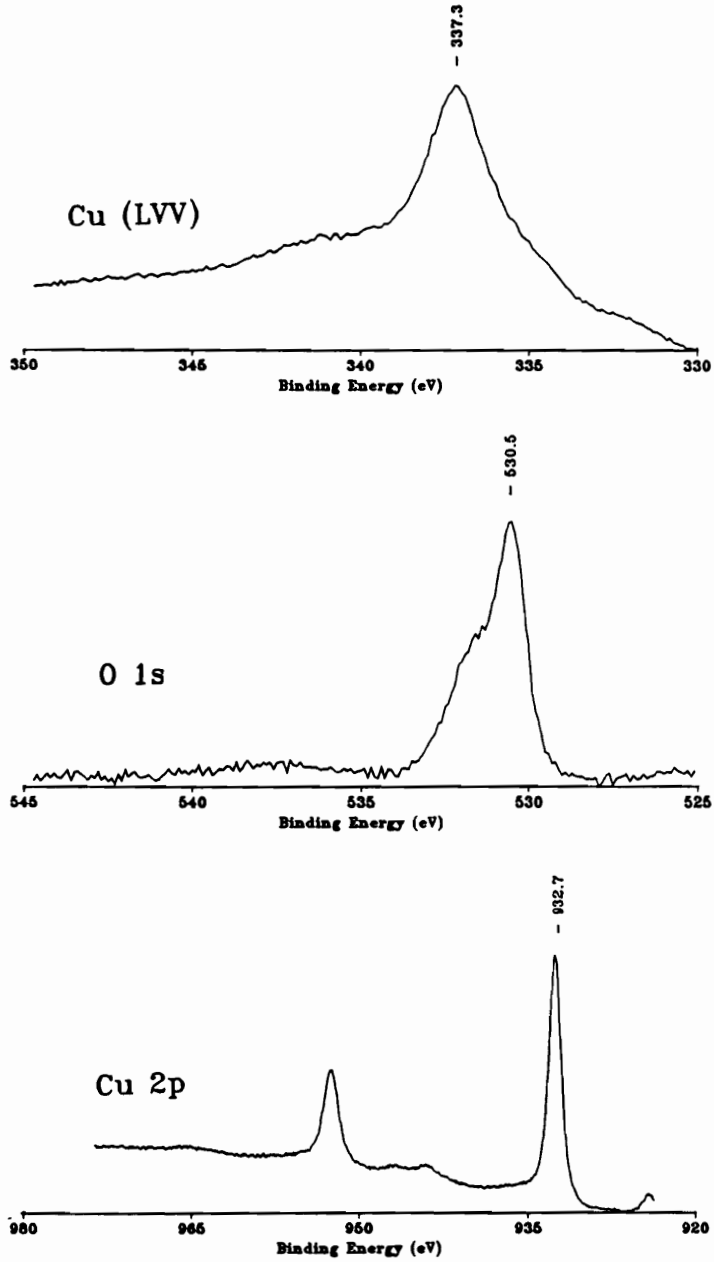


Figure 3.28 XPS analysis of a preoxidized vapor deposited copper substrate.

of these two photopeaks is commonly used to identify the oxidation state of copper (42,43). Also, the absence of significant 'shakeup' features in the Cu 2p spectrum associated with the Cu²⁺ state indicate that little cupric oxide is present. Figure 3.29 shows the variable temperature RAS analysis for the 814 - 820 cm⁻¹ absorbance band for both the first and second scans of peak intensity and position. The plot for the first scan looks very similar to those seen previously for both chromium and aluminum, indicating that the crystallization process from the quenched state is also similar for this metal. The second scan, however, clearly shows a very different behavior than that found for the previous two metals. No evidence for crystallization is found as both the peak position and intensity for the 814 - 820 cm⁻¹ band are very similar to those values for amorphous PPS. Analysis of the other absorbance bands also shows no evidence for recrystallization from the melt for PPS films coated on oxidized vapor deposited copper. To further understand the dynamic chemistry occurring in the interphase region with temperature, Figure 3.30 shows the analysis for the peak area of the copper oxide band near 650 cm⁻¹ for both the first and second scans. This plot shows a slowly decreasing function of peak area with temperature until approximately 280°C, where a sharp loss of oxide is observed. The results for the second run show little evidence for oxide and indicate that the original thin copper oxide layer has been completely lost at temperatures between 275 - 300°C. Since the samples were initially heated to 325 - 350°C and quenched in liquid nitrogen to form amorphous film samples, one might expect that the time and temperature of initial heating for PPS films on copper may play a critical role in the results. Figure 3.31 shows the results of a RAS thermal scan for a sample quenched from slightly higher temperatures of between 350 - 375°C. Clearly, little crystallization is observed, indicating that the loss in the crystallizability can occur at elevated temperatures after only short exposure times of PPS to copper under nitrogen environments as well. To understand the chemical changes in PPS films exposed to copper, Figure 3.32 shows the difference RAS spectrum for samples taken after the first and second scans.

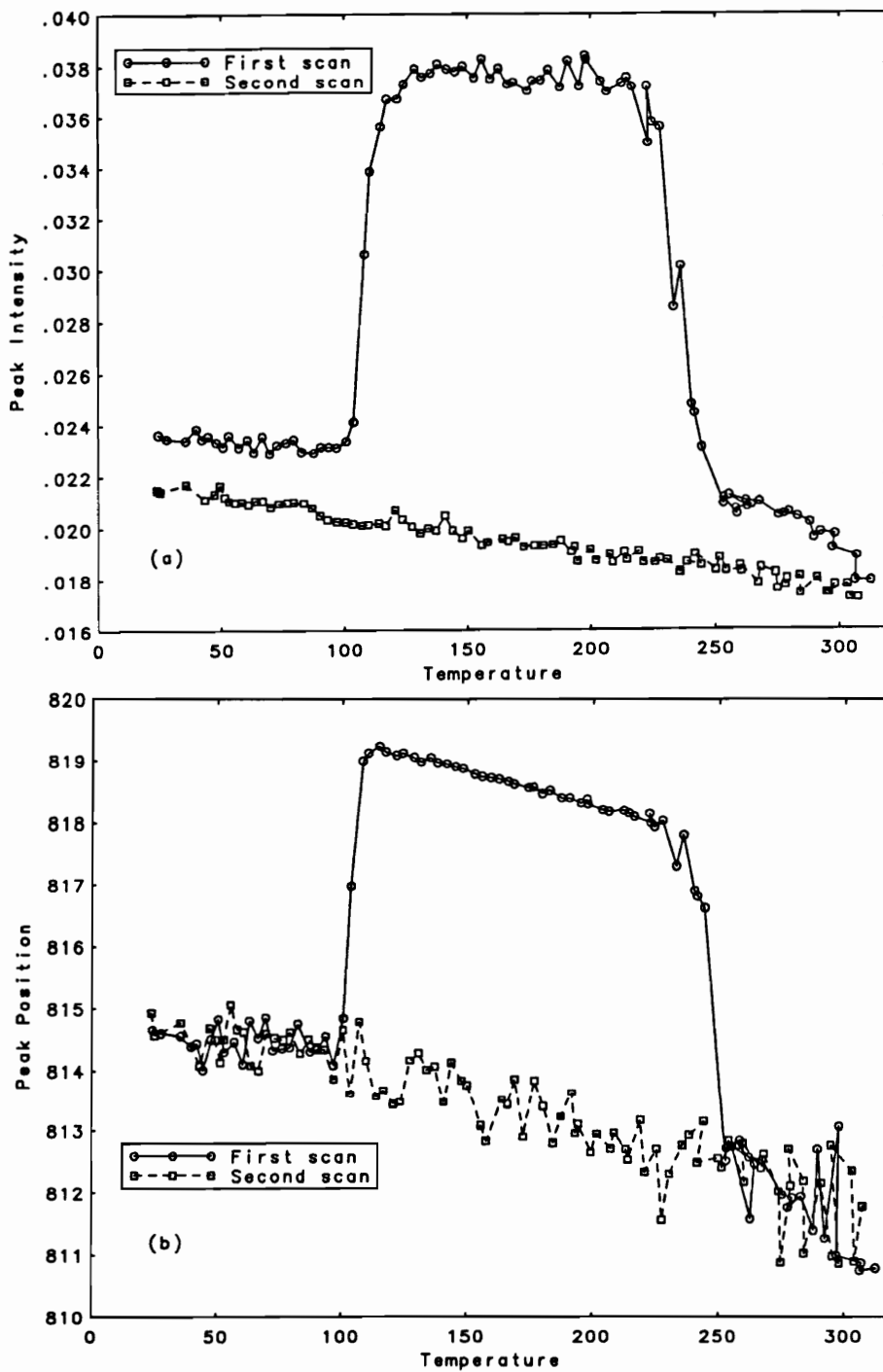


Figure 3.29 VTRAS analysis of the absolute (a) peak intensity and (b) peak position of the 814 - 820 cm^{-1} absorbance band for both first and second scans in the analysis of a 60-70 nm PPS film on copper.

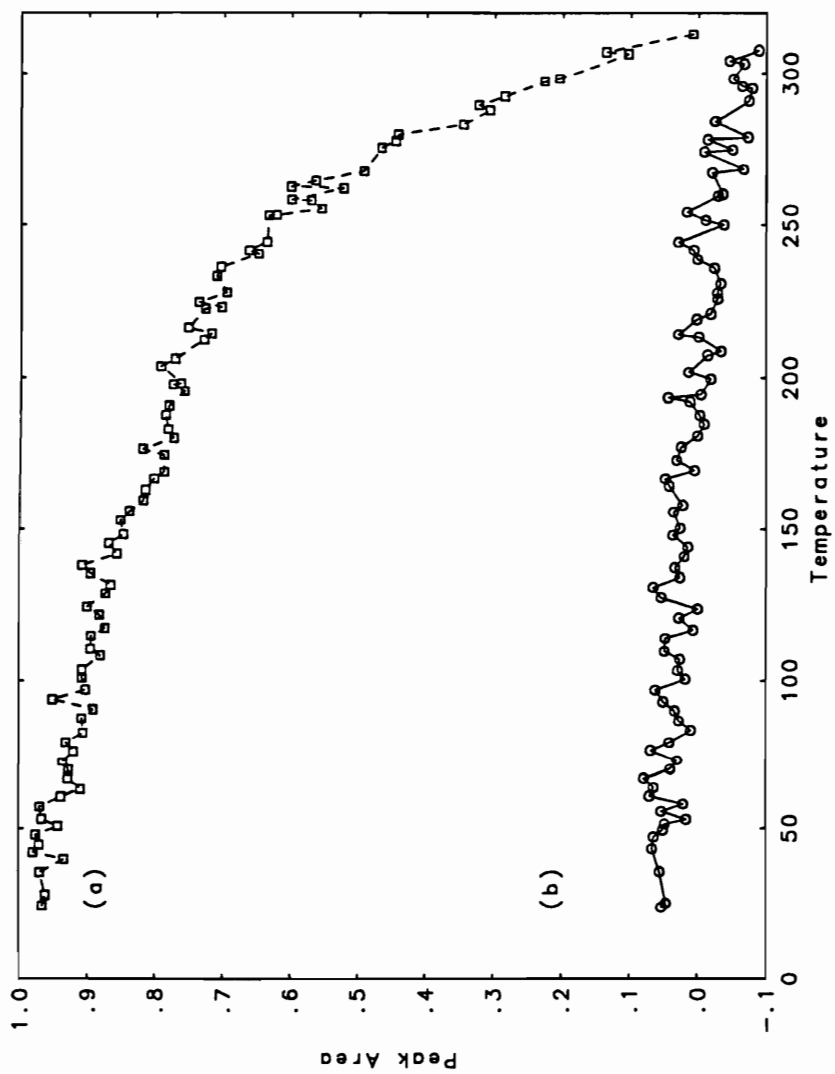


Figure 3.30 VTRAS analysis of the absolute peak area of the 650 cm^{-1} absorbance band for both the first and second scans in the analysis of a 60-70 nm film on copper.

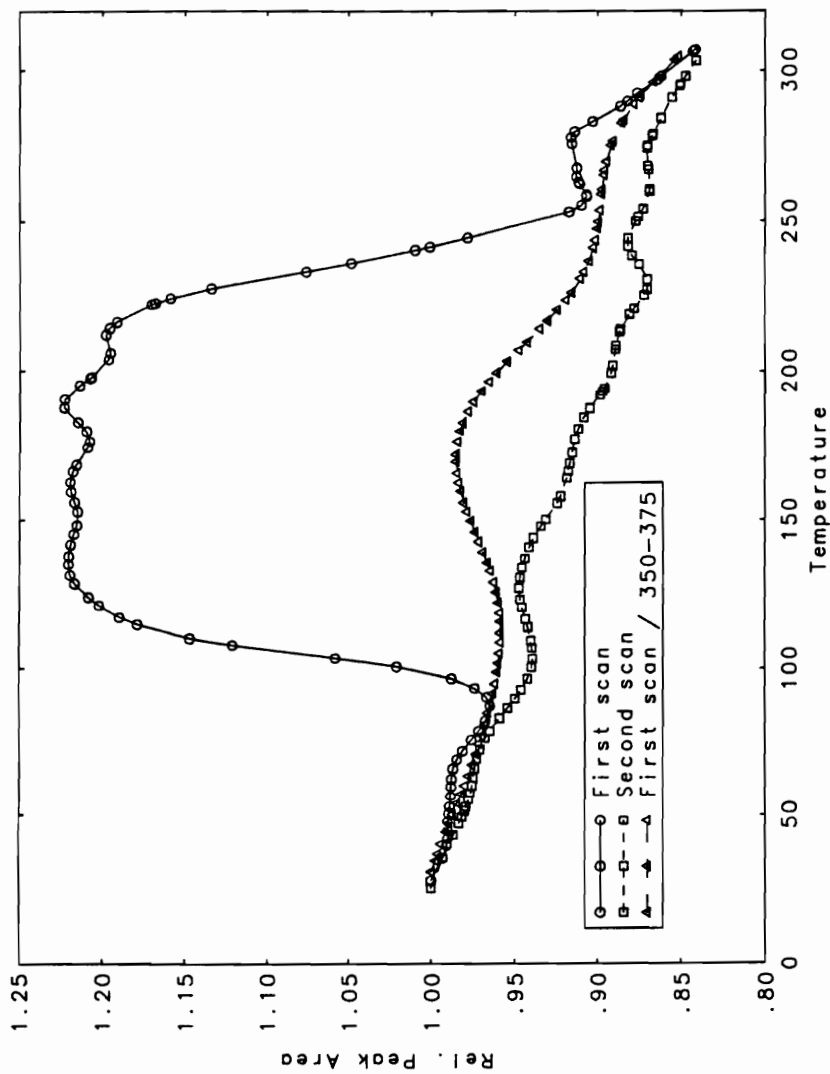


Figure 3.31 VTRAS analysis of the relative peak area changes for the 814 - 820 cm^{-1} absorbance band of a 60-70 nm PPS film on a copper substrate showing plots for both the first and second runs for films quenched from 320 - 340°C, and for a sample quenched after heating to 350 - 370°C.

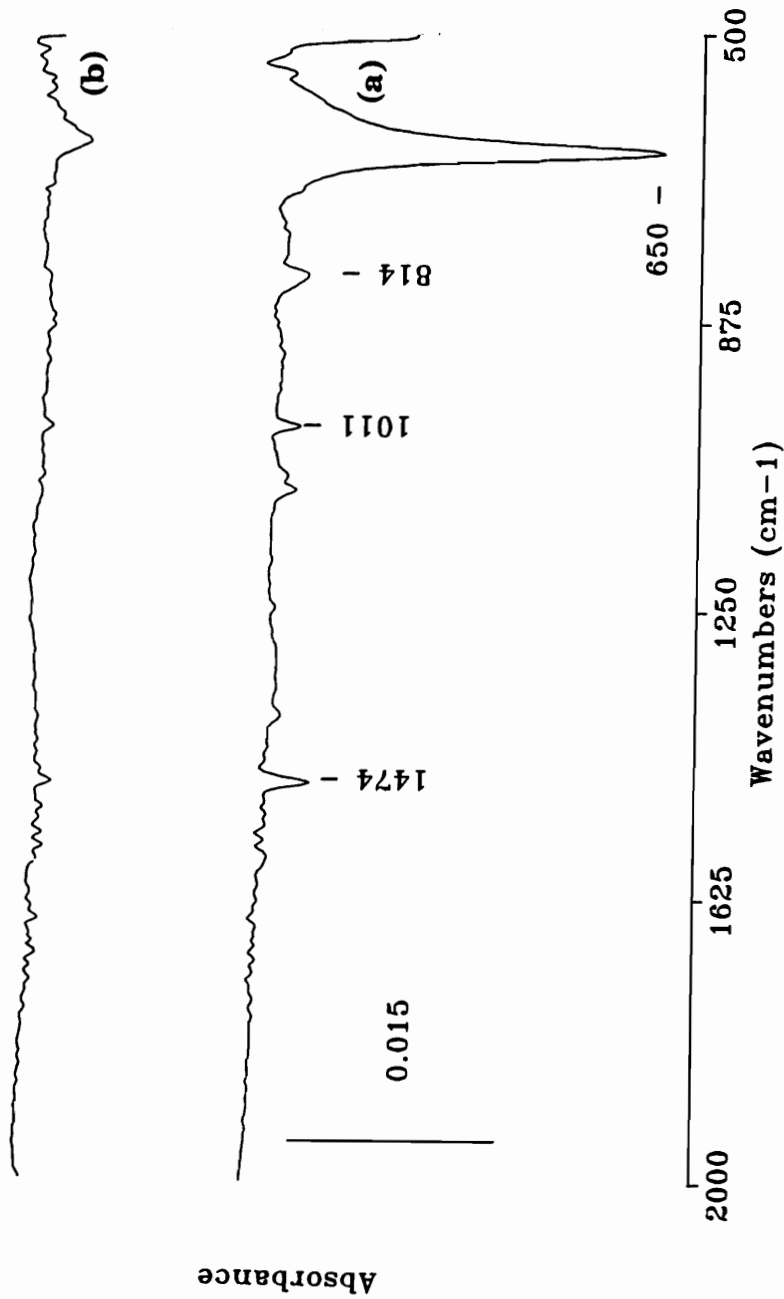
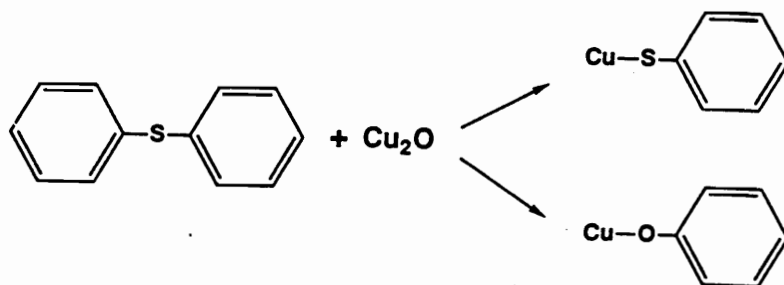


Figure 3.32 RAS difference spectrum for the analysis of 60 - 70 nm PPS films on copper. Shown are spectra for (a) the difference between the spectrum after the first scan and the initial spectrum, and (b) the difference between the spectrum after the second scan and the spectrum after the first scan.

The spectrum after the first scan is compared to the original spectrum, while the spectrum after the second scan is compared to that after the first. While some general decrease in all absorbance peak intensities is observed, no new absorbance bands are detected, indicating no new IR active functional groups are formed after exposure to copper. Thermal crosslinking would show new absorbance bands near 860 and 610 - 640 cm^{-1} due to tri- and tetra- substituted ring structures, and these are not observed. The reduction of cuprous oxide may be expected to result in polymer oxidation, although reduction could occur with loss of oxygen. No clear evidence of oxidized carbon or sulfur species is evident from the spectrum. It is possible, that volatile oxidation products including oxygen or oxidized forms of sulfur or carbon could be lost due to the vacuum conditions used in the analysis. Also, some reaction products including disulfides or copper sulfides may not show distinctive absorbance bands in the mid-infrared region. Clearly, however, the exposure of PPS coatings on copper to elevated temperatures under vacuum conditions has resulted in the chemical changes resulting in the loss of crystallizability.

The general loss of small amounts of material with loss of crystallizability, and the lack of evidence for thermal crosslinking suggests some type of chain scission mechanism of degradation of PPS against copper. While changes in molecular weight might be detected as an increase in the number of end group functionalities, the sensitivity of crystallization against a surface to this parameter is not known, and end group concentrations may be below detection limits. The reaction of diphenyl sulfide with copper oxide under high vacuum conditions has been documented (48), and the following reactions postulated:



While species A was detected, the phenoxide was not, and it was postulated that phenol was formed by the combination of this species with surface hydrogen (48). In this analysis, either group should give rise to unique absorbance bands, and no new bands were observed in the present work. It is possible that at elevated temperatures used here, such species decompose rapidly to form cuprous oxide, cuprous sulfide, diphenyl ether, and diphenyl sulfide. Such a mechanism would result in the loss of oxide, and also result in chain scission.

A second possibility would be that the copper metal, after oxide reduction, catalyzes the disproportionation reactions known to occur at higher temperatures for PPS under inert atmosphere conditions (49). Instead of chain extension, it may be possible that copper sulfide is formed by reaction during intermediate steps thus leading to polymer chain fragmentation.

3.3.4.1.4 Copper Oxide (Cu₂O)

To investigate the interaction of PPS with pure copper oxide in the absence of any copper underlayer, copper oxide was prepared by sputtering copper onto an acid cleaned ferrotype substrate followed by thermal annealing in air to provide a pure copper(I) oxide surface. XPS analysis of this substrate showed spectra similar to those recorded for oxidized copper metal with a Cu 2p_{3/2} photopeak at 932.9 eV, an Auger (LVV) photopeak at 337.1 eV and the major O 1s photopeak centered at 530.7 eV. A small shake-up feature was observed in the Cu 2p spectrum, however, probably indicating a very thin CuO layer. Ellipsometry indicated that the film was approximately 20 - 30 nm thick based on published values of the optical constants of cuprous oxide (47), and the infrared spectrum showed a typical peak absorbance for the Cu₂O band near 650 cm⁻¹. The RAS thermal scan for the peak intensity and position is shown in Figure 3.33 for both the first and second scans. The first scan shows a similar analysis to that obtained for chromium, aluminum and copper

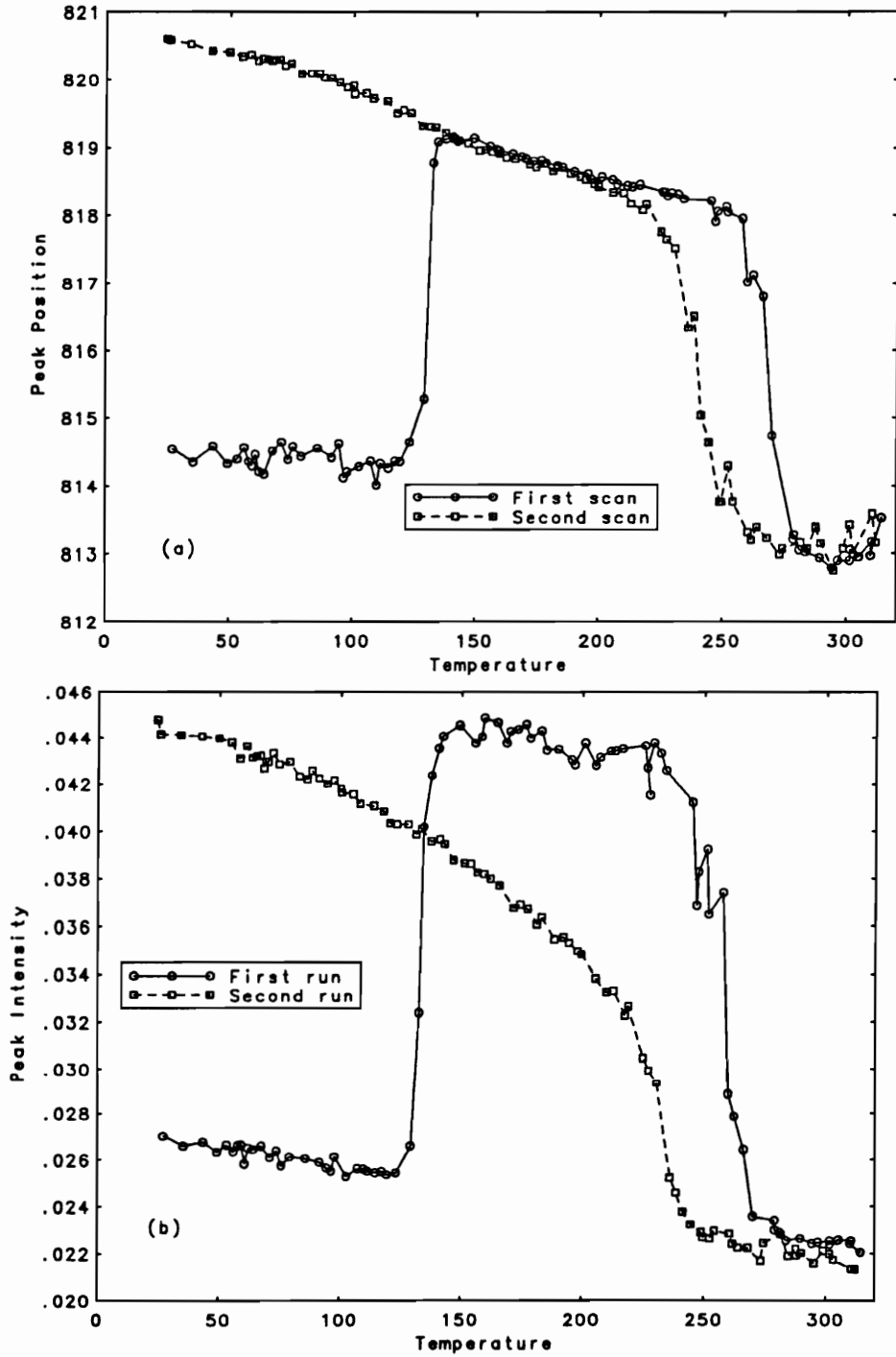


Figure 3.33 VTRAS analysis of the absolute (a) peak intensity and (b) peak position of the 814 - 820 cm^{-1} absorbance band for both first and second scans in the analysis of 60 - 70 nm PPS films on copper oxide.

although the crystallization temperature is slightly higher at 130 °C indicating the possibility a slight decreased ability for PPS to nucleate on this surface. The second scan, however, shows an interesting and significant result in that while the polymer can crystallize to some degree after cooling from the first scan, the absolute intensity value for the 820 cm^{-1} peak at the start of the second run is much less than that observed for both chromium and pre-oxidized vapor deposited copper. Also the melting temperature is decreased to approximately 230°C. This seems to indicate that while copper (I) oxide may damage the surface PPS film, it does not completely inhibit crystallization after the first scan as was the case with a thin layer of copper(I) oxide on copper metal. Figure 3.34 shows the infrared spectra of the PPS film before analysis and after the first and second scans. Some crystallization of the film is evident by the presence of the 820 cm^{-1} band after the first scan; however, crystallization is not observed after the second scan indicating that the degradation process may occur here also but at a slower rate than that found for a thin oxide layer on copper. Figure 3.35 shows the difference spectrum between spectra taken after the first run and the original spectrum. A small loss of polymer is indicated with some loss of oxide. Figure 3.36 shows the analysis of the peak area for the copper oxide band area for both the first and second scans and only a slight decrease in the peak area is observed indicating that this process is less important in the absence of an underlying metal layer. This may also indicate for the copper oxide (I) / copper system, that once the oxide is lost, accelerated degradation of the polymer may occur via the catalytic effect of copper metal.

The reduction of copper (I) oxide is not unique to PPS coated vapor deposited copper surfaces held under vacuum. Figure 3.37 shows the XPS analysis of the Cu 2p_{3/2} and Auger (LVV) photopeaks for methanol cleaned copper foil surfaces exposed to elevated temperatures under a flow of argon. The initial surface shows possible mixed oxides, and the presence of Cu²⁺ copper species is clearly indicated by the appearance of 'shake-up' satellites. At 220°C, the reduction of Cu²⁺ to Cu¹⁺ is evident and at 320°C,

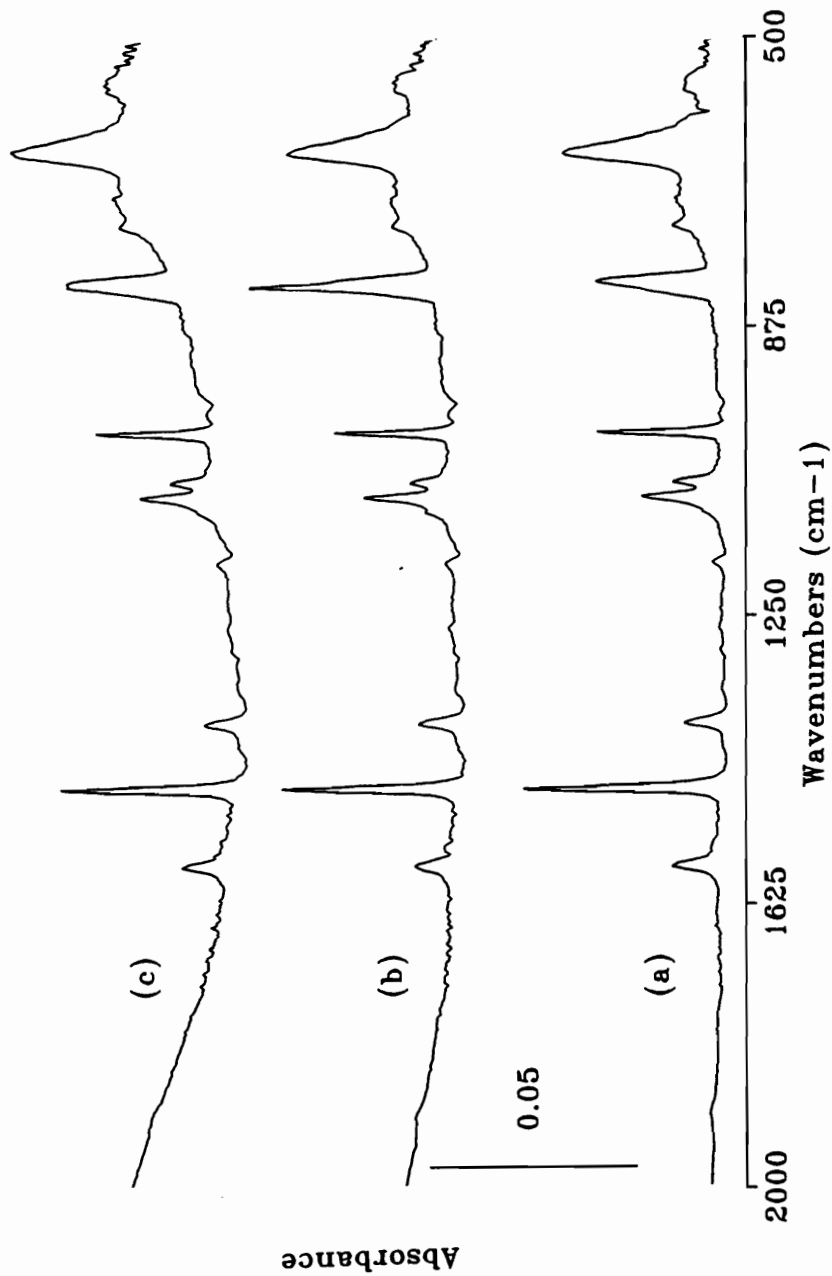


Figure 3.34 RAS spectrum for the analysis of 60 - 70 nm PPS films on copper oxide shown for (a) the original spectrum, (b) the spectrum taken after the first scan, and (c) the spectrum taken after the second scan.

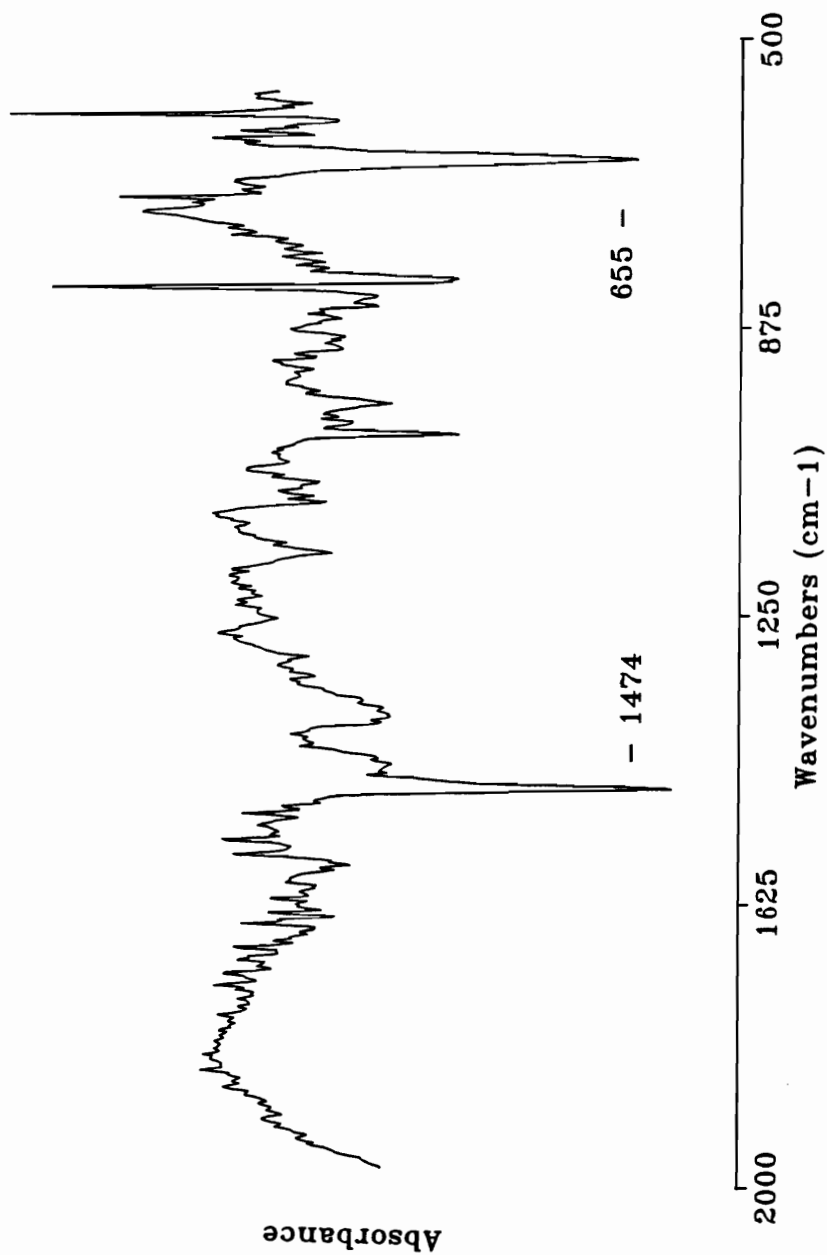


Figure 3.35 RAS difference spectrum for the analysis of 60 - 70 nm PPS films on copper oxide. Shown is the difference spectrum between the spectrum after the first run and the initial spectrum.

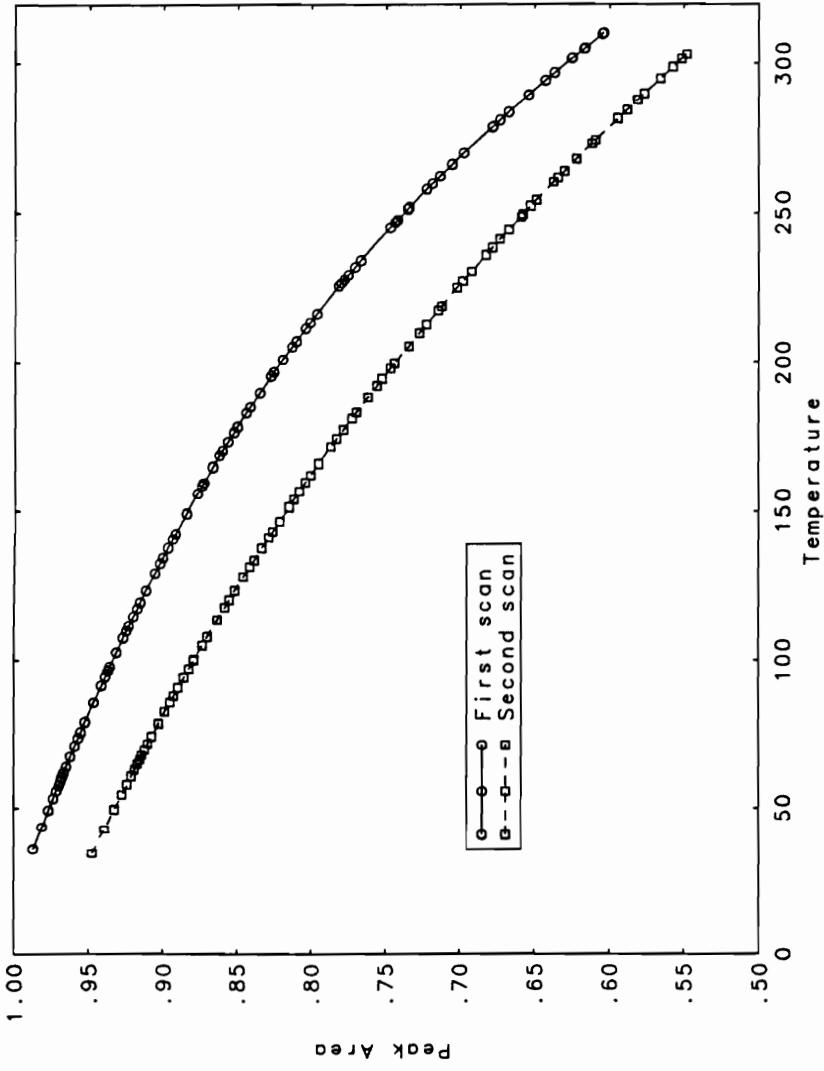


Figure 3.36 VTRAS analysis of the absolute peak area for the 650 cm^{-1} absorbance band for both the first and second scans in the analysis of a 60-70 nm film on copper oxide.

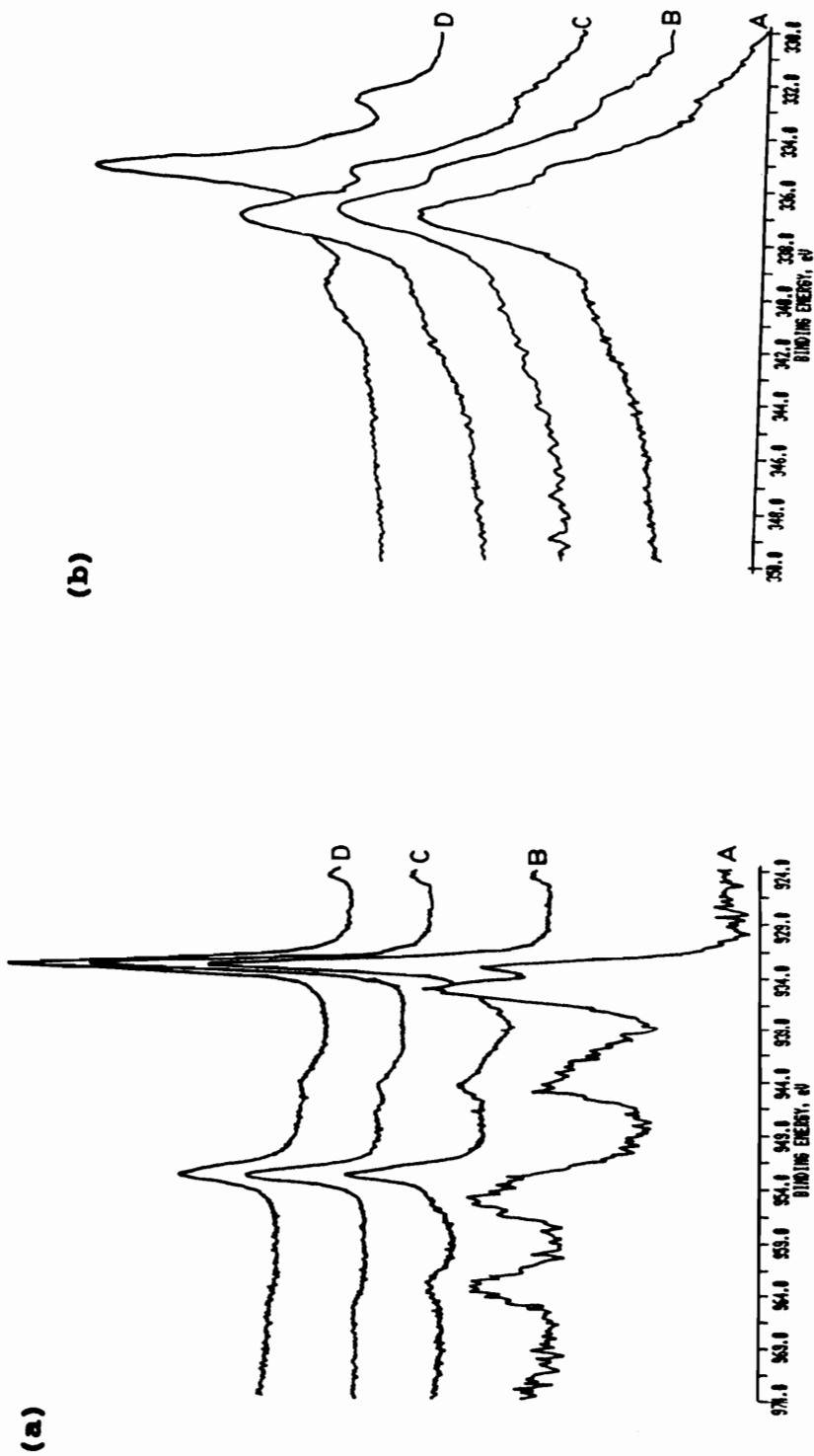


Figure 3.37 XPS analysis of the (a) Cu_{2p} 3/2 photopeak and the (b) Cu (LVV) photopeak for the analysis of methanol cleaned copper foil as a function of temperature under argon. Shown are 30 minute heat treatments at (A) room temperature, (B) 120°C, (C) 220°C, and (D) 320°C.

a large reduction of copper(I) oxide to metal is observed by the shift in the Auger photopeak from approximately 337 to near 335 eV . The reduction is most probably accompanied by the oxidation of surface contaminants and the evolution of CO₂ and H₂O, and this has been observed for the exposure of single crystal Cu₂O samples to elevated temperatures under high vacuum (42). Analysis of spin coated polyimide samples on pre-oxidized vapor deposited copper substrates at similar temperatures also shows a reduction in oxide indicating that this phenomenon is general in nature.

3.3.4.2 Polyetherimide

While variable temperature reflection absorption spectroscopy has been shown to be useful in the analysis of reorganization for a thin crystalline polymer on surfaces, analysis of purely amorphous materials can also be performed even though less dramatic changes occur at the glass transition temperature. Polyimides are commonly used in electronics applications and often spin coating techniques are utilized to form thin uniform polyimide layers to serve as dielectric layers. In the analysis of thin polyimide films on copper, various drying and annealing steps have been used prior to analysis by a variety of techniques (43,44). Since thin spin coated polyphenylene sulfide films to form oriented surface films, questions concerning the orientation of thin spin coated films of polyetherimide may be also addressed using the VTRAS technique.

Table 3.1 shows the chemical structure and gives the infrared band peak assignments for polyetherimide, and a typical infrared spectrum of a 60-70 nm film on copper metal foil is shown in Figure 3.38. Figure 3.39 shows the difference infrared spectrum for a polyetherimide film on a copper metal foil substrate after the first and second scan using a scan speed of 2.5 /minute and a maximum temperature of approximately 320°C. Samples for this analysis had been purposely dried at only 150°C, almost 70° below the reported glass transition temperature (45). While this would allow for the removal of most of the solvent in such a thin film, any orientation

Table 3.1 Infrared absorbance band assignments for Ultem™ polyetherimide.

<u>Peak Position</u>	<u>Assignment</u>
1732	C=O stretch
1601,1505,1480	C=C stretch
1363	Imide C-N stretch
1278	C-H bend
1239	Aromatic C-O stretch
1105	Phenyl-N-C bend
848 779	out-of-plane ring bends

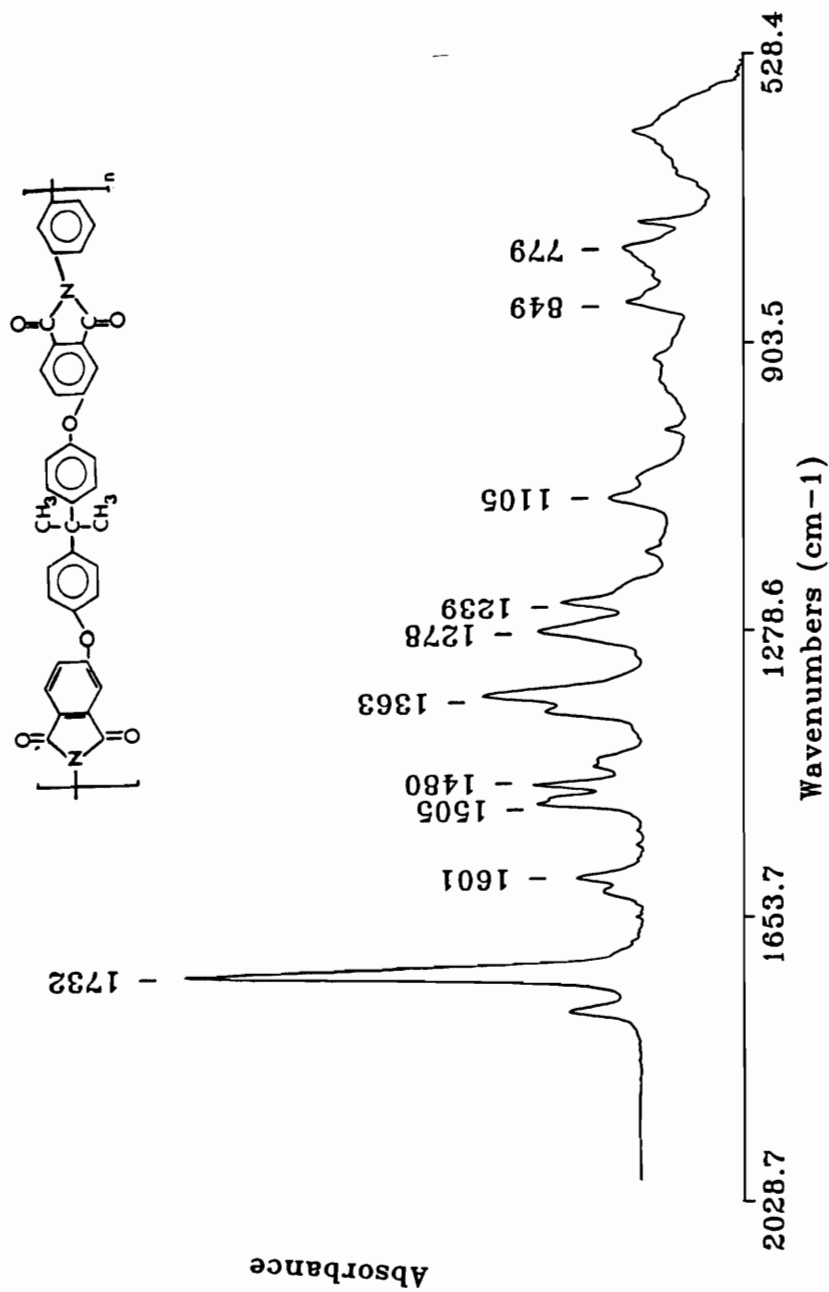


Figure 3.38 RAS spectrum of a thin spin coated film of polyetherimide on a 'brite dip' (See chapter 2, section 2.2.1.2) acid cleaned copper foil substrate.

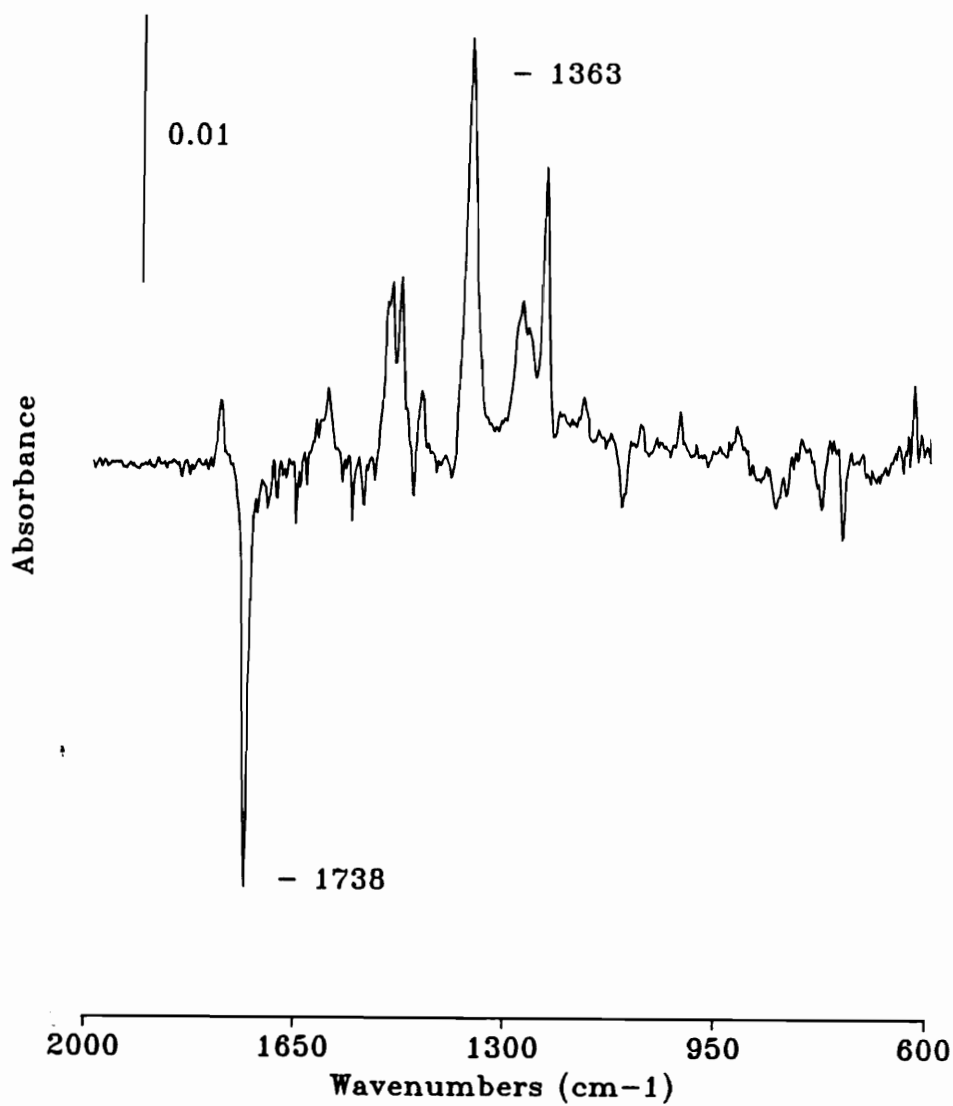


Figure 3.39 RAS difference spectrum comparing a polyetherimide thin film taken after the first temperature scan and the original spectrum after drying.

from spin coating would remain due to the lack of large scale segmental motion for the polymer at this temperature. After the first run, the spectrum shows a number of spectral changes including a loss in the carbonyl absorbance at 1738 cm^{-1} and an intensity increase for the 1363 cm^{-1} band due to the imide C-N stretch. The simultaneous loss of intensity for some bands and increase in others rules out the possibility of changes in density

or refractive index and suggests orientation effects. Figure 3.40 shows the thermal RAS scan for the 1738 cm^{-1} carbonyl peak and shows a linear decrease in the carbonyl peak intensity until near 200°C where the peak undergoes a sharp decrease in intensity to a new value followed by a further linear decrease in intensity. The second scan starts at a higher intensity value due to the lower temperature, and decreases almost linearly to merge with the first scan above approximately 240°C . The sharp transition in the temperature range of 190 to 230°C clearly indicates the onset of large scale segmental motion associated with the glass transition temperature which has been reported as 220°C for this polymer (45). The generally lower T_g associated with the start of motion, and the broad transition temperature range probably reflect the unique state of the spin coated film. Also this range probably reflects the increased free volume after solvent removal, and the longer time scale for the reorientation of the polymer against a surface. Figure 3.41 shows a similar analysis for the 1363 cm^{-1} band attributed to the C-N imide group. The results are similar to that obtained for the carbonyl band and show a similar transition region near 205°C .

The results for these two bands seem to indicate that the spin coating technique results in an orientated surface polymer layer that can only be relaxed as the temperature approaches the glass transition temperature of the polymer. The decreased carbonyl and out-of-plane C-H ring absorbance band intensities with increase the in-plane band intensities are consistent with an average polymer chain that was oriented in the plane of the substrate moving to a more random configuration after heating above the glass transition temperature. This would be

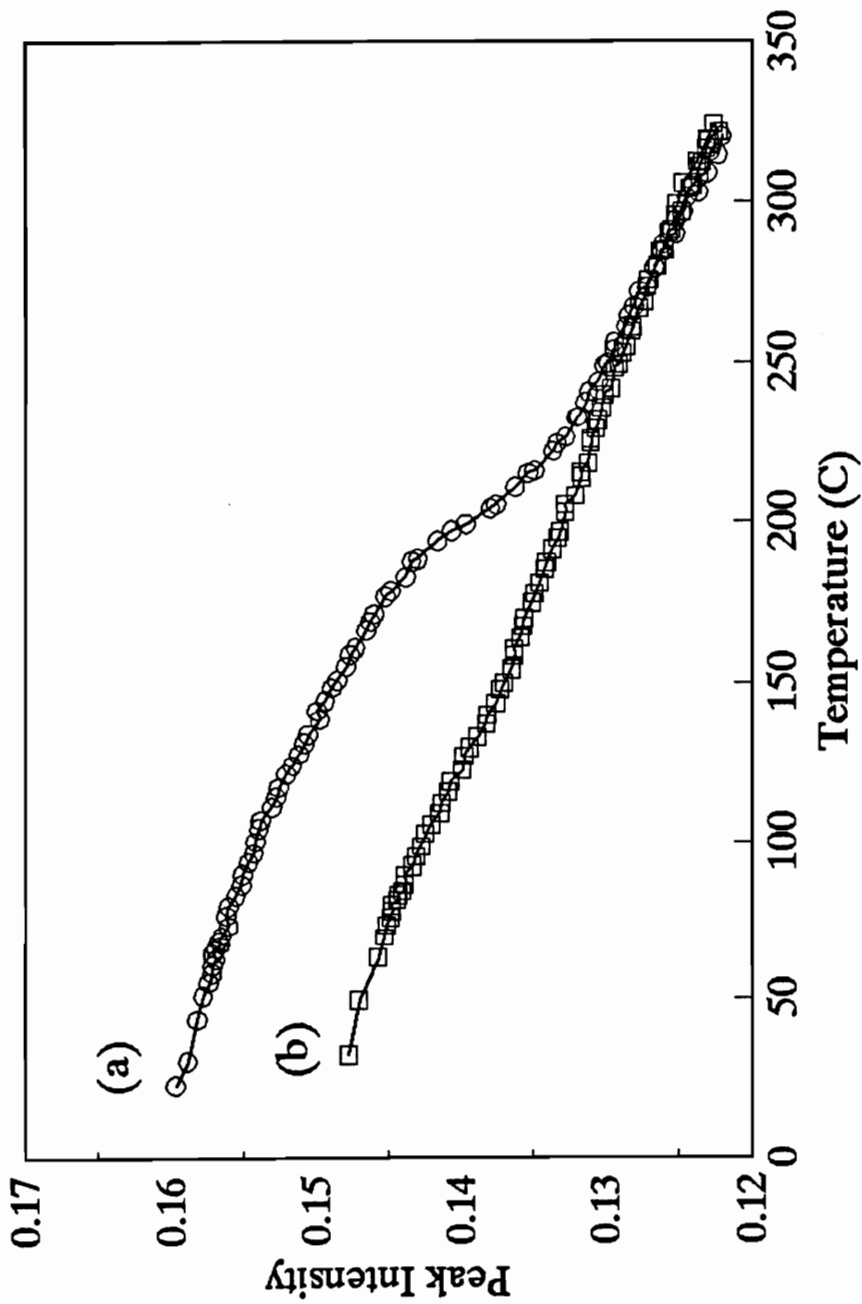


Figure 3.40 VTRAS analysis of the absolute peak intensity of the 1738 cm^{-1} carbonyl absorbance band for both the first and second scans in the analysis of a thin polyetherimide film on copper foil.

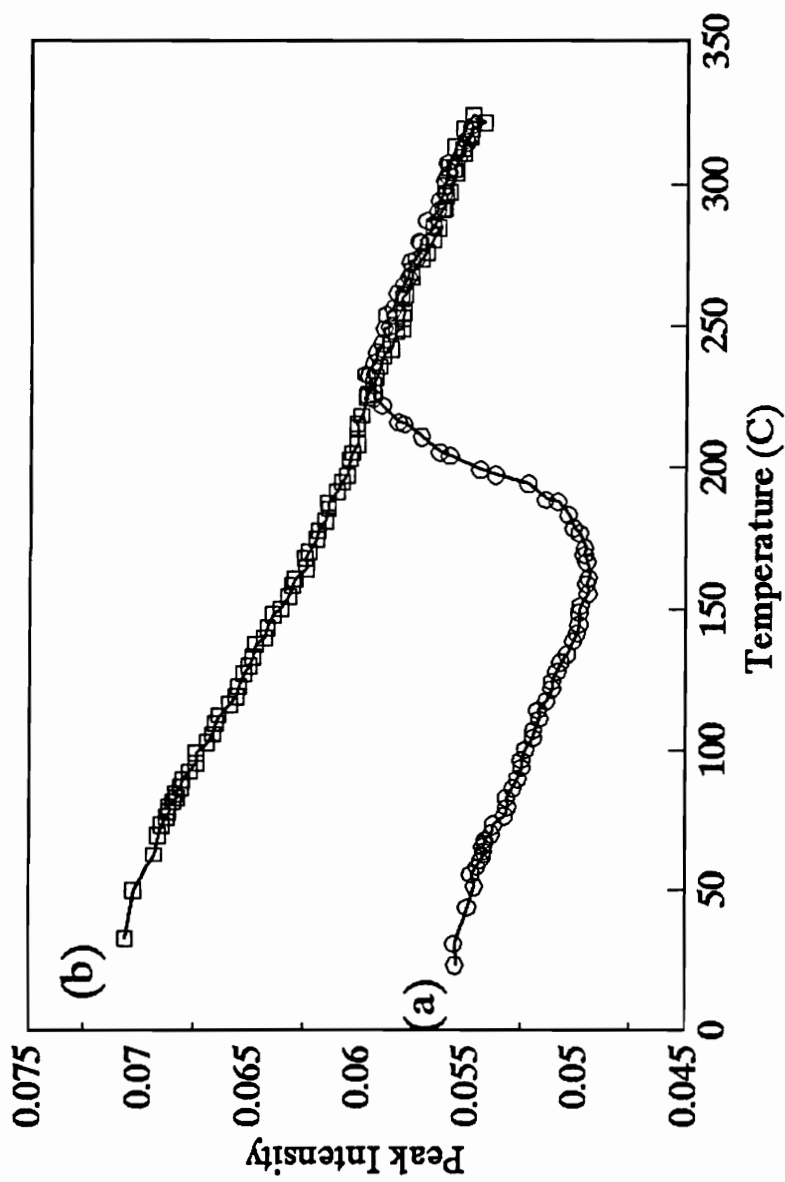


Figure 3.41 VTRAS analysis of the absolute peak intensity for the 1363 cm^{-1} C-N absorbance band for both the first and second scans in the analysis of a thin polyetherimide film on copper foil.

consistent with the spin coating technique which would produce shear forces in the plane of the substrate upon coating. While the results could also involve chemical interactions with the substrate, one might expect these to be more specific in nature, only affecting one or several of the absorbance bands for the polymer. This type of specific interaction has been observed in the analysis of the interaction of evaporated copper with polyimides under high vacuum conditions where the specific interaction of copper with the carbonyl group was reported (46). The results here seem to be more general in nature, involving the general relaxation of the polymer against the surface.

3.4 SUMMARY AND CONCLUSIONS

Variable temperature RAS analysis has proven useful in the analysis of the reorganization of thin PPS films against a variety of substrates. Both the onset of crystallization and melting can be detected by this technique and the transition temperatures were determined for all substrates analyzed. The much lower crystallization temperature for thin films on metal or metal oxide substrates compared to transmission measurements may reflect the large increase in available surface nucleation sites relative to the volume of the polymer present. For thin films of 60 - 70 nm thickness, the substrate surface area to volume ratio increases to 50 times that for a 2.5 micron film. The lower melting temperature probably reflects the unique structure of the PPS thin film. It has been observed in the DSC analysis of PPS composites that in some cases, two melting exotherms are observed for the first scan, one due to the bulk melting transition at 275°C, and a second lower value near 257°C (50). This effect is probably due to surface effects of reinforcing fibers and is dependent on the sample processing prior to analysis. Since the transition temperature is independent of the number of scans for aluminum and chromium substrates, the unique ordered structure at the interface is probably responsible for the lower value found here.

Exposure of PPS to pre-oxidized vapor deposited copper metal results in the degradation of the film leading to the loss in the ability to crystallize upon cooling from the melt. Due to the relatively few spectral changes for the polymer observed in *ex-situ* measurements, this shows an advantage of the VTRAS technique, where now the change in morphological behavior can be used as an indicator of interaction within the interphase. Copper(I) oxide is reduced at high temperatures, but this effect seems general in nature and is not specific to PPS. Thin films of PPS coated on copper(I) oxide films also degrade but at a slower rate than a thin oxide on a copper metal underlayer, indicating that degradation is in the presence of metal is much faster than that observed for the pure oxide.

3.5 REFERENCES

1. Schonhorn, H., Ryan, F. W. *J. Polym. Sci. Part A-2* **1970**, 8, 1545
2. López, L. C.; Wilkes, G. L. *Polym. Prep.* **1989**, 30, 207
3. Fitchmun, D. R., Newman, S. J. *Polym. Sci. Part A-2* **1968**, 6, 231
4. Fowkes, F. M. and Mostafa, M. A., *Ind. Eng. Chem. Prod. Res. Dev.* **1978**, 17, 3
5. Braun, J. M., and Guillet, *Adv. Polym Sci.* **1976**, 21, 107
6. Braun, J., M., and Guillet, J. E., *Macromolecules* **1975**, 8, 882
7. Ratner, B. D., In "Surface and Interfacial Aspects of Biomedical Polymers" Chapter 10, 373, J. D. Andrade, Ed., Plenum Press, New York (1985).
8. Ratner, B. D., Weathersby, P. K., Hoffman, A. S., Kelly, M. A., and Scharpen, L. H., *J. Appl. Polym. Sci.* **1978**, 22, 643
9. Lin, T., *M.S. Thesis*, Virginia Polytechnic Institute and State University, Blacksburg, VA, 1990
10. Gilpin, R. K., *J. Chromatographic Sci.* **1984**, 22, 371
11. Gilpin, R. K., *Anal. Chem.* **1985**, 57, 1465
12. Schaefer, J., *Macromolecules* **1973**, 6, 882
13. Nagaoka, S., Mori, Y., Takiuchi, H., Yokota, K, Tanzawa, H., and Nichiumi, S., *Polymer Preprints* **1983**, 24, 67
14. Yim, A., Chahal, R. S., and St. Pierre, L. E., *J. Colloid Interface Sci.* **1973**, 43, 583
15. Iisaka, K. and Shibayama, K., *J. Appl. Polym. Sci.* **1978**, 22, 3135
16. Richard, C., Kuntharet, H., and Schreiber, H. P., *Polym. Compos.* **1985**, 6, 201
17. Stupp, S. I., and Weldert, S. C., *Polym. Compos.* **1983**, 7, 224

18. Ko, C. U., Balcells, E., Ward, T. C., Wightman, J. P., *J. Adhesion*, **1989**, 28, 247
19. Wedgwood, A. R.; Seferis, J. C. *Pure Appl. Chem.* **1983**, 55, 873
20. Iwamoto, R.; Miya, M.; Mima, S. *J. Polym. Sci. Polym. Phys. Ed.* **1979**, 17, 1507
21. Higuchi, S., Tanaka, S., Kamada, H. *Spectrochim. Acta* **1972**, 28A, 1721
22. Hannon, M. J., Koenig, J. L. *J. Polym. Sci. A2* **1969**, 7, 1085
23. Herber, R. H., *Polyhedron* **1985**, 4, 1969
24. Joss, B. L., Bretzlaff, R. S., and Wool, R. P., *Polym. Eng. Sci.* **1984**, 24, 1130
25. Joss, B. L., Ph.D. Dissertation, University of Illinois, Urbana, Illinois, 1986
26. Anton, A., *J. Appl. Polym. Sci.* **1968**, 12, 2117
27. Ogura, K., *Br. Polym. Journal* **1975**, 7, 221
28. Fukawa, K., *Kogyo Kagaku Zasshi* **1965**, C8, 41
29. Huang, Y. S., and Koenig, J. L., *J. Appl. Polym. Sci.* **1971**, 15, 1237
30. Lin, S.-B., and Koenig, J. L., *J. Polym. Sci.: Polym. Phys. Ed.* **1983**, 21, 2067
31. Magonov, S. N., Shen, D., Qian, R., *Macromol. Chem.* **1989**, 190, 2565
32. Snyder, R. G., Maroncelli, M., Strauss, H. L., and Hallmark, V. M., *J. Phys. Chem.* **1986**, 90, 5624
33. Snyder, W. S., Sheen, C. W., and Painter, P. C., *Appl. Spectrosc.* **1988**, 42, 503
34. Schlotter, N. E., Rabolt, J. F., *Appl. Spectrosc.* **1985**, 6, 994
35. Swalen, J. D., Rabe, J. P., Brown, C. A., and Rabolt, J. F. In *Surface and Colloid Science in Computer Technology*; Mittal, K. L., Ed.; Plenum Press: New York, 1987; p.375
36. Rabolt, J. F., Hofer, D., Miller, R. D, *Macromolecules* **1986**, 19, 611
37. Greenler, R. G., *J. Chem. Phys.* **1966**, 44, 310

38. Greenler, R. G., Rahn, R. R., and Schwartz, J. P., *J. Catal.* **1971**, 23, 42
39. Allara, D. L., Baca, A., and Pryde, C. A., *Macromolecules* **1978**, 11, 1215
40. Boerio, F. J, Armogan, L., *Appl. Spectrosc.* **1978**, 32, 509
41. Poling, J., *Electrochem. Soc.* **1969**, 116, 958
42. Schulz, K. H.; Cox, D. F.; *Submitted to J. Phys. Chem.*
43. Russell, T. P.; Gugger, H.; Swalen, J. D.; *J. Polym. Sci.: Polym. Phys. Ed.*, **1983**, 21, 1745
44. Takahashi, N.; Yoon, D. Y.; Parrish, W. *Macromolecules* **1984**, 17, 2583
45. Devilbiss III, T. A., *Ph.D. Dissertation*, Virginia Polytechnic Institute and State University, 1987
46. Strunkus, T.; Hahn, C.; Frankel, D.; Grunze, M. *J. Vac. Sci. Technol.* **1991**, 9, 1272
47. Ribbing, C. G.; Roos, A. In *Handbook of Optical Constants II*; Palik, E.D., Ed.; Academic: San Diego, 1991; p. 875
48. Beecher, J. F. *Surf. Interf. Anal.* **1991**, 17, 245
49. Hawkins, R. T. *Macromolecules*, **1976**, 9, 189
50. Wilfong, D. L., *Polym. Compos.* **1989**, 10, 92

Chapter 4: Analysis of the Molecular Structure at PPS / Copper Interphases and its Role in Adhesion

4.0 INTRODUCTION

Due to the growing number of applications in the electronics industry, the interest in polymer/copper adhesion has increased greatly during the last two decades. Dielectric layers in multi-layer components at the chip level consist of either ceramic or polymeric thin films. Ceramics used include silicon dioxide, polycrystalline silicon, or silicon nitride and offer the advantage of strength and thermal stability (1-3). The disadvantage of these materials, however, are a high dielectric constant and poor line width resolution, and the film thicknesses are usually limited to less than two microns due to cracking problems (4). Polymers can have a much lower dielectric constant and can be patterned using lithographic techniques. Attention in recent years has focused on the use of polyimides due to a low dielectric constant, good thermal stability, and the ability to planarize the underlying substrate (5). Copper is usually the metal of choice in most studies due to good electrical conductivity.

Polymers have also been extensively used for the encapsulation of electrical and electronic devices and 90% of all semiconductor products are supplied with some type of plastic encapsulation (6). While encapsulation of electronic components has centered around the use of thermosetting epoxide based resins, polyphenylene sulfide, due to the relative ease of injection molding of this thermoplastic resin, has found applications in this area (7). The properties of PPS have been reviewed in an earlier section (See section 2.1.4).

In any application, the initial adhesive strength of the copper/polymer bond will be a critical factor in determining the performance and lifetime of the device. Also, bond durability and the effects of exposure to elevated temperatures or moisture must be determined. This is particularly important in circuit board applications where soldering processes result in localized exposure to high temperatures.

The physical and chemical characteristics of the polymer/copper interface region will be important in determining the strength and durability of the device. Sharpe

coined the phrase 'interphase' to describe the transition zone of properties when dissimilar materials are brought into contact (8). This region is often thought to be very different from the bulk regions of either phase. Individual material properties of the bulk can be chosen carefully to meet system requirements, but the interphase must be understood in terms of the physical and chemical properties resulting in the initial adhesion as well as changes occurring as a function of time and environment.

4.1 LITERATURE REVIEW

4.1.1 Surface Analysis of Copper

A number of surface analytical techniques have been employed to study copper surfaces including x-ray photoelectron spectroscopy (XPS), Auger electron spectroscopy (AES), infrared reflectance absorption spectroscopy (IRRAS), surface enhanced Raman scattering (SERS), and ellipsometry among others. The analysis of copper surfaces by XPS, IRRAS, and ellipsometry will be briefly reviewed here due to the relevance to this work.

4.1.1.1 X-ray Photoelectron Spectroscopy

XPS has probably been the most widely used tool to investigate the chemistry of copper surfaces for low surface area samples (plates, foils, etc.). The surface chemistry of copper has generally been deduced from an analysis of both the Cu 2p and x-ray induced Auger (LVV) photopeaks. Analysis of the Cu 2p photopeak has been used in a number of studies to distinguish between the Cu⁰ and Cu²⁺ oxidation states as the photopeak for the Cu²⁺ species is shifted approximately one electron volt higher than the photopeak position for the metal (9-12). Also, the presence of a characteristic shake up satellite located from seven to ten electron volts higher than the main photopeak position also serves as a quick indicator of the presence of Cu²⁺ species. A detailed analysis of the structure of the satellite has been used to distinguish between cupric oxide and cupric hydroxide (12). Analysis of the 2p photopeak alone, however, cannot distinguish between Cu⁰ and Cu⁺ oxidation states. To differentiate these oxidation states, the x-ray induced Auger photopeak (LVV) can be analyzed, and while

there is only a slight difference between the Cu^+ and Cu^{2+} states, there is a clear distinction between the Cu^0 and Cu^+ peak positions. This represents a good example of how both the photoelectron and Auger lines can be examined to determine the chemistry of a metal surface. Figure 4.1 shows typical spectra for the Cu 2p and Cu(LVV) photopeaks for copper metal, cupric oxide, and cuprous oxide (13). Combined with the analysis of the O1s photopeak, distinctions can be made between various copper oxides and copper hydroxide (12). Analysis of copper sulfides yield similar results and studies have been done to determine the binding energies for these compounds (11).

In addition to the absolute binding energies of the copper 2p and Auger photopeaks for identification, the "modified Auger parameter" (α') is often used (14). The term is defined as:

$$\alpha' = \text{KE}(\text{Auger}) + \text{BE}(\text{Photoelectron}) \quad [1]$$

where $\text{KE}(\text{Auger})$ is the kinetic energy for the strongest Auger line and $\text{BE}(\text{Photoelectron})$ is the binding energy of the photoelectron of interest.

Use of this parameter eliminates problems related to sample charging since this would have a positive effect on the photoelectron line and a negative effect on the Auger line, resulting in a constant difference. Wagner plots can then be constructed by plotting a combination of Auger parameter, kinetic energy of the Auger line, and binding energy of the photoelectron line (28). An example of this type of plot is shown in Figure 4.2 for various copper compounds (11). In addition, the valence band spectra have also been used to identify surface copper species (10,29).

Copper species have been extensively analyzed by XPS and Table 4.1 shows the results of data compiled from the literature for various oxygen and sulfur containing species prepared under a variety of conditions. While there is some disagreement, the binding energies are relatively close and differences probably arise from the referencing method used to correct for charging effects.

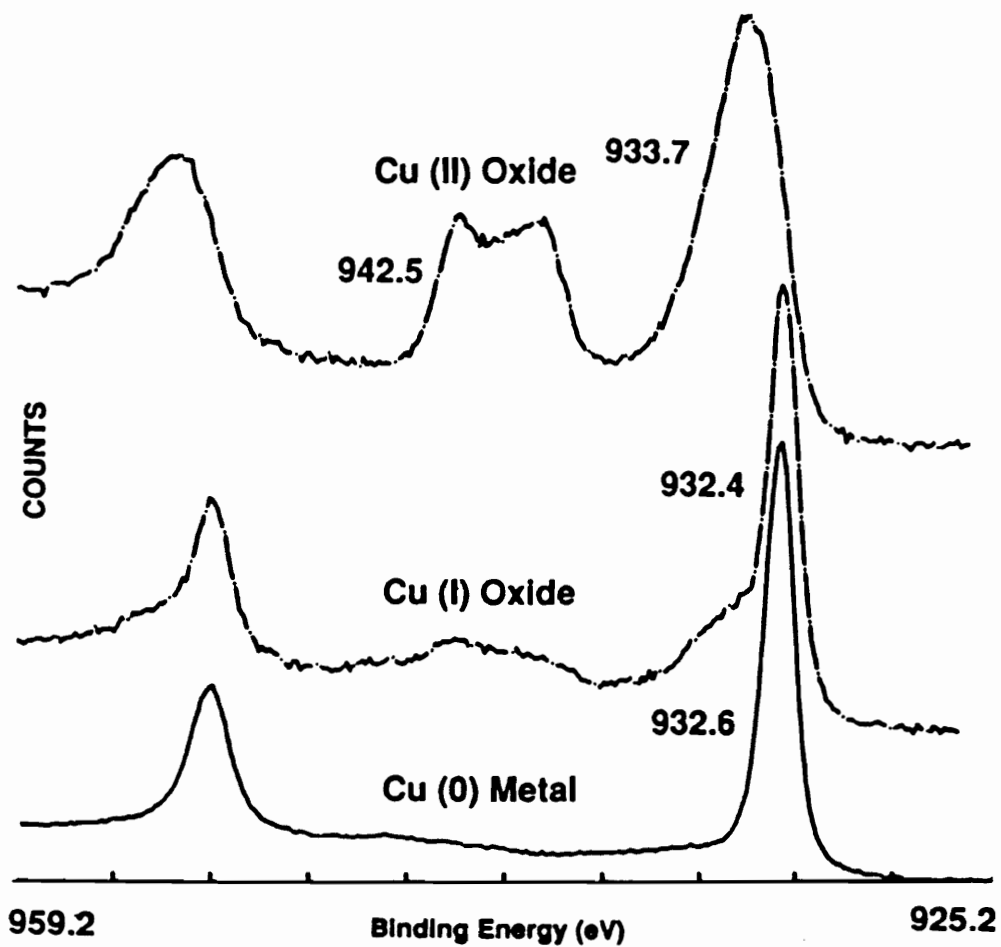


Figure 4.1 XPS analysis of the Cu 2p photopeak for copper metal and cupric and cuprous copper oxides (13).

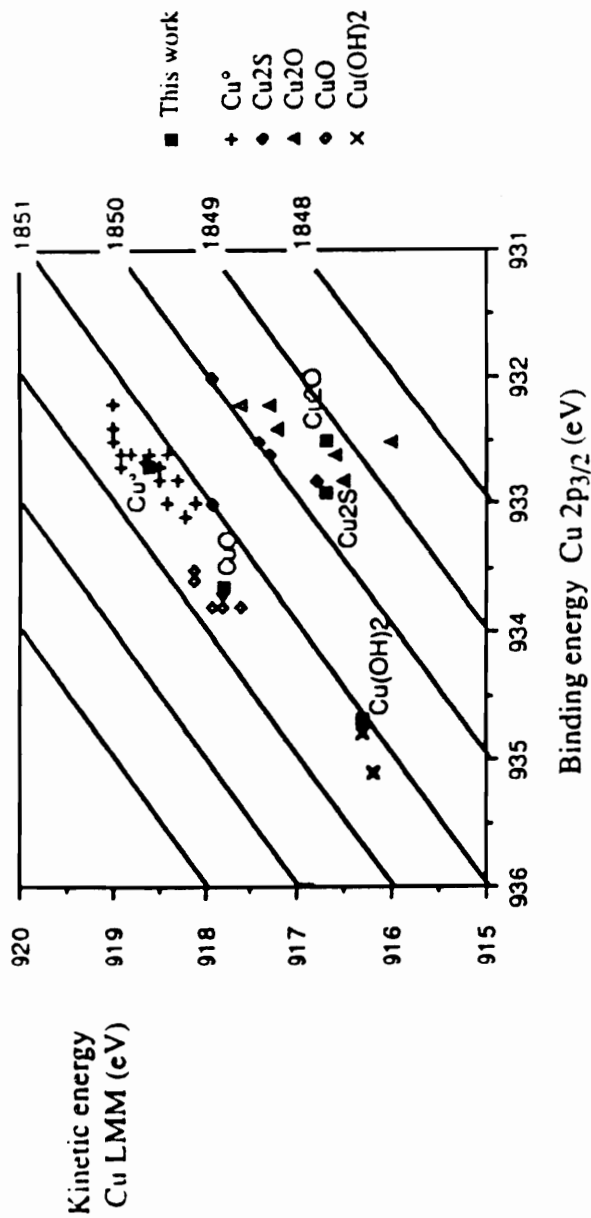


Figure 4.2 Typical Wagner plot for various copper compounds (11)

Table 4.1 XPS analysis of photopeak positions for several copper compounds.

<u>Compound</u>	<u>Cu2p</u>	<u>Cu (LVV)</u>	<u>α'</u>	<u>O1s</u>	<u>S2p</u>
<i>Cu (metal)</i>	932.8 ¹	335.1 ¹	1851.3 ¹	-----	-----
	932.7 ²	335.0 ²	1851.3 ²	-----	-----
	932.5 ³	-----	-----	-----	-----
<i>Cu₂O</i>	932.9 ¹	336.8 ¹	1849.7 ¹	-----	-----
	932.5 ²	337.1 ²	1849.0 ²	-----	-----
	932.5 ³	-----	-----	-----	530.5 ³
<i>CuO</i>	933.8 ¹	335.8 ¹	1851.6 ¹	-----	-----
	933.6 ²	335.8 ²	1851.4 ²	-----	-----
	933.8 ³	-----	-----	529.6 ³	-----
<i>Cu(OH)₂</i>	934.4 ³	-----	-----	530.9 ³	-----
<i>Cu₂S</i>	932.9 ²	336.9 ²	1849.6 ²	-----	161.9 ²

¹ - Ref. (10)

² - Ref. (11)

³ - Ref. (12)

XPS has also been used to analyze the surface chemistry associated with the exposure of samples to a variety of environments. Exposure of polycrystalline copper samples to ambient temperatures and humidities has been termed 'natural passivation' and studied by XPS (14,15). Results showed a surface layer of $\text{Cu}(\text{OH})_2$ or hydrated CuO with an underlayer of Cu_2O on copper metal (2), and an illustration for this layered surface structure is shown in Figure 4.3. Thermal oxidation of copper has been studied by a number of investigators, and the resultant surface chemistry is highly dependent on the temperature and atmosphere at which the oxidation was carried out. Oxidation near 150°C results in primarily a thin layer of cuprous oxide (16,17) although a defect structure of $\text{CuO}_{0.67}$ has been postulated for oxides formed at least up to 180°C (18). Heating near 200°C , however, results in the formation of an overlayer of CuO with a relatively thick underlayer of Cu_2O (16,19). Copper oxides formed by other methods have also been investigated including preparation of cuprous oxide films under high vacuum using high temperature solid state electrolysis (20). The formation of oxide films by electrochemical methods in solution has been extensively studied using XPS and ion scattering spectroscopy (ISS) and these studies show that either a Cu_2O layer or Cu_2O and CuO / $\text{Cu}(\text{OH})_2$ mixed layer can form depending on the electrode potential used (21-23). Speckman, et al. have used curve fitting techniques to analyze the copper (LVV) Auger signal and quantitatively determine the amount of cuprous oxide formed from electrochemical oxidation (24). Relatively thick cuprous oxide films with a surface cupric oxide layer having a needle-like morphology have also been prepared for solar collector surface coatings by chemical treatment with alkaline solutions of potassium persulfate (25-27).

4.1.1.2 Infrared Reflection Absorption Spectroscopy

Infrared analysis of copper oxidation has been reported by a number of researchers using the technique of reflection absorption infrared spectroscopy (IRRAS). Greenler investigated thin Cu_2O films on copper, and using calculations based on optical theory, predicted that the observed reflection spectra should show a single band at thicknesses less than 100 nm while two bands were predicted for thicker films (30).

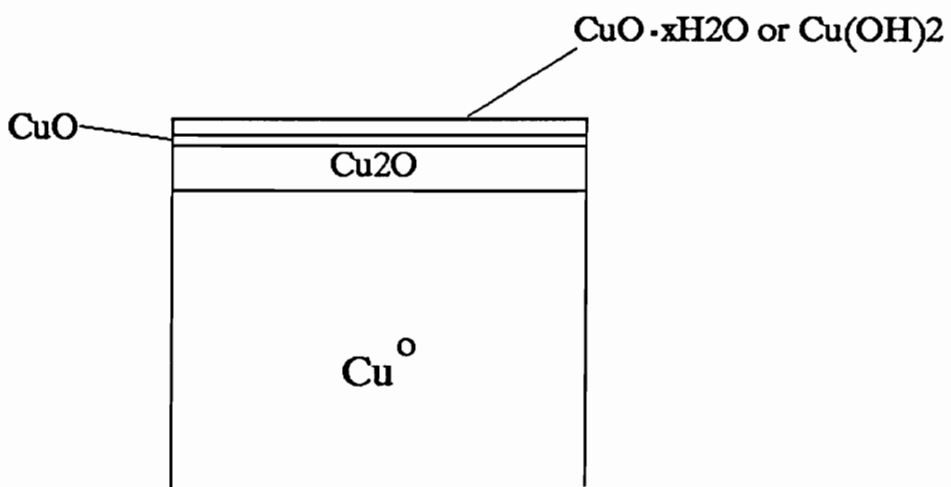


Figure 4.3 Illustration of the copper metal, oxide, and hydroxide layered structure typically found for the ambient oxidation of copper surfaces (15).

This behavior was attributed to the dispersion in the refractive index (See section 2.1.2.2). Boerio and Armogan experimentally showed two peaks at 655 and 612 cm^{-1} for thermally grown films at 150°C (17). For thicker oxide films ranging from 0.2 - 3 microns, very complicated spectra were predicted from optical theory and measured experimentally for cuprous oxide films thermally grown at approximately 300°C (31).

Heating freshly prepared copper substrates to temperatures near 150°C results in primarily a cuprous oxide surface (16,17) as determined by a single absorbance band near 650 cm^{-1} . Samples heated at higher temperatures, however, show evidence of the formation of cupric oxide. Ishitani et al. observed a band at 560 cm^{-1} attributed to CuO for copper plates heated at 200°C (16). Boerio and Armogan, upon heating copper plates to 300°C observed the conversion of Cu_2O to CuO by the disappearance of bands at 655 and 612 cm^{-1} due to Cu_2O to give a new absorbance band at 570 cm^{-1} attributed to CuO (17).

4.1.1.3 Ellipsometry

Ellipsometry has been used to characterize copper surfaces in a number of studies and the optical constants have been compiled for copper metal (32) and for both cupric and cuprous oxides (33). The technique has been used to monitor the kinetics of oxide formation for vapor deposited copper films (34). Ellipsometry has also been used for the routine *in-situ* monitoring of oxide growth on circuit boards during the heating cycle before soldering (35).

4.1.2 Copper Catalyzed Thermoxidative Degradation of Polymers

It has been well documented in the literature that the oxidation of polymers at elevated temperatures is accelerated in the presence of many copper compounds (36-39). While the specific mechanisms involved are still somewhat in question and are dependent on both the polymer studied and particular copper compound used, the copper catalyzed homolytic decomposition of hydroperoxides has been suggested in many studies (36-37). In early work, Hansen proposed the mechanism shown in Figure 4.4. This shows the reaction of hydroperoxides found in the normal oxidation

of polyolefins with cuprous ions through a mechanism that produces alkoxy radicals which propagate chain scission (36). The cupric ion can then react with the polymer itself to regenerate Cu^+ species for further reaction. Jellink, et al. have proposed that the catalysis is due primarily to initiation reactions involving copper ions that diffuse through the polymer bulk as carboxylate species (37). Catalysis would then result from both an initiation step involving the carboxylate species and the reaction of Cu^+ and Cu^{2+} copper species with hydroperoxides (37). They proposed that both Cu_2O and $\text{CuO}_{0.67}$ have defect structures capable of providing copper ions more readily than CuO , and therefore explain the more accelerated oxidation in the presence of the first two copper compounds. It was also found that the oxidation mechanism depended on whether reaction products (CO_2 and H_2O) had been removed during the course of the oxidation (37). In another study of ^{18}O labelled $\text{CuO}_{0.67}$, in the presence of getters to remove reaction products, reduction of copper oxide to metal without re-oxidation by ^{16}O oxygen was observed using ion scattering profiles (40,41) This result suggests a redox mechanism at the polymer/copper interface as an important step of the degradation process. In the absence of getters, the reduced copper was re-oxidized and the ratio of $^{16}\text{O}/^{18}\text{O}$ increased. Also, copper ions were found throughout the polymer film (40,41). Allara and coworkers have used infrared reflection absorption spectroscopy to study the interfacial reactions between polyolefins and copper (42-44). The results of these studies also show accelerated degradation and indicate that copper carboxylates form at the copper/polymer interface which subsequently diffuse into the bulk of the polymer.

While the studies above have dealt with copper oxide / copper metal systems, Allara and Chan have investigated a series of copper compounds based mainly on oxamide derivatives to investigate the possible inhibition of the copper catalyzed degradation of polyethylene (45). A list of the copper compounds used in the study and the rates of oxidation are given in Table 4.2. Of particular interest is the catalytic effect of copper stored in air which shows a polymer oxidation rate of almost one order of magnitude greater than found for cupric oxide. Also, copper complexes with oxanilide, oxamide, phthalocyanine, and oxalate ligands show greatly reduced

Table 4.2 Maximum Rate of Oxidation (R_c) as Functions of Catalyst Surface Area. (45)

Copper compound	Specific surface area, m^2/g^a	Range of total surface area per gram of polyethylene (σ) $\times 10^4$, $m^2 \cdot h$	k_c , ml/hr- m^2	k_c relative to k_c for Cu(BODH)
Cu(BODH)	1.5	15-300	44	1.0
Cu(oxanilide)	32.5	7.8-312	50	1.1
Cu(oxamide)	152.0	7.6-304	23	0.52
Cu(phthalocyanine)	50.0	25-250	~0	~0
Cu(glycinate), Cu(salicylaldehylenediimine)	4.5	4.5-45.0	305	7.0
Cu(oxalate)	2.3	2.1-20.7	490	11.3
Cu(oxalate)	11.5	11.2-112	<4	<0.1
Cu(benzoate), Cu(OH)(benzoate)	7.3	7.3-73.0	216	5.0
Cu(OH)(benzoate)	3.0	4.2-42.0	446	10.3
CuS ^c	0.8	4.0-160	132	3.0
CuO	0.5	1.3-30	55	1.3
Cu ₂ O	0.4	0.4-40	850 ^d	19.6
Cu (Stored in Air)	1.3	1.6-26	1660	38.2

^a Values reliable within $\pm 5\%$, as measured by BET method.

^b σ = weight percent of catalyst \times specific surface area/100.

^c Runs repeated with another sample of CuS, pulverized and baked *in vacuo* (100°C/10⁻⁵ torr). Both sets of runs were the same.

^d The initial part of the rate curve ($\sigma < 5 \times 10^{-4}$) gives $k_c \approx 8500$ ml/hr- m^2 . There is a sharp break at $\sigma = 5 \times 10^{-4}$, and for $\sigma > 5 \times 10^{-4}$, $k_c \approx 850$ ml/hr- m^2 .

catalytic activity (45). In another study, Allara and Roberts investigated the catalytic behavior of copper for the oxidation of hexadecane, and found that the particular surface treatment resulted in widely varying catalytic activity (46). Cuprous and cupric oxides accelerated the oxidation, while cupric hydroxide surfaces inhibited the reaction. It was postulated that Cu_2O and CuO reacted with hydroperoxides to yield free radical products which could propagate chain scission while copper hydroxide would react to form non-radical products thus trapping radicals and slowing oxidation (46).

While the polymers used in the above studies were simple polyolefins, degradation of more complex polymers has also been investigated. Burrell and coworkers studied the degradation of poly(ester imide) wire enamel coatings by XPS (47), XPS depth profiling (48), and infrared reflection absorption spectroscopy (49). Results showed that the degradation of coatings on copper was much more rapid than that on aluminum (49). XPS analysis showed that copper species were distributed throughout the film (47,48) and copper carboxylates were postulated from infrared measurements (49). Kelly, et al. investigated the curing of the polyamic acid precursor of a PMDA-ODA polyimide on copper and chromium in both air and nitrogen environments using surface infrared techniques (38). They showed little degradation on chromium substrates or on copper substrates in a nitrogen environment. On the other hand, severe degradation occurred for coatings on copper heated to 250°C in air, and copper carboxylates and nitriles were seen as degradation products (38). The accelerated degradation of poly(ether ether ketone) in the presence of copper has been documented by thermogravimetric analysis coupled with mass spectrometry (TGA / MS) (50). An increased evolution of benzoquinone was detected for oxidation in air. The interaction of PEEK with copper under high vacuum conditions has also been studied for thin coatings from extracts of the polymer on copper using *in-situ* XPS analysis (13). Little polymer degradation was observed for PEEK films on copper metal while spectral changes were observed at temperatures above 200°C for both cuprous and cupric oxide surfaces. Also, for the cupric oxide, reduction to cuprous oxide was observed (13).

Many of the findings of the copper catalyzed oxidative degradation of polymers can

be summarized as noted below. The formation of copper carboxylates has been observed in many studies (42-44) along with copper ion diffusion in the polymer matrix (40,41,47). Degradation seems to be restricted to heating in an oxidative environment, although degradation in a vacuum environment also has been observed. Most importantly, the particular copper compound present is critical in determining the catalytic activity observed (13,45,46).

4.1.3. Analysis of Polymer/Copper Adhesion

4.1.3.1 Copper Surface Pretreatment

Before adhesive bonding to a copper substrate, surface pretreatment is usually performed to remove contaminants and to generate a specific chemistry or morphology for bonding. A number of treatments can be used including cleaning with etches using nitric acid or ferric chloride in nitric acid, formation of chromate conversion coatings, or preparation of a thick 'black oxide' barrier layer (51,52). The latter process is particularly interesting due to the unique morphology generated by the treatment of copper in alkaline chlorite / phosphate solutions or by use of the commercially available Ebonol C solution (Enthron, Inc.) (53). This treatment leads to a dendritic surface layer of cupric oxide and it has been suggested that this morphology is responsible for the better peel adhesion for these surfaces (53,54). Often plain commercial copper foils show poor adhesion and corrosion stability, and foils have been developed to overcome these problems. Gould, Inc. introduced a copper foil with unique surface morphology, having a surface barrier layer of brass, and a final surface layer of chromium to provide superior adhesion characteristics and stability against corrosion (55).

In many applications, after a cleaning step, complexation of the copper surface with nitrogen-based compounds is used to inhibit oxidation or attack by corrosive gases. These compounds are usually azole base compounds including benzotriazole, benzimidazole and 2-mercaptobenzimidazole for examples. The surface complexes formed and the mechanism of corrosion inhibition have been extensively studied using a number of techniques including XPS (56,57), reflection absorption infrared

spectroscopy (58,59), surface enhanced Raman scattering (60), and ellipsometry (61). These small molecular weight compounds desorb at elevated temperatures, and recent efforts have focused on the use of polyvinylimidazole and polybenzimidazole as oxidation inhibitors (62,63). These polymers have also been evaluated as adhesion promoters for bonding to copper (63).

4.1.3.2 Analysis of the Interphase

With the increasing importance of polyimides as dielectric layers in electronic devices, many experimental studies have been conducted to investigate the interfacial chemistry in copper/polyimide systems. The copper / polyimide interface is usually formed by one of three preparation methods: (1) the polyamic acid precursor is dissolved and the solution is deposited on the metal substrate with subsequent heating to remove solvent, and to cure the polyimide (48,49,64). (2) the thermal evaporation (64-66) or sputter deposition (67) of copper directly on preimidized polymer (64,65), and (3) the co-deposition of polyimide monomer precursors under high vacuum followed by thermal imidization of these to form a surface film on a substrate. The particular chemistry involved in metal-on-polymer and polymer-on-metal systems has been shown to be different, with a high reactivity of the polyamic acid for the metal substrate in the latter case. It has been shown that a polymer/copper complex can form leading to oxide precipitates in the polymer on curing (68,69)

Particular emphasis has been placed on the "site" of interaction between the polyimide and copper, and comparing the interaction site and strength for copper with chromium and other metals. Mack concluded that copper metal interacted strongly with the imide portion of the molecule resulting in reduction of the carbonyl functionality to form copper oxide species (64). Ho, et al. used XPS and ultraviolet photoelectron spectroscopy (UPS) measurements to report a weak interaction with copper metal and the imide portion of the polyimide (70). Strunskus, et al. in studying the interaction of vapor deposited copper on vapor deposited polyimide films showed a preferential interaction with the carbonyl functionality in the imide portion of the molecule (65). In the same work, they also reported a smaller interaction with

the ether oxygen and this has also been reported by other workers (71). The much stronger interaction of chromium with polyimide has also been investigated by XPS (66) and this is thought to give rise to the much higher adhesive strength usually seen for these systems.

Analysis of the copper / polymer interphase for other polymer systems has also been conducted. Boerio showed in a study of epoxy adhesives that the anhydride curing agent can react with copper at the interphase to form relatively thick carboxylate layers (72). Studies on the interaction of copper with polyvinyl alcohol have also been done, and the formation of a copper/polymer complex was postulated (73).

4.1.3.3 Test Methods

Given the importance of polymer/copper adhesion for electrical and electronic applications, paint technology, and corrosion inhibition, considerable work has been devoted to the development of methods to evaluate the bond strength in metal / polymer film bonded systems. Methods include the use of the peel test (74,75), constrained blister test (76,77), island blister test (78,79), peninsula blister test (80), and the stretch deformation test (81,82). While each of these tests has particular geometry constraints with advantages and disadvantages, the ultimate goal of all tests is to provide a measure of the energy required to debond the polymer/metal interface. The most widely used method of analyzing copper/polymer adhesion has been the peel test (75, 83). In the case of no plastic deformation (elastic case), the peel force can yield the debond energy directly and the theoretical analysis for this case has been given in earlier works (84,85). A more typical case, however, is the situation where the adherend undergoes plastic deformation. In this case, the total peel force represents contributions from the interfacial debond energy, the energy to plastically deform the adherend, and any residual strain energy. The case of elastoplastic peeling has also been treated theoretically (74,75,86,87). Results show that in typical bonding situations, the peel strength measures the interfacial fracture energy only when $6E_p/\sigma_y^2 < t$ where E is the elastic modulus, σ_y is the yield stress, t is the

thickness and p is the peel strength (74,75,87). This condition is not met for typical copper films where the thickness is usually less than 1000 microns. Kim and Kim, through an analysis of copper films on polyimide substrates, showed that the peel strength depended on the thickness and ductility of the copper adherend, and on the compliance of the substrate (74). By analyzing the peel strength as a function of these factors for a given system, a universal peel diagram could be constructed from which the interfacial debond energy could be calculated (75). Even with the problems of adherend deformation, the peel test is often used to measure 'practical' adhesion if parameters including peel angle, peel rate, film thickness, and ambient atmosphere are kept constant (83). In this way, changes in surface pretreatment or durability may be monitored by changes in the 'practical' adhesion for the system. Buchwalter and coworkers have used the peel test extensively to evaluate the adhesion of polyimide to a variety of substrates to investigate the locus of failure (88), sensitivity to contamination (89), evaluation of acid-base interactions (90) and durability studies (91). A review of many aspects of the peel test and other aspects of polyimide/substrate adhesion have been given (92).

4.2 EXPERIMENTAL

4.2.1 Analysis of the Thermoxidative Degradation of PPS Coatings

4.2.1.1 Sample Preparation

Copper Foil

Copper foil samples (ETP 110 grade, Olin Corp.) were chemically polished using a 'brite dip' solution as previously described (see section 2.2.1.2). PPS films were prepared by spin coating 1.0 - 2.5% (wt/wt) solutions in benzophenone using the high temperature spin coating techniques previously described (see section 2.2.1.1). After coating, the samples were dried under vacuum (10^{-1} - 10^{-2}) torr for ten hours at 150°C.

Zinc Foil

Zinc foil (0.25mm, 99.98% purity, Johnson Matthey, Inc.) was degreased in methanol (Fisher, reagent grade) and cleaned by a one minute oxygen plasma

treatment prior to coating.

Chromium

Ferrotypes plates were cleaned using oxygen plasma treatment as described previously (see section 2.2.1.2). Samples were coated as above, and after coating, plates were dried under vacuum (10^{-1} - 10^{-2}) at 120 - 140°C for 12 hours prior to use.

Copper Oxide

Thin cuprous oxide films were prepared by sputter deposition on acid cleaned ferrotypes plates as described previously (see section 2.2.1.2). Samples were coated as above, and after coating, plates were dried under vacuum (10^{-1} - 10^{-2}) at 120 - 140°C for 12 hours prior to use.

Aluminum Foil

Aluminum foil (0.127mm thick, type 1100-0, Metal Foils, Inc.) samples were etched by treatment in 5% sodium hydroxide in distilled water for 30 seconds followed by two 15 second washes with distilled water and drying under nitrogen. PPS films were prepared and dried as with both chromium and copper oxide samples above.

4.2.1.2 X-ray Photoelectron Spectroscopy

For XPS analysis, coated substrates (spin coated from 2.5% (wt/wt) solutions) were heated in a oven to 210°C under ambient laboratory conditions, and samples were periodically removed for analysis. The film thicknesses for these samples, by comparison with ellipsometric analysis of films coated on chromium substrates could be estimated in the range of 200 - 300 nm.

4.2.1.3 Infrared Reflection Absorption Spectroscopy

For *ex-situ* analysis, samples were prepared by spin coating 1% PPS solutions in benzophenone onto copper and zinc substrates followed by drying under vacuum as before. Analysis was done using a retro mirror design reflection attachment and

specifics of the technique have been given previously (see section 2.2.3.2.5). For all samples, parallel polarization and an incidence angle of 85° were used. Aging for these samples was also done at 210°C in air, and an aging time of 15 minutes was typically used.

In-situ analysis of polymer aging was carried out using variable temperature reflection absorption spectroscopy. Experimental details have been previously described (see section 2.3.3), although instead of using vacuum conditions, aging was carried out in the chamber under a constant flow of dry air. The temperature was monitored by a thermocouple cemented directly to the foil surface using high temperature ceramic cement (Omega, Inc.). A temperature scan of 5°C / minute to approximately 300°C was used in all studies.

4.2.2 Analysis of Copper / PPS Adhesion

4.2.2.1 Sample Preparation

A number of copper foil pretreatment methods were used to prepare copper foil samples prior to bonding as noted below:

Solvent degrease

As received copper foil (ETP 110 grade, Olin Inc.) was degreased by a solvent wipe with methanol (Fisher, reagent grade). The procedure was repeated several times to remove any excess surface contamination.

Acid Etches

Two acid etches were used to remove the initial oxide and contamination before bonding. In the first case, copper foil was etched for 15 seconds in 20% (vol/vol) nitric acid (Fisher, 70%) followed by two distilled water rinses and drying with a stream of nitrogen. The second etch was a 'brite dip' chemical polish previously described (see section 2.2.1.2).

Chemical Oxidation

Chemical oxidation of the copper foil was done using a procedure designed to produce a thick 'black oxide' layer (25-27). Foil samples were first cleaned with a 'brite dip' chemical polish followed by an etch in an alkaline potassium persulfate solution. The etching bath was prepared as 60 g / liter sodium hydroxide and 16 g / liter potassium persulfate in distilled water. The bath temperature was maintained at 65 - 70°C and samples were treated for two minutes followed by a distilled water wash and drying under a stream of nitrogen. For 5.08 cm x 8.89 cm size foil samples, only two etches were performed per 200 ml of solution due to the degradation of the etch solution (25-27). Treatment by this method resulted in a substrate with a matt black surface finish.

Thermal Oxidation

Copper foil samples were chemically polished using a 'brite dip' solution previously described. Thermal oxidation was carried out in the hydraulic heated press immediately prior to bonding, and the inner surface of the foil was exposed to ambient air conditions for oxidation. An illustration of the procedure is shown in Figure 4.5. Typically an oxidation time of 60 to 90 seconds was used prior to the application of pressure and bonding. The foil temperature in the center of the sample was monitored for several samples and the temperature quickly exceeded 200°C during the first 15 seconds and reached a final temperature of approximately 260°C after 60 seconds.

4.2.2.2 Scanning Electron Microscopy (SEM)

Analysis of pretreated copper foil samples by scanning electron microscopy was done using a Model ISI-SX-40 (International Scientific Instruments, Inc.) All samples were sputter coated with gold prior to analysis using an Edwards (Model S1503) sputter coater to minimize sample charging.

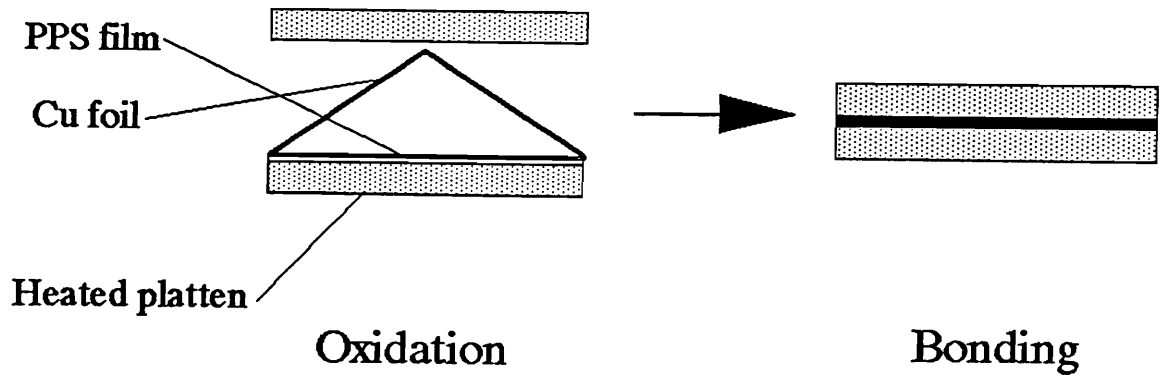


Figure 4.5 Illustration of the method of thermal oxidation of copper foil prior to bonding.

4.2.2.3 Bonding

Copper foil samples were cut to 5.08 cm x 8.89 cm, and after pretreatment, a laminate of copper foil, PPS, and ferrotype substrate was constructed as shown in Figure 4.6. Polyphenylene sulfide (Ryton™, Phillips Petroleum) was obtained as a 0.18 mm crystalline extruded film. In all cases a 0.10 mm stainless steel spacer were used to maintain a constant bond line thickness for all samples. A temperature of 320°C was used and typically a contact pressure of one minute was followed by a bonding time of two minutes at 800 - 1000 psi. The thin uniform nature of the laminate formed allowed fast heating and a rapid cycle time. After bonding, samples were removed and placed in a cold press and held under a pressure of approximately 550 - 700 psi. Samples were then annealed in an oven under ambient atmospheric conditions for 1 - 2 hours at 150°C and then analyzed immediately (<12 hours) by peel test analysis.

4.2.2.4 Peel Test Analysis

After bonding and annealing, approximately 12 mm sample strips were cut using a metal shear. The peel strength was then determined using a an Instrumentors, Inc. Model SP-102B-3M90 slip / peel tester by peeling the copper foil at a peel rate of 12 mm / min using a 180° peel configuration. All test were taken in ambient laboratory conditions.

4.2.2.5 Interphase Characterization: Failure Surface Analysis

After the peel test, both failure samples were immediately transferred (<1min) to the XPS spectrometer to minimize the changes due to exposure to atmospheric conditions. In some cases, analysis of the foil failure surface by infrared reflection absorption spectroscopy was attempted using the retro mirror design previously described.

Due to the difficulty in processing polyphenylene sulfide at elevated temperatures, studies were designed to investigate the interaction of copper with bis(4-phenyl thiophenyl) sulfide (PPS tetramer, Phillips Petroleum, Inc.). The oligomer was

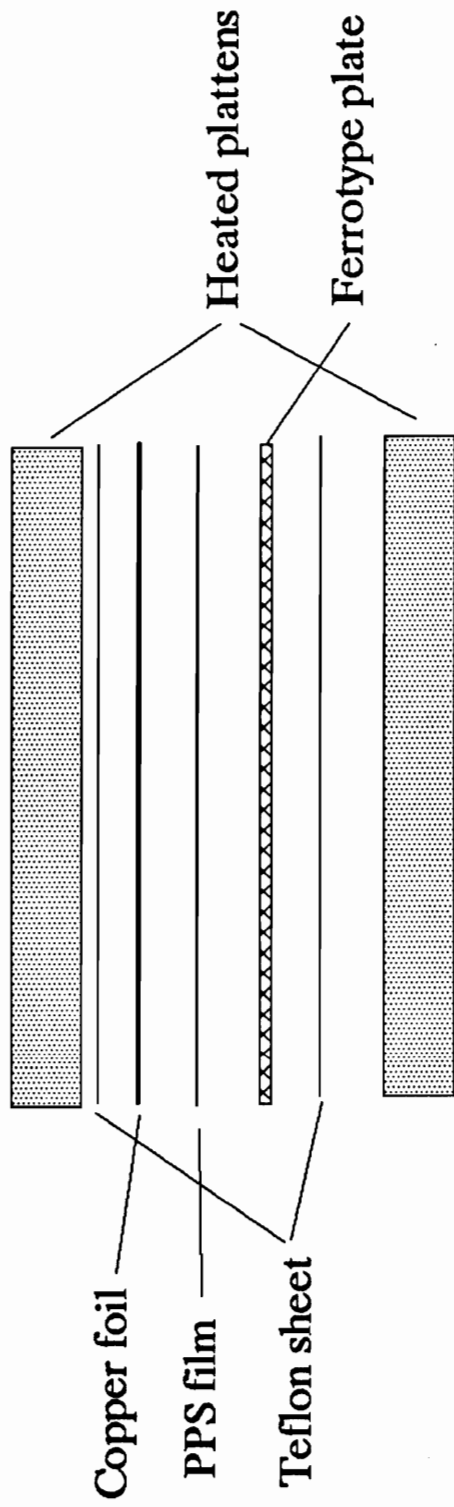


Figure 4.6 Schematic of the laminate structure used in the bonding of PPS to copper foil.

dissolved in tetrahydrofuran (Fisher, certified grade), precipitated into distilled water, washed several times, and dried under vacuum at approximately 60°C for 12 hours. This procedure was used to removed residual salts in the original material. The PPS oligomer was then placed between two sheets of pretreated copper or aluminum foil and held in place with two ferrotype plates of similar size. Samples were heated to approximately 320 - 340°C on a hot plate surface under a nitrogen environment. After high temperature exposure, foil samples were separated and either analyzed immediately, or after several rinses with tetrahydrofuran to remove excess oligomer. Samples were then analyzed by XPS.

4.3 RESULTS AND DISCUSSION

4.3.1 Analysis of the Copper Catalyzed Oxidative Degradation of PPS

4.3.1.1 XPS Analysis

Figure 4.7a shows the results of XPS analysis for the high temperature aging of 200 - 300 nm PPS films on copper foil substrates. The plot shows the changes in the calculated atomic concentrations calculated from the C 1s and O 1s photopeaks as a function of aging time. The plots indicate that the initial polymer film shows little evidence of oxygen functionality and this is in agreement with the structure of PPS. There are almost no changes in the atomic concentration during the first several hours of aging. After approximately 10 hours aging time, however, a marked increase in oxygen and reduction in carbon can be seen. Figure 4.7b shows a similar analysis using the Cu 2p and S 2p photopeaks and shows a dramatic increase in the copper concentration and reduction in the sulfur concentration in the surface region starting at approximately 10 hours aging time. Analysis of all photopeaks at longer aging times indicates the further increase in copper and oxygen with a decrease in carbon and sulfur, and at longer aging times (85 hours), no sulfur could be detected. The rapid loss of carbon and sulfur with the increase in copper and oxygen seem to indicate either a severe degradation of the polymer coating, or a migration of copper species through the film to the surface where growth can occur on top of the polyphenylene sulfide layer. The mechanism of copper diffusion through thin surface

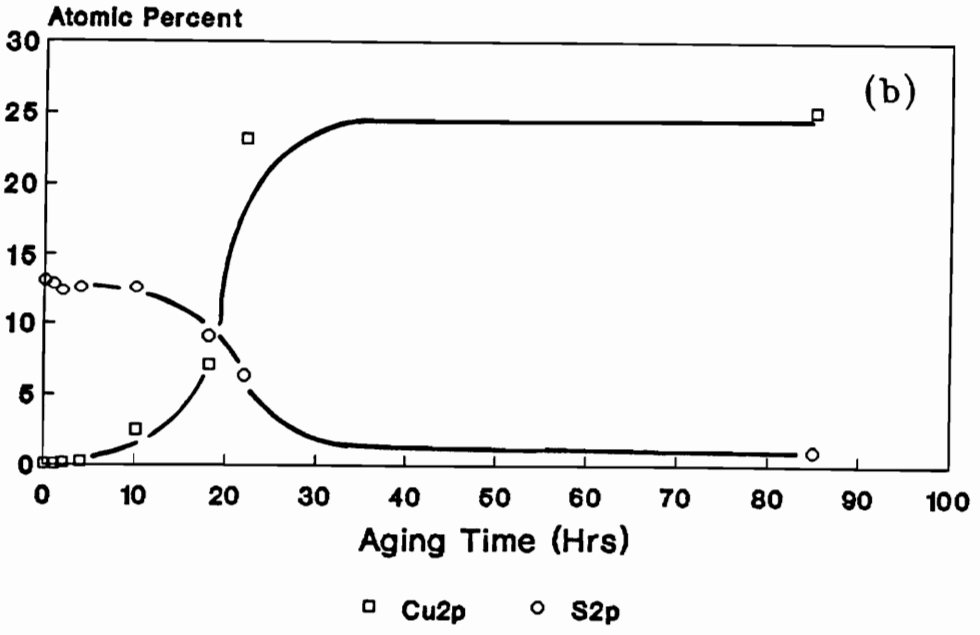
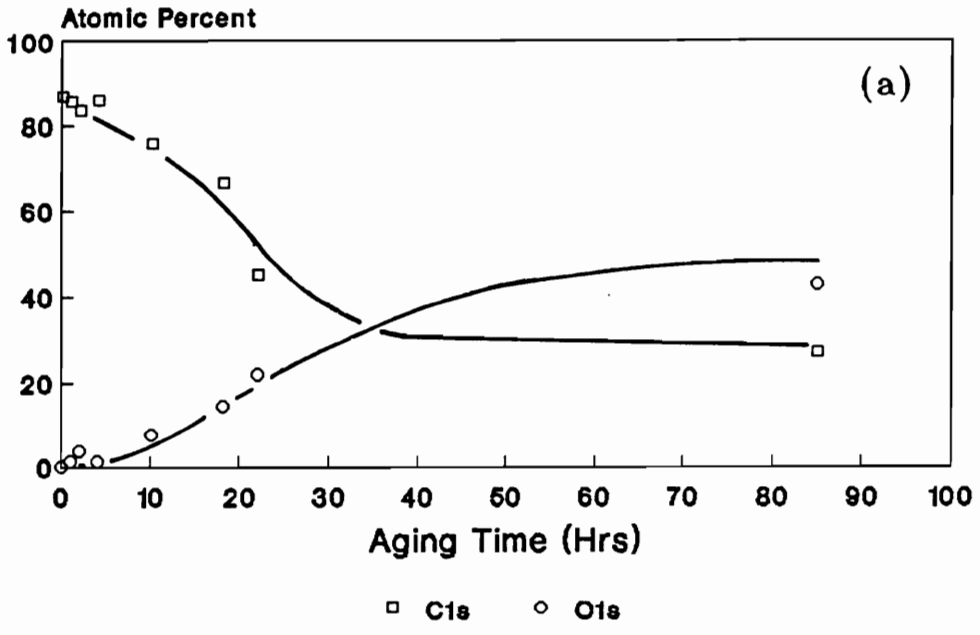


Figure 4.7 XPS analysis of the (a) C 1s and O 1s photopeak, and (b) Cu 2p and S 2p photopeak intensities at different aging times on copper foil at 210°C in air.

films has previously been proposed in the study of polyesterimide films of copper (47). It was postulated that copper either moved through the bulk of the film itself, or channeled through thin pinholes left after the spin coating procedure. Many other studies have also shown the migration of copper species as an important part of the degradation mechanism (40,41).

To investigate the nature of the identity of surface species after various aging times, the individual narrow scan photopeaks were examined. Figure 4.8a shows the analysis of the Cu 2p photopeak as a function of several aging times, and as can be seen, after one hour of aging at 220°C, no copper is detected on the film surface. After 10 hours of aging, however, the copper signal is evident with a peak maxima near 933.0 eV indicating a Cu⁺ surface species. This photopeak does have an asymmetric component at higher binding energy (934.6 eV), and this coupled with the appearance of weak shake up satellite features indicates the presence of a small amount of Cu²⁺. At longer times, a Cu²⁺ copper species component becomes the dominant surface species. Analysis of the O 1s photopeak in Fig. 4.8b indicates that while little oxygen is initially present after one hour of aging, at an aging time of ten hours, a photopeak doublet at 532.1 and 530.6 eV is evident. While the lower binding energy peak can be assigned to copper oxide, the higher binding energy component can be attributed to a O=C functionality, and is most probably associated with degradation products in the polymer film. This may be associated with copper carboxylate species often observed. Allara, in the study of copper catalyzed degradation of polyethylene, showed that the copper carboxylates could migrate hundreds of nanometers into the polymer film (45). At longer aging times, the 532.1 photopeak decreases in intensity relative to the oxide photopeak and probably represents the decomposition of copper carboxylates with time to yield copper oxide species. Figure 4.9 shows a similar analysis for the S 2p photopeak during aging. For one hour aging, the typical sulfur photopeak for PPS is observed, but at longer times, the appearance of a distinct peak at 168.3 eV indicates the presence of a highly oxidized sulfur species. This may indicate the presence of copper sulfate species and Sugama and Carriello, in the study of PPS bonded to cold-rolled, stainless, and galvanized steel surfaces in

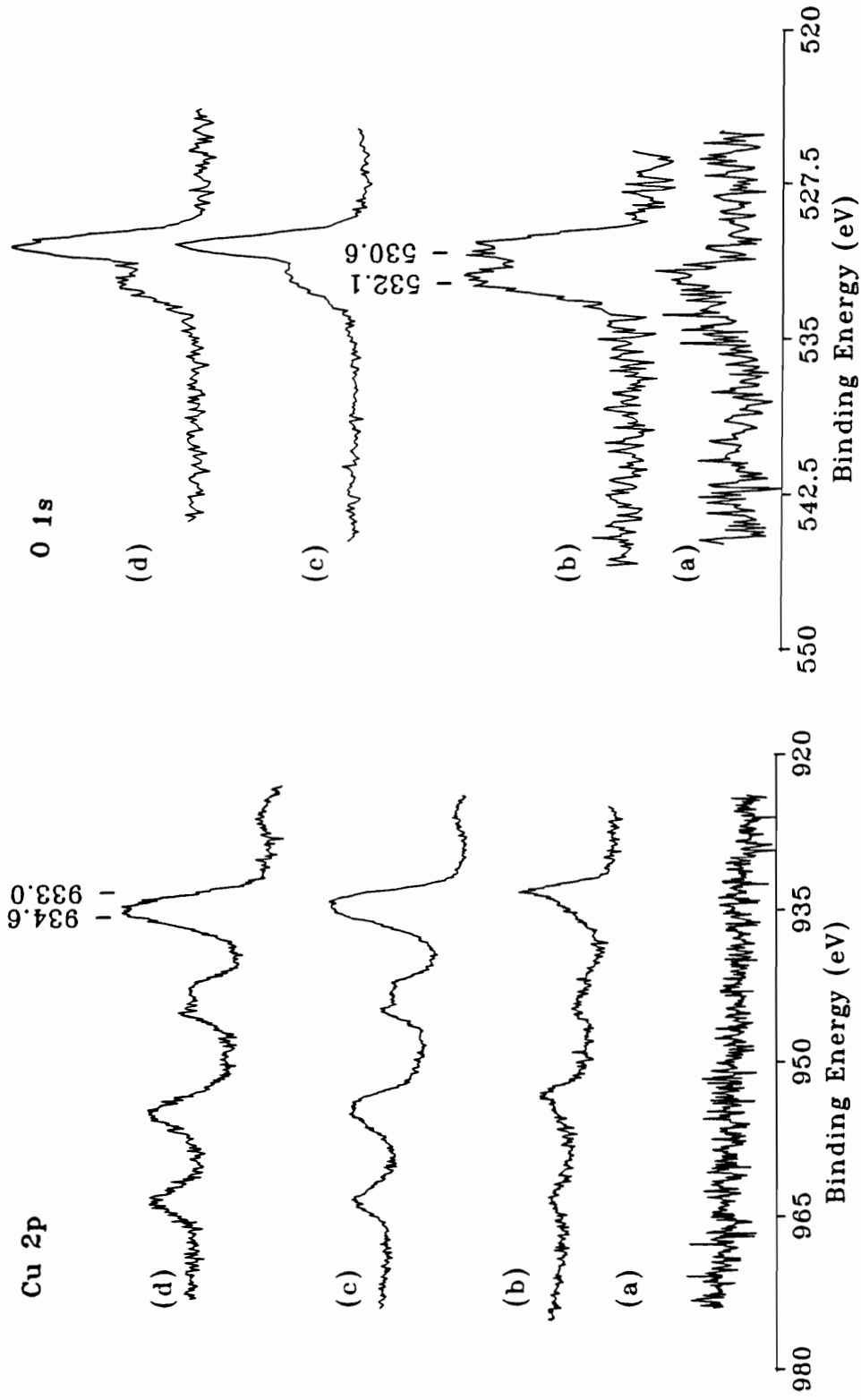


Figure 4.8 XPS analysis of the Cu 2p and O1s photopeaks at aging times of (a) 1 hour (b) 10 hours (c) 22 hours and (d) 85 hours for PPS films on copper foil at 210°C in air.

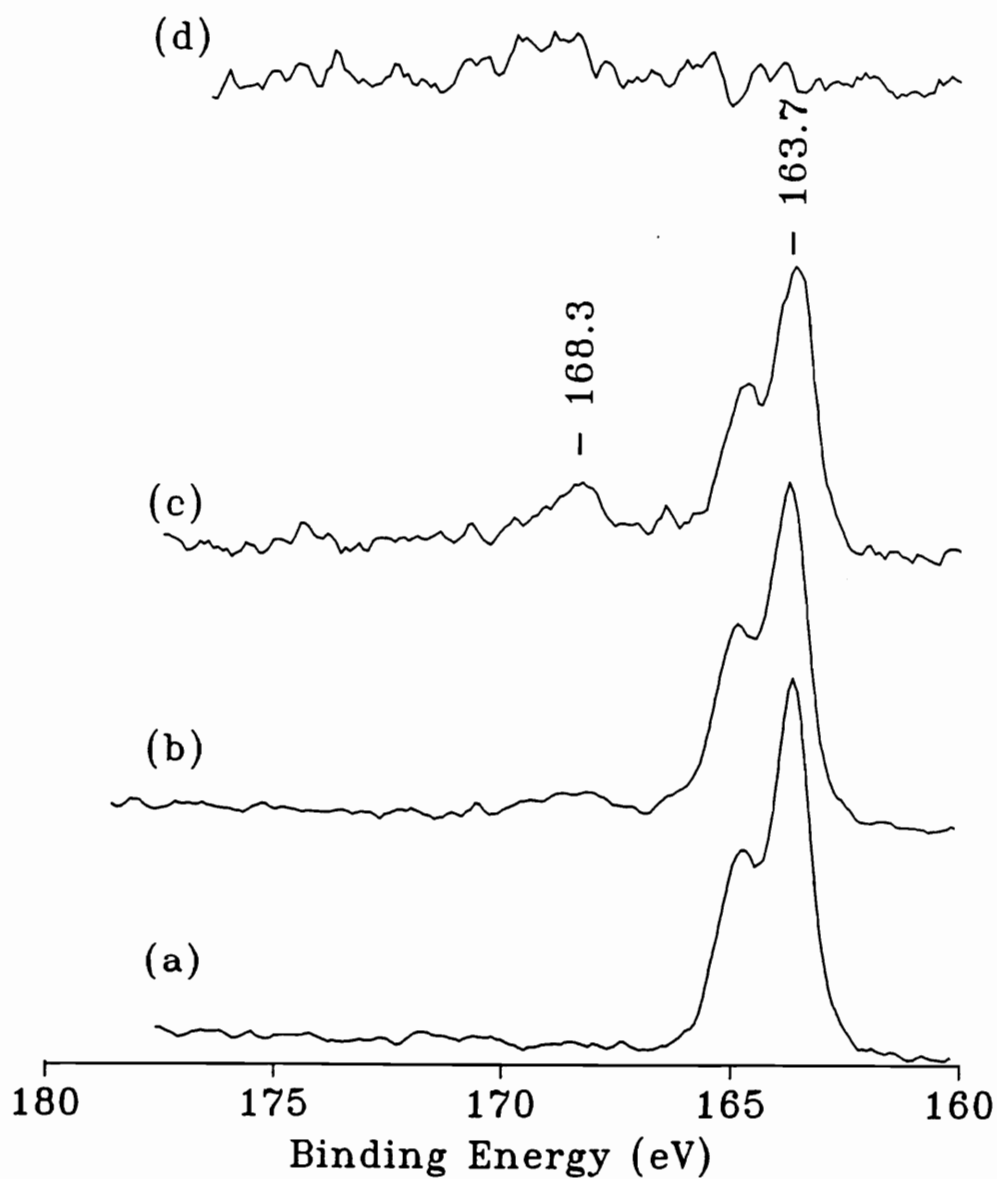


Figure 4.9 XPS analysis of the S 2p photopeak at aging times of (a) 1 hour (b) 10 hours (c) 22 hours and (d) 85 hours for PPS films on copper foil at 210° in air.

an air environment, showed that an iron sulfate interfacial species was formed with a S 2p peak position at 168.5 eV (95).

To compare the aging process of PPS coatings on another metal surface, Figure 4.10a shows a similar analysis of atomic concentration changes for the C 1s and O 1s photopeaks at different aging times on zinc. As is apparent, although a slight increase in the oxygen content is observed, little overall change in the atomic concentrations of these elements was detected. Fig 4.10b shows the analysis for the Zn 2p and S 2p photopeaks and indicates only a slight increase in zinc content and decrease in the sulfur content even after aging at 85 hours. This is in sharp contrast the results observed for copper, and shows that PPS coatings on zinc are relatively stable by comparison. Thus, the increases in oxygen content with loss of sulfur for PPS are distinctly related to the nature of the metal substrate.

4.3.1.2 IRRAS Analysis

While XPS analysis can provide information concerning the surface chemical changes associated with the aging of PPS films of copper, the technique is limited to approximately the top 10 nm of the film. This limits the information obtained to changes occurring in the surface regions of the coating. In contrast, infrared reflection absorption spectroscopy can sample the entire depth of the polymer film, and therefore can analyze the initial stages of polymer degradation. Figure 4.11 shows the ex-situ IRRAS analysis of a PPS coating (200 - 300 nm) on copper foil for an aging time of 15 minutes at 220°C. The spectrum shown represents the difference spectrum where the reference has been multiplied by a factor to account for the loss of material that was observed. Analysis of the spectrum shows two large peaks at 1549 and 1390 cm^{-1} and another at 1252 cm^{-1} . The first set of bands are associated with carboxylate functionality and similar spectral features have been seen in investigations of the aging of polyethylene of copper (42). The band at 1252 cm^{-1} can probably be attributed to aryl ether functionality associated with some oxidation of the surface film (94). Although not shown due to scaling problems, the most prominent feature in the aged film is a large band near 650 cm^{-1} associated with the formation of cuprous oxide. The

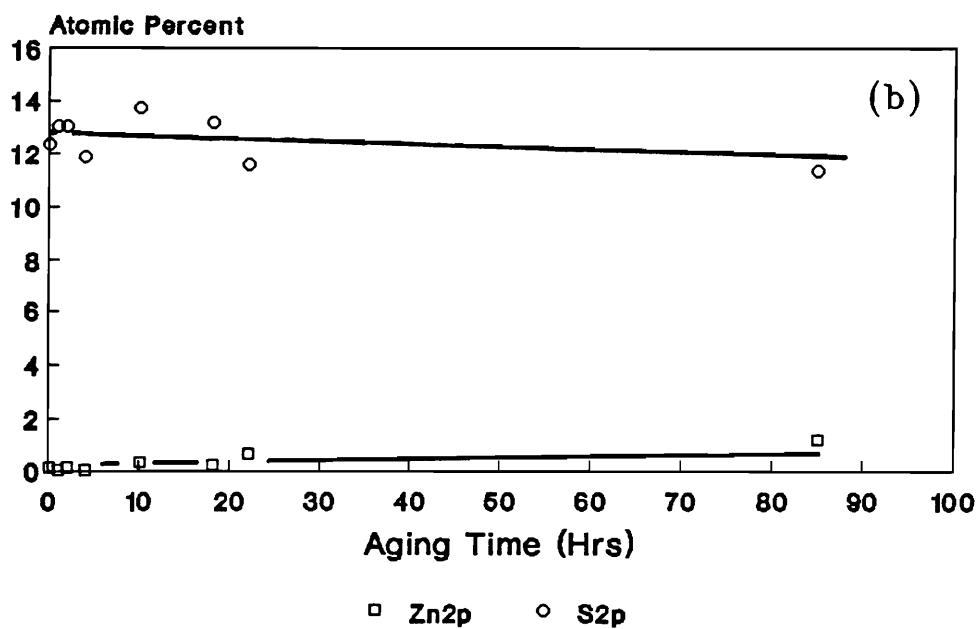
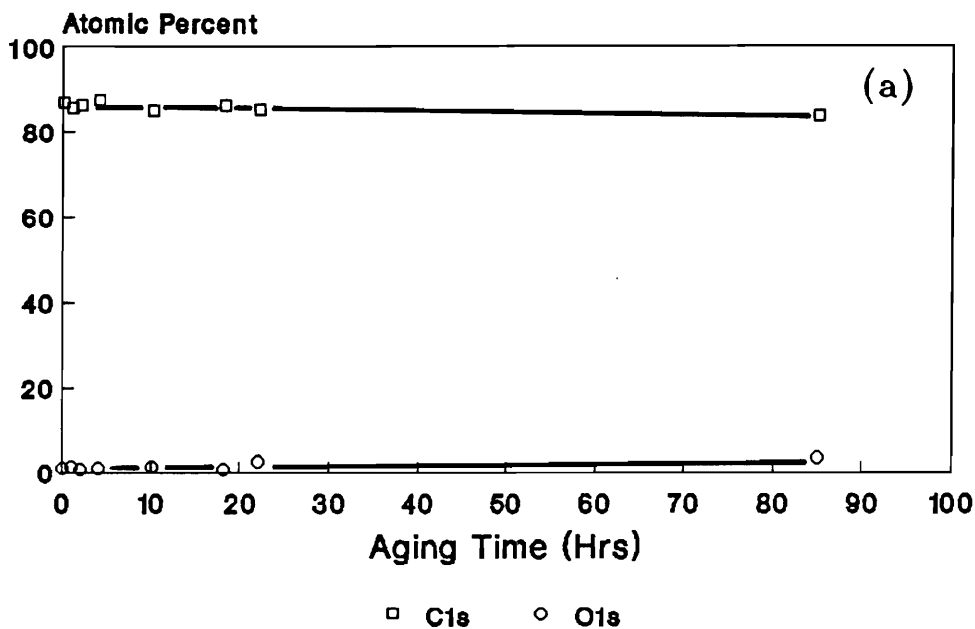


Figure 4.10 XPS analysis of the (a) C 1s and O 1s photopeak, and (b) Zn 2p and S 2p photopeak intensities at different aging times on zinc foil at 210°C in air.

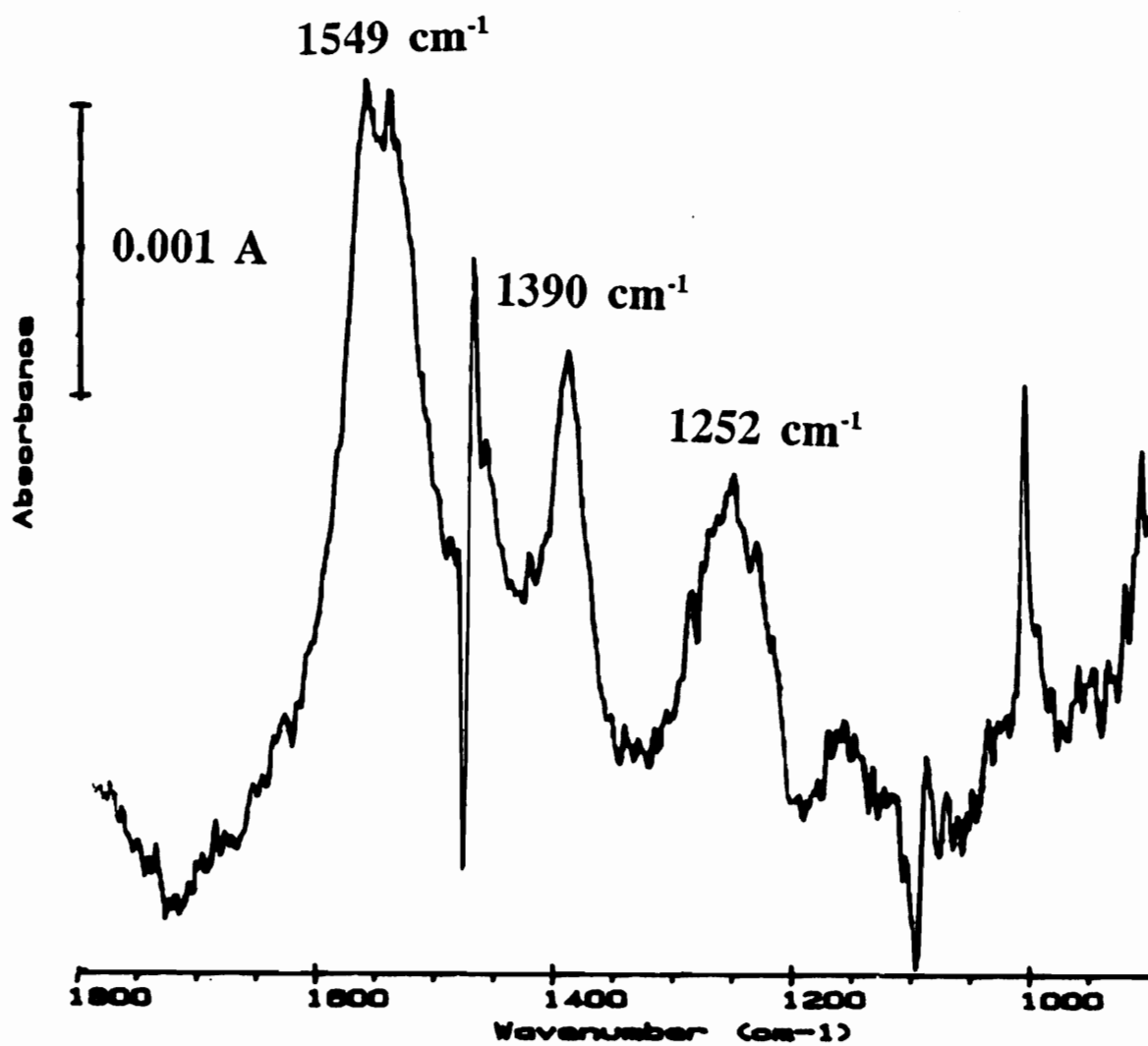


Figure 4.11 *Ex-situ* IRRAS analysis of PPS aging (1% spin coated) on a copper foil substrate after 15 minutes at 210°C.

general loss of polymer is also observed by an intensity loss in all absorbance bands. Similar analysis for PPS films on zinc substrates showed relatively few spectral changes.

To provide a more in depth analysis of the aging of PPS films by IRRAS, *in-situ* analysis was performed using variable temperature RAS. Figure 4.12 shows the spectral changes associated with exposure of a 200 - 300 nm PPS film on copper to elevated temperatures. The spectra show a large increase in cuprous oxide with elevated temperature exposure as evidence by the large absorbance near 625 cm^{-1} . The shift of this peak from 650 cm^{-1} to lower wavenumbers is due to the fact that the analysis was performed at an elevated temperature which tends to shift absorbances to lower frequencies. In addition to the increase in oxide, there is also a general decrease in all spectral features associated with the PPS surface film, and the appearance of a number of new absorbance bands. To further investigate this aging effect, Figure 4.13 shows the analysis of the same spectra in the limited spectral range of $1700\text{ to }1300\text{ cm}^{-1}$. As can be seen, new absorbance features appear near 1525 and 1400 cm^{-1} , and while the exact position is dependent on the temperature, the general features are clearly associated with carboxylate functionality. The results show that the formation of copper carboxylates are an important part of the degradation of PPS and this has been observed for the degradation of many polymers on copper substrates (38,42,49). Figure 4.14 shows the integrated peak areas versus temperature for the cuprous oxide absorbance band at $620 - 650\text{ cm}^{-1}$ and the C-H in-plane bend for PPS at approximately 1012 cm^{-1} . The plot shows little change in the relative amounts of oxide and polymer until approximately 175°C , where a rapid increase in oxide and loss of polymer is observed. This shows that the degradation of PPS occurs simultaneously with the formation of interfacial oxide. At longer times, no evidence for a surface polymer film can be seen.

To examine the aging of PPS films on other substrates surfaces, Figure 4.15 shows the IRRAS analysis of PPS coatings on chromium and a sputtered copper oxide surface, over a similar temperature range. As can be seen for both analyses, little degradation of the film is apparent. The fact that no carboxylate species are observed

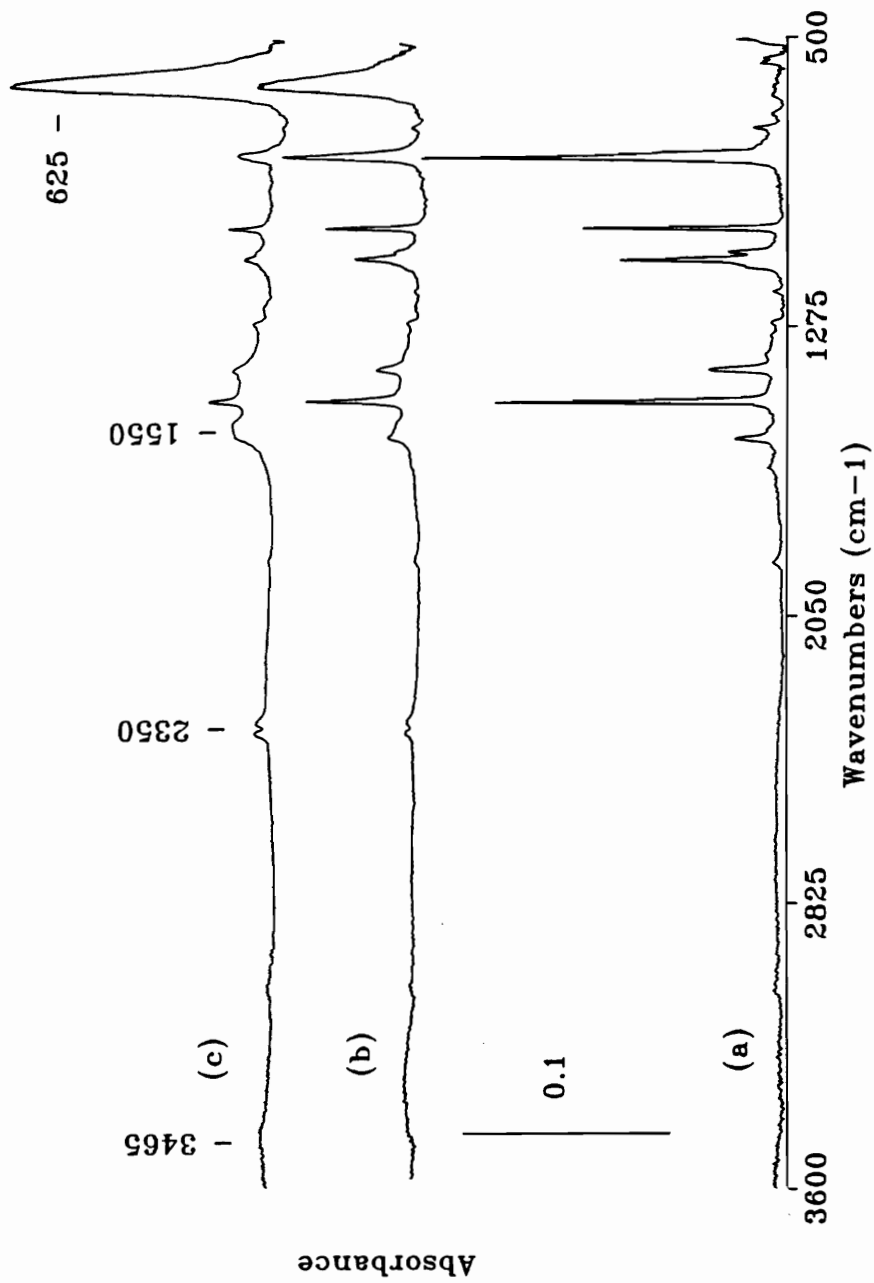


Figure 4.12 *In-situ* VTRAS analysis of a 2% (wt/wt) spin coated PPS film on copper foil in air. Spectra are shown at (a) room temperature, (b) 204°C, and (c) 221°C for a 5°C / min temperature ramp rate.

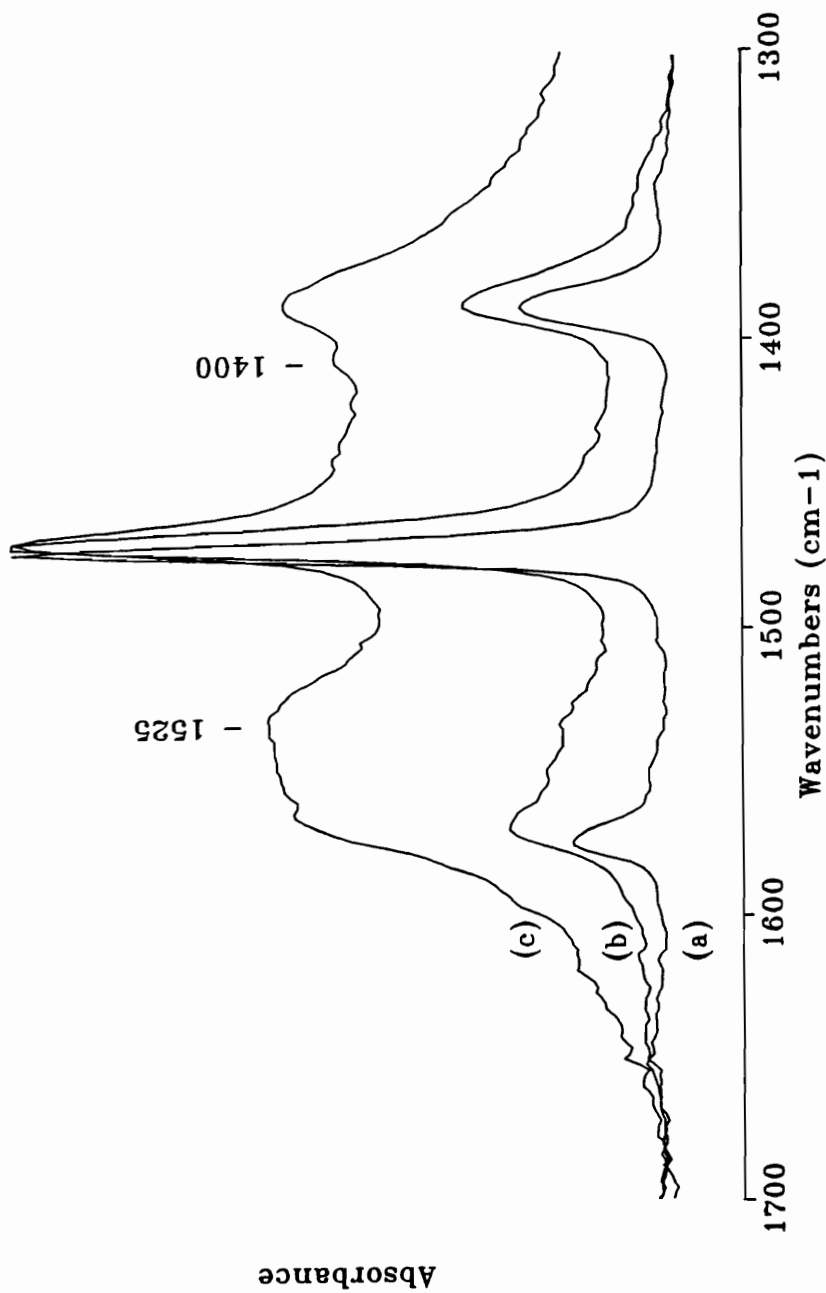


Figure 4.13 *In-situ* VTRAS analysis of a 2% (wt/wt) spin coated PPS film on copper foil in air in the 1300 - 1700 cm⁻¹ spectral region. Spectra are shown at (a) room temperature, (b) 204°C, and (c) 221°C for a 5°C / min temperature ramp rate.

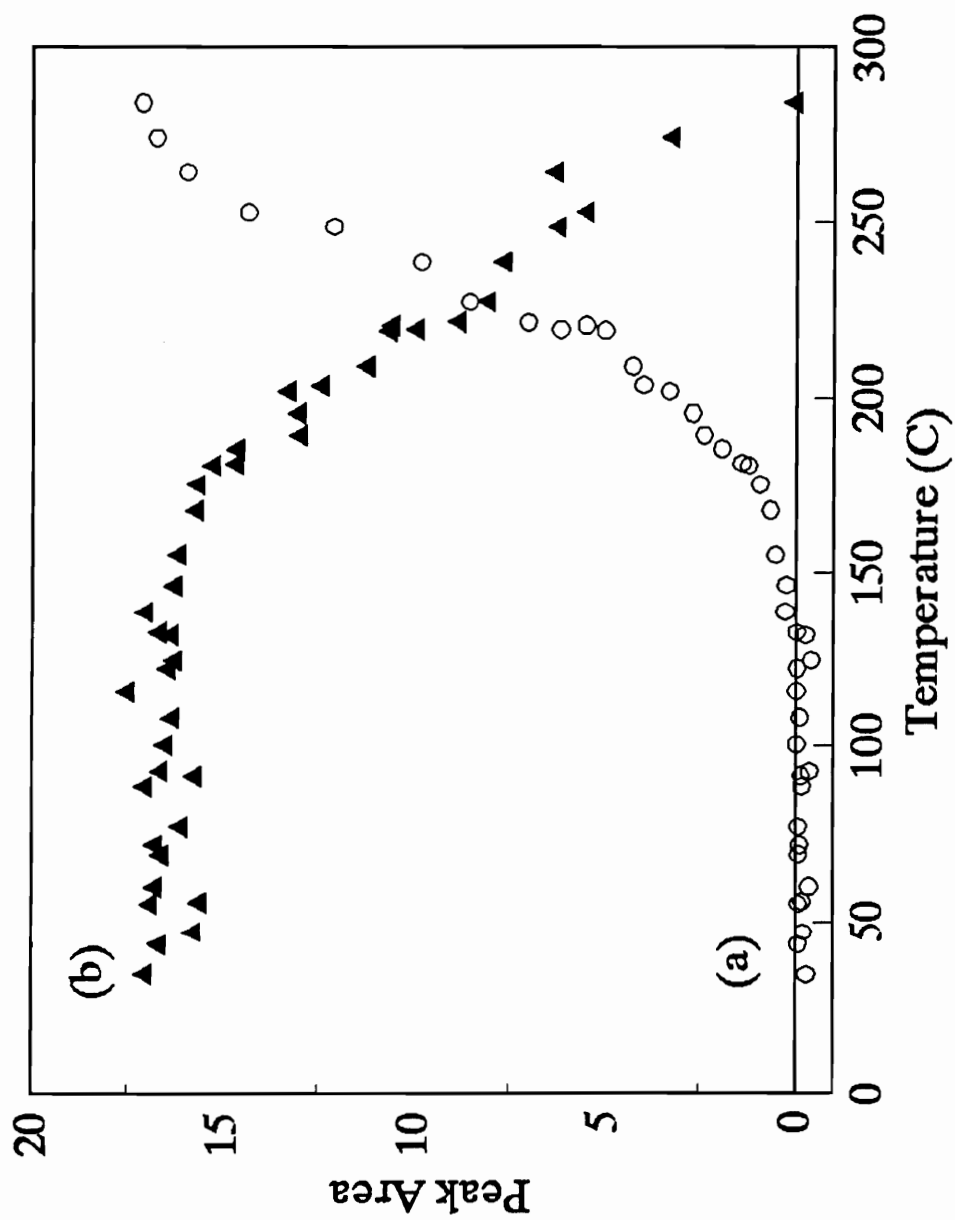


Figure 4.14 VTRAS analysis of the integrated peak areas versus temperature for the (a) 620 - 650 cm⁻¹, and (b) 1012 cm⁻¹ absorbance bands. Plot (b) was multiplied by a factor of 17.0 for scaling purposes.

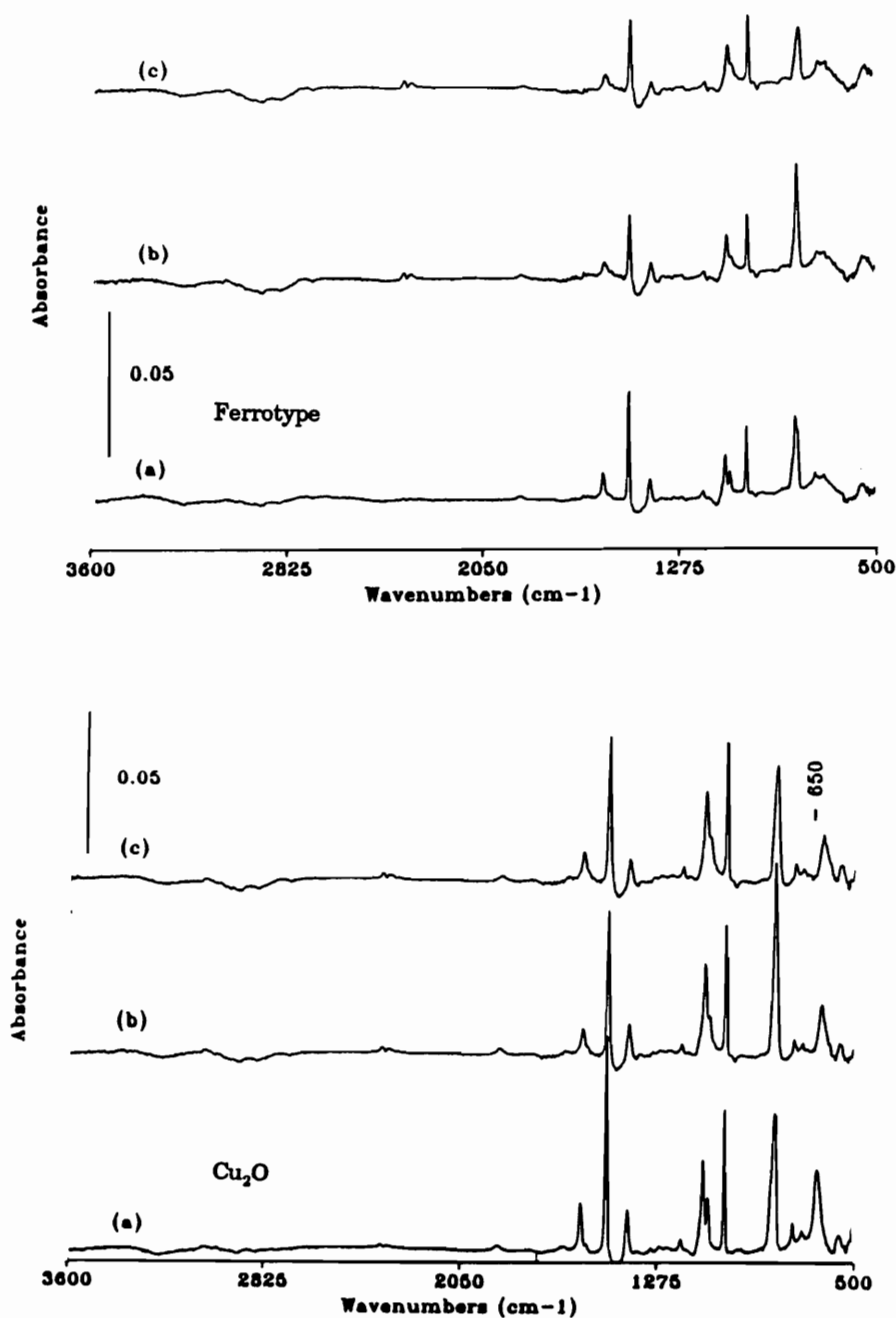


Figure 4.15 VTRAS analysis of a 1% (wt/wt) spin coated PPS film on a ferrottype substrate with spectra shown for (a) room temperature, (b) 194°C, and (c) 218°C. Also shown is the analysis for a 2% (wt/wt) spin coated PPS film on a sputtered cuprous oxide film for (a) room temperature, (b) 201°C, and (c) 223°C. A ramp rate of 5°C / min was used in all analyses.

for the copper oxide substrate indicates that the oxidation of copper metal plays a unique role in the formation of these species. After cooling, however, the spectrum showed some general loss of polymer for these surfaces, indicating some degradation may have occurred. Figure 4.16 shows a similar analysis for an aluminum substrate, and shows that even at temperatures near 300°C, there is little evidence for degradation. This result shows the unique role of copper metal in the degradation of PPS.

4.3.2 Bonding Studies

4.3.2.1 Analysis of Surface Pretreatment

Figure 4.17 shows the analysis of the Cu 2p and Cu(LVV) lines for copper foil surfaces pretreated with a methanol degrease, a nitric acid etch, and a 'brite dip' chemical polish. For the methanol degreased sample, the Cu 2p peak maximum near 935.1 eV, the broad Auger line centered near 337.0 eV, and the presence of shake up satellites in the Cu 2p spectrum most likely indicates a mixed oxide / hydroxide surface layer. Treatment by a nitric acid etch seems to remove most of the Cu⁺² species, and leaves a relatively thin surface cuprous oxide layer on copper metal. The evidence for metal is shown in the Auger line by a peak at 335.4 eV, and the 336.9 eV Auger peak with a corresponding O 1s peak position of 530.8 eV indicates that a layer of Cu₂O is present. The 'brite dip' polish appears to remove most of the surface oxide as only one major peak component due to copper metal is found for the copper Auger analysis at 335.4 eV. An O 1s signal at 531.6 eV may indicate a thin layer of surface carboxylate is present as might be expected from the large component of acetic acid in the etching solution. The effect of pretreatment by thermal oxidation is shown in Figure 4.18 and shows the XPS analysis before and after the oxidation step. Clearly, the shift of the Auger line from 335.4 to 337.4 eV with little change in the Cu 2p line indicates the formation of a surface cuprous oxide layer. An O 1s photopeak centered at 530.7 eV is in agreement with these results. Figure 4.19 shows the results of XPS analysis before and after chemical oxidation in and alkaline persulfate solution and the shift in the Cu 2p line from approximately 933 eV to 934 eV with a small shift in the Auger

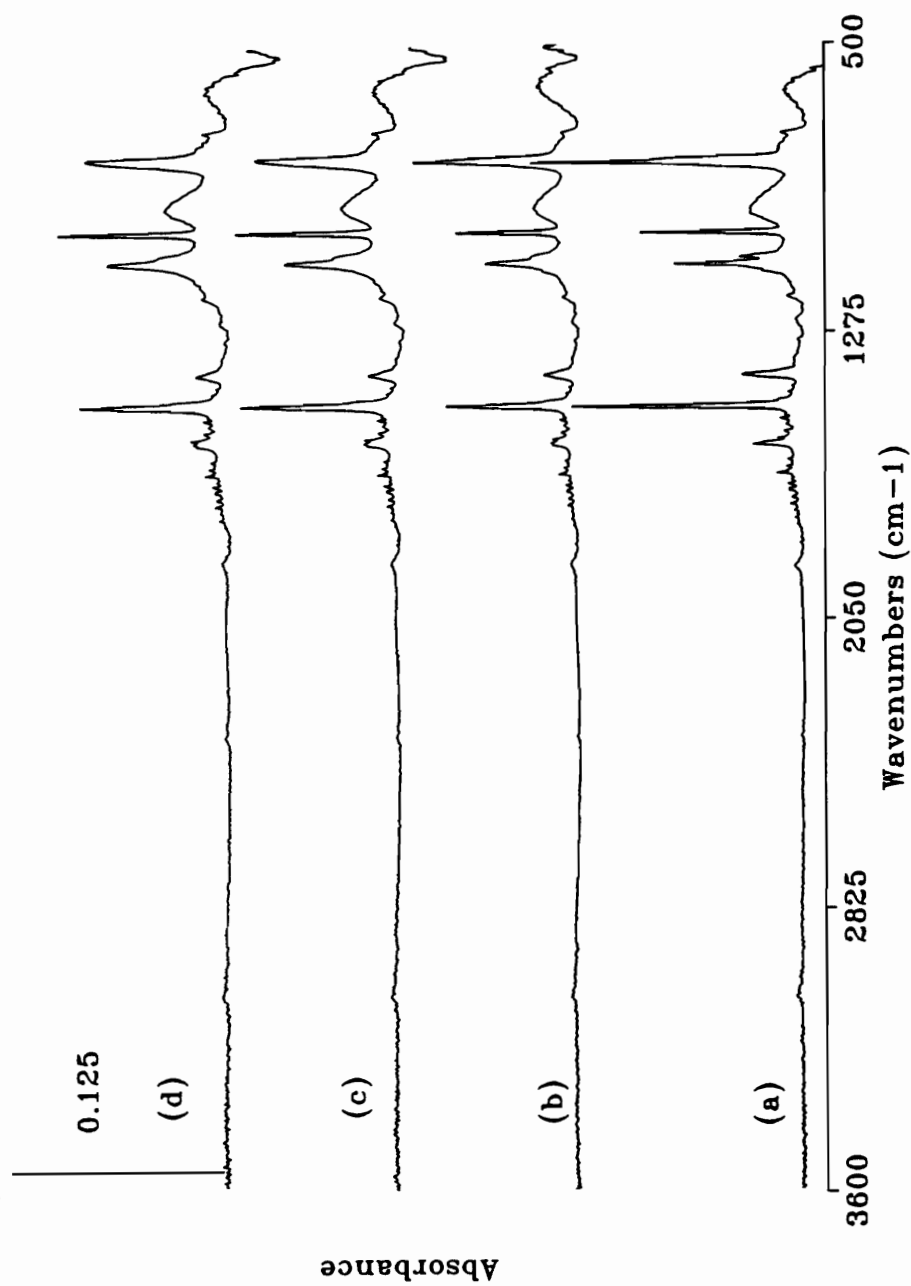


Figure 4.16 VTRAS analysis of a 2% (wt/wt) spin coated PPS film on an aluminum foil substrate. Shown are spectra for (a) room temperature, (b) 216°C, (c) 250°C, and (d) 282°.

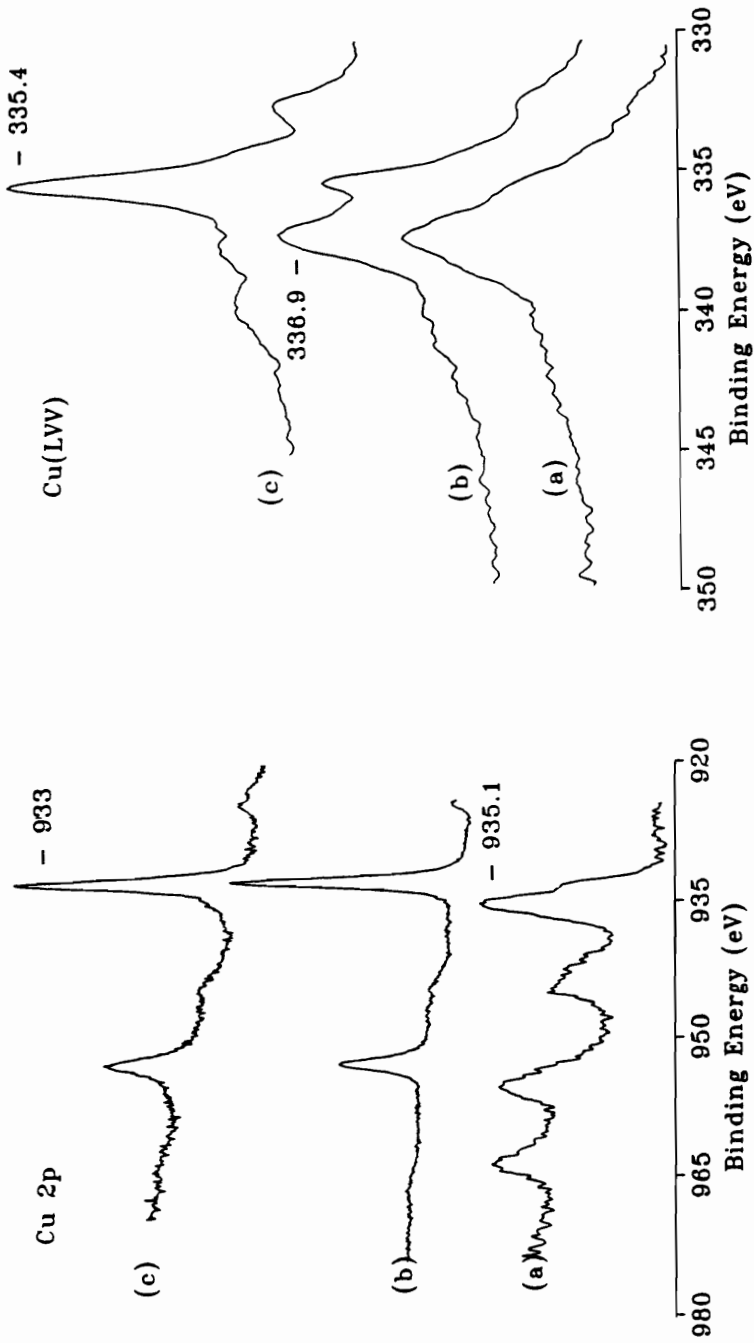


Figure 4.17 XPS analysis of the Cu 2p and Cu(LVV) spectral lines for (a) methanol washed, (b) nitric acid treated, and (c) 'brite dip' treated copper foil.

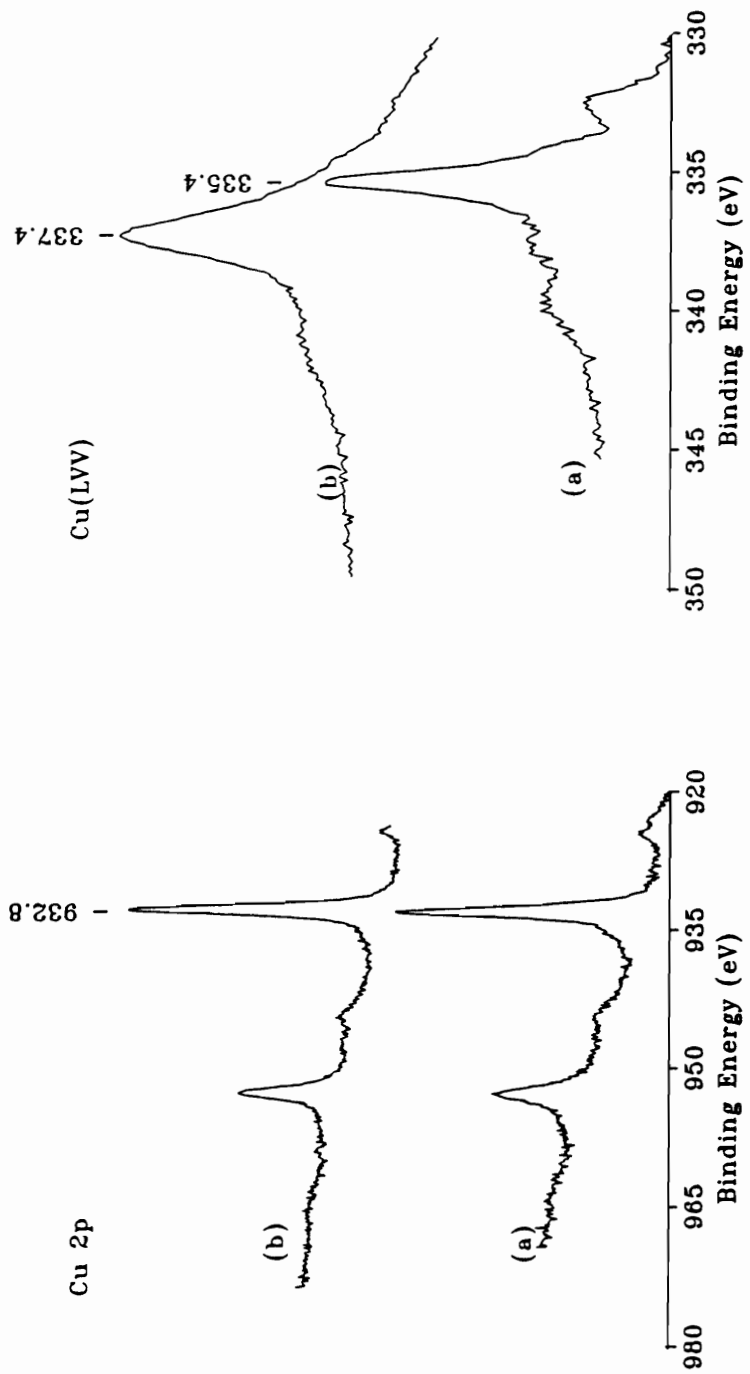


Figure 4.18 XPS analysis of the Cu 2p and Cu(LVV) spectral lines for (a) 'brite dip' treated, and (b) thermally oxidized copper foil.

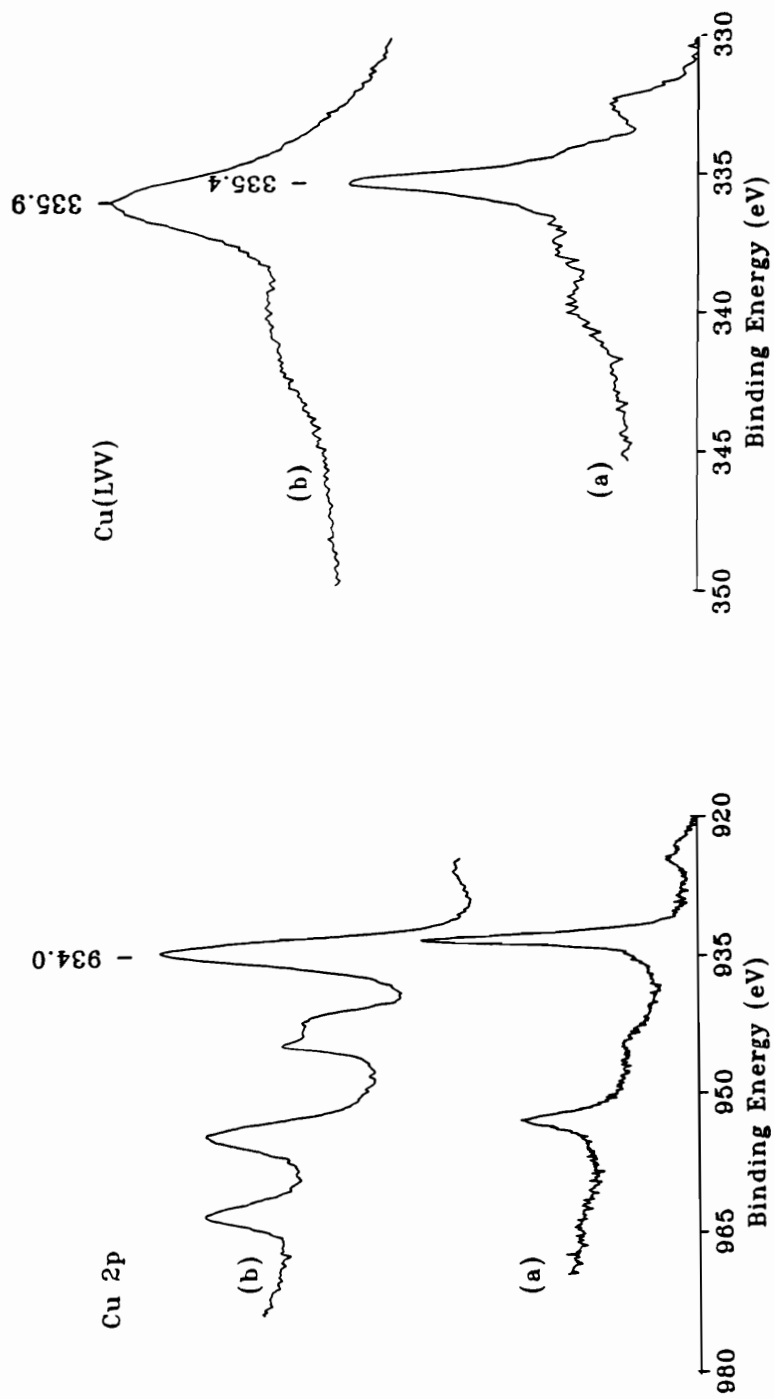


Figure 4.19 XPS analysis of the Cu 2p and Cu(LVV) spectral lines for (a) brite dip treated and (b) chemically oxidized copper foil.

line from 335.4 to 335.9 eV is consistent with a surface layer of cupric oxide. An O 1s photopeak position at 529.7 eV is in agreement with this, although a shoulder at 531.3 eV may indicate some surface hydroxide species. The complete XPS analysis for all surface pretreatments is given in Table 4.3. In general, the methanol wash probably does little to change the native surface oxide layer, while acid etches result in a metal substrate with a thin surface oxide or acetate layer. Thermal oxidation gives primarily a cuprous oxide surface while chemical oxidation yields primarily cupric oxide surface chemistry.

To investigate the morphological changes associated with the thermal and chemical treatment procedures, Figure 4.20 shows the SEM micrographs of both the 'brite dip' chemically polished and thermally oxidized foil samples. As can be seen, although the roller marks are clearly visible, there is little change due to the thermal oxidation step. Figure 4.21 shows the SEM analysis for the chemically oxidized foil sample and the unique morphology generated by this pretreatment is evident. The needle-like structures formed are in agreement with previous results reported for the pretreatment of copper sheets (27).

4.3.2.2 Peel Test Analysis

Table 4.4 shows the peel strengths obtained for the five pretreatments used in this study. The methanol degreased sample shows an extremely low peel strength, averaging only 3 g/mm for the samples tested. The use of acid etches also does not significantly improve the adhesive strength as might be expected. Chemical oxidation results in a dramatic improvement in bond strength and this might be expected given the given the needle-like morphology previously shown for this pretreatment (see Fig. 4.21). The most dramatic results, however, are found for the thermal oxidation pretreatment which shows an almost ten fold increase in the adhesive strength compared to the methanol degreased or acid etched samples. SEM analysis of the surface prior to bonding showed no major change in substrate morphology, and XPS indicated that a relatively simple cuprous oxide surface layer was present. The short

Table 4.3 XPS Atomic Concentrations for Pretreated Copper Foil Surfaces.

<u>Pretreatment</u>	<u>ELEMENT</u>					
	<u>C1s</u>	<u>O1s</u>	<u>S2p</u>	<u>Cu2p</u>	<u>Cu(A)</u>	<u>Cl2p</u>
<i>MeOH</i>	43.3 (285.0)	45.2 (531.8)	NSP -----	11.5 (935.1)	----- (337.4)	< 0.5 -----
<i>Nitric Acid</i>	46.3 (285.0)	27.4 (530.8)	NSP -----	26.0 (932.9)	----- (337.3) (335.4)	< 0.5 -----
<i>Brite Dip</i>	31.1 (285.0)	29.7 (531.6)	<0.5 -----	35.9 (933.1)	----- (335.4)	< 0.5 -----
<i>Thermal Oxidation</i>	58.8 (285.0)	26.4 (530.7)	NSP -----	12.1 (932.8)	----- (337.3)	2.7 (200.7)
<i>Chemical Oxidation</i>	38.6 (285.0)	42.2 (529.7) (531.3)	NSP -----	19.2 (934.0)	----- (335.9)	NSP -----

NSP - No significant peak. Binding energies are given in parenthesis 0.

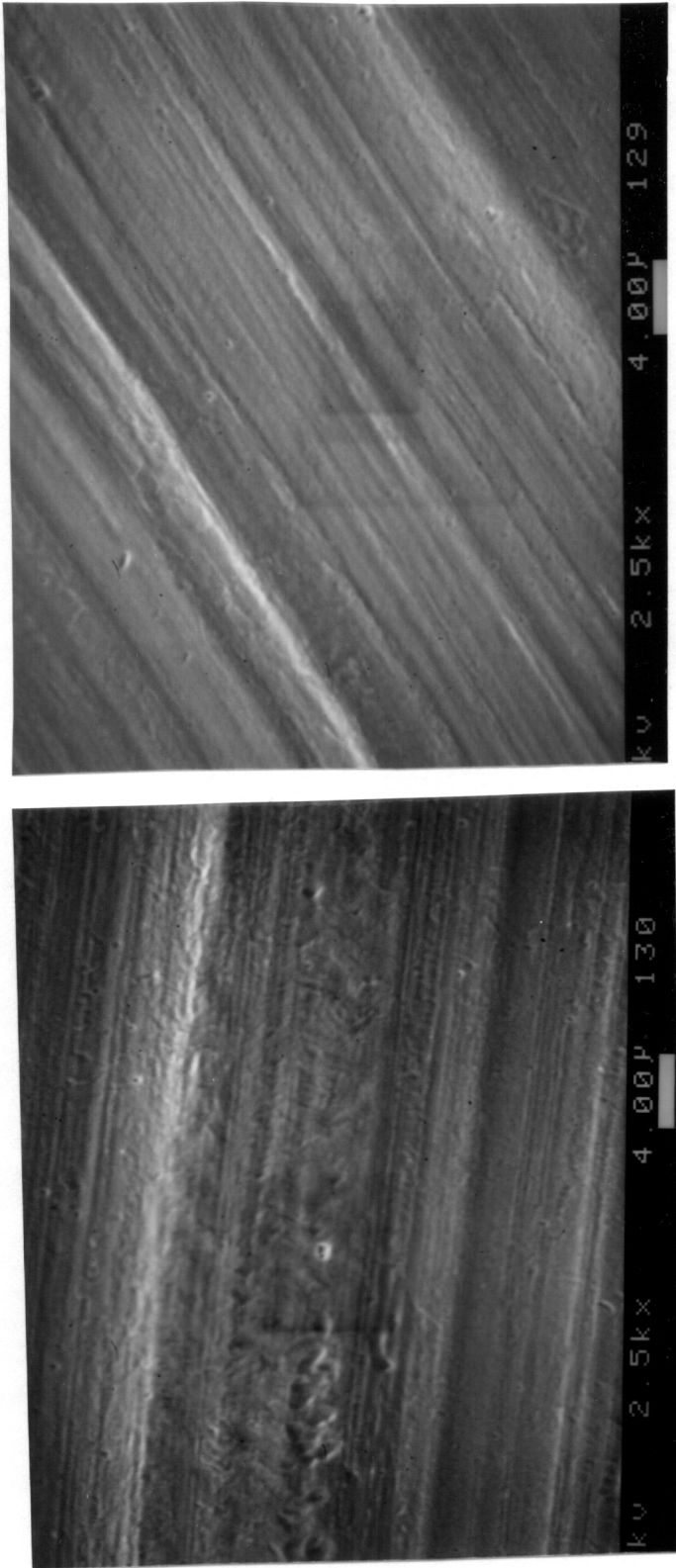


Figure 4.20 SEM analysis of copper foil surfaces for (a) 'brite dip' treated, and (b) thermally oxidized samples.

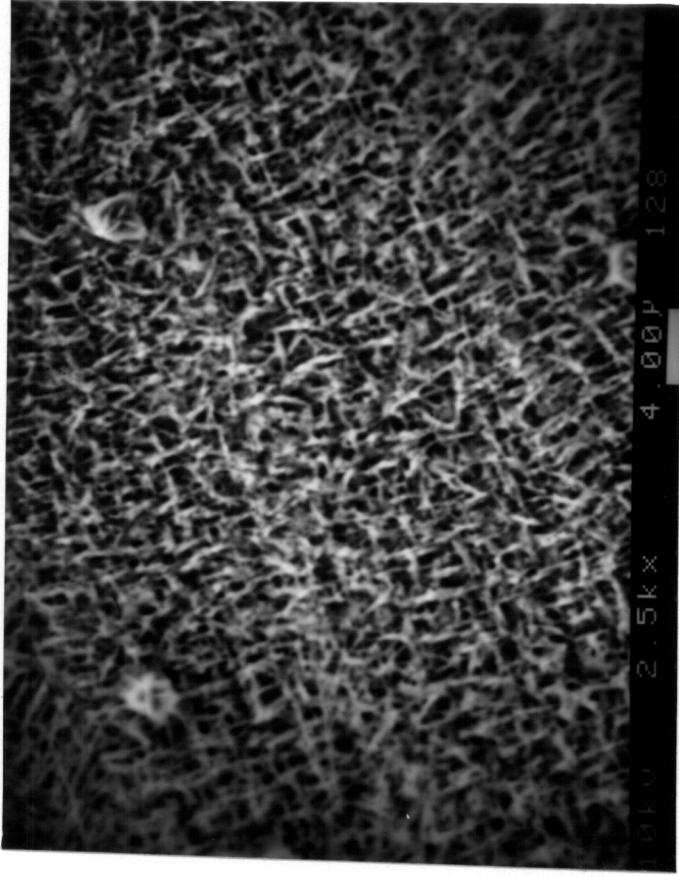


Figure 4.21 SEM analysis of a chemically oxidized copper foil sample.

Table 4.4 Peel Test Analysis of Copper / PPS Adhesion

<u>TREATMENT</u>	<u>PEEL STRENGTH (g/mm)</u>
MEOH	3 ± 2
20% Nitric Acid	3 ± 1
Brite Dip	5 ± 2
Thermal Oxidation	40 ± 6
Chemical Oxidation	27 ± 7

one minute oxidation step would also not be expected to significantly alter the mechanical properties of the copper film, thus leading to changes in peel strength. The results, therefore, must be related to the particular surface chemistry involved between PPS and this copper substrate.

4.3.2.3 Failure Surface Analysis

Figure 4.22 shows the results of the XPS analysis of the Cu 2p and Cu (LVV) lines for the failure surfaces for the methanol degreased copper foil samples. As is evident from analysis of both lines, the original surface consisting of a mixed oxide / hydroxide layer has been reduced to copper metal as evident by the Cu (LVV) Auger line at 335.3 eV. A second Auger peak at 336.9 eV is also apparent and with the Cu 2p photopeak position at 933.0 eV, indicates a Cu⁺ surface species. Figure 4.23 shows the analysis of the S 2p photopeak for both the adhesive and foil failure surfaces and it is apparent that considerable sulfur remains on the foil failure surface. The photopeak at 163.7 eV corresponds to a thin PPS layer (95) while the peak at 162.2 eV can be assigned to a copper sulfide species (31). Angular analysis indicated that the sulfide layer was beneath the thin PPS surface film, indicating that fracture occurred through a PPS surface layer with this assignment. In agreement, no copper was detected on the adhesive failure surface. Figure 4.24 shows a similar analysis of the S 2p and Cu (LVV) lines for the 'brite dip' cleaned copper foil. The Cu (LVV) shows the new peak at 336.9 eV for the foil failure surface and the sulfur line again shows the presence of copper sulfide at 162.2 eV. The Auger signal can be attributed in part to the presence of cuprous sulfide. Figure 4.25 gives the analysis for the nitric acid cleaned copper foil and shows the partial reduction of oxide to metal as shown by the increase in the 335.3 eV Auger line and decrease in the 336.9 eV oxide peak. Again, copper sulfide is indicated in the S 2p photopeak by the presence of the photopeak at 162.3 eV. Table 4.5 shows the complete analysis of the methanol and acid cleaned foil failure surfaces. The most noticeable general feature is the extremely small oxygen concentration found for the failure surfaces when compared to surfaces prior to bonding. Secondly, the appearance of copper sulfide is found for all foil failure

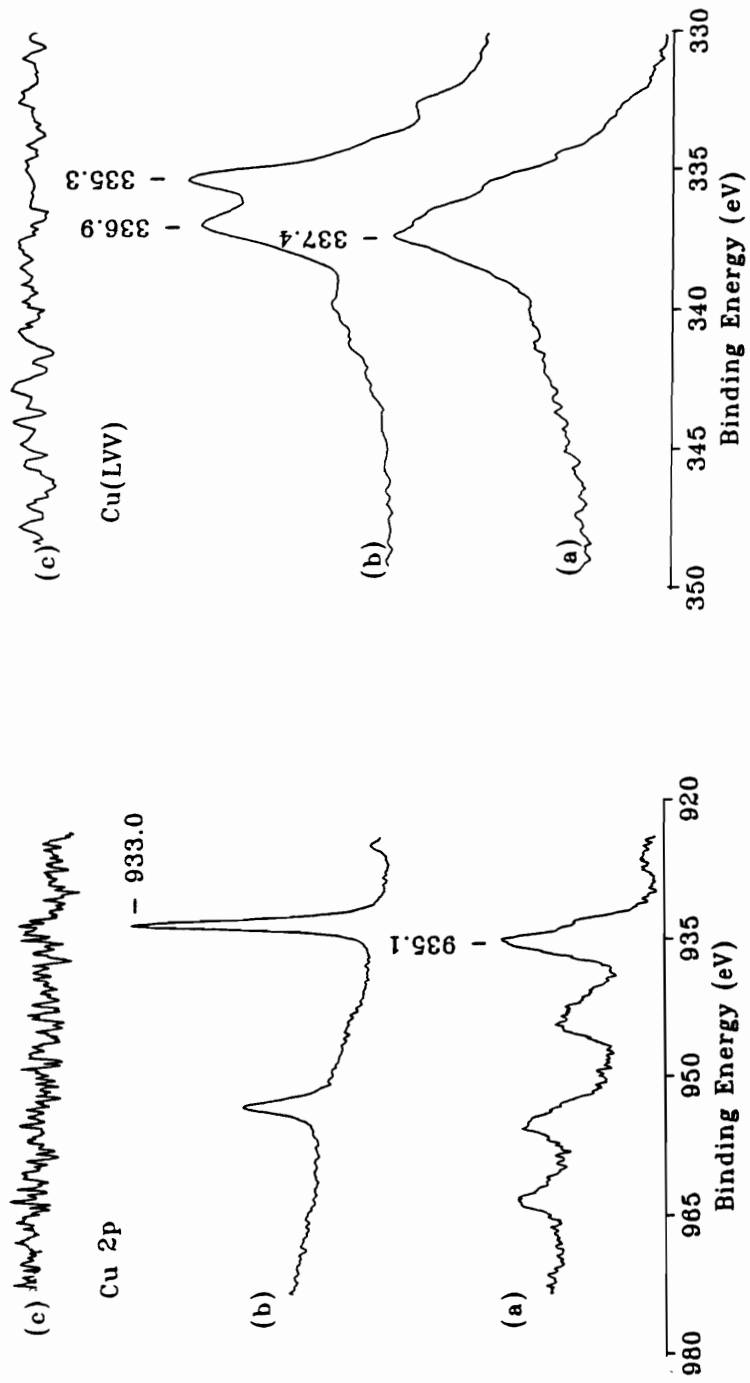


Figure 4.22 XPS analysis of the Cu 2p and Cu(LVV) lines for failure surfaces of PPS bonded to methanol degreased copper foil showing (a) the foil surface before bonding, (b) the foil failure surface, and (c) the adhesive failure surface.

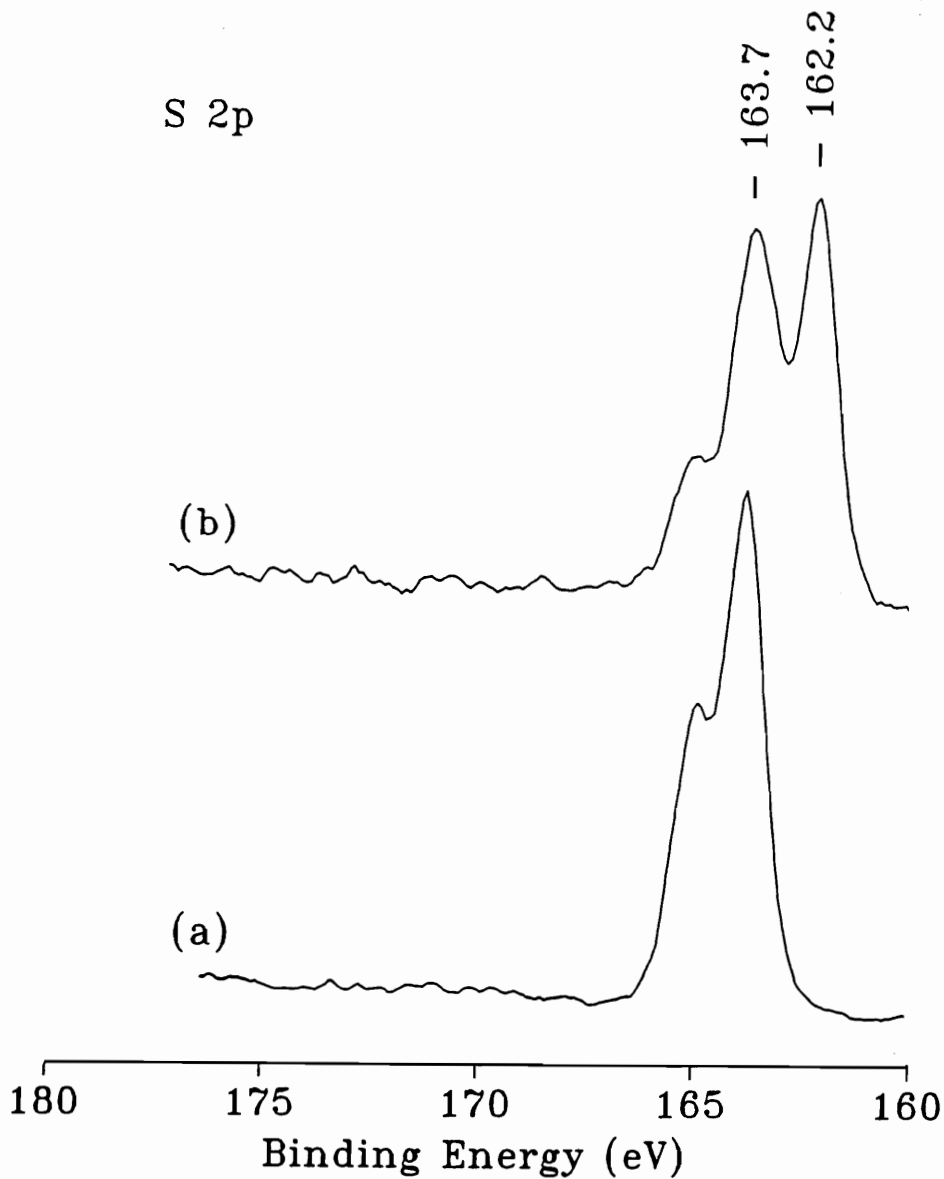


Figure 4.23 XPS analysis of the S 2p photopeak of failure surfaces for PPS bonded to methanol degreased copper foil for (a) the adhesive failure surface, and (b) the foil failure surface.

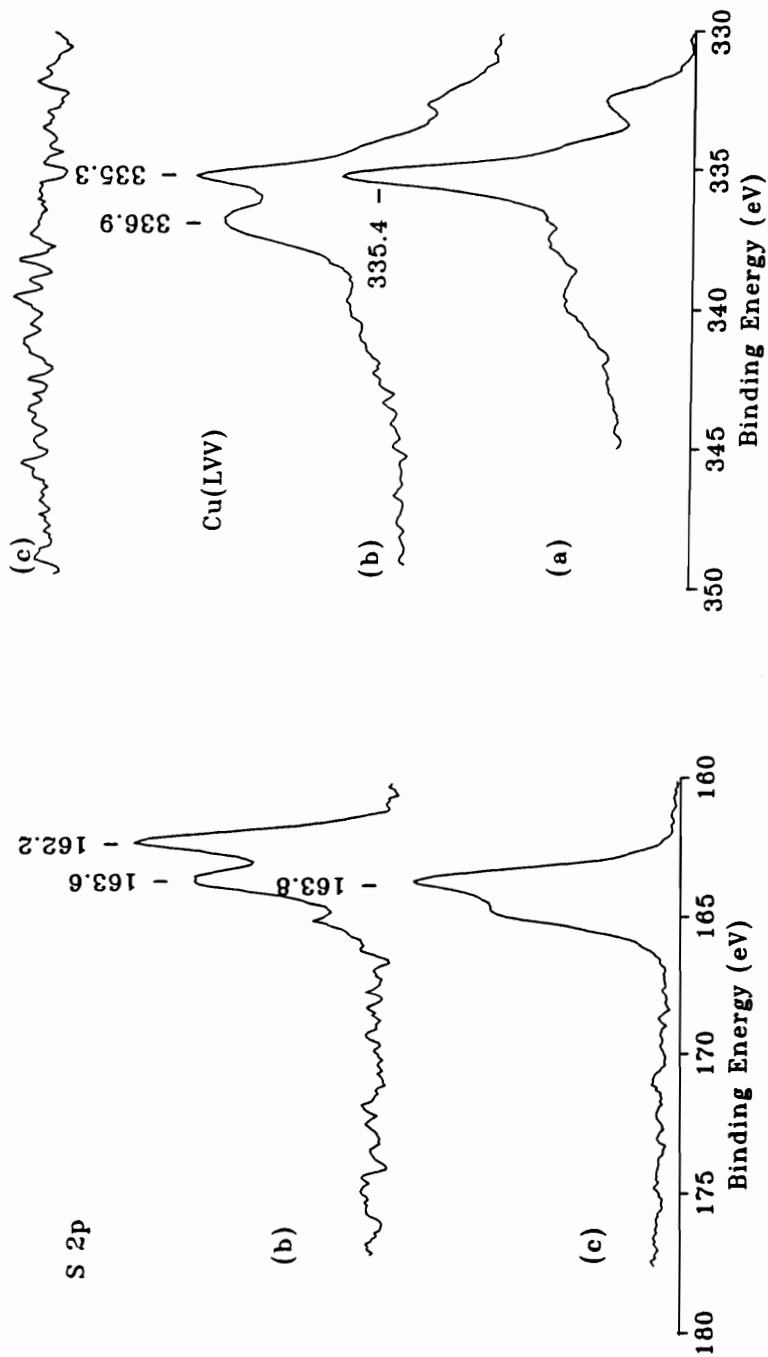


Figure 4.24 XPS analysis of the S 2p and Cu(LVV) peaks for failure surfaces of PPS bonded to 'brite dip' etched copper foil showing (a) the foil surface before bonding, (b) the foil failure surface, and (c) the adhesive failure surface.

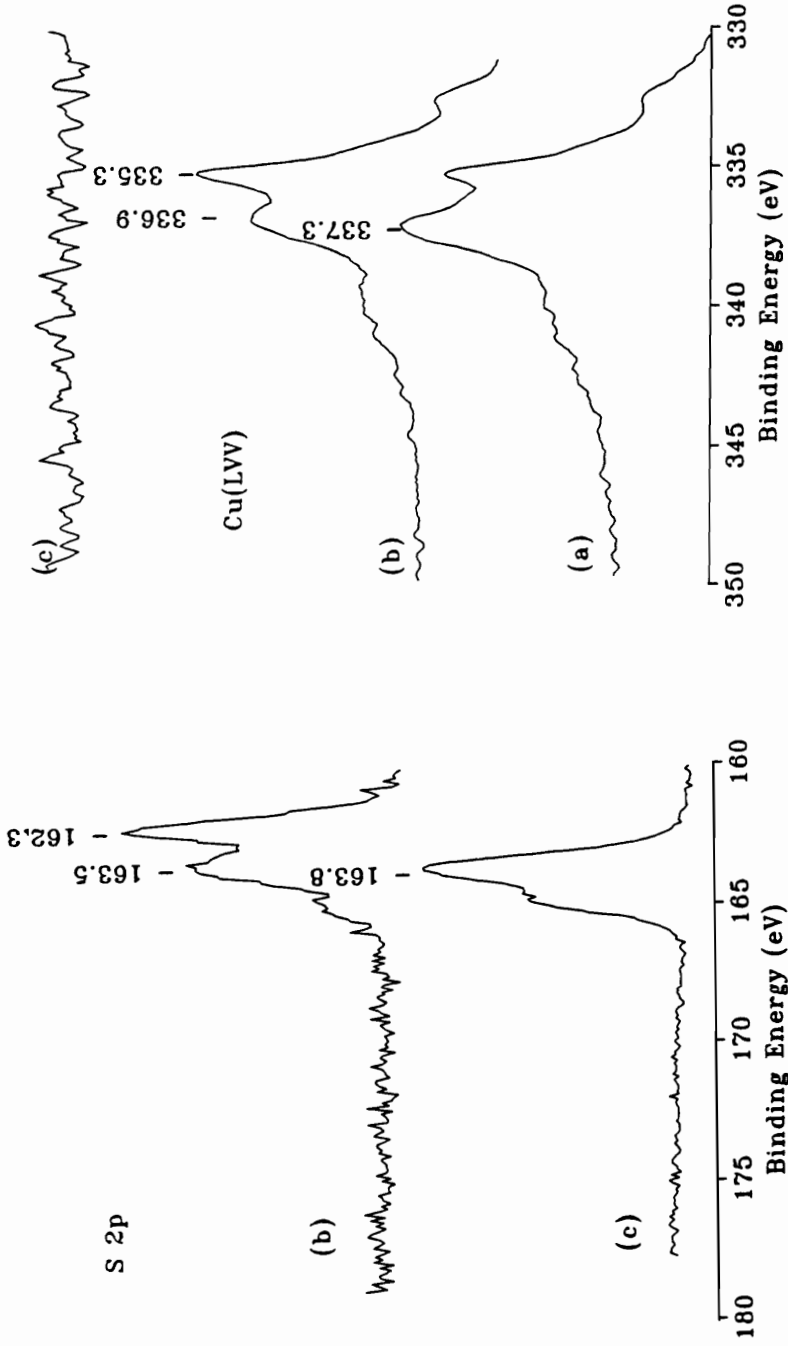


Figure 4.25 XPS analysis of the S 2p and Cu(LVV) peaks for failure surfaces of PPS bonded to nitric acid etched copper foil showing (a) the foil surface before bonding, (b) the foil failure surface, and (c) the adhesive failure surface.

Table 4.5 XPS Atomic Concentrations for Copper Foil/PPS Failure Surfaces.

	<u>SURFACE</u>	<u>ELEMENT</u>					
		<u>Cl1s</u>	<u>O1s</u>	<u>S2p</u>	<u>Cu2p</u>	<u>Cu(A)</u>	<u>Cl2p</u>
MEOH	<i>Foil side</i>	66.8 (285.0)	3.4 (531.8)	15.6 (163.7) (162.2)	11.5 (933.0)	----- (336.9) (335.3)	2.7 -----
	<i>Adh. side</i>	82.6 (285.0)	2.2 (532.3)	15.2 (163.8)	NSP -----	NSP -----	NSP -----
NITRIC ACID	<i>Foil side</i>	62.3 (285.0)	1.9 (531.6)	15.9 (163.5) (162.3)	16.7 (933.0)	----- (336.9) (335.3)	3.2 (198.9)
	<i>Adh. side</i>	84.9 (285.0)	1.0 (532.5)	14.1 (163.8)	NSP -----	NSP -----	NSP -----
BRITE DIP	<i>Foil side</i>	64.0 (285.0)	3.2 (531.2)	13.2 (163.6) (162.2)	19.6 (932.8)	----- (336.9) (335.3)	----- -----
	<i>Adh. side</i>	86.1 (285.0)	2.8 (533.1)	11.1 (163.8)	NSP -----	NSP -----	NSP -----

NSP - No significant peak. Binding energies are given in parenthesis ().

surfaces. An average oxygen content of only 1 - 3% for all failure surfaces is extremely interesting given the large oxygen content on the pretreated surfaces prior to bonding. It is important to note that foil failure surfaces rapidly oxidized on exposure to air, indicating the need for immediate analysis after debonding. A large sulfur signal ranging from 13 - 15% on the foil failure surfaces is seen, and a substantial amount of the total signal represents inorganic sulfur. The generally similar chemical composition for all samples implies that the interfacial chemistry involved for all these samples may be the same.

Figure 4.26 shows the analysis of the Cu (LVV) Auger and the S 2p lines for the thermally oxidized foil samples, and a dramatic difference can be seen when the plots are compared to those for methanol and acid clean foil surfaces above. For the Auger line, although a slight peak at 335.3 eV may indicate some reduction of oxide in the bonding process, the foil failure surface appears very similar to the original pretreated surface. Also, a small Auger signal at approximately 339.5 eV is seen on the adhesive failure surface, although the identity of such a high binding energy peak is not clear. Although the S 2p photopeak shows some evidence of inorganic sulfur at 162.3 eV, the relative amount present when compared to previous pretreatments is less, and indicates either a shift of the average failure plane into the adhesive, or a lower concentration of copper sulfide at the interface.

Figure 4.27 shows the XPS narrow scan plots for the Cu (LVV) line, and both the Cu 2p and S 2p photopeaks for chemically oxidized copper foil. The loss of shake up features and shift to 933 eV in the Cu 2p spectrum with a shift from 335.9 to 337.2 eV in the Auger plot show the general reduction of cupric to cuprous oxide. Also, analysis of the sulfur spectrum shows only the presence of organic sulfur due to PPS. Analysis of all plots indicates the same chemistry on both the foil and adhesive failure surfaces and shows a great deal of interdiffusion between the surface copper oxide and polymer with fracture occurring in the mixed layer. This could be expected given the fragile needle-like structure of the surface oxide formed during the chemical oxidation procedure. With the bonding conditions used, the surface structure is probably destroyed, and the oxide readily mixing with the molten PPS. The reduction of oxide

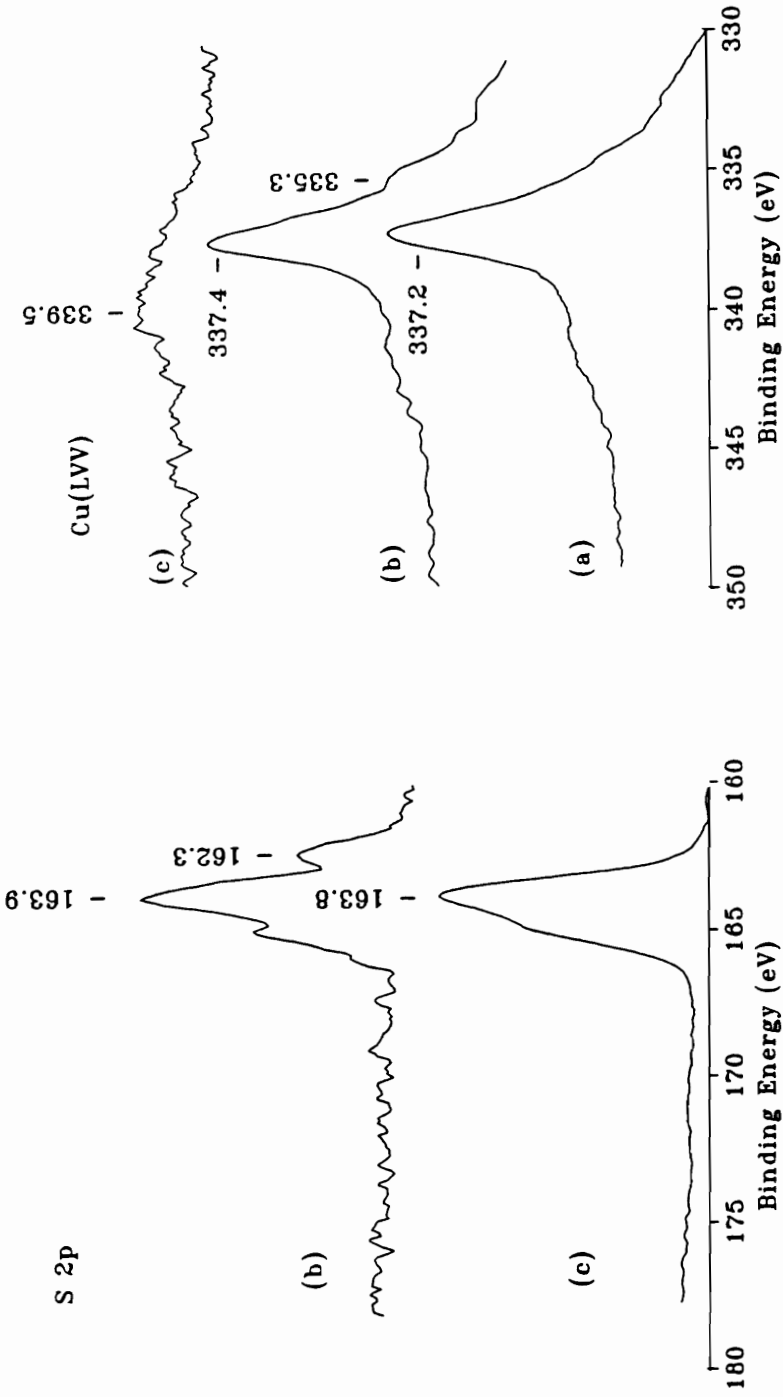


Figure 4.26 XPS analysis of the S 2p and Cu(LVV) peaks for failure surfaces of PPS bonded to thermally oxidized copper foil showing (a) the foil surface before bonding, (b) the foil failure surface, and (c) the adhesive failure surface.

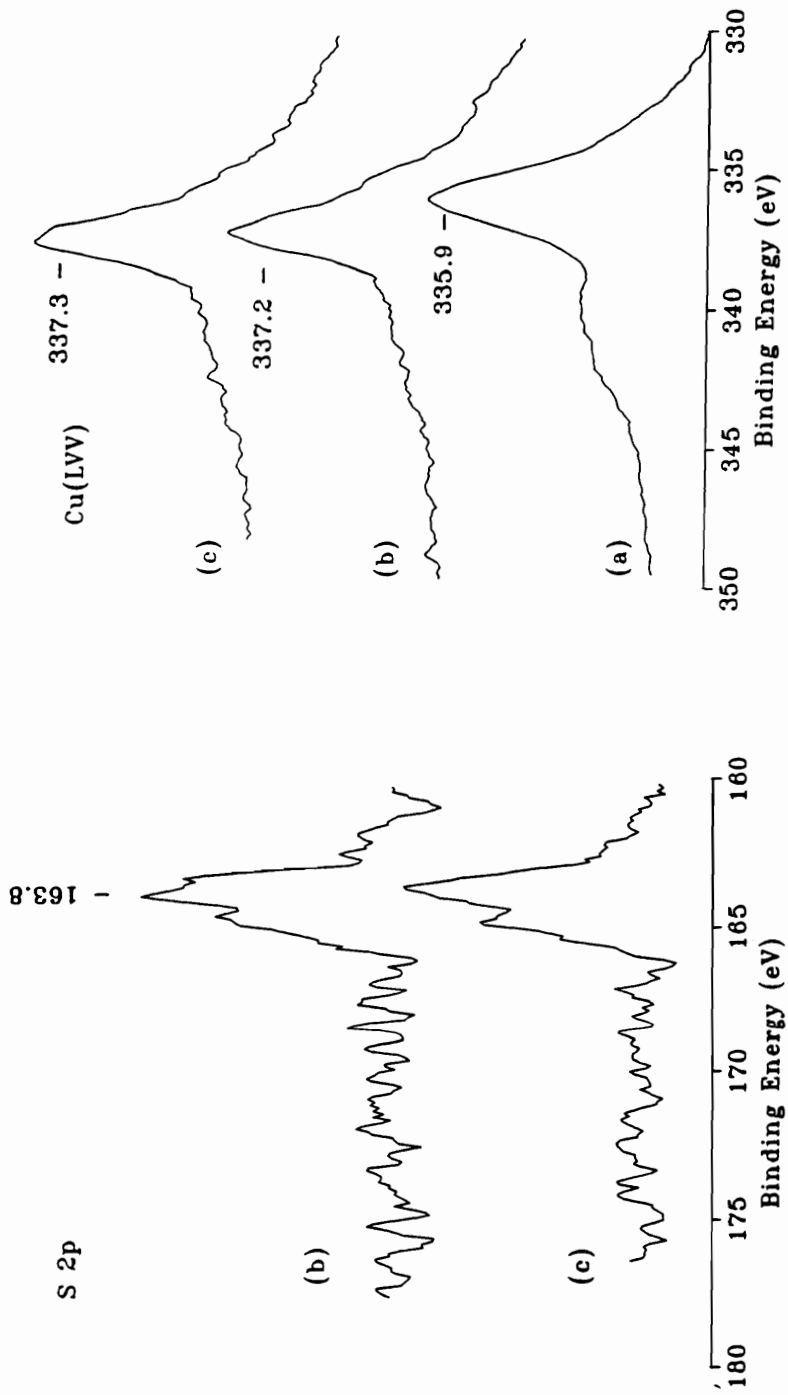


Figure 4.27 XPS analysis of the S 2p and Cu(LVV) peaks for failure surfaces of PPS bonded to chemically oxidized copper foil showing (a) the foil surface before bonding, (b) the foil failure surface, and (c) the adhesive failure surface.

may be due to the temperature involved in the bonding step since cupric oxide reduction can occur under inert conditions at these temperatures (See section 3.2.4.1.3). Also, this type of chemical oxidation forms a mixture of cupric and cuprous oxide (96), and ion milling indicates the formation of a dense cuprous oxide underlayer that supports a fragile cupric oxide surface layer (97). Given this structure, the mode of failure may occur in the deeper cuprous oxide layer. A complete analysis for thermally and chemically treated surfaces in Table 4.6 and an interesting point is the higher concentrations of oxygen found on the copper foil failure surfaces when compared to the other surface pretreatments studied (see Table 4.5).

Table 4.7 shows a more in depth analysis of the sulfur content on the foil failure surfaces. For this analysis, the S 2p photopeak was curve fit into two components indicating both organic (164.8 eV) and inorganic components (162.2 eV). Parameters used for the curve fitting procedure assumed a peak spacing of 1 - 1.2 eV for the S 2p^{3/2} and S 2p^{1/2} photopeaks, and a ratio of 1.8 - 2.2 for the S 2p^{3/2} to S 2p^{1/2} peak area ratio. The analysis shows that for the methanol degreased foil and the acid etched foil surfaces, a relatively high inorganic sulfur content of 9 - 10% was found for all cases. A smaller amount of organic sulfur indicative of a residual PPS film was also observed, and an inorganic sulfur to organic sulfur ratio of 1 - 2 was found for these three cases. For comparison, the thermal and chemical oxidation yielded values of 0.32 and 0.06 for this ratio, and the much lower inorganic sulfur content could arise from two possibilities. The first would be a much lower reactivity of copper to yield a lower sulfide concentration. The second possibility is that a shift in the average failure plane occurred to give a much thicker surface PPS film. This would cover the underlying sulfide layer and give a much lower sulfide signal due to the exponential nature of the XPS sampling depth. The total sulfur signal of only 5% seems to rule out the second possibility, and another measure of inorganic sulfur content can be obtained by examining the inorganic sulfide to copper ratio. These values are also given in Table 4.7, and the ratio of approximately 0.5 - 0.75 is much higher than the value of 0.01 - 0.09 found for the chemically and thermally oxidized

Table 4.6 XPS Atomic Concentrations for Copper Foil/PPS Failure Surfaces.

<u>SURFACE</u>	<u>ELEMENT</u>					
	<u>C1s</u>	<u>O1s</u>	<u>S2p</u>	<u>Cu2p</u>	<u>Cu(A)</u>	<u>Cl2p</u>
<i>Foil side</i>	58.2 (285.0)	13.5 (530.7)	7.1 (163.9) (162.3)	19.1 (932.8)	----- (337.4)	2.2 (198.8)
THERMAL OXIDATION						
<i>Adh. side</i>	80.5 (285.0)	6.3 (532.3)	11.4 (163.8)	1.8 (935.2)	----- (339.5)	NSP -----
<i>Foil side</i>	62.2 (285.0)	16.9 (530.7)	5.9 (163.8)	15.1 (932.9)	----- (337.3)	NSP -----
CHEMICAL OXIDATION						
<i>Adh. side</i>	61.0 (285.0)	16.5 (530.8)	5.8 (163.7)	----- (933.1)	NSP (337.2)	1.0 (199.0)

NSP - No significant peak. Binding energies are given in parenthesis ().

Table 4.7 XPS Analysis of Relative Concentrations of Inorganic and Organic Sulfur From Foil Failure Surfaces

<u>Pretreatment</u>	<u>Percent Composition</u>			
	<u>S 2p(o)</u>	<u>S 2p(i)</u>	<u>(i)/(o)</u>	<u>(i)/Cu</u>
MeOH	7.1 (163.8)	8.5 (162.2)	1.2	0.74
Nitric Acid	6.2 (163.8)	9.7 (162.1)	1.6	0.58
Brite Dip	4.0 (163.8)	9.2 (162.1)	2.3	0.47
Thermal Oxidation	5.4 (163.8)	1.7 (162.2)	0.32	0.09
Chemical Oxidation	5.4 (163.8)	0.4 (162.0)	0.08	0.01

(o) designates organic sulfur
 (i) designates inorganic sulfur

samples. This analysis again seems to indicate a much reduced inorganic sulfur content for the oxidized copper foil samples.

4.3.3 Interphase Characterization: Model Studies with PPS Tetramer

Due to the insolubility of PPS and requirement of high temperature spin coating techniques to prepare thin films, the use of a PPS oligomer provides a convenient method of monitoring interaction of PPS with copper surfaces prepared using a variety of pretreatments. Figure 4.28 shows the analysis of the S 2p photopeak for the interaction of oligomer with both the 'brite dip 'acid polished copper foil samples and sodium hydroxide etched aluminum foil samples. For both the copper and aluminum samples, no evidence for sulfur is observed for samples heat treated at 320 - 340 °C without oligomer. After heating to 320 - 340°C in the presence of oligomer, however, a new photopeak is evident on copper surfaces at approximately 161.9 eV indicative of copper sulfide species. This is interesting, since a thick oligomer film is visually present after treatment, and indicates that copper sulfide species may be present throughout the bulk of the remaining oligomer film. After the removal of excess oligomer with tetrahydrofuran, a residual amount of both inorganic and organic sulfur is detected, and the spectrum looks remarkably similar to that seen previously for the foil failure surfaces using this pretreatment. The shift in binding energy from 161.9 to 162.3 eV may also indicate that the inorganic film at the surface may be of different structure than that detected in the bulk of the oligomer. Beecher showed, in the analysis of the reaction of diphenyl sulfide with both cuprous and cupric oxides that a copper phenyl sulfide was formed having a binding energy of 162.9 eV which is higher than that observed here. It may be possible that a mixed state of PPS, copper sulfide, and copper phenyl sulfide exists in this surface film. Similar analysis for the aluminum foil substrate shows only the typical S 2p photopeak for the oligomer after foil separation, and after solvent washes, a thin residual film of oligomer is detected by a small photopeak at 163.8 eV. No evidence for significant amounts of other sulfur species were detected for this substrate.

Figure 4.29 shows a comparison of the S 2p photopeaks for the acid cleaned and

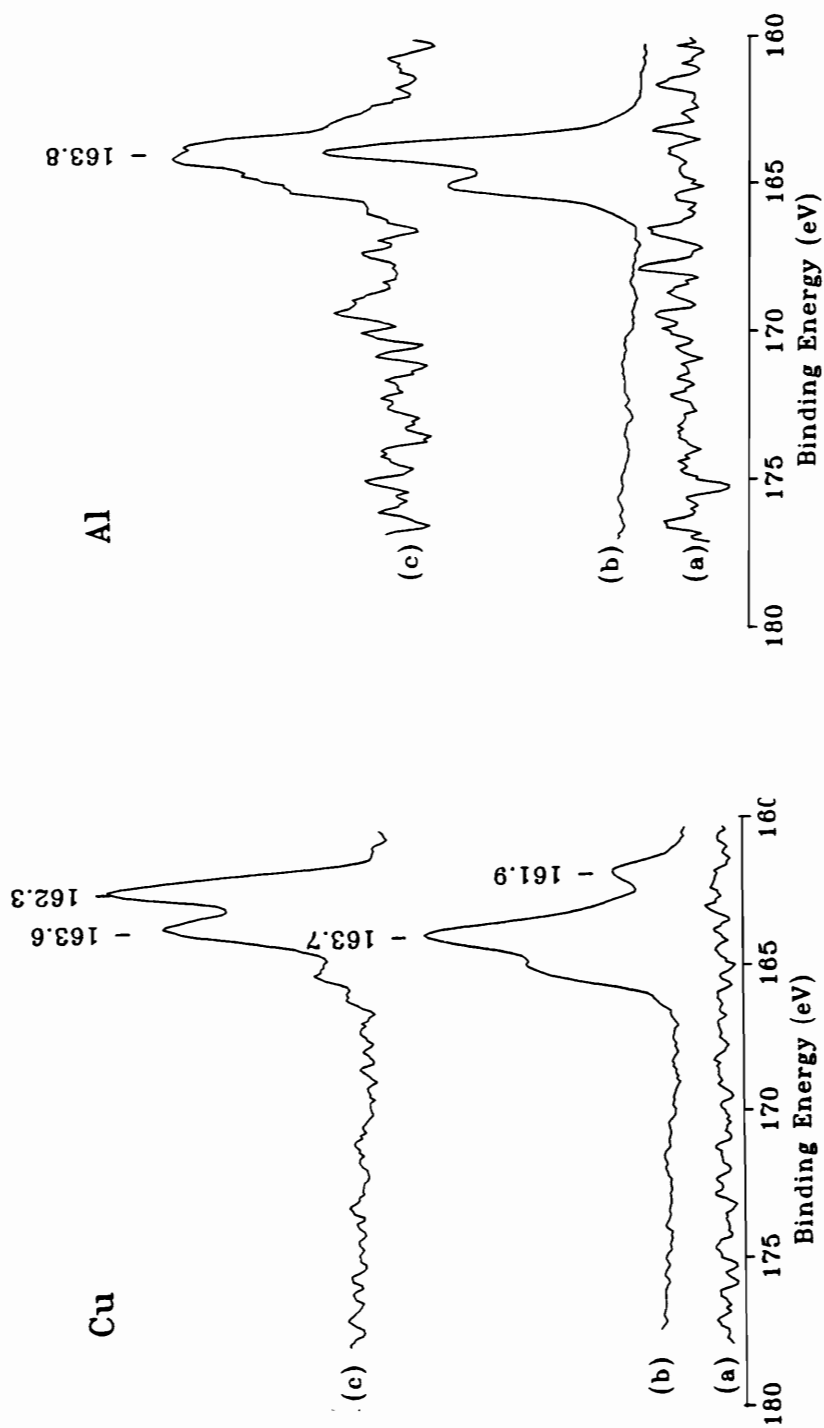


Figure 4.28 XPS analysis of the S 2p photopeaks for copper and aluminum foil samples after exposure to PPS oligomer for five minutes at 320 - 340°. Shown are spectra for (a) heat treatment without oligomer, (b) heat treatment with oligomer and no solvent wash, and (c) treatment with oligomer followed by several solvent washes.

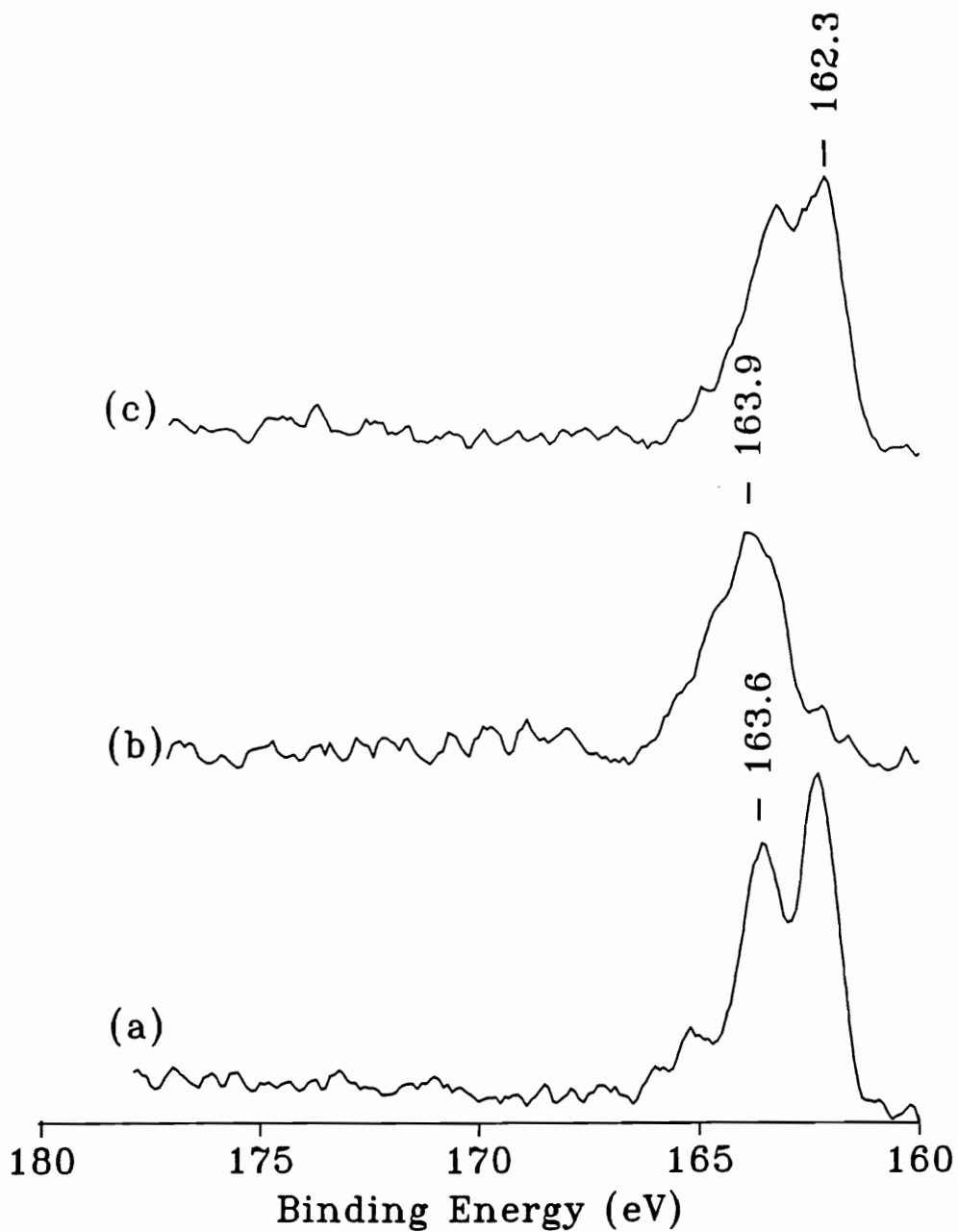


Figure 4.29 XPS analysis of the S 2p photopeaks for (a) 'brite dip' etched foil, (b) thermally oxidized, and (c) chemically oxidized copper foil after exposure to PPS oligomer for five minutes at 320 - 340° followed by several solvent washes.

oxidized foil surfaces after solvent washing to remove any residual oligomer. As is evident, the reaction with the chemically oxidized surface resulted in the formation copper sulfide surface species at 162.3 eV. The fact that sulfide species are seen in this case and not on foil failure surfaces may be due in part to the interaction of oligomer with only the fragile surface cupric oxide layer. Under bonding conditions, destruction of this surface layer would most probably occur. In contrast to chemically oxidized surfaces, little copper sulfide is detected for thermally oxidized surfaces and this is in agreement with the results from the foil failure surfaces. Figure 4.30 shows the results for a comparison of the Cu 2p and Cu (LVV) lines for the three pretreatments above. In the case of 'brite dip' polished samples, little change is seen in the Cu 2p photopeak, while the appearance of a new peak at 337.0 eV in the Auger line can probably be attributed to the formation of copper sulfide. For the chemically oxidized foil samples, analysis of the photopeak and Auger lines indicates that reduction of cupric oxide to cuprous oxide has occurred. For the case of thermal oxidation, the broadening of the Cu 2p line at 933.0 eV and the appearance of weak shake up satellite features is consistent with the formation of a Cu⁺² species. The broadening of the Cu (LVV) towards lower binding energies is in agreement with this. Table 4.8 shows a more complete analysis of the sulfur photopeak and indicates a relatively large copper sulfide content found for both the 'brite dip' cleaned and chemically oxidized surface film. In contrast very little inorganic sulfide was detected on the thermally oxidized copper foil, with mainly organic sulfur species detected for the aluminum foil substrate. Table 4.9 shows a complete analysis of the atomic concentrations found for all surfaces analyzed. The larger oxygen content found for these surfaces in comparison with the failure surfaces analyzed is probably due to the exposure to tetrahydrofuran during solvent washes. The oxygen binding energy at 530.4 eV indicates oxide for the thermally oxidized samples while the binding energy at 531.1eV and 531.6 eV for the chemically oxidized sample and 'brite dip' polished samples indicates another surface oxygen species.

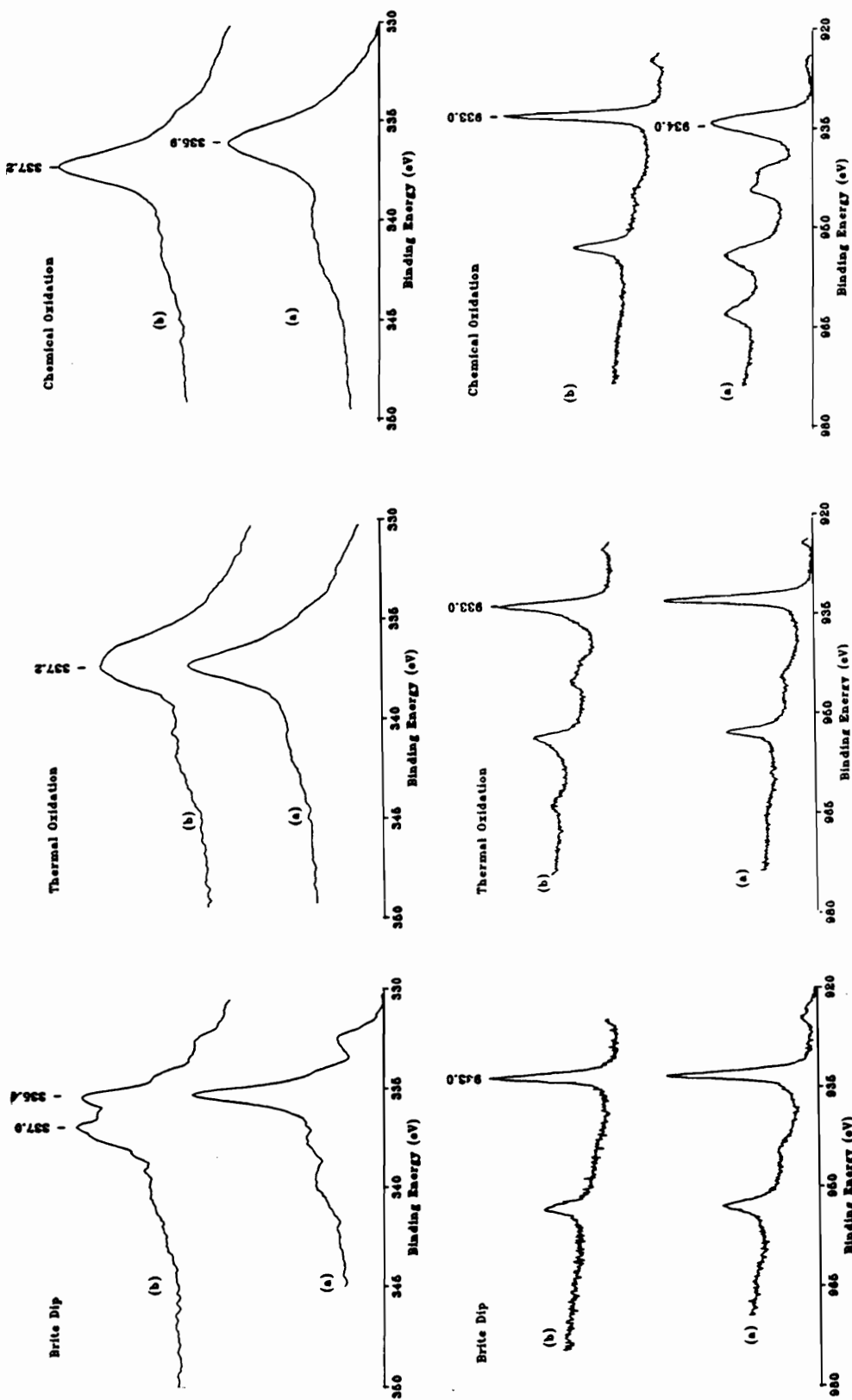


Figure 4.30 XPS analysis of the Cu 2p and Cu (LVV) peaks (a) before, and (b) after exposure to PPS oligomer for five minutes at 320 - 340° followed by several solvent washes for 'brite dip' etched, thermally oxidized, and chemically oxidized copper foil.

Table 4.8 XPS Analysis of Relative Concentrations of Inorganic and Organic Sulfur for PPS Oligomer Treated Copper Foil.

<u>Pretreatment</u>	<u>Percent Composition</u>			
	<u>S 2p(o)</u>	<u>S 2p(i)</u>	<u>(i)/(o)</u>	<u>(i)/Cu</u>
Brite Dip	3.8 (163.8)	7.7 (162.2)	2.0	1.0
Thermal Oxidation	5.1 (163.9)	1.1 (162.4)	0.22	0.07
Chemical Oxidation	3.4 (163.7)	6.8 (162.3)	2.0	0.41
Aluminum	1.33 (163.8)	0	0	---

(o) designates organic sulfur

(i) designates inorganic sulfur

Table 4.9 XPS Atomic Concentrations for Oligomer Treated Copper Foil Surfaces.

<u>Pretreatment</u>	<u>C1s</u>	<u>O1s</u>	<u>ELEMENT</u>			
			<u>S2p</u>	<u>Cu/Al2p</u>	<u>Cu(A)</u>	<u>Cl2p</u>
<i>Brite Dip</i>	64.2 (285.0)	16.5 (531.1)	11.5 (162.5) (163.5)	7.8 (933.0)	----- (337.3)	NSP -----
<i>Thermal Oxidation</i>	48.4 (285.0)	29.9 (530.4)	6.2 (163.9)	15.3 (933.0)	----- (337.2)	2.7 NSP
<i>Chemical Oxidation</i>	50.9 (285.0)	21.4 (529.7)	10.2 -----	16.5 (934.0)	----- (335.9)	1.1 (198.7)
<i>Aluminum*</i>	34.4 (285)	38.6	1.33 (163.8)	24.7 (72.1) (74.7)	-----	NSP

NSP - No significant peak. Binding energies are given in parenthesis ().
* - A small amount of tin was also observed.

4.4 SUMMARY AND CONCLUSIONS

4.4.1 Thermoxidative Degradation of PPS

XPS analysis for the aging of thin PPS films on copper has shown convincing evidence for a marked degradation of the film with eventual migration of copper species to the surface of the film. The initial species reaching the surface region was found to be a combination of copper oxide and possibly a O=C species probably indicative of carboxylate species. Infrared analysis confirms the presence of carboxylate species and this is in agreement with the general results for many other polymer systems (36-39). *In-situ* analysis also showed the appearance of carboxylate species at temperatures approaching 200°C and temperatures in excess of 175°C resulted in the rapid appearance of cuprous oxide and general loss of polymer. The aging of PPS on other surfaces including aluminum and chromium shows no evidence for such large scale degradation in comparison to copper foil substrates. The aging of PPS on sputtered cuprous oxide films did result in some loss of material but no carboxylates were detected indicating the unique role of the oxidation of copper *metal* in the formation of copper carboxylate species.

4.4.2 Analysis of PPS / Copper Adhesion

Given the lack of change in surface morphology for thermally oxidized foil samples, this pretreatment represents an interesting case where a relatively minor change in surface chemistry can result in a tremendous increase in adhesive strength. Results show a reduced concentration of inorganic sulfide when compared to solvent degreased acid etched samples, and this probably indicates that excessive sulfide formation at the interface is responsible for the almost complete loss in adhesive strength. van Ooij showed that while small amounts of copper sulfide were beneficial to bond strength in brass/ rubber adhesion, excessive formation of interfacial cuprous sulfide actually gave poor adhesion for these systems (98). Also, the bonding of rubber to pure copper gave poor adhesion due to the excessive interfacial cuprous sulfide formed. Given the simple mechanisms of copper phenyl sulfide and copper phenoxide formation proposed by Beecher for the interaction of diphenyl sulfide with cuprous and

cupric oxides, these reaction necessarily involve chain scission (99). The reduction of copper oxide for the methanol washed and nitric acid treated surfaces seems to be consistent with this analysis. The lower reactivity of a thick layer of cuprous oxide for thermally pre-treated surfaces versus a thin layer of oxide on metal for nitric acid treated samples indicates that the copper metal may play a catalytic role in the sulfide formation.

The formation of copper sulfide species may also occur during the disproportionation reactions which are known to occur for PPS polymers and oligomers held at elevated temperatures in inert environments (94). Since these reactions would still be expected to occur irrespective of substrate, the unique role of the copper surface chemistry in the formation of sulfide must again be considered. The extraction of sulfur to form copper bonded sulfur species would alter the physical polymer properties in the interphase region, and this is most likely responsible for the loss in crystallizability previously seen for thin films held at high temperatures against copper substrates under vacuum conditions (See section 3.3.4.1.3). The formation of an amorphous, fragmented polymer surface film would give a weak boundary layer, and failure would be expected to occur in this region. For thermally oxidized foil samples, where the amount of interfacial sulfide is relatively small, the degree of polymer damage would be much less, and although the fracture during peeling also occurs through a thin surface PPS layer, the polymer properties including crystallinity and molecular weight are probably similar to those of bulk PPS.

4.7 REFERENCES

- (1) Adams, A.C. In *VLSI Technology*; Sze, S.M., Ed.; McGraw Hill: New York, 1983
- (2) Kern, W. *Semicond. Inter.* **1985**, *8*, 228.
- (3) Kern, W.; Rosler, R.S. *J. Vac. Sci. Technol.* **1977**, *14*, 1082.
- (4) Wilson, A.M. *Thin Solid Films* **1981**, *83*, 145.
- (5) Saiki, A.; Mukai, K.; Harada, S. In *Polymer Materials for Electronic Applications*; Feit, E.D., Wilkins Jr., C., Eds.; ACS Symposium Series 184, American Chemical Society: Washington D. C., 1982, p. 123.
- (6) Merrett, R. P. In *Plastics for Electronics*; Goosey, M. T., Ed.; Elsevier Applied Science: London, 1985, Chapter 6
- (7) Goosey, M.T. In *Plastics for Electronics*; Goosey, M. T., Ed.; Elsevier Applied Science: London, 1985, Chapter 10
- (8) Sharpe, L.H. *J. Adhesion* **1972**, *4*, 51.
- (9) Panzer, G.; Egert, B.; Schmidt, H.P. *Surf. Sci.* **1985**, *151*, 400.
- (10) Fleisch, T.H.; Mains, G.J. *Appl. Surf. Sci.* **1982**, *10*, 51.
- (11) Deroubaix, G.; Marcus, P. *Surf. Interf. Anal.* **1992**, , 39.
- (12) McIntyre, N.S.; Cook, M.G. *Anal. Chem.* **1975**, *47*, 2208.
- (13) McElhaney, R.D.; Castner, D.G.; Ratner, B.D. In *ACS Symp. Series 440*; Sacher, E., Pireaux, J.J., Kowalczyk, S.P. Eds.; American Chemical Society: Washington, D.C., 1990, p.371.
- (14) Barr, T.L. *J. Vacuum Sci. Technol.* **1977**, *14*, 660.
- (15) Barr, T.L. *Surf. Interf. Anal.* **1982**, *4*, 185.
- (16) Ishitani, A.; Ishida, H.; Soeda, F.; Nagasawa, Y. *Anal. Chem.* **1982**, *54*, 682.
- (17) Boerio, F.J.; Armogan, L. *Appl. Spect.* **1978**, *32*, 509.
- (18) Wieder, H.; Czanderna, A.W. *J. Phys. Chem.* **1962**, *66*, 816.

- (19) Poling, G. J. *Electrochem. Soc.* **1969**, 116, 958.
- (20) Watanabe, N.; Kuwana, T. *Anal. Chem.* **1980**, 52, 1657.
- (21) Strehblow, H.H.; Titze, B. *Electrochim. Acta* **1980**, 25, 839.
- (22) Shoesmith, D.W.; Sunder, S.; Bailey, M.G.; Wallace, G.J.; Stanchell, F.W. *J. Electroanal. Chem.* **1983**, 143, 153.
- (23) Lohrengel, M.M.; Schultze, J.W.; Speckmann, H.D.; Strehblow, H.H. *Electrochim. Acta* **1987**, 32, 733.
- (24) Speckmann, H.D.; Haupt, S.; Strehblow, H.H. *Surf. Interf. Anal.* **1988**, 11, 148.
- (25) Scherer, A.; Inal, O.T.; Singh, A.J. *Solar Energy Mat.* **1983**, 9, 139.
- (26) Inal, O.T.; Scherer, A. *J. Mat. Sci.* **1986**, 21, 729.
- (27) Scherer, A.; Inal, O.T.; Pettit, R.B. *J. Mat. Sci.* **1988**, 23, 1923.
- (28) Wagner, C.D. *Faraday Discuss. Chem. Soc.* **1975**, 60, 291.
- (29) Barr, T.L.; Hackenberg, J.J. *Appl. Surf. Sci.* **1982**, 10, 523.
- (30) Greenler, R.G.; Rahn, R.R.; Schwartz, J.P. *J. Catal.* **1971**, 23, 42.
- (31) Machefert, J.M.; Calvar, M.Le.; Lenglet, M. *Surf. Interf. Anal.* **1992**, 18, 39.
- (32) Lynch, D. W.; Hunter, W. R. In *Handbook of Optical Constants*; Palik, E. D., Ed.; Academic: Orlando, 1985; p. 280
- (33) Ribbing, C. G.; Roos, A. In *Handbook of Optical Constants II*; Palik, E.D., Ed.; Academic: San Diego, 1991; p. 875
- (34) Schmidt, R.; WiBmann, P. *Surf. Interf. Anal.* **1988**, , 407.
- (35) Manara, A.; Sitori, V.; Mammarella, L. *Surf. Interf. Anal.*, **1992**, 18, 32.
- (36) Hansen, R.H. In *Thermal Stability of Polymers*; Conley, R.T., Ed.; Marcell Dekker: New York, 1970; Chapt. 6.
- (37) Jellinek, H.H.G.; Kachi, H.; Czanderna, A.; Miller, A.C. *J. Polym. Sci: Polym. Chem. Ed.* **1979**, 17, 1493.
- (38) Kelley, K.; Ishino, Y.; Ishida, H. *Thin Solid Films* **1987**, 154, 279.

- (39) Allara, D.L.; White, C.W.; Meek, R.L.; Briggs, T.H. *J. Polym. Sci.: Polym. Chem. Ed.* **1976**, *14*, 93.
- (40) Czandena, A.W.; Miller, A.C.; Jellinek, H.H.G.; Kachi, H. *J. Vac. Sci. Technol.* **1977**, *14*, 227.
- (41) Miller, A.C.; Czanderna, A.W.; Jellinek, H.H.G.; Kachi, H. *J. Colloid Interf. Sci.* **1982**, *85*, 244.
- (42) Chan, M.G.; Allara, D.L. *Polym. Eng. Sci.* **1974**, *14*, 12.
- (43) Chan, M.G.; Allara, D.L. *J. Colloid Interf. Sci.* **1974**, *47*, 697.
- (44) Allara, D.L. In *Characterization of Metal and Polymer Surfaces*; Lee, L.H., Ed.; Academic: New York, 1977; p. 193.
- (45) Allara, D.L.; Chan, M.G. *J. Polym. Sci.: Polym. Chem. Ed.* **1976**, *14*, 1857.
- (46) Allara, P.L.; Roberts, R.F. *J. Catal.* **1976**, *45*, 54.
- (47) Burrell, M.C.; Keane, J. *J. Surf. Intef. Anal.* **1988**, *11*, 487.
- (48) Burrell, M.C.; Fontana, J.; Chera, J.J. *J. Vac. Sci. Technol.* **1988**, *A6*, 2893.
- (49) Burrell, M.C.; Codella, P.J.; Fontana, J.A.; Chera, J.J. *J. Vac. Sci. Technol.* **1989**, *A7*, 1778.
- (50) Prime, R.B. *J. Polym. Sci.: Polym. Lett.* **1986**, *24*, 641.
- (51) Wegman, R. F. *Surface Preparation Techniques for Adhesive Bonding*; Noyes Publications: New Jersey, 1989; Chapter 5.
- (52) ASTM Method D2651, *Standard Practice for Preparation of Metal Surfaces for Adhesive Bonding*, Method E; American Society for Testing and Materials, Philadelphia, PA.
- (53) Evans, J.R.G.; Packham, D.E. *J. Adhesion* **1979**, *10*, 39.
- (54) Evans, J.R.G.; Packham, D.E. *J. Adhesion* **1978**, *9*, 267.
- (55) Bucci, G.D.; Savage, R.D. "Foil Technology for PCB Fabrication: Foil Manufacturing and Developments for Advanced PCB Designs"; presented at PCFAB Expo '86, May 12, 1986.
- (56) Roberts, R.F. *J. Electron Spectrosc. Rel. Phenom.* **1974**, *4*, 273.

- (57) Chadwick, D.; Hashemi, T. *J. Electron. Spectrosc. Rel. Phenom.* **1978**, 18, 39.
- (58) Yoshida, S.; Ishida, H. *J. Chem. Phys.* **1983**, 78, 6960.
- (59) Poling, G.W. *Corros. Sci.* **1970**, 10, 359.
- (60) Xue, G.; Zhang, J. *Appl. Spectrosc.* **1991**, 45, 760.
- (61) Thiboult, S. *Corros. Sci.* **1977**, 17, 701.
- (62) Eng, F.P.; Ishida, H. *J. Mat. Sci.* **1986**, 21, 1561.
- (63) Ishida, H.; Kelley, K. *J. Adhesion* **1991**, 36, 177.
- (64) Mack, R.G.; Grossman, E.; Unertl J. *Vac. Sci. Technol.* **1990**, 8, 3827.
- (65) Strunskus, T.; Hahn, D.; Frankel, D.; Grunze, M. *J. Vac. Sci. Technol.* **1991**, 9, 1272.
- (66) Haught, R.; White, R.C.; Silverman, B.D.; Ho, P.S. *J. Vac. Sci. Technol.* **1988**, 6, 2188.
- (67) Van Ooij, W.J.; Michael, R.S. In *Metallization of Polymers*; Sacher, E., Pireaux, J.J., Kowalczyk, S.P., Eds.; American Chemical Society: Washington, D.C., 1990; ACS Symp. Ser., No. 440, p. 60.
- (68) Kim, J.; Kowalczyk, S.P.; Kim, Y.H.; Chou, M.J.; Oh, T.S. In *Materials Reseach Soc. Proceed.* **1989**, 167, 137.
- (69) Kim, Y.H.; Walker, G.F.; Kim, J.; Park, J. *J. Adhes. Sci. Technol.* **1987**, 1, 331.
- (70) Ho, P.S.; Hahn, P.O.; Bartha, J.W.; Rugloff, G.W.; Legoues, F. K.; Silvermann, B.D. *J. Vac. Sci. Technol.* **1985**, 3, 739.
- (71) Sanda, P.N.; Bartha, J.W.; Clabes, J.G.; Jordan, J.L.; Feger, C.; Silvermann, B.D.; Ho, P.S. *J. Vac. Sci. Technol.* **1986**, 4, 1035.
- (72) Boerio, F.J.; Ondrus, D.J. *J. Colloid Inter. Sci.* **1990**, 139, 446.
- (73) Burkstrand, J. M. *J. Vac. Sci. Technol.* **1979**, 16, 363
- (74) Kim, K.S.; Aravas, N. *Int. J. Solids Structures* **1988**, 24, 417.
- (75) Kim, K.S.; Kim, J. *J. Eng. Mat. Technol.* **1988**, 110, 267.

- (76) Napolitano, M.J.; Chudnovsky, A.; Moet, A. *J. Adhes. Sci. Technol.* **1988**, *2*, 311.
- (77) Chang, Y.S.; Lai, Y.H.; Dillard, D.A. *J. Adhesion* **1989**, *27*, 197.
- (78) Allen, M.G.; Senturia, S.D. *J. Adhesion* **1988**, *25*, 303.
- (79) Allen, M.G.; Senturia, S.D. *J. Adhesion* **1989**, *29*, 219.
- (80) Dillard, D.A.; Bao, Y. *J. Adhesion* **1991**, *33*, 253.
- (81) Ho, P.S.; Faupel, F. *Appl. Phys. Lett.* **1988**, *53*, 1602.
- (82) Faupel, F.; Yang, C.H.; Chen, S.T.; Ho, P.S. *J. Appl. Phys.* **1989**, *65*, 1911.
- (83) Mittal, K.L. *Pure Appl. Chem.* **1989**, *52*, 1295.
- (84) Gent, A.N.; Hamed, G.R. *J. Adhesion* **1975**, *7*, 91.
- (85) Nicholson, D.W. *Int. J. Fracture* **1977**, *13*, 279.
- (86) Crocombe, A.D.; Adams, R.D. *J. Adhesion* **1982**, *13*, 241.
- (87) Gent, A.N.; Hamed, G.R. *J. Appl. Polym. Sci.* **1977**, *21*, 2817.
- (88) Buchwalter, L.P.; Greenblatt, J. *J. Adhesion* **1986**, *19*, 257.
- (89) Buchwalter, L.P.; Lacombe, R.H. *J. Adh. Sci. Technol.* **1988**, *2*, 463.
- (90) Oh, T.S.; Buchwalter, L.P.; Kim, J. *J. Adhes. Sci. Technol.* **1990**, *4*, 303.
- (91) Buchwalter, L.P.; Oh, T.S.; Kim, J. *J. Adhes. Sci. Technol.* **1991**, *4*, 333.
- (92) Buchwalter, L.P. *J. Adhes. Sci. Technol.* **1990**, *4*, 697.
- (93) Sugama, T.; Carciello, N. R. *Int. J. Adhes. Adh.* **1991**, *11*, 97
- (94) Hawkins, R. T. *Macromolecules*, **1976**, *9*, 189
- (95) Riga, J.; Boutique, J. P.; Pereaux, J. J.; Verbist, J. J. *In Physicochemical Aspects of Polymer Surfaces*; Mittal, K. L., Ed.; Plenum Press: New York, 1983; p.45
- (96) Inal, O. T.; Scherer, A. *J. Mater. Sci.* **1986**, *21*, 729
- (97) Scherer, A.; Inal, O. T. *Thin Solid Films* **1984**, *119*, 413

- (98) van Ooij, W. J. *Surf. Sci.* **1977**, 68, 1
- (99) Beecher, J. F. *Surf. Interf. Anal.* **1991**, 17, 245

Chapter 5: Overall Conclusions

Optical theory represents a relatively new approach in the analysis of polymer surface modification or the investigation of the polymer / metal interface. In this work, optical simulation was used to predict experimental reflectance spectra and the agreement of theory and experiment is a strong statement for the usefulness of this technique. Optical theory was also used with infrared reflection absorption spectroscopy (IRRAS) to prove the unique orientation of thin PPS films, and the orientation was observed to be in the plane of the substrate. Such alignment of polymer molecules most likely arises from the nature of the spin coating process itself.

Optical theory was also useful in the prediction of the experimental parameters necessary to observe thin plasma modified polymer surface layers. Oxygen plasma treatment of polystyrene showed a highly oxidized surface, and the depth of modification was determined to be approximately 2 nm. Given the thin nature of the surface layer and the sensitivity of current instrumentation, the importance of optimizing experimental parameters through the use of optical theory cannot be over emphasized. Treatment of polystyrene by an ammonia plasma resulted in a thicker modified layer, rich in hydrocarbon fragments and amine functionalities. The ability to use vibrational spectroscopy as a complementary technique to the more traditionally used technique of x-ray photoelectron spectroscopy (XPS) is clearly an advantage in surface analysis.

Results from the oxygen plasma treatment of poly(arylene ether) phosphine oxides showed a material highly resistant to oxidative attack. Both ellipsometry and surface acoustic wave analysis were used as relatively new methods to analyze polymer stability. This resistance is atypical of most polymers, and thus represents one of only several types of materials that behave in this manner. In depth analysis by XPS and IRRAS indicated that after plasma exposure, a surface layer of a phosphate material develops which inhibits further oxidation of the underlying polymer. Detailed analysis

showed that this material is probably polymeric in nature, and contains significant amounts of hydrocarbon and hydroxyl functionalities.

To analyze the dynamic behavior of thin oriented PPS films on a variety of substrates, the new technique of variable temperature reflection absorption spectroscopy (VTRAS) was used. Analysis showed that this technique was useful in examining the degradation processes involved in under both vacuum and ambient atmospheres. Under vacuum, the crystallization temperature and melting temperature could be determined reliably for a number of substrates, and all samples showed a T_m value 30 - 40°C below the value for bulk PPS. For aluminum and chromium substrates, little degradation was observed and the polymer could be re-crystallized after exposure to high temperatures (approximately 300°C). For copper substrates, however, a loss in crystallizability was observed after the first high temperature exposure. A loss of copper oxide was also observed, and due to a lack of other spectral features, it was postulated that chain scission mechanisms must be involved with the possible formation of copper sulfide. For the analysis of PPS films on cuprous oxide substrates in the absence of an underlying metal, a lesser degree of degradation was noted. This indicates that the degradation processes are specific to the particular copper chemistry present.

Analysis of degradation of PPS coatings of copper in air shows that a quite different degradation mechanism occurs. The growth of cuprous oxide was evident, and copper species were observed by XPS to migrate through the polymer film. *In-situ* VTRAS analysis also distinctly showed the formation of copper carboxylates. No degradation was observed on other metal substrates including zinc, chromium, and aluminum. Variable temperature infrared analysis was useful also in determining the exact temperature at which degradation starts, and the degradation mechanism seems to be coupled with the growth of copper oxide at the interface.

An investigation of PPS / copper bonding was also undertaken and results showed that a simple thermal oxidation step could increase bond strength almost one order of magnitude. Analysis by scanning electron microscopy showed that no new topographical surface features were formed, and the alteration of surface chemistry

was postulated to play a prominent role. Chemical oxidation of copper foil in an alkaline persulfate solution also increased peel strength, although the mechanisms involved are much more complicated due to the unique dendritic morphology formed by surface pretreatment. Analysis of failure surfaces and the interaction of pretreated copper with PPS tetramer, revealed that cuprous sulfide can readily form at the interface. It was also shown that the amount found was strongly dependent on the surface pretreatment. Thermally oxidized foil showed the least interfacial copper sulfide, and it was postulated that excess sulfide at the interface was responsible for the poor adhesion observed for other pretreatments.

APPENDIX 2.1

The problem of reflectance can be formulated as in Fig. 2.2. The approach treats multiple reflections as the vector sum of the waves traveling in a given direction in each medium.

Using solutions to Maxwell's equations for waves traveling in each phase, one can obtain the z dependent of the x and y components of the electric and magnetic vectors. A thorough presentation of development of the specific relationship from Maxwell's equations can be found elsewhere (Chapter 2, Ref. 2). These relationships can be written in terms of both perpendicular and parallel states of polarization of incident light and can be summarized as follows:

Parallel polarization

$$E_{jx} = (E_j^+ e^{-ipz} + E_j^- e^{+ipz}) \cos \phi_j \tag{A.1}$$

$$H_{jy} = (E_j^+ e^{-ipz} - E_j^- e^{+ipz}) n_j \tag{A.2}$$

Perpendicular polarization

$$E_{jy} = E_j^+ e^{-ipz} + E_j^- e^{+ipz} \tag{A.3}$$

$$H_{jx} = (-E_j^+ e^{-ipz} + E_j^- e^{+ipz}) n_j \cos \phi_j \tag{A.4}$$

where $E_{jx,y}$ and $H_{jx,y}$ represent the x and y components of the total electric and magnetic vectors in the j^{th} phase, $E_j^+, -$ represents the individual electric vectors traveling in the direction indicated in the j^{th} phase, n_j is the refractive index, ϕ is the angle of incidence to the j^{th} phase, z is the thickness of a given phase, and b represents the phase delay due to the presence of a film and can be written as $p = 2\pi/\lambda * n_j z_j \cos \phi_j$ where λ is the wavelength of the incident light. Applying the boundary conditions that the tangential components of the magnetic and electric vectors are equal at the interface between two phases (i.e., $E_{jx} = E_{(j+1)x}$ and $H_{jx} = H_{(j+1)x}$), the following two equations can be specified for each interface:

Parallel polarization

$$E_j^+ e^{-ipz} + E_j^- e^{+ipz} \cos\phi_j = (E_{j+1}^+ + E_{j+1}^- e^{+ipz}) \cos\phi_{j+1} \quad [\text{A.5}]$$

$$(E_j^+ e^{-ipz} - E_j^- e^{+ipz}) n_j = (E_{j+1}^+ e^{-ipz} - E_{j+1}^- e^{+ipz}) n_{j+1} \quad [\text{A.6}]$$

Perpendicular polarization

$$E_j^+ e^{-ipz} + E_j^- e^{+ipz} = E_{j+1}^+ e^{-ipz} + E_{j+1}^- e^{+ipz} \quad [\text{A.7}]$$

$$(-E_j^+ e^{-ipz} + E_j^- e^{+ipz}) n_j \cos\phi_j = (-E_{j+1}^+ e^{-ipz} + E_{j+1}^- e^{+ipz}) n_{j+1} \cos\phi_{j+1} \quad [\text{A.8}]$$

These equations are the same as those presented by Greenler, although they are shown here for non-absorbing systems. For a single surface, the phase terms can be removed since there is no film and the equations can be rearranged to yield E_1^-/E_1^+ and E_2^+/E_1^+ for each state of polarization, and are known as the Fresnel reflection and transmission coefficients. As an example, the reflection and transmission coefficients for parallel polarization is shown here:

$$r_1 = \frac{E_1^-}{E_1^+} = \frac{n_1 \cos\phi_2 - n_2 \cos\phi_1}{n_1 \cos\phi_2 + n_2 \cos\phi_1} \quad [\text{A.9}]$$

$$t_1 = \frac{E_2^+}{E_1^+} = \frac{2 n_1 \cos\phi_1}{n_1 \cos\phi_2 + n_2 \cos\phi_1} \quad [\text{A.10}]$$

In reflection absorption spectroscopy, the quantity desired is the power loss due to reflection from a surface covered with a thin film. Heavens has described a matrix method which can easily be employed to solve eqns. [A.5] through [A.8] for this more complicated system (40).

By using the expressions for the Fresnel coefficients in eqns [A.9] and [A.10], eqns. [A.5] and [A.6] can be written in the following notation:

$$E_j^+ = \frac{E_{j+1}^+ e^{i\delta_j} + r_{j+1} E_{j+1}^- e^{i\delta_j}}{t_{j+1}} \quad [\text{A.11}]$$

$$E_j^- = \frac{r_{j+1} E_{j+1}^+ e^{-i\delta_j} + E_{j+1}^- e^{-i\delta_j}}{t_{j+1}} \quad [\text{A.12}]$$

where

$$\delta_{j+1} = p \times \sum_{i=1}^j z_i$$

Since the same equation forms can be written for each interface, the expressions can be written in compact matrix form

$$\begin{bmatrix} E_j^+ \\ E_j^- \end{bmatrix} = \frac{1}{t_{j+1}} \begin{bmatrix} e^{i\delta_j} & r_j + e^{i\delta_j} \\ r_j + e^{-i\delta_j} & e^{-i\delta_j} \end{bmatrix} \begin{bmatrix} E_{j+1}^+ \\ E_{j+1}^- \end{bmatrix} \quad [\text{A.13}]$$

For a system with n layers, the previous relation can be expanded to

$$\begin{bmatrix} E_j^+ \\ E_j^- \end{bmatrix} = M \begin{bmatrix} E_{n+1}^+ \\ E_{n+1}^- \end{bmatrix} \quad [\text{A.14}]$$

where

$$M = \prod_{m=1}^{n+1} \frac{C_m}{t_m} \quad [\text{A.15}]$$

and

$$C_m = \begin{bmatrix} e^{i\delta_{m-1}} & r_m e^{i\delta_{m-1}} \\ r_m e^{-i\delta_{m-1}} & e^{-i\delta_{m-1}} \end{bmatrix} \quad [\text{A.16}]$$

If the term M represents a matrix $\begin{bmatrix} a & b \\ c & d \end{bmatrix}$ divided by $\prod_{m=1}^{n+1} t_m$, simple matrix multiplication yields

$$E_1^+ = \frac{[a E_{n+1}^+ + b E_{n+1}^-]}{\prod_{m=1}^{n+1} t_m} \quad [\text{A.17}]$$

$$E_1^- = \frac{[c E_{n+1}^+ + d E_{n+1}^-]}{\prod_{m=1}^{n+1} t_m} \quad [\text{A.18}]$$

Noting that there is no E_{n+1}^- term since there is no negative travelling wave in the last phase, solving for the ratio E_1^-/E_1^+ yields the value c/a for the reflectivity. The reflectance, which is the quantity desired for RAS, can be calculated by aa^*/cc^* where a^* and c^* are the complex conjugate of a and c respectively. Similarly, for transmission:

$$t = \frac{E_{n+1}^+}{E_1^+} = \prod_{m=1}^{n+1} \frac{t_m}{a} ; T = \frac{[\prod_{m=1}^{n+1} t_m \times \prod_{m=1}^{n+1} t_m^*]}{aa^*} \quad [\text{A.19}]$$

Exact solution of the previous equations was outlined in a detailed stepwise fashion by Heavens (40). Heavens limited this development to normal incidence only, the

following treatment will be totally general in nature although only the reflectance will be considered.

To evaluate the matrix M, one can conveniently express each element in the C_m matrix in complex notation

$$C_m = \begin{bmatrix} p_m + iq_m & r_m + is_m \\ t_m + iu_m & v_m + iw_m \end{bmatrix}$$

where each element of the product matrix can be determined by simple matrix multiplication. Double suffixes are used to represent the elements of product matrices, and for example, for the matrix $C_1 * C_2 * C_3$, the matrix element p_{13} can be defined as follows

$$p_{13} = p_{12}p_3 - q_{12}q_3 + r_{12}t_3 - s_{12}u_3$$

$$p_{12} = p_{11}p_2 - q_{11}q_2 + r_{11}t_2 - s_{11}u_2$$

$$q_{12} = q_{11}p_2 - p_{11}q_2 + s_{11}t_2 + r_{11}u_2$$

$$r_{12} = p_{11}r_2 - q_{11}s_2 + r_{11}v_2 - s_{11}w_2$$

$$s_{12} = q_{11}r_2 + p_{11}s_2 + s_{11}v_2 + r_{11}w_2$$

Similarly, expressions could be derived for all elements of the final matrix and this is done completely in Heaven treatment (Chap. 2., Ref. 2). To evaluate the original C_m matrix, several extensions must be added to Heavens treatment to allow for non-normal incidence with absorbing materials.

For normal incidence of absorbing materials, or non-normal incidence of non-absorbing, the planes of constant phase of the penetrating wave are parallel to those of constant amplitude (Chap. 2, Ref. 2), and under this condition, Snell's law is obeyed. When the material is absorbing, the planes of constant phase and those of constant amplitude are no longer parallel, and the effective values of n and k depend

on the angle of incidence.

These effective values $n'(\alpha)$ and $k'(\beta)$, as well as the angle between the planes of constant phase and those of constant amplitude can be calculated from the following equations (Chap. 2, Ref. 12):

$$\alpha^2 - \beta^2 = n^2 - k^2 \quad [\text{A.20}]$$

$$\alpha\beta \cos\phi_j = nk \quad [\text{A.21}]$$

$$\sin \phi_1 = \alpha \sin \phi_j \quad [\text{A.22}]$$

To solve for each element of the C_m matrix, the Fresnel coefficients will be assumed to be complex in the general case, and of the form $(g + ih)$. To solve for the real and imaginary components of the Fresnel coefficients, they must be written to include the general case of absorbing films at non normal incidence. To accomplish this, using the same method as Greenler (Chap. 2, Ref. 7), $\alpha \cos\phi_j - i\beta_j$ is substituted for $n_j \cos\phi_j$ and $n_j - ik_j$ is substituted for other values of n_j where α , β , and ϕ are given by Eqns [20-22]. If similar substitutions are made for the phase shift term b , the following equations result

$$e^{i\delta_j} = e^{2\pi d/\lambda[\beta + i\alpha \cos\phi]} \quad [\text{A.23}]$$

$$e^{i\delta_j} = e^{\sigma} e^{i\gamma_j} \quad [\text{A.24}]$$

where

$$\sigma_j = 2\pi d_j \beta_j / \lambda \text{ and } \gamma_j = 2\pi d / \lambda [\alpha_j \cos\phi_j] \quad [\text{A.25}]$$

Using the relationships $[e^{i\delta} = \cos\delta + i \sin\delta]$ and $[e^{-i\delta} = \cos\delta - i \sin\delta]$ and the definitions $r_m = g_m + i h_m$, the C_m matrix can be determined in terms familiar quantities given below:

$$p_m = e^{\alpha m - 1} \cos\phi_{m-1}$$

$$q_m = e^{\alpha m - 1} \sin\gamma_{m-1}$$

$$r_m = e^{\alpha m - 1} [g_m \cos\gamma_{m-1} - h_m \sin\gamma_{m-1}]$$

$$s_m = e^{\alpha m - 1} [h_m \cos\gamma_{m-1} + g_m \sin\gamma_{m-1}]$$

$$t_m = e^{-\alpha m-1} [g_m \cos l_{m-1} + h_m \sin \gamma_{m-1}]$$

$$u_m = e^{-\alpha m-1} [h_m \cos l_{m-1} - g_m \sin \gamma_{m-1}]$$

$$v_m = e^{-\alpha m-1} \cos \gamma_{m-1}$$

$$w_m = -e^{-\alpha m-1} \sin \gamma_{m-1}$$

For reflectance, the reflectivity and reflectance can be calculated using the final matrix C_{1m} . The reflectivity (r) and the reflectance (R) can be expressed as the following equations

$$r = \frac{t_{1_m} + i u_{1_m}}{p_{1_m} + i q_{1_m}} \quad [\text{A.26}]$$

$$R = \frac{t_{1_m}^2 + u_{1_m}^2}{p_{1_m}^2 + q_{1_m}^2} \quad [\text{A.27}]$$

The formulation given here can most easily be handled by computer except in the most simple cases.

APPENDIX 2.2 COMPUTER PROGRAMS

RASI4.FOR

C This program is designed to calculate the reflectance and transmittance for a series stratified isotropic layers as a function of frequency according using a matrix method:

C See:

C Heavens, O. S. Optical Properties of Thin Solid Films; Dover: New York, Chapter 4 or Born, M; Wolf, E. Principles of Optics; Pergamon: Oxford, 1975.

C 0 - 5 films can be designated with this program

C This program will input the optical constants for several stratified layers and calculate the reflectance and transmittance for both parallel and perpendicular polarization. The optical constant data for each layer must be given at the same frequency values for each program to operate correctly. For ratioed spectra, individual spectra must be calculated for background or reference and the ratio or subtraction done in a separate program.

C Variables used in this program:

C FINAME(I)- File name of the optical constants of C individual layers.

C PHI - angle of incidence (degrees)

C FRQ(I) - frequency (cm-1)

C D(I) - thickness (angstroms)

C KF(I) - attenuation coefficient (no units)

C NF(I) - refractive index (no units)

C N(I) - complex index of refraction (N - i)

C RRP(I) - reflectance / parallel polarization

C RRS(I) - reflectance / perpendicular polarization

C TTP(I) - transmittance / parallel polarization

C TTS(I) - transmittance / perpendicular polarization

INTEGER M,TST,POSINT

REAL D(10),SAVE(10),LAMBDA,PHI,NF(5,3000),KF(5,3000)

REAL FRQ(3000),FFRQ(5,3000)
DOUBLE PRECISION PSI,DELTA,TRNP,TRNS,RFLP,RFLS
DOUBLE PRECISION
RRP(1,3000),RRS(1,3000),TTP(1,3000),TTS(1,3000)
DOUBLE PRECISION RFCP(3000),RFCS(3000),TFCP(3000)
DOUBLE PRECISION
TFCS(3000),RAP(3000),RAS(3000),TAP(3000)
DOUBLE PRECISION TAS(3000),RRTEST,ITTEST
COMPLEX*16 N(0:11)
CHARACTER NAME*12, NAMED*12, DESCRIP*40
CHARACTER*12 FLNAME(5)
C PI=3.14159265358979
C
PRINT *, 'NUMBER OF FILM LAYERS?'
READ *, M
PRINT *, M
PRINT *, 'FILE FOR AMBIENT LAYER'
READ (*,'(A)') FLNAME(0)
PRINT *, FLNAME(0)
DO 3 I=1,M+1
PRINT *, 'FILE NAME FOR LAYER?', I
READ (*,'(A)') FLNAME(I)
PRINT *, FLNAME(I)
3 CONTINUE
TST=1
DO J=0,M+1
OPEN (9,FILE=FLNAME(J),STATUS='OLD')
PRINT *, 'Loading File #', J
CNT=0
DO WHILE (.NOT. EOF(9))
CNT=CNT+1
READ (9,*) FFRQ(J,CNT),NF(J,CNT),KF(J,CNT)
PRINT *, FFRQ(J,CNT),NF(J,CNT),KF(J,CNT)
END DO
CLOSE(9)
END DO
PTS=CNT
PRINT *, PTS
11 FORMAT (F7.1)

```

14 FORMAT (F6.3)
15 FORMAT (F7.3)

DO 17, I=1,PTS
FRQ(I)=FFRQ(1,I)
17 CONTINUE

20 PRINT *,'Enter incident angle:'
READ *,PHI
PRINT *, PHI

C
DO 25 I=1,M
PRINT *,'Enter Film Thickness:'
PRINT *,'Layer #', I
READ *,D(I)
PRINT *,D(I)
25 CONTINUE

PRINT *,'Please wait, simulating Spectrum'
DO 200 II=1,2

DO 30 JJ=1,PTS
DO 29 K=0,M+1
N(K)=DCMPLX(NF(K,JJ),-KF(K,JJ))
29 CONTINUE

LAMBDA=(1/FRQ(JJ))*10**8

CALL
CDPSIM(M,N,D,LAMBDA,PHI,DELTA,PSI,TRNP,TRNS,RFLP,RF
LS)

RRP(II,JJ)=RFLP
RRS(II,JJ)=RFLS
TTP(II,JJ)=TRNP
TTS(II,JJ)=TRNS
30 CONTINUE
200 CONTINUE

C-----
C Store data in a format for graphing

```

```

C-----
PRINT *,'NAME OF FILE TO STORE DATA?'
READ *,(A) NAME
POSINT=10
212 IF (NAME(POSINT:POSINT).EQ.' ') THEN
POSINT = POSINT + 1
GO TO 212
END IF

C-----
C Store Reflectance for parallel polarization
C-----
NAMES=NAME(:POSINT) // '.RP'
OPEN (9,FILE=NAMES,STATUS='NEW')
DO 230 J=1,PTS
WRITE (9,*) FRQ(J),RRP(1,J)
230 CONTINUE
CLOSE(9)

C-----
C Store reflectance for perpendicular polarization
C-----
NAMES=NAME(:POSINT) // '.RS'
OPEN (9,FILE=NAMES,STATUS='NEW')
DO 235 J=1,PTS
WRITE (9,*) FRQ(J),RRS(1,J)
235 CONTINUE
CLOSE(9)

C-----
C Store transmittance for parallel polarization
C-----
NAMES=NAME(:POSINT) // '.TP'
OPEN (9,FILE=NAMES,STATUS='NEW')
DO 240 J=1,PTS
WRITE (9,*) FRQ(J),TTP(1,J)
240 CONTINUE
CLOSE(9)

C-----
C Store transmittance for perpendicular polarization
C-----
NAMES=NAME(:POSINT) // '.TS'
OPEN (9,FILE=NAMES,STATUS='NEW')
DO 245 J=1,PTS
WRITE (9,*) FRQ(J),TTS(1,J)
245 CONTINUE

```

```

CLOSE(9)
END

SUBROUTINE
CDPSIM(M,N,D,LAMBDA,PHI,DELTA,PSI,TRNP,TRNS,RFLP,RF
LS)
REAL LAMBDA,D(10),PHI
DOUBLE PRECISION PI,PHIO,PSI,DELTA,PA,PB,SA,SB
COMPLEX*16 N(0:11),COSP(0:11),BETA(10),SNELL,RHO
COMPLEX*16
SP(0:5,2),SS(0:5,2),RP(0:10),RS(0:10),TMP(2,2)
COMPLEX*16 TP(0:10),TS(0:10),EX3(6),EX4(6)
DOUBLE PRECISION RFLP,RFLS,TRNS,TRNP
PI=3.14159265358979
PHIO=PHI*PI/180
SNELL=N(0)*DSIN(PHIO)
COSP(0)=DCOS(PHIO)

DO 1 J=1,M+1
COSP(J)=CDSQRT(1-(SNELL/N(J))**2)

RS(J-1)=(N(J-1)*COSP(J-1)-N(J)*COSP(J))/(N(J-1)*COSP(J-1)+
& N(J)*COSP(J))
RP(J-1)=(N(J-1)*COSP(J)-N(J)*COSP(J-1))/(N(J-1)*COSP(J)+
& N(J)*COSP(J-1))

TS(J-1)=(2*N(J-1)*COSP(J-1))/(N(J-1)*COSP(J-1)+N(J)*COSP(J))
TP(J-1)=(2*N(J-1)*COSP(J-1))/(N(J-1)*COSP(J)+N(J)*COSP(J-1))
IF (J.EQ.(M+1)) GO TO 1
BETA(J)=2*PI*D(J)*N(J)*COSP(J)/LAMBDA
EX3(J)=CDEXP(0,1)*BETA(J)
EX4(J)=CDEXP(0,-1)*BETA(J)
1 CONTINUE
DO 2 J=1,2
SP(0,J,J)=(1,0)
SS(0,J,J)=(1,0)
2 CONTINUE
SP(0,1,2)=RP(0)
SP(0,2,1)=RP(0)

```

```

SS(0,1,2)=RS(0)
SS(0,2,1)=RS(0)
IF (M.EQ.0) THEN
GOTO 7
ENDIF
DO 3 J=1,M
SP(J,1,1)=EX3(J)
SP(J,2,1)=RP(J)*EX4(J)
SP(J,1,2)=RP(J)*EX3(J)
SP(J,2,2)=EX4(J)
SS(J,1,1)=EX3(J)
SS(J,2,1)=RS(J)*EX4(J)
SS(J,1,2)=RS(J)*EX3(J)
SS(J,2,2)=EX4(J)
3 CONTINUE

TMP(1,1)=1
TMP(2,1)=0
TMP(1,2)=0
TMP(2,2)=1
DO 5, J=0,M
CALL MM(SP,TMP,J)
5 CONTINUE

SP(M,1,1)=TMP(1,1)
SP(M,2,1)=TMP(2,1)
SP(M,1,2)=TMP(1,2)
SP(M,2,2)=TMP(2,2)
TMP(1,1)=1
TMP(2,1)=0
TMP(1,2)=0
TMP(2,2)=1
DO 6, J=0,M
CALL MM(SS,TMP,J)
6 CONTINUE

SS(M,1,1)=TMP(1,1)
SS(M,2,1)=TMP(2,1)
SS(M,1,2)=TMP(1,2)
SS(M,2,2)=TMP(2,2)
7 CONTINUE

SA=SP(M,2,1)*DCONJG(SP(M,2,1))
SB=SP(M,1,1)*DCONJG(SP(M,1,1))

```

```

RFLP=SA/SB
PA=SS(M,2,1)*DCONJG(SS(M,2,1))
PB=SS(M,1,1)*DCONJG(SS(M,1,1))
RFLS=PA/PB

TRNP=1
TRNS=1

DO 100 J =1,M+1
TRNP=TRNP*(TP(J-1)*DCONJG(TP(J-1)))
TRNS=TRNS*(TS(J-1)*DCONJG(TS(J-1)))
100 CONTINUE
TRNP=TRNP/SB
TRNS=TRNS/PB
RETURN
END

C MM is a FORTRAN subroutine which calculates
multiplication of two
C (2x2) matrices: C=AxB.
C
SUBROUTINE MM(A,TMP,J)
COMPLEX*16 TMP(2,2),A(0:5,2,2),C(2,2)
INTEGER J
C(1,1)=TMP(1,1)*A(J,1,1)+TMP(1,2)*A(J,2,1)
C(1,2)=TMP(1,1)*A(J,1,2)+TMP(1,2)*A(J,2,2)
C(2,1)=TMP(2,1)*A(J,1,1)+TMP(2,2)*A(J,2,1)
C(2,2)=TMP(2,1)*A(J,1,2)+TMP(2,2)*A(J,2,2)
TMP(1,1)=C(1,1)
TMP(2,1)=C(2,1)
TMP(1,2)=C(1,2)
TMP(2,2)=C(2,2)
RETURN
END

```

NK10.FOR

C This program is designed to calculate the optical
 C constants of a polymer film if the thickness, high
 C frequency refractive index are known. Experimental
 C data is in the form a transmittance spectrum.

C For general review of optical theory, see Heavens,
 C O. S. Optical Properties of Thin Solid Films; Dover:
 C New York, Chapter 4 or Born, M; Wolf, E. Principles
 C of Optics; Pergamon: Oxford, 1975.

C For a detailed analysis of this procedure for thin
 C films, see the work of Jones and coworkers:

C Spectrochim Acta 1976, 32A, 75
 C Spectrochim Acta 1976, 32A, 85
 C Spectrochim Acta 1976, 32A, 99
 C Spectrochim Acta 1976, 32A, 111
 C Appl. Spectrosc. 1980, 34, 652

C Variable used in this program:

C PHI - angle of incidence (degrees)
 C FRQ(I) - frequency (cm-1)
 C D(I) - thickness (angstroms)
 C KF(I) - attenuation coefficient (no units)
 C NF(I) - refractive index (no units)
 C N(I) - complex index of refraction (N - iK)
 C NIFIN - high frequency refractive index
 C TRORG(I) - original transmittance spectrum
 C ORG(I) - original k spectrum calculated from TRORG
 C DEL - error in the original transmittance spectrum
 C and the calc.

C M - number of layers
 C SC - scaling factor - original spectrum can be
 C multiplied by a factor
 C correct for differences between sample and
 C background throughput
 C SEG - number of segments - This variable is
 C important as it limits the number of data points
 C entered. The number of data points is limited to

C 2500 due to limitations on the size of the compiled
 C program. SEG allows one to enter data at different
 C resolutions (i.e. one segment may be at 2 cm-1,
 C while another may be at 4cm-1, etc. SEG is the
 C number of different segments to enter.
 C Another point is that this type of feature can only
 C be used here where the KK algorithm does not
 C require equal spaced data points as is used in this
 C program. It will not work with KK algorithms using
 C Simpson's or Trapezoid formula.
 C PART(I) - cutoff frequencies for analysis
 C INT(I) - data point interval - will define resolution
 C NUM - number of iterations

INTEGER M, POSINT, PTS, X, ITNUM, NUM, SEG, CH
 REAL D(10), LAMBDA, PHI, NF(3,2500), KF(3,2500), DEL, SC
 REAL FRQ(2500), NIFIN, ERROR, PART(10), INT(10)
 DOUBLE PRECISION PSI, DELTA, TRNP, TRNS, RFLP, RFLS
 REAL TR(2500), TRORG(2500), A(2500), B(2500), TMP0, TMP1
 REAL ORG(2500), KTN(2500), AAA, NFREQ, AO(2500), BO(2500)
 COMPLEX*16 N(0:11)
 CHARACTER NAME*10,
 NAME*10, NAMED*10, DESCRIP*40
 CHARACTER*40 FLNAME
 PI=3.14159265358979
 X=0
 ERROR=0
 M=1

PRINT *, 'FILE NAME FOR TRANSMISSION DATA?'
 READ (*, '(A)') FLNAME
 OPEN (9, FILE=FLNAME, STATUS='OLD')
 PRINT *, '100% (1) OR 1.0 (2) FORMAT FOR MAX
 REFLECTION?'
 READ *, CH

PRINT *, 'SCALING FACTOR'
 READ *, SC

PRINT *, 'NUMBER OF DATA SEGMENTS'
 READ *, SEG
 DO I=1, SEG

```

7 FORMAT (I4)
8 FORMAT (F6.4)
9 FORMAT (G7.7,1X,G7.7)
11 FORMAT (F3.1)
C The incident angle for transmission is zero degrees.
PHI=0
PRINT *,'Enter Film Thickness:'
READ *,D(1)
PRINT *,D(1)
PRINT *,'Enter refractive index at infinite frequency'
READ *,NFIN
N(0)=(1,0)
AAA=2.30258
DO I=1,PTS
DEN=4*PI*D(1)*FRQ(I)/I0**8
ORG(I)=(AAA*LOG10(1/TR(I)))/DEN
KF(1,I)=ORG(I)
END DO
C Iteration Procedure
DO ITNUM=1,NUM
PRINT *,ITNUM,PTS,FRQ(1),FRQ(PTS)
DO V=1,PTS
END DO
C Calculate the slope and intercept values for each consecutive
set of data
C pairs
DO I=1,PTS-1
A(I)=(FRQ(I+1)*KF(1,I)-FRQ(I)*KF(1,I+1))/(FRQ(I+1)-FRQ(I))
B(I)=(KF(1,I+1)-KF(1,I))/(FRQ(I+1)-FRQ(I))
END DO
PRINT *,WAIT, CALCULATING N VALUES FOR

```

```

PRINT *,'CUTOFF FREQUENCY FOR PART,I
READ *,PART(I)
PRINT *,'DATA POINT INTERVAL?'
READ *,INT(I)
END DO
P=1
PRINT *,WAIT, ENTERING POINTS'
PTS=0
CNT=1
DO WHILE (.NOT. EOF(9))
IF (CNT.EQ.INT(P))THEN
PTS=PTS+1
READ (9,*) FRQ(PTS),TRORG(PTS)
IF(CH.EQ.1)THEN
TRORG(PTS)=TRORG(PTS)/100*SC
ELSE
END IF
TR(PTS)=TRORG(PTS)
CNT=1
ELSE
READ (9,9) TMP0,TMP1
CNT=CNT+1
END IF
IF (FRQ(PTS).GE.PART(P)) THEN
P=P+1
END IF
END DO
CLOSE(9)
PRINT *,TOTAL NUMBER OF POINTS',PTS
PRINT *,NUMBER OF ITERATIONS'
READ *,NUM
DO 5 I=1,PTS
NF(2,I)=1
KF(2,I)=0
5 CONTINUE
6 FORMAT (F8.2)

```

ROUND,ITNUM

```
CALL NCALC(FRQ,A,B,NF,PTS,NIFIN,PI,NFREQ)
DO V=1,PTS-2
NF(1,V)=(NF(1,V)+NF(1,V+1))/2
KF(1,V)=KF(1,V+1)
ORG(V)=ORG(V+1)
FRQ(V)=FRQ(V+1)
TRORG(V)=TRORG(V+1)
END DO
PTS=PTS-2

DO JJ=1,PTS
DO K=1,M+1
N(K)=DCMPLX(NF(K,JJ),-KF(K,JJ))
END DO
LAMBDA=(1/FRQ(JJ))*10**8
IF (JJ.EQ.1)THEN
PRINT *,WAIT, CALCULATING NEW TRANSMISSION
SPECTRUM'
END IF
CALL
CDPSIM(M,N,D,LAMBDA,PHI,DELTA,PSI,TRNP,TRNS,RFLP,RF
LS)
TR(JJ)=TRNP
END DO

CALL KCALC(TR,FRQ,PTS,D,KTN)
DO W=1,PTS
DEL=ORG(W)-KTN(W)
ERROR=ERROR+DEL
KF(1,W)=KF(1,W)+DEL
END DO
ERROR=ABS(ERROR)/PTS
PRINT *,ERROR

END DO
```

C-----
C Store data in a format for graphing in the form
C frequency (cm-1), n, k, original trans. spectrum, last calc.

spectrum

```
C-----  
PRINT *,NAME OF FILE TO STORE DATA?  
READ (*,'A') NAME  
POSINT=10  
222 IF (NAME=POSINT:POSINT) .EQ. ' ') THEN  
POSINT = POSINT - 1  
GO TO 222  
END IF  
NAMER2=NAME(:POSINT) // 'PLT'  
OPEN (8,FILE=NAMER2,STATUS='NEW')  
DO J=1,PTS  
WRITE (8,*) FRQ(J),KF(1,J),NF(1,J),TRORG(J),TR(J)  
END DO  
CLOSE(8)  
END  
SUBROUTINE  
CDPSIM(M,N,D,LAMBDA,PHI,DELTA,PSI,TRNP,TRNS,RFLP,RF  
LS)  
REAL LAMBDA,D(10),PHI  
DOUBLE PRECISION PI,PHI0,PSI,DELTA,PA,PB,SA,SB  
COMPLEX*16 N(0:11),COSPO(0:11),BETA(10),SNELL,RHO  
COMPLEX*16  
SP(0:5,2,2),SS(0:5,2,2),RP(0:10),RS(0:10),TMP(2,2)  
COMPLEX*16 TP(0:10),TS(0:10),EX3(5),EX4(6)  
DOUBLE PRECISION RFLP,RFLS,TRNS,TRNP  
PI=3.14159265358979  
PHI0=PHI*PI/180  
SNELL=N(0)*DSIN(PHI0)  
COSPO(0)=DCOS(PHI0)  
DO 1 J=1,M+1  
COSPO(J)=CDSQRT(1-(SNELL/N(J))**2)  
RS(J-1)=(N(J-1)*COSPO(J-1)-N(J)*COSPO(J))/(N(J-1)*COSPO(J-1)+  
& N(J)*COSPO(J))  
RP(J-1)=(N(J-1)*COSPO(J)-N(J)*COSPO(J-1))/(N(J-1)*COSPO(J)+  
& N(J)*COSPO(J-1))
```

```

TS(J-1)=(2*N(J-1)*COSP(J-1))/(N(J-1)*COSP(J-1)+N(J)*COSP(J))
TP(J-1)=(2*N(J-1)*COSP(J-1))/(N(J-1)*COSP(J)+N(J)*COSP(J-1))
IF (J.EQ. (M+1)) GO TO 1
BETA(J)=2*PI*D(J)*N(J)*COSP(J)/LAMBDA
EX3(J)=CDEXP(0,1)*BETA(J)
EX4(J)=CDEXP(0,-1)*BETA(J)
1 CONTINUE
DO 2 J=1,2
SP(0,J,J)=(1,0)
SS(0,J,J)=(1,0)
2 CONTINUE
SP(0,1,2)=RP(0)
SP(0,2,1)=RP(0)
SS(0,1,2)=RS(0)
SS(0,2,1)=RS(0)
IF (M.EQ. 0) THEN
GOTO 7
END IF
DO 3 J=1,M
SP(J,1,1)=EX3(J)
SP(J,2,1)=RP(J)*EX4(J)
SP(J,1,2)=RP(J)*EX3(J)
SP(J,2,2)=EX4(J)
SS(J,1,1)=EX3(J)
SS(J,2,1)=RS(J)*EX4(J)
SS(J,1,2)=RS(J)*EX3(J)
SS(J,2,2)=EX4(J)
3 CONTINUE

TMP(1,1)=1
TMP(2,1)=0
TMP(1,2)=0
TMP(2,2)=1
DO 6, J=0,M
CALL MM(SS,TMP,J)
6 CONTINUE
SS(M,1,1)=TMP(1,1)
SS(M,2,1)=TMP(2,1)
SS(M,1,2)=TMP(1,2)
SS(M,2,2)=TMP(2,2)

7 CONTINUE
SA=SP(M,2,1)*DCONJG(SP(M,2,1))
SB=SP(M,1,1)*DCONJG(SP(M,1,1))
RFLP=SA/SB
PA=SS(M,2,1)*DCONJG(SS(M,2,1))
PB=SS(M,1,1)*DCONJG(SS(M,1,1))
RFLS=PA/PB

TRNP=1
TRNS=1

DO 100 J =1,M+1
TRNP=TRNP*(TP(J-1)*DCONJG(TP(J-1)))
TRNS=TRNS*(TS(J-1)*DCONJG(TS(J-1)))
100 CONTINUE
TRNP=TRNP/SB
TRNS=TRNS/PB
RHO=(SP(M,2,1)/SP(M,1,1))*SS(M,1,1)/SS(M,2,1)
PSI=DATAN(CDABS(RHO))*180/PI
DELTA=DATAN2(DIMAG(RHO),DREAL(RHO))*180/PI
RETURN
END

C
C MM is a FORTRAN subroutine which calculates
multiplication of two
C (2x2) matrices: C=AxB.
C
SUBROUTINE MM(A,TMP,J)
COMPLEX*16 TMP(2,2),A(0:5,2,2),C(2,2)
INTEGER J
C(1,1)=TMP(1,1)*A(J,1,1)+TMP(1,2)*A(J,2,1)

```

```

C(1,2)=TMP(1,1)*A(J,1,2)+TMP(1,2)*A(J,2,2)
C(2,1)=TMP(2,1)*A(J,1,1)+TMP(2,2)*A(J,2,1)
C(2,2)=TMP(2,1)*A(J,1,2)+TMP(2,2)*A(J,2,2)
TMP(1,1)=C(1,1)
TMP(2,1)=C(2,1)
TMP(1,2)=C(1,2)
TMP(2,2)=C(2,2)
RETURN
END

SUBROUTINE KCALC(TR,FRQ,PTS,D,KTN)
C KCALC is a subroutine that estimates k values from the
C transmission spectrum
REAL D(10),FRQ(2500)
REAL TR(2500),KTN(2500)
REAL DEN,AA
INTEGER PTS
PI=3.14159265358979
AAA=2.30258
DO 100 I=1,PTS
C THICKNESS MUST BE EXPRESS IN CM TO
CORRESPOND TO CM-1
DEN=4*PI*D(I)*FRQ(I)/10**8
KTN(I)=(AAA*LOG10(1/TR(I)))/DEN
100 CONTINUE
RETURN
END

SUBROUTINE NCALC(FRQ,A,B,NF,PTS,NIFIN,PI,NFREQ)
C This program calculates n values from input k values
approximated from
C the transmission spectrum. This is done through the use of
the Kramers-
C Kronig transform
C
REAL FRQ(2500),KF(3,2500),NF(3,2500),NFREQ
REAL NIFIN,INTEG,INTEGS,NADJ
REAL MNX(2500),SL
REAL A(2500),B(2500),X1,X2,T
INTEGER PTS,MARK
MARK=0
DO I=1,PTS-1
NF(1,I)=0
MNX(I)=(FRQ(I+1)+FRQ(I))/2.0
DO J=1,PTS-1
X1=FRQ(J)
X2=FRQ(J+1)
IF((MNX(I).LT.X1).OR.(MNX(I).GT.X2)) THEN
NF(1,I)=NF(1,I)+INTEG(X1,X2,A(J),B(J),MNX(I))
ELSE
NF(1,I)=NF(1,I)+INTEGS(X1,X2,A(J),B(J),MNX(I))
END IF
END DO
NF(1,I)=NIFIN+NF(1,I)*2/PI

IF(MNX(I).GE.NFREQ.AND.MARK.EQ.0)THEN
NADJ=NF(1,I)
MARK=1
ELSE
END IF
END DO
REAL FUNCTION INTEG(X1,X2,AA,BB,EE)
REAL AA,BB,CC,DD,X1,X2,EE
CC=-LOG((X2-EE)/(X1-EE))
DD=LOG((X2+EE)/(X1+EE))
INTEG=0.5*((AA+BB*EE)*CC+(AA-BB*EE)*DD)+BB*(X2-X1)

```

```
RETURN
END

REAL FUNCTION INTEGS(X1,X2,AA,BB,EE)
REAL X1,X2,AA,BB,EE

INTEGS=0.5*((AA-BB*EE)*LOG((3*X2+X1)/(3*X1+X2))+2*BB*(X2
-X1))
RETURN
END
```

RASGEN.FOR

C C This program is designed to calculate the reflectance
 C C and transmittance for a series stratified isotropic
 C C layers using a matrix method. See:
 C C Heavens, O. S. Optical Properties of Thin Solid
 C C Films; Dover: New York, Chapter 4 or Born, M; Wolf,
 C C E. Principles of Optics; Pergamon: Oxford, 1975.
 C C
 C C 0 - 2 films can be designated with this program
 C C
 C C The program is designed to allow the variation of
 C C one variable with the others held constant. First
 C C enter all variables, then pick the one to vary and
 C C give the minimum, maximum values wanted with
 C C the scan increment. Only 300 data points are
 C C allowed.
 C C Variable used in this program:
 C C PHI - angle of incidence (degrees)
 C C FRQ(I) - frequency (cm-1)
 C C D(I) - thickness (angstroms)
 C C KF(I) - attenuation coefficient (no units)
 C C NF(I) - refractive index (no units)
 C C N(I) - complex index of refraction (N - iK)
 C C RRP(I) - reflectance / parallel polarization
 C C RRS(I) - reflectance / perpendicular polarization
 C C TTP(I) - transmittance / parallel polarization
 C C TTS(I) - transmittance / perpendicular polarization
 C C RAP(I) - absorbance factor (Ro-R)/Ro / parallel
 C C polarization
 C C RAS(I) - absorbance factor (Ro-R)/Ro / perpendicular
 C C polarization
 C C AP(I) - absorbance -log(R/Ro) / parallel polarization
 C C AS(I) - absorbance -log(R/Ro) / perpendicular
 C C polarization
 C C TP(I) - absorbance -log(T/To) / parallel polarization
 C C TS(I) - absorbance -log(T/To) / perpendicular
 C C polarization
 C C PSI - ellipsometric amplitude relation psi
 C C DEL - ellipsometric phase relation delta

```

INTEGER M,TST,POSIT,INTERVAL(6),PTS,JJ,OPTION
REAL D(10),SAVE(10),LAMBDA,PHI,NF(0:300),KF(0:300)
REAL FRQ(100),VAR,ST,ED,DIV
DOUBLE PRECISION PSI,DELTA,TRNP,TRNS,RFLP,RFLS
DOUBLE PRECISION
RRP(1,300),RRS(1,300),TTP(1,300),TTS(1,300)
DOUBLE PRECISION RFCP(300),RFCS(300),TFCP(300)
DOUBLE PRECISION
TFCS(300),RAP(300),RAS(300),TAP(300)
DOUBLE PRECISION AS(300),AP(300),TS(300),TP(300)
DOUBLE PRECISION TAS(300),RRTST,TTEST
COMPLEX*16 N(0:11)
CHARACTER NAME*10, NAMED*10,DESCRIP*40
CHARACTER*10
NAME1,NAME2,NAME3,NAME4,NAME5,NAME6,NAME7
PTS=1
JJ=1
PI=3.14159265358979

PRINT *,'NUMBER OF FILM LAYERS?'
READ *,M
PRINT *,M
DO 5 I=0,M+1
PRINT *,'ENTER N,K FOR LAYER NUMBER,I
IF (I.EQ. M+1) THEN
PRINT *,'SUBSTRATE'
ELSE
END IF
READ *, NF(I)
READ *, KF(I)
PRINT *, NF(I),KF(I)
5 CONTINUE

20 PRINT *,'Enter incident angle:'
READ *,PHI
PRINT *, PHI
PRINT *,'Enter wavenumber'
READ *,FRQ(1)

DO 25 I=1,M
PRINT *,'Enter Film Thickness:'

```

```

PRINT *,LAYER#,I
READ *,D(I)
PRINT *,D(I)
25 CONTINUE
IF(M.GT.0) THEN
DO I=1,M
PRINT *,3*I-3,'...REFRACTIVE INDEX, LAYER',I
PRINT *,3*I-2,'...K VALUE, LAYER',I
PRINT *,3*I-1,'...FILM THICKNESS, LAYER',I
END DO
I=I-1
PRINT *,3*I,'...REFRACTIVE INDEX VALUE, SUBSTRATE'
PRINT *,3*I+1,'...K VALUE OF SUBSTRATE'
PRINT *,3*I+2,'...FREQUENCY (CM-1)'
PRINT *,3*I+3,'...INCIDENCE ANGLE'
ELSE
I=0
PRINT *,3*I,'...REFRACTIVE INDEX VALUE, SUBSTRATE'
PRINT *,3*I+1,'...K VALUE OF SUBSTRATE'
PRINT *,3*I+2,'...FREQUENCY (CM-1)'
PRINT *,3*I+3,'...INCIDENCE ANGLE'
END IF
PRINT *,'VARY WHICH VARIABLE?'
READ *,OPTION
PRINT *,'STARTING VALUE'
READ *,ST
PRINT *,'ENDING VALUE'
READ *,ED
PRINT *,'NUMBER OF DIVISIONS'
READ *,DIV
CALL INITINFO
JJ=1
DO 200 VAR=ST,ED,(ED-ST)/DIV
CALL SELECTION(OPTION,M,NF,KF,D,FRQ,PHI,VAR)
DO 190 II=1,2
IF (II.EQ.1) THEN
DO K=1,M
SAVE(KQ)=KF(K)
KF(KQ)=0
END DO
ELSE
DO K=1,M
KF(KQ)=SAVE(K)
END DO
END IF
DO 29 K=0,M+1
N(K)=DCMLPX(NF(K),-KF(K))
29 CONTINUE
LAMBDA=(1/FRQ(1))*10**8
CALL
CDPSIM(M,N,D,LAMBDA,PHI,DELTA,PSI,TRNP,TRNS,RFLP,RF
LS)
RRP(II,JJ)=RFLP
RRS(II,JJ)=RFLS
TTP(II,JJ)=TRNP
TTS(II,JJ)=TRNS
IF (II.EQ.2) THEN
RAP(JJ)=(RRP(1,JJ)-RRP(2,JJ))/RRP(1,JJ)
RAS(JJ)=(RRS(1,JJ)-RRS(2,JJ))/RRS(1,JJ)
AP(JJ)=-LOG10(RRP(2,JJ)/RRP(1,JJ))
AS(JJ)=-LOG10(RRS(2,JJ)/RRS(1,JJ))
TP(JJ)=-LOG10(TTP(2,JJ)/TTP(1,JJ))
TS(JJ)=-LOG10(TTS(2,JJ)/TTS(1,JJ))
CALL
STOREINFO(VAR,II,JJ,RRP,RRS,TTP,TTS,PSI,DELTA,RAS,RAP,
&AS,AP,TS,TP)
ELSE
END IF

```

```

190 END DO
200 END DO
END
SUBROUTINE INITINFO
C-----
C Initinfo() is a subprogram designed to initialize files for
C data storage. Files are opened to store the following data:
C Reflectance, parallel polarization *.RP
C Reflectance, perpendicular polarization *.RS
C Transmittance, parallel polarization *.TP
C Transmittance, perpendicular polarization *.TS
C Absorbance factor for reflectance (see Greenler, J. Chem.
C Phys. 1966, 44,310
C (Ro-R)/Ro *.AFP and *.AFS for parallel and perpendicular pol.
C Absorbance -log(R/Ro) *.ABP and *.ABS for parallel and
C perpen. pol.
C Absorbance -log(T/To) *.ATP and *.ATS for parallel and
C perpen. pol.
C PSI, *.psi and DEL, *.del
C-----
CHARACTER*10 NAMEA, NAMEB, NAMEC, NAMEE, NAMEF, NAMEG, NAMEH, NAMEI,
NAMEJ,
NAMEK, NAMEL, NAMEM, NAMEO, NAMEP, NAMEQ, NAMER, NAMES, NAMEV,
NAMEW,
NAMEX, NAMEY, NAMEZ, NAMEAA, NAMEAB, NAMEAC, NAMEAD, NAMEAE, NAMEAF,
NAMEAG,
NAMEAH, NAMEAJ, NAMEAK, NAMEAL, NAMEAM, NAMEAN, NAMEAO, NAMEAP, NAMEAQ,
NAMEAR,
NAMEAS, NAMEAT, NAMEAU, NAMEAV, NAMEAW, NAMEAX, NAMEAY, NAMEAZ, NAMEBA,
NAMEBB,
NAMEBC, NAMEBD, NAMEBE, NAMEBF, NAMEBG, NAMEBH, NAMEBJ, NAMEBK, NAMEBL,
NAMEBM,
NAMEBN, NAMEBO, NAMEBP, NAMEBQ, NAMEBR, NAMEBS, NAMEBT, NAMEBU, NAMEBV,
NAMEBW,
NAMEBX, NAMEBY, NAMEBZ, NAMECA, NAMECB, NAMECC, NAMECD, NAMECE, NAMECF,
NAMECG,
NAMECH, NAMECJ, NAMECK, NAMECL, NAMECM, NAMECN, NAMECO, NAMECP, NAMECQ,
NAMECR,
NAMECS, NAMECT, NAMECU, NAMECV, NAMECW, NAMECX, NAMECY, NAMECZ, NAMEDA,
NAMEDB,
NAMEDC, NAMEDD, NAMEDE, NAMEDF, NAMEDG, NAMEDH, NAMEDJ, NAMEDK, NAMEDL,
NAMEDM,
NAMEDN, NAMEDO, NAMEDP, NAMEDQ, NAMEDR, NAMEDS, NAMEDT, NAMEDU, NAMEDV,
NAMEDW,
NAMEDX, NAMEDY, NAMEDZ, NAMEEA, NAMEEB, NAMEEC, NAMEED, NAMEEE, NAMEEF,
NAMEEG,
NAMEEH, NAMEEJ, NAMEEK, NAMEEL, NAMEEM, NAMEEN, NAMEEO, NAMEEP, NAMEEQ,
NAMEER,
NAMEES, NAMEET, NAMEEU, NAMEEV, NAMEEW, NAMEEX, NAMEEY, NAMEEZ, NAMEFA,
NAMEFB,
NAMEFC, NAMEFD, NAMEFE, NAMEFF, NAMEFG, NAMEFH, NAMEFJ, NAMEFK, NAMEFL,
NAMEFM,
NAMEFN, NAMEFO, NAMEFP, NAMEFQ, NAMEFR, NAMEFS, NAMEFT, NAMEFU, NAMEFV,
NAMEFW,
NAMEFX, NAMEFY, NAMEFZ, NAMEGA, NAMEGB, NAMEGC, NAMEGD, NAMEGE, NAMEGF,
NAMEGG,
NAMEGH, NAMEGJ, NAMEGK, NAMEGL, NAMEGM, NAMEGN, NAMEGO, NAMEGP, NAMEGQ,
NAMEGR,
NAMEGS, NAMEGT, NAMEGU, NAMEGV, NAMEGW, NAMEGX, NAMEGY, NAMEGZ, NAMEHA,
NAMEHB,
NAMEHC, NAMEHD, NAMEHE, NAMEHF, NAMEHG, NAMEHJ, NAMEHK, NAMEHL, NAMEHM,
NAMEHN,
NAMEHO, NAMEHP, NAMEHQ, NAMEHR, NAMEHS, NAMEHT, NAMEHU, NAMEHV, NAMEHW,
NAMEHX,
NAMEHY, NAMEHZ, NAMEIA, NAMEIB, NAMEIC, NAMEID, NAMEIE, NAMEIF, NAMEIG,
NAMEIH,
NAMEIJ, NAMEIK, NAMEIL, NAMEIM, NAMEIN, NAMEIO, NAMEIP, NAMEIQ, NAMEIR,
NAMEIS,
NAMEIT, NAMEIU, NAMEIV, NAMEIW, NAMEIX, NAMEIY, NAMEIZ, NAMEJA, NAMEJB,
NAMEJC,
NAMEJD, NAMEJE, NAMEJF, NAMEJG, NAMEJH, NAMEJJ, NAMEJK, NAMEJL, NAMEJM,
NAMEJN,
NAMEJO, NAMEJP, NAMEJQ, NAMEJR, NAMEJS, NAMEJT, NAMEJU, NAMEJV, NAMEJW,
NAMEJX,
NAMEJY, NAMEJZ, NAMEKA, NAMEKB, NAMEKC, NAMEKD, NAMEKE, NAMEKF, NAMEKG,
NAMEKH,
NAMEKJ, NAMEKK, NAMEKL, NAMEKM, NAMEKN, NAMEKO, NAMEKP, NAMEKQ, NAMEKR,
NAMEKS,
NAMEKT, NAMEKU, NAMEKV, NAMEKW, NAMEKX, NAMEKY, NAMEKZ, NAMELA, NAMELB,
NAMELC,
NAMELD, NAMELE, NAMELF, NAMELG, NAMELJ, NAMELK, NAMELL, NAMELM, NAMELN,
NAMELO,
NAMELP, NAMELQ, NAMELR, NAMELS, NAMELT, NAMELU, NAMELV, NAMELW, NAMELX,
NAMELY,
NAMELZ, NAMEMA, NAMEMB, NAMEMC, NAMEMD, NAMEME, NAMEMF, NAMEMG, NAMEMH,
NAMEMJ,
NAMEMK, NAMEML, NAMEMN, NAMEMO, NAMEMP, NAMEMQ, NAMEMR, NAMEMS, NAMEMT,
NAMEMU,
NAMEMV, NAMEMW, NAMEMX, NAMEMY, NAMEMZ, NAMENA, NAMENB, NAMENC, NAMEND,
NAMENE,
NAMENF, NAMENG, NAMENH, NAMENJ, NAMENK, NAMENL, NAMENM, NAMENO, NAMENP,
NAMENQ,
NAMENR, NAMENS, NAMENT, NAMENU, NAMENV, NAMENW, NAMENX, NAMENY, NAMENZ,
NAMEOA,
NAMEOB, NAMEOC, NAMEOD, NAMEOE, NAMEOF, NAMEOG, NAMEOH, NAMEOJ, NAMEOK,
NAMEOL,
NAMEOM, NAMEON, NAMEOP, NAMEOQ, NAMEOR, NAMEOS, NAMEOT, NAMEOU, NAMEOV,
NAMEOW,
NAMEOX, NAMEOY, NAMEOZ, NAMEPA, NAMEPB, NAMEPC, NAMEPD, NAMEPE, NAMEPF,
NAMEPG,
NAMEPH, NAMEPJ, NAMEPK, NAMEPL, NAMEPM, NAMEPN, NAMEPO, NAMEPP, NAMEPQ,
NAMEPR,
NAMEPS, NAMEPT, NAMEPU, NAMEPV, NAMEPW, NAMEPX, NAMEPY, NAMEPZ, NAMEQA,
NAMEQB,
NAMEQC, NAMEQD, NAMEQE, NAMEQF, NAMEQG, NAMEQH, NAMEQJ, NAMEQK, NAMEQL,
NAMEQM,
NAMEQN, NAMEQO, NAMEQP, NAMEQQ, NAMEQR, NAMEQS, NAMEQT, NAMEQU, NAMEQV,
NAMEQW,
NAMEQX, NAMEQY, NAMEQZ, NAMERA, NAMERB, NAMERC, NAMERD, NAMERE, NAMERF,
NAMERG,
NAMERH, NAMERJ, NAMERK, NAMERL, NAMERM, NAMERN, NAMERO, NAMERP, NAMERQ,
NAMERR,
NAMERS, NAMERT, NAMERU, NAMERV, NAMERW, NAMERX, NAMERY, NAMERZ, NAMESA,
NAMESB,
NAMESC, NAMESD, NAMESE, NAMESF, NAMESG, NAMESH, NAMESJ, NAMESK, NAMESL,
NAMESM,
NAMESN, NAMESO, NAMESP, NAMESQ, NAMESR, NAMESS, NAMEST, NAMESU, NAMESV,
NAMESW,
NAMESX, NAMESY, NAMESZ, NAMETA, NAMETB, NAMETC, NAMETD, NAMETE, NAMETF,
NAMETG,
NAMETH, NAMETJ, NAMETK, NAMETL, NAMETM, NAMETN, NAMETO, NAMETP, NAMETQ,
NAMETR,
NAMETS, NAMETU, NAMETV, NAMETW, NAMETX, NAMETY, NAMETZ, NAMEUA, NAMEUB,
NAMEUC,
NAMEUD, NAMEUE, NAMEUF, NAMEUG, NAMEUH, NAMEUJ, NAMEUK, NAMEUL, NAMEUM,
NAMEUN,
NAMEUO, NAMEUP, NAMEUQ, NAMEUR, NAMEUS, NAMEUT, NAMEUU, NAMEUV, NAMEUW,
NAMEUX,
NAMEUY, NAMEUZ, NAMEVA, NAMEVB, NAMEVC, NAMEVD, NAMEVE, NAMEVF, NAMEVG,
NAMEVH,
NAMEVJ, NAMEVK, NAMEVL, NAMEVM, NAMEVN, NAMEVO, NAMEVP, NAMEVQ, NAMEVR,
NAMEVS,
NAMEVT, NAMEVU, NAMEVV, NAMEVW, NAMEVX, NAMEVY, NAMEVZ, NAMEWA, NAMEWB,
NAMEWC,
NAMEWD, NAMEWE, NAMEWF, NAMEWG, NAMEWH, NAMEWJ, NAMEWK, NAMEWL, NAMEWM,
NAMEWN,
NAMEWO, NAMEWP, NAMEWQ, NAMEWR, NAMEWS, NAMEWT, NAMEWU, NAMEWV, NAMEWW,
NAMEWX,
NAMEWY, NAMEWZ, NAMEXA, NAMEXB, NAMEXC, NAMEXD, NAMEXE, NAMEXF, NAMEXG,
NAMEXH,
NAMEXJ, NAMEXK, NAMEXL, NAMEXM, NAMEXN, NAMEXO, NAMEXP, NAMEXQ, NAMEXR,
NAMEXS,
NAMEXT, NAMEXU, NAMEXV, NAMEXW, NAMEXX, NAMEXY, NAMEXZ, NAMEYA, NAMEYB,
NAMEYC,
NAMEYD, NAMEYE, NAMEYF, NAMEYG, NAMEYH, NAMEYJ, NAMEYK, NAMEYL, NAMEYM,
NAMEYN,
NAMEYO, NAMEYP, NAMEYQ, NAMEYR, NAMEYS, NAMEYT, NAMEYU, NAMEYV, NAMEYW,
NAMEYX,
NAMEYY, NAMEYZ, NAMEZA, NAMEZB, NAMEZC, NAMEZD, NAMEZE, NAMEZF, NAMEZG,
NAMEZH,
NAMEZJ, NAMEZK, NAMEZL, NAMEZM, NAMEZN, NAMEZO, NAMEZP, NAMEZQ, NAMEZR,
NAMEZS,
NAMEZT, NAMEZU, NAMEZV, NAMEZW, NAMEZX, NAMEZY, NAMEZZ
212 IF (NAME(:POSINT).EQ.' ') THEN
POSINT = POSINT - 1
GO TO 212
END IF
NAMEA=NAME(:POSINT) // '.RP'
OPEN (1,FILE=NAMEA,STATUS='NEW')
NAMEB=NAME(:POSINT) // '.RS'
OPEN (2,FILE=NAMEB,STATUS='NEW')
NAMEC=NAME(:POSINT) // '.TP'
OPEN (3,FILE=NAMEC,STATUS='NEW')
NAMEE=NAME(:POSINT) // '.PSI'
OPEN (5,FILE=NAMEE,STATUS='NEW')
NAMEF=NAME(:POSINT) // '.DEL'
OPEN (6,FILE=NAMEF,STATUS='NEW')
NAMEG=NAME(:POSINT) // '.AFP'
OPEN (7,FILE=NAMEG,STATUS='NEW')
NAMEH=NAME(:POSINT) // '.AFS'
OPEN (8,FILE=NAMEH,STATUS='NEW')
NAMEI=NAME(:POSINT) // '.ABP'
OPEN (9,FILE=NAMEI,STATUS='NEW')
NAMEJ=NAME(:POSINT) // '.ABS'
OPEN (10,FILE=NAMEJ,STATUS='NEW')
NAMEK=NAME(:POSINT) // '.ATP'
OPEN (11,FILE=NAMEK,STATUS='NEW')
NAMEL=NAME(:POSINT) // '.ATS'
OPEN (12,FILE=NAMEL,STATUS='NEW')
END
SUBROUTINE
STOREINFO(VAR,II,JJ,RRP,RRS,TRP,TRS,PSI,DELTA,RAS,RAP,
&AS,AP,TS,TP)
INTEGER II,JJ
REAL VAR
DOUBLE PRECISION
RRP(2,300),RRS(2,300),RAP(300),RAS(300),AS(300)
DOUBLE PRECISION
TRP(2,300),TRS(2,300),PSI,DELTA,AP(300)
WRITE (1,*) VAR,RRP(II,JJ)
WRITE (2,*) VAR,RRS(II,JJ)
WRITE (3,*) VAR,TRP(II,JJ)

```

```

WRITE (4,*) VAR,TTS(I,J,J)
WRITE (6,*) VAR,PSI
WRITE (6,*) VAR,DELTA
WRITE (7,*) VAR,RAP(JJ)
WRITE (8,*) VAR,RAS(JJ)
WRITE (9,*) VAR,AP(JJ)
WRITE (10,*) VAR,AS(JJ)
WRITE (11,*) VAR,TP(JJ)
WRITE (12,*) VAR,TS(JJ)
END

```

```

SUBROUTINE
CDFSIM(M,N,D,LAMBDA,PHI,DELTA,PSI,TRNP,TRNS,RFLP,RF
LS)

```

```

REAL LAMBDA,D(10),PHI
DOUBLE PRECISION PI,PHI0,PSI,DELTA,PA,PB,SA,SB
COMPLEX*16 N(0:11),COSP(0:11),BETA(10),SNELL,RHO
COMPLEX*16

```

```

SP(0:5,2),SS(0:5,2),RP(0:10),RS(0:10),TMP(2,2)
COMPLEX*16 TP(0:10),TS(0:10),EX3(6),EX4(6)
DOUBLE PRECISION RFLP,RFLS,TRNS,TRNP
PI=3.14159266358979
PHI0=PI*PI/180
SNELL=N(0)*DSIN(PHI0)
COSP(0)=DCOS(PHI0)
DO 1 J=1,M+1
COSP(J)=CDSQRT(1-(SNELL/N(J))**2)

```

```

RS(J-1)=(N(J-1)*COSP(J-1)-N(J)*COSP(J))/(N(J-1)*COSP(J-1)+
& N(J)*COSP(J))
RP(J-1)=(N(J-1)*COSP(J)-N(J)*COSP(J-1))/(N(J-1)*COSP(J)+
& N(J)*COSP(J-1))

```

```

TS(J-1)=(2*N(J-1)*COSP(J-1))/(N(J-1)*COSP(J-1)+N(J)*COSP(J))
TP(J-1)=(2*N(J-1)*COSP(J-1))/(N(J-1)*COSP(J)+N(J)*COSP(J-1))
IF (J.EQ. (M+1)) GO TO 1
BETA(J)=2*PI*D(J)*N(J)*COSP(J)/LAMBDA
EX3(J)=CDEXP(0,1)*BETA(J)
EX4(J)=CDEXP(0,-1)*BETA(J)
1 CONTINUE

```

```

DO 2 J=1,2
SP(0,J)=1,0
SS(0,J)=1,0
2 CONTINUE
SP(0,1,2)=RP(0)
SP(0,2,1)=RP(0)
SS(0,1,2)=RS(0)
SS(0,2,1)=RS(0)
IF (M.EQ. 0) THEN
GOTO 7
ENDIF

```

```

DO 3 J=1,M
SP(J,1,1)=EX3(J)
SP(J,2,1)=RP(J)*EX4(J)
SP(J,1,2)=RP(J)*EX3(J)
SP(J,2,2)=EX4(J)
SS(J,1,1)=EX3(J)
SS(J,2,1)=RS(J)*EX4(J)
SS(J,1,2)=RS(J)*EX3(J)
SS(J,2,2)=EX4(J)
3 CONTINUE

```

```

TMP(1,1)=1
TMP(2,1)=0
TMP(1,2)=0
TMP(2,2)=1
DO 5, J=0,M
CALL MM(SP,TMP,J)

```

```

5 CONTINUE
SP(M,1,1)=TMP(1,1)
SP(M,2,1)=TMP(2,1)
SP(M,1,2)=TMP(1,2)
SP(M,2,2)=TMP(2,2)
TMP(1,1)=1
TMP(2,1)=0
TMP(1,2)=0
TMP(2,2)=1
DO 6, J=0,M
CALL MM(SS,TMP,J)
6 CONTINUE
SS(M,1,1)=TMP(1,1)
SS(M,2,1)=TMP(2,1)

```

```

SS(M,1,2)=TMP(1,2)
SS(M,2,2)=TMP(2,2)

7 PRINT *,*
SA=SP(M,2,1)*DCONJG(SP(M,2,1))
SB=SP(M,1,1)*DCONJG(SP(M,1,1))
RFLP=SA/SB
PA=SS(M,2,1)*DCONJG(SS(M,2,1))
PB=SS(M,1,1)*DCONJG(SS(M,1,1))
RFLS=PA/PB

TRNP=1
TRNS=1

DO 100 J =1,M+1
TRNP=TRNP*(TP(J-1)*DCONJG(TP(J-1)))
TRNS=TRNS*(TS(J-1)*DCONJG(TS(J-1)))
100 CONTINUE

TRNP=TRNP/SB
TRNS=TRNS/PB
RHO=(SP(M,2,1)/SP(M,1,1))*SS(M,1,1)/SS(M,2,1)
PSI=DATAN(CDABS(RHO))*180/PI
DELTA=DATAN2(DIMAG(RHO),DREAL(RHO))*180/PI
RETURN
END

C MM is a FORTRAN subroutine which calculates
multiplication of two
C (2x2) matrices: C=AxB.
C
SUBROUTINE MM(A,TMP,J)
COMPLEX*16 TMP(2,2),A(0:5,2,2),C(2,2)
INTEGER J
C(1,1)=TMP(1,1)*A(J,1,1)+TMP(1,2)*A(J,2,1)
C(1,2)=TMP(1,1)*A(J,1,2)+TMP(1,2)*A(J,2,2)
C(2,1)=TMP(2,1)*A(J,1,1)+TMP(2,2)*A(J,2,1)
C(2,2)=TMP(2,1)*A(J,1,2)+TMP(2,2)*A(J,2,2)
TMP(1,1)=C(1,1)
TMP(2,1)=C(2,1)
TMP(1,2)=C(1,2)
TMP(2,2)=C(2,2)
RETURN
END

SUBROUTINE
SELECTION(OPTION,M,NF,KF,D,FRQ,PHI,VAR)
C-----
C The subroutine selection() allows the variable management
necessary to vary any one of the optical parameters for a given
system setup.
C-----
REAL D(10),PHI,NF(0:300),KF(0:300)
REAL FRQ(100),VAR
INTEGER M,OPTION
c PRINT *,HERE,M,OPTION
c READ *,RRR
IF (M.EQ.0) THEN
SELECT CASE (OPTION)
CASE(0)
NF(0)=VAR
CASE(1)
KF(0)=VAR
CASE(2)
FRQ(1)=VAR
CASE(3)
PHI=VAR
END SELECT
ELSE IF (M.EQ.1) THEN
SELECT CASE (OPTION)
CASE(0)
NF(1)=VAR
CASE(1)
KF(1)=VAR
CASE(2)
D(1)=VAR
CASE(3)
NF(2)=VAR
CASE(4)
KF(2)=VAR
CASE(5)
FRQ(1)=VAR
CASE(6)
PHI=VAR
END SELECT
C PRINT
*,M,NF(0),NF(1),NF(2),KF(0),KF(1),KF(2),D(1),FRQ(1),PHI
C READ *,RRR

```

```
ELSE IF (M.EQ.2) THEN
SELECT CASE (OPTION)
CASE(0)
NF(1)=VAR
CASE(1)
KF(1)=VAR
CASE(2)
D(1)=VAR
CASE(3)
NF(2)=VAR
CASE(4)
KF(2)=VAR
CASE(5)
D(2)=VAR
CASE(6)
NF(3)=VAR
CASE(7)
KF(3)=VAR
CASE(8)
FRQ(1)=VAR
CASE(9)
PHI=VAR
END SELECT
ELSE
END IF
END
```

ANGLE3.FOR

The program angle3.for was written by Renaldo Gonzalez, a graduate student working for Dr. Zalen in the Physics department at Va. Tech. It is designed to calculate the electric field intensity $\langle E \rangle^2$ for the x,y, and z directions.

```

parameter(m2 = 21,ndim = 3000,ncurve = 7)
real zthet(ndim),plott(ndim),plot(ncurve,ndim),htot,thint,thfin,
& n(0:m2),k(0:m2),h(0:m2),w,pi,rs,rr,trs,rrp,frs,frp,fts,
& frp,ix,iy,ip,theta,notheta,thetrad,deltaz,iz,sai,delta
complex nc(0:m2),cosc(0:m2),csqrt,cmplx,identity(2,2)
integer m,j,il,nmax,iguess
character fname*12,name*12
common /com1/pi
common /com2/identity
data pi/3.14159265, identity/1.,0.,0.,1./
print*,'Angle scan analysis'
print*,'
print*,'input data filename -> '
read(*,110)fname
110 format(a12)
open(1,file = fname, status = 'old')
read(1,*)m
do i = 0,m+1
  read(1,*)n(i),k(i),h(i)
end do
print*,'incident light energy [cm-1] -> '
read*,w
nmax = 100
print*,'z-position of (Ez*Ez) evaluation [um] -> '
read*,z
hd = 0.
j = 0
if (z.lt. 0.) then
  delz = z
end if
do while ((z.ge. hd) .and. (j.ne. m+1))
  j = j+1
  hd = hd + h(j)
end do
delz = z - (hd-h(j))
do l = 0, m+1
  nc(l) = cmplx(n(l),k(l))
end do
print*,'initial angle [deg] -> '
read*,thint
print*,'final angle [deg] -> '
read*,thfin
print*,'what to plot? '
print*,'rf1-tra and Intensities --> [1]'
print*,'phase - sai -delta --> [2]'
print*,'Choose option -->'
read*,iguess
do i = 1, nmax
  zthet(i) = thint + (thfin-thint)*(i-1.)/real(nmax)
  thetrrad = zthet(i) * pi / 180.
  notheta = n(0) * sin(thetrad)
  do l = 0, m+1
    cosc(l) = csqrt(1 - (notheta/nc(l))**2)
  end do
  call calculation(nc,cosc,h,w,notheta,j,deltaz,m,m2,rs,rr,trs,
& trp,frs,frp,fts,frp,ix,iy,iz,ip,sai,delta)
  if (iguess.eq. 1) then
    plot(1,i) = rp
    plot(2,i) = rs
    plot(3,i) = trp
    plot(4,i) = trs
    plot(5,i) = iz
    plot(6,i) = iy
    plot(7,i) = ix
  else if (iguess.eq. 2) then
    plot(1,i) = frp
    plot(2,i) = frs
    plot(3,i) = ffp
    plot(4,i) = fts
    plot(5,i) = sai
    plot(6,i) = delta
  end if
end do

```

```

end do

print *, 'Name of file to store data'
read (*, '(A)') name
open(9, file=name, status='new')

do j = 1, nmax
  write(9, *) zthet(j), plot(7, j), plot(6, j), plot(5, j)
end do
close(9)

do ii = 1, 3, 2
  10 continue
  call howplt(0, 1, 2)
  call legpos(0.67, 0.88)
  call legend('rt_p')
  call rtemy(ndim, ncurve, nmax, plot, plott, ii)
  call curv(nmax, zthet, plott)
  call howplt(0, 1, 3)
  call legend('rt_s')
  call rtemy(ndim, ncurve, nmax, plot, plott, ii+1)
  call curv(nmax, zthet, plott)
  call vg
  if(loopin0 .eq. 1) go to 10
  call newpag
end do

20 continue
  call howplt(0, 1, 2)
  call legpos(0.67, 0.88)
  call legend('iz')
  call rtemy(ndim, ncurve, nmax, plot, plott, 5)

  call curv(nmax, zthet, plott)
  call howplt(0, 1, 3)
  call legend('iy')
  call rtemy(ndim, ncurve, nmax, plot, plott, 6)
  call curv(nmax, zthet, plott)
  if (iguess .eq. 1) then

call howplt(0, 1, 4)
call legend('ix')
call rtemy(ndim, ncurve, nmax, plot, plott, 7)
call curv(nmax, zthet, plott)
end if
call vg
if(loopin0 .eq. 1) go to 20
call newpag

stop
end

c*****
c
c*****
  subroutine rtemy(ndim, ncurve, max_freq, x, y, i)
  real x(ncurve, ndim), y(ndim)
  do j = 1, max_freq
    y(j) = x(i, j)
  end do
  return
end
c*****
c*
c*****
  subroutine calculation(nc, cosec, h, w, notheta, j, delz, m, m2,
    &rs, rp, trs, trp, frs, frp, fts, ftp, ix, iy, iz, ip, ssi, delta)
  real h(0:m2), w, notheta, pi, delz, sai, delta
  &rs, rp, trs, trp, frs, frp, fts, ftp, ix, iy, iz, ip, hd
  complex tp(20), ts(20), cp(20, 2, 2), cs(20, 2, 2), nc(0:m2), cosec(0:m2),
  & d0s(2, 2), djs(2, 2), t0s, tjs, d0p(2, 2), djp(2, 2), t0p, tjp, csqrt,
  & cmlpx, crs, crp, cts, ctp, kzjdelz, epjp, epjs, emjp, emjs, ex, ey, ez, cexp,
  & expkzjdelz, conjg
  common /com1/pi
  integer j, m, m2

  call product(nc, cosec, h, w, t0s, t0p, d0s, d0p, djs, djp, tjs, tjp, m, j, m2)

  crs = d0s(2, 1)/d0s(1, 1)
  cts = t0s/d0s(1, 1)
  rs = crs * conjg(crs)
  trs = real(nc(m+1)*cosec(m+1)/(nc(0)*cosec(0))) * cts * conjg(cts)

```

```

    ts = 2*nc1*cosc1/dens

return
end
c*****
c
c*****
subroutine product(nc,cosc,h,w,t0s,t0p,d0s,d0p,djs,djp,tjs,tjp,
& mj,m2)
complex d0s(2,2),d0p(2,2),djs(2,2),djp(2,2),t0s,t0p,tjs,tjp,
&identity(2,2),cs(2,2),cp(2,2),dis(2,2),dlp(2,2),delta,
&cexp,csqrt,cmplx,nc(0:m2),cosc(0:m2),ts,tp
integer mj,m2
real pi,w,h(0:m2)
common /com1/pi
common /com2/identity

d0s = identity
d0p = identity
t0s = 1.
t0p = 1.
tjs = 1.
tjp = 1.

do i = 0, m
  if (m-i .eq. j) then
    djs = d0s
    djp = d0p
  end if

  call interph(nc(m-i),cosc(m-i),nc(m+1-i),cosc(m+1-i),cs(1,2),
& cp(1,2),ts,tp)
  delta = 2*pi*w*h(m-i)*nc(m-i)*cosc(m-i)/1.e4
  cs(2,2) = cexp(cmplx(-imag(delta),real(delta)))
  cp(2,2) = cs(2,2)
  cs(2,1) = cs(1,2)*cs(2,2)
  cp(2,1) = cp(1,2)*cp(2,2)
  cs(1,1) = 1./cs(2,2)
  cp(1,1) = 1./cp(2,2)
  cs(1,2) = cs(1,2)*cs(1,1)
  cp(1,2) = cp(1,2)*cp(1,1)

  t0s = t0s * ts

```

```

call phase(crs,frs)
call phase(cts,fts)
crp = d0p(2,1)/d0p(1,1)
ctp = t0p/d0p(1,1)
rp = crp * conjg(crp)
trp =
real((conjg(nc(m+1))*cosc(m+1)/(conjg(nc(0))*cosc(0)))*ctp*co
&njg(ctp)
call phase(crp,frp)
call phase(ctp,ftp)

delta = frp - frs
sai = atan2(abs(crp),abs(crs))*180./pi

kzjdelz = 2*pi*w*nc(i)*cosc(i)*delz/1.e4
expkzjdelz = cexp(cmplx(-imag(kzjdelz),real(kzjdelz)))

epjs = expkzjdelz*tjs * djs(1,1)/d0s(1,1)
emjs = tjs * djs(2,1)/(d0s(1,1)*expkzjdelz)
epjp = expkzjdelz*tjp * djp(1,1)/d0p(1,1)
emjp = tjp * djp(2,1)/(d0p(1,1)*expkzjdelz)

ex = (epjp - emjp) * cosc(i)
ey = epjs + emjs
ez = (epjp + emjp) * notheta/nc(i)
ix = ex * conjg(ex)
iy = ey * conjg(ey)
iz = ez * conjg(ez)
ip = ix + iz

return
end
c*****
c
c*****
subroutine interph(nc1,cosc1,nc2,cosc2,rs,rp,ts,tp)
complex tp,ts,rp,rs,nc1,nc2,cosc1,cosc2,denp,dens

denp = nc1*cosc2 + nc2*cosc1
rp = (-nc1*cosc2 + nc2*cosc1)/denp
tp = 2*nc1*cosc1/denp
dens = nc2*cosc2 + nc1*cosc1
rs = (nc1*cosc1 - nc2*cosc2)/dens

```

```

t0p =t0p * tp
call matprod(cs,d0s,d1s)
call matprod(cp,d0p,d1p)
d0s = d1s
d0p = d1p
if (m-i+1 .le. j) then
  tjs = tjs * ts
  tjp = tjp * tp
end if
end do
if (j .eq. 0) then
  djs = d0s
  tjs = 1.
  djp = d0p
  tjp = 1.
end if
return
end
c*****
c
c*****
subroutine matprod(m1,m2,mm)
complex m1(2,2),m2(2,2),mm(2,2)
do i=1,2
  do j=1,2
    mm(i,j)=0.
  end do
end do
do i =1,2
  do j=1,2
    do k =1,2
      mm(i,j)=m1(i,k)*m2(k,j)+mm(i,j)
    end do
  end do
end do
return
end
c*****
c
c*****
subroutine phase(crs,frs)
complex crs

```

```

real frs
common /com1/pi
if (real(crs) .lt. 1.e-6) then
  frs = 90.
else if (real(crs) .lt. 0.) then
  frs = atan2(imag(crs),real(crs))*180./pi
  frs = frs + 180.
else
  frs = atan2(imag(crs),real(crs))*180./pi
end if
return
end
c*****
c*****

```

APPENDIX 3.1 COMPUTER PROGRAMS

RASINT3.AB

```
free
temp=#s(lfreq,ffreq)
setxtype 1
setytype 2
setleft lfreq, ffreq
#s=#s+offset
ll=temp(1)+offset
rr=temp(np-1)+offset
av=(ll+rr)/2
see
peaktable 9, 2, n
if n=0 then print #2,ii,0:gosub 2000:pauseon:goto 890
free area, inten, pkpos
dim area(n), inten(n), pkpos(n)
FOR i = 0 TO n - 1
  peaktable 14, i, area(i)
  peaktable 10, i, pkpos(i)
  peaktable 11, i, inten(i)
  pauseon
NEXT
print #2,ii,n
FOR i = 0 TO n - 1
  PRINT #2, pkpos(i)
PRINT #2, inten(i)
print #2, (inten(i)-av)
NEXT
peaktable 3
890 noshow
  gosub 4000
  print #2,ar
  if n=0 then pauseon:print 'No peaks for this spectrum':
  pauseoff
input "Base name of file to import", $base
INPUT "First index", fin
INPUT "Last index", lin
input "Base name of file to store data", $store
open #2, $store
INPUT "First frequency", ffreq
INPUT "Last frequency", lfreq
INPUT "Y axis offset", offset
FOR ii = fin TO lin
  FOR j = 0 TO 5
    name(j)=base(j)
    if name(j)=0 then i=j:j=5:goto 25
  NEXT
  25 huns = INT(ii / 100)
  tens = INT(ii / 10) - huns * 10
  ones = ii - huns * 100 - tens * 10
  name(i)=huns+48
  name(i+1)=tens+48
  name(i+2)=ones+48
  name(i+3)=46
  name(i+4)=83
  name(i+5)=80
  name(i+6)=67
  name(i+7)=0
  onerror 1000
loadspc $name
onerror -1
np=npfs(#s(lfreq,ffreq))
free temp
dim temp(np)
```

```
900 NEXT ii
CLOSE #2
```

```
END
```

```
' Error handling
```

```
1000 onerror -1: BEEP: pauseon:PRINT "File #", ii,"not found":
    pauseoff
    goto 900
```

```
2000 PRINT #2, 0
    print #2, 0
    PRINT #2, 0
    return
```

```
3000 onerror -1: GOTO 200
```

```
4000 free slope
```

```
    pauseon
    dim slope(np)
    fillbeg temp(0)
    fillinc (temp(0)-temp(np-1))/(np-1)
    slope = fill(slope) 'create baseline correcting straight line
    temp=temp+slope
    off=temp(0):temp=temp-off      'set offset to zero

4500 ar=(sum(temp)-(temp(0)+temp(np-1))/2)*abs(lfreq-ffreq)/(np-1)
    return
```

```

RASCNTL4.BAS
DIM d%(16), CH%(16), YL%(16)

DIM tm(12000), stores(12000)
COMMON SHARED d%0
DECLARE SUB das8 (mode%, BYVAL dummy%, flag%)
DECLARE SUB calibrate (avg!)
DECLARE SUB normalplot (m$, gr$, x!0, y!0, a!, B!, c!, d!, x!1,
x!2!, y!1!, y!2!, minx!, maxx!, miny!, maxy!, xfc!, yfc!, aa!, BB!)
DECLARE SUB customplot (m$, x!0, y!0, gr$, a!, B!, c!, d!, x!1,
x!2!, y!1!, y!2!, minx!, maxx!, miny!, maxy!, xfc!, yfc!, aa!, BB!)
DECLARE SUB boxdraw (a!0, B!0, c!0, d!0, menu!)
DECLARE SUB menudisplay (f$, title$, menu!, label!0, CH$,0,
m$,0, cnt!0, a!0, B!0, c!0, d!0, z!0, zz!0, yy!0)

DECLARE SUB menu1 (minx!, maxx!, miny!, maxy!, gr$, m$,0)
DECLARE SUB setup (a!, B!, c!, d!, x!1!, x!2!, y!1!, y!2!, minx!, maxx!,
miny!, maxy!, xfc!, yfc!, aa!, BB!)
DECLARE SUB grid (minx!, maxx!, xfc!, miny!, maxy!, yfc!, x!1,
x!2!, y!1!, y!2!)
DECLARE SUB dataplot (numpt, m$,0, gr$, x!1!, x!2!, y!1!, y!2!, x!0,
y!0, minx!, maxx!, miny!, maxy!, xfc!, yfc!)
DECLARE SUB normnum (minx!, maxx!, miny!, maxy!, aa!)

DIM CH$(10, 10): DIM m$(10, 10), cnt(10)
DIM mny(7)
DIM xval(1000), yval(1000)
DIM x(1000), y(1000), zzz(1000)
DIM a(20), B(20), c(20), d(20), z(20), zz(20), yy(20)
DIM time(1000), tm$(1000)
%$DYNAMIC

DIM dio%(30)

%$STATIC

' The $ Metacommands are necessary for proper compilation using
BC in DOS.

'----- Initialize section
B% = &H300 %Set this for correct base address

```

```

'Initialize DAS8/DAS8-PGA
md% = 0: flag% = 0: NCHAN% = 8: d%(0) = B%
'get base of first board in system

```

```

CALL das8(md%, VARPTR(d%(0)), flag%)

md% = 1: d%(0) = 0: d%(1) = 0 %set mux for full scan
CALL das8(md%, VARPTR(d%(0)), flag%)

```

```

INPUT "Name of File", file$
file$ = "c:" + file$

```

```

INPUT "Description", descrip$
OPEN "c", #1, file$
WRITE #1, file$, sz
WRITE #1, descrip$
CLOSE #1

```

```

CLS
'Set time for derivative control
cnt = 1: incnt = 1: cnt2 = 1: testime = 0
count = 0: mark1 = 0: mark2 = 0

```

```

pick:
LOCATE 1, 1: INPUT "Constant (c) or variable (v) control",
choice$

```

```

IF choice$ <> "c" AND choice$ <> "v" THEN GOTO pick:
constant:

```

```

INPUT "Setpoint temperature", setpoint
INPUT "Second setpoint", setpoint2

```

```

INPUT "1st ramp rate (deg/min)", rate
rate = rate / 60
INPUT "2nd ramp rate (deg/min)", rate2

```

```

rate2 = rate2 / 60
pp1 = (setpoint - 25) / rate
pp2 = ABS((setpoint - setpoint2)) / rate2

INPUT "Derivative time,(seconds)", dtime

PRINT "Total time to reach first setpoint (Mins)", pp1 / 60
PRINT "Total time to reach second setpoint (Mins)", pp2 / 60
INPUT "Total Time", ttime

CALL menu1(minx!, maxx!, miny!, maxy!, gr$, m$(0))

sumwt = 0
wtcnt = 0

sumtemp = 0
temptemp = 0

offset = 0
propertime = 1000
propcntrl = .025
tottemp = 400
pconst = 250
pvar = 500
ptot = 400
OPEN "a", #1, file$
WRITE #1, "First setpoint", setpoint
WRITE #1, "Second setpoint", setpoint2
WRITE #1, "First ramp rate", rate * 60
WRITE #1, "Second ramp rate", rate2 * 60
WRITE #1, "Derivative time (sec)", dtime
WRITE #1, "Wait, constant part", pconst
WRITE #1, "Wait, variable part", pvar
WRITE #1, "Wait, Total span", ptot
WRITE #1, "Total time", ttime
CLOSE #1
CLS
ON TIMER(dtime) GOSUB deriv:
PRINT "Hit any key to start"
GOSUB menuplot
LOCATE 20, 1: PRINT "Press any key to begin"

DO
LOOP WHILE INKEY$ = ""
LOCATE 20, 1: PRINT "
TIMER ON
numpt = 1: datacnt = 1

main:
IF tetime / 60 > ttime THEN GOTO prostop:

GOSUB temp:
IF count = 1 THEN ftemp = temp

sumtemp = sumtemp + temp
temptemp = temptemp + 1

GOSUB setpoint:

upper = setpoint + (tottemp * propcntrl)
lower = setpoint - (tottemp * propcntrl)
percent = ((upper - temp - deriv - offset) / (upper - lower))

LOCATE 1, 60: PRINT "Setpoint="; setpoint
LOCATE 3, 60: PRINT "Temp,="; CINT(temp)
LOCATE 5, 60: PRINT "wt="; wt
LOCATE 7, 60: PRINT "Time="; tetime / 60
LOCATE 9, 60: PRINT "Derivative"; deriv
LOCATE 11, 60: PRINT "Offset"; offset
LOCATE 13, 60: PRINT "Heater";
LOCATE 15, 60: PRINT "Time"; TIME$

IF percent > 1 THEN percent = 1
IF percent < 0 THEN percent = 0

GOSUB cntrl:
GOTO main:

cntrl:
total = proptime

```

```

wt = pconat + (pvar - (pvar * (temp / ptot)))

part1 = percent * total
part2 = total - part1

md% = 14: op% = 3: flag% = 1: d%(0) = 1
CALL das8(md%, VARPTR(d%(0)), flag%)
LOCATE 13, 67: PRINT "*"

FOR i = 1 TO CINT(part1)
NEXT i

md% = 14: flag% = 1: d%(0) = 0
CALL das8(md%, VARPTR(d%(0)), flag%)
LOCATE 13, 67: PRINT ""

FOR i = 1 TO CINT(part2)
: NEXT i

FOR i = 1 TO wt
NEXT i
RETURN

temp = count + 1
count = count + 1
md% = 4
CALL das8(md%, VARPTR(d%(0)), flag%)/do A/D conversions
B = d%(0)
B = B * 2.4414 * 10 / 11 / 10
temp = B
RETURN

setpoint:
IF choice$ = "c" THEN GOTO p4:
IF temp >= final THEN GOSUB prostop:

IF mark1 = 1 THEN GOTO p1:
IF temp >= (start - 10) THEN mark1 = 1: testime = 0: f2temp =
temp: GOTO p1:
setpoint = ftemp + ((2 / 60) * testime)
PRINT "first"

wt = pconat + (pvar - (pvar * (temp / ptot)))

p1:
IF mark2 = 1 THEN GOTO p2:
IF temp >= start THEN mark2 = 1: testime = 0: GOTO p4:
setpoint = f2temp + (rate * testime)
PRINT "second"
GOTO p4:

p2:
PRINT "third"
setpoint = start + (rate * testime)

GOTO p5:

p4:
IF mark1 = 0 THEN storeset = setpoint: storeset2 = setpoint2
mark1 = 1

setpoint = ftemp + (rate * testime)
IF setpoint >= storeset AND mark3 = 0 THEN mark3 = 1
IF mark3 = 1 THEN setpoint = storeset - (rate2 * (testime -
timeset))

IF setpoint <= storeset2 AND mark3 = 1 THEN mark4 = 1
IF mark4 = 1 THEN setpoint = storeset2: rate = 0: rate2 = 0

p5:
RETURN

deriv:
testime = testime + dtime
temp = sumtemp / tempcnt: sumtemp = 0: tempcnt = 0
IF testime MOD 30 = 0 THEN datacnt = datacnt + 1: GOSUB
datalog

IF datacnt = 2 THEN GOSUB store: datacnt = 1
GOSUB integral:
tm(cnt) = temp

```

```

factor = 4.5
IF cnt = 1 THEN GOTO rtt:
IF mark3 = 0 THEN deriv = ABS(((tm(cnt) - tm(cnt - 1)) / (dtime /
60)) - rate) * factor
IF mark3 = 1 THEN deriv = ABS(((tm(cnt) - tm(cnt - 1)) / (dtime /
60)) - rate2) * factor

rtt:
cnt = cnt + 1
rttt:
RETURN

integral:
IF mark4 = 0 THEN GOTO continue2:
IF temp < lower THEN GOTO continue2:
IF temp > upper THEN GOTO continue2:
dev = ABS(temp - setpoint)
sum = sum + dev

IF incnt < 5 THEN GOTO continue:

store(cnt2) = sum / 5: incnt = 1: sum = 0
IF cnt2 = 1 THEN min = ABS(store(cnt2)): GOTO ttt:

change = (ABS(store(cnt2)) - ABS(min)) * ABS(((temp - setpoint) /
10))

IF temp < setpoint THEN sign = -1
IF temp > setpoint THEN sign = 1
saveoff = offset

IF ABS(store(cnt2)) > min THEN offset = offset + change * sign
IF ABS(offset) > ABS((setpoint - lower)) THEN offset = saveoff

IF ABS(store(cnt2)) <= min THEN min = store(cnt2)

ttt:
cnt2 = cnt2 + 1
continue:

incnt = incnt + 1
continue2:
RETURN

datalog:
y(numpt) = temp
tm$(numpt) = TIME$
time(numpt) = testime / 60
x(numpt) = time(numpt)
CALL dataplot(numpt, m$, gr$, x1, x2, y1, y2, x'0, y'0, minx,
maxx, miny, maxy, xfc, yfc)
numpt = numpt + 1
RETURN

prostop:
md% = 14: flag% = 1: d%(0) = 0
CALL das8(md%, VARPTR(d%(0)), flag%)
STOP

menuplot:
GOTO cust:
CALL normalplot(m$, gr$, x'0, y'0, a!, B!, c!, d!, x1, x2, y1, y2,
minx, maxx, miny, maxy, xfc, yfc, aa!, BB!)
GOTO stopper:

custom:
IF k = 1 THEN a = 50: B = 350: c = 1: d = 120
IF k = 2 THEN a = 400: B = 700: c = 1: d = 120
cust:
a = 75: B = 375: c = 1: d = 120

LET aa = 10: LET BB = 4
CALL customplot(m$, x'0, y'0, gr$, a!, B!, c!, d!, x1, x2, y1, y2,
minx, maxx, miny, maxy, xfc, yfc, aa!, BB!)

stopper:
RETURN

store:
OPEN "a", #1, file$

```

```

FOR ii = numpt - 1 TO numpt - 1
WRITE #1, ii, x(ii), zzz(ii), y(ii), tm$(ii)
NEXT ii
CLOSE #1
RETURN

SUB boxdraw (a(0), B(0), c(0), d(0), menu) STATIC

LOCATE a(menu), B(menu): PRINT CHR$(218)
LOCATE c(menu), B(menu): PRINT CHR$(192)
LOCATE a(menu), d(menu): PRINT CHR$(191)
LOCATE c(menu), d(menu): PRINT CHR$(217)

FOR i = B(menu) + 1 TO d(menu) - 1: LOCATE a(menu), i: PRINT
CHR$(196); : NEXT i
FOR i = B(menu) + 1 TO d(menu) - 1: LOCATE c(menu), i: PRINT
CHR$(196); : NEXT i
FOR i = a(menu) + 1 TO c(menu) - 1: LOCATE i, B(menu): PRINT
CHR$(179): NEXT i
FOR i = a(menu) + 1 TO c(menu) - 1: LOCATE i, d(menu): PRINT
CHR$(179): NEXT i

END SUB

SUB customplot (m$(0), x(0), y(0), gr$, a!, B!, c!, d!, x1!, x2!, y1!, y2!,
minx!, maxx!, miny!, maxy!, xfc!, yfc!, aal!, BBl)
DIM a$(16)

CALL setup(a!, B!, c!, d!, x1!, x2!, y1!, y2!, minx!, maxx!, miny!,
maxy!, xfc!, yfc!, aal!, BBl)

IF gr$ = "Y" THEN CALL grid(minx!, maxx!, xfc!, miny!, maxy!,
yfc!, x1!, x2!, y1!, y2!)

LET a = 5: LET B = 4

LET p = 1
FOR j = x1 TO x2 STEP (x2 - x1) / a
GOSUB xnumbers:
LET p = p + 1
NEXT j

LET p = 1
FOR kk = y1 TO y2 STEP (y2 - y1) / a
GOSUB ynumbers:
LET p = p + 1
NEXT kk

GOTO endplot:

xnumbers:
FOR i = 1 TO 10: LET a$(i) = ""; NEXT i
LET no = minx + ((maxx - minx) / a) * (p - 1): LET no = (INT(no *
100) / 100)
LET a$ = STR$(no)
LET q = 0

checkx:
LET a$(q + 1) = LEFT$(a$, 1)
IF LEFT$(a$, 1) = "" THEN GOTO xadjust:
LET a$ = MID$(a$, 2)
LET q = q + 1: GOTO checkx:

xadjust:
IF no < 0 THEN q = q + 1
LET m = 3
LET ps = j - (q * m) / 2 - ((q - 1) * m) / 2
N = 0: c = 15
PSET (ps, y2 + 15), 0
LET sign = 2
IF no < 0 THEN sign = 1

FOR i = sign TO q
GOSUB number:
DRAW "BR3"
NEXT i
RETURN

ynumbers:

```

```

FOR i = 1 TO 10: LET a$(i) = "": NEXT i
LET no = maxy - ((maxy - miny) / a) * (p - 1): no = (INT(no * 100) /
100)
LET a$ = STR$(no)
LET q = 0

```

```

checky:
IF no < 0 THEN q = q + 1
LET a$(q + 1) = LEFT$(a$, 1)
IF LEFT$(a$, 1) = "" THEN GOTO yadjust:
LET a$ = MID$(a$, 2)
LET q = q + 1: GOTO checky:

```

```

yadjust:
LET ps = (x1 - 10) - (q * 8) + ((q - 1) * 3)
LET m = 3: N = 0: c = 15
PSET (ps, kk), 0
FOR i = 2 TO q
GOSUB number:
DRAW "BR3"
NEXT i
RETURN

```

'Number Control

```

number:
IF a$(i) = "1" THEN GOSUB one:
IF a$(i) = "2" THEN GOSUB two:
IF a$(i) = "3" THEN GOSUB three:
IF a$(i) = "4" THEN GOSUB four:
IF a$(i) = "5" THEN GOSUB five:
IF a$(i) = "6" THEN GOSUB six:
IF a$(i) = "7" THEN GOSUB seven:
IF a$(i) = "8" THEN GOSUB eight:
IF a$(i) = "9" THEN GOSUB nine:
IF a$(i) = "0" THEN GOSUB zero:
IF a$(i) = "." THEN GOSUB decimal:
IF a$(i) = "-" THEN GOSUB minus:
RETURN

```

'Number drawing

```

zero:
DRAW "C=" + VARPTR$(c) + "S=" + VARPTR$(m) + "A=" +

```

```

VARPTR$(N) + "BR8 L8 D8 R8 U8"
RETURN
one:
DRAW "C=" + VARPTR$(c) + "S=" + VARPTR$(m) + "A=" +
VARPTR$(N) + "BR4 NG3 D8 NL3 NR3 BR4 BU8"
RETURN
two:
DRAW "C=" + VARPTR$(c) + "S=" + VARPTR$(m) + "A=" +
VARPTR$(N) + "R8 D4 L8 D4 R8 BU8"
RETURN
three:
DRAW "C=" + VARPTR$(c) + "S=" + VARPTR$(m) + "A=" +
VARPTR$(N) + "R8 D4 NL4 D4 NL8 BU8"
RETURN
four:
DRAW "C=" + VARPTR$(c) + "S=" + VARPTR$(m) + "A=" +
VARPTR$(N) + "D4 R8 L2 ND4 U4 BR2"
RETURN
five:
DRAW "C=" + VARPTR$(c) + "S=" + VARPTR$(m) + "A=" +
VARPTR$(N) + "NR8 D4 R8 D4 L8 BU8 BR8"
RETURN
six:
DRAW "C=" + VARPTR$(c) + "S=" + VARPTR$(m) + "A=" +
VARPTR$(N) + "NR8 D4 R8 D4 L8 U4 BU4 BR8"
RETURN
seven:
DRAW "C=" + VARPTR$(c) + "S=" + VARPTR$(m) + "A=" +
VARPTR$(N) + "R8 D8 BU8"
RETURN
eight:
DRAW "C=" + VARPTR$(c) + "S=" + VARPTR$(m) + "A=" +
VARPTR$(N) + "R8 D8 L8 U4 NR8 U4 BR8"
RETURN
nine:
DRAW "C=" + VARPTR$(c) + "S=" + VARPTR$(m) + "A=" +
VARPTR$(N) + "R8 D4 ND4 L8 U4 BR8"
RETURN
decimal:
DRAW "C=" + VARPTR$(c) + "S=" + VARPTR$(m) + "A=" +
VARPTR$(N) + "BD8 BR4 U1 R1 D1 L1 BU8 BR4"
RETURN
minus:

```

```

DRAW "C=" + VARPTR$(c) + "S=" + VARPTR$(m) + "A=" +
VARPTR$(N) + "BD4 BR2 R4 D1 L4 U1 BU4 BR4"
RETURN

endplot:
END SUB

SUB dataplot (numpt, m$, gr$, x1, x2, y1, y2, x10, y10, minx,
maxx, miny, maxy, xfc, yfc) STATIC

i = numpt
LET x = x1 - (minx * xfc) + (x(i) * xfc): LET y = y2 + (miny * yfc) -
(y(i) * yfc)

'IF DATA OFF SCALE...

IF x > x2 OR x < x1 THEN GOTO 38600
IF y > y2 OR y < y1 THEN GOTO 38600

'PLOT POINTS

CIRCLE (x, y), 1

38600

END SUB

SUB grid (minx, maxx, xfc, miny, maxy, yfc, x1, x2, y1, y2)
STATIC

gr = 10
FOR i = x1 TO x2 STEP (x2 - x1) / gr
LINE (i, y1)-(i, y2), , &H888
NEXT i

FOR i = y1 TO y2 STEP (y2 - y1) / gr
LINE (x1, i)-(x2, i), , &H888
NEXT i

IF minx < 0 AND maxx > 0 THEN xx = x1 - (minx * xfc): LINE
(xx, y1)-(xx, y2), , &H7777
IF miny < 0 AND maxy > 0 THEN yy = y2 + (miny * yfc): LINE
(x1, yy)-(x2, yy), , &H7777

END SUB

SUB menu1 (minx, maxx, miny, maxy, gr$, m$(0) STATIC

'MENU PROGRAM
CLS
SCREEN 0
CLS

LET numlab1 = 4: numlab2 = 6

LET a = 3: LET B = 1: LET c = 2 * numlab2: LET d = 22: GOSUB
box:
a = numlab2 + 8: B = 1: c = numlab2 + 10: d = 22
GOSUB box:

'a,b are upper left hand coord. y,x
'c,b are lower left hand coord.
'a,d are upper right hand coord.
'c,d are lower right hand coord.
FOR i = 1 TO 10: LET aa(i) = 15: BB(i) = 0: NEXT i
LET aa(1) = 0: LET BB(1) = 15: LET cnt = 1

CH$(1, 1) = "Minimum x": m(1) = minx
CH$(1, 2) = "Maximum x": m(2) = maxx

```

```

CH$(1, 3) = "Minimum y": m(3) = miny
CH$(1, 4) = "Maximum y": m(4) = maxy
CH$(1, 5) = "Grid pattern":
CH$(1, 6) = "Line Connect"

COLOR 0, 15: LOCATE 4, 2: PRINT " PLOT PARAMETERS "

pt:
LET z = 5: zz = 15: yy = 2
FOR i = 1 TO numlab2
  LOCATE z + i, yy: COLOR aa(i), BB(i): PRINT CH$(1, i); " ...."
  IF i <= numlab1 THEN LOCATE z + i, zz: PRINT USING
    "###.##"; m(i)
  IF i > numlab1 THEN LOCATE z + i, zz + 5: PRINT m$(1, i)
NEXT i

100 LET f$ = INKEY$
IF f$ <> CHR$(32) AND f$ <> CHR$(13) AND f$ <> CHR$(9)
AND f$ <> CHR$(27) THEN GOTO 100
IF f$ = CHR$(13) AND cnt <= numlab1 THEN GOTO update1:
IF f$ = CHR$(13) AND cnt > numlab1 THEN GOTO update2:

IF f$ = CHR$(27) THEN minx = m(1): maxx = m(2): miny = m(3):
gr$ = m$(1, 5): maxy = m(4): GOTO gobet:

IF f$ = CHR$(32) THEN LET aa(cnt) = 15: BB(cnt) = 0:
LOCATE z + cnt, yy: COLOR aa(cnt), BB(cnt): PRINT CH$(1, cnt);
" ....":
IF cnt <= numlab1 THEN LOCATE z + cnt, zz: PRINT USING
"###.##"; m(cnt)
IF cnt > numlab1 THEN LOCATE z + cnt, zz + 5: PRINT m$(1,
cnt)
cnt = cnt + 1

```

```

IF cnt = numlab2 + 1 THEN LET cnt = cnt - numlab2
LET aa(cnt) = 0: LET BB(cnt) = 15
LOCATE z + cnt, yy: COLOR aa(cnt), BB(cnt): PRINT CH$(1, cnt);
" ...."
IF cnt <= numlab1 THEN LOCATE z + cnt, zz: PRINT USING
"###.##"; m(cnt)
IF cnt > numlab1 THEN LOCATE z + cnt, zz + 5: PRINT m$(1,
cnt)
GOTO 100

update1:
COLOR 0, 15
LOCATE a + 1, B + 1: PRINT "
LOCATE a + 1, B + 1: PRINT CH$(1, cnt); " ...
LOCATE a + 1, B + 11: INPUT m(cnt)
LOCATE a + 1, B + 1: PRINT "

LOCATE z + cnt, yy: PRINT CH$(1, cnt); " ....";
LOCATE z + cnt, zz: PRINT USING "###.##"; m(cnt)
GOTO 100

update2:
COLOR 0, 15
again:
LOCATE a + 1, B + 1: PRINT "
LOCATE a + 1, B + 1: PRINT CH$(1, cnt); " ...

LOCATE a + 1, B + 15: INPUT m$(1, cnt)
m$(1, cnt) = UCASE$(m$(1, cnt))
IF m$(1, cnt) <> "Y" AND m$(1, cnt) <> "N" THEN GOTO again:

LOCATE a + 1, B + 1: PRINT "

LOCATE z + cnt, yy: PRINT CH$(1, cnt); " ....";
LOCATE z + cnt, zz + 5: PRINT m$(1, cnt)

```

```

GOTO 100
box:
LOCATE a, B: PRINT CHR$(218)
LOCATE c, B: PRINT CHR$(192)
LOCATE a, d: PRINT CHR$(191)
LOCATE c, d: PRINT CHR$(217)

FOR i = B + 1 TO d - 1: LOCATE a, i: PRINT CHR$(196); : NEXT
i
FOR i = B + 1 TO d - 1: LOCATE c, i: PRINT CHR$(196); : NEXT
i
FOR i = a + 1 TO c - 1: LOCATE i, B: PRINT CHR$(179): NEXT i
FOR i = a + 1 TO c - 1: LOCATE i, d: PRINT CHR$(179): NEXT i
RETURN
,
gohet:
END SUB

SUB menudisplay (f$, title$, menu, label$, CH$, m$, cnt$,
a$, B$, c$, d$, z$, z$, yy$(0) STATIC
SCREEN 0
COLOR 15, 0

CLS
CALL boxdraw(a$, B$, c$, d$, menu)

FOR i = 1 TO 10: LET aa(i) = 15: BB(i) = 0: NEXT i
LET aa(1) = 0: LET BB(1) = 15: LET cnt(menu) = 1
COLOR 0, 16: LOCATE 4, 2: PRINT " "; title$(menu); " "
pt2:
FOR i = 1 TO label(menu)
LOCATE z(menu) + i, yy(menu): COLOR aa(i), BB(i): PRINT
CH$(menu, i); " ...."
LOCATE z(menu) + i, zz(menu) + 5: PRINT m$(menu, i)
NEXT i
1002 LET f$ = INKEY$
IF f$ <> CHR$(32) AND f$ <> CHR$(13) AND f$ <> CHR$(9)
AND f$ <> CHR$(27) THEN GOTO 1002
IF f$ = CHR$(13) OR f$ = CHR$(27) THEN GOTO updater:

IF f$ = CHR$(32) THEN LET aa(cnt(menu)) = 16: BB(cnt(menu)) =
0:
LOCATE z(menu) + cnt(menu), yy(menu): COLOR aa(cnt(menu)),
BB(cnt(menu)): PRINT CH$(menu, cnt(menu)); " ....":
LOCATE z(menu) + cnt(menu), zz(menu) + 5: PRINT m$(menu,
cnt(menu))
cnt(menu) = cnt(menu) + 1

IF cnt(menu) = label(menu) + 1 THEN LET cnt(menu) = cnt(menu)
- label(menu)
LET aa(cnt(menu)) = 0: LET BB(cnt(menu)) = 15
LOCATE z(menu) + cnt(menu), yy(menu): COLOR aa(cnt(menu)),
BB(cnt(menu)): PRINT CH$(menu, cnt(menu)); " ....":
LOCATE z(menu) + cnt(menu), zz(menu) + 5: PRINT m$(menu,
cnt(menu))
GOTO 1002

updater:
END SUB

SUB normalplot (m$, gr$, x$(0), y$(0), a!, B!, c!, d!, x1!, x2!, y1!, y2!,
minx!, maxx!, miny!, maxy!, xfc!, yfc!, aa!, BB!) STATIC
LET a = 89: B = 560: c = 20: d = 180
LET aa = 10: LET BB = 4
CALL setup(a!, B!, c!, d!, x1!, x2!, y1!, y2!, minx!, maxx!, miny!,
maxy!, xfc!, yfc!, aa!, BB!)
IF gr$ = "Y" THEN CALL grid(minx!, maxx!, xfc!, miny!, maxy!,
yfc!, x1!, x2!, y1!, y2!)
CALL normnum(minx!, maxx!, miny!, maxy!, aa)

```

```

END SUB
SUB normnum (minx!, maxx!, miny!, maxy!, aa) STATIC
    LOCATE start, 4
    PRINT USING "###.###"; yleg;
    start = start - 2
    NEXT v

adj:
    IF aa = 10 THEN LET aa = aa * 5: LET BB = 2: GOTO normnx
END SUB

SUB setup (a!, B!, c!, d!, x1!, x2!, y1!, y2!, minx!, maxx!, miny!,
maxy!, xfc!, yfc!, aa!, BB!) STATIC

SCREEN 2:
IF k = 1 THEN CLS
LET x1 = a: LET x2 = B: LET y1 = c: LET y2 = d

LET xfc = (x2 - x1) / (maxx - minx)
LET yfc = (y2 - y1) / (maxy - miny)
LINE (x1, y1)-(x2, y2), , B: LINE (x1 - 1, y1 - 1)-(x2 + 1, y2 + 1), ,
B

FOR i = 1 TO BB / 2
    LET p = 1
    FOR j = x1 TO x2 STEP (x2 - x1) / aa
        PSET (j, y2 - i)
    NEXT j
NEXT i

FOR i = 1 TO BB / 2
    FOR kk = y1 TO y2 STEP (y2 - y1) / aa
        PSET (x1 + i, kk)
    NEXT kk
NEXT i

END SUB

normy:
    IF aa <> 10 THEN GOTO adj:
    qq = (maxx - minx) / aa
    start = 9
    FOR v = 1 TO aa + 1
        LET xleg = minx + (v - 1) * qq
        IF ABS(maxx) >= ABS(minx) THEN abxmax = ABS(maxx) ELSE
        abxmax = ABS(minx)
        xexp = INT(LOG(abxmax) / 2.3): xleg = xleg / (10 ^ xexp)
    NEXT v

LOCATE 24, start
PRINT USING "###.###"; xleg;

start = start + 6
NEXT v

normy:
    IF aa <> 10 THEN GOTO adj:
    qq = (maxy - miny) / aa
    start = 23
    FOR v = 1 TO aa + 1
        LET yleg = miny + (v - 1) * qq
        IF ABS(maxy) >= ABS(miny) THEN abymax = ABS(maxy) ELSE
        abymax = ABS(miny)
        LET yexp = INT(LOG(abymax) / 2.3): yleg = yleg / (10 ^ yexp)
    LOCATE 10, 1: PRINT "E"
    LOCATE 11, 1: PRINT ".-"; yexp

```

VTTODVVT.BAS

VTTODVVT.BAS is a program designed to convert the .vt data file containing all information concerning a VTRAS run into the critical parameters of time versus temperature. The new x,y file will have the extension .dvt

```
DIM tm(1000), pt(1000), temp(1000), a$(1000)
ON ERROR GOTO 1000:
10:
CLS
LOCATE 10, 10:
INPUT "Name of input data file (do not put .vt ext)", nme$
nme2$ = nme$ + ".vt"
OPEN "i", #1, nme2$
INPUT #1, a$, a
INPUT #1, b$
FOR i = 1 TO 9
INPUT #1, a$, a
NEXT i
LOCATE 9, 5: PRINT "pt# Time(min) ---
Temperature Time$"
cnt = 0
op:
IF EOF(1) THEN GOTO cl:
cnt = cnt + 1
INPUT #1, pt(cnt), tm(cnt), a, temp(cnt), a$(cnt)
LOCATE 10, 5
PRINT pt(cnt), tm(cnt), a, temp(cnt), a$(cnt)
GOTO op:
cl:
numdata = cnt
CLOSE #1
out$ = nme$ + ".dvt"
OPEN "o", #1, out$
FOR i = 1 TO numdata
WRITE #1, tm(i), temp(i)
NEXT i
```

```
CLOSE #1
GOTO ed:
1000:
CLS
LOCATE 10, 10:
PRINT "There is an error (probably bad file name), try again"
DO
LOOP WHILE INKEY$ = ""
RESUME 10
ed:
INPUT "Another?", a$
IF a$ <> "y" AND a$ <> "n" THEN GOTO ed:
IF a$ = "y" THEN GOTO 10:
IF a$ = "n" THEN END
```

TIMCONV6.BAS

Timconv6.bas is the 6th version of the timconv.bas program to determine the temperature associated with each ir scan when a temperature ramp is used.

The program is designed to:

- (1) Help determine the exact time required to take and store a data file using the STS and MTS Nicolet SX commands.
- (2) Once the interval is known, the exact time at the midpoint can be calculated and the temperature interpolated from known time vs. temperature data located in the *.dvt files.

```
DIM t(1000) AS DOUBLE
DIM snum(1000)
DIM ta$(1000)
DIM hrs(1000), mins(1000), secs(1000)
DIM temp(1000), pt(1000), tm(1000), a$(1000)
DIM ttemp(1000), tot$(1000)
```

```
CLS
GOSUB filein
CLS
```

```
.....
'Enter the total time between scans, i.e. the time given by
comparing
'successive results obtained from the SX command STS and
represents the
'time at the beginning of each spectrum taken.
'Enter the scan time given by the SX command MTS
'The store time, stn is then calculated.
'.....
```

```
INPUT "Total time increment between scans ", in
INPUT "Scan time ", scn
stn = in - scn
PRINT "Store time is - "; stn
'.....
```

```
.....
'Enter the total time of linear temperature control. This number is
given by
'the cntrl6.bas program during the setup procedure. From this, the
number of
'spectra in the ramp region will be calculated. This makes sure
that only spectra
'in the linear ramp region (not cool down etc.) will be analyzed.
'Also enter the initial temperature so the data between the first
and second
'data points can be interpolated
'.....
```

```
INPUT "Total time of linear temperature control ", tanaal
numdnt = INT(tanaal * 60 / in)
totime = tanaal
PRINT "Number of spectra in this region", numdnt
INPUT "Initial temperature", temp(0)
askk:
```

```
.....
'To calculate the exact time for each scan, a comparison of the
Nicolet scan times
'and those calculated is done until times given by the STS command
match those
'calculated. Enter the initial time "XX:XX:XX" and the approximate
interval.
'This can be obtained by comparing two successive times using the
STS command.
'Times will be generated for each spectra taken. Adjust the total
time per
'spectrum until all times match:
'Press space bar to continue running list of times.
'Press "e" to enter another total time value.
'.....
```

```
INPUT "Comparison of calc. and exp. times? ", aa$
IF aa$ <> "y" AND aa$ <> "n" THEN GOTO askk:
IF aa$ = "y" THEN INPUT "Starting Time", ta$ ELSE ta$ =
"00:00:00"
start0:
```

```
p1$ = MID$(ta$, 1, 2)
```

```

p2$ = MID$(ta$, 4, 2)
p3$ = MID$(ta$, 7, 2)
'PRINT p1$, p2$, p3$

p1 = VAL(p1$)
p2 = VAL(p2$)
p3 = VAL(p3$)

total = 3600 * p1 + 60 * p2 + p3
timesum = 0

FOR i = 1 TO totime
  snum(i) = i
  timesum = timesum + i
  t(i) = CINT(timesum) + total

IF t(i) / 3600 < 1 THEN hrs(i) = 0: GOTO min:
temp1 = t(i) MOD 3600
hrs(i) = (t(i) - temp1) / 3600

min:
IF (t(i) - (hrs(i) * 3600)) / 60 < 1 THEN mins(i) = 0: GOTO sec:
temp2 = (t(i) - (hrs(i) * 3600))
temp3 = temp2 MOD 60
mins(i) = (temp2 - temp3) / 60

sec:
secs(i) = (t(i) - (hrs(i) * 3600) - (mins(i) * 60))
t(i) = (t(i) - total) / 60
q1 = (scn / 2) / 60
t(i) = t(i) + q1
NEXT i
t(0) = q1

FOR i = 1 TO totime
  s1$ = STR$(hrs(i))
  s2$ = STR$(mins(i))
  s3$ = STR$(secs(i))
  tot$(i) = s1$ + ":" + s2$ + ":" + s3$
  IF aa$ = "n" THEN GOTO nnnn
  PRINT i, tot$(i)

```

```

tester:
IF INKEY$ = "s" THEN
GOTO 1000:
ELSE IF INKEY$ = "" THEN GOTO tester:
END IF
nnnn:
NEXT i
CLS

```

This section of the program is an interpolation routine to calculate the temperature at the midpoint of a spectrum. To do this, the time in the middle of a scan is calculated from the scan time and the total time to take and store a scan

Example: if the scan time is 60 seconds, the first spectrum time will be 30 seconds (in the middle of the scan). If the total time to take and store a scan is 80 seconds, the second scan time would be 80 + 30 = 110 seconds, the third: 2 x 80 + 30 Once times are calculated, temperatures are interp.

from values of time vs. temp from the *.dvt files.

```

FOR i = 0 TO numdt - 1
tempor = t(i)

FOR j = 1 TO numdata
IF tm(j) > tempor THEN mk = j - 1: GOTO nxt:
NEXT j
nxt:
delta = (tempor(mk + 1) - tempor(mk)) / (tm(mk + 1) - tm(mk))
ttemp(i) = delta * (t(i) - tm(mk)) + tempor(mk)

** DISPLAY **

COLOR 5, 0
LOCATE 10, 10: PRINT "Spectrum #"
COLOR 6, 0

LOCATE 10, 22: PRINT i
COLOR 3, 0
LOCATE 11, 10: PRINT "Time at mid-spectrum interval"; t(i)
LOCATE 12, 10: PRINT "Temperature at mid-spectrum interval";
ttemp(i)

```

```

LOCATE 13, 10: PRINT "Interpolated between times"; tm(mk);
"and"; tm(mk + 1)
LOCATE 14, 10: PRINT "For temperatures"; temp(mk); "and";
temp(mk + 1)
COLOR 0, 15: LOCATE 16, 10: PRINT "Press any key to
continue"; COLOR 16, 0

DO
LOOP WHILE INKEY$ = ""
NEXT i

GOSUB fileout:
END

'-----
DATA output routine to store data as spectrum number vs.
temperature
'-----
fileout:
flout$ = nme$ + ".tmp"

OPEN "o", #1, flout$
FOR i = 0 TO numdt - 1
WRITE #1, i, ttemp(i)
NEXT i
CLOSE #1
RETURN

'-----
'Data input routine to import time vs. temperature data from *.dvt
files
'-----
filein:

INPUT "Name of input data file (.dvt will be added) ", nme$
OPEN "i", #1, nme$ + ".dvt"
cnt = 0

op:
IF EOF(1) THEN GOTO cl:
cnt = cnt + 1
INPUT #1, tm(cnt), temp(cnt)
PRINT tm(cnt), temp(cnt)
IF cnt = 2 THEN tminc = tm(2) - tm(1)

```

```

GOTO op:
cl:
numdata = cnt
CLOSE #1
RETURN:

1000 :
INPUT "New time increment?", in
GOTO start0:
RETURN

```

NEWMRG3.BAS

This program is the third version of the newmrg.bas routine to combine infrared information versus file# data with temperature versus file# information. Data can be input either from the labcalc format (using RASINT3.AB) or from x,y data. If x,y data are input, there is also an option to multiply the data by a factor. If for the lab calc format several peaks are detected for one temperature, the user must select which band is of interest since the output will be generated as peak position, peak intensity, and peak area versus temperature.

```

DIM area2(1000)
DIM ppos(8, 1000), inten(8, 1000), area1(8, 1000), rawint(8, 1000)
DIM jy(1000)
DIM tnum(1000), num(1000), numpk(1000), temp(1000)
CLS

LOCATE 10, 10: INPUT "Name of ir data (after lc) file", a$
LOCATE 12, 10: INPUT "Name of temperature (after
interpolation) data", temp$
LOCATE 14, 10: INPUT "Multiplication Factor for data", mult
typ:
LOCATE 16, 10: INPUT "Lab Calc file (l) or (X,Y) file (x)", type$
IF type$ <> "l" AND type$ <> "x" THEN GOTO typ:

IF type$ = "l" THEN GOSUB labcalc:
IF type$ = "x" THEN GOSUB xy:
IF type$ = "l" THEN GOSUB store1:
IF type$ = "x" THEN GOSUB store2:

PRINT "Finished"
END

labcalc:
OPEN "i", #1, a$
OPEN "i", #2, temp$
LOCATE 18, 10: INPUT "Starting Index Number", index
cnt = 0
cnt2 = 0
'INPUT #1, a$
CLS

DO
IF EOF(1) OR EOF(2) THEN GOTO stp:

cnt = cnt + 1
cnt2 = cnt2 + 1

INPUT #1, num(cnt), numpk(cnt)
'PRINT num(cnt), numpk(cnt)
IF numpk(cnt) = 0 THEN numpk(cnt) = 1

FOR j = 1 TO numpk(cnt)
INPUT #1, ppos(j, cnt)
INPUT #1, rawint(j, cnt)
INPUT #1, inten(j, cnt)
NEXT j
INPUT #1, area1(1, cnt)

IF numpk(cnt) > 1 THEN
CLS
LOCATE 10, 10: PRINT "Several peaks detected for one region"
FOR j = 1 TO numpk(cnt)
PRINT "(:; j: "; ppos(j, cnt); inten(j, cnt)
NEXT j
LOCATE 17, 10: INPUT "Which band? ", band
IF band > 1 THEN
ppos(1, cnt) = ppos(band, cnt)
rawint(1, cnt) = rawint(band, cnt)
inten(1, cnt) = inten(band, cnt)
ELSE
END IF
ELSE
END IF

ELSE
END IF

st:
IF EOF(2) THEN GOTO stp:
INPUT #2, tnum(cnt), temp(cnt)

```

```

'PRINT cnt, num(cnt), tnum(cnt)
'DO
'LOOP WHILE INKEY$ = ""

IF num(cnt) - index <> tnum(cnt) THEN PRINT "IR and
temperature data are not in synch": GOTO tst:

'PRINT cnt, num(cnt), tnum(cnt)
LOCATE 17, 10: PRINT "Peak position Peak Intensity Peak Area
Temperature"
LOCATE 18, 10: PRINT ppos(1, cnt), inten(1, cnt), areal(1, cnt),
temp(cnt)
'DO
'LOOP WHILE INKEY$ = ""
LOOP
stp:
CLOSE #1
CLOSE #2
RETURN:

xy:
OPEN "i", #1, s$
OPEN "i", #2, temp$
INPUT "Starting Index Number", index

cnt2 = 0
cnt = 0
DO
IF EOF(1) OR EOF(2) THEN GOTO stp:

cnt = cnt + 1
cnt2 = cnt2 + 1

INPUT #1, num(cnt), yy(cnt)
yy(cnt) = yy(cnt) * nlt
CLS

LOCATE 10, 10: PRINT "Data Entry Number ", num(cnt)
LOCATE 11, 10: PRINT "Y value", yy(cnt)

tstt:
IF EOF(2) THEN GOTO stp:
INPUT #2, tnum(cnt), temp(cnt)

LOCATE 13, 10: PRINT "Data Number (Temp.)", tnum(cnt)
LOCATE 14, 10: PRINT "Temperature", temp(cnt)

IF num(cnt) - index <> tnum(cnt) THEN PRINT "IR and
temperature data are not in synch": GOTO tstt:

DO
LOOP WHILE INKEY$ = ""
LOOP

stp:
CLOSE #1
CLOSE #2

RETURN:
acqold:
RETURN

store1:
INPUT "Base name of file", base$

OPEN "o", #1, base$ + ".pos"
OPEN "o", #2, base$ + ".raw"
OPEN "o", #3, base$ + ".int"
OPEN "o", #4, base$ + ".are"

FOR i = 1 TO cnt
WRITE #1, temp(i), ppos(1, i)
NEXT i

FOR i = 1 TO cnt
WRITE #2, temp(i), rawint(1, i)

```

The output filespec should not be longer than 5 characters since with
 'the extension added the name cannot exceed 8 characters.
 Extensions
 'are not assumed to exceed 999.

ON ERROR GOTO erhandle:

```
CLS
LOCATE 10, 10
INPUT "Input file spec. (Root name)", inbase$
```

```
CLS
LOCATE 10, 10
INPUT "Output file spec. (Root name)", outbase$
CLS
LOCATE 10, 10
INPUT "Starting File Number", start
CLS
```

```
LOCATE 10, 10
INPUT "Ending File Number", finish
```

```
FOR n = start TO finish
PRINT "File #", n
```

```
n$ = STR$(n)
```

```
IF n < 10 THEN n$ = RIGHT$(n$, 1): n$ = "00" + n$
IF n < 100 AND n >= 10 THEN n$ = RIGHT$(n$, 2): n$ = "0" + n$
IF n > 100 THEN n$ = RIGHT$(n$, 3)
```

```
filename$ = inbase$ + "." + n$
PRINT "Old filename"; filename$
```

```
OPEN "i", #1, filename$
```

```
newfile$ = outbase$ + n$ + ".nic"
PRINT "New filename"; newfile$
CLOSE #1
NAME filename$ AS newfile$
```

```
NEXT i
```

```
FOR i = 1 TO cnt
WRITE #3, temp(i), inten(1, i)
NEXT i
```

```
FOR i = 1 TO cnt
WRITE #4, temp(i), area1(1, i)
NEXT i
```

```
FOR i = 1 TO 4
CLOSE #1
NEXT i
RETURN
```

```
store2:
INPUT "Base name of file (With proper extension)", base$
```

```
OPEN "o", #1, base$
```

```
FOR i = 1 TO cnt
WRITE #1, temp(i), yy(i)
NEXT i
```

```
CLOSE #1
RETURN
```

```
NIC.BAS
```

'Nic.bas is a program designed to rename large numbered data files

'exported by Nicolet SX (Kermit) to a form that can be entered as a batch file into Lab Calc.

'The base file must remain constant and the file number entered as the
 'extension (i.e. TEST.000,TEST.001, TEST.002, etc.)

'The program will output files incorporating the file number into
 'the main name and adding the .nic extension (i.e. TEST000.nic,
 etc.)

```
GOTO 100:
erhandle:
CLS
LOCATE 10, 10: PRINT "File - "; filename$; "not found"
LOCATE 11, 10: PRINT "Press any key to continue to next file"
DO
LOOP WHILE INKEY$ = ""
CLS

RESUME 100

100 :
NEXT n
```

VITA

The author, Harold Francis Webster II, was born in Richmond, Virginia on May 7, 1959. The son of Mr. and Mrs. Harold F. Webster, he lived in Goochland Co. and attended public school there for twelve years, graduating valedictorian of his class in 1977. After graduation, he attended Virginia Polytechnic Institute and State University and majored in Biochemistry. During his stay, he was inducted into the Phi Beta Kappa, Phi Kappa Phi, and Phi Sigma honor societies, and graduated magna cum laude in 1981.

After graduation, he worked in the biochemistry department at the University of Virginia with Dr. T. E. Thompson, investigating the physical properties of synthetic membrane systems. In February, 1983, he returned to VPI and worked for Dr. J. P. Wightman, researching topics of coal moisture and adhesion of insects to aircraft. He entered graduate school in September 1983. The author was elected to associate membership in Sigma Xi honorary research society in 1984, and received the Master of Science degree in the fall of 1985.

He was married to Janet Grome Brown of Bel Air, Maryland on September 8, 1984. After receiving the M.S. degree, he and his wife served as rural development officers with the Peace Corps in Papua New Guinea where they lived and worked with the Faiwol and Angkiak people. After returning from overseas in 1988, he rejoined Dr. Wightman's group to investigate the adhesion of polymer coatings on optical fibers. He entered the Ph.D. program in the fall of 1989 and researched various aspects of polyphenylene sulfide / copper adhesion. He co-authored several papers and presented results at meetings including the annual meetings of the Adhesion Society, both national and regional ACS meetings, and the Virginia Academy of Science.

He and Janet were proud parents of a baby girl, Rebekah Ireland, on April 9, 1992 and he received his Ph.D. degree in August of the same year. He has taken a position as an assistant professor on the faculty at Radford University.

